

**Defining the molecular mechanisms that regulate
breast cancer cell migration**

by

Alexander Kiepas

A thesis submitted to McGill University in partial fulfillment
of the requirements of the degree Doctor of Philosophy

© Alexander Kiepas, 2021

McGill University
Faculty of Medicine
Department of Physiology
Montreal, Quebec, Canada

TABLE OF CONTENTS

| | |
|---|--------------|
| TABLE OF CONTENTS | II |
| ABSTRACT | VI |
| RÉSUMÉ | VIII |
| ACKNOWLEDGEMENTS | X |
| PUBLICATIONS ARISING FROM THIS WORK | XII |
| AUTHOR CONTRIBUTIONS | XIV |
| ORIGINAL CONTRIBUTIONS TO KNOWLEDGE | XV |
| PREFACE | XVII |
| LIST OF TABLES | XVIII |
| LIST OF FIGURES | XIX |
| LIST OF ABBREVIATIONS | XXII |
| CHAPTER 1 – General Introduction and Literature Review | 1 |
| 1.1 CANCER OVERVIEW | 2 |
| 1.2 BREAST CANCER | 2 |
| 1.2.1 Molecular classification of breast cancers | 2 |
| 1.2.1.1 Luminal breast cancers | 3 |
| 1.2.1.2 ErbB2 ⁺ breast cancers | 3 |
| 1.2.1.3 Basal and triple-negative breast cancers | 3 |
| 1.2.1.4 Normal-like breast cancers | 4 |
| 1.2.2 Integrated approaches to breast cancer classification | 4 |
| 1.2.3 Breast cancer progression | 5 |
| 1.2.3.1 Epithelial-to-mesenchymal transition (EMT)..... | 6 |
| 1.2.4 TGFβ signaling pathway | 7 |
| 1.2.4.1 Smad signaling pathway..... | 7 |
| 1.2.4.2 Dichotomous role of TGFβ..... | 8 |
| 1.2.5 ErbB2 signaling pathway..... | 8 |
| 1.2.5.1 ShcA adapter protein..... | 9 |
| 1.2.5.2 PTB domain of ShcA..... | 10 |
| 1.2.5.3 SH2 domain of ShcA..... | 10 |
| 1.2.5.4 CH1 domain of ShcA | 11 |
| 1.2.6 ErbB2 and TGFβ synergy..... | 12 |
| 1.2.7 Breast cancer metastasis | 13 |
| 1.3 CELL MIGRATION | 13 |
| 1.3.1 Modes of cell migration..... | 14 |
| 1.3.1.1 Mesenchymal migration | 14 |
| 1.3.1.2 Ameboid migration | 15 |
| 1.3.1.3 Collective migration | 15 |
| 1.3.2 Cell-matrix adhesions | 16 |
| 1.3.2.1 Integrin engagement of the ECM | 17 |
| 1.3.2.2 Structural organization of effector layers | 17 |
| 1.3.2.3 Adhesions and mechanobiology | 17 |
| 1.3.3 ECM stiffness and cell migration | 18 |

| | | |
|------------|---|-----------|
| 1.3.4 | ECM stiffness and cell invasion | 18 |
| 1.3.5 | ECM stiffness and breast cancer progression | 19 |
| 1.4 | LIPOMA PREFERRED PARTNER (LPP) | 20 |
| 1.4.1 | LPP protein domain organization | 20 |
| 1.4.2.1 | <i>LPP localization to the nucleus</i> | 21 |
| 1.4.2.2 | <i>LPP localization to adhesions</i> | 21 |
| 1.4.2 | LPP interaction partners | 22 |
| 1.4.2.1 | <i>α-actinin</i> | 22 |
| 1.4.2.2 | <i>LASP</i> | 22 |
| 1.4.2.3 | <i>Palladin</i> | 23 |
| 1.4.2.4 | <i>PP2A</i> | 23 |
| 1.4.2.5 | <i>Scrib</i> | 23 |
| 1.4.2.6 | <i>Supervillin</i> | 24 |
| 1.4.2.7 | <i>VASP</i> | 24 |
| 1.4.3 | Biological functions of LPP | 25 |
| 1.4.4 | LPP augments the malignant phenotypes of cancer cells | 25 |
| 1.4.5 | LPP as a suppressor of malignant cancer phenotypes | 27 |
| 1.4.6 | LPP as a mechanosensor | 27 |
| 1.5 | MICROSCOPY | 28 |
| 1.5.1 | Contrast | 28 |
| 1.5.2 | Fluorescence | 29 |
| 1.5.2.1 | <i>Organic fluorophores</i> | 29 |
| 1.5.2.2 | <i>Fluorescent proteins</i> | 30 |
| 1.5.3 | Photobleaching and phototoxicity | 31 |
| 1.5.4 | Reactive oxygen species (ROS) | 31 |
| 1.5.4.1 | <i>Superoxide dismutase (SOD)</i> | 32 |
| 1.5.4.2 | <i>Catalase</i> | 32 |
| 1.5.4.3 | <i>Glutathione peroxidase (GPx)</i> | 33 |
| 1.5.4.4 | <i>Peroxiredoxins (Prx) and thioredoxins (Trx)</i> | 33 |
| 1.5.4.5 | <i>Fluorescent probes for detecting ROS</i> | 34 |
| 1.5.5 | Mitigating photobleaching and phototoxicity | 34 |
| 1.5.5.1 | <i>Oxygen scavengers</i> | 34 |
| 1.5.5.2 | <i>Singlet oxygen quenchers</i> | 35 |
| 1.5.5.3 | <i>Triplet state quenchers (TSQ)</i> | 35 |
| 1.5.5.4 | <i>Other methods</i> | 35 |
| 1.6 | LIGHT MICROSCOPY TECHNIQUES | 36 |
| 1.6.1 | Widefield fluorescence microscopy | 36 |
| 1.6.1.1 | <i>Excitation light sources</i> | 36 |
| 1.6.1.2 | <i>Multi-color imaging</i> | 37 |
| 1.6.1.3 | <i>Emission light detectors</i> | 37 |
| 1.6.2 | Confocal microscopy | 38 |
| 1.6.2.1 | <i>Excitation light sources</i> | 38 |
| 1.6.2.2 | <i>Multi-color imaging</i> | 39 |
| 1.6.2.3 | <i>Emission light detectors</i> | 39 |

| | |
|---|------------|
| 1.6.3 Spinning disk (SD) confocal microscopy | 40 |
| 1.6.4 Total internal reflection fluorescence (TIRF) microscopy | 41 |
| 1.6.5 Fluorescence resonance energy transfer (FRET) microscopy | 42 |
| 1.6.5.1 Tension sensors | 43 |
| 1.6.5.2 Vinculin tension sensor (<i>VinTS</i>) | 43 |
| 1.6.5.3 Talin tension sensor (<i>TalinTS</i>) | 44 |
| 1.7 SUPER-RESOLUTION MICROSCOPY TECHNIQUES | 44 |
| 1.7.1 Stochastic optical reconstruction microscopy (STORM) | 45 |
| 1.7.2 Photoactivated localization microscopy (PALM) | 47 |
| 1.7.3 3D single molecule localization microscopy | 47 |
| 1.7.3.1 Interference PALM (<i>iPALM</i>) | 48 |
| 1.8 RATIONALE | 48 |
| 1.9 REFERENCES | 50 |
| 1.10 FIGURES AND LEGENDS | 77 |
| CHAPTER 2 – Optimizing live-cell fluorescence imaging conditions to minimize phototoxicity | 83 |
| 2.1 PREFACE | 84 |
| 2.2 ABSTRACT | 85 |
| 2.3 INTRODUCTION | 86 |
| 2.4 RESULTS | 88 |
| 2.5 DISCUSSION | 99 |
| 2.6 MATERIALS AND METHODS | 102 |
| 2.7 AUTHOR CONTRIBUTIONS | 115 |
| 2.8 ACKNOWLEDGEMENTS | 116 |
| 2.9 REFERENCES | 117 |
| 2.10 FIGURES AND LEGENDS | 120 |
| 2.11 SUPPLEMENTARY INFORMATION | 134 |
| CHAPTER 3 – Microscope Hardware and Software Delays Cause Photo-Toxicity | 155 |
| 3.1 PREFACE | 156 |
| 3.2 ABSTRACT | 157 |
| 3.3 INTRODUCTION | 158 |
| 3.4 RESULTS | 160 |
| 3.5 DISCUSSION | 163 |
| 3.6 MATERIALS AND METHODS | 164 |
| 3.7 AUTHOR CONTRIBUTIONS | 167 |
| 3.8 ACKNOWLEDGEMENTS | 168 |
| 3.9 REFERENCES | 169 |
| 3.10 FIGURES AND LEGENDS | 170 |
| CHAPTER 4 – The SHCA adapter protein cooperates with lipoma-preferred partner in the regulation of adhesion dynamics and invadopodia formation | 182 |
| 4.1 PREFACE | 183 |
| 4.2 ABSTRACT | 184 |
| 4.3 INTRODUCTION | 185 |
| 4.4 RESULTS | 187 |

| | |
|---|------------|
| 4.5 DISCUSSION..... | 195 |
| 4.6 MATERIALS AND METHODS..... | 199 |
| 4.7 AUTHOR CONTRIBUTIONS..... | 212 |
| 4.8 ACKNOWLEDEMENTS..... | 213 |
| 4.9 REFERENCES | 214 |
| 4.10 FIGURES AND LEGENDS..... | 220 |
| 4.11 SUPPLEMENTARY INFORMATION | 241 |
| CHAPTER 5 - LPP is a mechanosensitive protein that mediates HER2 and triple-negative breast cancer metastasis..... | 264 |
| 5.1 PREFACE..... | 265 |
| 5.2 ABSTRACT | 266 |
| 5.3 INTRODUCTION | 267 |
| 5.4 RESULTS | 269 |
| 5.5 DISCUSSION..... | 274 |
| 5.6 MATERIALS AND METHODS..... | 278 |
| 5.7 REFERENCES | 288 |
| 5.8 FIGURES AND LEGENDS..... | 293 |
| 5.9 SUPPLEMENTARY INFORMATION | 307 |
| CHAPTER 6 – General Discussion and Future Directions..... | 313 |
| 6.1 SUMMARY | 314 |
| 6.2 MITIGATING PHOTOTOXICITY | 315 |
| 6.2.1 Changing the light dose delivery method..... | 315 |
| 6.2.2 Reducing ROS..... | 316 |
| 6.3 NEW IMAGING APPROACHES ENABLE NOVEL BIOLOGICAL QUESTIONS..... | 317 |
| 6.3.1 Live-cell imaging of multiple adhesion components..... | 317 |
| 6.3.2 Live-cell imaging of invadopodia..... | 319 |
| 6.3.3 Live-cell imaging of adhesion tension and traction force mapping..... | 320 |
| 6.4 ROLE OF LPP IN CELLULAR MECHANOMEMORY | 321 |
| 6.5 OTHER EXTRACELLULAR FORCES THAT INFLUENCE CELL BEHAVIOR | 322 |
| 6.5.1 Viscoelasticity | 322 |
| 6.5.2 Fractionability..... | 323 |
| 6.6 LIMITATIONS OF 2D CELL MIGRATION AND INVASION MODELS | 324 |
| 6.7 3D CELL MIGRATION | 326 |
| 6.8 MOVING BEYOND 3D CELL MIGRATION MODELS..... | 327 |
| 6.9 CONCLUDING REMARKS | 328 |
| 6.10 REFERENCES | 330 |

ABSTRACT

Many physiological processes, including angiogenesis, neurodevelopment and wound healing, rely on the directed movement of cells through the extracellular matrix (ECM). Cell migration is also a fundamental process involved in cancer metastasis. Indeed, proteins that enhance focal adhesion and actin cytoskeletal dynamics are often upregulated in invasive and metastatic cancer cells. In this thesis, we show that the adapter proteins ShcA (p46/52 isoforms) and lipoma-preferred partner (LPP) are required for the migration and invasion of ErbB2-overexpressing breast cancer cells in response to transforming growth factor β (TGF β). Live-cell microscopy techniques reveal that ShcA and LPP are both required for TGF β -enhanced assembly and disassembly of adhesions. Moreover, p46/52ShcA must be phosphorylated on three key tyrosine residues (Y239/Y240/Y313) and LPP must interact with the actin cytoskeleton through its α -actinin binding domain (ABD) to mediate these effects. Using a BioID proximity labeling approach, we show that p46/52ShcA exists in a complex with various adhesion and actin cytoskeletal proteins, including paxillin and LPP. Total internal reflection fluorescence (TIRF) and 3D super-resolution iPALM microscopy confirm that p46/52ShcA is a novel component of adhesions and its localization to these structures precedes LPP.

In addition to acting as a scaffold, the ECM provides biophysical cues that direct cell migration. We demonstrate that LPP is required for ErbB2⁺ breast cancer cells to sense substrate stiffness. Cells expressing wildtype LPP exhibit enhanced migration rates on intermediate stiffnesses (30-50 kPa), and slower migration rates on soft (<10 kPa) and stiff (>90kPa) substrates; in contrast, cells lacking LPP expression migrate at a constant speed. ErbB2⁺ cells also modulate invasive activity based on substrate stiffness. In particular, cells invade maximally on soft (<5 kPa) and hard (>100 kPa) substrates where migration is significantly reduced. This is the first study to demonstrate that LPP mediates mechanosensitivity in breast cancer cells.

Breast cancer is a highly heterogenous disease with considerable cellular, molecular and pathological differences between patients. We find that LPP also plays an important role during TGF β -enhanced migration and invasion of triple-negative breast cancer (TNBC) cells. Human MDA-MB-231 cells with lower levels of LPP expression fail to exhibit TGF β -enhanced migration and invasion. Mouse 4T1 cells, and 4T1 derivatives that preferentially metastasize to the lungs (4T1-526) and liver (4T1-2776), also fail to exhibit TGF β -enhanced migration and invasion when

LPP expression is reduced. Consequently, 4T1-2776 cells lacking LPP develop fewer liver metastases following splenic injection.

Many of experimental results described in this thesis were obtained with live-cell fluorescence microscopy. Fluorescence microscopy provides a convenient, selective and sensitive way to observe live-cell dynamics; however, phototoxicity is a significant limitation of this technique. In this thesis, we show that much of the phototoxicity and photobleaching experienced with live-cell fluorescence imaging occurs as a result of “illumination overhead” (IO). This occurs when a sample is illuminated but fluorescence emission is not being captured by the microscope camera. As a result, we developed a workflow to optimize imaging conditions on any standard microscope. The workflow includes a guide on how to (1) determine the maximum image exposure time for a dynamic process, (2) optimize excitation light intensity, and (3) assess cell health with mitochondrial markers.

Overall, the work described in this thesis defines p46/52ShcA and LPP as important focal adhesion components that underlie the cooperation between ErbB2 and TGF β signaling pathways during breast cancer cell migration and invasion. Additionally, our work shows that LPP is required for mechanosensitivity and TNBC migration, invasion and metastasis to the liver.

RÉSUMÉ

Plusieurs processus physiologiques, y compris l'angiogenèse, le développement neural et la cicatrisation, dépendent du mouvement dirigé des cellules au travers de la matrice extracellulaire (MEC). Cette migration cellulaire est également un processus fondamental impliqué dans les métastases cancéreuses. En effet, les protéines qui améliorent l'adhésion focale et la dynamique du cytosquelette d'actine sont souvent surexprimées dans les cellules cancéreuses invasives et métastatiques. Dans cette thèse, nous démontrons que les isoformes p46/52 de la protéine adaptatrice ShcA ainsi que la protéine LPP (partenaire préféré des lipomes) sont nécessaires pour la migration et l'invasion, en réponse au TGF β (facteur de croissance transformant β), des cellules cancéreuses du sein qui surexpriment ErbB2. Les techniques de microscopie des cellules vivantes révèlent que ShcA et LPP sont tous deux nécessaires pour l'assemblage et le désassemblage des complexes d'adhésion en réponse au TGF β . Pour ce faire, il est nécessaire que p46/52ShcA soit phosphorylé en trois résidus tyrosine clés (Y239/Y240/Y313) et que LPP interagisse avec le cytosquelette d'actine via son domaine de liaison à l' α -actinine (ABD). En utilisant une approche de marquage de proximité BioID, nous avons observé que p46/52ShcA se retrouve au sein d'un complexe composé de diverses protéines d'adhésion et du cytosquelette d'actine comprenant paxilline et LPP. La fluorescence par réflexion interne totale (TIRF) et la microscopie iPALM à super-résolution 3D confirment que p46/52ShcA est un nouveau composant des adhésions cellulaires et que sa localisation dans ces structures précède celle de LPP.

En plus d'agir comme support, la MEC envoie des signaux biophysiques pour diriger la migration cellulaire. Nous démontrons que LPP est nécessaire pour la détection de la rigidité du substrat par les cellules du cancer du sein ErbB2⁺. Ainsi, les cellules exprimant LPP présentent des taux de migration supérieurs sur les rigidités intermédiaires (30-50 kPa) et des taux de migration plus lents sur les substrats souples (<10 kPa) ou rigides (90 kPa). Au contraire, les cellules dépourvues d'expression de LPP migrent à une vitesse constante quel que soit le substrat. Les cellules ErbB2⁺ modulent également la capacité invasive en fonction de la rigidité du substrat. En conséquence, les cellules envahissent plus facilement les substrats mous (<5 kPa) et durs (>100 kPa) sur lesquels la migration est significativement réduite. Il s'agit de la première étude à démontrer que LPP est une protéine mécanosensible exprimée par les cellules cancéreuses du sein.

Le cancer du sein est une maladie hétérogène avec des différences cellulaires, moléculaires et pathologiques considérables entre patients. Nous observons que LPP est aussi un

médiateur critique de la migration et de l'invasion des cellules du cancer du sein triple négatif (CSTN) en réponse au TGF β . Ainsi, la migration et l'invasion Les cellules humaines MDA-MB-231 ne répondent plus au TGF β lorsque l'expression de LPP est atténuée. Similairement, les cellules 4T1 de souris et les lignées cellulaires dérivées qui métastasent préférentiellement vers les poumons (4T1-526) ou le foie (4T1-2776), ne parviennent également pas à présenter une migration et une invasion exacerbée en réponse au TGF β lorsque l'expression de LPP est réduite. Par conséquent, les cellules 4T1-2776 dépourvues de LPP développent moins de métastases hépatiques après injection splénique.

De nombreux résultats expérimentaux présentés dans cette thèse ont été obtenus par microscopie à fluorescence sur cellules vivantes. Cette technique offre un moyen pratique, sélectif et sensible pour observer la dynamique des cellules vivantes. Toutefois, la phototoxicité est une limitation non négligeable. Dans cette thèse, nous montrons qu'une grande partie de cette phototoxicité et du photoblanchiment observés avec l'imagerie par fluorescence des cellules vivantes se produit à la suite de « l'illumination par le dessus » (IO). Cela se produit lorsqu'un échantillon est éclairé mais que l'émission de fluorescence n'est pas capturée par la caméra du microscope. En conséquence, nous avons développé un processus de travail pour optimiser les conditions d'imagerie sur n'importe quel microscope standard. Ceci comprend un guide sur la façon de (1) déterminer le temps maximum d'exposition de l'image pour un processus dynamique, (2) optimiser l'intensité de la lumière d'excitation et (3) évaluer la santé cellulaire avec des marqueurs mitochondriaux.

Dans l'ensemble, les travaux décrits dans cette thèse définissent p46/52ShcA et LPP comme des composants importants des complexes d'adhésion focale et qui suggère une coopération entre les voies de signalisation ErbB2 et TGF β pendant la migration et l'invasion des cellules du cancer du sein. De plus, nos travaux identifient LPP comme une nouvelle protéine mécanosensible et un régulateur essentiel de la migration, de l'invasion et des métastases des CSTN vers le foie.

ACKNOWLEDGEMENTS

I would like to acknowledge my funding sources for providing stipend support during my Ph.D. studies: Department of Physiology Graduate Excellence Award, Goodman Cancer Research Centre (GCRC) Canderel Studentship award, Fonds de Recherche Nature et Technologies (FRQNT) Master's award, and Fonds de Recherche Sante (FRQS) Doctoral award. I would also like to thank the Department of Physiology and the GCRC for providing several GREAT and Canderel travel awards, respectively. These awards allowed me to present my work at many national and international conferences, which greatly enriched my scientific development. Furthermore, I would like to thank McGill University for providing a Graduate Mobility Award to perform cutting-edge microscopy experiments at Janelia Research Campus in Ashburn, Virginia, USA. In turn, I am very grateful to Ulrike Boehm, Teng-Leong Chew and other members of the Advanced Imaging Center (AIC) at Janelia for hosting me for three weeks in January 2020. Finally, I would like to thank the Departments of Physiology and Medicine for nominating me and supporting my travel to the 2019 Canadian Student Health Research Forum in Winnipeg, Manitoba. It was truly an incredible experience to present my research at this premier conference and attend the Gairdner Foundation Gala afterwards.

My amazing academic journey at McGill University would not have been possible without the support of my co-supervisors Dr. Peter Siegel and Dr. Claire Brown.

To Dr. Peter Siegel, thank you for providing an unparalleled research experience full of challenging problems, thoughtful discussions and rewarding triumphs. Your enthusiasm for science always motivated me to push through and overcome even the most difficult hurdles, and your extensive knowledge about cancer never ceased to impress me. Thank you also for having an open-door policy (even during COVID-19). Finally, thank you for providing the intellectual freedom to drive my own project. The communication, leadership and research skills I learned in your lab are invaluable.

To Dr. Claire Brown, thank you for your kindness and support throughout my Ph.D. Your patience and understanding created a research environment where I felt that my input was always valued. Your excitement for furthering microscopy techniques also led to the development of interesting collaborative and interdisciplinary work. I gained a vast amount of knowledge about advanced microscopy. These skills will be undoubtedly fundamental in my science career. I am grateful that you reached out and invited me to join your research group in 2015.

I would like to thank my Thesis Advisory Committee: Dr. Luke McCaffrey, Dr. Reza Sharif-Naeini and Dr. Allen Ehrlicher. Thank you for invaluable input throughout my Ph.D. career. Thank you also for collaborative research efforts that exposed to me to the fields of 3D cell migration, calcium signaling, and cellular mechanosensing. Your experience in these research areas helped expand my scientific vision and frame my research interests. Furthermore, I would like to acknowledge Dr. Josie Ursini-Siegel (from the Lady Davis Institute) and Dr. Nicolas Bisson (from

Universite Laval) who helped advance projects described in this thesis. I am especially grateful to Dr. Ursini-Siegel for involving me in the p66ShcA project. This project inspired me to learn new experimental techniques and explore the role of LPP in triple-negative breast cancer.

To past and present members of the Siegel laboratory, I express my deepest gratitude for your friendship, support and thoughtful discussions throughout the years. Thank you to Matthew Annis, Sebastien Tabaries, Marco Biondini, Elena Voorand, Matthew Dankner, Alex Nowakowski, Brian Hsu, Elaine Ngan, Sylvia Andrzejewski, Julien Senecal, Camille Lehuede, and all other undergrads who spent time in the lab. I would especially like to acknowledge,

Matt A: First and foremost, thank you for your patience. I am extremely grateful for your willingness to answer questions, help with experiments, and interpret confusing results. You helped me solve countless problems that would have otherwise prevented me from accomplishing many of the things described in this thesis! Thank you also for your friendship, kindness and great sense of humor.

Seb: Thank you for your help with experiments and advice on future directions. It was a privilege to work alongside such an experienced mentor. I hope that there will be more opportunities to work together in the future.

Elena: Thank you for your friendship and support. I had an amazing time working with you in the lab and attending various conferences. I am especially grateful for your help during iPALM imaging in Virginia; I would not have been able to do it without you.

Marco: Thank you for including me in so many different projects. It was a pleasure working with such a positive and kind-hearted person. Your friendliness, generosity and sincerity made the lab an enjoyable and cooperative working environment.

Additionally, I would like to thank members of the Brown, Ehrlicher and Ursini-Siegel laboratories for help with experiments, techniques and thoughtful discussions: Abira Rajah, Firas Mubaid, and Jessica Lyda; Haruka Yoshie; Jesse Hudson, Kyle Lewis, and Ryuhjin Ahn. I would also like to thank past and present members of the Advanced Bioimaging Facility (ABIF): Dr. Erika Wee, Dr. Anne-Marie Ladouceur, Dr. Nelly Vuillemin and Samuel Brown.

Last but not least, I would like to thank my family. To my fiancée, Rebecca Flessner: your love and encouragement helped me to take on ambitious challenges and push myself. Thank you for making me smile even when times were tough. I cannot imagine what my years in Montreal would have looked like without you at my side. To my parents, Monika and Roman: this thesis would not have been possible without your unwavering support. Thank you for giving me the strength to reach for the stars and pursue my dreams. Your incredible work ethic inspired me to complete my work to the highest standard and excel during my Ph.D.

PUBLICATIONS ARISING FROM THIS WORK

Portions of Chapter 1 were published in the following review article:

Elaine Ngan*, Alex Kiepas*, Claire M. Brown and Peter M. Siegel. *Emerging roles for LPP in metastatic cancer progression*. **Journal of Cell Signalling and Communication**, 2018 (*equal contribution)

Chapter 2 was published as a peer-reviewed original research article:

Alex Kiepas, Elena Voorand, Firas Mubaid, Peter M. Siegel and Claire M. Brown. *Optimizing live-cell fluorescence imaging conditions to minimize phototoxicity*. **Journal of Cell Science**, 2020

Chapter 3 was published as a research article:

Alex Kiepas and Claire M. Brown. *Microscope hardware and software delays cause phototoxicity*. **Microscopy Today**, 2020

Chapter 4 was published as a peer-reviewed original research article:

Alex Kiepas, Elena Voorand, Julien Senecal, Ryuhjin Ahn, Matthew G. Annis, Kevin Jacquet, George Tali, Nicolas Bisson, Josie Ursini-Siegel, Peter M. Siegel and Claire M. Brown. *The ShcA adapter protein cooperates with LPP to mediate adhesion dynamics and invadopodia formation*. **Journal of Biological Chemistry**, 2020

Chapter 5 is a manuscript in preparation:

Alex Kiepas, Elena Voorand, Alex Nowakowski, Sebastien Tabaries, Julien Senecal, Haruka Yoshie, Ulrike Boehm, Matthew G. Annis, Teng-Leong Chew, Allen J. Ehrlicher, Claire M. Brown and Peter M. Siegel. *LPP is a mechanosensitive protein that mediates HER2 and triple-negative breast cancer metastasis*. (In preparation)

The following publications arose from work that was performed during my Ph.D. but are not presented in this thesis:

Kyle Lewis*, **Alex Kiepas***, Jesse Hudson*, Julien Senecal, Jacqueline R. Ha, Elena Voorand, Matthew G. Annis, Valerie Sabourin, Ryuhjin Ahn, Rachel La Selva, Sebastien Tabaries, Brian E. Hsu, Matthew J. Siegel, Matthew Dankner, Eduardo Cepeda Canedo, Mathieu Lajoie, Ian R. Watson, Claire M. Brown, Peter M. Siegel and Josie Ursini-Siegel. *p66ShcA functions as a contextual promoter of breast cancer metastasis*. **Breast Cancer Research**, 2020, 22:7 (*equal contribution)

Marco Biondini, **Alex Kiepas**, Leeanna El-Houjeiri, Matthew G. Annis, Brian E. Hsu, Anne-Marie Fortier, Geneviève Morin, José A. Martina, Isabelle Sirois, Adriana Aguilar-Mahecha, Tina Gruosso, Shawn McGuirk, April A.N. Rose, Unal M. Tokat, Radia M. Johnson, Ozgur Sahin, Eric Bareke, Julie St-Pierre, Morag Park, Mark Basik, Jacek Majewski, Rosa Puertollano, Arnim Pause, Sidong Huang, Tibor Keler and Peter M. Siegel. *HSP90 inhibitors*

induce GPNMB cell surface expression by modulating lysosomal positioning and sensitize breast cancer cells to Glembatumumab Vedotin. (under review at **Cell Reports**)

AUTHOR CONTRIBUTIONS

The work presented in this thesis would not have been possible without contributions from other members of the Brown and Siegel laboratories, as well as collaborations within the Goodman Cancer Research Centre (GCRC) and other academic institutions. The specific contributions of different authors on published manuscripts and unpublished results are listed below:

Chapter 2: A.K. generated fluorescently-labelled constructs and cell lines, performed the majority of experiments, analyzed data, and created MATLAB codes. E.V. assisted with microtubule dynamics acquisition and image analysis (Figures 2.4 and S2.4). F.M. assisted with cell migration (Figures 2.2D,E and 2.3D,E) and photobleaching experiments (Figures 2.4J and 2.6H). A.K. and C.M.B. conceptualized the idea. C.M.B. supervised the project. A.K. and C.M.B. wrote the manuscript with contributions from E.V. and P.M.S.

Chapter 3: A.K. performed the experiments, analyzed the data, and prepared figures. A.K. and C.M.B. interpreted the results and wrote the manuscript.

Chapter 4: A.K. generated fluorescently-labelled constructs, performed immunoblotting and microscopy experiments, analyzed data, and created MATLAB codes. E.V. performed gelatin degradation assays (Figures 4.9 and S4.11) and assisted with immunoblotting experiments (Figure S4.10A). J.S. (under the supervision of A.K.) helped with microscopy, image analysis and immunoblotting experiments. R.A. performed streptavidin pulldown assays (Figure S4.5). M.G.A. generated ShcA-iRFP constructs. K.J. and N.B. performed mass spectrometry analysis (Tables 4.1 and S4.1). G.T. generated preliminary results for cell migration. J.U.-S. contributed to the design and analysis of ShcA BioID data. P.M.S. and C.M.B. conceptualized and supervised the project. A.K., E.V., P.M.S. and C.M.B. wrote and edited the manuscript.

Chapter 5: A.K. generated fluorescently-labelled constructs and cell lines, performed immunoblotting and microscopy experiments, analyzed data, and created MATLAB codes. E.V. performed gelatin degradation assays, assisted A.K. with 3D super-resolution imaging of LPP, α -actinin and p46/52ShcA (Figure 5.2), and assisted H.Y. with the generation of polydimethylsiloxane (PDMS) substrates (Figure 5.3). A.N. and J.S. (under the supervision of A.K.) assisted with cell migration experiments. A.N. also assisted with vinculin tension sensor (Figure 5.1) and adhesion size and number (Figure 5.6) experiments. S.T. performed/analyzed animal experiments and immunohistochemistry (Figure 5.7). M.G.A. helped generate a ShcA-WT-mEos construct. U.B. and T.-L.C. helped acquire and analyze iPALM images. A.J.E. contributed to the design of PDMS substrates. P.M.S., C.M.B. and A.K. conceptualized the project. P.M.S. and C.M.B. supervised the project. A.K. interpreted the results and prepared the figures with edits from P.M.S. and C.M.B.

ORIGINAL CONTRIBUTIONS TO KNOWLEDGE

1. Fluorescence illumination can negatively affect living samples by producing radical oxygen species (ROS). I show that hardware and software delays are largely responsible for excessive ROS production during live-cell fluorescence imaging. These delays contribute to inappropriate delays between images and fluorescence illumination beyond the camera exposure time, termed “illumination overhead” (IO). IO is especially problematic when imaging fast processes that require short exposure times, such as microtubule, mitochondrial and lysosomal dynamics. I provide researchers with a guide on how to (1) determine the maximum image exposure time for a dynamic process, (2) optimize excitation light intensity, and (3) assess cell health with mitochondrial markers.
2. p46/52ShcA is a novel focal adhesion component that is required for the formation of small, dynamic adhesions in response to TGF β treatment. Live-cell time-lapse imaging techniques revealed that p46/52ShcA enhances single-cell migration of ErbB2-overexpressing breast cancer cells by increasing the assembly and disassembly of paxillin-bearing adhesions. p46/52ShcA also preceded and regulated the recruitment of lipoma preferred partner (LPP) to adhesions. Interferometric photoactivated localization microscopy (iPALM) suggested that p46/52ShcA and LPP are localized to distinct layers within adhesions.
3. Phosphorylation of three key tyrosine residues (Y239/Y240/Y313) on p46/52ShcA is required for TGF β -enhanced migration and invasion of ErbB2⁺ breast cancer cells. We demonstrated that cells expressing a ShcA-3F mutant (Y239F/Y240F/Y313F) cannot enhance adhesion dynamics or invadopodia formation in response to TGF β stimulation.
4. LPP must localize to adhesions through its LIM1 domain and interact with the actin cytoskeleton via its α -actinin binding domain (ABD) to facilitate TGF β -enhanced single-cell migration. ErbB2⁺ cells expressing LPP with a mutated LIM domain (mLIM1) or a deleted ABD domain (Δ ABD) failed to exhibit TGF β -induced migration and adhesion dynamics.
5. LPP influences the migration and invasion of breast cancer cells in response to substrate stiffness. ErbB2⁺ cells expressing wildtype LPP migrated maximally on polydimethylsiloxane (PDMS) substrates with intermediate stiffnesses (~40 kPa) and invaded maximally on soft (<5 kPa) and hard (>100 kPa) substrates. In contrast, cells lacking LPP were insensitive to substrate stiffness. Furthermore, LPP was required for TGF β -mediated increases in adhesion tension. Live-cell confocal microscopy experiments using a fluorescence resonance energy transfer (FRET)-based tension sensor revealed that TGF β enhances adhesion tension through the LPP/ α -actinin linkage.
6. In addition to its roles in ErbB2⁺ breast cancer cells, LPP is also required for TGF β -enhanced migration and invasion of triple-negative breast cancer (TNBC) cells. Various TNBC cell lines migrated faster and further in response to TGF β treatment. Stable

diminishment of LPP expression in these cell lines abrogated TGF β -enhanced migration and invasion. Cells with reduced LPP expression also exhibited significantly less liver metastasis following splenic injection.

PREFACE

This is a manuscript-based thesis. It contains one published review article (incorporated into *Chapter 1*), two peer-reviewed original research articles (*Chapters 2* and *4*), and a research article reviewed by the editor (*Chapter 3*). Unpublished results that provide the basis for future experimental directions are described in *Chapter 5*.

This thesis is divided into 6 sections:

Chapter 1: A general introduction to breast cancer, cell migration/invasion and microscopy.

Chapter 2: Published manuscript describing a novel imaging technique for optimizing live-cell fluorescence imaging and minimizing phototoxicity with its own preface, abstract, introduction, results, discussion, materials and methods, author contributions, acknowledgements, references, figures, and supplemental information.

Chapter 3: Published manuscript describing how hardware and software delays affect live-cell fluorescence time-lapse microscopy experiments with its own preface, abstract, introduction, results, discussion, materials and methods, author contributions, acknowledgements, references and figures.

Chapter 4: Published manuscript describing the role of p46/52ShcA and LPP in mediating ErbB2⁺ breast cancer cell migration, adhesion dynamics and invadopodia formation with its own preface, abstract, introduction, results, discussion, materials and methods, author contributions, acknowledgements, references, figures, and supplemental information.

Chapter 5: Unpublished results implicating LPP as a mechanosensitive protein in breast cancer cells and important mediator of triple-negative breast cancer metastasis with its own preface, abstract, introduction, results, discussion, materials and methods, references and figures.

Chapter 6: A general discussion of all the results, future directions and references.

LIST OF TABLES

CHAPTER 2

| | |
|---|-----|
| Table S2.1. Illumination overhead continues to be a widespread and relatively unknown phenomenon affecting many microscopes..... | 146 |
| Table S2.2. Illumination conditions used to capture live-cell migration data for CHO-K1 cells expressing paxillin-EGFP | 147 |
| Table S2.3. Illumination conditions used to measure CHO-K1 cell migration speeds in response to increasing light power..... | 148 |
| Table S2.4. Illumination conditions for paxillin-EGFP used to observe mitochondrial morphology in migrating cells..... | 149 |
| Table S2.5. Illumination conditions for BFP, mCherry and iRFP excitation on the widefield microscope | 150 |
| Table S2.6. Signal-to-noise ratio of paxillin-EGFP in response to different exposure times | 151 |
| Table S2.7. Signal-to-noise ratio of paxillin-EGFP in response to increasing light power | 152 |
| Table S2.8. Illumination conditions used to show the effect of IO on the spinning disk confocal microscope | 153 |
| Table S2.9. Summary of illumination conditions used to capture cellular dynamics on the spinning disk confocal microscope..... | 154 |

CHAPTER 4

| | |
|---|-----|
| Table S4.1. Mass spectrometry data for BioID analysis to identify novel SHCA-interacting proteins..... | 249 |
|---|-----|

LIST OF FIGURES

INTRODUCTION

- Figure 1.1.** Schematic depicting the domain structure of LPP..... 78
- Figure 1.2.** Schematic illustrating distinct points within the metastatic cascade that rely on LPP-regulated cellular functions..... 80
- Figure 1.3.** Cellular mechanisms that eliminate reactive oxygen species (ROS) 82

CHAPTER 2

- Figure 2.1.** Standard imaging protocols deliver additional sample illumination beyond input camera exposure time 121
- Figure 2.2.** Total light dose and ROS are tightly linked processes that cause phototoxicity..... 123
- Figure 2.3.** Longer exposure times reduce the impact of IO..... 125
- Figure 2.4.** Object shape can be used to determine the longest exposure time for a dynamic process 127
- Figure 2.5.** Spatial and temporal binning can be used to improve S/N of images 129
- Figure 2.6.** Continuous imaging provides enhanced temporal resolution to reveal quantifiable fast adhesion dynamics 131
- Figure 2.7.** Flowchart for optimizing live-cell fluorescence imaging..... 133

- Figure S2.1.** Light source activation through USB causes a significant amount of IO which affects many cell types regardless of fluorophore localization or excitation wavelength..... 135
- Figure S2.2.** DLD can generate images with comparable signal-to-noise as CLD 137
- Figure S2.3.** Power must be increased exponentially to recover signal-to-noise lost to IO 139
- Figure S2.4.** Median filtering improves S/N without affecting morphology 141
- Figure S2.5.** Spatial and temporal binning of lysosomes and mitochondria results in greater S/N 143
- Figure S2.6.** Continuous imaging provides enhanced temporal resolution of fast adhesion dynamics in CHO-K1 cells 145

CHAPTER 3

- Figure 3.1.** USB connection must be disabled for TTL to eliminate IO..... 171
- Figure 3.2.** IO generates a significant amount of ROS 173
- Figure 3.3.** IO may vary with exposure time due to software delays 175
- Figure 3.4.** Software delays lead to inappropriate delays between images..... 177

| | |
|--|-----|
| Figure 3.5. Stream acquisition reduces IO and delays between images | 179 |
| Figure 3.6. Stream acquisition captures rapid lysosomal dynamics accurately | 181 |

CHAPTER 4

| | |
|--|-----|
| Figure 4.1. TGF β stimulates the migration of ErbB2-NT-expressing breast cancer cells | 221 |
| Figure 4.2. The SHCA adapter protein is required for TGF β -induced migration | 223 |
| Figure 4.3. SHCA is required for the formation of small, dynamic adhesions in breast cancer cells exposed to TGF β | 225 |
| Figure 4.4. Loss of SHCA phosphorylation abrogates TGF β -induced increase in migration speed of ErbB2-expressing breast cancer cells | 227 |
| Figure 4.5. LPP targeting to adhesions in response to TGF β requires SHCA..... | 230 |
| Figure 4.6. LPP is required for TGF β -induced migration and adhesion dynamics | 232 |
| Figure 4.7. SHCA is found in adhesions and co-localizes with LPP upon TGF β treatment | 234 |
| Figure 4.8. SHCA localization to adhesions precedes LPP recruitment..... | 236 |
| Figure 4.9. SHCA promotes breast cancer cell-mediated gelatin degradation | 238 |
| Figure 4.10. SHCA promotes the formation of small, dynamic adhesions in the presence of TGF β by acting as a nucleator of focal complex formation | 240 |
| | |
| Figure S4.1. TGF β stimulates the migration of ErbB2-NT expressing breast cancer cells in independent mammary tumor explant cell lines | 242 |
| Figure S4.2. The SHCA adapter protein is required for TGF β -induced migration in independent mammary tumor explant cell lines..... | 244 |
| Figure S4.3. SHCA phosphorylation on Y239/Y240 or Y313 is sufficient for enhanced cell migration in response to TGF β | 246 |
| Figure S4.4. Loss of SHCA phosphorylation on Y239/Y240/Y313 abrogates TGF β -induced migration of ErbB2-NT expressing breast cancer cells | 248 |
| Figure S4.5. SHCA-BirA biotinylates LPP | 251 |
| Figure S4.6. LPP is a component of cellular adhesions in breast cancer cells | 253 |
| Figure S4.7. LPP localization to adhesions requires intact LIM domains..... | 255 |
| Figure S4.8. LPP must localize to adhesions and interact with the actin cytoskeleton for TGF β -induced migration and adhesion dynamics | 257 |
| Figure S4.9. Migratory behavior of breast cancer cells with reduced SHCA levels is successfully rescued with SHCA-WT-iRFP but not SHCA-3F-iRFP | 259 |
| Figure S4.10. MAPK and PI3K signaling are required for the formation of small, dynamic adhesions in response to TGF β stimulation | 261 |

Figure S4.11. Invasive behavior of breast cancer cells is successfully rescued with SHCA-WT-iRFP but not SHCA-3F-iRFP 263

CHAPTER 5

Figure 5.1. LPP mediates TGF β -enhanced adhesion tension through its α -actinin binding domain 294

Figure 5.2. LPP localizes to the same adhesion layer as α -actinin 296

Figure 5.3. LPP is required for sensing substrate stiffness 298

Figure 5.4. LPP is an important regulator of triple-negative breast cancer cell migration and invasion 300

Figure 5.5. LPP is required for TGF β -enhanced migration and invasion of 4T1 derivatives that preferentially metastasize to the lungs and liver 302

Figure 5.6. TGF β enhances adhesion dynamics in liver metastatic cells in an LPP-dependent manner 304

Figure 5.7. Loss of LPP expression reduces liver-metastatic potential of TNBC cells 306

Figure S5.1. Spectral capture and linear unmixing can be used to measure adhesion tension .. 308

Figure S5.2. LPP is required for TGF β -enhanced invasion of ErbB2⁺ cells 310

Figure S5.3. 4T1 triple-negative breast cancer cells exhibit enhanced invasion following TGF β stimulation 312

LIST OF ABBREVIATIONS

| | |
|---------------------------------|---|
| 2D/3D: | 2-dimension/3-dimension |
| 4T1: | mouse triple-negative breast cancer cells |
| 2776: | 4T1-derived liver metastatic cells |
| 526: | 4T1-derived lung metastatic cells |
| ABD: | α -actinin binding domain |
| AOTF: | acousto-optic tunable filter |
| Arp2: | actin-related protein 2 |
| BF: | brightfield |
| BFP: | blue fluorescent protein |
| CAM: | chick chorioallantoic membrane |
| CCD: | charge-coupled device |
| CH: | collagen homology |
| CHIP: | chromatin immunoprecipitation |
| CHO-K1: | Chinese hamster ovary K1 cells |
| CLD: | condensed light delivery |
| COX-2: | cyclooxygenase-2 |
| Ctn: | cortactin |
| DCIS: | ductal carcinoma in situ |
| DLD: | diffuse light delivery |
| EB3: | end-binding protein 3 |
| ECM: | extracellular matrix |
| EGF: | epidermal growth factor |
| EGFR: | epidermal growth factor receptor |
| EGFP: | enhanced green fluorescent protein |
| EMT: | epithelial-to-mesenchymal transition |
| ER: | estrogen receptor |
| ErbB2: | avian erythroblastosis oncogene B |
| ERK: | extracellular signal-related kinase |
| FAK: | focal adhesion kinase |
| FN: | fibronectin |
| FRET: | fluorescence resonance energy transfer |
| H ₂ O ₂ : | hydrogen peroxide |
| H&E: | hematoxylin and eosin |
| HGMA2: | high mobility group AT-Hook 2 |
| IO: | illumination overhead |
| iRFP670: | far-red fluorescent protein |
| LAP: | leucine rich repeat and PDZ |
| LASP: | LIM and SH3 protein |
| LED: | light emitting diode |

| | |
|-----------------------|--|
| LLC-PK1: | pig kidney cells |
| LNAME: | nitro L-arginine methyl ester |
| LPP: | lipoma preferred partner |
| LPP ^{endo} : | cells expressing luciferase targeting shRNA |
| LPP ^{KD} : | cells expressing LPP targeting shRNA |
| LPP-mLIM1: | LPP construct with mutation in the first LIM domain |
| LPP- Δ ABD: | LPP construct with a deletion in the α -actinin binding domain |
| MAPK: | mitogen-activated protein kinase |
| MDA-MB-231: | human triple-negative breast cancer cells |
| MEF: | mouse embryonic fibroblast cells |
| MMP: | matrix metalloproteinase |
| ND: | neutral density |
| NES: | nuclear export signal |
| NF- κ B: | nuclear factor κ B |
| NLS: | nuclear localization signal |
| NMuMG: | normal murine mammary gland cells |
| NOS: | nitric oxide synthase |
| NT: | constitutively active ErbB2 receptor (V664E point mutation) |
| NYPD: | constitutively active ErbB2 receptor with five autophosphorylation sites (Y1028, Y1144, Y1201, Y1226/Y1227 and Y1253) mutated to phenylalanine (F) |
| $^1\text{O}_2$: | excited state singlet oxygen |
| $^3\text{O}_2$: | ground state molecular oxygen |
| O_2^- : | superoxide anion |
| OD: | optical density |
| OH \cdot : | hydroxyl radical |
| PALM: | photoactivated localization microscopy |
| PBS: | phosphate buffered saline |
| PDMS: | polydimethylsiloxane |
| PEI: | polyethylenimine |
| PFA: | paraformaldehyde |
| PI3K: | phosphoinositide-3-kinase |
| PP2A: | protein phosphatase 2A |
| PR: | progesterone receptor |
| PRR: | proline rich region |
| PTB: | phosphotyrosine-binding domain |
| PRX1: | paired-related homeobox gene 1 |
| RAM: | random access memory |
| RCHOP: | Rituximab, cyclophosphamide, doxorubicin, vincristine, prednisone |
| ROS: | reactive oxygen species |

| | |
|------------------------|---|
| SAINT: | significance analysis of interactome |
| sCMOS: | scientific complementary metal-oxide-semiconductor |
| SD: | spinning disk |
| SH2: | Src homology 2 domain |
| ShcA: | Src homology and collagen (p46, p52 and p66 isoforms) |
| ShcA ^{endo} : | cells expressing luciferase targeting shRNA |
| ShcA ^{low} : | cells expressing ShcA targeting shRNA |
| shRNA: | short hairpin ribonucleic acid |
| siRNA: | small interfering ribonucleic acid |
| SMC: | smooth muscle cells |
| S/N: | signal-to-noise ratio |
| Src: | avian sarcoma (Schmidt-Ruppin A-2) viral oncogene |
| STORM: | stochastic optical reconstruction microscopy |
| SVIL: | supervillin |
| TGF β : | transforming growth factor β |
| TIRF: | total internal reflection fluorescence |
| TFP: | teal fluorescent protein |
| Tks5: | tyrosine kinase substrate with 5 SH3 domains |
| TNBC: | triple-negative breast cancer |
| TSM: | tension sensing module |
| TTL: | transistor-transistor logic |
| USB: | universal serial bus |
| VASP: | vasodilator stimulated phosphoprotein |
| VinTS: | vinculin tension sensor |
| WASP: | Wiskott-Aldrich syndrome protein |
| WT: | wildtype |
| 313F: | p46/52ShcA construct with tyrosine 313 mutated to phenylalanine |
| 2F: | p46/52ShcA construct with tyrosines 239 and 240 mutated to phenylalanine |
| 3F: | p46/52ShcA construct with tyrosines 239, 240 and 313 mutated to phenylalanine |

CHAPTER 1 – General Introduction and Literature Review

1.1 CANCER OVERVIEW

Cancer arises from defects in regulatory circuits that regulate normal cell processes. More than 100 different types of cancers have been characterized, many of which are further classified into distinct subtypes [1]. Given this complexity, researchers have attempted to identify a number of underlying principles that govern the transformation of normal cells into malignant cancers. Several lines of evidence suggest that tumor cells acquire (1) a self-sufficiency in growth signals, (2) an insensitivity to growth suppression, (3) limitless replicative potential, (4) sustained angiogenesis, (5) the ability to evade apoptosis, and (6) activation of invasion and metastasis programs [2].

Tissues are comprised of many different cell types that work in concert to effect normal physiology. Over the past few years, it has become increasingly apparent that cancer cells can influence disease initiation and progression through various interactions with the microenvironment [3-5]. As a result, the hallmarks of cancer have been updated to include (7) tumor-promoting inflammation, (8) evasion of immune-mediated tumor clearance, (9) deregulation of cellular energetics, and (10) genomic instability and mutation [6]. These characteristics enable tumor cells to outgrow and dominate their local tissue environment.

1.2 BREAST CANCER

Breast cancer is the most commonly diagnosed cancer in women with over 1.38 million cases worldwide [7]. In Canada, 1 in 8 women will develop breast cancer during their lifetime [8]. Treatment of primary tumors has significantly improved over the past two decades; patients with localized disease experience a 5-year relative survival rate of about 99% [9, 10]. However, there are still many unresolved clinical and scientific problems in the areas of prevention, diagnosis, tumor progression, treatment, recurrence and therapeutic resistance. Many patients present with advanced disease [9]. Unfortunately, metastatic tumors, which form when the cancer spreads from the primary tumor site to essential organs, are particularly challenging to treat. As a result, 14 women still die of breast cancer every day [8].

1.2.1 Molecular classification of breast cancers

Gene expression profiling analyses have allowed researchers to stratify breast cancers into distinct subtypes with unique clinical outcomes [11-13]. Initial studies identified five distinct

groups: luminal A, luminal B, ErbB2⁺, basal, and normal-like [14, 15]. About 23.7% of patients present with the luminal A subtype, 52.8% with luminal B, 11.2% with ErbB2⁺, 12.3% with basal, and 7.8% with normal-like [16, 17].

1.2.1.1 Luminal breast cancers: Luminal breast cancers are characterized by high expression of estrogen receptor (ER) [11]. Luminal A is positive for both ER and progesterone receptor (PR) while luminal B is positive for ER only [18]. In addition, more than 25% of luminal B cancers also overexpress ErbB2 [19]. Luminal A cancers are associated with good clinical outcomes as they are generally responsive to endocrine therapies such as anti-estrogens (tamoxifen, fulvestrant) or aromatase inhibitors (letrozole, anastrozole, exemestane) [20, 21]. Luminal B cancers, on the other hand, are associated with intermediate outcomes due to a higher proliferation rate (Ki-67) and increased axillary lymph node involvement [11, 17, 22].

1.2.1.2 ErbB2⁺ breast cancers: ErbB2⁺ breast cancers are associated with amplification and overexpression of the HER2/ErbB2/Neu receptor tyrosine kinase. *TP53* and *PIK3CA* are also frequently mutated in primary and metastatic tumors; *TP53* is mutated in 39% of primary and 58% of metastatic tumors while *PIK3CA* is mutated in 33% of primary and 45.5% of metastatic tumors [23]. Increased activation of downstream signaling pathways that control cell proliferation, differentiation, survival, and invasion promotes the formation of highly aggressive metastatic tumors [24-26]. Indeed, transgenic mouse models that overexpress ErbB2 in the mammary epithelium spontaneously develop primary tumors with a high incidence of lung metastasis [27-30]. Consequently, patients with ErbB2 amplification have significantly lower overall survival rates and shorter time to relapse [24]. There are currently three types of targeted therapy available for the treatment of ErbB2⁺ breast cancers: (1) humanized monoclonal antibodies (trastuzumab, pertuzumab), (2) antibody-drug conjugates (ado-trastuzumab emtansine) and (3) tyrosine kinase inhibitors (lapatinib, neratinib) [31]. Unfortunately, many patients receiving these targeted therapies eventually relapse and develop progressive disease [32, 33].

1.2.1.3 Basal and triple-negative breast cancers: Basal breast cancers are characterized by high expression of cytokeratins 5 and 17, laminin and fatty acid binding protein 7 [14, 15]. These cancers do not express ErbB2 and expression of ER may be absent or low [14, 15]. Basal cancers that do not express ER, PR or ErbB2 are considered triple-negative [34]. In addition, a majority of triple-negative breast cancers (TNBC) exhibit mutations in *TP53* (68% of primary and 79% of metastatic tumors); *PIK3CA* is much less frequently mutated (18% of primary and 19% of

metastatic tumors) [23]. Due to a lack of well-defined clinical targets, chemotherapy is the standard of care treatment [35, 36]. Some cancers are sensitive to chemotherapy; however, many patients experience local and systemic relapse resulting in a poor overall outcome [11, 37, 38].

Although many basal-like cancers are triple-negative, and the majority of TNBCs are basal-like, there is up to 30% discordance between gene expression signatures and immunohistochemistry analysis [39]. High heterogeneity within this subtype has led to further subclassifications [40]. Claudin-low breast cancers are now considered to be a distinct subtype characterized by absent or low expression of ER, PR, ErbB2, claudin 3, claudin 4, claudin 7 and E-cadherin [41, 42]. Claudin-low tumors are also highly enriched for EMT markers and cancer stem cell-like features [43, 44]. Loss of claudin expression and stemness contribute to chemoresistance [45-47]. On the other hand, claudin-low tumors express lower levels of proliferation genes than basal, ErbB2⁺ and luminal B subtypes [48]. Thus, patients with this subtype have a slightly better prognosis than those with basal breast cancer; albeit, clinical outcomes are still poor [43]. Molecular-based therapies are now being investigated for TNBC, including inhibitors against EGFR, KIT, Src, PI3K/AKT/mTOR, HDAC, PARP, NOTCH and angiogenesis [36].

1.2.1.4 Normal-like breast cancers: Normal-like breast cancers are poorly characterized. They have (1) weak expression of luminal epithelial genes and (2) strong expression of basal epithelial genes [15]. Due to (3) high expression of many genes found in adipose tissue and other non-epithelial cell types, this subtype has the same signature as fibroadenomas and normal breast samples [14]. Consequently, there is controversy whether this subtype constitutes a *bona fide* subgroup or arises from contamination of tumour samples with normal breast tissue [49]. Indeed, a retrospective analysis of grade III invasive ductal carcinomas (IDCs) was unable to identify any normal-like breast cancers [50].

1.2.2 Integrated approaches to breast cancer classification

Gene expression profiling analyses initially categorized breast cancer into 5 different subtypes; however, it is increasingly evident that tumors within these groups are still highly heterogenous. For example, unsupervised clustering of tumors based on DNA methylation patterns revealed 3 groups of breast cancer with characteristic methylation patterns. These 3 groups corresponded to luminal A, luminal B and basal-like, with ErbB2⁺ and normal-like subtypes

distributed amongst the groups [51]. Thus, tumors with similar gene expression profiles may belong to epigenetically different subtypes [52]. A more expansive analysis of primary breast cancers by genomic DNA copy number, DNA methylation, exome sequencing, mRNA arrays, microRNA sequencing and reverse phase protein arrays subsequently confirmed that tumors within previously identified subtypes possess significant heterogeneity [53]. In line with these results, an integrated genomic/transcriptomic analysis of breast cancers from METABRIC (Molecular Taxonomy of Breast Cancer International Consortium) identified 10 clusters with distinct clinical outcomes [54]. Consequently, bioinformatic approaches to integrate genomics, transcriptomics, proteomics, metabolomics and histopathology data from various sources (blood samples, biopsies, genetically engineering mouse models and patient derived xenografts) have become instrumental in identifying tumor aggressiveness, response to therapy and patient outcome [55]. Single cell sequencing is a powerful new tool that is also being employed to understand the evolution and diversity of breast cancer [56-59]. Together, these techniques will help identify new therapeutic targets and advance efforts towards “personalized medicine.”

1.2.3 Breast cancer progression

There are many different risk factors that contribute to the formation of breast cancer [60]. Increased exposure to estrogen and progesterone (reproductive) [61, 62] and family history of early onset breast cancer (genetic) [63] are the most important factors. Transforming events in the mammary epithelium lead to abnormal proliferation and the formation of atypical ductal hyperplasia (ADH) [2, 64-66]. Atypical hyperplasias are considered to be precancerous lesions because of their small (<2 mm) and focal (<2 separate ducts) histopathology [67]; however, the genes conferring invasive growth advantage are already active [65]. As a result, women who develop ADH have a high risk of progressing to ductal carcinoma *in situ* (DCIS) [68-70]. DCIS are cancerous lesions characterized by widespread proliferation of malignant epithelial cells within the ductal-lobular system [66, 67]. Hyperplasias and carcinomas have multiple cellular layers, partial loss of cell polarity and reduced intercellular adhesion [71, 72]. As cancer cells proliferate and acquire more genetic modifications, they may breach the basement membrane and invade the surrounding stroma to form an invasive ductal carcinoma (IDC) [66, 73]. Cancer cells can then migrate towards blood vessels, enter the circulation, and metastasize to the lungs (71%), liver (62%), bone (71%) and brain (21%) [74]. The expression of different gene sets appear to regulate

where breast cancer cells metastasize [75-78]; however, further investigation into the mechanisms regulating organ-specific preference is required.

1.2.3.1 Epithelial-to-mesenchymal transition (EMT): EMT is a normal physiological process that can be co-opted by transformed epithelial cells to loosen cell-cell contacts and acquire metastatic properties. EMT typically occurs during embryogenesis, development, wound healing and inflammation [79, 80]; however, it can also be employed by cancer cells to enhance cell migration and invasion, avoid apoptosis, and bypass senescence checkpoints [80-82]. The expression of Twist1, an important transcription factor for EMT, enhances the invasion of mammary organoids in 3D culture [83]. Accordingly, mesenchymal-like cells have been identified at invasive front of tumors and in circulation [84, 85]. Conversely, conditional knockout of Snail1, another key EMT transcription factor, significantly blunts breast cancer metastasis [86].

Lineage tracing experiments have recently challenged the notion that EMT is required for cancer metastasis. Lung metastases isolated from transgenic mice with a Cre-switchable fluorescent marker and *fibroblast specific protein-1 (Fsp1)*-Cre did not contain any breast cancer cells that underwent EMT [87]. Lung metastasis was also not reduced with miR-200 inhibition of the EMT transcription factor Zeb1 [87]. Similarly, *α -smooth muscle actin (α SMA)*- and *Fsp1*-Cre reporters in mice with spontaneous pancreatic ductal adenocarcinoma (PDAC) showed that metastases were primarily epithelial; metastatic cancer cells exhibiting a partial EMT were restricted to single cancer cells or micrometastases [88]. Inhibition of Snail or Twist1 did not affect the invasion and metastasis of PDAC [89]; however, a subsequent study noted that expression of Zeb1 is required [90]. Together, these studies have shifted our view of EMT from a binary process to a spectrum where full transition to a mesenchymal phenotype is not required for metastasis [91]. For example, E-cadherin expression is required for breast cancer cells during systemic circulation and initial metastatic seeding [92]. Cells lacking E-cadherin frequently undergo apoptosis following dissemination due to increased reactive oxygen species (ROS) levels [92]. It is now appreciated that epithelial-mesenchymal plasticity supports metastasis in a context-dependent manner [93]. This is neatly demonstrated by the fact that breast cancer cells migrate out of the primary tumor as strands led by distinct cells, which are more metabolically active and may undergo a reversible, partial EMT [94-97]. TGF β is known to induce EMT via Smad2/3-dependent and Smad-independent pathways [98]. Consequently, TGF β signaling has important implications in breast cancer [99].

1.2.4 TGF β signaling pathway

The TGF β superfamily of growth factors consists of more than 35 members that regulate a diverse array of processes including embryonic development, angiogenesis, skeletal morphogenesis, body composition and fertility [100]. The mammalian TGF β isoforms TGF β 1, TGF β 2 and TGF β 3 are a small subset of this family that play an important role in cell proliferation, cell differentiation, ECM production and wound healing [101]. All three isoforms are secreted as latent precursors that are tethered to the ECM or cell-membrane-associated mannose-6-phosphate receptor [102]. Proteolytic cleavage by plasmin, matrix metalloproteinases (MMPs) or other enzymes releases TGF β , allowing it to exert autocrine and paracrine effects [103-105].

TGF β initiates intracellular signaling by binding the extracellular domain of TGF β type II receptor (T β RII), a constitutively active transmembrane serine/threonine kinase [101]. Upon ligand binding, T β RII recruits and phosphorylates one of two potential TGF β type I receptor (T β RI) partners: activin receptor-like kinase-1 (ALK1) or -5 (ALK5) [106, 107]. ALK5 propagates further downstream signaling through TGF β -associated Smad2/3 while ALK1 leads to a divergence from the TGF β pathway by interacting with bone morphogenic protein (BMP)-associated Smad1/5/8. Consequently, ALK5 is commonly referred to as T β RI [108].

1.2.4.1 Smad signaling pathway: Following T β RI activation, Smad2 and Smad3 are phosphorylated and form hetero-oligomers with Smad4 [107]. These complexes are then translocated into the nucleus where they modulate gene expression [101]. Although most Smad proteins can bind DNA directly through Smad-binding elements (SBEs), several cofactors help Smads achieve high affinity and selectively for specific subsets of genes [109]. Furthermore, the recruitment of transcriptional coactivators or corepressors determines whether the expression of a target gene is induced or inhibited [110]. A particularly important consequence of Smad2/3 activity is the loss of characteristic epithelial cell proteins and the acquisition of mesenchymal traits [111].

Smad-dependent activation of EMT involves three families of transcription factors: Snail, ZEB and helix-loop-helix (HLH). In particular, Smad3 binds the promoter of Snail1 to activate its expression. Snail1 subsequently enhances vimentin and fibronectin expression while suppressing E-cadherin to facilitate the dissolution of cell-cell tight junctions and stimulate cell migration [98]. Smad3 also interacts with ZEB proteins to directly repress epithelial marker genes. This effect may be mediated by the recruitment of CtBP, a known co-repressor [112]. Finally, TGF β stimulation

dramatically increases the expression of high mobility group A2 (HMGA2) through Smad3/4 activation. HMGA2 then induces the expression of Snail1/2 and Twist1, an HLH protein that increases vimentin and N-cadherin expression while decreasing E-cadherin, occludin and claudin-7 [98].

1.2.4.2 Dichotomous role of TGF β : Although TGF β is often portrayed as a tumor promoter, it is important to note that TGF β acts as a tumor suppressor in normal epithelial cells. Transgenic mice expressing active TGF β 1 under the control of an MMTV promoter are more resistant to mammary tumor formation following carcinogen exposure [113]. Similarly, conditional knockout of T β RII shortens tumor latency and increases pulmonary metastasis [114]. Genetic alterations allow epithelial cells to overcome the cytostatic effects of TGF β and co-opt this pathway for tumor-progression [115, 116]. For example, normal mammary epithelial cells treated with TGF β do not exhibit an increase in migration or invasion; however, cells with ErbB2 overexpression form invasive structures upon TGF β application. This effect is dependent on ErbB2 and TGF β synergy as ErbB2 alone is not sufficient to stimulate the formation of invasive structures in 3D basement membrane cultures [117]. Tumors that co-express ErbB2 and active TGF β type I receptor (T β RI) are also more invasive and metastatic to the lung than ErbB2 alone [116, 118].

1.2.5 ErbB2 signaling pathway

ErbB2 belongs to the EGFR family comprised of EGFR/ErbB1/HER1, ErbB3/HER3 and ErbB4/HER4 [119]. All ErbB family members possess an extracellular ligand-binding region, a single pass transmembrane domain, and a cytoplasmic domain with intrinsic protein tyrosine kinase activity. Ligand binding to the extracellular domain causes receptor homo- or heterodimerization. This leads to autophosphorylation of specific residues in the cytoplasmic tail and the recruitment of various signaling molecules. Interestingly, the extracellular domain of ErbB2 does not bind any known ligands [120]. It exists in a fixed conformation that resembles the ligand bound form of other family members [121]. This unique structure allows ErbB2 to be the preferred heterodimerization partner of all ErbB proteins [122].

Several cell and transgenic mouse models have been generated to understand the biological and mechanistic contributions of ErbB2 to breast cancer development. Overexpression of constitutively active ErbB2 (ErbB2-NT) results in the efficient transformation of mammary epithelial cells and the development of multiple tumors [28]. In contrast, epithelial cells with active

ErbB2 that cannot phosphorylate five specific tyrosine residues (Y1028, Y1144, Y1201, Y1266/Y1227 and Y1253) in its cytoplasmic tail (ErbB2-NYPD) fail to form large primary tumors or lung metastases [123]. Using a panel of add-back receptors that couple to distinct signaling pathways downstream of ErbB2, residues Y1144 and Y1266/Y1227 were found to be particularly important for breast cancer development. Grb2 signaling through Y1144 (Neu-YB) results in the formation of focal mammary tumors with slow growth but a high rate of metastasis. ShcA signaling through Y1226/Y1227 (Neu-YD), on the other hand, leads to the development of multifocal tumors with fast growth kinetics but a lower metastatic burden [124]. Interestingly, ShcA knockdown significantly impairs both primary tumor growth and metastatic burden even in the presence of fully functional ErbB2 (ErbB2-NT/ShcA^{low}). Together, this data indicates that ShcA is an essential adaptor protein for ErbB2 signaling in mammary epithelial cells [125].

1.2.5.1 ShcA adapter protein: ShcA is an adapter protein that mediates interactions between proteins in a variety of intracellular signaling cascades. It is part of a Src-homology/collagen (Shc) family of proteins that also includes ShcB, ShcC and ShcD. Alternative translational initiation and RNA splicing result in the expression of three different ShcA isoforms: p46, p52 and p66 [126, 127]. All three isoforms possess an N-terminal phosphotyrosine binding (PTB) domain, a collagen homology 1 (CH1) domain, and a C-terminal Src homology 2 (SH2) domain. The longer p66ShcA isoform contains an additional glycine/proline-rich CH2 domain in the N-terminal region [127]. p46ShcA and p52ShcA are ubiquitously expressed while p66ShcA is mainly found in epithelial cells. In contrast, ShcB and ShcC expression is largely limited to neuronal cells [128] and ShcD is expressed in the adult brain and skeletal muscle [129]. As a result, ShcA has been implicated in a variety of human disorders including Alzheimer's [130], cancer [131], and heart failure [132].

p46/52ShcA signaling in breast cancer has been extensively studied. As mentioned above, tumor formation and progression are significantly delayed when the cytoplasmic tail of ErbB2 cannot bind p46/52ShcA (ErbB2-NYPD). A similar phenotype is observed when polyomavirus (PyV) middle T antigen (MT) is mutated to Y250F and cannot bind p46/52ShcA [133]. Interestingly, tumors that eventually grow and metastasize restore p46/52ShcA binding to MT through somatic mutations [133]. These results imply that there is selective pressure for retention of p46/52ShcA signaling during breast cancer development. Indeed, genetic ablation of p52ShcA

significantly attenuates mammary tumor formation in rats dosed with 7,12-dimethylbenz(a)anthracene (DMBA) [134].

In contrast, p66ShcA has a complex and context-dependent role in cancer development, which is evidenced by conflicting reports about its pro-tumorigenic capacity. One study found that p66ShcA is overexpressed in breast cancer cell lines and primary tumors with high metastatic potential [135], while another showed that elevated p66ShcA levels and decreased p46/52ShcA signaling is associated with good outcome [136]. More recently, *in vivo* experiments revealed that p66ShcA knockout has no effect on breast cancer progression [134]. On the other hand, work from our group shows that p66ShcA overexpression induces EMT in luminal breast cancer cells, resulting in enhanced migration and invasion [137]. TNBC cells with elevated levels of p66ShcA require continued expression to support baseline migration speeds, as p66ShcA knockdown significantly reduces adhesion dynamics and impairs lung metastasis [138]. p66ShcA translocation into mitochondria is also required for TNBC metastasis. Phosphorylation-deficient p66ShcA (S36A) supports enhanced cell migration but fails to rescue the metastatic fitness of p66ShcA-null cells due to an inability to survive systemic circulation [138]. Therefore, we hypothesize that p66ShcA overexpression in naïve breast cancer cells is not sufficient to increase lung metastasis, but cells that have acquired high levels of p66ShcA require its continued expression to retain metastatic fitness.

1.2.5.2 PTB domain of ShcA: The PTB domain allows ShcA to interact with ErbB2 and PyV MT [139-141]. An R175Q mutation in the PTB domain (ShcR175Q) reduces ShcA binding to ErbB2 and abrogates TGF β -induced migration and invasion [125, 142]. Paradoxically, however, tumor outgrowth and angiogenesis are robustly increased when ErbB2-NT/ShcR175Q breast cancer cells are injected into the mammary fat pad of nude mice [143]. This phenomenon is thought to occur via SH2-dependent activation of Src and Fyn tyrosine kinases [144].

1.2.5.3 SH2 domain of ShcA: The biological significance of the ShcA SH2 domain during breast cancer progression is just beginning to emerge. Similar to the PTB domain, SH2 interacts with phosphotyrosine residues in a sequence specific manner. Arginine 397 is particularly important for this function [142, 145]. MMTV/MT transgenic mice that express a mutant ShcA allele with a non-functional SH2 domain (R397K) show a modest delay in tumor onset [146]. ShcR397K is unable to form a molecular complex with 14-3-3 ζ and the p85 α subunit of PI3K resulting in significantly more apoptosis and reduced tumor volume 4 and 6 weeks post-palpation.

Hence, the SH2 domain of ShcA appears to be important for the recruitment of PI3K and activation of Akt to enhance survival [146]. More recently, it has been shown that the SH2 domain is necessary for the activation of Src family kinases (SFKs) [144]. Mutating the SH2 domain (PTB/SH2^{MUT}) decreases SFK phosphorylation which significantly impairs tumor growth potential. Interestingly, PTB/SH2^{MUT} breast cancer cells that manage to form a primary tumor demonstrate high levels of SFK phosphorylation at endpoint. The SH2 domain of ShcA most likely activates Src through an indirect mechanism. Further studies are required to identify the protein or molecular complex responsible for this interaction [144].

1.2.5.4 CH1 domain of ShcA: The CH1 domain of ShcA contains three phosphotyrosine residues that are critical for breast cancer cell migration, invasion and metastasis: Y239/Y240 and Y313. Loss of phosphorylation at any of these sites results in decreased lung metastasis [125]. Tyrosines 239/240 are thought to recruit growth factor receptor-bound protein 2 (Grb2), a ubiquitously expressed adapter protein that is essential for a variety of cellular functions [147]. Grb2 has been implicated in several oncogenic signaling pathways due to its role in cell cycle progression and actin-based motility. For example, Grb2 is known to activate Ras/MAPK signaling through an interaction with SOS leading to enhanced cell proliferation [146, 148]. Additionally, it can directly interact with the cytoskeleton-associated protein Wiskott-Aldrich syndrome protein (WASP) to enhance cancer cell migration and invasion [149, 150]. Several reports suggest that Y313 may also contribute to Grb2 recruitment; however, this interaction appears to be highly cell type and cell context dependent [151-153]. Importantly, Y313 was found to be dispensable for Grb2 recruitment to ShcA in mouse embryonic fibroblasts (MEFs). Loss of Y239/Y240 phosphorylation (ShcA-2F) partially blocked this recruitment while loss of all three tyrosines (ShcA-3F) completely abrogated the association between Grb2 and ShcA [142]. Instead, Y313 is thought to bind Crk, another adapter protein involved in cell adhesion, migration, proliferation, apoptosis and gene expression [154]. Nevertheless, breast cancer cells bearing ShcA-3F do not exhibit increased cell migration and invasion in response to TGF β stimulation [125].

NMuMG-ErbB2 cells expressing ShcA-3F develop primary tumors at a slower rate than ShcA-WT cells [125]. A recent study found that p46/52ShcA signalling through Y239/Y240/Y313 enhances peroxisome proliferator-activated receptor gamma coactivator 1-alpha (PGC-1 α)-driven metabolic reprogramming of breast cancer cells to augment the metabolic rate of mammary tumors [155]. Loss of signalling through these phosphotyrosine residues (ShcA-3F) decreases glucose

metabolism and enhances the glutamine dependency of breast cancer cells [155]. Phosphotyrosine-dependent p46/52ShcA signaling also promotes breast cancer immune suppression; phosphorylation of Y239/Y240 enhances signal transducer and activator of transcription 3 (STAT3) while Y313 inhibits STAT1 [156]. By balancing STAT3 and STAT1 signaling, p46/52ShcA is able to inhibit cytotoxic T lymphocytes and enhance programmed death-ligand 1 (PD-L1) levels in mammary tumors [156].

1.2.6 ErbB2 and TGF β synergy

The dual role of TGF β is partially attributed to the cooperation of ErbB2 and TGF β signaling pathways. One possible mechanism for this synergy involves the production of soluble ErbB-family ligands. Conditioned media from cells stimulated with ErbB2 and TGF β enhances the migration of normal epithelial cells. Interestingly, this heightened activity can be reduced by ErbB1-inhibitory antibodies and ErbB1-specific pharmacological inhibitors, suggesting that at least one EGF-family ligand is secreted [117]. Recently, ErbB2 was shown to induce Smad3 phosphorylation via AKT leading to the expression of genes related to EMT [157]. ErbB2 inhibition or Smad3 knockdown is sufficient to impair TGF β -induced breast cancer cell migration [157].

Another possible mechanism for synergy involves ShcA. Src-mediated phosphorylation of Y284 within T β RII creates a docking site for ShcA and Grb2 [158]. In a similar manner, T β RI recruits and directly phosphorylates tyrosine and serine residues on ShcA following TGF β stimulation [159, 160]. This process allows ShcA to associate with Grb2/SOS, thereby initiating the MAPK signaling pathway. TGF β can also cause clustering of ErbB2 and integrins α_6 , β_1 and β_4 at the cell membrane [161]. Immunoprecipitation experiments show that TGF β induces the association of ErbB2 with actin and actinin [162]. This raises the possibility that ShcA may be present in cellular adhesions. Indeed, phosphoproteomic analysis of adhesions recently identified ShcA within isolated adhesion complexes [163]. Tension applied to human endothelial cells via fibronectin-bound paramagnetic beads also stimulates the recruitment of ShcA (p46, p52 and p66 isoforms) to adhesions [164].

While controversy exists regarding the clinical relevance of TGF β 1 levels in serum [165-170], ErbB2-overexpressing mammary epithelial cells with active T β RI produce a gene signature that matches tumors of patients with poor relapse-free and overall survival [171]. Moreover, TGF β

reduces the sensitivity of ErbB2-overexpressing cells to trastuzumab, effectively decreasing the utility of this therapy [171]. Collectively, this data demonstrates that TGF β signaling can augment the pro-metastatic behavior of ErbB2-overexpressing cells.

1.2.7 Breast cancer metastasis

The spread of breast cancer cells from the primary tumor to distant organs and tissues continues to be the biggest challenge to successful treatment. While the five-year survival rate for women with stage 0 or I breast cancer is close to 100%, the relative survival for stage IV metastatic cancers is only 22% [10]. There are currently two views used to describe metastatic progression. The linear progression model (see section 1.2.3) suggests that epithelial cells acquire genetic alterations in a step-wise fashion before they are able to invade the stroma, access the vasculature, and colonize metastatic sites [2, 172]. In contrast, the parallel progression model proposes that dissemination is an early event in the metastatic cascade which can occur in the absence of a large primary tumor [173, 174]. This notion is supported by clinical reports that show that 5-10% of cancer diagnoses in the US and Europe are metastatic cancers of unknown primary origin [175, 176]. Mathematical modeling of systemic cancer progression indicates metastatic growth is a rare stochastic event that allows cells to disseminate from the primary site shortly after transformation [177]. Consequently, further research is required to understand the mechanisms governing cancer cell dissemination.

1.3 CELL MIGRATION

Cell migration is required for the proper development and maintenance of multicellular organisms. Many physiological processes, including angiogenesis, neurodevelopment and wound healing, rely on the directed movement of cells. Unfortunately, migratory programs are also engaged in pathological conditions, such as cancer progression, where they contribute to tumor cell dissemination [178].

There are many intrinsic and extrinsic cues that regulate migration. Importantly, all cells acquire a polarized morphology with leading and trailing edges. This spatial reorganization arises from (1) biochemical or physical gradients leading to directed migration; or (2) microscopic non-uniformities in ligand concentration causing random migration [179]. In both cases, polarization requires the proper assembly of complex intracellular structures. The chemical and structural

composition of the ECM strongly influences the molecular mechanisms that are engaged. For example, $\alpha_5\beta_1$ integrins are recruited to bind fibronectin; $\alpha_2\beta_1$ binds fibrillar collagen; and $\alpha_6\beta_1$ or $\alpha_6\beta_4$ binds laminin [180]. Stiffness, viscoelasticity, pore size and many other physical barriers have also been shown to affect cell migration [181]. Thus, it is important to understand how the extracellular environment impacts migration patterns, and the assembly and cooperation of molecular machinery responsible for migration.

1.3.1 Modes of cell migration

Cell migration can be classified into three main modes based on the morphology of migration patterns: collective, mesenchymal and ameboid. Each mode is governed by a set of molecular mechanisms that regulate cytoskeletal organization, cell-ECM interaction and force generation [182]. Collective cell migration occurs when cells are mechanically held together by versatile cell-cell adhesion receptors called cadherins (E-cadherin in epithelial cells; VE-cadherin in endothelial cells; N-cadherin in stromal cells) [72, 183, 184]. An intermediate state where cells exhibit weak cadherin interactions (partial EMT) results in repetitive short-lived contacts that permit the individual, but coordinated, migration of many cells. Complete dissolution of cell-cell contacts (full EMT) permits individual cell migration in all directions [185]. Mesenchymal migration resembles the movement of fibroblasts and relies on integrin-based adhesions for force generation. In contrast, individual cells that rely on the formation and elongation of protrusions exhibit ameboid or bleb-based motility. Interestingly, cancer cells can adopt all three modes of migration to disseminate from the primary tumor [180, 186].

1.3.1.1 Mesenchymal migration: TGF β -induced EMT is one mechanism that allows epithelial cells to de-differentiate and acquire a mesenchymal phenotype. It is predominantly found in soft tissue sarcomas and epithelial cells that progressively de-differentiate [186]. In principle, the lower the differentiation stage, the more likely the tumor will spread as individual cells [187]. Mesenchymal cell migration is characterized by four key events: (1) protrusion of the leading edge, (2) adhesion to the ECM, (3) cell body translocation, and (4) retraction of the trailing edge [179, 185, 188]. This mode of cell migration is relatively slow (0.1 to 1 $\mu\text{m min}^{-1}$) for three reasons. First, the formation of lamellipodial protrusions requires the coordinated assembly of branching actin filaments through an Arp2/3-dependent mechanism [189, 190]. Integrin-based focal adhesions must then assemble, couple to the actin cytoskeleton, generate traction forces, and

disassemble. This process generally occurs on the order of minutes [191]. Finally, cells must secrete proteases or express membrane bound MMPs to clear a path through the ECM [192]. As a result, it is thought that mesenchymal cells can switch modes of migration when it is no longer favorable (or possible) to use adhesions and proteases [193-195]. Mathematical modelling supports this notion, demonstrating that migration plasticity can be advantageous in terms of distance travelled under heterogenous, highly structured ECM conditions [196].

1.3.1.2 Ameboid migration: EMT allows cancer cells to loosen cell-cell contacts and detach from the primary tumor; however, metastasizing tumor cells must then migrate through a dense environment filled with other cell types and highly crosslinked fibers [197]. Cancer cells may undergo transient mesenchymal-to-ameboid transitions (MAT) to squeeze through confining pores [186]. Ameboid migration mechanistically resembles the movement of *Dictyostelium discoideum* amoeba [186]. This type of cell migration typically occurs in cells with low adhesion force or high actomyosin-mediated contractility. Accordingly, cells have small or diffusely organized adhesion sites [198] and rely on microtubule polymerization at the leading edge to migrate [199]. Ameboid migration is relatively fast ($20 \mu\text{m min}^{-1}$) and involves rapid changes that occur in response to the current state of the microenvironment [200]. Indeed, physical confinement of human breast carcinoma cells induces cytoskeletal changes that reduce adhesion-contraction force coupling. Thus, EMT allows cancer cells to detach from the tumor while MAT allows cells to move through ECM quickly and efficiently [201]. For example, mammary carcinoma cells transformed by oncogenic Ras display ameboid migration, which allow them to undergo early detachment and spread from a small primary tumor [180]. Conversely, vinculin upregulation via ERa suppresses ameboid migration and reduces metastasis [202].

1.3.1.3 Collective migration: Recent studies show that many breast cancer cells metastasize as clusters [94, 97]; the maintenance of some cell-cell contacts reduces ROS-mediated apoptosis and enhances cell survival [92]. These cells migrate away from the primary tumor as a sheet or strand of cells. Such collective migration depends on the “supracellular” coordination of cytoskeleton dynamics through cell-cell contacts [186]. The cluster behaves as a “mega cell” with specialized leader cells at the front that produce MMPs to form a path for trailing cells [203]. Accordingly, leader cells exhibit increased metabolism [95]. Traction force analyses demonstrate that leader cells also produce greater forces than follower cells, resulting in a global tug-of-war through E-cadherin junctions [204]. Stretch-induced ERK activation triggers cell contraction via

EGFR, resulting in waves of traction force as the monolayer migrates [205]. As a result, intercellular coupling of ERK-mediated mechanochemical feedback yields long-distance transmission of guidance cues [205]. Interestingly, mechanical force applied to a single C-cadherin molecule (the primary cadherin in *Xenopus*) is sufficient to induce polarized cell protrusion and persistent migration away from the applied force [206]. The magnitude of this pulling force is comparable to the tugging stresses (5 Pa) reported for the Madin-Darby canine kidney epithelial sheets described above. A positive feedback mechanism may sustain directional cell migration. In addition to reducing ROS-mediated apoptosis, the large cell mass also protects inner cells from immunological assaults by lymphocytes and natural-killer cells [180]. Collective cell migration is observed in many different types of cancers [207, 208]. Importantly, collective cell migration does not preclude cells from undergoing a partial EMT [209].

1.3.2 Cell-matrix adhesions

Mesenchymal migration is highly dependent on adhesion dynamics. Adhesions are multiprotein complexes that allow cells to grow and function in physiological environments with diverse connective tissue components. They consist of a complex network of integrins and cytoplasmic proteins that form a <200 nm plaque of at least 156 components with 690 interactions [210, 211]; multidimensional protein identification technology mass spectrometry (MudPIT MS) of isolated adhesions suggests that there are as many as 905 proteins [212].

There are four main classes of adhesions which can be distinguished by their size, protein composition and lifetime: nascent adhesion, focal complex, focal adhesion and fibrillar adhesion [213]. Nascent adhesions at the leading edge of migratory cells are <1 μm in diameter, primarily composed of integrins, talin and paxillin, and have a lifespan <60 s [214-217]. Nascent adhesions mature into focal complexes upon vinculin recruitment and attachment to the actin cytoskeleton [218]. Mechanical force promotes recruitment of more scaffold proteins and strengthening of the adhesion-actin cytoskeleton link, leading to the formation of focal adhesions [219, 220]. Focal adhesions are larger than focal complexes (1 μm wide \times 3-5 μm long), contain zyxin, and have a considerably longer lifetime (>8.5 min) [214, 221]. Continued force application transitions focal adhesions into fibrillar adhesions by translocating ligand-occupied $\alpha_5\beta_1$ integrins along bundles of actin filaments [222]. Fibrillar adhesions are significantly longer, contain tensin, and have a very long lifetime (~42 min) [221, 222]. Adhesions typically form along ECM bundles of collagen and

fibronectin [223, 224]. Collectively, nascent adhesions, focal complexes, focal adhesions and fibrillar adhesions are often referred to as focal adhesions to distinguish them from cell-cell adhesion contacts.

1.3.2.1 Integrin engagement of the ECM: The primary role of adhesions is to link the internal cellular actin cytoskeleton to the ECM. This is achieved through various integrins that directly interact with ECM components [225]. Integrins are heterodimeric transmembrane receptors comprised of an α and a β subunit that associate through noncovalent interactions. Both subunits possess a globular head region that participates in binding ligands such as fibronectin, collagen, and laminins. Ligand binding alters the coordination of a Mg^{2+} ion which causes a conformational change that shifts integrin into an open conformation. This change increases ligand affinity and causes adhesion strengthening [226].

1.3.2.2 Structural organization of effector layers: Three-dimensional super-resolution microscopy reveals that integrins and actin filaments are separated by a core region that spans ~40 nm. This region can be stratified into three spatial and functional compartments: an integrin signaling layer, a force transduction layer, and an actin regulatory layer [210]. Focal adhesion kinase (FAK) and paxillin appear to be key players in the membrane-proximal integrin signaling layer; talin and vinculin are observed in the broader central zone which is responsible for force transduction; and vasodilator-stimulated phosphoprotein (VASP) and zyxin localize to the uppermost region that constitutes the actin regulatory layer.

1.3.2.3 Adhesions and mechanobiology: Adhesions were initially thought to play a strictly structural role; however, it is now clear that they are multifunctional organelles that allow cells to respond to an extraordinary number of physical signals. Most cells require a solid surface that allows them to spread and engage adhesion molecules [227]. This anchorage dependence underscores the importance of integrin signaling and actin engagement for cell survival and proliferation. Cells can also sense the topography, rigidity and anisotropy of the underlying ECM through their adhesions [228]. These physical cues can manifest into local responses like adhesion maturation [229], or global responses such as growth, differentiation or programmed cell death [230-234]. More recently, it has been shown that cells are sensitive to the elasticity of their environment and adopt different migration strategies based on this parameter [235]. Consequently, there is a growing interest to determine the nanoscale architecture of adhesions and identify specific proteins that allow adhesions to function as mechanosensitive structures.

1.3.3 ECM stiffness and cell migration

Adhesions play an important role in sensing and responding to substrate stiffness. Nascent adhesions are initially formed at the leading edge of cells in a force- and stiffness-independent fashion [217, 220]. Many of these small adhesions quickly decay while a few continue to increase in size and move towards the cell interior [236]. Substrate stiffness increases the fraction of adhesions that mature into large complexes [237] by unmasking additional binding sites on adhesion proteins [238, 239]. Force fluctuations within adhesions are also converted into biochemical signals through a FAK/phosphopaxillin/vinculin signaling pathway [240]. As a result, cells migrate towards stiffer areas almost immediately after substrate stretching or compression [241]. This cellular response to extracellular stiffness is known as durotaxis [242].

While durotaxis is a stimulus for cell migration, an optimal range of stiffness likely exists that promotes maximal cell migration. Indeed, a biphasic relationship between substrate stiffness and migration appears to exist: very soft substrates fail to support traction forces required for cell migration while very stiff substrates induce maturation and hyper-stabilization of adhesions, which impedes cell migration [219, 241]. Mathematical models of steady-state cell speed suggest that fibroblasts migrate best on substrates with a Young's modulus of ~30-40 kPa [243, 244]. In agreement with these models, traction force mapping shows that lung fibroblasts treated with TGF β exhibit greater root-mean-square traction on elastic moduli greater than 13 kPa when compared with untreated controls [245]. Stiffer substrates induce cell spreading, the formation of more adhesions, and increased stability of adhesions; collectively this results in slower migration [237, 246]. These data suggest that intermediate substrate stiffness might be favorable for migration [247], with soft or very stiff substrates both resulting in less cell migration.

1.3.4 ECM stiffness and cell invasion

During cell migration, the actin cytoskeleton couples to adhesions in a tangential orientation to generate traction forces [248]. In contrast, perpendicular alignment of actin filaments with respect to the underlying ECM results in the formation of invadopodia, which create protrusive forces as MMPs degrade matrix [248]. Invadopodia allow invasive carcinoma cells to (1) escape the primary tumor, (2) intravasate into the circulatory and lymphatic systems, (3) extravasate into the parenchyma of distant tissues, and (4) initiate the formation of metastasis [249,

250]. *Ex vivo* models demonstrate that breast carcinoma cells form invadopodia when seeded onto urinary bladder-derived basement membrane [251] and invasive colorectal cells form invadopodia that breach basement membrane barriers through physical and enzymatic mechanisms [252]. Accordingly, there is evidence to suggest a direct correlation between the propensity of cancer cells to form invadopodia and poor prognosis in breast cancer patients [253]. Sophisticated imaging approaches are now producing direct evidence of their involvement during tumor cell intravasation and extravasation *in vivo* [254-257].

Invadopodia are also mechanosensory structures that form optimally on substrates of varying stiffness [251, 258]. Indeed, breast carcinoma cells have been shown to demonstrate peak invadopodia-associated ECM degradation on 30 kPa and 2 GPa substrates, with significantly less activity on intermediate rigidities [251]. Other studies have shown that soft matrices (0.1-0.4 kPa) can increase MMP secretion, promote MMP activity, and induce invadopodia formation [259]. It has been suggested that a minimum stiffness of 0.165 kPa is required for invadopodia formation [260]; however, cancer cells exhibit significantly less invadopodia on 0.36 kPa substrates compared to 3.3 kPa [261]. Similarly, head and neck squamous cell carcinoma cells show less ECM degradation on rigidities of 1.0 kPa when compared to 22.7 kPa [262]. These data suggest that invadopodia may optimally form on softer substrates relative to those that induce peak cell migration. Interestingly, very stiff substrates that impair cell migration may re-engage invadopodia for effective cell invasion.

1.3.5 ECM stiffness and breast cancer progression

The cellular and biochemical components of the primary tumor and metastatic environments have long been areas of interest; however, the biophysical microenvironment is emerging as a key modular of cancer cell behavior [258, 263]. It is well documented that breast density is positively correlated with cancer development [264-266]. Normal fatty breast tissue has a stiffness of ~5-7 kPa, benign lesions measure $\sim 45 \pm 40$ kPa, and malignant lesions reach $\sim 147 \pm 40$ kPa [267]. Although tumor stiffness is highly variable (64-181 kPa), this parameter increases along with the grade of DCIS [268] and with larger tumors of higher grade [269].

ECM deposition, modification, degradation and organization are modified during breast cancer progression [270]. Collagen crosslinking and matrix stiffening promote adhesion formation and maturation [271, 272]. Increased ECM stiffness also induces EMT and enables a

mesenchymal-like mode of cancer cell migration [273]. Accordingly, upregulation of proteins that enhance actin cytoskeleton and adhesion dynamics is often observed in invasive and metastatic cancer cells, while inhibition of these mediators is beneficial in blocking cell migration [274-276]. Furthermore, breast cancer transformation is accompanied by progressive linearization and thickening of interstitial collagen adjacent to the invasive tumor front [277]. Together, these changes enhance tumor progression by inducing cell migration and invasion. Indeed, *in vivo* experiments show that increased stromal collagen within mouse mammary tissue significantly increases tumor formation and lung metastasis [278]. A better understanding of how mechanical properties within the surrounding stromal tissue regulate molecular mechanisms engaged in cancer cells may lead to the identification of new targets for intervention that can suppress malignant cancer phenotypes.

1.4 LIPOMA PREFERRED PARTNER (LPP)

LIM domain containing proteins play a pivotal role in regulating the actin cytoskeleton. Lipoma Preferred Partner (LPP), a member of the zyxin family of LIM proteins, has long been characterized as a promoter of mesenchymal/fibroblast cell migration. More recently, LPP has emerged as a critical inducer of ErbB2⁺ breast cancer cell migration, invasion and metastasis [279-281]. LPP is thought to contribute to these malignant phenotypes by virtue of its ability to shuttle into the nucleus, localize to adhesions, and promote invadopodia formation. Interestingly, LPP is also emerging as a mechanosensory and potentially mechanoregulatory protein, which is consistent with the fact that both adhesions and invadopodia are mechanosensory cellular structures [263, 282]. The notion that biophysical cues that direct LPP to adhesions or signal LPP-mediated invadopodia formation is an exciting prospect.

1.4.1 LPP protein domain organization

LPP spans a genomic region of over 400 kb and produces an mRNA transcript of approximately 10 kb [283]. The main promoter element within intron 2 has an open reading frame of 1836 nucleotides, which encodes an 80 kDa protein. Although LPP mRNA levels are found in almost all human tissues (except the brain and peripheral blood), LPP protein is highly expressed in smooth muscle cells (SMCs) particularly in the ileum, stomach, corpus cavernosum, uterus, portal vein, aorta and bladder [284]. It is important to note that a smaller transcript has been

detected in the testes [283], which in mice, is generated through an alternative promoter located in intron 7 [285].

LPP was initially described as a novel group 3 LIM domain containing protein based on motif composition and its highly modular organization [283]. Further characterization, however, led to the re-classification of LPP as a zyxin family member due to high sequence similarity within the LIM domains and a similar overall domain structure to zyxin [286]. The zyxin family currently consists of zyxin, LPP, TRIP6/ZRP-1, Ajuba, LIMD1, WT1P and FBLP-1/migifilin/Cal, all of which regulate cellular proliferation, cytoskeletal rearrangements, cellular motility, cell migration/invasion and tumorigenesis [287-292]. Although LPP shares the greatest amino acid sequence similarity to TRIP6/ZRP-1 (53%), its domain organization most closely resembles zyxin (with 41% amino acid similarity) [293, 294].

LPP contains three carboxyl-terminal LIM domains that are preceded by a Proline-Rich amino-terminal region (PRR) (Fig. 1.1). The LIM domains span amino acid residues 413 to 612 in human LPP and are formed by cysteine and histidine rich double zinc finger protein motifs [283]. These motifs are comprised of approximately 55 residues with the following consensus sequence: CX₂CX₁₆₋₂₃HX₂CX₂CX₂CX₁₆₋₂₃CX₂C (where X is any amino acid) [295, 296]. The remaining domain sequence is highly variable and thought to confer protein-protein binding specificity [297]. It is unclear whether a single LIM domain binds several proteins simultaneously, or whether tandem LIM domains co-operate to bind a single interaction partner. Discrete consensus binding sequences or structural features that define LIM domain interactions with specific partners have not yet emerged.

1.4.2.1 LPP localization to the nucleus: LPP possesses a classic leucine-rich nuclear export signal (NES) within its PRR (residues 117-128, sequence LDAEIDSLTSIL). Only a very small amount of LPP can be detected in the nucleus (1-6% of cells) under steady state conditions [298]. Interestingly, expression of exogenous LIM 1-3 alone can displace LPP and vinculin from adhesions and increase nuclear accumulation [295]. It is unclear how LPP translocates into the nucleus as it does not possess a predicted Nuclear Localization Signal (NLS) and its molecular weight is too large to permit passive diffusion. Even so, data has emerged to suggest that LPP can shuttle to the nucleus and perform distinct functions [289, 299].

1.4.2.2 LPP localization to adhesions: LIM domain-containing proteins typically function as scaffold and/or adaptor proteins to mediate protein-protein interactions and signal transduction.

They have been implicated in the regulation of actin structure and dynamics, integrin-dependent adhesion/signaling, neuronal pathfinding, cell-fate determination and tissue-specific gene expression [297].

The ability of GFP-tagged LPP to localize at cell-cell contacts and adhesions was first observed in fibroblasts [298]. The second LIM domain is an important determinant of this process, as mutation of conserved zinc-binding cysteine and histidine residues significantly impairs LPP targeting to adhesions [295]. The most severe phenotype occurs when both LIM 1 and 2 are mutated, while mutations in the third LIM domain only modestly diminish adhesion targeting [295]. These results are in agreement with the observation that the LIM 3 sequence of LPP is more divergent than LIM 1 and 2 [295]. Others have since described co-localization of LPP with vinculin in rat aortic cells [284], palladin in smooth muscle tissues [300], and protein phosphatase 2A (PP2A) in HT1080 fibrosarcoma cells [301]. The precise functional roles of LPP within adhesions have yet to be elucidated, although recent evidence strongly suggests an important role in regulating cell migration and invasion [279, 280].

1.4.2 LPP interaction partners

LPP is a highly modular protein with numerous protein-protein interaction motifs (Fig. 1.1). Binding sites for α -actinin, LIM and SH3 protein (LASP), palladin, PP2A, scrib, supervillin and VASP have implicated LPP in multiple biological and cellular processes.

1.4.2.1 α -actinin: α -actinin is an actin-binding protein that localizes to the leading edge of cells [302], lamellipodia [303], filopodia [304], adhesions [305, 306], invadopodia [307], and stress fibers [303, 308]. While α -actinin lacks G-actin binding and actin initiation/nucleation ability, it functions to crosslink actin, promote cell migration [309, 310], stimulate adhesion maturation [220], and promote invadopodia formation [311]. It interacts with LPP through an α -actinin binding domain (ABD) in the PRR (amino acid residues 41-57) [294, 295]. Six core residues (FAPVVA in human LPP and YAPVVA in mouse LPP) allow LPP to bind the central-rod region of α -actinin, which contains spectrin-like repeats 2 and 3 [294]. Interestingly, overexpression of α -actinin isoforms has been identified in many different cancers, including breast cancer [312].

1.4.2.2 LASP: LASP is a nebulin-family LIM containing protein involved in actin binding and cytoskeletal re-organization. It was first identified from a cDNA library of metastatic axillary

lymph nodes and since then LASP overexpression has been implicated in breast and ovarian cancers [313]. LASP interacts with an XPPPP motif within the PRR of LPP via its SH3 domain [314]. Interestingly, MEFs that lack LASP (LASP^{-/-}) migrate more rapidly and exhibit increased adhesion dynamics. It has been postulated that these effects are due to compensation by LPP, which is upregulated by 2-fold in the absence of LASP [315].

1.4.2.3 Palladin: Palladin is a member of the palladin/myotilin/myopalladin family of actin-associated scaffolds responsible for cell shape, adhesion, motility, contraction and invadopodia formation [316-318]. Like LPP, palladin is abundantly expressed in mesenchymal cells and has been found in stress fibers, adhesions and cell-cell junctions [316]. In human iliac vein SMCs, palladin is found to co-localize with LPP and α -actinin during cell spreading [300]. Palladin interacts with the first and second LIM domains of LPP through an N-terminal region [300]. LPP and palladin expression appear to be co-regulated, as FAK null cells exhibit decreased LPP and palladin levels; however, their expression can be rescued by paired-related homeobox gene-1 (PRX1) and angiotensin II [300].

1.4.2.4 PP2A: PP2A is a ubiquitously expressed serine/threonine phosphatase that regulates many cellular processes including cell proliferation, signal transduction, cell motility and cytoskeletal dynamics [319]. Its core structure is composed of a 36 kDa catalytic C subunit (PPP2CA/B, α and β isoforms) and a 65 kDa structural/scaffold A subunit (PR65 or PPP2R1A/B, α and β isoforms), which is frequently associated with a regulatory B subunit (B, B', B'' or B''') that dictates subcellular localization and substrate specificity [320, 321]. It has recently been shown that the B'' subunit PR130 interacts with the LIM domains of LPP [301]. PP2A activity is required for efficient cell migration on collagen I as siRNA-mediated knockdown of PR130 impairs wound closure. Interestingly, PR130 is absent from mature (non-dynamic) adhesions where LPP accumulates. This suggests that PR130 must dissociate from the LIM domains of LPP for adhesion stabilization to occur [301]. Alterations of PP2A subunits and binding proteins have been implicated in many cancers including brain, breast, liver and lung [319, 322].

1.4.2.5 Scrib: Scrib is a member of the leucine-rich repeat and PDZ (LAP) family of proteins involved in cell shape, adhesion and polarity [323]. LPP-scrib interactions are mediated through the C-terminal region of LPP and the PDZ domain of scrib [323]. Both proteins are co-localized at cell-cell contacts; however, scrib is dispensable for LPP targeting. Likewise, LPP is dispensable for targeting scrib to cell-cell contacts and adhesions [323]. In zebrafish, the proteins

cooperate to mediate convergence & extension movements during gastrulation [324]. Scrib has been found to act as either a tumor suppressor or tumor promoter depending on the context, and has also been implicated in skin carcinogenesis [325], lung cancer [326] and prostate cancer [327]. Its mislocalization or dysregulation has been implicated in breast cancer formation and metastasis [328-330].

1.4.2.6 *Supervillin:* Supervillin (SVIL) belongs to the gelsolin superfamily of proteins responsible for actin organization [331]. It was first characterized as a tightly bound peripheral membrane protein that interacts with actin filaments [332]. Further studies showed that SVIL and other family members (gelsolin, adseverin, advillin, villin, CapG and flightless I) sever actin filaments by weakening non-covalent bonds between individual actin molecules [331, 333]. In doing so, SVIL can regulate actin assembly and disassembly within the cytosol. Gelsolin family members have been implicated in numerous cellular processes including, but not limited to, cell migration and invasion. SVIL can interact directly with the LIM domains of LPP and TRIP6, but not zyxin, through residues 342-571 [334]. SVIL localization to TRIP6 containing adhesions enhances their assembly and disassembly rates [334] while SVIL binding to myosin II mediates cellular contractility and podosome dynamics [335]. SVIL can also increase Rac1 activation to promote cell spreading [336]. Overexpression of SVIL has been found to enhance gelatin degradation and invadopodia formation through binding to cortactin [337]. Indeed, SVIL is observed in cortactin/Tks5/cdc42 labeled podosomes and invadopodia [337].

1.4.2.7 *VASP:* VASP is a member of the Ena/VASP family of proteins comprised of VASP, Mena and Evl. VASP is often found in lamellipodia, filopodia and adhesions [338], and plays a role in cell adhesion, cell motility and actin polymerization [339-342]. LPP has 2 ActA repeats (FPPPP) located in its PRR that bind the EVH1 domains of VASP family members [343]. VASP also interacts with G and F-actin, and regulates actin assembly, cellular contraction and invadopodia formation [248]. Moreover, VASP increases the rate of actin polymerization, promotes F-actin elongation, and blocks the barbed end of growing actin filaments from binding capping proteins [344]. Overexpression and phosphorylation of Ena/VASP family members have been implicated in the formation of breast [345-349], colon [350-352] and lung cancers [353].

1.4.3 Biological functions of LPP

LPP's complex domain structure and diversity of interacting partners allow it to regulate distinct biological processes relevant to cell migration and invasion. As previously mentioned, LPP is abundantly expressed in SMCs [284]. LPP knockdown in SMCs results in decreased cell migration [354], while transfection of EGFP-LPP causes a 2-fold increase in EGF-induced migration [300]. Moreover, exogenous expression of LPP rescues cell spreading and EGF-stimulated motility in FAK null embryonic fibroblasts [300]. In Madin-Darby canine kidney cells, LPP co-localizes to adhesions in the basal plane and cell-cell contacts in the apical plane [355]. Knockdown of LPP diminishes E-cadherin dependent cell-cell adhesion and tight junction formation, but increases cell-substrate adhesion [355]. LPP localization to cell-cell junctions likely occurs through interactions with α -actinin [356].

Knockout/knockdown studies in model organisms demonstrate the cumulative effect of changes in LPP dependent cell-cell and cell-ECM adhesion. Morpholino-mediated knockdown of LPP in zebrafish impairs convergence & extension movements during gastrulation due to reduced directed migration of paraxial cells [324]. Interestingly, LPP expression is significantly diminished in zebrafish treated with morpholinos targeting Wnt11. Loss of LPP in female C57BL/5 J mice results in partial embryonic lethality [285]. While male $LPP^{-/-}$ mice exhibit normal fertility, females in $LPP^{-/-} \times LPP^{-/-}$ crosses produce low numbers of offspring. $LPP^{-/-}$ mice that reach adulthood do not display any overt phenotypes; however, $LPP^{-/-}$ MEFs migrate more slowly and exhibit decreased viability compared to $LPP^{+/+}$ MEFs. Furthermore, $LPP^{-/-}$ MEFs have reduced expression of LPP binding partners, including α -actinin, PR130 and scrib [285].

1.4.4 LPP augments the malignant phenotypes of cancer cells

The first associations between LPP and cancer emerged with the discovery of High Motility Group AT-Hook2 (HMGA2)-LPP fusion proteins in lipoma and other mesenchymal tumors [295, 298]. Indeed, exogenous expression of HMGA2-LPP induces malignant transformation of NIH3T3 cells while wildtype HMGA2 does not. Consequently, HMGA2-LPP transformed cells grow in soft agar and induce tumors in athymic mice [357].

LPP was subsequently identified as one of the most upregulated proteins in invasive endometrial carcinomas [299]. In this context, it was found to enhance cell migration and invasion by acting as a transcriptional regulatory partner of ETV5. ETV5 is a member of the Polyomavirus

Enhancer Activator protein (PEA3) subfamily of ETS transcription factors. It activates the zinc finger E-box binding transcription factor Zeb1, which represses E-cadherin to facilitate EMT [299]. LPP responds to extracellular EGF stimulation in an ETV5-dependent manner and induces a complete re-organization of cell-cell and cell-substrate contacts to promote tumor invasion [299].

Most recently, work by our group shows that LPP is an important driver of cell migration, invasion and metastasis in breast cancer [279-281]. LPP is required for TGF β -induced migration of ErbB2-expressing cells; cells expressing endogenous levels of LPP exhibit an increase in cell migration following EMT, while shRNA-mediated knockdown of LPP abolishes this effect [279, 281]. TGF β enhances LPP localization to adhesions which permits faster assembly and disassembly of these structures [281]. Accordingly, LPP constructs harboring a mutant LIM domain (LPP-mLIM1) or a deleted α -actinin binding domain (LPP- Δ ABD) fail to support TGF β -induced cell migration [280, 281]. LPP is also required for invadopodia formation, breast cancer cell extravasation, and the establishment of lung metastases [280]. *In vitro* gelatin degradation assays indicate that knockdown of LPP significantly impairs invadopodia formation in response to TGF β without influencing MMP expression or activity. Furthermore, LPP co-localizes with actin and Tks5, an obligate component of invadopodia [253], at sites of gelatin degradation. The ability of LPP to support invadopodia formation requires LIM1 and ABD domains. *Ex ovo* imaging of LPP and Tks5 in a chick chorioallantoic membrane assay shows that breast cancer cells harboring LPP-mLIM1 and LPP- Δ ABD fail to extravasate out of the vasculature [280]. Consequently, the ability of LPP-mLIM1 and LPP- Δ ABD mutants to rescue the formation of lung metastases is significantly impaired compared to wildtype LPP [280]. Finally, LPP is a Src substrate and phosphorylation of three tyrosine residues (Y245/Y301/Y302) is required for TGF β -induced breast cancer cell invasion. *In vivo* data demonstrates that simultaneous mutation of Y245/Y301/Y302 significantly decreases the number of surface metastatic lesions, albeit not to the same extent as knockdown of LPP [280]. Interestingly, these phosphorylation events are dispensable for TGF β -induced increases in breast cancer cell migration [280]. Taken together, these data support a novel role for LPP in modulating two fundamental processes linked to breast cancer metastasis: (1) increased cell migration via growth factor stimulation and (2) enhanced invasion through the promotion of invadopodia formation (Fig. 2.2).

1.4.5 LPP as a suppressor of malignant cancer phenotypes

Interestingly, studies in other cancer models have implicated LPP as a negative regulator of cancer progression. In lung cancer, MMP15 is a direct transcriptional target of LPP and ETV5, which degrades N-cadherin to weaken cell-cell interactions [358]. Knockdown of LPP and ETV5 in PC14PE6 cells increases cell-cell adhesion, which fosters collective cell migration and enhances lung cancer cell dissemination [358]. Thus, loss of LPP, ETV5 or MMP15 is a prognostic marker for increased malignancy in this context.

In a similar fashion, LPP was identified as a predictor of better survival in B-cell lymphoma [359]. LPP, LMO2, MME and FOXP1 are part of a cell-of-origin signature in diffuse large B-cell lymphoma. When highly expressed, this signature is correlated with better overall survival and progression free survival in patients treated with RCHOP (Rituximab, cyclophosphamide, doxorubicin, vincristine, prednisone) [359]. These results indicate that the ability of LPP to modulate the malignant phenotypes of cancer cells can be highly context dependent.

1.4.6 LPP as a mechanosensor

Recent studies implicate LPP as a mechanosensitive protein capable of responding to extracellular forces. In the myocardium, increased LPP expression is observed in the hearts of aortic-banded rats (pressure overload induced cardiac hypertrophy), suggesting that hemodynamic load can regulate LPP levels [360]. Nitro-L-arginine methyl ester (LNAME), an inhibitor of nitric oxide synthase (NOS), significantly increases LPP expression in cardiac myocytes [360, 361]. Conversely, cyclic mechanical stretching of myocytes, which mimics *in vivo* mechanical stress, causes a decrease in LPP expression and membrane localization [360, 361]. In cultured cells, LPP expression and subcellular localization also appear to be regulated by substrate stiffness. LPP localizes to long, broad adhesions at the periphery of SMCs cultured on rigid surfaces. In contrast, cells grown on compliant matrices show LPP localization to small adhesions and punctate structures [362].

Taken together, these observations implicate LPP as a mechanosensor that responds to diverse cues in physiological conditions such as myofibrillogenesis [360, 361] and vascular injury [362]. This is not unexpected as the role of LIM domain-containing proteins in sensing mechanical changes in the ECM is now starting to emerge [363]. While zyxin serves as the “prototype” mechanosensor [292, 364-368], considerably less is known about the mechanobiology of LPP. It

would be interesting to determine whether LPP expression and localization are correlated with ECM composition, protein density and mechanical stiffness. An intriguing hypothesis is that LPP expression and localization dictate cellular modes of migration in response to matrix stiffness.

1.5 MICROSCOPY

The overarching aim of the current thesis was to define the molecular mechanisms that regulate breast cancer progression. Previous studies by our group demonstrate that TGF β enhances the migration and invasion of breast cancer cells through Boyden chamber assays in a p46/52ShcA- and LPP-dependent manner [123, 125, 279, 280]. While transwell assays are useful for defining gross cellular phenotypes at a population level, they fail to provide insight into the mechanisms of cell migration at the single cell level. To gain a more in-depth understanding of how p46/52ShcA and LPP regulate breast cancer cell migration, we employed a variety of advanced microscopy techniques. In the following sections, we describe how light, fluorescence and super-resolution microscopy can be used to observe the structure and function of living cells, subcellular compartments, protein dynamics and even protein-protein interactions involved in cancer cell migration.

1.5.1 Contrast

Most cellular tissue is transparent and colorless. The intensity of a given object and the local background tend to be very similar when performing brightfield microscopy making it difficult to identify any details. Several different techniques have now been developed to enhance the interest contrast of living specimens, including phase contrast and differential interference contrast (DIC).

Phase contrast microscopy utilizes an etched glass plate to ‘speed up’ surrounding light that passes directly through the sample relative to light diffracted by the sample. Destructive interference between the two components causes thick, or high refractive index areas, of the specimen to appear dark on a light background [369]. On the other hand, DIC microscopy capitalizes on the birefringent properties of modified Wollaston prisms to translate phase shifts into measurable amplitude differences [370-372]. A condenser prism generates two orthogonal sheared light waves, known as ordinary and extraordinary rays, which interact with different regions of the sample. Subsequent recombination of these rays with an objective prism causes

constructive and destructive interference which generates contrast. DIC produces images with a higher resolution than phase contrast because it can utilize the microscope at full numerical aperture without the masking effect of phase plates or condenser annuli; however, DIC prisms are generally much more expensive than phase contrast objectives.

1.5.2 Fluorescence

Cells and tissue samples can also be labelled with fluorescent dyes. Fluorescence is a sensitive technique that can be used to observe subcellular structures in fixed and living samples. It is a naturally occurring process that arises when a molecule in its relaxed ground state absorbs a photon of light [373, 374]. This excess energy causes the molecule to enter an excited state where it is unstable. Vibrational relaxation and other non-radiative transitions provide some relief; ultimately though, the molecule returns to the ground state by releasing energy in the form of a photon. The energy associated with fluorescence emission is less than the excitation light due to vibrations, heat and other processes. As a result, the wavelength of emitted light is always greater than the wavelength of absorbed light. This difference in wavelength, known as Stokes' shift, is important for fluorescence microscopy as it allows for the separation of signals with a filter cube. Molecules that undergo this process of light absorption and immediate release (within nanoseconds) are called fluorophores. DNA, lipids and proteins can be labelled directly or indirectly with a variety of extrinsic fluorophores. In the field of cell biology, proteins are commonly visualized with organic fluorophores and genetically encoded fluorescent proteins.

1.5.2.1 Organic fluorophores: Organic fluorophores are typically conjugated to 'secondary' antibodies that recognize 'primary' antibodies bound to a protein of interest. They have a large aromatic structure with π bonds that support electron delocalization following light excitation. Fluorescein (λ_{abs} 490 nm, λ_{em} 525 nm) and rhodamine (tetramethyl rhodamine isothiocyanate) (λ_{abs} 557 nm, λ_{em} 576 nm) were widely used for the first fluorescently conjugated antibodies. Since then, numerous other fluorophores (Alexa Fluor, Janelia Fluor, STAR, ATTO series) have been generated through chemical modification of these core scaffolds and others [375-377]. Molecular substitutions have generated fluorescent probes with fine-tuned absorption and emission spectra that span the entire visible spectrum and extend into the infrared. These synthetic dyes also have improved brightness and photostability, which allow them to be used for super-resolution applications. One major drawback of this labelling technique is the requirement for

primary antibodies to specifically label the protein of interest. Commercially produced antibodies are not available for many proteins. Of those that are available, many are also not suited for immunofluorescence due to non-specific binding or poor reproducibility between batches and cell lines [378]. Moreover, the sample must be permeabilized with a detergent for the antibodies to reach their target.

1.5.2.2 Fluorescent proteins: Fluorescent proteins provide a powerful alternative for labelling proteins in living and fixed samples. These proteins can be genetically encoded to tag nearly any protein of interest. Green fluorescent protein (GFP) was the first fluorescent protein to be expressed in eukaryotic cells [379-381]. GFP is a 238 amino acid protein folded into an 11-stranded β barrel that accommodates an internal distorted helix [382, 383]. Posttranslational modification of amino acid residues 65-67 within the helix form the chromophore group responsible for fluorescence [384, 385]. Wildtype GFP isolated from the jellyfish *Aequorea victoria* has a maximum absorption wavelength of 395 nm and an emission wavelength of 508 nm [386, 387]. Modification of serine 65 to threonine (S65T) suppressed the 395 nm excitation peak and enhanced a secondary 475 nm peak five- to six-fold [388]. Subsequent modification of phenylalanine 64 to leucine (F64L) increased the brightness of GFP, leading to the creation of enhanced GFP (EGFP) with a maximum absorption wavelength of 488 nm and an emission wavelength of 508 nm [389]. Additional mutations to the chromophore (especially Y66) and adjacent amino acid residues resulted in an array of blue-shifted and red-shifted variants [381, 383, 390]. Finally, other mutations were introduced to improve protein folding efficiency at 37°C, reduce aggregation at high concentrations and increase diffusibility within cells [381, 391, 392].

Following the success of GFP, researchers searched for fluorescent proteins in other marine organisms resulting in the discovery and cloning of approximately 30 distinct fluorescent proteins [393, 394]. Interestingly, these fluorescent proteins possessed the same arrangement of key secondary structure elements as GFP [393]. Intensive engineering of these fluorescent proteins further led to a diverse array of tags that span the visible spectrum. For example, the red-shifted protein dsFP593 (λ_{abs} 573 nm, λ_{em} 593 nm) isolated from *Discosoma* coral [395] was modified to generate a new color series of fluorescent proteins, including mCherry [396]. More recently, bacterial phytochromes (BphPs) that absorb light in the range of 650-700 nm [397] have been used to generate infrared fluorescent proteins such as mIFP and iRFP [398-403]. These fluorescent proteins have a markedly different protein structure than GFP family members. BphPs are

covalently bound to the chromophore biliverdin, a linear tetrapyrrole with conjugated double bonds that is produced by heme catabolism [404, 405]. Together, GFP, dsRed and BphP fluorescent proteins facilitate multi-color imaging of different protein targets within living cells.

1.5.3 Photobleaching and phototoxicity

Organic fluorophores and fluorescent proteins typically undergo thousands of excitation and relaxation events. An electron in a singlet ground state ($\uparrow\downarrow$) is usually excited to a higher singlet state while maintaining its spin [406]. Occasionally, however, the spin of the electron is reversed giving rise to an excited triplet state; this excited electron is no longer able to relax to the ground state through photon emission, thereby trapping the fluorescent molecule in a 'dark' triplet state [373, 407, 408]. The probability of this forbidden transition is low due to the Pauli exclusion principle, and the molecule can eventually exit the triplet state through radiative decay known as phosphorescence; however, this is a relatively slow process (μs to ms) compared to fluorescence (ns) [373]. As a result, it is possible to push almost all available fluorescent molecules into the dark state. Stochastic optical reconstruction microscopy (STORM) is a super-resolution microscopy technique that exploits this phenomenon (see section 1.7.1). In general, however, intersystem crossing into the triplet state is undesirable as excited fluorescent molecules can react with molecular oxygen ($^3\text{O}_2$), resulting in permanent destruction of the fluorophore (photobleaching) and the production of damaging oxygen radicals (phototoxicity) [408]. Therefore, it is useful to consider the photostability of a fluorophore, which describes the rate of photobleaching or the time it takes for emission intensity to reach half of its initial value [409].

1.5.4 Reactive oxygen species (ROS)

ROS species such as superoxide anion (O_2^-), hydrogen peroxide (H_2O_2) and hydroxyl radical ($\text{OH}\bullet$) can negatively impact cell health by damaging DNA, lipids and proteins [410-412]. $\text{OH}\bullet$ radicals add to the double bonds of heterocyclic DNA bases (adenine, cytosine, guanine, thymine, uracil), giving rise to DNA radicals that further react to generate modified bases and sugars, base-free sites, strand breaks, DNA-protein cross-links. For example, $\text{OH}\bullet$ can react with thymine bases to form 5-(uracilyl)methyl radicals, which can further react with neighboring guanine and adenine bases to produce intra-strand or possibly inter-strand crosslinks [410]. Similarly, guanine radical cations created by $\text{OH}\bullet$ can undergo addition with lysine to form DNA-

protein cross-links [410]. Collectively, these reactions lead to genomic instability. ROS can also interfere with mitochondrial function by reacting with lipids within membranes, in a process known as lipid peroxidation [411]. For example, H₂O₂ treatment decreases NADH/FAD⁺ redox ratio and mitochondrial membrane potential ($\Delta\Psi_m$) in a concentration-dependent manner [413]. Finally, ROS can interfere with the enzyme activity of a protein or the binding capacity of a transcription factor by oxidizing the sulfhydryl group on cysteine amino acids [414]. Oxidation of cysteine residues can also cause the formation of disulfide linkages within or between two proteins. In the latter case, this may cause di- or oligomerization [414].

1.5.4.1 Superoxide dismutase (SOD): ROS production can be counterbalanced by antioxidant enzymes such as superoxide dismutase (SOD), catalase, glutathione peroxidase, peroxiredoxins and thioredoxins. SOD proteins are the first line of defense against ROS. They are ubiquitous enzymes that use metal ions to catalyze the conversion of O₂⁻ to H₂O₂ and O₂ ($2O_2^- + 2H^+ \rightarrow H_2O_2 + O_2$) [415]. All aerobic organisms express SOD proteins because numerous metabolic reactions, such as the mitochondrial electron transport chain, produce ROS [416]. Loss of SOD activity severely impacts organism survival due to increased levels of oxidative damage [417-420]. Mammals possess three classes of SOD proteins [421, 422]. Cu/ZnSOD (also known as SOD1 in humans) is primarily localized to the cytoplasm with a smaller fraction localized to the intermembrane space of mitochondria [423, 424]. Another Cu/ZnSOD with a distinct protein structure (known as SOD3 in humans) is found extracellularly [425, 426]. In contrast, MnSOD (also known as SOD2 in humans) localizes to the mitochondrial matrix [424].

1.5.4.2 Catalase: While SOD proteins effectively eliminate highly reactive O₂⁻ within cellular compartments, H₂O₂ must also be eliminated to prevent cellular damage. Catalases convert H₂O₂ into H₂O and O₂ with high efficiency ($2H_2O_2 \rightarrow 2H_2O + O_2$). There are three classes of catalases; however, only class I are found in mammalian cells [427]. Class I catalases possess a prosthetic group of ferric (Fe^{III}) protoporphyrin IX, which is first oxidized to a high-valent iron intermediate, known as Compound I (Fe^{IV}=O), and then reduced back to the resting state by reacting with another H₂O₂ [428]. These catalases are mainly found in peroxisomes due to the presence of a peroxisome-targeting signal sequence [429]; however, a smaller fraction has also been identified in mitochondria [430]. Catalase treatment prevents the degeneration of Down's syndrome neurons, which exhibit three- to four-fold more intracellular ROS than normal neurons [431]. Addition of exogenous catalase can also attenuate apoptosis induced by antitumor drugs

[432]. Thus, class I catalase enzymes play an important role in reducing intracellular ROS arising from a variety of sources.

1.5.4.3 Glutathione peroxidase (GPx): Glutathione peroxidase (GPx) catalyzes the breakdown of H₂O₂ and other hydroperoxides into water (ROOH + 2 glutathione → glutathione disulfide + ROH + H₂O) [433]. The reaction is comprised of two independent events: (1) oxidation of reduced GPx by hydroperoxide and (2) reduction of oxidized GPx by glutathione. As a result, GPx requires several other enzymes and cofactors to reduce H₂O₂ levels: glutathione reductase, glucose-6-phosphate dehydrogenase (G6PD), reduced glutathione, nicotinamide adenine dinucleotide phosphate (NADPH) and glucose 6-phosphate [433]. There are at least eight different isozymes of GPx in humans; GPx1-4 and 6 contain a selenocysteine residue while GPx5, 7 and 8 are selenium-independent [434-436]. GPx1 is the most abundant isozyme and is expressed in almost all tissues [437, 438]. It is primarily localized to the mitochondria and cytoplasm, with some localization to peroxisomes [439-441]. GPx1 is protective against many apoptotic stimuli, including H₂O₂ and paraquat treatment [442-444]. GPx4 is another important isozyme that catalyzes the reduction of lipid peroxides and repairs oxidatively damaged DNA [445-452]. Targeted disruption of the GPx4 locus (^{-/-}) causes embryonic death by mid-gestation (E7.5) and MEFs derived from GPx4 (^{+/-}) mice are more sensitive to inducers of oxidative stress, such paraquat, tert-butylhydroperoxide and H₂O₂, compared to wildtype littermate controls [449].

1.5.4.4 Peroxiredoxins (Prx) and thioredoxins (Trx): Peroxiredoxins (Prx) are ubiquitous family of enzymes that reduce H₂O₂, peroxyxynitrite and other organic hydroperoxides using redox-active cysteine residues (ROOH + 2e⁻ → ROH + H₂O) [453]. There are three classes of Prx enzymes: ‘typical’ 2-Cys (PrxI, PrxII, PrxIII and PrxIV), ‘atypical’ 2-Cys (PrxV) and 1-Cys (PrxVI) [434, 453]. Prx I, II and VI are primarily localized to the cytoplasm; PrxIII is restricted to mitochondria; PrxIV is primarily localized to the endoplasmic reticulum; and Prx5 is found in the cytoplasm, mitochondria and peroxisomes [454]. Following oxidation, typical 2-Cys and atypical 2-Cys are reduced by thioredoxin (Trx) [453-455], whereas 1-Cys enzymes are reduced by glutathione [456, 457].

Trx are a small group of ubiquitous proteins with two active cysteine residues that undergo reversible oxidation/reduction [458]. Two Trx isoforms have been identified in mammals. Trx1 is mainly localized to the cytoplasm but it can translocate to the nucleus or be secreted extracellularly [459-461]. In contrast, Trx2 is predominantly found in the mitochondria [462]. Trx proteins are

reduced by thioredoxin reductase (TrxR) using flavin adenine dinucleotide (FAD) and NADPH [463-467]. Cellular mechanisms for eliminating ROS are summarized in Fig. 1.3.

1.5.4.5 Fluorescent probes for detecting ROS: Numerous fluorescent probes have been developed to detect ROS production within cells. MitoSOXTM Red is a cationic derivative of dihydroethidium that reacts with O₂⁻ to form 2-hydroxyethidium. Once generated, 2-hydroxyethidium exhibits a fluorescence excitation/emission at ~400/590 nm. Oxidation products generated by other ROS species do not possess these spectral characteristics, making MitoSOXTM Red highly specific for O₂⁻ [468]. CellROXTM Deep Red is another commercially available probe that simultaneously detects O₂⁻ and OH•. In its oxidized form, CellROXTM Deep Red exhibits strong fluorescence excitation/emission at ~644/665 nm [469]. MitoSOXTM Red is selectively targeted to the mitochondria whereas CellROXTM Deep Red is localized to the cytoplasm. Although MitoSOXTM and CellROXTM are commonly used, it is important to note that there are many other fluorescent molecules for the sensitive and selection detection of ROS, reactive nitrogen species and reactive sulfur species [470]. Numerous probes are compatible with live-cell imaging; however, dye concentration and imaging conditions must be adjusted to prevent phototoxicity from the dyes themselves.

1.5.5 Mitigating photobleaching and phototoxicity

Oxygen plays a complex role in photobleaching and phototoxicity. On one hand, ³O₂ can undergo an electron transfer reaction with an unstable triplet state fluorophore to facilitate its return to the ground state. In doing so, oxygen restores the number of fluorescent molecules available for photon excitation. However, electron transfer to ³O₂ results in the formation of highly reactive singlet oxygen (¹O₂), which can permanently destroy fluorophores through structural alterations (photobleaching). ¹O₂ can also form O₂⁻ which reacts with DNA, lipids and proteins leading to phototoxicity [471]. Several strategies have been employed to decrease photobleaching: removing ground state ³O₂, excited state ¹O₂, or excited triplet state molecules [472, 473].

1.5.5.1 Oxygen scavengers: Oxygen scavenging systems such as glucose oxidase/catalase (GOX/CAT) and protocatechuic acid/protocatechuate-3,4-dioxygenase (PCG) reduce dissolved ³O₂ levels by directly reacting with ³O₂. GOX/CAT uses the enzyme glucose oxidase to catalyze a reaction between glucose and ³O₂. The reaction generates gluconic acid and H₂O₂, which is subsequently broken down into ³O₂ and H₂O by catalase [474]. PCG is a more efficient system

that consumes $^3\text{O}_2$ without producing H_2O_2 [475]. Oxygen scavengers have been shown to reduce the rate of photobleaching; however, removal of oxygen enhances the lifetime of triplet state fluorophores [476-478]. The main consequences of trapping more fluorescent molecules in the dark state is that the sample appears dimmer and fluorophores can undergo blinking [479]. Depending on experimental conditions, there is also a greater probability that triplet state fluorophores will absorb a second photon of light, resulting in structural changes to the molecule and photobleaching [480-482].

1.5.5.2 Singlet oxygen quenchers: Another method to decrease the rate of photobleaching is to reduce the population of $^1\text{O}_2$ that can react with fluorescent molecules in the ground state. Singlet oxygen quenching may be physical and/or chemical [483]. Molecules with many electrons, such as amines, azides, iodide, phenols and sulfides, form charge transfer complexes with singlet oxygen to facilitate a transition to the triplet state ($^1\text{O}_2 \rightarrow ^3\text{O}_2$) [484, 485]. Ascorbic acid (vitamin C), β -carotene, peptides, tocopherols and phenolics can also reduce singlet oxygen ($^1\text{O}_2 \rightarrow \text{O}_2^-$) [485-487]. SOD enzymes convert O_2^- into H_2O_2 , which is further degraded into H_2O and $^3\text{O}_2$ by ascorbic acid and glutathione [488]. Accordingly, *n*-propyl gallate (nPG) [475, 486, 489, 490], ascorbic acid [475, 482, 486], 6-hydroxy-2,5,7,8-tetramethylchroman-2-carboxylic acid (Trolox: a water-soluble vitamin E analog) [491, 492] and glutathione [493] have all been shown to reduce photobleaching. These chemicals are more advantageous than oxygen scavengers because molecular oxygen is still present to facilitate triplet state fluorophore relaxation.

1.5.5.3 Triplet state quenchers (TSQ): Triplet state quenchers (TSQs) undergo electron transfer reactions directly with triplet state fluorescent molecules to facilitate fluorophore return to the ground state and reduce the formation of $^1\text{O}_2$ [472]. For example, a fluorescent molecule in the triplet state (^3dye) transfers energy to 1,3,5,7-cyclooctatetraene (COT) in the ground state (^1COT), resulting in dye relaxation ($^3\text{dye} \rightarrow ^1\text{dye}$) and COT excitation ($^1\text{COT} \rightarrow ^3\text{COT}$). ^3COT has a relatively low energy triplet state and returns to the ground state with minimal energy loss via conformational changes [494]. Accordingly, COT [486, 492] and other TSQ molecules, including β -mercaptoethanolamine (MEA) [477], *para*-nitrobenzyl alcohol (NBA) [492] and 1,4-diazabicyclo[2,2,2]octane (DABCO) [493], have been shown to reduce photobleaching. Unfortunately, many of these molecules are toxic to living samples.

1.5.5.4 Other methods: Oxygen scavengers, singlet oxygen quenchers, and TSQs enhance photostability to varying degrees depending on the fluorophore. These protective agents can be

applied in various combinations to achieve even greater photostability; however, they may also adversely affect cell health [472, 479]. Other techniques such as points accumulation for imaging in nanoscale technology (PAINT) [495] and DNA-PAINT [496, 497] have been developed to prevent signal decay by using fluorescent probes that transiently bind to a target and switch on. Fluorescence intensity remains constant throughout the imaging session because fluorescent molecules are replenished from a large pool of probes in the surrounding medium; however, photobleaching and thus ROS production continue to occur. As a result, recent efforts have focused on developing novel microscopy techniques that reduce unnecessary light exposure. For example, light sheet [498, 499] and lattice light sheet microscopy [500] illuminate cross-sections of the sample rather than the entire 3D volume. Previous studies propose that lower light levels with longer exposure times can also reduce photobleaching and phototoxicity [501-504]. We continued to explore this idea in the present thesis as it can be applied relatively easily to any standard microscope.

1.6 LIGHT MICROSCOPY TECHNIQUES

1.6.1 Widefield fluorescence microscopy

Widefield fluorescence microscopy is an imaging technique that uses a parallel beam of light to illuminate a sample and excite fluorophores within the field of view. It is similar to brightfield microscopy in that a light source is used to visualize the sample; however, filter cubes are used to limit which wavelengths of light illuminate the sample [505]. Each filter cube contains (1) an excitation filter to select wavelengths of excitation light, (2) a dichroic mirror which reflects excitation light but passes emission light, and (3) an emission filter which selects fluorescence emission of the sample while blocking any reflected incident light [506, 507].

1.6.1.1 Excitation light sources: There are many different types of light sources available for fluorescence imaging, including mercury short arc lamps, mercury halide lamps and light emitting diodes (LEDs) [508]. LEDs are slowly replacing all other light sources due to their many benefits and relatively few cons. They have discrete color peaks to excite almost any fluorophore, a very long lifetime (~10,000 h), do not decay over time, and do not contain mercury [509]. Moreover, LEDs can be triggered to turn on and off within microseconds, light intensity can be precisely controlled, and they do not generate heat [510].

1.6.1.2 Multi-color imaging: Filter turrets can be used to switch between filter cubes and image multiple fluorescent dyes or proteins sequentially. ‘Single’ filter cubes with one excitation filter, one dichroic mirror, and one emission filter are preferred for multi-color imaging because they can be equipped with long pass or wide band pass emission filters that capture a large range of wavelengths. This results in a brighter image for the same excitation light intensity. Unfortunately, filter switching may not be amenable to multi-color time-lapse imaging of rapid events due to a significant delay between colors (hundreds of milliseconds) [511]. One solution is to image multiple fluorescent proteins with ‘dual’, ‘triple’ or ‘quad’ filter cubes [512]. These filter cubes possess multiple sets of excitation filters, dichroic mirrors and emission filters to image two, three, or four different sets of fluorophores simultaneously. A major drawback of these filter cubes is that they have decreased sensitivity for each color due to narrow band pass filters. There is also potential for crosstalk between channels if fluorophores have wide emission spectra. Another solution is to split the emission signal and capture fluorescence data on multiple detectors [513]. A long band pass filter can be used for each color in this scenario resulting in brighter images. A major drawback of this technique is that the detectors must be spatially aligned in x,y,z by manual adjustment and post-image processing.

1.6.1.3 Emission light detectors: Interline-charged coupled devices (CCD), electron multiplied (EM)-CCD cameras, and scientific complementary metal oxide semi-conductors (sCMOS) are commonly used for scientific imaging [514-517]. Interline-CCD cameras use potential wells to capture light in the form of electrons. Photoactive pixels are excited by light, followed by a horizontal shift of electrons to an opaque mask and a vertical shift to the serial register. Pixels are read out one at a time by a readout amplifier and converted to a digital signal to be displayed on a computer. Read speed is an important consideration when performing a time-lapse experiment that requires rapid acquisition of many frames. Serial read-out of information can be a slow process, resulting in lower frame rates. EM-CCD cameras have a slightly greater frame rate and possess a high voltage serial register to multiply electrons. This makes them particularly suited for imaging dim samples. Unfortunately, read noise is relatively high because noise pixels are also amplified. In contrast, sCMOS cameras are affordable and fast because every pixel has its own amplifier circuit for converting electrons to a voltage signal. Pixels can be read out simultaneously to image rapidly occurring events. In the past, these detectors had a relatively high dark current compared to interline-CCD and EM-CCD cameras resulting in noisier images

when using longer exposure times; however, recent advancements have significantly reduced dark noise, making sCMOS cameras the preferred detector for most fluorescence microscopy applications [518].

1.6.2 Confocal microscopy

Conventional fluorescence microscopy techniques illuminate the entire 3D volume within a field of view; an objective lens projects a beam of light that passes through the sample and collects all corresponding fluorescence emission. As a result, secondary fluorescence outside of the focal plane is also captured. This secondary fluorescence often interferes with the resolution of features that are in focus, especially if the sample is thick. One method of eliminating out-of-focus light is to place a pinhole in front of the detector.

Confocal laser scanning microscopes (CLSMs) use a light source pinhole to focus excitation light into a point within the focal plane of the objective [519]. Computer-controlled mirrors driven by galvanometers scan the point (in x,y) across the field of view. Fluorescence emission captured by the objective is “descanned” by the mirrors and passes through a secondary pinhole situated in a conjugate plane (confocal) to the light source pinhole aperture before reaching a detector. The excitation point is a narrow beam of light with x , y and z dimensions. Therefore, the size of the pinhole can be adjusted to regulate the amount of out-of-focus light (optical section thickness) that can pass to the detector.

1.6.2.1 Excitation light sources: CLSMs use a variety of lasers to excite fluorescent molecules. Gas lasers such as argon ion (Ar), krypton (Kr), krypton-argon and helium neon (HeNe) have discrete excitation wavelengths [520-522]. For example, Ar lasers emit 12 wavelengths of light between 351.1 and 528.7 nm and another wavelength at 1092.3 nm; the most powerful bands are 488 and 514.5 nm. In contrast, most HeNe lasers operate at 632.8 nm. Solid state lasers use a solid medium to generate a single wavelength of light. A single crystal is infused with a small percentage of a “doping” element such as chromium (Cr), neodymium (Nd), erbium (Er), thulium (Tm) or ytterbium (Yb) [521-523]. Energy is transferred (or pumped) from an external source into the crystal to generate light. Diode-pumped solid-state (DPSS) lasers are typically used. Finally, semiconductor lasers use a multi-layered medium composed of semiconductor materials to generate a single wavelength of light [522, 524, 525]. The base substrate is either gallium arsenide (GaAs) or indium phosphide (InP). Alloys made of Group III (aluminum [Al], Ga, In) and Group

V (phosphorus [P], As) elements are precisely layered on top of the base substrate, ensuring that they are lattice-matched to one another. GaAs-based lasers emit at any wavelength between 630 and 1100 nm, while InP-based lasers emit at any wavelength between 1100 and 2000 nm. As is the case with DPSS lasers, shorter wavelengths can be achieved by doubling or tripling the frequency of electrical pumping.

1.6.2.2 Multi-color imaging: CLSMs do not use a filter cube to select excitation and emission wavelengths when acquiring images. An excitation filter with a very narrow band (typically <0.4% of the desired wavelength) is used to select a laser line [519]. This filter (or plate) is especially important for gas lasers with several discrete excitation wavelengths. A diffraction grating or prism subsequently separates fluorescence emission into a continuous spectrum. Finally, a variable slit selects a band of wavelengths allowed to pass to the detector. The position and width of slit can be adjusted to select any part of the visible spectrum.

1.6.2.3 Emission light detectors: Most fluorescence microscopy techniques, including widefield (section 1.6.1), spinning disk confocal (section 1.6.3), TIRF (section 1.6.4), STORM (section 1.7.1) and PALM (section 1.7.2), use CCD, EMCCD or sCMOS cameras to generate images. Unfortunately, these cameras are not compatible with the laser scanning process used to illuminate samples on CLSMs. CLSMs use photomultiplier tubes (PMT), spectral detectors, avalanche photodiode (APD), and hybrid detectors (HyD) to amplify small emission signals captured during laser scanning [526-531].

PMTs are highly sensitive detectors that amplify fluorescence light emission through a series of electrodes. A photocathode at the tube opening converts incoming photons into electrons. These electrons are then passed through a series of metal channel dynodes and collected by an anode at the end of the tube. Each dynode releases additional electrons following impact resulting in a large signal amplification; the voltage (or gain) of the PMT can be adjusted to regulate the degree of amplification [526, 529]. Gallium arsenide phosphide (GaAsP) activated with cesium (Cs) is commonly used for fluorescence microscopy applications because of its relatively flat and high quantum efficiency for wavelengths within the visible spectrum (300-720 nm) [532].

Spectral detectors use an array of detectors to acquire several images of the same field of view at different wavelengths. A diffraction grating is used to separate fluorescence emission into its individual components. The size of the diffraction grating can be adjusted to change the degree of light separation and therefore the width of the band entering each PMT. For example,

fluorescence emission can be split into 9.8 nm segments across 32 detectors to generate a separate image from each channel. Images can then be added together to create a single three-dimensional image (x, y, λ) which reveals the relative contribution of each spectral band to the combined image [527, 528]. Spectral profiles of individual fluorophores are useful for untangling mixed fluorescence signals arising from multiple fluorophores. Mathematical algorithms can perform linear unmixing to resolve the spatial contribution of each fluorophore. This allows multiple fluorophores with similar emission spectra to be imaged within the same sample.

1.6.3 Spinning disk (SD) confocal microscopy

CLSM successfully eliminates out of focus light with a pinhole to enhance contrast. By controlling the depth of field, optical sections of thick specimens can be serially captured to generate 3D volumes (x, y, z) . Unfortunately, there are several drawbacks of single-beam scanning. First, laser scanning is a relatively slow process that requires extremely precise control of galvanometer mirrors. The mirrors are fixed and tilt back and forth to produce a ‘stretched’ image that must be ‘descanned’ to provide an accurate representation of the sample. Image acquisition speed can be increased by scanning in the forwards and reverse directions; however, bidirectional scanning can introduce jaggedness artifacts due to the varying speed of forward and backward acquisitions [533]. Alternatively, acquisition speed can be increased by reducing the pixel dwell time of the laser. Faster scanning allows the laser to cover image pixels in a shorter amount of time; however, this reduces the signal-to-noise ratio (S/N) of images as less photon excitation and emission occurs in each part of the image. Consequently, CLSMs are often inadequate for capturing rapid dynamics in living cells. The excitation light source is also focused into a small point which can enhance photobleaching and phototoxicity.

Spinning disk (SD) confocal microscopy is an alternative to CLSMs that uses hundreds of pinholes on an opaque Nipkow disk to achieve optical sectioning [534]. The pinholes are arranged in spirals so that when the disk is spun, the pinholes scan across the sample in rows. A CCD, EMCCD or sCMOS camera with a sufficiently long exposure time builds up the image as the disk rotates [535]. Fluorescence excitation is achieved with a laser. Excitation light passes through a filter and is projected onto an upper Nipkow disk covered with microlenses. The microlenses focus the light into a series of beams that illuminate the sample. The upper disk is perfectly matched to a lower Nipkow disk so that the pinholes are confocal. Fluorescence emission returning through

the lower Nipkow disk is reflected by a beam splitter and passes through an emission filter before reaching the camera.

SD confocal microscopy is significantly faster than CLSM due to the extremely large number of pinholes (up to 20,000) and high rotation speed of the disks (up to 10,000 revolutions per minute) [535]. In theory, the fastest spinning disks can support camera exposure times as low as 0.5 ms. The large number of pinholes also reduces photobleaching and phototoxicity. Incoming laser light is diffused by the spinning disk, rather than concentrated into a single point. One major disadvantage of SD confocal microscopy is the inability to adjust pinhole diameter during an imaging session. CLSMs can adjust the pinhole diameter for each fluorophore separately to ensure that only 1 Airy unit of emission light is captured. Pinhole spacing must also be adjusted on an SD microscope to prevent pinhole crosstalk [535]. If the distance between pinholes is too small, out-of-focus light can pass through neighboring pinholes, increasing background signal. Conversely, if the distance between pinholes is too far, gaps or stripes of lower intensity appear in the final image. Nevertheless, SD confocal microscopes can approach the axial resolution performance of CLSMs while capturing images significantly faster and delivering less photobleaching and phototoxicity.

1.6.4 Total internal reflection fluorescence (TIRF) microscopy

Total internal reflection fluorescence (TIRF) microscopy is an optical technique that illuminates a thin region of a sample near the surface. While the optical thickness (z) of a confocal section is >500 nm, TIRF microscopy captures an optical section that is 100-200 nm. Incident light from a laser source is sent at a high angle (critical angle) such that when it strikes the interface of two materials, its refraction direction becomes parallel to the interface [536, 537]. This parallel beam of light generates a highly restricted electromagnetic field that emanates into the second medium. The intensity of the evanescent wave decays at an exponential rate with distance. Consequently, fluorophores close to the surface are primarily excited. Fluorescence emission is collected by the objective, reflected by a beam splitter, and passed through an emission filter before being captured on a CCD, EMCCD or sCMOS camera.

TIRF microscopy provides a selective way of observing structures close to the cell membrane, such as cell-matrix adhesions [538]. The thin optical section (100-200 nm) effectively increases the signal-to-background of these structures by reducing fluorescence contributions from

the cytoplasm. This makes it easier to segment adhesions and track their fluorescence intensity over time. It is important to note that CLSM and SD confocal microscopy can be used to study adhesion dynamics as well; however, the thicker optical sectioning (>500 nm) of these techniques captures more background signal from the cytoplasm, giving less contrast and making it more difficult to segment and track adhesions.

1.6.5 Fluorescence resonance energy transfer (FRET) microscopy

Förster or fluorescence resonance energy transfer (FRET) is a photophysical process that describes energy transfer from an excited ‘donor’ fluorophore to a ground state ‘acceptor’ fluorophore [539]. The emission spectrum of the ‘donor’ fluorophore must overlap with the excitation spectrum of the ‘acceptor’ fluorophore for FRET to occur. In addition, the fluorophores must be sufficiently close to each other. Maximum energy transfer typically occurs when the donor and acceptor are 2 nm within each other; FRET efficiency decreases with distance (sigmoid decay) such that there is almost no FRET between donor-acceptor pairs when they are more than 8 nm apart:

$$FRET\ efficiency = \frac{1}{1 + \left(r/R_0\right)^6} \quad (1)$$

where r is the distance between donor-acceptor pairs and R_0 is the distance at which energy transfer is 50% [540]. Acceptor-donor pairs have different R_0 depending on the relative orientation of the chromophore transition dipoles and the overall quantum yield for donor fluorescence [541, 542].

FRET can be captured with epifluorescence and confocal microscopy techniques [543]. For example, a widefield microscope equipped with an LED light source can be used to excite donor fluorophores and capture acceptor emission via a filter cube. The excitation filter should select wavelengths of light that excite the donor fluorophore but do not excite the acceptor fluorophore. Similarly, the emission filter should pass wavelengths that correspond to acceptor, but not donor, emission. Depending on the donor-acceptor pair chosen, it may not be possible to completely avoid direct acceptor excitation and donor emission. The degree of direct excitation and emission crosstalk can be determined by acquiring images of each fluorophore independently. Experimental FRET images can then be corrected based on these reference images. Alternatively, FRET microscopy can be performed on a CLSM with spectral capture and linear unmixing [527,

528]. A laser light source with a discrete wavelength excites the donor fluorophore. The variable slit is set to pass all wavelengths of light corresponding to donor and acceptor emission. This complex 3D image (x, y, λ) can then be unmixed based on the reference spectra of donor fluorophore alone and acceptor fluorophore alone. Spectral capture with linear unmixing is a more convenient way of acquiring FRET data because it does not require additional images to be collected for FRET image correction. In addition, linear unmixing can be performed automatically by the microscope software.

Traditionally, FRET was used visualize protein-protein interactions, quantify the distance between biomolecules, and determine the stoichiometry of protein complexes. More recently, genetically encoded FRET biosensors have been engineered to measure calcium (Ca^{2+}) concentration [544], metabolite concentration [545, 546], enzyme and kinase activity [547-549], membrane voltage [550]; tension across cell-cell contacts [551], focal adhesions [552, 553] and the cytoskeleton [554-556]; and many other cellular processes [557, 558].

1.6.5.1 Tension sensors: Cell-cell adhesion, focal adhesion and cytoskeleton tension sensors contain a tension sensing module (TSM) comprised of two fluorescent proteins separated by an elastic linker. E-cadherin [551], vinculin [552], talin [553] and nesprin-2G [556] have been made into tension sensors by inserting a repetitive amino acid motif (GPGGA₈) into the structure of each protein. This sequence (derived from the spider silk protein flagelliform) is linearly elastic between 1 and 6 piconewtons (pN), allowing for precise measurements of force across each molecule. For example, the vinculin tension sensor (VinTS) experiences ~2.5 pN of tension in stable adhesions [552], which is in line with other studies showing that focal adhesions can generate up to 75 nanonewtons (nN) of traction force [559, 560].

1.6.5.2 Vinculin tension sensor (VinTS): Vinculin is a 117 kDa protein that primarily localizes to integrin-based adhesions. It contains a globular head region, a flexible proline-rich neck region, and a tail region. The head domain binds talin and localizes vinculin to adhesions, while the tail domain interacts with F-actin [561, 562]. VinTS was created by inserting a TSM between the head and tail domains [552]. Teal fluorescent protein (mTFP1) and venusA206K (venus) are donor and acceptor fluorophores, respectively. Under low tension conditions, mTFP1 and venus are close together; mTFP1 excitation by 405 nm light results in FRET emission at 528 nm due to energy transfer (equivalent to 492 nm). Under high tension conditions, the fluorophores

are far apart and mTFP1 excitation does not lead to significant FRET; emission at 492 nm is much stronger than 528 nm in this case.

1.6.5.3 Talin tension sensor (TalinTS): A talin tension sensor (TalinTS) with EGFP and tagRFP was developed using the same principle. Talin is a 270 kDa protein that plays a key role in adhesion mechanosensing. It contains a head domain that directly binds β integrin tails and a rod domain with three actin binding sites [563, 564]. The TSM was inserted between the head and rod domains to ensure proper talin function and localization [553]. EGFP excitation by 488 nm light results in FRET emission at 584 nm. Interestingly, talinTS undergoes significantly more FRET in cells seeded onto soft substrates (~3 vs. 30 kPa) [553]. These experiments neatly demonstrate the utility of FRET-based biosensors for studying cellular mechanosensing.

1.7 SUPER-RESOLUTION MICROSCOPY TECHNIQUES

Conventional microscopy techniques can perform multicolor acquisition of several different fluorophores to observe a variety of targets simultaneously. Although it is possible to determine the relative colocalization of targets, conventional microscopy techniques are unable to reveal direct interactions. The wave nature of light imposes a fundamental restriction on the maximum lateral (x,y) and axial (z) resolution that can be achieved. Resolution is determined by the wavelength (λ) of fluorescence emission, numerical aperture (NA) of the objective, and refractive index (η) of the medium between the objective and the specimen [565]:

$$\text{Widefield resolution}_{x,y} = \frac{0.61\lambda}{NA} \quad (2a)$$

$$\text{Widefield resolution}_z = \frac{2\lambda\eta}{NA^2} \quad (2b)$$

In turn, NA depends on the angular aperture (θ) of the objective [566]:

$$NA = \eta \times \sin(\theta) \quad (3)$$

Air objectives have a practical upper limit of 72° resulting in a maximum NA of ~0.95 [567]. Immersion oils with an η of ~1.51 can substantially increase NA (up to ~1.51 for objectives with θ of 1). Nevertheless, the theoretical resolution of two fluorophores emitting in the visible spectrum (>400 nm) is >162 nm in x,y and >530 nm in z , much greater than the size of individual proteins. A pinhole set to ≤ 1 Airy unit can slightly improve resolution by generating a narrower point spread

function (PSF) [568, 569]. For CLSMs, the theoretical resolution is >98 nm in x,y and >371 nm in z :

$$\text{Confocal resolution}_{x,y} = \frac{0.37\lambda}{NA} \quad (4a)$$

$$\text{Confocal resolution}_z = \frac{1.4\lambda\eta}{NA^2} \quad (4b)$$

While this is a substantial improvement, most microscopes cannot achieve this level of resolution due to light scattering by the sample and optical imperfections [570]. More substantial gains in resolution can be obtained by limiting the number of fluorophores allowed to emit light at any given point in time. Super-resolution microscopy techniques such as stochastic optical reconstruction microscopy (STORM) and photoactivated localization microscopy (PALM) exploit the mechanisms of fluorescence to take advantage of this idea and bypass the diffraction limit of light.

1.7.1 Stochastic optical reconstruction microscopy (STORM)

STORM is a super-resolution technique that determines the precise location of diffraction-limited spots from hundreds of fluorescent events [571-574]. As previously described (section 1.5.3), fluorophores can enter a dark triplet state (OFF state) if electron spin is reversed upon excitation. Fluorophores trapped in long-lived OFF states can return to the ground state by transferring the additional electron to another molecule; however, this process is significantly slower than fluorescence. STORM takes advantage of this phenomenon by pushing fluorophores into the OFF state with a high-powered laser. Fluorophores sporadically return to the ground state and may undergo a few cycles of excitation-emission (i.e., blinking) before returning to the OFF state. A TSQ such as MEA is usually added to reduce the length of the triplet state, and oxygen scavenger systems such as GOX/CAT and PCA are used to prevent photobleaching through reactions with O_2 [575]. An EMCCD camera capable of rapid image acquisition captures thousands of images with a short exposure time (<50 ms) during this process. Fluorophores attached to a target have unlimited rotational freedom within a fixed distance. Therefore, target location can be predicted with statistics. When S/N is sufficiently high (≥ 4) [576-578], the relationship may be approximated as:

$$\sigma_{position} \approx \frac{s}{\sqrt{N}} \quad (5)$$

where s is the width of the observed PSF and N is the number of photons captured from the fluorophore. For a single spot with a diameter well below the diffraction limit of light, the PSF is >162 nm in x,y (equation 2a). A fluorophore attached to this spot could yield a resolution of $\sim 2-3$ nm with ~ 6500 blinks at 400 nm [579, 580]; however, there are several practical elements that must be considered. First, fluorophores undergo a finite number of blinks before photobleaching [575]. Second, fluorescence emission is usually >510 nm. Third, most oil immersion objectives have an NA around 1.4 [567]. Together, these factors increase PSF to >222 nm and reduce STORM resolution to ~ 10 nm.

The type of strategy used to label the target also affects resolution. Antibody dye conjugates frequently used to visualize proteins have the dimensions $14.5 \times 8.5 \times 4.0$ nm [581]. While IgG antibodies are much smaller than the PSF produced by widefield and confocal microscopes, the fluorophore is located at a relatively large distance away from the protein for STORM. Labeling with primary antibody alone is typically not sufficient to produce a robust signal and secondary antibodies must also be applied to amplify fluorescence signal. Overall, the addition of primary and secondary antibodies may reduce localization precision to ~ 30 nm. Secondary antibodies can be digested to yield smaller antigen-binding fragments (F_{ab}) that are ~ 10 nm in length [582-584]; however, primary antibodies must retain their F_c domain for secondary antibody recognition. Consequently, several new labeling strategies have been developed to reduce fluorophore distance from the protein of interest, including HaloTag, SNAP and CLIP [585-589]. These labelling strategies use genetically encoded enzymes that irreversibly bind a single fluorescent ligand to the protein of interest.

Finally, it is important to consider labelling density and dye properties when performing super-resolution microscopy [590]. The Nyquist-Shannon theorem dictates that sampling frequency should be at least 2.3 times the highest frequency in the signal [591]. For single molecule localization techniques that achieve ~ 20 nm resolution, fluorescent dyes should be spaced <8.7 nm apart to accurately reproduce subcellular structures. A homogenous structure with tightly packed proteins will exhibit gaps if labelling density is inadequate [592]. These effects are often missed with widefield and confocal microscopy because the PSF is sufficiently large to smooth out issues with density. Furthermore, blinking events must be spatially separated to reduce localization

errors. A fluorophore that undergoes many switching cycles (ON state \leftrightarrow OFF state) and spends a short amount of time in the ON state (low on-off duty cycle) is desired [575]. The fluorophore should also be photostable and release many photons in the ON state to capture high S/N images.

1.7.2 Photoactivated localization microscopy (PALM)

Photoactivated localization microscopy (PALM) is a single molecule localization technique analogous to STORM that uses photoactivatable or ‘caged’ fluorophores to resolve the spatial details of tightly packed molecules [593]. Photoactivation regulates the number of fluorophores available for excitation to increase spatiotemporal separation between blinks. For example, UV-violet light (~380 nm) can cause photolysis of a protecting group, such as 2-nitrobenzyl or its derivatives, to release organic fluorophores from an inactive state [594]. Similarly, light can induce conformational changes within the chromophore of certain fluorescent proteins [405, 595, 596] to activate [597, 598], inactivate [599, 600] or alter the excitation/emission spectra of fluorescent proteins (also known as photochromism) [601-604]. The rate of fluorophore activation is matched to intersystem crossing and photobleaching to maintain a constant density of resolvable single molecules during image acquisition [605]. Camera exposure time is then adjusted to acquire an image of each fluorophore before it is bleached. Interestingly, high-powered 405 nm light may also return fluorophores trapped in the OFF state back to the ON state [606]. This phenomenon generates additional blinking events which can be captured with shorter exposure times.

mEos [601], mMaple [603] and PA-mCherry [598] are commonly used for PALM. Importantly, fluorescent proteins are directly conjugated to the protein of interest, allowing PALM to achieve ~2-25 nm resolution [607]. These fluorescent proteins can be combined with HaloTag, SNAP, CLIP or antibody labelling methods to perform PALM and STORM on the same system.

1.7.3 3D single molecule localization microscopy

PALM/STORM systems substantially improve x,y resolution; however, the widefield nature of these platforms precludes z localization [608]. TIRF illumination was initially employed to reduce background signal and determine molecule localizations within a thin optical slice. A variety of techniques have now been developed to perform 3D localization, including astigmatism [609], biplane [610-612], single helix [613], double helix [614, 615] and interference [616].

1.7.3.1 Interference PALM (iPALM): Interference microscopy is commonly used to visualize surface topography (see DIC, section 1.5.1); however, interference between coherent light waves from two optical paths can also be used to perform sub-nanometer measurements [617]. Interference PALM (iPALM) achieves exceptional z resolution (9.8 nm from ~1500 photons) by collecting fluorescence emission through two separate objectives and allowing the optical paths to interfere in a special 3-way beam splitter [616]. The microscope is calibrated so that reference beads below the sample produce three waves with amplitudes that oscillate 120° out of phase. A separate EMCCD camera is used to capture each interference wave. The z position of an emitter in the sample directly affects upper and lower path lengths, resulting in a phase shift that can be quantified. Once the z position of an emitter is determined, x,y localization can be calculated from the frame triplets. The interference process does not affect lateral resolution obtained with STORM/PALM. As a result, iPALM is able to achieve <20 nm resolution in x , y and z [210, 616].

1.8 RATIONALE

ErbB2 and TGF β pathways synergize to promote breast cancer progression. Our group previously identified the adapter proteins p46/52ShcA and LPP as critical mediators of ErbB2⁺ breast cancer cell migration, invasion, and metastasis [123, 125, 279, 280]. TGF β is known to induce clustering of ErbB2 and integrin complexes [161, 162]. In addition, our recent BioID data indicates that p46/52ShcA and LPP exist within the same interaction. Therefore, the primary objective of this thesis was to characterize the interaction and investigate the impact of these proteins on cellular migratory mechanisms. We show that p46/52ShcA is a novel component of adhesions which precedes and regulates LPP recruitment to these structures in response to TGF β . Furthermore, we show that LPP interaction with α -actinin supports enhanced adhesion tension. Finally, we demonstrate that LPP is required for breast cancer cells to sense substrate stiffness.

Patients with triple-negative breast cancer (TNBC) exhibit the worst overall outcomes. TNBC cells often co-express epithelial and myoepithelial genes and can be driven to undergo further EMT with TGF β treatment [618-626]. Therefore, we extended our studies on LPP to TNBC and found that LPP is also an important mediator of cell migration, invasion and metastasis in this subtype.

During my PhD project, I used several live-cell fluorescence microscopy techniques to capture and quantify cellular behavior. The process of imaging fluorescent molecules with light can cause phototoxicity. Many biological researchers are unaware that small changes to the way a sample is imaged can have a profound impact on cell health. Thus, another key aim of this thesis was to bring attention to this prevalent issue and help researchers create an imaging protocol that minimizes harm. We show that “illumination overhead” beyond the camera exposure time causes an exponential increase in ROS, which damages mitochondria.

Overall, this thesis will discuss novel roles played by p46/52ShcA and LPP in breast cancer progression, and ways to optimize live-cell fluorescence imaging conditions to minimize phototoxicity.

1.9 REFERENCES

1. Institute, N.C. *Cancer Stat Facts: Female Breast Cancer Subtypes*. Available from: <https://seer.cancer.gov/statfacts/html/breast-subtypes.html>.
2. Hanahan, D. and R.A. Weinberg, *The hallmarks of cancer*. Cell, 2000. **100**(1): p. 57-70.
3. Quail, D.F. and J.A. Joyce, *Microenvironmental regulation of tumor progression and metastasis*. Nat Med, 2013. **19**(11): p. 1423-37.
4. Joyce, J.A. and J.W. Pollard, *Microenvironmental regulation of metastasis*. Nat Rev Cancer, 2009. **9**(4): p. 239-52.
5. Polyak, K., *Breast cancer: origins and evolution*. J Clin Invest, 2007. **117**(11): p. 3155-63.
6. Hanahan, D. and R.A. Weinberg, *Hallmarks of cancer: the next generation*. Cell, 2011. **144**(5): p. 646-74.
7. Ferlay, J., et al., *Estimates of worldwide burden of cancer in 2008: GLOBOCAN 2008*. Int J Cancer, 2010. **127**(12): p. 2893-917.
8. Society, C.C. *Breast cancer statistics*. Available from: <https://www.cancer.ca/en/cancer-information/cancer-type/breast/statistics/?region=on>.
9. Institute, N.C. *Cancer stat facts: female breast cancer*. Available from: <https://seer.cancer.gov/statfacts/html/breast.html>.
10. Society, C.C. *Survival statistics for breast cancer*. Available from: <https://www.cancer.ca/en/cancer-information/cancer-type/breast/prognosis-and-survival/survival-statistics/?region=on>.
11. Sorlie, T., et al., *Repeated observation of breast tumor subtypes in independent gene expression data sets*. Proc Natl Acad Sci U S A, 2003. **100**(14): p. 8418-23.
12. Sotiriou, C., et al., *Breast cancer classification and prognosis based on gene expression profiles from a population-based study*. Proc Natl Acad Sci U S A, 2003. **100**(18): p. 10393-8.
13. Sotiriou, C. and M.J. Piccart, *Taking gene-expression profiling to the clinic: when will molecular signatures become relevant to patient care?* Nat Rev Cancer, 2007. **7**(7): p. 545-53.
14. Perou, C.M., et al., *Molecular portraits of human breast tumours*. Nature, 2000. **406**(6797): p. 747-52.
15. Sorlie, T., et al., *Gene expression patterns of breast carcinomas distinguish tumor subclasses with clinical implications*. Proc Natl Acad Sci U S A, 2001. **98**(19): p. 10869-74.
16. Smid, M., et al., *Subtypes of breast cancer show preferential site of relapse*. Cancer Res, 2008. **68**(9): p. 3108-14.
17. Cheang, M.C., et al., *Ki67 index, HER2 status, and prognosis of patients with luminal B breast cancer*. J Natl Cancer Inst, 2009. **101**(10): p. 736-50.
18. Goldhirsch, A., et al., *Personalizing the treatment of women with early breast cancer: highlights of the St Gallen International Expert Consensus on the Primary Therapy of Early Breast Cancer 2013*. Ann Oncol, 2013. **24**(9): p. 2206-23.
19. Dai, X., et al., *Breast cancer intrinsic subtype classification, clinical use and future trends*. Am J Cancer Res, 2015. **5**(10): p. 2929-43.
20. Geisler, J., *Differences between the non-steroidal aromatase inhibitors anastrozole and letrozole-of clinical importance?* Br J Cancer, 2011. **104**(7): p. 1059-66.
21. Lumachi, F., D.A. Santeufemia, and S.M. Basso, *Current medical treatment of estrogen receptor-positive breast cancer*. World J Biol Chem, 2015. **6**(3): p. 231-9.
22. Inic, Z., et al., *Difference between Luminal A and Luminal B Subtypes According to Ki-67, Tumor Size, and Progesterone Receptor Negativity Providing Prognostic Information*. Clin Med Insights Oncol, 2014. **8**: p. 107-11.
23. Angus, L., et al., *The genomic landscape of metastatic breast cancer highlights changes in mutation and signature frequencies*. Nat Genet, 2019. **51**(10): p. 1450-1458.
24. Slamon, D.J., et al., *Human breast cancer: correlation of relapse and survival with amplification of the HER-2/neu oncogene*. Science, 1987. **235**(4785): p. 177-82.

25. Moasser, M.M., *The oncogene HER2: its signaling and transforming functions and its role in human cancer pathogenesis*. *Oncogene*, 2007. **26**(45): p. 6469-87.
26. Jones, R.B., et al., *A quantitative protein interaction network for the ErbB receptors using protein microarrays*. *Nature*, 2006. **439**(7073): p. 168-74.
27. Muller, W.J., et al., *Single-step induction of mammary adenocarcinoma in transgenic mice bearing the activated c-neu oncogene*. *Cell*, 1988. **54**(1): p. 105-15.
28. Guy, C.T., R.D. Cardiff, and W.J. Muller, *Activated neu induces rapid tumor progression*. *J Biol Chem*, 1996. **271**(13): p. 7673-8.
29. Guy, C.T., et al., *Expression of the neu protooncogene in the mammary epithelium of transgenic mice induces metastatic disease*. *Proceedings of the National Academy of Sciences of the United States of America*, 1992. **89**(22): p. 10578-10582.
30. Siegel, P.M., et al., *Elevated expression of activated forms of Neu/ErbB-2 and ErbB-3 are involved in the induction of mammary tumors in transgenic mice: implications for human breast cancer*. *The EMBO journal*, 1999. **18**(8): p. 2149-2164.
31. Society, A.C. *Targeted therapy for breast cancer*. Available from: <https://www.cancer.org/cancer/breast-cancer/treatment/targeted-therapy-for-breast-cancer>.
32. Arteaga, C.L., et al., *Treatment of HER2-positive breast cancer: current status and future perspectives*. *Nat Rev Clin Oncol*, 2011. **9**(1): p. 16-32.
33. Rexer, B.N. and C.L. Arteaga, *Intrinsic and acquired resistance to HER2-targeted therapies in HER2 gene-amplified breast cancer: mechanisms and clinical implications*. *Crit Rev Oncog*, 2012. **17**(1): p. 1-16.
34. Cleator, S., W. Heller, and R.C. Coombes, *Triple-negative breast cancer: therapeutic options*. *Lancet Oncol*, 2007. **8**(3): p. 235-44.
35. Rodler, E., L. Korde, and J. Gralow, *Current treatment options in triple negative breast cancer*. *Breast Dis*, 2010. **32**(1-2): p. 99-122.
36. Bertucci, F., P. Finetti, and D. Birnbaum, *Basal breast cancer: a complex and deadly molecular subtype*. *Curr Mol Med*, 2012. **12**(1): p. 96-110.
37. Foulkes, W.D., I.E. Smith, and J.S. Reis-Filho, *Triple-negative breast cancer*. *N Engl J Med*, 2010. **363**(20): p. 1938-48.
38. Rodriguez-Pinilla, S.M., et al., *Prognostic significance of basal-like phenotype and fascin expression in node-negative invasive breast carcinomas*. *Clin Cancer Res*, 2006. **12**(5): p. 1533-9.
39. Bertucci, F., et al., *How basal are triple-negative breast cancers?* *Int J Cancer*, 2008. **123**(1): p. 236-40.
40. Lehmann, B.D., et al., *Identification of human triple-negative breast cancer subtypes and preclinical models for selection of targeted therapies*. *J Clin Invest*, 2011. **121**(7): p. 2750-67.
41. Herschkowitz, J.I., et al., *Identification of conserved gene expression features between murine mammary carcinoma models and human breast tumors*. *Genome Biol*, 2007. **8**(5): p. R76.
42. Dias, K., et al., *Claudin-Low Breast Cancer; Clinical & Pathological Characteristics*. *PLoS One*, 2017. **12**(1): p. e0168669.
43. Prat, A., et al., *Phenotypic and molecular characterization of the claudin-low intrinsic subtype of breast cancer*. *Breast Cancer Res*, 2010. **12**(5): p. R68.
44. Hennessy, B.T., et al., *Characterization of a naturally occurring breast cancer subset enriched in epithelial-to-mesenchymal transition and stem cell characteristics*. *Cancer Res*, 2009. **69**(10): p. 4116-24.
45. Shang, X., et al., *Claudin-3 and claudin-4 regulate sensitivity to cisplatin by controlling expression of the copper and cisplatin influx transporter CTR1*. *Mol Pharmacol*, 2013. **83**(1): p. 85-94.
46. Abdullah, L.N. and E.K. Chow, *Mechanisms of chemoresistance in cancer stem cells*. *Clin Transl Med*, 2013. **2**(1): p. 3.
47. Creighton, C.J., et al., *Residual breast cancers after conventional therapy display mesenchymal as well as tumor-initiating features*. *Proc Natl Acad Sci U S A*, 2009. **106**(33): p. 13820-5.

48. Sabatier, R., et al., *Claudin-low breast cancers: clinical, pathological, molecular and prognostic characterization*. Mol Cancer, 2014. **13**: p. 228.
49. Parker, J.S., et al., *Supervised risk predictor of breast cancer based on intrinsic subtypes*. J Clin Oncol, 2009. **27**(8): p. 1160-7.
50. Weigelt, B., et al., *Breast cancer molecular profiling with single sample predictors: a retrospective analysis*. Lancet Oncol, 2010. **11**(4): p. 339-49.
51. Holm, K., et al., *Molecular subtypes of breast cancer are associated with characteristic DNA methylation patterns*. Breast cancer research : BCR, 2010. **12**(3): p. R36-R36.
52. Rønneberg, J.A., et al., *Methylation profiling with a panel of cancer related genes: association with estrogen receptor, TP53 mutation status and expression subtypes in sporadic breast cancer*. Molecular oncology, 2011. **5**(1): p. 61-76.
53. Cancer Genome Atlas, N., *Comprehensive molecular portraits of human breast tumours*. Nature, 2012. **490**(7418): p. 61-70.
54. Curtis, C., et al., *The genomic and transcriptomic architecture of 2,000 breast tumours reveals novel subgroups*. Nature, 2012. **486**(7403): p. 346-352.
55. Kristensen, V.N., et al., *Principles and methods of integrative genomic analyses in cancer*. Nature Reviews Cancer, 2014. **14**(5): p. 299-313.
56. Wang, Y., et al., *Clonal evolution in breast cancer revealed by single nucleus genome sequencing*. Nature, 2014. **512**(7513): p. 155-60.
57. Nik-Zainal, S., et al., *The Life History of 21 Breast Cancers*. Cell, 2012. **149**(5): p. 994-1007.
58. Hwang, B., J.H. Lee, and D. Bang, *Single-cell RNA sequencing technologies and bioinformatics pipelines*. Experimental & Molecular Medicine, 2018. **50**(8): p. 96.
59. Muciño-Olmos, E.A., et al., *Unveiling functional heterogeneity in breast cancer multicellular tumor spheroids through single-cell RNA-seq*. Scientific Reports, 2020. **10**(1): p. 12728.
60. Pearlman, M.D. and J.L. Griffin, *Benign Breast Disease*. Obstetrics & Gynecology, 2010. **116**(3).
61. Kelsey, J.L., M.D. Gammon, and E.M. John, *Reproductive factors and breast cancer*. Epidemiol Rev, 1993. **15**(1): p. 36-47.
62. Investigators, W.G.f.t.W.s.H.I., *Risks and Benefits of Estrogen Plus Progestin in Healthy Postmenopausal Women Principal Results From the Women's Health Initiative Randomized Controlled Trial*. JAMA, 2002. **288**(3): p. 321-333.
63. Colditz, G.A., et al., *Family history, age, and risk of breast cancer. Prospective data from the Nurses' Health Study*. Jama, 1993. **270**(3): p. 338-43.
64. Deng, G., et al., *Loss of heterozygosity in normal tissue adjacent to breast carcinomas*. Science, 1996. **274**(5295): p. 2057-9.
65. Ma, X.J., et al., *Gene expression profiles of human breast cancer progression*. Proc Natl Acad Sci U S A, 2003. **100**(10): p. 5974-9.
66. Arpino, G., R. Laucirica, and R.M. Elledge, *Premalignant and In Situ Breast Disease: Biology and Clinical Implications*. Annals of Internal Medicine, 2005. **143**(6): p. 446-457.
67. Ellis, I.O., *Intraductal proliferative lesions of the breast: morphology, associated risk and molecular biology*. Modern Pathology, 2010. **23**(2): p. S1-S7.
68. Page, D.L., et al., *Atypical hyperplastic lesions of the female breast. A long-term follow-up study*. Cancer, 1985. **55**(11): p. 2698-708.
69. Dupont, W.D. and D.L. Page, *Risk Factors for Breast Cancer in Women with Proliferative Breast Disease*. New England Journal of Medicine, 1985. **312**(3): p. 146-151.
70. Hartmann, L.C., et al., *Benign breast disease and the risk of breast cancer*. N Engl J Med, 2005. **353**(3): p. 229-37.
71. Bilder, D., *Epithelial polarity and proliferation control: links from the Drosophila neoplastic tumor suppressors*. Genes Dev, 2004. **18**(16): p. 1909-25.
72. Ewald, A.J., et al., *Collective epithelial migration and cell rearrangements drive mammary branching morphogenesis*. Dev Cell, 2008. **14**(4): p. 570-81.

73. Gupta, G.P. and J. Massagué, *Cancer metastasis: building a framework*. Cell, 2006. **127**(4): p. 679-95.
74. Witzel, I., et al., *Breast cancer brain metastases: biology and new clinical perspectives*. Breast Cancer Research, 2016. **18**(1): p. 8.
75. Minn, A.J., et al., *Lung metastasis genes couple breast tumor size and metastatic spread*. Proceedings of the National Academy of Sciences of the United States of America, 2007. **104**(16): p. 6740-6745.
76. Bos, P.D., et al., *Genes that mediate breast cancer metastasis to the brain*. Nature, 2009. **459**(7249): p. 1005-9.
77. Minn, A.J., et al., *Genes that mediate breast cancer metastasis to lung*. Nature, 2005. **436**(7050): p. 518-24.
78. Kang, Y., et al., *A multigenic program mediating breast cancer metastasis to bone*. Cancer Cell, 2003. **3**(6): p. 537-49.
79. Thiery, J.P., et al., *Epithelial-mesenchymal transitions in development and disease*. Cell, 2009. **139**(5): p. 871-90.
80. Yang, J. and R.A. Weinberg, *Epithelial-mesenchymal transition: at the crossroads of development and tumor metastasis*. Dev Cell, 2008. **14**(6): p. 818-29.
81. Weinberg, R.A., *Twisted epithelial-mesenchymal transition blocks senescence*. Nat Cell Biol, 2008. **10**(9): p. 1021-3.
82. Tiwari, N., et al., *EMT as the ultimate survival mechanism of cancer cells*. Semin Cancer Biol, 2012. **22**(3): p. 194-207.
83. Georgess, D., et al., *Twist1-Induced Epithelial Dissemination Requires Prkd1 Signaling*. Cancer Res, 2020. **80**(2): p. 204-218.
84. Lapin, M., et al., *Single-cell mRNA profiling reveals transcriptional heterogeneity among pancreatic circulating tumour cells*. BMC Cancer, 2017. **17**(1): p. 390.
85. Paterson, E.L., et al., *Down-Regulation of the miRNA-200 Family at the Invasive Front of Colorectal Cancers with Degraded Basement Membrane Indicates EMT Is Involved in Cancer Progression*. Neoplasia, 2013. **15**(2): p. 180-IN22.
86. Tran, H.D., et al., *Transient SNAIL1 Expression Is Necessary for Metastatic Competence in Breast Cancer*. Cancer Research, 2014. **74**(21): p. 6330.
87. Fischer, K.R., et al., *Epithelial-to-mesenchymal transition is not required for lung metastasis but contributes to chemoresistance*. Nature, 2015. **527**(7579): p. 472-476.
88. Chen, Y., et al., *Dual reporter genetic mouse models of pancreatic cancer identify an epithelial-to-mesenchymal transition-independent metastasis program*. EMBO Molecular Medicine, 2018. **10**(10): p. e9085.
89. Zheng, X., et al., *Epithelial-to-mesenchymal transition is dispensable for metastasis but induces chemoresistance in pancreatic cancer*. Nature, 2015. **527**(7579): p. 525-530.
90. Krebs, A.M., et al., *The EMT-activator Zeb1 is a key factor for cell plasticity and promotes metastasis in pancreatic cancer*. Nature Cell Biology, 2017. **19**(5): p. 518-529.
91. Nieto, M.A., et al., *EMT: 2016*. Cell, 2016. **166**(1): p. 21-45.
92. Padmanaban, V., et al., *E-cadherin is required for metastasis in multiple models of breast cancer*. Nature, 2019. **573**(7774): p. 439-444.
93. Aiello, N.M. and Y. Kang, *Context-dependent EMT programs in cancer metastasis*. J Exp Med, 2019. **216**(5): p. 1016-1026.
94. Cheung, K.J., et al., *Collective invasion in breast cancer requires a conserved basal epithelial program*. Cell, 2013. **155**(7): p. 1639-51.
95. Zhang, J., et al., *Energetic regulation of coordinated leader–follower dynamics during collective invasion of breast cancer cells*. Proceedings of the National Academy of Sciences, 2019. **116**(16): p. 7867.

96. Yang, C., et al., *Inducible formation of leader cells driven by CD44 switching gives rise to collective invasion and metastases in luminal breast carcinomas*. *Oncogene*, 2019. **38**(46): p. 7113-7132.
97. Cheung, K.J., et al., *Polyclonal breast cancer metastases arise from collective dissemination of keratin 14-expressing tumor cell clusters*. *Proceedings of the National Academy of Sciences*, 2016. **113**(7): p. E854.
98. Xu, J., S. Lamouille, and R. Derynck, *TGF- β -induced epithelial to mesenchymal transition*. *Cell Research*, 2009. **19**(2): p. 156-172.
99. Massagué, J., *TGFbeta in Cancer*. *Cell*, 2008. **134**(2): p. 215-230.
100. Chang, H., C.W. Brown, and M.M. Matzuk, *Genetic analysis of the mammalian transforming growth factor-beta superfamily*. *Endocr Rev*, 2002. **23**(6): p. 787-823.
101. Massague, J., *TGF-beta signal transduction*. *Annu Rev Biochem*, 1998. **67**: p. 753-91.
102. Clark, D.A. and R. Coker, *Transforming growth factor-beta (TGF-beta)*. *Int J Biochem Cell Biol*, 1998. **30**(3): p. 293-8.
103. Khalil, N., et al., *Plasmin regulates the activation of cell-associated latent TGF-beta 1 secreted by rat alveolar macrophages after in vivo bleomycin injury*. *Am J Respir Cell Mol Biol*, 1996. **15**(2): p. 252-9.
104. Lyons, R.M., et al., *Mechanism of activation of latent recombinant transforming growth factor beta 1 by plasmin*. *J Cell Biol*, 1990. **110**(4): p. 1361-7.
105. Annes, J.P., J.S. Munger, and D.B. Rifkin, *Making sense of latent TGFbeta activation*. *J Cell Sci*, 2003. **116**(Pt 2): p. 217-24.
106. Moustakas, A., S. Souchelnytskyi, and C.H. Heldin, *Smad regulation in TGF-beta signal transduction*. *J Cell Sci*, 2001. **114**(Pt 24): p. 4359-69.
107. ten Dijke, P., K. Miyazono, and C.H. Heldin, *Signaling inputs converge on nuclear effectors in TGF-beta signaling*. *Trends Biochem Sci*, 2000. **25**(2): p. 64-70.
108. ten Dijke, P., et al., *Identification of type I receptors for osteogenic protein-1 and bone morphogenetic protein-4*. *J Biol Chem*, 1994. **269**(25): p. 16985-8.
109. Massague, J., J. Seoane, and D. Wotton, *Smad transcription factors*. *Genes Dev*, 2005. **19**(23): p. 2783-810.
110. Massague, J. and D. Wotton, *Transcriptional control by the TGF-beta/Smad signaling system*. *EMBO J*, 2000. **19**(8): p. 1745-54.
111. Kalluri, R. and R.A. Weinberg, *The basics of epithelial-mesenchymal transition*. *The Journal of clinical investigation*, 2009. **119**(6): p. 1420-1428.
112. Postigo, A.A., et al., *Regulation of Smad signaling through a differential recruitment of coactivators and corepressors by ZEB proteins*. *EMBO J*, 2003. **22**(10): p. 2453-62.
113. Pierce, D.F., Jr., et al., *Mammary tumor suppression by transforming growth factor beta 1 transgene expression*. *Proc Natl Acad Sci U S A*, 1995. **92**(10): p. 4254-8.
114. Forrester, E., et al., *Effect of conditional knockout of the type II TGF-beta receptor gene in mammary epithelia on mammary gland development and polyomavirus middle T antigen induced tumor formation and metastasis*. *Cancer Res*, 2005. **65**(6): p. 2296-302.
115. Bierie, B. and H.L. Moses, *Tumour microenvironment: TGFbeta: the molecular Jekyll and Hyde of cancer*. *Nat Rev Cancer*, 2006. **6**(7): p. 506-20.
116. Siegel, P.M., et al., *Transforming growth factor {beta} signaling impairs Neu-induced mammary tumorigenesis while promoting pulmonary metastasis*. *Proceedings of the National Academy of Sciences*, 2003. **100**(14): p. 8430-8435.
117. Seton-Rogers, S.E., et al., *Cooperation of the ErbB2 receptor and transforming growth factor beta in induction of migration and invasion in mammary epithelial cells*. *Proc Natl Acad Sci U S A*, 2004. **101**(5): p. 1257-62.
118. Muraoka, R.S., et al., *Increased Malignancy of Neu-Induced Mammary Tumors Overexpressing Active Transforming Growth Factor {beta}1*. *Mol. Cell. Biol.*, 2003. **23**(23): p. 8691-8703.

119. Yarden, Y. and M.X. Sliwkowski, *Untangling the ErbB signalling network*. Nat Rev Mol Cell Biol, 2001. **2**(2): p. 127-37.
120. Holbro, T. and N.E. Hynes, *ErbB receptors: directing key signaling networks throughout life*. Annu Rev Pharmacol Toxicol, 2004. **44**: p. 195-217.
121. Lemmon, M.A., *Ligand-induced ErbB receptor dimerization*. Exp Cell Res, 2009. **315**(4): p. 638-48.
122. Graus-Porta, D., et al., *ErbB-2, the preferred heterodimerization partner of all ErbB receptors, is a mediator of lateral signaling*. EMBO J, 1997. **16**(7): p. 1647-55.
123. Northey, J.J., et al., *Signaling through ShcA is required for TGF- β and Neu/ErbB-2 induced breast cancer cell motility and invasion*. Mol. Cell. Biol., 2008: p. MCB.01734-07.
124. Dankort, D., et al., *Grb2 and Shc adapter proteins play distinct roles in Neu (ErbB-2)-induced mammary tumorigenesis: implications for human breast cancer*. Mol Cell Biol, 2001. **21**(5): p. 1540-51.
125. Northey, J.J., et al., *Distinct phosphotyrosine-dependent functions of the ShcA adaptor protein are required for transforming growth factor beta (TGF β)-induced breast cancer cell migration, invasion, and metastasis*. J Biol Chem, 2013. **288**(7): p. 5210-22.
126. Pelicci, G., et al., *A novel transforming protein (SHC) with an SH2 domain is implicated in mitogenic signal transduction*. Cell, 1992. **70**(1): p. 93-104.
127. Migliaccio, E., et al., *Opposite effects of the p52shc/p46shc and p66shc splicing isoforms on the EGF receptor-MAP kinase-*fos* signalling pathway*. EMBO J, 1997. **16**(4): p. 706-16.
128. Pelicci, G., et al., *A family of Shc related proteins with conserved PTB, CH1 and SH2 regions*. Oncogene, 1996. **13**(3): p. 633-41.
129. Jones, N., et al., *Analysis of a Shc family adaptor protein, ShcD/Shc4, that associates with muscle-specific kinase*. Mol Cell Biol, 2007. **27**(13): p. 4759-73.
130. Russo, C., et al., *The amyloid precursor protein and its network of interacting proteins: physiological and pathological implications*. Brain Res Brain Res Rev, 2005. **48**(2): p. 257-64.
131. Ursini-Siegel, J. and W.J. Muller, *The ShcA adaptor protein is a critical regulator of breast cancer progression*. Cell Cycle, 2008. **7**(13): p. 1936-43.
132. Mlih, M., et al., *The Src homology and collagen A (ShcA) adaptor protein is required for the spatial organization of the costamere/Z-disk network during heart development*. J Biol Chem, 2015. **290**(4): p. 2419-30.
133. Webster, M.A., et al., *Requirement for both Shc and phosphatidylinositol 3' kinase signaling pathways in polyomavirus middle T-mediated mammary tumorigenesis*. Mol Cell Biol, 1998. **18**(4): p. 2344-59.
134. Wright, K.D., et al., *The p52 isoform of SHC1 is a key driver of breast cancer initiation*. Breast Cancer Res, 2019. **21**(1): p. 74.
135. Jackson, J.G., et al., *Elevated levels of p66 Shc are found in breast cancer cell lines and primary tumors with high metastatic potential*. Clin Cancer Res, 2000. **6**(3): p. 1135-9.
136. Davol, P.A., et al., *Shc proteins are strong, independent prognostic markers for both node-negative and node-positive primary breast cancer*. Cancer Res, 2003. **63**(20): p. 6772-83.
137. Hudson, J., et al., *p66ShcA promotes breast cancer plasticity by inducing an epithelial-to-mesenchymal transition*. Mol Cell Biol, 2014. **34**(19): p. 3689-701.
138. Lewis, K., et al., *p66ShcA functions as a contextual promoter of breast cancer metastasis*. Breast Cancer Res, 2020. **22**(1): p. 7.
139. Kavanaugh, W.M., C.W. Turck, and L.T. Williams, *PTB domain binding to signaling proteins through a sequence motif containing phosphotyrosine*. Science, 1995. **268**(5214): p. 1177-9.
140. Dankort, D.L., et al., *Distinct tyrosine autophosphorylation sites negatively and positively modulate neu-mediated transformation*. Mol Cell Biol, 1997. **17**(9): p. 5410-25.
141. Campbell, K.S., et al., *Polyoma middle tumor antigen interacts with SHC protein via the NPTY (Asn-Pro-Thr-Tyr) motif in middle tumor antigen*. Proc Natl Acad Sci U S A, 1994. **91**(14): p. 6344-8.

142. Hardy, W.R., et al., *Combinatorial ShcA docking interactions support diversity in tissue morphogenesis*. Science, 2007. **317**(5835): p. 251-6.
143. Ahn, R., et al., *The ShcA PTB domain functions as a biological sensor of phosphotyrosine signaling during breast cancer progression*. Cancer Res, 2013. **73**(14): p. 4521-32.
144. Ha, J.R., et al., *Integration of Distinct ShcA Signaling Complexes Promotes Breast Tumor Growth and Tyrosine Kinase Inhibitor Resistance*. Mol Cancer Res, 2018. **16**(5): p. 894-908.
145. Ravichandran, K.S., *Signaling via Shc family adapter proteins*. Oncogene, 2001. **20**(44): p. 6322-30.
146. Ursini-Siegel, J., et al., *The ShcA SH2 domain engages a 14-3-3/PI3'K signaling complex and promotes breast cancer cell survival*. Oncogene, 2012. **31**(48): p. 5038-44.
147. Giubellino, A., T.R. Burke, Jr., and D.P. Bottaro, *Grb2 signaling in cell motility and cancer*. Expert Opin Ther Targets, 2008. **12**(8): p. 1021-33.
148. Margolis, B. and E.Y. Skolnik, *Activation of Ras by receptor tyrosine kinases*. J Am Soc Nephrol, 1994. **5**(6): p. 1288-99.
149. She, H.Y., et al., *Wiskott-Aldrich syndrome protein is associated with the adapter protein Grb2 and the epidermal growth factor receptor in living cells*. Mol Biol Cell, 1997. **8**(9): p. 1709-21.
150. Fernando, H.S., H.G. Kynaston, and W.G. Jiang, *WASP and WAVE proteins: vital intrinsic regulators of cell motility and their role in cancer (review)*. Int J Mol Med, 2009. **23**(2): p. 141-8.
151. Faisal, A., S. Kleiner, and Y. Nagamine, *Non-redundant role of Shc in Erk activation by cytoskeletal reorganization*. J Biol Chem, 2004. **279**(5): p. 3202-11.
152. Patrussi, L., et al., *Cooperation and selectivity of the two Grb2 binding sites of p52Shc in T-cell antigen receptor signaling to Ras family GTPases and Myc-dependent survival*. Oncogene, 2005. **24**(13): p. 2218-28.
153. Stevenson, L.E., K.S. Ravichandran, and A.R. Frackelton, Jr., *Shc dominant negative disrupts cell cycle progression in both G0-G1 and G2-M of ErbB2-positive breast cancer cells*. Cell Growth Differ, 1999. **10**(1): p. 61-71.
154. Birge, R.B., et al., *Crk and CrkL adaptor proteins: networks for physiological and pathological signaling*. Cell Commun Signal, 2009. **7**: p. 13.
155. Im, Y.K., et al., *Interplay between ShcA Signaling and PGC-1alpha Triggers Targetable Metabolic Vulnerabilities in Breast Cancer*. Cancer Res, 2018. **78**(17): p. 4826-4838.
156. Ahn, R., et al., *The Shc1 adaptor simultaneously balances Stat1 and Stat3 activity to promote breast cancer immune suppression*. Nat Commun, 2017. **8**: p. 14638.
157. Huang, F., et al., *HER2/EGFR-AKT Signaling Switches TGFβ from Inhibiting Cell Proliferation to Promoting Cell Migration in Breast Cancer*. Cancer Res, 2018. **78**(21): p. 6073-6085.
158. Galliher, A.J. and W.P. Schiemann, *Src phosphorylates Tyr284 in TGF-beta type II receptor and regulates TGF-beta stimulation of p38 MAPK during breast cancer cell proliferation and invasion*. Cancer Res, 2007. **67**(8): p. 3752-8.
159. Lee, M.K., et al., *TGF-beta activates Erk MAP kinase signalling through direct phosphorylation of ShcA*. Embo j, 2007. **26**(17): p. 3957-67.
160. Zhang, Y.E., *Non-Smad pathways in TGF-beta signaling*. Cell Res, 2009. **19**(1): p. 128-39.
161. Wang, S.E., et al., *Transforming growth factor beta induces clustering of HER2 and integrins by activating Src-focal adhesion kinase and receptor association to the cytoskeleton*. Cancer research, 2009. **69**(2): p. 475-82.
162. Wang, S.E., et al., *HER2/Neu (ErbB2) signaling to Rac1-Pak1 is temporally and spatially modulated by transforming growth factor beta*. Cancer research, 2006. **66**(19): p. 9591-600.
163. Robertson, J., et al., *Defining the phospho-adhesome through the phosphoproteomic analysis of integrin signalling*. Nat Commun, 2015. **6**: p. 6265.
164. Wu, R.F., et al., *p66(Shc) Couples Mechanical Signals to RhoA through Focal Adhesion Kinase-Dependent Recruitment of p115-RhoGEF and GEF-H1*. Mol Cell Biol, 2016. **36**(22): p. 2824-2837.
165. Wakefield, L.M., et al., *Transforming growth factor-beta1 circulates in normal human plasma and is unchanged in advanced metastatic breast cancer*. Clin Cancer Res, 1995. **1**(1): p. 129-36.

166. Lebrecht, A., et al., *Transforming growth factor beta 1 serum levels in patients with preinvasive and invasive lesions of the breast*. Int J Biol Markers, 2004. **19**(3): p. 236-9.
167. Kong, F.M., et al., *Elevated plasma transforming growth factor-beta 1 levels in breast cancer patients decrease after surgical removal of the tumor*. Ann Surg, 1995. **222**(2): p. 155-62.
168. Sheen-Chen, S.M., et al., *Serum levels of transforming growth factor beta1 in patients with breast cancer*. Arch Surg, 2001. **136**(8): p. 937-40.
169. Ivanovic, V., et al., *Elevated plasma levels of transforming growth factor-beta 1 (TGF-beta 1) in patients with advanced breast cancer: association with disease progression*. Eur J Cancer, 2003. **39**(4): p. 454-61.
170. Ivanovic, V., et al., *Elevated plasma TGF-beta1 levels correlate with decreased survival of metastatic breast cancer patients*. Clin Chim Acta, 2006. **371**(1-2): p. 191-3.
171. Wang, S.E., et al., *Transforming growth factor beta engages TACE and ErbB3 to activate phosphatidylinositol-3 kinase/Akt in ErbB2-overexpressing breast cancer and desensitizes cells to trastuzumab*. Molecular and cellular biology, 2008. **28**(18): p. 5605-20.
172. Kroigard, A.B., et al., *Clonal expansion and linear genome evolution through breast cancer progression from pre-invasive stages to asynchronous metastasis*. Oncotarget, 2015. **6**(8): p. 5634-49.
173. Klein, C.A., *Parallel progression of primary tumours and metastases*. Nat Rev Cancer, 2009. **9**(4): p. 302-12.
174. Koscielny, S. and M. Tubiana, *Parallel progression of tumour and metastases*. Nat Rev Cancer, 2010. **10**(2): p. 156.
175. Abbruzzese, J.L., et al., *Unknown primary carcinoma: natural history and prognostic factors in 657 consecutive patients*. J Clin Oncol, 1994. **12**(6): p. 1272-80.
176. van de Wouw, A.J., et al., *Epidemiology of unknown primary tumours; incidence and population-based survival of 1285 patients in Southeast Netherlands, 1984-1992*. Eur J Cancer, 2002. **38**(3): p. 409-13.
177. Klein, C.A. and D. Holzel, *Systemic cancer progression and tumor dormancy: mathematical models meet single cell genomics*. Cell Cycle, 2006. **5**(16): p. 1788-98.
178. Horwitz, R. and D. Webb, *Cell migration*. Curr Biol, 2003. **13**(19): p. R756-9.
179. Lauffenburger, D.A. and A.F. Horwitz, *Cell migration: a physically integrated molecular process*. Cell, 1996. **84**(3): p. 359-69.
180. Friedl, P. and K. Wolf, *Tumour-cell invasion and migration: diversity and escape mechanisms*. Nat Rev Cancer, 2003. **3**(5): p. 362-74.
181. Friedl, P., et al., *New dimensions in cell migration*. Nat Rev Mol Cell Biol, 2012. **13**(11): p. 743-7.
182. Friedl, P. and K. Wolf, *Plasticity of cell migration: a multiscale tuning model*. Journal of Cell Biology, 2009. **188**(1): p. 11-19.
183. Vitorino, P. and T. Meyer, *Modular control of endothelial sheet migration*. Genes Dev, 2008. **22**(23): p. 3268-81.
184. Friedl, P. and D. Gilmour, *Collective cell migration in morphogenesis, regeneration and cancer*. Nat Rev Mol Cell Biol, 2009. **10**(7): p. 445-57.
185. Friedl, P. and K. Wolf, *Plasticity of cell migration: a multiscale tuning model*. J Cell Biol, 2010. **188**(1): p. 11-9.
186. Friedl, P. and S. Alexander, *Cancer invasion and the microenvironment: plasticity and reciprocity*. Cell, 2011. **147**(5): p. 992-1009.
187. Thiery, J.P., *Epithelial-mesenchymal transitions in tumour progression*. Nat Rev Cancer, 2002. **2**(6): p. 442-54.
188. Welf, E.S. and J.M. Haugh, *Signaling pathways that control cell migration: models and analysis*. Wiley Interdiscip Rev Syst Biol Med, 2011. **3**(2): p. 231-40.
189. Huber, F., J. Kas, and B. Stuhmann, *Growing actin networks form lamellipodium and lamellum by self-assembly*. Biophys J, 2008. **95**(12): p. 5508-23.

190. Nicholson-Dykstra, S., H.N. Higgs, and E.S. Harris, *Actin dynamics: growth from dendritic branches*. *Curr Biol*, 2005. **15**(9): p. R346-57.
191. Berginski, M.E., et al., *High-resolution quantification of focal adhesion spatiotemporal dynamics in living cells*. *PLoS One*, 2011. **6**(7): p. e22025.
192. Friedl, P. and K. Wolf, *Proteolytic interstitial cell migration: a five-step process*. *Cancer Metastasis Rev*, 2009. **28**(1-2): p. 129-35.
193. Liu, Y.J., et al., *Confinement and low adhesion induce fast amoeboid migration of slow mesenchymal cells*. *Cell*, 2015. **160**(4): p. 659-672.
194. Sahai, E. and C.J. Marshall, *Differing modes of tumour cell invasion have distinct requirements for Rho/ROCK signalling and extracellular proteolysis*. *Nat Cell Biol*, 2003. **5**(8): p. 711-9.
195. Wolf, K., et al., *Compensation mechanism in tumor cell migration: mesenchymal-amoeboid transition after blocking of pericellular proteolysis*. *J Cell Biol*, 2003. **160**(2): p. 267-77.
196. Talkenberger, K., et al., *Amoeboid-mesenchymal migration plasticity promotes invasion only in complex heterogeneous microenvironments*. *Sci Rep*, 2017. **7**(1): p. 9237.
197. Frantz, C., K.M. Stewart, and V.M. Weaver, *The extracellular matrix at a glance*. *Journal of Cell Science*, 2010. **123**(24): p. 4195.
198. Lammermann, T. and M. Sixt, *Mechanical modes of 'amoeboid' cell migration*. *Curr Opin Cell Biol*, 2009. **21**(5): p. 636-44.
199. Balzer, E.M., et al., *Physical confinement alters tumor cell adhesion and migration phenotypes*. *FASEB J*, 2012. **26**(10): p. 4045-56.
200. Pankova, K., et al., *The molecular mechanisms of transition between mesenchymal and amoeboid invasiveness in tumor cells*. *Cell Mol Life Sci*, 2010. **67**(1): p. 63-71.
201. Condeelis, J. and J.E. Segall, *Intravital imaging of cell movement in tumours*. *Nat Rev Cancer*, 2003. **3**(12): p. 921-30.
202. Gao, Y., et al., *Loss of ERalpha induces amoeboid-like migration of breast cancer cells by downregulating vinculin*. *Nat Commun*, 2017. **8**: p. 14483.
203. Wolf, K., et al., *Multi-step pericellular proteolysis controls the transition from individual to collective cancer cell invasion*. *Nat Cell Biol*, 2007. **9**(8): p. 893-904.
204. Trepats, X., et al., *Physical forces during collective cell migration*. *Nature Physics*, 2009. **5**(6): p. 426-430.
205. Hino, N., et al., *ERK-Mediated Mechanochemical Waves Direct Collective Cell Polarization*. *Developmental Cell*, 2020. **53**(6): p. 646-660.e8.
206. Weber, G.F., M.A. Bjerke, and D.W. DeSimone, *A mechanoresponsive cadherin-keratin complex directs polarized protrusive behavior and collective cell migration*. *Dev Cell*, 2012. **22**(1): p. 104-15.
207. Yang, Y., et al., *An emerging tumor invasion mechanism about the collective cell migration*. *American journal of translational research*, 2019. **11**(9): p. 5301-5312.
208. Sahai, E., *Mechanisms of cancer cell invasion*. *Curr Opin Genet Dev*, 2005. **15**(1): p. 87-96.
209. Campbell, K., et al., *Collective cell migration and metastases induced by an epithelial-to-mesenchymal transition in Drosophila intestinal tumors*. *Nature Communications*, 2019. **10**(1): p. 2311.
210. Kanchanawong, P., et al., *Nanoscale architecture of integrin-based cell adhesions*. *Nature*, 2010. **468**(7323): p. 580-4.
211. Zaidel-Bar, R., et al., *Functional atlas of the integrin adhesome*. *Nat Cell Biol*, 2007. **9**(8): p. 858-67.
212. Kuo, J.C., et al., *Analysis of the myosin-II-responsive focal adhesion proteome reveals a role for beta-Pix in negative regulation of focal adhesion maturation*. *Nat Cell Biol*, 2011. **13**(4): p. 383-93.
213. Wolfenson, H., I. Lavelin, and B. Geiger, *Dynamic regulation of the structure and functions of integrin adhesions*. *Developmental cell*, 2013. **24**(5): p. 447-458.

214. Zaidel-Bar, R., et al., *Early molecular events in the assembly of matrix adhesions at the leading edge of migrating cells*. J Cell Sci, 2003. **116**(Pt 22): p. 4605-13.
215. Laukaitis, C.M., et al., *Differential dynamics of alpha 5 integrin, paxillin, and alpha-actinin during formation and disassembly of adhesions in migrating cells*. J Cell Biol, 2001. **153**(7): p. 1427-40.
216. Yu, C.H., et al., *Early integrin binding to Arg-Gly-Asp peptide activates actin polymerization and contractile movement that stimulates outward translocation*. Proc Natl Acad Sci U S A, 2011. **108**(51): p. 20585-90.
217. Nayal, A., et al., *Paxillin phosphorylation at Ser273 localizes a GIT1-PIX-PAK complex and regulates adhesion and protrusion dynamics*. J Cell Biol, 2006. **173**(4): p. 587-9.
218. DePasquale, J.A. and C.S. Izzard, *Evidence for an actin-containing cytoplasmic precursor of the focal contact and the timing of incorporation of vinculin at the focal contact*. J Cell Biol, 1987. **105**(6 Pt 1): p. 2803-9.
219. Galbraith, C.G., K.M. Yamada, and M.P. Sheetz, *The relationship between force and focal complex development*. J Cell Biol, 2002. **159**(4): p. 695-705.
220. Choi, C.K., et al., *Actin and alpha-actinin orchestrate the assembly and maturation of nascent adhesions in a myosin II motor-independent manner*. Nat Cell Biol, 2008. **10**(9): p. 1039-50.
221. Zaidel-Bar, R., et al., *A paxillin tyrosine phosphorylation switch regulates the assembly and form of cell-matrix adhesions*. J Cell Sci, 2007. **120**(Pt 1): p. 137-48.
222. Pankov, R., et al., *Integrin dynamics and matrix assembly: tensin-dependent translocation of alpha(5)beta(1) integrins promotes early fibronectin fibrillogenesis*. J Cell Biol, 2000. **148**(5): p. 1075-90.
223. Doyle, A.D., et al., *Local 3D matrix microenvironment regulates cell migration through spatiotemporal dynamics of contractility-dependent adhesions*. Nature Communications, 2015. **6**(1): p. 8720.
224. Harunaga, J.S. and K.M. Yamada, *Cell-matrix adhesions in 3D*. Matrix biology : journal of the International Society for Matrix Biology, 2011. **30**(7-8): p. 363-368.
225. Humphries, J.D., A. Byron, and M.J. Humphries, *Integrin ligands at a glance*. J Cell Sci, 2006. **119**(Pt 19): p. 3901-3.
226. EHJ, D. *Integrins: An Overview of Structural and Functional Aspects*. Madame Curie Bioscience Database 2000-2013; Available from: <https://www.ncbi.nlm.nih.gov/books/NBK6259/>.
227. Assoian, R.K., *Anchorage-dependent cell cycle progression*. J Cell Biol, 1997. **136**(1): p. 1-4.
228. Geiger, B., J.P. Spatz, and A.D. Bershadsky, *Environmental sensing through focal adhesions*. Nat Rev Mol Cell Biol, 2009. **10**(1): p. 21-33.
229. Walcott, S., et al., *Nucleation and decay initiation are the stiffness-sensitive phases of focal adhesion maturation*. Biophys J, 2011. **101**(12): p. 2919-28.
230. Ingber, D.E. and J. Folkman, *Mechanochemical switching between growth and differentiation during fibroblast growth factor-stimulated angiogenesis in vitro: role of extracellular matrix*. J Cell Biol, 1989. **109**(1): p. 317-30.
231. Engler, A.J., et al., *Matrix elasticity directs stem cell lineage specification*. Cell, 2006. **126**(4): p. 677-89.
232. Wells, R.G., *The role of matrix stiffness in regulating cell behavior*. Hepatology, 2008. **47**(4): p. 1394-400.
233. Zhang, Y.H., et al., *Substrate stiffness regulates apoptosis and the mRNA expression of extracellular matrix regulatory genes in the rat annular cells*. Matrix Biol, 2011. **30**(2): p. 135-44.
234. Khavari, A., et al., *Composite alginate gels for tunable cellular microenvironment mechanics*. Sci Rep, 2016. **6**: p. 30854.
235. Petrie, R.J., et al., *Nonpolarized signaling reveals two distinct modes of 3D cell migration*. J Cell Biol, 2012. **197**(3): p. 439-55.
236. Parsons, J.T., A.R. Horwitz, and M.A. Schwartz, *Cell adhesion: integrating cytoskeletal dynamics and cellular tension*. Nat Rev Mol Cell Biol, 2010. **11**(9): p. 633-43.

237. Discher, D.E., P. Janmey, and Y.L. Wang, *Tissue cells feel and respond to the stiffness of their substrate*. Science, 2005. **310**(5751): p. 1139-43.
238. del Rio, A., et al., *Stretching single talin rod molecules activates vinculin binding*. Science, 2009. **323**(5914): p. 638-41.
239. Horton, E.R., et al., *Mechanosensitivity of integrin adhesion complexes: role of the consensus adhesome*. Exp Cell Res, 2016. **343**(1): p. 7-13.
240. Plotnikov, S.V., et al., *Force fluctuations within focal adhesions mediate ECM-rigidity sensing to guide directed cell migration*. Cell, 2012. **151**(7): p. 1513-27.
241. Lo, C.M., et al., *Cell movement is guided by the rigidity of the substrate*. Biophys J, 2000. **79**(1): p. 144-52.
242. DuChez, B.J., et al., *Durotaxis by Human Cancer Cells*. Biophys J, 2019. **116**(4): p. 670-683.
243. Pelham, R.J., Jr. and Y. Wang, *Cell locomotion and focal adhesions are regulated by substrate flexibility*. Proc Natl Acad Sci U S A, 1997. **94**(25): p. 13661-5.
244. Dokukina, I.V. and M.E. Gracheva, *A model of fibroblast motility on substrates with different rigidities*. Biophys J, 2010. **98**(12): p. 2794-803.
245. Marinkovic, A., et al., *Improved throughput traction microscopy reveals pivotal role for matrix stiffness in fibroblast contractility and TGF-beta responsiveness*. Am J Physiol Lung Cell Mol Physiol, 2012. **303**(3): p. L169-80.
246. Lange, J.R. and B. Fabry, *Cell and tissue mechanics in cell migration*. Exp Cell Res, 2013. **319**(16): p. 2418-23.
247. Pathak, A. and S. Kumar, *Independent regulation of tumor cell migration by matrix stiffness and confinement*. Proc Natl Acad Sci U S A, 2012. **109**(26): p. 10334-9.
248. Albiges-Rizo, C., et al., *Actin machinery and mechanosensitivity in invadopodia, podosomes and focal adhesions*. J Cell Sci, 2009. **122**(Pt 17): p. 3037-49.
249. Eddy, R.J., et al., *Tumor Cell Invadopodia: Invasive Protrusions that Orchestrate Metastasis*. Trends Cell Biol, 2017. **27**(8): p. 595-607.
250. Paterson, E.K. and S.A. Courtneidge, *Invadosomes are coming: new insights into function and disease relevance*. FEBS J, 2017.
251. Parekh, A., et al., *Sensing and modulation of invadopodia across a wide range of rigidities*. Biophys J, 2011. **100**(3): p. 573-82.
252. Schoumacher, M., et al., *Actin, microtubules, and vimentin intermediate filaments cooperate for elongation of invadopodia*. J Cell Biol, 2010. **189**(3): p. 541-56.
253. Blouw, B., et al., *The invadopodia scaffold protein Tks5 is required for the growth of human breast cancer cells in vitro and in vivo*. PLoS One, 2015. **10**(3): p. e0121003.
254. Leong, H.S., et al., *Invadopodia are required for cancer cell extravasation and are a therapeutic target for metastasis*. Cell Rep, 2014. **8**(5): p. 1558-70.
255. Harney, A.S., et al., *Real-Time Imaging Reveals Local, Transient Vascular Permeability, and Tumor Cell Intravasation Stimulated by TIE2hi Macrophage-Derived VEGFA*. Cancer Discov, 2015. **5**(9): p. 932-43.
256. Carmona, G., et al., *Lamellipodin promotes invasive 3D cancer cell migration via regulated interactions with Ena/VASP and SCAR/WAVE*. Oncogene, 2016. **35**(39): p. 5155-69.
257. Harney, A.S., et al., *Extended Time-lapse Intravital Imaging of Real-time Multicellular Dynamics in the Tumor Microenvironment*. J Vis Exp, 2016(112).
258. Kai, F., H. Laklai, and V.M. Weaver, *Force Matters: Biomechanical Regulation of Cell Invasion and Migration in Disease*. Trends Cell Biol, 2016. **26**(7): p. 486-497.
259. Gu, Z., et al., *Soft matrix is a natural stimulator for cellular invasiveness*. Mol Biol Cell, 2014. **25**(4): p. 457-69.
260. Aung, A., et al., *3D traction stresses activate protease-dependent invasion of cancer cells*. Biophys J, 2014. **107**(11): p. 2528-37.
261. Alexander, N.R., et al., *Extracellular matrix rigidity promotes invadopodia activity*. Curr Biol, 2008. **18**(17): p. 1295-9.

262. Jerrell, R.J. and A. Parekh, *Cellular traction stresses mediate extracellular matrix degradation by invadopodia*. *Acta Biomater*, 2014. **10**(5): p. 1886-96.
263. Parekh, A. and A.M. Weaver, *Regulation of invadopodia by mechanical signaling*. *Exp Cell Res*, 2016. **343**(1): p. 89-95.
264. Li, T., et al., *The association of measured breast tissue characteristics with mammographic density and other risk factors for breast cancer*. *Cancer Epidemiol Biomarkers Prev*, 2005. **14**(2): p. 343-9.
265. McCormack, V.A. and I. dos Santos Silva, *Breast density and parenchymal patterns as markers of breast cancer risk: a meta-analysis*. *Cancer Epidemiol Biomarkers Prev*, 2006. **15**(6): p. 1159-69.
266. Boyd, N.F., et al., *Evidence that breast tissue stiffness is associated with risk of breast cancer*. *PLoS One*, 2014. **9**(7): p. e100937.
267. Athanasiou, A., et al., *Breast lesions: quantitative elastography with supersonic shear imaging--preliminary results*. *Radiology*, 2010. **256**(1): p. 297-303.
268. Bae, J.S., et al., *Prediction of invasive breast cancer using shear-wave elastography in patients with biopsy-confirmed ductal carcinoma in situ*. *Eur Radiol*, 2017. **27**(1): p. 7-15.
269. Evans, A., et al., *Differentiating benign from malignant solid breast masses: value of shear wave elastography according to lesion stiffness combined with greyscale ultrasound according to BI-RADS classification*. *Br J Cancer*, 2012. **107**(2): p. 224-9.
270. Winkler, J., et al., *Concepts of extracellular matrix remodelling in tumour progression and metastasis*. *Nature Communications*, 2020. **11**(1): p. 5120.
271. Levental, K.R., et al., *Matrix crosslinking forces tumor progression by enhancing integrin signaling*. *Cell*, 2009. **139**(5): p. 891-906.
272. Provenzano, P.P., et al., *Matrix density-induced mechanoregulation of breast cell phenotype, signaling and gene expression through a FAK-ERK linkage*. *Oncogene*, 2009. **28**(49): p. 4326-43.
273. Wei, S.C., et al., *Matrix stiffness drives epithelial-mesenchymal transition and tumour metastasis through a TWIST1-G3BP2 mechanotransduction pathway*. *Nat Cell Biol*, 2015. **17**(5): p. 678-88.
274. Jiang, W.G., et al., *Tissue invasion and metastasis: Molecular, biological and clinical perspectives*. *Semin Cancer Biol*, 2015. **35 Suppl**: p. S244-75.
275. Wendt, M.K. and W.P. Schiemann, *Therapeutic targeting of the focal adhesion complex prevents oncogenic TGF-beta signaling and metastasis*. *Breast Cancer Res*, 2009. **11**(5): p. R68.
276. Yamaguchi, H. and J. Condeelis, *Regulation of the actin cytoskeleton in cancer cell migration and invasion*. *Biochim Biophys Acta*, 2007. **1773**(5): p. 642-52.
277. Acerbi, I., et al., *Human breast cancer invasion and aggression correlates with ECM stiffening and immune cell infiltration*. *Integr Biol (Camb)*, 2015. **7**(10): p. 1120-34.
278. Provenzano, P.P., et al., *Collagen density promotes mammary tumor initiation and progression*. *BMC Med*, 2008. **6**: p. 11.
279. Ngan, E., et al., *A complex containing LPP and alpha-actinin mediates TGFbeta-induced migration and invasion of ErbB2-expressing breast cancer cells*. *J Cell Sci*, 2013. **126**(Pt 9): p. 1981-91.
280. Ngan, E., et al., *LPP is a Src substrate required for invadopodia formation and efficient breast cancer lung metastasis*. *Nat Commun*, 2017. **8**: p. 15059.
281. Kiepas, A., et al., *The SHCA adapter protein cooperates with lipoma-preferred partner in the regulation of adhesion dynamics and invadopodia formation*. *J Biol Chem*, 2020. **295**(31): p. 10535-10559.
282. Schiller, H.B. and R. Fassler, *Mechanosensitivity and compositional dynamics of cell-matrix adhesions*. *EMBO Rep*, 2013. **14**(6): p. 509-19.
283. Petit, M.M., et al., *LPP, the preferred fusion partner gene of HMGIC in lipomas, is a novel member of the LIM protein gene family*. *Genomics*, 1996. **36**(1): p. 118-29.
284. Gorenne, I., et al., *LPP, a LIM protein highly expressed in smooth muscle*. *Am J Physiol Cell Physiol*, 2003. **285**(3): p. C674-685.
285. Vervenne, H.B., et al., *Targeted disruption of the mouse Lipoma Preferred Partner gene*. *Biochem Biophys Res Commun*, 2009. **379**(2): p. 368-73.

286. Macalma, T., et al., *Molecular characterization of human zyxin*. J Biol Chem, 1996. **271**(49): p. 31470-8.
287. Beckerle, M.C., *Zyxin: zinc fingers at sites of cell adhesion*. Bioessays, 1997. **19**(11): p. 949-57.
288. Wu, C., *Migfilin and its binding partners: from cell biology to human diseases*. J Cell Sci, 2005. **118**(Pt 4): p. 659-64.
289. Grunewald, T.G., S.M. Pasedag, and E. Butt, *Cell Adhesion and Transcriptional Activity - Defining the Role of the Novel Protooncogene LPP*. Transl Oncol, 2009. **2**(3): p. 107-16.
290. Willier, S., et al., *Defining the role of TRIP6 in cell physiology and cancer*. Biology of the cell / under the auspices of the European Cell Biology Organization, 2011. **103**(12): p. 573-91.
291. Grunewald, T.G., et al., *The Zyxin-related protein thyroid receptor interacting protein 6 (TRIP6) is overexpressed in Ewing's sarcoma and promotes migration, invasion and cell growth*. Biol Cell, 2013. **105**(11): p. 535-47.
292. Hirata, H., H. Tatsumi, and M. Sokabe, *Zyxin emerges as a key player in the mechanotransduction at cell adhesive structures*. Communicative & integrative biology, 2008. **1**(2): p. 192-195.
293. Yi, J. and M.C. Beckerle, *The human TRIP6 gene encodes a LIM domain protein and maps to chromosome 7q22, a region associated with tumorigenesis*. Genomics, 1998. **49**(2): p. 314-6.
294. Li, B., et al., *The lipoma preferred partner LPP interacts with alpha-actinin*. J Cell Sci, 2003. **116**(Pt 7): p. 1359-66.
295. Petit, M.M., S.M. Meulemans, and W.J. Van de Ven, *The focal adhesion and nuclear targeting capacity of the LIM-containing lipoma-preferred partner (LPP) protein*. J Biol Chem, 2003. **278**(4): p. 2157-68.
296. Majesky, M.W., *Organizing Motility: LIM Domains, LPP, and Smooth Muscle Migration*. Circ Res, 2006. **98**(3): p. 306-308.
297. Kadrmas, J.L. and M.C. Beckerle, *The LIM domain: from the cytoskeleton to the nucleus*. Nat Rev Mol Cell Biol, 2004. **5**(11): p. 920-31.
298. Petit, M.M., et al., *LPP, an actin cytoskeleton protein related to zyxin, harbors a nuclear export signal and transcriptional activation capacity*. Mol Biol Cell, 2000. **11**(1): p. 117-29.
299. Colas, E., et al., *ETV5 cooperates with LPP as a sensor of extracellular signals and promotes EMT in endometrial carcinomas*. Oncogene, 2012. **31**(45): p. 4778-88.
300. Jin, L., et al., *Angiotensin II, focal adhesion kinase, and PRX1 enhance smooth muscle expression of lipoma preferred partner and its newly identified binding partner palladin to promote cell migration*. Circ Res, 2007. **100**(6): p. 817-25.
301. Janssens, V., et al., *PP2A binds to the LIM domains of lipoma-preferred partner through its PR130/B" subunit to regulate cell adhesion and migration*. J Cell Sci, 2016. **129**(8): p. 1605-18.
302. Knight, B., et al., *Visualizing muscle cell migration in situ*. Curr Biol, 2000. **10**(10): p. 576-85.
303. Langanger, G., et al., *Ultrastructural localization of alpha-actinin and filamin in cultured cells with the immunogold staining (IGS) method*. J Cell Biol, 1984. **99**(4 Pt 1): p. 1324-34.
304. Xue, F., D.M. Janzen, and D.A. Knecht, *Contribution of Filopodia to Cell Migration: A Mechanical Link between Protrusion and Contraction*. Int J Cell Biol, 2010. **2010**: p. 507821.
305. Wehland, J., M. Osborn, and K. Weber, *Cell-to-substratum contacts in living cells: a direct correlation between interference-reflexion and indirect-immunofluorescence microscopy using antibodies against actin and alpha-actinin*. J Cell Sci, 1979. **37**: p. 257-73.
306. David-Pfeuty, T. and S.J. Singer, *Altered distributions of the cytoskeletal proteins vinculin and alpha-actinin in cultured fibroblasts transformed by Rous sarcoma virus*. Proc Natl Acad Sci U S A, 1980. **77**(11): p. 6687-91.
307. Hirooka, S., et al., *Localization of the invadopodia-related proteins actinin-1 and cortactin to matrix-contact-side cytoplasm of cancer cells in surgically resected lung adenocarcinomas*. Pathobiology, 2011. **78**(1): p. 10-23.
308. Feramisco, J.R., *Microinjection of fluorescently labeled alpha-actinin into living fibroblasts*. Proc Natl Acad Sci U S A, 1979. **76**(8): p. 3967-71.

309. Le Clainche, C. and M.F. Carrier, *Regulation of actin assembly associated with protrusion and adhesion in cell migration*. *Physiol Rev*, 2008. **88**(2): p. 489-513.
310. Foley, K.S. and P.W. Young, *The non-muscle functions of actinins: an update*. *Biochem J*, 2014. **459**(1): p. 1-13.
311. Yamaguchi, H., et al., *Actinin-1 and actinin-4 play essential but distinct roles in invadopodia formation by carcinoma cells*. *Eur J Cell Biol*, 2017.
312. Honda, K., *The biological role of actinin-4 (ACTN4) in malignant phenotypes of cancer*. *Cell Biosci*, 2015. **5**: p. 41.
313. Grunewald, T.G. and E. Butt, *The LIM and SH3 domain protein family: structural proteins or signal transducers or both?* *Mol Cancer*, 2008. **7**: p. 31.
314. Keicher, C., et al., *Phosphorylation of mouse LASP-1 on threonine 156 by cAMP- and cGMP-dependent protein kinase*. *Biochem Biophys Res Commun*, 2004. **324**(1): p. 308-16.
315. Zhang, H., et al., *Lasp1 gene disruption is linked to enhanced cell migration and tumor formation*. *Physiol Genomics*, 2009. **38**(3): p. 372-85.
316. Parast, M.M. and C.A. Otey, *Characterization of palladin, a novel protein localized to stress fibers and cell adhesions*. *J Cell Biol*, 2000. **150**(3): p. 643-56.
317. Otey, C.A., et al., *The palladin/myotilin/myopalladin family of actin-associated scaffolds*. *Int Rev Cytol*, 2005. **246**: p. 31-58.
318. Najm, P. and M. El-Sibai, *Palladin regulation of the actin structures needed for cancer invasion*. *Cell Adh Migr*, 2014. **8**(1): p. 29-35.
319. Seshacharyulu, P., et al., *Phosphatase: PP2A structural importance, regulation and its aberrant expression in cancer*. *Cancer Lett*, 2013. **335**(1): p. 9-18.
320. Eichhorn, P.J., M.P. Creighton, and R. Bernards, *Protein phosphatase 2A regulatory subunits and cancer*. *Biochim Biophys Acta*, 2009. **1795**(1): p. 1-15.
321. Bononi, A., et al., *Protein kinases and phosphatases in the control of cell fate*. *Enzyme Res*, 2011. **2011**: p. 329098.
322. Perrotti, D. and P. Neviani, *Protein phosphatase 2A: a target for anticancer therapy*. *Lancet Oncol*, 2013. **14**(6): p. e229-38.
323. Petit, M.M., et al., *The tumor suppressor Scrib selectively interacts with specific members of the zyxin family of proteins*. *FEBS Lett*, 2005. **579**(22): p. 5061-8.
324. Vervenne, H.B., et al., *Lpp is involved in Wnt/PCP signaling and acts together with Scrib to mediate convergence and extension movements during zebrafish gastrulation*. *Dev Biol*, 2008. **320**(1): p. 267-77.
325. Pearson, H.B., et al., *The polarity protein Scrib mediates epidermal development and exerts a tumor suppressive function during skin carcinogenesis*. *Mol Cancer*, 2015. **14**: p. 169.
326. Elsum, I.A., et al., *Scrib heterozygosity predisposes to lung cancer and cooperates with KRas hyperactivation to accelerate lung cancer progression in vivo*. *Oncogene*, 2014. **33**(48): p. 5523-33.
327. Pearson, H.B., et al., *SCRIB expression is deregulated in human prostate cancer, and its deficiency in mice promotes prostate neoplasia*. *J Clin Invest*, 2011. **121**(11): p. 4257-67.
328. Anastas, J.N., et al., *A protein complex of SCRIB, NOS1AP and VANGL1 regulates cell polarity and migration, and is associated with breast cancer progression*. *Oncogene*, 2012. **31**(32): p. 3696-708.
329. Feigin, M.E., et al., *Mislocalization of the cell polarity protein scribble promotes mammary tumorigenesis and is associated with basal breast cancer*. *Cancer Res*, 2014. **74**(11): p. 3180-94.
330. Savi, F., et al., *miR-296/Scribble axis is deregulated in human breast cancer and miR-296 restoration reduces tumour growth in vivo*. *Clin Sci (Lond)*, 2014. **127**(4): p. 233-42.
331. Silacci, P., et al., *Gelsolin superfamily proteins: key regulators of cellular functions*. *Cell Mol Life Sci*, 2004. **61**(19-20): p. 2614-23.
332. Pestonjampasp, K.N., et al., *Supervillin (p205): A novel membrane-associated, F-actin-binding protein in the villin/gelsolin superfamily*. *J Cell Biol*, 1997. **139**(5): p. 1255-69.

333. Sun, H.Q., et al., *Gelsolin, a multifunctional actin regulatory protein*. J Biol Chem, 1999. **274**(47): p. 33179-82.
334. Takizawa, N., et al., *Supervillin modulation of focal adhesions involving TRIP6/ZRP-1*. J Cell Biol, 2006. **174**(3): p. 447-58.
335. Bhuwania, R., et al., *Supervillin couples myosin-dependent contractility to podosomes and enables their turnover*. J Cell Sci, 2012. **125**(Pt 9): p. 2300-14.
336. Son, K., T.C. Smith, and E.J. Luna, *Supervillin binds the Rac/Rho-GEF Trio and increases Trio-mediated Rac1 activation*. Cytoskeleton (Hoboken), 2015. **72**(1): p. 47-64.
337. Crowley, J.L., et al., *Supervillin reorganizes the actin cytoskeleton and increases invadopodial efficiency*. Mol Biol Cell, 2009. **20**(3): p. 948-62.
338. Krause, M., et al., *The Ena/VASP enigma*. J Cell Sci, 2002. **115**(Pt 24): p. 4721-6.
339. Holt, M.R., D.R. Critchley, and N.P. Brindle, *The focal adhesion phosphoprotein, VASP*. Int J Biochem Cell Biol, 1998. **30**(3): p. 307-11.
340. Reinhard, M., T. Jarchau, and U. Walter, *Actin-based motility: stop and go with Ena/VASP proteins*. Trends Biochem Sci, 2001. **26**(4): p. 243-9.
341. Krause, M., et al., *Ena/VASP proteins: regulators of the actin cytoskeleton and cell migration*. Annu Rev Cell Dev Biol, 2003. **19**: p. 541-64.
342. Kwiatkowski, A.V., F.B. Gertler, and J.J. Loureiro, *Function and regulation of Ena/VASP proteins*. Trends Cell Biol, 2003. **13**(7): p. 386-92.
343. Hansen, M.D. and M.C. Beckerle, *Opposing roles of zyxin/LPP ACTA repeats and the LIM domain region in cell-cell adhesion*. J Biol Chem, 2006. **281**(23): p. 16178-88.
344. Hansen, S.D. and R.D. Mullins, *VASP is a processive actin polymerase that requires monomeric actin for barbed end association*. J Cell Biol, 2010. **191**(3): p. 571-84.
345. Hu, L.D., et al., *EVL (Ena/VASP-like) expression is up-regulated in human breast cancer and its relative expression level is correlated with clinical stages*. Oncol Rep, 2008. **19**(4): p. 1015-20.
346. Philippar, U., et al., *A Mena invasion isoform potentiates EGF-induced carcinoma cell invasion and metastasis*. Dev Cell, 2008. **15**(6): p. 813-28.
347. Di Modugno, F., et al., *The cooperation between hMena overexpression and HER2 signalling in breast cancer*. PLoS One, 2010. **5**(12): p. e15852.
348. Gertler, F. and J. Condeelis, *Metastasis: tumor cells becoming MENAcing*. Trends Cell Biol, 2011. **21**(2): p. 81-90.
349. Doppler, H., et al., *The phosphorylation status of VASP at serine 322 can be predictive for aggressiveness of invasive ductal carcinoma*. Oncotarget, 2015. **6**(30): p. 29740-52.
350. Toyoda, A., et al., *Aberrant expression of human ortholog of mammalian enabled (hMena) in human colorectal carcinomas: implications for its role in tumor progression*. Int J Oncol, 2009. **34**(1): p. 53-60.
351. Zuzga, D.S., et al., *Phosphorylation of vasodilator-stimulated phosphoprotein Ser239 suppresses filopodia and invadopodia in colon cancer*. Int J Cancer, 2012. **130**(11): p. 2539-48.
352. Ali, M., L.K. Rogers, and G.M. Pitari, *Serine phosphorylation of vasodilator-stimulated phosphoprotein (VASP) regulates colon cancer cell survival and apoptosis*. Life Sci, 2015. **123**: p. 1-8.
353. Dertsiz, L., et al., *Differential expression of VASP in normal lung tissue and lung adenocarcinomas*. Thorax, 2005. **60**(7): p. 576-81.
354. Gorenne, I., et al., *LPP expression during in vitro smooth muscle differentiation and stent-induced vascular injury*. Circ Res, 2006. **98**(3): p. 378-85.
355. Van Itallie, C.M., et al., *Biotin ligase tagging identifies proteins proximal to E-cadherin, including lipoma preferred partner, a regulator of epithelial cell-cell and cell-substrate adhesion*. J Cell Sci, 2014. **127**(Pt 4): p. 885-95.
356. Gregory Call, S., et al., *A zyxin-nectin interaction facilitates zyxin localization to cell-cell adhesions*. Biochem Biophys Res Commun, 2011. **415**(3): p. 485-9.

357. Fedele, M., et al., *Truncated and chimeric HMGI-C genes induce neoplastic transformation of NIH3T3 murine fibroblasts*. *Oncogene*, 1998. **17**(4): p. 413-8.
358. Kuriyama, S., et al., *LPP inhibits collective cell migration during lung cancer dissemination*. *Oncogene*, 2016. **35**(8): p. 952-64.
359. Jais, J.P., et al., *The expression of 16 genes related to the cell of origin and immune response predicts survival in elderly patients with diffuse large B-cell lymphoma treated with CHOP and rituximab*. *Leukemia*, 2008. **22**(10): p. 1917-24.
360. Hooper, C.L., P.R. Dash, and S.Y. Boateng, *Lipoma preferred partner is a mechanosensitive protein regulated by nitric oxide in the heart*. *FEBS Open Bio*, 2012. **2**: p. 135-44.
361. Hooper, C.L., et al., *Modulation of stretch-induced myocyte remodeling and gene expression by nitric oxide: a novel role for lipoma preferred partner in myofibrillogenesis*. *Am J Physiol Heart Circ Physiol*, 2013. **304**(10): p. H1302-13.
362. Jin, L., et al., *Mechanical properties of the extracellular matrix alter expression of smooth muscle protein LPP and its partner palladin; relationship to early atherosclerosis and vascular injury*. *J Muscle Res Cell Motil*, 2009. **30**(1-2): p. 41-55.
363. Smith, M.A., L.M. Hoffman, and M.C. Beckerle, *LIM proteins in actin cytoskeleton mechanoresponse*. *Trends Cell Biol*, 2014. **24**(10): p. 575-83.
364. Yoshigi, M., et al., *Mechanical force mobilizes zyxin from focal adhesions to actin filaments and regulates cytoskeletal reinforcement*. *J Cell Biol*, 2005. **171**(2): p. 209-15.
365. Hirata, H., H. Tatsumi, and M. Sokabe, *Mechanical forces facilitate actin polymerization at focal adhesions in a zyxin-dependent manner*. *Journal of cell science*, 2008. **121**(Pt 17): p. 2795-804.
366. Uemura, A., et al., *The LIM domain of zyxin is sufficient for force-induced accumulation of zyxin during cell migration*. *Biophysical journal*, 2011. **101**(5): p. 1069-75.
367. Hoffman, L.M., et al., *Stretch-induced actin remodeling requires targeting of zyxin to stress fibers and recruitment of actin regulators*. *Mol Biol Cell*, 2012. **23**(10): p. 1846-59.
368. Smith, M.A., et al., *LIM domains target actin regulators Paxillin and zyxin to sites of stress fiber strain*. *PLoS One*, 2013. **8**(8): p. e69378.
369. MicroscopyU. *Introduction to Phase Contrast Microscopy*. February 8, 2021]; Available from: <https://www.microscopyu.com/techniques/phase-contrast/introduction-to-phase-contrast-microscopy>.
370. Olympus. *Differential Interference Contrast - Introduction*. February 8, 2021]; Available from: <https://www.olympus-lifescience.com/en/microscope-resource/primer/techniques/dic/dicoverview/>.
371. Olympus. *Comparison of Phase Contrast and DIC Microscopy*. February 8, 2021]; Available from: <https://www.olympus-lifescience.com/en/microscope-resource/primer/techniques/dic/dicphasecomparison/>.
372. MicroscopyU. *Comparison of Phase Contrast and DIC Microscopy*. February 8, 2021]; Available from: <https://www.microscopyu.com/tutorials/comparison-of-phase-contrast-and-dic-microscopy>.
373. Lichtman, J.W. and J.A. Conchello, *Fluorescence microscopy*. *Nat Methods*, 2005. **2**(12): p. 910-9.
374. Lakowicz, J.R., *Principles of fluorescence spectroscopy*. 2010, New York: Springer Science+Business Media.
375. Lavis, L.D. and R.T. Raines, *Bright building blocks for chemical biology*. *ACS Chem Biol*, 2014. **9**(4): p. 855-66.
376. Jun, J.V., D.M. Chenoweth, and E.J. Petersson, *Rational design of small molecule fluorescent probes for biological applications*. *Org Biomol Chem*, 2020. **18**(30): p. 5747-5763.
377. Sun, X.-y., et al., *Synthesis and application of coumarin fluorescence probes*. *RSC Advances*, 2020. **10**(18): p. 10826-10847.
378. Bordeaux, J., et al., *Antibody validation*. *Biotechniques*, 2010. **48**(3): p. 197-209.
379. Prasher, D.C., et al., *Primary structure of the *Aequorea victoria* green-fluorescent protein*. *Gene*, 1992. **111**(2): p. 229-33.

380. Chalfie, M., et al., *Green fluorescent protein as a marker for gene expression*. Science, 1994. **263**(5148): p. 802-5.
381. Tsien, R.Y., *The green fluorescent protein*. Annu Rev Biochem, 1998. **67**: p. 509-44.
382. Thorn, K., *Genetically encoded fluorescent tags*. Mol Biol Cell, 2017. **28**(7): p. 848-857.
383. Chudakov, D.M., et al., *Fluorescent Proteins and Their Applications in Imaging Living Cells and Tissues*. Physiological Reviews, 2010. **90**(3): p. 1103-1163.
384. Cody, C.W., et al., *Chemical structure of the hexapeptide chromophore of the Aequorea green-fluorescent protein*. Biochemistry, 1993. **32**(5): p. 1212-8.
385. Ormo, M., et al., *Crystal structure of the Aequorea victoria green fluorescent protein*. Science, 1996. **273**(5280): p. 1392-5.
386. Morise, H., et al., *Intermolecular energy transfer in the bioluminescent system of Aequorea*. Biochemistry, 1974. **13**(12): p. 2656-62.
387. Ward, W.W., et al., *SPECTROPHOTOMETRIC IDENTITY OF THE ENERGY TRANSFER CHROMOPHORES IN RENILLA AND AEQUOREA GREEN-FLUORESCENT PROTEINS*. Photochemistry and Photobiology, 1980. **31**(6): p. 611-615.
388. Heim, R., A.B. Cubitt, and R.Y. Tsien, *Improved green fluorescence*. Nature, 1995. **373**(6516): p. 663-4.
389. Patterson, G.H., et al., *Use of the green fluorescent protein and its mutants in quantitative fluorescence microscopy*. Biophys J, 1997. **73**(5): p. 2782-90.
390. Heim, R. and R.Y. Tsien, *Engineering green fluorescent protein for improved brightness, longer wavelengths and fluorescence resonance energy transfer*. Curr Biol, 1996. **6**(2): p. 178-82.
391. Zacharias, D.A., et al., *Partitioning of lipid-modified monomeric GFPs into membrane microdomains of live cells*. Science, 2002. **296**(5569): p. 913-6.
392. Fisher, A.C. and M.P. DeLisa, *Laboratory evolution of fast-folding green fluorescent protein using secretory pathway quality control*. PLoS One, 2008. **3**(6): p. e2351.
393. Matz, M.V., et al., *Fluorescent proteins from nonbioluminescent Anthozoa species*. Nat Biotechnol, 1999. **17**(10): p. 969-73.
394. Labas, Y.A., et al., *Diversity and evolution of the green fluorescent protein family*. Proc Natl Acad Sci U S A, 2002. **99**(7): p. 4256-61.
395. Fradkov, A.F., et al., *Novel fluorescent protein from Discosoma coral and its mutants possesses a unique far-red fluorescence*. FEBS Lett, 2000. **479**(3): p. 127-30.
396. Shaner, N.C., et al., *Improved monomeric red, orange and yellow fluorescent proteins derived from Discosoma sp. red fluorescent protein*. Nat Biotechnol, 2004. **22**(12): p. 1567-72.
397. Karniol, B., et al., *Phylogenetic analysis of the phytochrome superfamily reveals distinct microbial subfamilies of photoreceptors*. Biochem J, 2005. **392**(Pt 1): p. 103-16.
398. Filonov, G.S., et al., *Bright and stable near-infrared fluorescent protein for in vivo imaging*. Nat Biotechnol, 2011. **29**(8): p. 757-61.
399. Shu, X., et al., *Mammalian expression of infrared fluorescent proteins engineered from a bacterial phytochrome*. Science, 2009. **324**(5928): p. 804-7.
400. Yu, D., et al., *An improved monomeric infrared fluorescent protein for neuronal and tumour brain imaging*. Nat Commun, 2014. **5**: p. 3626.
401. Shcherbakova, D.M. and V.V. Verkhusha, *Near-infrared fluorescent proteins for multicolor in vivo imaging*. Nat Methods, 2013. **10**(8): p. 751-4.
402. Shcherbakova, D.M., et al., *Bright monomeric near-infrared fluorescent proteins as tags and biosensors for multiscale imaging*. Nat Commun, 2016. **7**: p. 12405.
403. Yu, D., et al., *A naturally monomeric infrared fluorescent protein for protein labeling in vivo*. Nat Methods, 2015. **12**(8): p. 763-5.
404. Auldridge, M.E. and K.T. Forest, *Bacterial phytochromes: more than meets the light*. Crit Rev Biochem Mol Biol, 2011. **46**(1): p. 67-88.
405. Rodriguez, E.A., et al., *The Growing and Glowing Toolbox of Fluorescent and Photoactive Proteins*. Trends Biochem Sci, 2017. **42**(2): p. 111-129.

406. Expressions, M. *Basic Concepts in Fluorescence*. 2003 November 13, 2015 February 8, 2021]; Available from: <https://micro.magnet.fsu.edu/primer/techniques/fluorescence/fluorescenceintro.html>.
407. Kasha, M., *Characterization of electronic transitions in complex molecules*. Discussions of the Faraday Society, 1950. **9**(0): p. 14-19.
408. Stennett, E.M.S., M.A. Ciuba, and M. Levitus, *Photophysical processes in single molecule organic fluorescent probes*. Chemical Society reviews, 2014. **43**(4): p. 1057-75.
409. Eggeling, C., et al., *Photostability of Fluorescent Dyes for Single-Molecule Spectroscopy: Mechanisms and Experimental Methods for Estimating Photobleaching in Aqueous Solution*, in *Applied Fluorescence in Chemistry, Biology and Medicine*, W. Rettig, et al., Editors. 1999, Springer Berlin Heidelberg: Berlin, Heidelberg. p. 193-240.
410. Cadet, J. and J.R. Wagner, *DNA base damage by reactive oxygen species, oxidizing agents, and UV radiation*. Cold Spring Harb Perspect Biol, 2013. **5**(2).
411. Cui, H., Y. Kong, and H. Zhang, *Oxidative stress, mitochondrial dysfunction, and aging*. J Signal Transduct, 2012. **2012**: p. 646354.
412. Dizdaroglu, M., et al., *Free radical-induced damage to DNA: mechanisms and measurement*. Free Radic Biol Med, 2002. **32**(11): p. 1102-15.
413. Armstrong, J.A., et al., *Oxidative stress alters mitochondrial bioenergetics and modifies pancreatic cell death independently of cyclophilin D, resulting in an apoptosis-to-necrosis shift*. J Biol Chem, 2018. **293**(21): p. 8032-8047.
414. Bienert, G.P., J.K. Schjoerring, and T.P. Jahn, *Membrane transport of hydrogen peroxide*. Biochim Biophys Acta, 2006. **1758**(8): p. 994-1003.
415. Fridovich, I., *Superoxide anion radical (O₂⁻), superoxide dismutases, and related matters*. J Biol Chem, 1997. **272**(30): p. 18515-7.
416. Holmstrom, K.M. and T. Finkel, *Cellular mechanisms and physiological consequences of redox-dependent signalling*. Nat Rev Mol Cell Biol, 2014. **15**(6): p. 411-21.
417. Van Remmen, H., et al., *Life-long reduction in MnSOD activity results in increased DNA damage and higher incidence of cancer but does not accelerate aging*. Physiol Genomics, 2003. **16**(1): p. 29-37.
418. Elchuri, S., et al., *CuZnSOD deficiency leads to persistent and widespread oxidative damage and hepatocarcinogenesis later in life*. Oncogene, 2005. **24**(3): p. 367-80.
419. Strassburger, M., et al., *Heterozygous deficiency of manganese superoxide dismutase results in severe lipid peroxidation and spontaneous apoptosis in murine myocardium in vivo*. Free Radic Biol Med, 2005. **38**(11): p. 1458-70.
420. Li, Y., et al., *Dilated cardiomyopathy and neonatal lethality in mutant mice lacking manganese superoxide dismutase*. Nat Genet, 1995. **11**(4): p. 376-81.
421. Wang, Y., et al., *Superoxide dismutases: Dual roles in controlling ROS damage and regulating ROS signaling*. J Cell Biol, 2018. **217**(6): p. 1915-1928.
422. Perry, J.J., et al., *The structural biochemistry of the superoxide dismutases*. Biochim Biophys Acta, 2010. **1804**(2): p. 245-62.
423. Culotta, V.C., M. Yang, and T.V. O'Halloran, *Activation of superoxide dismutases: putting the metal to the pedal*. Biochim Biophys Acta, 2006. **1763**(7): p. 747-58.
424. Okado-Matsumoto, A. and I. Fridovich, *Subcellular distribution of superoxide dismutases (SOD) in rat liver: Cu,Zn-SOD in mitochondria*. J Biol Chem, 2001. **276**(42): p. 38388-93.
425. Folz, R.J. and J.D. Crapo, *Extracellular superoxide dismutase (SOD3): tissue-specific expression, genomic characterization, and computer-assisted sequence analysis of the human EC SOD gene*. Genomics, 1994. **22**(1): p. 162-71.
426. Marklund, S.L., E. Holme, and L. Hellner, *Superoxide dismutase in extracellular fluids*. Clin Chim Acta, 1982. **126**(1): p. 41-51.
427. Glorieux, C. and P.B. Calderon, *Catalase, a remarkable enzyme: targeting the oldest antioxidant enzyme to find a new cancer treatment approach*. Biol Chem, 2017. **398**(10): p. 1095-1108.

428. Alfonso-Prieto, M., et al., *The molecular mechanism of the catalase reaction*. J Am Chem Soc, 2009. **131**(33): p. 11751-61.
429. Purdue, P.E. and P.B. Lazarow, *Targeting of human catalase to peroxisomes is dependent upon a novel COOH-terminal peroxisomal targeting sequence*. J Cell Biol, 1996. **134**(4): p. 849-62.
430. Radi, R., et al., *Detection of catalase in rat heart mitochondria*. J Biol Chem, 1991. **266**(32): p. 22028-34.
431. Busciglio, J. and B.A. Yankner, *Apoptosis and increased generation of reactive oxygen species in Down's syndrome neurons in vitro*. Nature, 1995. **378**(6559): p. 776-9.
432. Sancho, P., et al., *Differential effects of catalase on apoptosis induction in human promonocytic cells. Relationships with heat-shock protein expression*. Mol Pharmacol, 2003. **63**(3): p. 581-9.
433. Toppo, S., et al., *Catalytic mechanisms and specificities of glutathione peroxidases: variations of a basic scheme*. Biochim Biophys Acta, 2009. **1790**(11): p. 1486-500.
434. Kang, D.H. and S.W. Kang, *Targeting cellular antioxidant enzymes for treating atherosclerotic vascular disease*. Biomol Ther (Seoul), 2013. **21**(2): p. 89-96.
435. Chen, Y.I., et al., *NPGPx (GPx7): a novel oxidative stress sensor/transmitter with multiple roles in redox homeostasis*. Am J Transl Res, 2016. **8**(4): p. 1626-40.
436. Cardoso, B.R., et al., *Glutathione peroxidase 4: a new player in neurodegeneration?* Mol Psychiatry, 2017. **22**(3): p. 328-335.
437. Chambers, I., et al., *The structure of the mouse glutathione peroxidase gene: the selenocysteine in the active site is encoded by the 'termination' codon, TGA*. EMBO J, 1986. **5**(6): p. 1221-7.
438. Lei, X.G., W.H. Cheng, and J.P. McClung, *Metabolic regulation and function of glutathione peroxidase-1*. Annu Rev Nutr, 2007. **27**: p. 41-61.
439. Asayama, K., et al., *Purification and immunoelectron microscopic localization of cellular glutathione peroxidase in rat hepatocytes: quantitative analysis by postembedding method*. Histochemistry, 1994. **102**(3): p. 213-9.
440. Singh, A.K., et al., *Demonstration of glutathione peroxidase in rat liver peroxisomes and its intraorganellar distribution*. Arch Biochem Biophys, 1994. **315**(2): p. 331-8.
441. Esworthy, R.S., Y.S. Ho, and F.F. Chu, *The Gpx1 gene encodes mitochondrial glutathione peroxidase in the mouse liver*. Arch Biochem Biophys, 1997. **340**(1): p. 59-63.
442. Cheng, W.H., et al., *Cellular glutathione peroxidase is the mediator of body selenium to protect against paraquat lethality in transgenic mice*. J Nutr, 1998. **128**(7): p. 1070-6.
443. Cheng, W., et al., *Selenium-dependent cellular glutathione peroxidase protects mice against a pro-oxidant-induced oxidation of NADPH, NADH, lipids, and protein*. FASEB J, 1999. **13**(11): p. 1467-75.
444. de Haan, J.B., et al., *Mice with a homozygous null mutation for the most abundant glutathione peroxidase, Gpx1, show increased susceptibility to the oxidative stress-inducing agents paraquat and hydrogen peroxide*. J Biol Chem, 1998. **273**(35): p. 22528-36.
445. Seiler, A., et al., *Glutathione peroxidase 4 senses and translates oxidative stress into 12/15-lipoxygenase dependent- and AIF-mediated cell death*. Cell Metab, 2008. **8**(3): p. 237-48.
446. Bao, Y., et al., *Reduction of thymine hydroperoxide by phospholipid hydroperoxide glutathione peroxidase and glutathione transferases*. FEBS Lett, 1997. **410**(2-3): p. 210-2.
447. Pushpa-Rekha, T.R., et al., *Rat phospholipid-hydroperoxide glutathione peroxidase. cDNA cloning and identification of multiple transcription and translation start sites*. J Biol Chem, 1995. **270**(45): p. 26993-9.
448. Arai, M., et al., *Import into mitochondria of phospholipid hydroperoxide glutathione peroxidase requires a leader sequence*. Biochem Biophys Res Commun, 1996. **227**(2): p. 433-9.
449. Yant, L.J., et al., *The selenoprotein GPX4 is essential for mouse development and protects from radiation and oxidative damage insults*. Free Radic Biol Med, 2003. **34**(4): p. 496-502.
450. Liang, H., et al., *Short form glutathione peroxidase 4 is the essential isoform required for survival and somatic mitochondrial functions*. J Biol Chem, 2009. **284**(45): p. 30836-44.

451. Pfeifer, H., et al., *Identification of a specific sperm nuclei selenoenzyme necessary for protamine thiol cross-linking during sperm maturation*. *FASEB J*, 2001. **15**(7): p. 1236-8.
452. Conrad, M., et al., *The nuclear form of phospholipid hydroperoxide glutathione peroxidase is a protein thiol peroxidase contributing to sperm chromatin stability*. *Mol Cell Biol*, 2005. **25**(17): p. 7637-44.
453. Wood, Z.A., et al., *Structure, mechanism and regulation of peroxiredoxins*. *Trends Biochem Sci*, 2003. **28**(1): p. 32-40.
454. Rhee, S.G., et al., *Peroxiredoxin functions as a peroxidase and a regulator and sensor of local peroxides*. *J Biol Chem*, 2012. **287**(7): p. 4403-10.
455. Seo, M.S., et al., *Identification of a new type of mammalian peroxiredoxin that forms an intramolecular disulfide as a reaction intermediate*. *J Biol Chem*, 2000. **275**(27): p. 20346-54.
456. Ralat, L.A., et al., *Direct evidence for the formation of a complex between l-cysteine peroxiredoxin and glutathione S-transferase pi with activity changes in both enzymes*. *Biochemistry*, 2006. **45**(2): p. 360-72.
457. Fisher, A.B., *Peroxiredoxin 6: a bifunctional enzyme with glutathione peroxidase and phospholipase A(2) activities*. *Antioxid Redox Signal*, 2011. **15**(3): p. 831-44.
458. Powis, G., D. Mustacich, and A. Coon, *The role of the redox protein thioredoxin in cell growth and cancer*. *Free Radic Biol Med*, 2000. **29**(3-4): p. 312-22.
459. Hirota, K., et al., *AP-1 transcriptional activity is regulated by a direct association between thioredoxin and Ref-1*. *Proc Natl Acad Sci U S A*, 1997. **94**(8): p. 3633-8.
460. Maruyama, T., et al., *Induction of thioredoxin, a redox-active protein, by ovarian steroid hormones during growth and differentiation of endometrial stromal cells in vitro*. *Endocrinology*, 1999. **140**(1): p. 365-72.
461. Rubartelli, A., et al., *Secretion of thioredoxin by normal and neoplastic cells through a leaderless secretory pathway*. *J Biol Chem*, 1992. **267**(34): p. 24161-4.
462. Bodenstein, J. and H. Follmann, *Characterization of two thioredoxins in pig heart including a new mitochondrial protein*. *Z Naturforsch C J Biosci*, 1991. **46**(3-4): p. 270-9.
463. Collet, J.F. and J. Messens, *Structure, function, and mechanism of thioredoxin proteins*. *Antioxid Redox Signal*, 2010. **13**(8): p. 1205-16.
464. Mustacich, D. and G. Powis, *Thioredoxin reductase*. *Biochem J*, 2000. **346 Pt 1**: p. 1-8.
465. Arner, E.S., *Focus on mammalian thioredoxin reductases--important selenoproteins with versatile functions*. *Biochim Biophys Acta*, 2009. **1790**(6): p. 495-526.
466. Gasdaska, P.Y., et al., *Cloning and sequencing of a human thioredoxin reductase*. *FEBS Lett*, 1995. **373**(1): p. 5-9.
467. Miranda-Vizuete, A., et al., *Human mitochondrial thioredoxin reductase cDNA cloning, expression and genomic organization*. *Eur J Biochem*, 1999. **261**(2): p. 405-12.
468. Johnson, I.D., *Molecular Probes Handbook: A Guide to Fluorescent Probes and Labeling Technologies*. 2010: Life Technologies Corporation.
469. Invitrogen, *Shedding light on oxidative stress*. 2011.
470. Wu, L., et al., *Reaction-Based Fluorescent Probes for the Detection and Imaging of Reactive Oxygen, Nitrogen, and Sulfur Species*. *Accounts of Chemical Research*, 2019. **52**(9): p. 2582-2597.
471. Saito, I., T. Matsuura, and K. Inoue, *Formation of superoxide ion from singlet oxygen. Use of a water-soluble singlet oxygen source*. *Journal of the American Chemical Society*, 1981. **103**(1): p. 188-190.
472. Gong, W., et al., *Redefining the photo-stability of common fluorophores with triplet state quenchers: mechanistic insights and recent updates*. *Chem Commun (Camb)*, 2019. **55**(60): p. 8695-8704.
473. Zheng, Q., et al., *Ultra-stable organic fluorophores for single-molecule research*. *Chem Soc Rev*, 2014. **43**(4): p. 1044-56.
474. Benesch, R.E. and R. Benesch, *Enzymatic removal of oxygen for polarography and related methods*. *Science*, 1953. **118**(3068): p. 447-8.

475. Aitken, C.E., R.A. Marshall, and J.D. Puglisi, *An oxygen scavenging system for improvement of dye stability in single-molecule fluorescence experiments*. *Biophys J*, 2008. **94**(5): p. 1826-35.
476. Widengren, J. and R. Rigler, *Mechanisms of photobleaching investigated by fluorescence correlation spectroscopy*. *Bioimaging*, 1996. **4**(3): p. 149-157.
477. Song, L., et al., *Influence of the triplet excited state on the photobleaching kinetics of fluorescein in microscopy*. *Biophys J*, 1996. **70**(6): p. 2959-68.
478. Zheng, Q., et al., *On the Mechanisms of Cyanine Fluorophore Photostabilization*. *J Phys Chem Lett*, 2012. **3**(16): p. 2200-2203.
479. Ha, T. and P. Tinnefeld, *Photophysics of fluorescent probes for single-molecule biophysics and super-resolution imaging*. *Annu Rev Phys Chem*, 2012. **63**: p. 595-617.
480. Eggeling, C., et al., *Photobleaching of Fluorescent Dyes under Conditions Used for Single-Molecule Detection: Evidence of Two-Step Photolysis*. *Anal Chem*, 1998. **70**(13): p. 2651-9.
481. Eggeling, C., et al., *Analysis of photobleaching in single-molecule multicolor excitation and Forster resonance energy transfer measurements*. *J Phys Chem A*, 2006. **110**(9): p. 2979-95.
482. Dijk, M.A., et al., *Combining optical trapping and single-molecule fluorescence spectroscopy: enhanced photobleaching of fluorophores*. *J Phys Chem B*, 2004. **108**(20): p. 6479-84.
483. Jovanovic, S.V., et al., *Antioxidant Potential of Gallocatechins. A Pulse Radiolysis and Laser Photolysis Study*. *Journal of the American Chemical Society*, 1995. **117**(39): p. 9881-9888.
484. Mukai, K., S. Nagai, and K. Ohara, *Kinetic study of the quenching reaction of singlet oxygen by tea catechins in ethanol solution*. *Free Radic Biol Med*, 2005. **39**(6): p. 752-61.
485. Petrou, A.L., et al., *A Possible Role for Singlet Oxygen in the Degradation of Various Antioxidants. A Meta-Analysis and Review of Literature Data*. *Antioxidants (Basel)*, 2018. **7**(3).
486. Widengren, J., et al., *Strategies to improve photostabilities in ultrasensitive fluorescence spectroscopy*. *J Phys Chem A*, 2007. **111**(3): p. 429-40.
487. Krumova, K. and G. Cosa, *Chapter 1 Overview of Reactive Oxygen Species*, in *Singlet Oxygen: Applications in Biosciences and Nanosciences, Volume 1*. 2016, The Royal Society of Chemistry. p. 1-21.
488. Noctor, G. and C.H. Foyer, *ASCORBATE AND GLUTATHIONE: Keeping Active Oxygen Under Control*. *Annu Rev Plant Physiol Plant Mol Biol*, 1998. **49**: p. 249-279.
489. Giloh, H. and J.W. Sedat, *Fluorescence microscopy: reduced photobleaching of rhodamine and fluorescein protein conjugates by n-propyl gallate*. *Science*, 1982. **217**(4566): p. 1252-5.
490. Gaigalas, A.K., et al., *Photodegradation of Fluorescein in Solutions Containing n-Propyl Gallate*. *The Journal of Physical Chemistry A*, 2004. **108**(20): p. 4378-4384.
491. Rasnik, I., S.A. McKinney, and T. Ha, *Nonblinking and long-lasting single-molecule fluorescence imaging*. *Nat Methods*, 2006. **3**(11): p. 891-3.
492. Dave, R., et al., *Mitigating unwanted photophysical processes for improved single-molecule fluorescence imaging*. *Biophys J*, 2009. **96**(6): p. 2371-81.
493. Dittrich, P.S. and P. Schwille, *Photobleaching and stabilization of fluorophores used for single-molecule analysis. with one- and two-photon excitation*. *Applied Physics B*, 2001. **73**(8): p. 829-837.
494. Frutos, L.M., et al., *A theory of nonvertical triplet energy transfer in terms of accurate potential energy surfaces: the transfer reaction from pi,pi* triplet donors to 1,3,5,7-cyclooctatetraene*. *J Chem Phys*, 2004. **120**(3): p. 1208-16.
495. Sharonov, A. and R.M. Hochstrasser, *Wide-field subdiffraction imaging by accumulated binding of diffusing probes*. *Proc Natl Acad Sci U S A*, 2006. **103**(50): p. 18911-6.
496. Jungmann, R., et al., *Multiplexed 3D cellular super-resolution imaging with DNA-PAINT and Exchange-PAINT*. *Nat Methods*, 2014. **11**(3): p. 313-8.
497. Schnitzbauer, J., et al., *Super-resolution microscopy with DNA-PAINT*. *Nat Protoc*, 2017. **12**(6): p. 1198-1228.
498. Huisken, J. and D.Y.R. Stainier, *Selective plane illumination microscopy techniques in developmental biology*. *Development*, 2009. **136**(12): p. 1963.

499. Power, R.M. and J. Huisken, *A guide to light-sheet fluorescence microscopy for multiscale imaging*. Nat Methods, 2017. **14**(4): p. 360-373.
500. Chen, B.C., et al., *Lattice light-sheet microscopy: imaging molecules to embryos at high spatiotemporal resolution*. Science, 2014. **346**(6208): p. 1257998.
501. Dixit, R. and R. Cyr, *Cell damage and reactive oxygen species production induced by fluorescence microscopy: effect on mitosis and guidelines for non-invasive fluorescence microscopy*. Plant J, 2003. **36**(2): p. 280-90.
502. Icha, J., et al., *Phototoxicity in live fluorescence microscopy, and how to avoid it*. Bioessays, 2017. **39**(8).
503. Magidson, V. and A. Khodjakov, *Circumventing photodamage in live-cell microscopy*. Methods Cell Biol, 2013. **114**: p. 545-60.
504. Mubaid, F. and C.M. Brown, *Less is More: Longer Exposure Times with Low Light Intensity is Less Photo-Toxic*. Microscopy Today, 2017. **25**(6): p. 26-35.
505. MicroscopyU. *Introduction to Fluorescence Microscopy*. February 8, 2021]; Available from: <https://www.microscopyu.com/techniques/fluorescence/introduction-to-fluorescence-microscopy>.
506. Olympus. *Fluorescence Filters*. February 8, 2021]; Available from: <https://www.olympus-lifescience.com/en/microscope-resource/primer/techniques/fluorescence/filters/>.
507. Expressions, M. *Brief Overview of Fluorescence Filters*. 1998 September 11, 2018 February 8, 2021]; Available from: <https://micro.magnet.fsu.edu/primer/techniques/fluorescence/fluorofiltershome.html>.
508. Zeiss. *Microscope Light Sources*. February 8, 2021]; Available from: <http://zeiss-campus.magnet.fsu.edu/articles/lightsources/index.html>.
509. Mubaid, F., et al., *Fluorescence microscope light source stability*. Histochemistry and Cell Biology, 2019. **151**(4): p. 357-366.
510. Albeanu, D.F., et al., *LED arrays as cost effective and efficient light sources for widefield microscopy*. PLoS One, 2008. **3**(5): p. e2146.
511. Zeiss. *Filter Wheel Wavelength Selection*. February 8, 2021]; Available from: <http://zeiss-campus.magnet.fsu.edu/tutorials/filterwheel/indexflash.html>.
512. MicroscopyU. *Fluorescence Filter Combinations*. February 8, 2021]; Available from: <https://www.microscopyu.com/techniques/fluorescence/nikon-fluorescence-filter-sets>.
513. Photometrics, T. *Introduction to splitters*. February 8, 2021]; Available from: <https://www.photometrics.com/products/imaging-splitters/introduction-to-splitters>.
514. MicroscopyU. *Fundamentals of Digital Imaging*. February 8, 2021]; Available from: <https://www.microscopyu.com/digital-imaging/fundamentals-of-digital-imaging>.
515. Hamamatsu. *A visual guide to CCD vs. EM-CCD vs. CMOS*. February 8, 2021]; Available from: https://camera.hamamatsu.com/jp/en/technical_guides/visual_guide/index.html.
516. Olympus. *Digital Imaging in Optical Microscopy*. February 8, 2021]; Available from: <https://www.olympus-lifescience.com/en/microscope-resource/primer/digitalimaging/digitalimagingdetectors/>.
517. Olympus. *Introduction to CMOS Image Sensors*. February 8, 2021]; Available from: <https://www.olympus-lifescience.com/en/microscope-resource/primer/digitalimaging/cmosimagesensors/>.
518. Instruments, O. *EMCCD vs sCMOS Cameras | A Comparison*. April 8, 2021]; Available from: <https://andor.oxinst.com/learning/view/article/comparing-scmos>.
519. Olympus. *Introduction to Confocal Microscopy*. February 8, 2021]; Available from: <https://www.olympus-lifescience.com/en/microscope-resource/primer/techniques/confocal/confocalintro/>.
520. Expressions, M. *Laser Systems for Optical Microscopy*. 2002 November 13, 2015 February 8, 2021]; Available from: <https://micro.magnet.fsu.edu/primer/techniques/microscopylasers.html>.
521. Abramczyk, H., *4 - Lasers*, in *Introduction to Laser Spectroscopy*, H. Abramczyk, Editor. 2005, Elsevier Science: Amsterdam. p. 59-106.

522. Gratton, E. and M.J. vandeVen, *Laser Sources for Confocal Microscopy*, in *Handbook Of Biological Confocal Microscopy*, J.B. Pawley, Editor. 2006, Springer US: Boston, MA. p. 80-125.
523. Šulc, J. and H. Jelínková, 5 - *Solid-state lasers for medical applications*, in *Lasers for Medical Applications*, H. Jelínková, Editor. 2013, Woodhead Publishing. p. 127-176.
524. Expressions, M. *Diode Lasers*. 2002 February 27, 2016 February 8, 2021]; Available from: <https://micro.magnet.fsu.edu/primer/java/lasers/diodelasers/index.html>.
525. Koch, S.W. and M.R. Hofmann, *Semiconductor Lasers*, in *Encyclopedia of Modern Optics (Second Edition)*, B.D. Guenther and D.G. Steel, Editors. 2018, Elsevier: Oxford. p. 462-468.
526. Olympus. *Electronic Light Detectors: Photomultipliers*. February 9, 2021]; Available from: <https://www.olympus-lifescience.com/en/microscope-resource/primer/techniques/confocal/pmtintro/>.
527. Zeiss. *Spectral Imaging and Linear Unmixing*. February 8, 2021]; Available from: <http://zeiss-campus.magnet.fsu.edu/articles/spectralimaging/index.html>.
528. MicroscopyU. *Spectral Imaging and Linear Unmixing*. February 9, 2021]; Available from: <https://www.microscopyu.com/techniques/confocal/spectral-imaging-and-linear-unmixing>.
529. Art, J., *Photon Detectors for Confocal Microscopy*, in *Handbook Of Biological Confocal Microscopy*, J.B. Pawley, Editor. 2006, Springer US: Boston, MA. p. 251-264.
530. Michalet, X., et al., *Hybrid photodetector for single-molecule spectroscopy and microscopy*. Proceedings of SPIE--the International Society for Optical Engineering, 2008. **6862**(68620F): p. 68620F_1.
531. Olympus. *Avalanche Photodiodes*. February 9, 2021]; Available from: <https://www.olympus-lifescience.com/en/microscope-resource/primer/java/digitalimaging/avalanche/>.
532. Hamamatsu, *Photomultiplier Tubes: Basics and Applications*. 2007.
533. Papiez, B.W., et al., *Image-Based Artefact Removal in Laser Scanning Microscopy*. IEEE Trans Biomed Eng, 2020. **67**(1): p. 79-87.
534. Zeiss. *Spinning Disk Confocal Microscopy*. February 8, 2021]; Available from: <http://zeiss-campus.magnet.fsu.edu/articles/spinningdisk/index.html>.
535. Zeiss. *Introduction to Spinning Disk Confocal Microscopy*. [cited February 9, 2021; Available from: <http://zeiss-campus.magnet.fsu.edu/articles/spinningdisk/introduction.html>.
536. MicroscopyU. *Total Internal Reflection Fluorescence (TIRF) Microscopy*. February 8, 2021]; Available from: <https://www.microscopyu.com/techniques/fluorescence/total-internal-reflection-fluorescence-tirf-microscopy>.
537. Axelrod, D., *Total Internal Reflection Fluorescence Microscopy*, in *Encyclopedia of Cell Biology*, R.A. Bradshaw and P.D. Stahl, Editors. 2016, Academic Press: Waltham. p. 62-69.
538. Worth, D.C. and M. Parsons, *Advances in imaging cell–matrix adhesions*. Journal of Cell Science, 2010. **123**(21): p. 3629.
539. MicroscopyU. *Basics of FRET Microscopy*. February 8, 2021]; Available from: <https://www.microscopyu.com/techniques/fluorescence/basics-of-fret-microscopy>.
540. Forster, T., **ZWISCHENMOLEKULARE ENERGIEWANDERUNG UND FLUORESZENZ*. Annalen Der Physik, 1948. **2**(1-2): p. 55-75.
541. Bajar, B.T., et al., *A Guide to Fluorescent Protein FRET Pairs*. Sensors (Basel), 2016. **16**(9).
542. Patterson, G.H., D.W. Piston, and B.G. Barisas, *Förster distances between green fluorescent protein pairs*. Anal Biochem, 2000. **284**(2): p. 438-40.
543. Broussard, J.A., et al., *Fluorescence resonance energy transfer microscopy as demonstrated by measuring the activation of the serine/threonine kinase Akt*. Nature protocols, 2013. **8**(2): p. 265-281.
544. Miyawaki, A., et al., *Fluorescent indicators for Ca²⁺ based on green fluorescent proteins and calmodulin*. Nature, 1997. **388**(6645): p. 882-7.
545. Mohsin, M., A. Ahmad, and M. Iqbal, *FRET-based genetically-encoded sensors for quantitative monitoring of metabolites*. Biotechnol Lett, 2015. **37**(10): p. 1919-28.

546. Imamura, H., et al., *Visualization of ATP levels inside single living cells with fluorescence resonance energy transfer-based genetically encoded indicators*. Proc Natl Acad Sci U S A, 2009. **106**(37): p. 15651-6.
547. Pertz, O. and K.M. Hahn, *Designing biosensors for Rho family proteins--deciphering the dynamics of Rho family GTPase activation in living cells*. J Cell Sci, 2004. **117**(Pt 8): p. 1313-8.
548. Mukherjee, A., et al., *A Fyn biosensor reveals pulsatile, spatially localized kinase activity and signaling crosstalk in live mammalian cells*. Elife, 2020. **9**.
549. Ni, Q., D.V. Titov, and J. Zhang, *Analyzing protein kinase dynamics in living cells with FRET reporters*. Methods, 2006. **40**(3): p. 279-86.
550. Tsutsui, H., et al., *Improving membrane voltage measurements using FRET with new fluorescent proteins*. Nat Methods, 2008. **5**(8): p. 683-5.
551. Borghi, N., et al., *E-cadherin is under constitutive actomyosin-generated tension that is increased at cell-cell contacts upon externally applied stretch*. Proc Natl Acad Sci U S A, 2012. **109**(31): p. 12568-73.
552. Grashoff, C., et al., *Measuring mechanical tension across vinculin reveals regulation of focal adhesion dynamics*. Nature, 2010. **466**(7303): p. 263-6.
553. Kumar, A., et al., *Talin tension sensor reveals novel features of focal adhesion force transmission and mechanosensitivity*. J Cell Biol, 2016. **213**(3): p. 371-83.
554. Meng, F., T.M. Suchyna, and F. Sachs, *A fluorescence energy transfer-based mechanical stress sensor for specific proteins in situ*. FEBS J, 2008. **275**(12): p. 3072-87.
555. Meng, F. and F. Sachs, *Visualizing dynamic cytoplasmic forces with a compliance-matched FRET sensor*. J Cell Sci, 2011. **124**(Pt 2): p. 261-9.
556. Arsenovic, P.T., et al., *Nesprin-2G, a Component of the Nuclear LINC Complex, Is Subject to Myosin-Dependent Tension*. Biophys J, 2016. **110**(1): p. 34-43.
557. Lindenburg, L. and M. Merkx, *Engineering genetically encoded FRET sensors*. Sensors (Basel), 2014. **14**(7): p. 11691-713.
558. Algar, W.R., et al., *FRET as a biomolecular research tool — understanding its potential while avoiding pitfalls*. Nature Methods, 2019. **16**(9): p. 815-829.
559. Balaban, N.Q., et al., *Force and focal adhesion assembly: a close relationship studied using elastic micropatterned substrates*. Nat Cell Biol, 2001. **3**(5): p. 466-72.
560. Tan, J.L., et al., *Cells lying on a bed of microneedles: an approach to isolate mechanical force*. Proc Natl Acad Sci U S A, 2003. **100**(4): p. 1484-9.
561. Ziegler, W.H., et al., *Integrin connections to the cytoskeleton through talin and vinculin*. Biochem Soc Trans, 2008. **36**(Pt 2): p. 235-9.
562. Carisey, A. and C. Ballestrem, *Vinculin, an adapter protein in control of cell adhesion signalling*. Eur J Cell Biol, 2011. **90**(2-3): p. 157-63.
563. Klapholz, B. and N.H. Brown, *Talin - the master of integrin adhesions*. J Cell Sci, 2017. **130**(15): p. 2435-2446.
564. Calderwood, D.A., I.D. Campbell, and D.R. Critchley, *Talins and kindlins: partners in integrin-mediated adhesion*. Nat Rev Mol Cell Biol, 2013. **14**(8): p. 503-17.
565. MicroscopyU. *Resolution*. February 9, 2021]; Available from: <https://www.microscopyu.com/microscopy-basics/resolution>.
566. MicroscopyU. *Numerical Aperture*. February 9, 2021]; Available from: <https://www.microscopyu.com/microscopy-basics/numerical-aperture>.
567. MicroscopyU. *Properties of Microscope Objectives*. February 9, 2021]; Available from: <https://www.microscopyu.com/microscopy-basics/properties-of-microscope-objectives>.
568. Olympus. *Resolution and Contrast in Confocal Microscopy*. February 9, 2021]; Available from: <https://www.olympus-lifescience.com/en/microscope-resource/primer/techniques/confocal/resolutionintro/>.
569. Ruzin, S. *Resolution in a confocal system*. February 9, 2021]; Available from: <http://microscopy.berkeley.edu/courses/TLM/clsm/resolution.html>.

570. Cole, R.W., T. Jinadasa, and C.M. Brown, *Measuring and interpreting point spread functions to determine confocal microscope resolution and ensure quality control*. Nat Protoc, 2011. **6**(12): p. 1929-41.
571. MicroscopyU. *Single-Molecule Super-Resolution Imaging*. February 9, 2021]; Available from: <https://www.microscopyu.com/techniques/super-resolution/single-molecule-super-resolution-imaging>.
572. Zhuang, X., *Nano-imaging with Storm*. Nature photonics, 2009. **3**(7): p. 365-367.
573. Rust, M.J., M. Bates, and X. Zhuang, *Sub-diffraction-limit imaging by stochastic optical reconstruction microscopy (STORM)*. Nature methods, 2006. **3**(10): p. 793-795.
574. MicroscopyU. *Stochastic Optical Reconstruction Microscopy (STORM) Imaging*. February 9, 2021]; Available from: <https://www.microscopyu.com/tutorials/stochastic-optical-reconstruction-microscopy-storm-imaging>.
575. Dempsey, G.T., et al., *Evaluation of fluorophores for optimal performance in localization-based super-resolution imaging*. Nat Methods, 2011. **8**(12): p. 1027-36.
576. Cheezum, M.K., W.F. Walker, and W.H. Guilford, *Quantitative comparison of algorithms for tracking single fluorescent particles*. Biophys J, 2001. **81**(4): p. 2378-88.
577. Thompson, R.E., D.R. Larson, and W.W. Webb, *Precise nanometer localization analysis for individual fluorescent probes*. Biophys J, 2002. **82**(5): p. 2775-83.
578. Bates, M., S.A. Jones, and X. Zhuang, *Stochastic optical reconstruction microscopy (STORM): a method for superresolution fluorescence imaging*. Cold Spring Harb Protoc, 2013. **2013**(6): p. 498-520.
579. Yildiz, A., et al., *Myosin V walks hand-over-hand: single fluorophore imaging with 1.5-nm localization*. Science, 2003. **300**(5628): p. 2061-5.
580. Qu, X., et al., *Nanometer-localized multiple single-molecule fluorescence microscopy*. Proc Natl Acad Sci U S A, 2004. **101**(31): p. 11298-303.
581. Tan, Y.H., et al., *A nanoengineering approach for investigation and regulation of protein immobilization*. ACS Nano, 2008. **2**(11): p. 2374-84.
582. Coulter, A. and R. Harris, *Simplified preparation of rabbit Fab fragments*. J Immunol Methods, 1983. **59**(2): p. 199-203.
583. Saber, R., et al., *High resolution imaging of IgG and IgM molecules by scanning tunneling microscopy in air condition*. Scientia Iranica, 2011. **18**(6): p. 1643-1646.
584. San Paulo, A. and R. García, *High-Resolution Imaging of Antibodies by Tapping-Mode Atomic Force Microscopy: Attractive and Repulsive Tip-Sample Interaction Regimes*. Biophysical Journal, 2000. **78**(3): p. 1599-1605.
585. Los, G.V., et al., *HaloTag: a novel protein labeling technology for cell imaging and protein analysis*. ACS Chem Biol, 2008. **3**(6): p. 373-82.
586. Keppler, A., et al., *A general method for the covalent labeling of fusion proteins with small molecules in vivo*. Nat Biotechnol, 2003. **21**(1): p. 86-9.
587. Gautier, A., et al., *An engineered protein tag for multiprotein labeling in living cells*. Chem Biol, 2008. **15**(2): p. 128-36.
588. Pegg, A.E., *Repair of O(6)-alkylguanine by alkyltransferases*. Mutat Res, 2000. **462**(2-3): p. 83-100.
589. Erdmann, R.S., et al., *Labeling Strategies Matter for Super-Resolution Microscopy: A Comparison between HaloTags and SNAP-tags*. Cell Chem Biol, 2019. **26**(4): p. 584-592 e6.
590. MicroscopyU. *Molecular Density in Super-Resolution Microscopy*. February 9, 2021]; Available from: <https://www.microscopyu.com/tutorials/molecular-density-in-superresolution-microscopy>.
591. Shannon, C.E., *COMMUNICATION IN THE PRESENCE OF NOISE*. Proceedings of the Institute of Radio Engineers, 1949. **37**(1): p. 10-21.
592. Shroff, H., et al., *Live-cell photoactivated localization microscopy of nanoscale adhesion dynamics*. Nat Methods, 2008. **5**(5): p. 417-23.

593. Zeiss. *Introduction to Photoactivated Localization Microscopy*. February 8, 2021]; Available from: <http://zeiss-campus.magnet.fsu.edu/articles/superresolution/palm/introduction.html>.
594. Li, W.H. and G. Zheng, *Photoactivatable fluorophores and techniques for biological imaging applications*. *Photochem Photobiol Sci*, 2012. **11**(3): p. 460-71.
595. Lippincott-Schwartz, J. and G.H. Patterson, *Photoactivatable fluorescent proteins for diffraction-limited and super-resolution imaging*. *Trends Cell Biol*, 2009. **19**(11): p. 555-65.
596. Lukyanov, K.A., et al., *Innovation: Photoactivatable fluorescent proteins*. *Nat Rev Mol Cell Biol*, 2005. **6**(11): p. 885-91.
597. Patterson, G.H. and J. Lippincott-Schwartz, *A photoactivatable GFP for selective photolabeling of proteins and cells*. *Science*, 2002. **297**(5588): p. 1873-7.
598. Subach, F.V., et al., *Photoactivatable mCherry for high-resolution two-color fluorescence microscopy*. *Nat Methods*, 2009. **6**(2): p. 153-9.
599. Ando, R., H. Mizuno, and A. Miyawaki, *Regulated fast nucleocytoplasmic shuttling observed by reversible protein highlighting*. *Science*, 2004. **306**(5700): p. 1370-3.
600. Habuchi, S., et al., *Photo-induced protonation/deprotonation in the GFP-like fluorescent protein Dronpa: mechanism responsible for the reversible photoswitching*. *Photochemical & Photobiological Sciences*, 2006. **5**(6): p. 567-576.
601. Zhang, M., et al., *Rational design of true monomeric and bright photoactivatable fluorescent proteins*. *Nat Methods*, 2012. **9**(7): p. 727-9.
602. McKinney, S.A., et al., *A bright and photostable photoconvertible fluorescent protein*. *Nat Methods*, 2009. **6**(2): p. 131-3.
603. Wang, S., et al., *Characterization and development of photoactivatable fluorescent proteins for single-molecule-based superresolution imaging*. *Proc Natl Acad Sci U S A*, 2014. **111**(23): p. 8452-7.
604. Gurskaya, N.G., et al., *Engineering of a monomeric green-to-red photoactivatable fluorescent protein induced by blue light*. *Nat Biotechnol*, 2006. **24**(4): p. 461-5.
605. Hess, S.T., T.P. Girirajan, and M.D. Mason, *Ultra-high resolution imaging by fluorescence photoactivation localization microscopy*. *Biophys J*, 2006. **91**(11): p. 4258-72.
606. Dickson, R.M., et al., *On/off blinking and switching behaviour of single molecules of green fluorescent protein*. *Nature*, 1997. **388**(6640): p. 355-8.
607. Betzig, E., et al., *Imaging intracellular fluorescent proteins at nanometer resolution*. *Science*, 2006. **313**(5793): p. 1642-5.
608. Deschout, H., et al., *Precisely and accurately localizing single emitters in fluorescence microscopy*. *Nat Methods*, 2014. **11**(3): p. 253-66.
609. Huang, B., et al., *Three-dimensional super-resolution imaging by stochastic optical reconstruction microscopy*. *Science*, 2008. **319**(5864): p. 810-3.
610. Prabhat, P., et al., *Simultaneous imaging of different focal planes in fluorescence microscopy for the study of cellular dynamics in three dimensions*. *IEEE Trans Nanobioscience*, 2004. **3**(4): p. 237-42.
611. Juette, M.F., et al., *Three-dimensional sub-100 nm resolution fluorescence microscopy of thick samples*. *Nat Methods*, 2008. **5**(6): p. 527-9.
612. Toprak, E., et al., *Three-dimensional particle tracking via bifocal imaging*. *Nano Lett*, 2007. **7**(7): p. 2043-5.
613. Lew, M.D., et al., *Corkscrew point spread function for far-field three-dimensional nanoscale localization of pointlike objects*. *Opt Lett*, 2011. **36**(2): p. 202-4.
614. Pavani, S.R. and R. Piestun, *Three dimensional tracking of fluorescent microparticles using a photon-limited double-helix response system*. *Opt Express*, 2008. **16**(26): p. 22048-57.
615. Thompson, M.A., et al., *Localizing and tracking single nanoscale emitters in three dimensions with high spatiotemporal resolution using a double-helix point spread function*. *Nano Lett*, 2010. **10**(1): p. 211-8.

616. Shtengel, G., et al., *Interferometric fluorescent super-resolution microscopy resolves 3D cellular ultrastructure*. Proc Natl Acad Sci U S A, 2009. **106**(9): p. 3125-30.
617. Bhushan, B., J.C. Wyant, and C.L. Koliopoulos, *Measurement of surface topography of magnetic tapes by Mirau interferometry*. Appl Opt, 1985. **24**(10): p. 1489.
618. Kim, S., et al., *Elevated TGF- β 1 and - β 2 expression accelerates the epithelial to mesenchymal transition in triple-negative breast cancer cells*. Cytokine, 2015. **75**(1): p. 151-8.
619. Drasin, D.J., T.P. Robin, and H.L. Ford, *Breast cancer epithelial-to-mesenchymal transition: examining the functional consequences of plasticity*. Breast Cancer Res, 2011. **13**(6): p. 226.
620. Côme, C., et al., *Snail and slug play distinct roles during breast carcinoma progression*. Clin Cancer Res, 2006. **12**(18): p. 5395-402.
621. Yang, J., et al., *Twist, a master regulator of morphogenesis, plays an essential role in tumor metastasis*. Cell, 2004. **117**(7): p. 927-39.
622. Taube, J.H., et al., *Core epithelial-to-mesenchymal transition interactome gene-expression signature is associated with claudin-low and metaplastic breast cancer subtypes*. Proc Natl Acad Sci U S A, 2010. **107**(35): p. 15449-54.
623. Kim, S., et al., *Berberine Suppresses Cell Motility Through Downregulation of TGF- β 1 in Triple Negative Breast Cancer Cells*. Cellular Physiology and Biochemistry, 2018. **45**(2): p. 795-807.
624. Terashima, M., et al., *Synergistic antitumor effects of S-1 with eribulin in vitro and in vivo for triple-negative breast cancer cell lines*. Springerplus, 2014. **3**: p. 417.
625. Brown, K.A., et al., *Induction by transforming growth factor- β 1 of epithelial to mesenchymal transition is a rare event in vitro*. Breast Cancer Research, 2004. **6**(3): p. R215.
626. Luwor, R.B., et al., *Single live cell TGF- β signalling imaging: breast cancer cell motility and migration is driven by sub-populations of cells with dynamic TGF- β -Smad3 activity*. Molecular Cancer, 2015. **14**(1): p. 50.

1.10 FIGURES AND LEGENDS

Lipoma Preferred Partner (LPP)

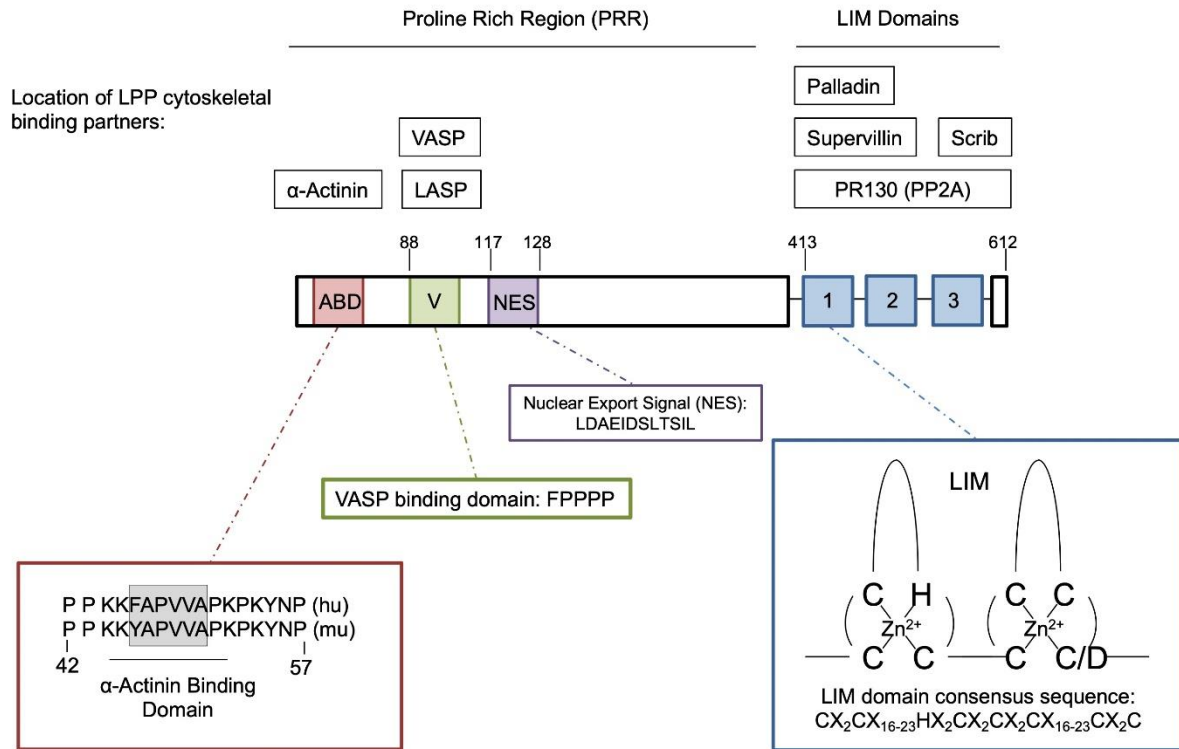


Figure 1.1. Schematic depicting the domain structure of LPP. LPP can be divided into the N-terminal Proline Rich Region (PRR) and the C-terminal LIM domains. Distinct domains within LPP are indicated: ABD: α -actinin binding domain; V: VASP binding domain; NES: nuclear export signal; 1/2/3: LIM domains. LPP interacting proteins are listed above the LPP schematic. Consensus sequences for the LPP α -actinin binding domain (ABD) and LIM domains are depicted below the LPP schematic. Numbers refer to the amino acid position within LPP.

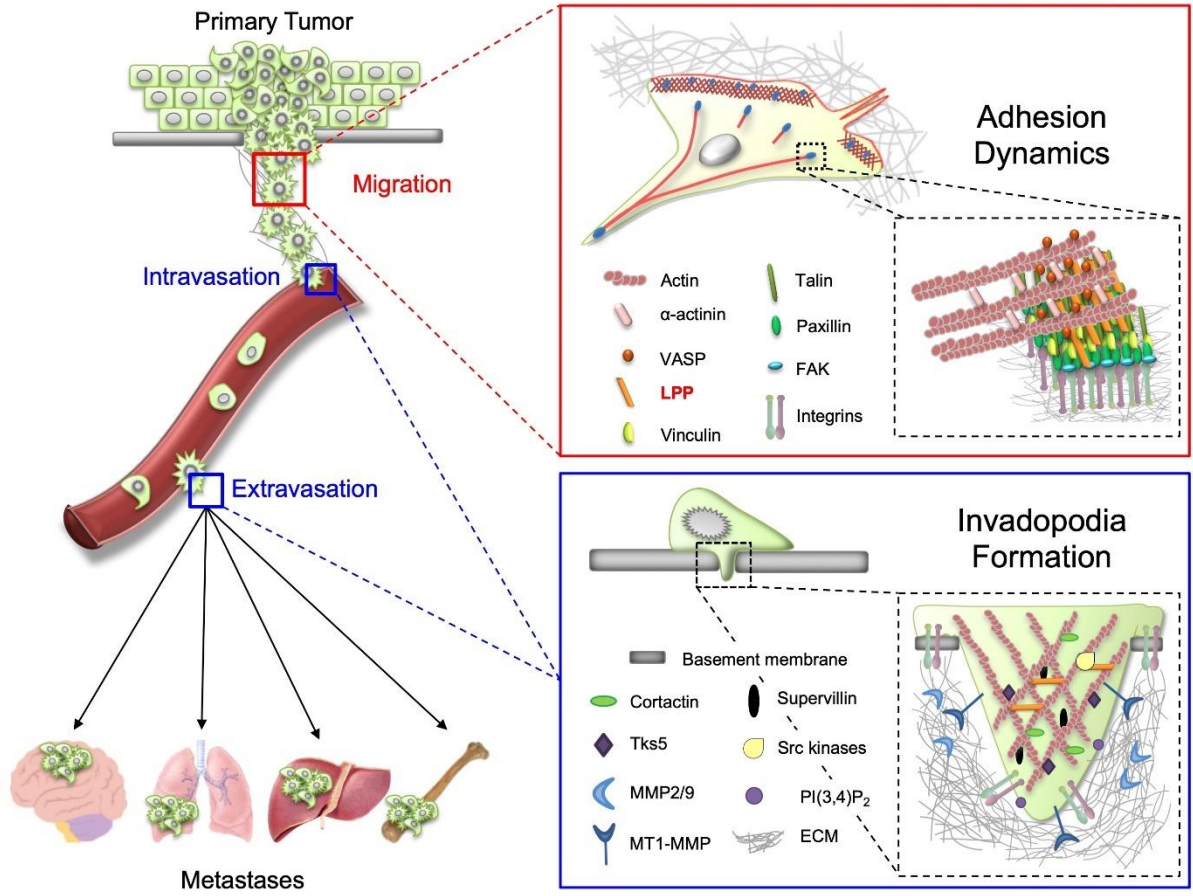
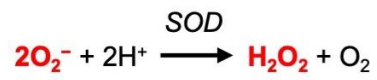


Figure 1.2. Schematic illustrating distinct points within the metastatic cascade that rely on LPP-regulated cellular functions (*left panel*). LPP is localized to adhesions, which are cellular structures on the ventral surface of cells that are critical for their migration. LPP is situated where the actin cable connects to components of the adhesion (*upper right panel*). Invadopodia are actin-rich structures with associated proteolytic activity that are responsible for localized degradation of ECM components (*lower right panel*). Recently, LPP has been shown to be a constituent of cellular adhesions and also required for efficient invadopodia formation, cancer cell invasion and metastasis.

1. Superoxide dismutase (SOD)



2. Catalase



3. Glutathione peroxidase (GPx)



4. Peroxiredoxins (Prx), thioredoxins (Trx) and thioredoxin reductase (TrxR)

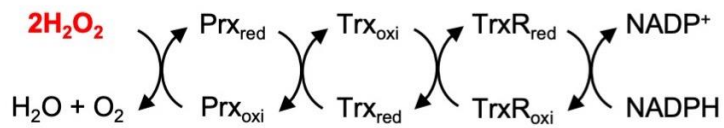


Figure 1.3. Cellular mechanisms that eliminate reactive oxygen species (ROS). Cells possess numerous enzymes designed to neutralize ROS, including (1) superoxide dismutase (SOD); (2) catalase; (3) glutathione peroxidase (GPx); and (4) peroxiredoxins (Prx), thioredoxins (Trx) and thioredoxin reductases (TrxR).

CHAPTER 2 – Optimizing live-cell fluorescence imaging conditions to minimize phototoxicity

Alex Kiepas^{1,2}, Elena Voorand^{2,3}, Firas Mubaid¹, Peter M. Siegel^{2,3,4,5} and Claire M. Brown^{1,5,6,7,8}

¹Department of Physiology, ²Goodman Cancer Research Centre, ³Department of Biochemistry, ⁴Department of Medicine, ⁵Department of Anatomy & Cell Biology, ⁶Advanced BioImaging Facility (ABIF), ⁷Cell Information Systems and ⁸Centre for Applied Mathematics in Bioscience and Medicine (CAMBAM), McGill University, Montreal, Quebec, Canada

This chapter is an original research article published in:
Journal of Cell Science, 2020

2.1 PREFACE

Microscopes allow us to observe the behavior of living cells in real-time. Unfortunately, the process of imaging fluorescent molecules with light can cause phototoxicity. Small changes in sample illumination often have a profound impact on cell health due to the production of radical oxygen species (ROS). Additional fluorescence illumination beyond the camera exposure time, termed “illumination overhead” (IO), significantly impacts cell health. Transistor-transistor logic (TTL) circuits between the camera and the light source can efficiently eliminate IO; however, many core-facility users around the world still rely on bulb-based microscopy platforms that cannot be configured with such technologies. Therefore, we investigated an alternative solution to maximize the utility of microscopy platforms to image both slow and fast cellular processes without harming cells. The overall goal of the present study was to bring awareness to the issue of phototoxicity and help researchers develop imaging protocols that more accurately capture cellular events.

2.2 ABSTRACT

Fluorescence illumination can cause phototoxicity that negatively affects living samples. This study demonstrates that much of the phototoxicity and photobleaching experienced with live-cell fluorescence imaging occurs as a result of ‘illumination overhead’ (IO). This occurs when a sample is illuminated but fluorescence emission is not being captured by the microscope camera. Several technological advancements have been developed, including fast-switching LED lamps and transistor-transistor logic (TTL) circuits, to diminish phototoxicity caused by IO. These advancements are not standard features on most microscopes and many biologists are unaware of their necessity for live-cell imaging. IO is particularly problematic when imaging rapid processes that require short exposure times. This study presents a workflow to optimize imaging conditions for measuring both slow and dynamic processes while minimizing phototoxicity on any standard microscope. The workflow includes a guide on how to (1) determine the maximum image exposure time for a dynamic process, (2) optimize excitation light intensity and (3) assess cell health with mitochondrial markers.

2.3 INTRODUCTION

Fluorescence microscopy provides a convenient, selective and sensitive way to observe living systems. Although modern microscopes are capable of capturing live-cell dynamics with incredible spatial and temporal resolution, phototoxicity has emerged as a significant limitation [1, 2]. Normally, fluorescent molecules absorb light energy and enter an excited state. A proportion of these excited fluorescent molecules can photobleach resulting in the production of singlet oxygen species during the imaging process [3]. It is generally thought that phototoxicity of live samples is tightly linked to the release of highly reactive oxygen species (ROS) during photobleaching [4].

Cells have several physiological mechanisms to deal with ROS production, including the induction of catalases, peroxidases and superoxide dismutases, the synthesis of antioxidants, and cell cycle delay [5]. Under physiological conditions, most growing cells can successfully manage ROS generated by aerobic metabolism. Additional ROS generated by fluorescent illumination, however, may overwhelm enzymes and mechanisms typically in place to limit damage. In particular, the quantity of ROS production may affect the ability of cells to effectively detoxify ROS. Consequently, two general approaches have been proposed for reducing photobleaching and phototoxicity: (1) increasing the exposure time and decreasing excitation light power (diffuse light delivery; DLD); or (2) decreasing the exposure time and increasing excitation light power (condensed light delivery; CLD). Proponents of the former approach argue that generating lower doses of ROS over a longer period of time alleviates pressure on cellular mechanisms designed to eliminate ROS [6-8]. Indeed, dye oxidation is reversible if cells are exposed to low irradiation levels [6]. In contrast, proponents of the latter approach argue that photobleaching and phototoxicity depend on total light dose rather than exposure time [9, 10].

Thus, the goal of the present study is to provide a comprehensive workflow to minimize phototoxicity during live-cell fluorescence imaging and explore CLD and DLD approaches. Using cell migration and mitochondrial morphology as sensitive readouts of cell health, we demonstrate that ‘illumination overhead’ (IO) beyond the camera exposure time causes a significant amount of phototoxicity and photobleaching. This is especially significant under CLD conditions when short exposure times with high light powers are employed. The results show that longer camera exposure times and stream acquisition can be implemented to circumvent the negative effects caused by IO without the need for specialized equipment. We use the microtubule tip-binding protein EB3 (also

known as MAPRE3) to demonstrate how the maximum exposure time for a fast process, such as microtubule tip tracking ($0.5 \mu\text{m s}^{-1}$) [11, 12], can be determined. Additionally, we show how the signal-to-noise ratio (S/N) of images can be improved through median filtering, spatial binning and temporal binning to access even lower illumination powers. Finally, using adhesion dynamics as an example, we demonstrate how the workflow can be used to detect often unobserved cellular processes and answer novel biological questions. Overall, the conclusion of the study is to maximize the image exposure time, avoid time delays between subsequent images, and minimize the light intensity to reduce the impact of IO and minimize phototoxicity.

2.4 RESULTS

2.4.1 IO is a widespread problem in fluorescence imaging

The optimal method for reducing phototoxicity depends on the microscope hardware. For example, older bulb-based light sources need to warm up for ~30 min before use [13] and cannot be repeatedly turned on and off. Thus, mechanical shutters are necessary to control sample illumination [14]. Mechanical shutters require tens or hundreds of milliseconds to open and close [15]. Consequently, samples receive additional light exposure, termed ‘illumination overhead’ (IO), where the sample is exposed to light but fluorescence emission is not being captured by the detector.

Recent advancements in electronics engineering have essentially eliminated the need for physical shutters through the use of light sources that can be turned on and off electronically (e.g. LED light sources and solid-state lasers). Unfortunately, delays in camera initiation, unsynchronized light source activation, and software and data handling delays can still contribute to IO. Transistor-transistor logic (TTL) circuits can be implemented between the camera and light source to limit the ‘on time’ of the light source precisely to the camera exposure time. However, measuring IO, implementing TTL or minimizing IO in other ways can be technically challenging. Indeed, there is a general need to create awareness of the problem as a survey conducted by Canada BioImaging (CBI) of 14 light microscopy facilities and 41 facility users (from across Canada) revealed that 21% of facility managers and 51% of facility users were unaware of IO (Table S2.1). A further 43% of facility managers and 66% of facility users were unaware that IO could occur on the order of hundreds of milliseconds when mechanical shutters are used (Table S2.1). In addition, there are over 100 widefield microscopes in use in the facilities surveyed, and 65-70% of facilities rely on bulb-based light sources that require mechanical shutters and cannot take advantage of direct TTL triggering. Half of the facilities have one or more spinning disk (SD) confocal microscopes in use and 30% of facility users employ an SD microscope for their research.

2.4.2 TTL circuits can sometimes eliminate IO caused by hardware and software delays

Live-cell fluorescence imaging is commonly conducted on widefield, SD confocal or total internal reflection fluorescence (TIRF) microscopes [16]. There are several different ways of controlling fluorescence light delivery to samples on these platforms including shutters (bulb-based systems), USB software triggering of LED lamps or solid-state lasers, or a TTL circuit where

electrical current is only sent to the light source when the camera is actively acquiring fluorescence photons (Fig. 2.1A). For USB triggering, careful synchronization between the light source and camera is required to avoid software delays in executing the command and saving acquired data that can contribute to IO.

In addition to light source activation, there are also two different methods of acquiring time-lapse data: interval imaging and stream acquisition (Fig. 2.1A). Interval imaging allows users to set a time delay between image acquisitions. Following each acquisition, the image is saved to the hard drive of the computer before the next image is captured. In contrast, stream acquisition attempts to capture images as quickly as possible (up to the camera frame rate) while the sample is constantly illuminated. Importantly, images can be temporarily stored on the random-access memory (RAM) of the computer to permit faster write speeds for rapid imaging.

Given this information, the total illumination time and IO were determined for an LED light source and several solid-state lasers using the imaging protocols outlined in Fig. 2.1A. Experiments with the LED light source were conducted on a widefield microscope that could be configured with a direct TTL trigger, a USB connection or a mechanical shutter. Measurements with an oscilloscope demonstrated that both TTL and USB control of the light source resulted in rapid on and off switching within less than half a millisecond (Fig. 2.1B). In contrast, the mechanical shutter required ~ 10 ms to open and ~ 10 ms to close (Fig. 2.1B). Next, the camera exposure time was set to 24 ms in the microscope image acquisition software and total sample exposure to light was measured as an image was captured with each configuration. Although TTL and USB triggered the light source in almost exactly the same amount of time, only the TTL trigger was accurate in limiting the total exposure time of the sample to precisely 24 ms (Fig. 2.1C). In fact, the total exposure time delivered with the USB configuration (137 ms) was almost six times longer than the desired exposure time (Fig. 2.1C). Image acquisition with the mechanical shutter was almost 10 times longer than the exposure time (230 ms) (Fig. 2.1C).

Similar experiments were conducted on an SD confocal microscope with solid state lasers. The SD microscope was configured so that laser intensity and shuttering were regulated by an acousto-optic tunable filter (AOTF) controlled by the microscope image acquisition software connected through a USB cable. The activation and deactivation times for the lasers were found to be less than 0.5 ms and independent of the laser line (Fig. 2.1D). The total illumination time

was measured and, for a 100 ms exposure time, stream acquisition added ~17 ms of IO, while interval imaging added ~42 ms (Fig. 2.1E).

2.4.3 Total light dose determines photobleaching and phototoxicity

Several studies report that longer exposure times coupled with lower light intensities (DLD), improve cell health (reviewed in [7]). Therefore, photobleaching and phototoxicity were measured in response to different exposure times. An optical power meter was used to measure incident light intensity at the focus of the imaging lens. Camera exposure times were scaled with illumination power to maintain a constant number of photons during image acquisition (Table S2.2). Chinese Hamster Ovary K1 (CHO-K1) cells stably expressing paxillin-EGFP were seeded onto fibronectin-coated glass coverslips, allowed to adhere and grow overnight, and then fixed with paraformaldehyde (PFA). Samples were left in PBS supplemented with sodium azide to avoid bacterial growth. Fixed cells were imaged with a 20×0.8 NA objective lens on the widefield microscope equipped with TTL. For the lowest light power setting (DLD), 0.0911 mW of incident light power was delivered to the sample over a 15,909 ms exposure time. This power corresponded to a final intensity of 0.03% from the light source [3% power, 1% neutral density (ND) filter (optical density (OD)=2)]. For the highest light power setting (CLD), 61.6 mW of incident light power was delivered over a 24 ms exposure time. Regardless of the light power, the amount of paxillin-EGFP signal remaining after 300 frames was not statistically different between imaging conditions that ranged from DLD to CLD when TTL was employed (Fig. 2.2A). This demonstrates that the total number of photons impacting the sample determines the degree of photobleaching, rather than how light is delivered. To further characterize the photobleaching, fixed cells expressing paxillin-EGFP were imaged in the presence of CellROXTM, a fluorogenic probe used for measuring cellular oxidative stress. Exposure time did not affect the amount of ROS produced when the number of photons between conditions was kept constant (Fig. 2.2B); however, if the light power was increased, the amount of ROS production was directly related to the total light dose (Fig. 2.2C).

Phototoxicity is often measured by quantifying cell division or cell death after live-cell experiments [2, 9, 17]. These assays can measure the impact of phototoxicity but they take a long time to conduct and more subtle phototoxic effects may go unnoticed. Our previous experience shows that cell migration rates are sensitive to phototoxicity [18, 19]. Therefore, the migration

speeds of CHO-K1 cells expressing paxillin-EGFP were assessed in response to different illumination conditions (Table S2.2). Cell migration speeds from fluorescence images generated with CLD (61.6 mW×24 ms) were similar to those measured with DLD (0.245 mW×60,000 ms) (Fig. 5.2D,E). Importantly, the migration rates measured from both sets of fluorescence images were not significantly different than those measured from brightfield images (Fig. 2.2D,E). A camera exposure time of 60,000 ms was chosen to fill the delay time of 1 min between images (continuous illumination). The 0.0245 mW of power used corresponded to a power density (i.e. irradiance) of 1.52 mW cm⁻² (Table S2.2) or 0.007% light source intensity, which is significantly lower than that used by most researchers for live-cell experiments [7% lamp intensity, 10% ND filter (OD=1) and 1% ND filter (OD=2)]. Given that ROS production is dependent on total light dose rather than exposure time, cell migration experiments were subsequently repeated with an increased frequency of TTL pulses (Fig. 2.2F) or incident light power (Fig. 2.2G; Table S2.3). Increasing the imaging frequency of CLD had a similar effect on cell migration speeds when compared to increasing the light power of DLD. Cell migration speeds remained unaffected up to a 3-fold increase in total light dose but were significantly reduced with further increases in light power (Fig. 2.2H,I). Thus, total light dose, rather than exposure time, is the main determinant of ROS production and cell health. As a result, it is best to implement TTL light triggering if possible.

2.4.4 Longer exposure times reduce the impact of IO and improve cell health

Although TTL triggering of LED and solid-state light sources has been in use for over a decade, TTL is not yet a standard feature on most microscopy platforms. Moreover, these microscope configurations are not well known in the biological imaging community and implementation of TTL circuits may require an override of the microscope software control. Given the measurements showing that USB lamp control and mechanical shutters result in substantially longer exposure times than the desired input (Fig. 2.1C), the relative impact of IO with different imaging conditions was measured.

Similar to the experiments shown in Fig. 2.2, camera exposure times were scaled with illumination power to maintain a constant number of photons during image acquisition but without accounting for the contribution from IO (Table S2.2). In our experience, this is how most microscope users configure a live-cell imaging experiment. USB triggering was used to control the LED light source as installed and configured by the manufacturer. Strikingly, IO had the largest

impact with short exposure times; in particular, the percentage contribution of IO was $\sim 470\%$ for an input camera exposure time of 24 ms (CLD) (Fig. 2.3A; Fig. 2.1C). In contrast, the percentage contribution for 60,000 ms (DLD) was only 0.67% (Fig. 2.3A; Fig. S2.1D). As a result, increasing the exposure time significantly reduced the amount of photobleaching experienced by CHO-K1 cells expressing paxillin-EGFP (Fig. 2.3B) and exponentially decreased the amount of ROS produced (Fig. 2.3C). This is because the relative contribution of IO was reduced at lower powers when longer exposure times were used (Fig. S2.1A-D). The CHO-K1 cell migration assay was used to test the impact of IO on cell health. Longer exposure times with lower light powers (DLD), resulted in significantly faster cell migration speeds than short exposure, high light power conditions (CLD) (Fig. 2.3D,E). In particular, cell migration speeds measured from fluorescence images captured with exposure times greater than 1060 ms were similar to those measured with brightfield imaging (Fig. 2.2E).

Changes in mitochondrial morphology are thought to occur early in the apoptotic process [20]. Studies indicate that excessive ROS production causes the release of cytochrome c and other pro-apoptotic proteins, which results in mitochondrial remodeling and fragmentation [21]. Thus, mitochondrial morphology was assessed as an additional sensitive readout of cell health. Live cells were stained with MitoTrackerTM Red and immediately fixed with PFA. Cells exposed to CLD (61.6 mW \times 24 ms) exhibited condensed/fragmented mitochondrial networks in the perinuclear region (Fig. 2.3F), similar to the positive controls (cells treated with H₂O₂, a ROS inducer; [22]) (Fig. 2.3F). In contrast, mitochondrial morphology was maintained following DLD (0.0245 mW \times 60,000 ms) even after 16 h of continuous illumination (Fig. 2.3F). To verify that changes in mitochondrial morphology were the direct result of light exposure, mitochondria were imaged in live cells over time using a high resolution 63 \times 1.4 NA oil objective lens (Table S2.4). Cells illuminated with DLD (0.0093 mW \times 60,000 ms) had a healthy mitochondrial network even after 4 h of continuous light exposure (Fig. 2.3G). In contrast, CLD (21.3 mW \times 24 ms) led to a retracted and fragmented mitochondrial network (Fig. 2.3H) due to excess light from IO. Measurements of cell and mitochondrial morphology indicated that cells were rapidly affected by CLD (Fig. 2.3I,J).

To determine the general applicability to other biological systems and fluorescent probes, the cell migration assay was conducted on normal murine mammary gland (NMuMG)-ErbB2 cells derived from mouse tumor explants (118; [23]; and 87, [24]) and 4T1 cells derived from liver metastases [25] (Table S2.5). NMuMG-ErbB2 cells expressing LifeAct tagged with blue

fluorescent protein (BFP-LifeAct) showed dramatically reduced speeds under CLD (34 mW×24 ms), but not DLD (0.015 mW×60,000 ms) (Fig. S2.1E). Similarly, 4T1 cells expressing the cell matrix adhesion protein lipoma preferred partner (LPP) fused to mCherry, were significantly affected by CLD (58 mW×100 ms), but not DLD (0.099 mW×60,000 ms) (Fig. S2.1F). Finally, cell migration speeds of NMuMG-ErbB2 cells expressing the adapter protein ShcA (also known as SHC1) tagged with a far-red fluorescent protein, miRFP670 [26], were significantly affected by CLD (63 mW×100 ms), but not DLD (0.110 mW×60,000 ms) (Fig. S2.1G). These results demonstrate that DLD is a simple and generalized method to minimize photobleaching and phototoxicity when TTL triggering of the light source is not possible.

2.4.5 Images collected with DLD conditions are of high quality

Charge-coupled device (CCD) cameras are commonly used to acquire fluorescence microscopy images. CCD cameras are primarily affected by shot noise and dark noise. Shot noise results from the inherent variation in the arrival rate of photons at the camera. Because it is dependent on the signal level measured, shot noise is insignificant when the signal is sufficiently large [27]. In contrast, dark noise arises from a random number and location of electrons thermally generated within the sensor [28]. Dark noise is essentially negligible with short exposure times because of camera cooling; however, long exposure times can cause significant buildup on the camera [29]. Read noise is also important but it is not dependent on exposure time.

To explore the impact of noise on the quality of images, fixed cells expressing paxillin-EGFP were imaged with a 20×0.8 NA objective lens and 12 different illumination settings (Table S2.6). The intensity of paxillin-EGFP was similar between illumination conditions as the number of photons applied to the sample was kept constant; however, the standard deviation of the background increased linearly with exposure time (Fig. S2.2A-F). Consequently, images captured with exposure times greater than 23 s had significantly lower signal-to-noise ratios (S/N) than images captured with 24 ms exposure time (Fig. S2.2D). Importantly, S/N was not significantly different for exposure times between 1 and 23 s, which were found to be conducive to good cell health.

In general, images captured with DLD conditions retained reasonable S/N; however, S/N could be substantially improved by slightly increasing the excitation light power (Fig. S2.2G,H; Table S2.7). A 3-fold increase still maintained a low light power (0.070 mW×60,000 ms) and

surpassed the S/N of images captured with CLD (61.6 mW×24 ms). Importantly, a 3-fold increase in power did not cause a significant reduction in cell migration speeds (Fig. 2.2*D*). Collectively, these results demonstrate that DLD conditions can be used to generate high-quality images that are comparable to those captured with CLD conditions.

2.4.6 Imaging of dynamic processes is severely impacted by IO

IO can significantly impact image quality and photobleaching of fluorescent dyes (Fig. 2.3*B*). More importantly, it can lead to additional phototoxic effects on the sample (Fig. 2.3*D-H*). Therefore, the impact of IO on dynamic processes, which require shorter exposure times and higher resolution objective lenses, was explored on the SD microscope.

LLC-PK1 cells stably expressing the microtubule-associated protein EB3, fused to Emerald (EB3-mEmerald), were imaged with a 63×1.40 NA oil objective lens. EB3 transiently binds to the tip of growing microtubules, which develop at a speed of at least 0.5 $\mu\text{m s}^{-1}$ [11, 12]. Accordingly, an sCMOS camera capable of acquiring high resolution images (0.0586 $\mu\text{m pixel}^{-1}$) with fast frame rates (10 ms) was used to capture this dynamic process. Images were captured with stream acquisition, as this method eliminates the need for repeated triggering of the light source and synchronization with the camera. Thus, the only major contributing factor to IO was the read speed of the camera and time for the computer to save the digital image. IO was measured to be 17 ms (Fig. 2.1*E*). Consequently, with shorter exposure times, IO comprised a significantly greater proportion of overall light exposure. For example, with the camera exposure time set to 10 ms, IO comprised ~170% of the total illumination time (Fig. 2.4*A*). In contrast, IO led to an additional ~8% of light exposure when the camera exposure time was set to 217 ms (Fig. 2.4*A*). The impact of different exposure times on S/N was explored. Given the fact that IO contributes to phototoxicity, light power was adjusted to compensate for IO so that the same total light dose was delivered for each imaging condition (Table S2.8). The S/N of EB3 dramatically improved with increasing exposure time as the percentage contribution of IO decreased (Fig. 2.4*B,C*). To collect images with a comparable S/N, light power needed to be increased for shorter exposure times (Fig. S2.3). These higher light powers caused rapid photobleaching after just 2 min (Fig. 2.4*D*). Indeed, only 26% of mEmerald signal remained after 2 min of CLD (0.922 mW), while DLD (0.0167 mW) resulted in little photobleaching (Fig. 2.4*D*). Thus, IO is especially detrimental when imaging dynamic processes with short exposure times under CLD conditions.

2.4.7 Systematic determination of maximum image exposure time for dynamic processes

Longer camera exposure times can be used to improve image S/N and reduce photobleaching and phototoxicity caused by IO. Unfortunately, longer exposure times can also cause object blurring when capturing dynamic processes. As a result, a workflow was developed to systematically determine the longest exposure time possible to generate high S/N images but avoid image blur from rapidly moving structures. Dynamic EB3-mEmerald structures were used to demonstrate the workflow.

First, temporal image stacks of EB3-mEmerald were acquired with a 10 ms exposure time. Maximum intensity projections of several frames were then generated to mimic longer exposure times (Fig. 2.4E). Camera exposure times appropriate for measuring cell migration resulted in significant motion blur of EB3 (Fig. 2.4E). To objectively determine the maximum exposure time without significant image blur, image analysis software was used to determine the area, roundness and length of EB3 spots localized to microtubule tips in the maximum projection images that mimicked different exposure times (Fig. 2.4F-H). Based on these parameters, it was clear that microtubule dynamics should be imaged with an exposure time no longer than ~500 ms (Fig. 2.4F-H). Longer exposure times caused significant blur and distorted the size and shape of EB3 structures, such that images were no longer representative of accurate EB3 localization.

Imaging two fluorescent probes in the same live sample has a higher chance of causing phototoxicity, and dual infection or transfection of fluorescent proteins can make cells more sensitive to external stressors [30]. The LLC-PK1 cells were engineered to co-express EB3-mEmerald and the histone binding protein H2B-mCherry. Therefore, dual-color live-cell imaging of both probes was performed. Given the fact that mEmerald is a relatively unstable fluorophore [31], light levels were reduced to the lowest possible level while maintaining sufficient S/N for EB3 microtubule tip-tracking analysis. With a modest exposure time of 200 ms (<500 ms maximum exposure determined above), images of EB3-mEmerald (491 nm; 0.020 mW) and H2B-mCherry (561 nm; 0.010 mW) were collected simultaneously with a beam splitter and two sCMOS cameras (Fig. 2.4I). Importantly, these laser powers caused minimal photobleaching on fixed samples (Fig. 2.4J).

2.4.8 Image processing can be used to improve S/N of images and subsequent image analysis

Image processing techniques can be used to enhance S/N as an alternative to increasing total light dose. First, temporal image stacks of EB3-mEmerald were summed to simulate images taken with longer exposure times (Fig. S2.4A). A 2×2 median filter was then applied to the images to remove spurious noise (Fig. S2.4C). For each exposure time tested, there was approximately a 4-fold increase in S/N due to increased signal and reduced noise (Fig. S2.4B,D). Filtering did significantly reduce mean intensity at most exposure times (likely due to the removal of high intensity noise pixels) but did not affect EB3 morphology (area, roundness and length) (Fig. S2.4E-H). Finally, a 2×2 median filter was applied to dual-color EB3 time-lapse data described in Fig. 2.4I. Filtering improved object detection and tracking by removing spurious noise (Fig. S2.4I). As a result, measurements of area, roundness and length were determined more precisely from filtered images (Fig. S2.4J). Importantly, the mean and standard deviation of EB3 speed was found to be identical between raw and filtered data, and in line with previously published results [11, 12].

Spatial and temporal binning are two other image processing techniques that may be used to improve the S/N of images. To demonstrate the benefit of binning, lysosomal structures in CHO-K1 cells stained with LysoTrackerTM Green were imaged on the SD microscope (Table S2.9). Note that spatial binning on sCMOS cameras is performed post image acquisition and does not provide as much benefit in speed as with CCD cameras. Thus, spatial binning can simply be performed as a post image acquisition processing step. Previous studies have shown that lysosomes move at $\sim 0.38 \mu\text{m s}^{-1}$ [32]. Accordingly, a 100 ms exposure time was fast enough to image lysosomes using a 63×1.40 NA oil immersion objective lens without any evidence of motion blur (Fig. 2.5A, *top left image*). Moreover, images collected with 100 ms exposure time had sufficient S/N for automated tracking (data not shown). Spatial pixel binning (post image acquisition processing) of high-resolution sCMOS images could be used to improve S/N (Fig. 2.5A, *moving across rows*). This method of image processing greatly increased the signal for each lysosomal structure (Fig. S2.5A) without significantly affecting lysosomal area (Fig. 2.5B). Temporal addition of successive image frames could also be used to improve S/N (Fig. 2.5A, *moving down columns*; Fig. S2.5B). There was a limit, however, as temporal addition of eight images resulted in significant motion blur of fast-moving lysosomes (Fig. 2.5C,D). Therefore, spatial pixel addition would be the preferred method of increasing S/N if objects are moving rapidly and temporal resolution must be maintained.

Spatial and temporal pixel binning were then investigated as tools for measuring mitochondrial dynamics. CHO-K1 cells were stained with MitoTrackerTM Red and imaged with a 63×1.40 NA oil objective (Table S2.9). In line with the lysosomal data, spatial addition generated images with higher S/N without significantly impacting mitochondrial morphology (Fig. 2.5E). Mitochondria are much less dynamic than lysosomes [33]. As a result, temporal binning of 100 ms images could also be used to improve S/N without introducing any obvious spatial blur (Fig. 2.5E). Combining both spatial binning of 4×4 pixels and temporal addition of eight sequential time-lapse image frames tremendously increased the signal captured for MitoTrackerTM Red (Fig. S2.5C). Therefore, conditions to capture a three-dimensional video of mitochondrial dynamics were explored. Images could be acquired continuously with a z-stack of 15 images for ~5 min without any evidence of phototoxicity. After spatially binning images (2×2) and removing spurious noise with a median filter (2×2), the volume of the mitochondrial networks was determined over time with a pixel resolution of 0.1172 μm in x,y and 0.25 μm in z with no evidence of motion blur (Fig. 2.5F).

2.4.9 DLD can be used to reveal and measure fast adhesion dynamics

Having explored the relationship between exposure time and cell health, continuous imaging of cell matrix adhesion dynamics with high temporal resolution was explored. Nascent adhesions found at the protruding edge of the cell are typically sub-resolution (<1 μm in diameter) and have a short lifespan (<1 min) [34, 35]. Traditionally, however, adhesion dynamics have been measured with a temporal resolution of 15-30 s [36-38]. With this knowledge in mind, camera exposure time on the SD microscope was set to 5 s. 4T1-derived lung-metastatic breast cancer cells (4T1-537; [39]) were then transfected with mCherry-paxillin and continuously imaged with DLD conditions for 20 min using a 63×1.40 NA oil immersion objective (Fig. 2.6A; Table S2.9). This resulted in high S/N images with superior temporal resolution for measuring adhesion dynamics and minimal contributions from IO. High S/N images and improved temporal resolution achieved with continuous imaging improved the ability of automated tracking algorithms to accurately segment adhesions and determine slow and intermediate adhesion assembly and disassembly rates [Fig. 2.6B, *red* (slow), *orange* (intermediate) traces]. Furthermore, rapid adhesion dynamics that were not detected with previous image acquisition settings were easily visualized and quantified (Fig. 2.6B, *green* traces). In contrast, measuring adhesion dynamics with

a time delay of 20-30 s between images resulted in a significant loss of information (Fig. 2.6C), which contributed to a lower accuracy in determining adhesion assembly and disassembly rates (Fig. 2.6D-F). These experiments were repeated with CHO-K1 cells expressing paxillin-EGFP (Fig. S2.6; Table S2.9). A 20 s time resolution also resulted in a significant underestimation of adhesion assembly and disassembly rates in these cells (Fig. S2.6).

Given the success in capturing fast adhesion dynamics, DLD was explored for the simultaneous capture of adhesion and actin dynamics in migrating cells. Using continuous imaging, rapid actin cytoskeleton dynamics were captured in parental NMuMG cells stably expressing LifeAct-EGFP with no evidence of photobleaching or phototoxicity (see Movie 7 in online publication; Table S2.9). CHO-K1 cells expressing paxillin-EGFP were then transfected with LifeAct-mRuby and continuously imaged with a 5 s time resolution (Table S2.9). Dual-color imaging of the actin cytoskeleton and adhesions was performed with little photobleaching and no evidence of phototoxicity (see Movie 8 in online publication).

Finally, DLD was used to image NMuMG-ErbB2 cells stably expressing a vinculin tension sensor, which contains the relatively unstable teal (TFP) and venus fluorescent proteins [40]. High S/N images with minimal phototoxicity were obtained using a 63×1.40 NA oil immersion objective. TFP was excited with 0.013 mW from a 448 nm laser over a period of 20 min and venus fluorescent protein was excited with 0.007 mW from a 491 nm laser for an additional 20 min (Fig. 2.6G; Table S2.9). Dynamic adhesions were observed with a camera exposure time of 5 s despite the reduced photostability of these proteins compared to EGFP [31]. In fact, photobleaching of these proteins in fixed samples was minimal with continuous DLD imaging conditions (Fig. 2.6H).

In general, the results presented here show that the entire time delay between images can be harnessed to collect light from low-power fluorescence excitation. DLD allows researchers to capture more information about biological processes without artifacts from cell damage. On the other hand, more rapid biological events may not be observed if shorter exposure times with higher light levels and longer delays between successive images (CLD) are used on microscopes without TTL.

2.5 DISCUSSION

In the present study, we show that photobleaching and ROS production are tightly linked processes that lead to phototoxicity. Conventional live-cell imaging protocols recommend the use of short exposure times with higher light powers (CLD) [1, 16, 17, 41]. On the other hand, several studies cite the benefit of longer exposure times with lower light powers (DLD) [7]. Proponents of the latter approach argue that DLD alleviates pressure on cellular mechanisms designed to eliminate ROS. This study shows that CLD and DLD produce similar levels of ROS. Instead, much of the phototoxicity caused by high power fluorescence illumination can be attributed to additional light exposure beyond the camera exposure time (i.e. IO). If microscopes are not configured with a TTL trigger, such that the sample is only exposed to light during the acquisition time, then phototoxicity caused by IO is much more of an issue with CLD than DLD. Opening and closing of physical shutters, electronic switching of light sources, ramp up/down times for the light source to reach peak power and delays in camera software drivers can all impact IO. Software control that leaves the light source enabled during image read time, analog-to-digital conversion, and image write time to the computer memory or hard drive can further impact IO. In some cases, IO can be effectively eliminated by installing a TTL circuit between the camera and light source. By allowing the camera to control light source activation, microscope software does not need to synchronize camera acquisition, illumination and data saving.

Unfortunately, TTL implementation is not always possible, such as with bulb-based widefield microscopes and the SD confocal microscope used in this study. These types of light sources and microscopes are broadly used in the bioimaging community. Measuring actual light delivery during microscopy imaging may also be technically challenging. As a general solution, this work shows that researchers can implement longer exposure times (DLD) on microscopy platforms without the need for TTL. DLD can generate high S/N images and does not require the addition of chemicals to living samples, such as reducing agents or ROS scavengers, which may alter the physiological properties under study [17, 42, 43]. In addition, it does not require the removal of nutrients that may be required by living samples [44, 45]. DLD can be broadly applied to image blue, cyan, green, yellow, red and far-red fluorescent proteins and dyes with minimal photodamage to live cells. DLD also does not restrict live-cell imaging to slow biological processes. Stream acquisition or continuous illumination with longer exposure times can be used to measure rapid cellular processes, on the scale of milliseconds, such as lysosomal, mitochondrial

and microtubule tip dynamics. By acquiring fluorescence emission during the entire time delay between image frames, sufficient temporal resolution and S/N can be obtained for fast dynamics and three-dimensional time-lapse movies. Furthermore, DLD can enable more frequent capture of fluorescence images because the percentage contribution of IO decreases exponentially as exposure time increases. Finally, DLD can reveal cellular events with unprecedented detail and accuracy, which are not detected with previous CLD configurations.

To help researchers reduce photobleaching and phototoxicity on microscopes without TTL, and more generally, to determine ideal image acquisition limits, a workflow for optimizing exposure time and light power is presented (Fig. 2.7). Firstly, researchers should estimate the camera exposure time required to capture a given biological process based on the Nyquist-Shannon frequency of known dynamics (*step 1*). Images should then be acquired at a much higher frequency (*step 2*) to determine the longest exposure time that does not result in image artifacts (e.g. blur) (*step 3*). Interval delays should be eliminated to harness the entire interval time for gathering fluorescence emission and minimize the impact of hardware delays. Using this newly determined exposure time, light intensity should be reduced to the lowest possible power such that image S/N is still suitable for image analysis (e.g. identification of objects, or measurements of morphology and tracking) (*step 4*). In our experience, a S/N of 2 is typically required for thresholding and the identification of objects without the need for extensive image processing. A quick assay for cell health, such as end-point imaging of mitochondrial morphology, should then be performed to verify lack of phototoxicity and determine whether light levels are compatible with live-cell imaging (*step 5*). Finally, if cells are viable, light intensity may be increased incrementally until a compromise between S/N and cell viability is reached (*step 6*). If image quality (i.e. S/N) is insufficient with these conditions, image processing techniques can be applied (*step 7*). In the current study, we demonstrate the utility of median filtering, spatial binning and temporal binning; however, there are now many more advanced image processing techniques. Denoising filters [1, 46], deconvolution [47] or newer machine-learning methods for denoising [48] and content-aware image restoration [49] may also be applied to significantly improve S/N. These techniques can be particularly useful if object centers need to be tracked. However, the methods must be validated if quantitative measurements of structural area, volume, morphology or intensity are required.

Situations may arise where optimal conditions cannot be achieved. In these instances, the instrument or sample could be modified. First and foremost, researchers should consider

implementing TTL on their microscope system if it is possible. IO may be difficult to overcome for very dynamic processes that require exceptionally short exposure times. Measuring the total exposure time with an oscilloscope will reveal the extent of IO. In addition, constitutive expression of brighter, more stable fluorophores can improve S/N by generating more emission light with the same excitation intensity. Alternatively, more sensitive detectors or different forms of microscopy can be used to capture more signal or deliver light in a less concentrated fashion (e.g. light sheet).

On microscopes without TTL, applying the concept of DLD will allow researchers to generate high S/N images with minimal phototoxicity, while retaining reasonable temporal resolution, to study a wide range of biological processes. Unfortunately, it is becoming increasingly difficult to employ lower light levels as light sources continue to be developed with higher power outputs. Moreover, commercial microscopes report illumination power in arbitrary percentage power rather than watts. Thus, seemingly small changes in percentage power may result in large changes in light power and have a dramatic effect on cell health. Access to light sources with refined control over incident light powers, and high stability at low power settings, would increase support for live-cell imaging and permit cell biologists to capture rapid cellular events with DLD illumination conditions.

2.6 MATERIALS AND METHODS

2.6.1 Cell culture

Wild-type Chinese Hamster Ovary-K1 (CHO-K1) cells were obtained from the American Type Culture Collection (cat. no.: CCL-61, ATCC). CHO-K1 cells stably expressing paxillin-EGFP were obtained from the lab of Dr. Rick Horowitz (University of Virginia, Charlottesville, VA). CHO-K1 cells were grown in low glucose (1.0 g l^{-1}) Dulbecco's modified Eagle's medium (DMEM; cat. no. 11,885-084, Thermo Fisher Scientific) supplemented with 10% fetal bovine serum (FBS; cat. no. 10082-147, Thermo Fisher Scientific), 1% non-essential amino acids (cat. no. 11140-050, Thermo Fisher Scientific), 25 mM 4-(2-hydroxyethyl)-1-piperazineethanesulfonic acid (HEPES; cat. no. 15630-080, Thermo Fisher Scientific) and 1% penicillin-streptomycin (cat. no. 10378-016, Thermo Fisher Scientific). Cells were maintained in 0.5 mg ml^{-1} Geneticin-418 (G418; cat. no. 11811-031, Thermo Fisher Scientific) antibiotic selection to maintain paxillin-EGFP expression.

Normal murine mammary gland (NMuMG) cells were obtained from the ATCC (cat. no. CRL-1636) and grown in high glucose (4.5 g l^{-1}) DMEM (cat. no. 319-005-CL, Wisent Bioproducts) supplemented with 5% FBS, $10 \text{ } \mu\text{g ml}^{-1}$ insulin (cat. no. 511-016-CM, Wisent Bioproducts), 1 mM L-glutamine (cat. no. 609-065-CM, Wisent Bioproducts), 1% penicillin-streptomycin and 0.2% amphotericin B (cat. no. 450-105-QL, Wisent Bioproducts). NMuMG cells were infected with a pMSCV-blast viral vector harboring LifeAct-EGFP to label the actin cytoskeleton. Cells were maintained in $5 \text{ } \mu\text{g ml}^{-1}$ blasticidin (cat. no. BLL-40-01, InvivoGen) antibiotic selection to maintain LifeAct-EGFP expression.

NMuMG-ErbB2 cells were previously generated in the laboratory of P.M.S. by infecting parental NMuMG cells with a pMSCV-hygromycin viral vector harboring the rat ortholog of ErbB2 with an activating transmembrane point mutation V664E [50]. NMuMG-ErbB2 cells were subsequently infected with a pMSCV-blast viral vector containing the vinculin tension sensor (VinculinTS) [40]. Cells were cultured as described above with the addition of 0.8 mg ml^{-1} hygromycin B (cat. no. 450-141-XL, Wisent Bioproducts) antibiotic selection to maintain ErbB2 expression and $5 \text{ } \mu\text{g ml}^{-1}$ blasticidin to maintain VinculinTS expression.

To generate explants 87 and 118, NMuMG-ErbB2 cells were injected into the mammary fat pad of athymic mice and subsequently explanted from primary tumors [23, 24]. Explant 118 was infected with a pMSCV-blast viral vector containing LifeAct-BFP. Cells were maintained in

5 $\mu\text{g ml}^{-1}$ blasticidin to maintain LifeAct-BFP expression. In contrast, explant 87 was infected with a pMSCV-puromycin viral vector containing an shRNA against endogenous ShcA (an adapter protein involved in ErbB2 signaling). These cells were then infected with a pMSCV-blast viral vector harboring ShcA-iRFP. Cells were maintained in 2 $\mu\text{g ml}^{-1}$ puromycin (cat. no. QLL-40-01, InvivoGen) to maintain knockdown and 5 $\mu\text{g ml}^{-1}$ blasticidin to maintain re-expression.

Liver-metastatic (4T1-2776; [25]) and lung-metastatic (4T1-537; [39]) breast cancer cells were derived from 4T1 breast cancer cells, a model of triple-negative breast cancer. Both explants were grown in high glucose (4.5 g l^{-1}) DMEM supplemented with 10% FBS, 1% penicillin-streptomycin and 0.2% amphotericin B. 4T1-2776 cells were subsequently infected with mCherry-LPP using a pMSCV-blast viral vector and kept in 5 $\mu\text{g ml}^{-1}$ blasticidin to maintain expression. In contrast, 4T1-537 cells were transiently transfected with pmCherry-paxillin (Addgene #50526). Proximal kidney tubule (LLC-PK1) cells stably expressing EB3-mEmerald and H2B-mCherry were a gift from Michael W. Davidson (National High Magnet Laboratory, Florida State University, FL). LLC-PK1 cells were grown in DMEM-F12 (cat. no. 21331-020, Thermo Fisher Scientific) supplemented with 10%FBS, 15 mM HEPES, 1 mM L-glutamine and 1% penicillin-streptomycin.

Mycoplasma screening was routinely performed using MycoAlert mycoplasma detection kit (cat. no. LT07-318, Lonza). Cells were not authenticated following acquisition from the ATCC.

2.6.2 DNA constructs

All viruses were expressed using theMSCVvector system. To create NMuMG cells expressing BFP- and EGFP-LifeAct, NheI and NotI restriction sites were first used to clone mTagBFP-Lifeact-7 (Addgene #54496) into pSL301. BglIII and XhoI restriction enzymes were then used to clone BFP-LifeAct into pMSCV-blast. Finally, BamHI and NotI restriction enzymes were used to replace mTagBFP with EGFP from mGFP-Lifeact-7 (Addgene #54610).

To create NMuMG-ErbB2 cells expressing VinculinTS, EcoRI and HindIII restriction sites were used to clone VinculinTS (Addgene #26019) into pBlueScript. HindIII and XhoI restriction enzymes were then used to move VinculinTS into pMSCV-blast.

To create 2776-4T1 cells expressing mCherry-LPP, LPP was PCR amplified from a previously generated construct (pMSCV-eGFP-WT-LPP; [51]) with the following primers: 5'-ATTGCGGCCGCGATGTCTCACCCATCTTGG-3' and 5'-GAGACGTGCTACTTC

CATTTGTC-3'. EcoRI and NotI restriction enzymes were then used to replace paxillin in a previously generated pMSCV-mCherry-paxillin construct with the amplified product.

To create NMuMG-ErbB2 cells expressing ShcA-iRFP, ShcA was PCR amplified from a previously generated construct (pMSCV-ShcA-WT; [24]) with the following primers: 5'-CCCTTGAACCTCCTCGTTCGACC-3' and 5'-TAGGTACCGCCTTGTCATCGT CATCCT-3'. XhoI and KpnI restriction enzymes were then used to insert the amplified product into pCMV-miRFP670 [26]. Finally, 5'-CGCAAATGGGCGGTAGGC GTG-3' and 5'-TATAGAATTCTTAGCTCTCAAGCGCGG-3' primers with EcoRI and BglII restriction sites were used to shuttle ShcA-iRFP into pMSCV-blast. Retroviruses were generated in 293VSV cells according to the manufacturer's instructions (Clontech).

2.6.3 Cell migration assays

CHO-K1 cells expressing paxillin-EGFP were seeded onto μ -slide 8-well plates (cat. no. 80821, IBIDI) coated with $2 \mu\text{g ml}^{-1}$ (or $0.21 \mu\text{g cm}^{-2}$) fibronectin (cat. no. F-0895, Sigma-Aldrich) diluted in $1\times$ phosphate-buffered saline (PBS). Cells were allowed to adhere and grow under exponential conditions for at least 12 h prior to experimentation. Images were acquired on a Zeiss AxioObserver fully automated inverted microscope equipped with a Plan ApoChromat 20×0.8 NA objective, AxioCam 506 camera (Carl Zeiss, Jena, Germany) and ChamSlide TC-LZ003 stage top environmental control incubator (Live Cell Instrument, Seoul, South Korea). For baseline measurements of cell motility, cells were illuminated with a halogen lamp (HAL 100, Carl Zeiss). To determine the effects of fluorescence illumination, an EGFP filter cube (filter set 10; 450–490 nm excitation, 515–565 nm emission; Carl Zeiss) was used in combination with an X-Cite 120LED lamp (Excelitas Technologies, Waltham, MA) and several incident light powers. Camera exposure times were adjusted for each setting to maintain a constant number of photons impacting the sample during image acquisition (Table S5.2). The light source was directly triggered by USB or TTL without the use of a mechanical shutter. To test the effects of increasing light dose, CHO-K1 cells were illuminated more frequently (condensed light delivery; $61.6 \text{ mW}\times 24 \text{ ms}$) or with increasing incident light power (diffuse light delivery; $0.0245 \text{ mW}\times 60,000 \text{ ms}$) (Table S5.3). Images were acquired for at least 2 h.

In a similar manner, NMuMG-ErbB2 (118) with BFP-LifeAct, 4T1-2776 with mCherry-LPP and NMuMG-ErbB2 (87) with ShcA-iRFP cells were seeded onto μ -slide 8-well plates coated

with 5 $\mu\text{g cm}^{-2}$ fibronectin (Cat. no. FC010, EMD Millipore). Cells were imaged on the Zeiss AxioObserver with a Plan ApoChromat 20 \times 0.8 NA objective. BFP-LifeAct was captured with brightfield, 33.90 mW for 24 ms, and 0.015 mW for 60,000 ms; mCherry-LPP cells were captured with brightfield, 58.40 mW for 100 ms, and 0.099 mW for 60,000 ms; and ShcA-iRFP was captured with brightfield, 33.90 mW for 24 ms, and 0.015 mW for 60,000 ms (Table S5.5). BFP excitation was delivered through a custom filter cube [365–395 nm excitation, long pass (LP) 420 nm emission]; mCherry excitation was delivered through filter set 00 (530–585 nm excitation, LP 615 nm emission; Carl Zeiss); and iRFP excitation was delivered through filter set 49006 (590–650 nm excitation, 662.5–737.5 nm emission; Chroma). Images were acquired every minute for a total of 3 h.

2.6.3.1 Analysis of cell migration: Cells were manually tracked in ImageJ (NIH, Bethesda, MD) using the manual tracking plugin. The center of the nucleus was used as the reference point for each cell. User bias was minimized by having several authors track the cells. x,y position data for each cell track was then exported to MATLAB (v. 8.6, Rel. R2015b; The MathWorks, Natick, MA). Rose plots of cell movement were created by superimposing the starting position of each track on the origin (0,0). The average speed of each 10-min segment was then calculated by determining the mean distance traveled between each time point over the imaging interval. The average speed of each cell was calculated in a similar fashion. The data shown represents the mean \pm s.e.m. for all cells analyzed from three independent experiments.

2.6.3.2 Mitochondrial morphology following cell tracking experiments: CHO-K1 cells expressing paxillin-EGFP were stained with 100 nM MitoTrackerTM Red CMXRos (cat. no. M7512, Thermo Fisher Scientific) for 10 min. Cells were then fixed with 4% PFA preheated to 37°C for 10 min, washed with PBS and kept in PBS solution. As a negative control, cells that did not receive fluorescence illumination were also stained and fixed. Similarly, cells treated with 250 μM H₂O₂ (cat. no. 216763, Sigma-Aldrich) for 3 h were included as a positive control. Note that the 0.0245 mW condition depicts cells imaged continuously (60,000 ms) for 16 h. Images of mitochondrial morphology were acquired on a Leica DMI6000B inverted microscope equipped with a Quorum WaveFx-X1 spinning disk confocal system (Quorum Technologies, Guelph, ON), HCX PL APO 63 \times 1.40 NA oil DIC objective, and two Prime BSI sCMOS cameras (Photometrics, Tucson, AZ). Each cell was illuminated with 491 and 561 nm diode lasers to capture paxillin-

EGFP and MitoTrackerTM Red signals, respectively. The pinhole size of the spinning disk was fixed at 50 μm .

2.6.4 Mitochondrial morphology during cell tracking experiments

CHO-K1 cells expressing paxillin-EGFP were seeded onto μ -dish 35 mm high glass bottom dishes (cat. no. 81158, IBIDI) coated with 0.21 $\mu\text{g cm}^{-2}$ fibronectin. Cells were allowed to adhere and grow under exponential conditions for at least 12 h. Cells were then stained with 50 nM MitoTrackerTM Red diluted in cell culture medium (pre-heated to 37°C) for 10 min. After staining, cells were washed once with fresh medium and placed in new cell culture medium for imaging. Images were acquired on the Zeiss AxioObserver with a PlanApo 63 \times 1.4 NA oil immersion objective. Paxillin-EGFP was excited every minute with 0.0093 mW or 21.3 mW of incident light (Table S5.4). Exposure time was set to 60,000 ms for the low power condition and 24 ms for the high-power condition. MitoTrackerTM Red was excited every 6 min with a total light dose of 360 mW \times ms using filter set 43 (532.5–557.5 nm excitation, 570–640 nm emission; Carl Zeiss). The 120LED light source was activated through a USB connection. Images were subsequently imported into ImageJ to assess cell and mitochondrial morphology over time. Cell area was determined by manually outlining each cell. In contrast, analysis of mitochondrial morphology required several pre-processing steps. Briefly, we applied (1) a despeckling filter, (2) enhanced local contrast (CLAHE) with blocksize 9 and maximum slope 4 and (3) sharpened the image. This image was then (4) duplicated and (5) mean filtered with a 10 \times 10 grid. Finally, the duplicated image was subtracted from the enhanced image (3–5) and imported into Imaris (v. 9.1.2; Bitplane AG, Zurich, CH) to analyze mitochondrial area with the Surfaces function. Detail from the surfaces function was smoothed and set to 0.140 μm with a local background subtraction of 0.140 μm . Surfaces smaller than 3 voxels were removed by filtering. Measurements for cell and mitochondrial area were normalized to initial values. The data shown represents the mean \pm s.e.m. for five cells from three independent experiments.

2.6.5 Photobleaching assays for paxillin-EGFP

CHO-K1 cells expressing paxillin-EGFP were seeded onto μ -slide 8-well plates and fixed with PFA. Images were acquired on the Zeiss AxioObserver microscope with a Plan ApoChromat 20 \times 0.8 NA objective. Cells were repeatedly imaged for at least 300 frames with different

illumination conditions. Camera exposure times were adjusted for each setting to maintain a constant number of photons impacting the sample during image acquisition (Table S5.2). The light source was directly triggered by USB or TTL without the use of a mechanical shutter. Definite Focus.2 (Carl Zeiss, Jena, Germany) was used to keep the z-focus constant throughout the experiment. Image drift in x,y was corrected in Imaris by tracking the position of an adhesion over time relative to the first frame. Image stacks were subsequently analyzed in ImageJ. Three regions of interest (30×30 pixels) were drawn and averaged to determine intensity decay over time for each condition. A 50×50 pixel region of interest was used to correct decay curves for fluctuations in background intensity. Curves were normalized by the maximum fluorescence intensity of each experiment. The data shown represents the mean±s.e.m. for three independent experiments.

2.6.6 ROS production in response to different illumination conditions

CHO-K1 cells expressing paxillin-EGFP were seeded onto μ -slide 8-well plates. Cells were stained with 0.83 μ M CellRoxTM Deep Red Reagent (cat. no. C10422, Thermo Fisher Scientific). Images were taken on the Zeiss AxioObserver with a Plan ApoChromat 20×0.8 NA objective (TTL triggering) or a PlanApo 63×1.4 NA objective (USB triggering). CellRoxTM was imaged before and after paxillin-EGFP photobleaching (400 frames) with a total light dose of 1030 mW×ms delivered through filter set 49006 (590–650 nm excitation, 662.5–737.5 nm emission; Chroma). Exposure time was set to 1000 ms. ImageJ was used to determine the mean intensity of CellROXTM in each cell. The data shown represents the mean±s.e.m. for nine cells from three independent experiments.

To determine ROS production as a function of total light dose, paxillin-EGFP photobleaching was performed with increasing incident light powers. Camera exposure time for paxillin-EGFP was set to 100 ms. Changes in CellROXTM intensity were performed as described above.

2.6.7 Signal-to-noise ratio of widefield images

CHO-K1 cells expressing paxillin-EGFP were seeded onto μ -slide 8-well plates and fixed with PFA. Cells were subsequently stained with DAPI diluted to 0.5 mg ml⁻¹ in water. Images were acquired on the Zeiss AxioObserver with a 20×0.8 NA objective and 15 illumination settings (Tables S5.2 and S5.3). For each setting, the same field of view was captured to directly compare

S/N (Tables S5.6 and S5.7). A single DAPI image was taken with 100 ms exposure time using filter set 49 (365 nm excitation, 420–470 nm emission; Carl Zeiss). Images were then analyzed in MetaXpress using the multi wavelength cell scoring application. Briefly, the minimum and maximum width of nuclei was set to 10 and 32 μm , respectively, while minimum and maximum width of the cytoplasm was set to 2.3 and 90.8 μm , respectively. Finally, the mean intensity of each cell was background subtracted and divided by the standard deviation of the background (σ_{bkg}). σ_{bkg} was determined from a 125 \times 125 pixel region of interest without cells. The data shown represents the mean \pm s.e.m. for three independent experiments.

2.6.8 IO severely impacts image quality of dynamic processes

LLC-PK1 cells stably expressing EB3-mEmerald and H2B-mCherry were seeded onto 35 mm glass-bottom dishes (cat. no. FD35, World Precision Instruments; WPI) coated with 5 $\mu\text{g cm}^{-2}$ fibronectin. Cells were allowed to adhere and grow under exponential conditions for at least 12 h prior to experimentation. Cells were then imaged with an HCX PL APO 63 \times 1.40 NA oil objective on the spinning disk confocal system described above. ACU-501 stage-top incubator system (Live Cell Instrument, Seoul, South Korea) was used to maintain cells in a 37 $^{\circ}\text{C}$ environment with 5% CO_2 . Images of EB3-mEmerald were captured with 10 different illumination settings (Table S5.8). Imaris was then used to determine the S/N of EB3. Detail from the surfaces function was smoothed and set to 0.150 μm with a local background subtraction of 0.300 μm . Manual refinement of the autothreshold feature was used to mask EB3 tip proteins. Finally, surfaces smaller than 10 voxels were removed by filtering. The mean intensity of EB3-mEmerald in each image was background subtracted and divided by σ_{bkg} (250 \times 250 pixel region of interest). Cells were then continuously imaged for 2 min with an exposure time of 400 ms and a variety of laser powers to evaluate photobleaching (0.0167, 0.031, 0.0517, 0.0914, 0.181, 0.333, 0.558 and 0.922 mW). Stream to RAM acquisition was used in MetaMorph (Molecular Devices, Sunnyvale, CA) to minimize the delay in saving images. Initial and final mean intensities of EB3-mEmerald were determined using Imaris. Initial intensity was set to 1. The data shown represents the mean \pm s.e.m. for at least three independent experiments.

2.6.9 Determining the maximum exposure time for microtubule dynamics

LLC-PK1 cells expressing EB3-mEmerald and H2B-mCherry were seeded onto 35 mm dishes (WPI). EB3-mEmerald was rapidly imaged with a 10 ms exposure time for a total of 5.005 s (stream acquisition). A 491 nm laser set to 1.35 mW was used to capture sufficient S/N for morphology analysis. Image stacks were imported into ImageJ to generate maximum intensity projections corresponding to exposure times of 37, 64, 91, 199, 388, 496, 604, 1009, 1495, 2008, 3007, 3493, 4006, 4492 and 5005 ms. These images were then imported into Imaris (including the first 10 ms exposure) to determine the area, roundness and length of EB3 (see parameters above). Values were normalized on a scale of 0-1. The data shown represents the mean \pm s.e.m. for five independent experiments.

2.6.10 Dual-color imaging of EB3-mEmerald and H2B-mCherry

LLC-PK1 cells were continuously illuminated for over 2 min with the 491 nm laser set to 0.020 mW and a 561 nm diode laser set to 0.010 mW (Table S5.9). A dichroic mirror set to reflect light below, and pass light above, 565 nm, combined with a 565 nm long pass filter (Chroma Technologies, Bellows Falls, VT) was used to send the emission signals to two separate Prime BSI sCMOS cameras and thereby capture both signals simultaneously. Camera exposure times were set to 200 ms.

2.6.11 Effect of image processing on EB3 morphology

EB3-mEmerald images captured with a 10 ms exposure time for a total of 5.005 s (stream acquisition) were summed in ImageJ to generate exposure times of 37, 64, 91, 199 and 388 ms. A 2 \times 2 median filter was then applied to the images (including the first 10 ms exposure). Raw and filtered images were analyzed in Imaris to determine the area, roundness and length of EB3 (see parameters above). Measurements determined from filtered images were normalized to values calculated from raw data to determine relative changes in morphology. Values greater or less than 1.5 times the standard deviation were considered outliers. S/N was determined as described above. Linescan analysis was used to visually show the signal for each exposure time before and after filtering.

2.6.12 Tracking microtubule tip-binding proteins

Dual-color image stacks were loaded into Imaris and analyzed using the Spots function. The estimated x,y diameter for EB3-mEmerald was set to 0.650 μm with background subtraction enabled. A quality filter was then used to select positive signals. Finally, tip proteins were tracked using an autoregressive algorithm with a maximum distance of 0.800 μm and gap size of 3 time points. Tracks shorter than 4 s were removed by filtering. Finally, a custom algorithm in MATLAB was used to determine the average speed of each tip protein from x,y position data.

2.6.13 Imaging mitochondrial and lysosomal dynamics

CHO-K1 cells were seeded onto μ -slide 8-well plates and stained with 100 nM MitoTrackerTM Red or 500 nM LysoTrackerTM Green DND-26 (Cat. no. L7526, Thermo Fisher Scientific) for 10 min. Images were acquired with an HCX PL APO 63 \times 1.40 NA oil objective on the spinning disk confocal system. Each cell was illuminated for \sim 5 min with the 561 nm diode laser set to 0.037 mW (MitoTrackerTM Red) or the 491 nm laser set to 0.020 mW (LysoTrackerTM Green) (Table S5.9). Camera exposure time was set to 100 ms.

2.6.13.1 Analysis of mitochondrial and lysosomal dynamics: MitoTrackerTM Red and LysoTrackerTM Green image stacks were imported into ImageJ. Spatial binning (or addition) was accomplished by summing 2 \times 2, 3 \times 3 or 4 \times 4 pixels within the same image. Temporal binning was accomplished by summing 2, 4 or 8 images. Lysosomal images were then loaded into Imaris for morphology analysis. Detail from the surfaces function was smoothed and set to 0.100 μm with a local background subtraction of 0.200 μm . Manual refinement of the autothreshold feature was then used to mask lysosomes. Finally, splitting touching objects was set to a seed points diameter of 0.500 μm . The data shown represents the mean \pm s.e.m. for five cells from four independent experiments.

2.6.13.2 Three-dimensional imaging of mitochondrial dynamics: CHO-K1 cells were seeded onto μ -slide 8-well plates and stained with 50 nM MitoTrackerTM Red for 10 min. Images were acquired with an HCX PL APO 63 \times /1.40NA oil objective on the spinning disk confocal system. Cells were continuously imaged for over 5 min. Z-stacks with a step size of 0.25 μm were captured as frequently as possible (1.74-1.88 s) to observe mitochondrial volume over time. An MS-2000 piezo stage (ASI, Eugene, OR) and stream acquisition were used to capture focal planes with minimal IO. Camera exposure time was set to 50 ms with 2 \times 2 pixel binning.

3D image stacks were imported into Imaris to mask mitochondrial volume. Detail from the surfaces function was smoothed and set to 0.180 μm with a local background subtraction of 0.350 μm . Manual refinement of the autothreshold feature was then used to mask mitochondria. Surfaces smaller than 10 voxels were removed by filtering. Finally, mitochondrial networks were statistically coded for volume using a spectrum colormap.

2.6.14 Imaging adhesion dynamics

Lung-metastatic 4T1 breast cancer cells (4T1-537) were seeded onto 35 mm dishes (WPI) coated with 5 $\mu\text{g cm}^{-2}$ fibronectin. Cells were transfected with 1 μg of pmCherry-paxillin using Effectine reagent (cat. no. 301425, QIAGEN) and allowed to recover for an additional 24 h before imaging. Images were acquired with an HCX PL APO 63 \times 1.40 NA oil objective on the spinning disk confocal system; however, an ORCA-Flash4.0 sCMOS camera (Hamamatsu Photonics K.K., Hamamatsu City, Japan) was used in this set of experiments. Each cell was continuously illuminated for 20 min with a 561 nm diode laser set to 0.031 mW (Table S5.9). Camera exposure time was set to 5 s with 2 \times 2 pixel binning.

Similarly, CHO-K1 cells expressing paxillin-EGFP were seeded onto 35 mm dishes (WPI) coated with 0.21 $\mu\text{g cm}^{-2}$ fibronectin. Each cell was continuously illuminated for 20 min with a 491 nm diode laser set to 0.016 mW (Table S5.9). Camera exposure time was set to 5 s with 2 \times 2 pixel binning.

2.6.14.1 Processing adhesion dynamics: To remove hot pixels and other sources of background noise, an area of the sample without cells was acquired for 8.75 min. A maximum intensity projection of this image stack was created to extract only the persistent noise pixels. This ‘hot’ pixel noise image was then subtracted from the raw data. To simulate data captured every 20 or 30 s, every fourth or sixth image was duplicated into a new image stack, respectively.

2.6.14.2 Tracking adhesions: Each image stack was loaded into Imaris to analyze adhesion dynamics with the Surfaces function. A protruding edge of each cell was manually selected using the region of interest tool. Detail from the surfaces function was smoothed and set to 0.200 μm with a local background subtraction of 0.200 μm . Adhesions were then masked by a manual refinement of the autothreshold feature. Splitting touching objects was set to a seed points diameter of 0.500 μm . Finally, adhesions were tracked over time using an autoregressive algorithm with a maximum distance of 0.700 μm and maximum gap size of three time points. Surfaces smaller than

5 voxels were removed by filtering. Note that for each cell, the same parameters used to analyze the continuous series were applied to the simulated 20 and 30 s interval series to ensure consistency.

2.6.14.3 Calculating adhesion dynamics: Mean intensity data for each adhesion tracked in Imaris was exported to MATLAB for further analysis. A spline curve was first fitted to each intensity trace to identify segments of assembly and disassembly. The difference in intensity between each time point was calculated, and changes greater than 20% were considered to be significant. A string of six or more points upwards was interpreted as assembly, while six or more points downwards was interpreted as disassembly. A log-linear fitting method was then used to determine the rate for each event. Fits with an R^2 value greater than 0.7 were considered to be significant. Finally, assembly and disassembly rates were pooled together to determine the mean \pm s.e.m. rate for each condition.

2.6.15 Imaging actin cytoskeleton dynamics

NMuMG cells stably expressing LifeAct-EGFP were seeded onto 35 mm dishes (WPI). Images were acquired with an HCX PL APO 63 \times 1.40 NA oil objective on the spinning disk confocal system. Each cell was continuously illuminated for 30 min with the 491 nm diode laser set to 0.060 mW (Table S5.9). The camera exposure time was set to 5 s with 2 \times 2 pixel binning.

2.6.16 Dual-color imaging of adhesion and cytoskeletal dynamics

CHO-K1 cells stably expressing paxillin-EGFP were transfected with 1 μ g of LifeAct-mRuby (Addgene #54560) using Lipofectamine 2000 reagent (cat. no. 11668027; Thermo Fisher Scientific). Cells were then seeded onto 35 mm dishes (WPI). Images were acquired with an HCX PL APO 63 \times 1.40NA oil objective on the spinning disk confocal system. Each cell was continuously illuminated for 20 min with the 491 nm laser set to 0.016 mW and the 561 nm diode laser set to 0.031 mW (Table S5.9). A dichroic mirror set was used to send the emission signals to two separate cameras. Camera exposure times were set to 5 s with 2 \times 2 pixel binning.

2.6.17 Continuous illumination of less stable fluorescent proteins

NMuMG-ErbB2 cells stably expressing VinculinTS were seeded onto 35 mm dishes (WPI). Images were acquired with an HCX PL APO 63 \times 1.40NA oil objective on the spinning disk

confocal system. Each cell was continuously illuminated for 20 min with a 448 nm laser set to 0.013 mW to image teal fluorescent protein. Immediately following this, cells were illuminated for another 20 min with the 491 nm laser set to 0.007 mW to image venus fluorescent protein (Table S5.9). Camera exposure time was set to 5 s with 2×2 pixel binning.

2.6.18 Photobleaching assays for all other fluorescent dyes and proteins

Cells were fixed with PFA immediately following live-cell imaging. Images were acquired on the spinning disk confocal system with the same settings used to acquire live-cell data. Three separate image stacks were collected for each condition. Three regions of interest (100×100 pixels) were drawn and averaged for each stack to determine the intensity decay over time. For relative comparison, photobleaching curves were normalized by the maximum fluorescence intensity of each experiment.

2.6.19 Measurements of exposure time

A digital oscilloscope (DS1054Z; Rigol, Beijing, China) coupled to a DET36A/M Si Based Detector (Thorlabs, Dachau, Germany) was used to measure the total illumination time delivered by the mechanical shutter, USB or TTL light source activation. Voltage values were normalized on a scale of 0-1 and plotted in MATLAB.

2.6.20 Power measurements

An X-Cite optical power measurement system (XR2100) with an XP750 external sensor (Excelitas Technologies) was used to measure incident light intensity through air objectives (Plan ApoChromat 20×0.8NA on the widefield microscope). A PM400 Optical Power and Energy Meter with an S170C Microscope Slide Power Sensor (Thorlabs) was used to measure incident light intensity through oil objectives (PlanApo 63×1.4 NA on the widefield microscope; HCX PL APO 63×1.40NA on the spinning disk confocal system).

2.6.21 Power density measurements

Cells were seeded onto 35 mm glass-bottom dishes (WPI) coated with fluorescently conjugated gelatin (Oregon Green 488; cat. no. G13186, Invitrogen), as previously described [51]. Cells were then fixed with PFA and used to focus the desired objective lens (20×0.8 NA and

63×1.4 NA on the widefield microscope; 63×1.40 NA on the spinning disk confocal system). Fluorescent gelatin was photobleached with high-power light for at least 1 min. Finally, a lower magnification lens (5× or 10×) was used to capture an image of the photobleached area. Measurements of illumination area for each objective were performed in ImageJ.

2.6.22 Statistical analyses

Statistical significance values (*P*-values) were obtained by performing two-tailed Student's *t*-tests or Mann–Whitney *U*-tests. The tests were used to make pairwise comparisons between a base value (indicated in each figure legend) and a test condition. Data are presented as mean±s.e.m. Values were normalized where indicated. Experiments were performed at least three times. For cell migration experiments, an $n \approx 30$ was chosen to account for normal distribution. For mitochondrial and EB3 morphology experiments, cell averages were chosen as the *n* value to prevent *p* value skewing [52]. For adhesion dynamics experiments, all assembly and disassembly rates were pooled together to reflect the increased amount of information obtained with continuous imaging.

2.7 AUTHOR CONTRIBUTIONS

Conceptualization: A.K., C.M.B.; Methodology: A.K., C.M.B.; Validation: A.K., E.V.; Formal analysis: A.K., E.V., F.M.; Investigation: A.K.; Data curation: A.K.; Writing - original draft: A.K., C.M.B.; Writing - review & editing: A.K., E.V., P.M.S., C.M.B.; Visualization: A.K.; Supervision: P.M.S., C.M.B.; Project administration: C.M.B.; Funding acquisition: P.M.S., C.M.B.

2.8 ACKNOWLEDGEMENTS

We thank the late Dr. Michael W. Davidson (National High Magnet Laboratory, Florida State University, FL) for providing LLC-PK1 cells stably expressing EB3-mEmerald and H2B-mCherry. We also thank Rebecca Flessner (McGill University, QC) and members of the Brown and Siegel laboratories for thoughtful discussions about the manuscript. We thank the following imaging facilities for participating in the Canada BioImaging (CBI) survey: Cell Imaging Facility, CHUM Research Center; Molecular and Cellular Microscopy Platform (MCMP), Douglas Hospital Research Center; CAMiLoD, University of Toronto; Genomic Centre for Cancer Research and Diagnosis, University of Manitoba; Biology Microscopy Core, University of Saskatchewan; Plateforme de microscopie photonique, University of Sherbrooke; Centre for Microscopy and Cellular Imaging, Concordia University; BMM Microscopy, University of Montreal; Neuro Microscopy Imaging Centre, Montreal Neurological Institute; MultiScale Imaging Facility, McGill University; Plateforme d'Imagerie Microscopique, CHU Sainte-Justine Research Centre; Advanced Optical Microscopy Facility (AOMF), University Health Network. Imaging experiments were performed at the McGill Life Sciences Complex Advanced BioImaging Facility (ABIF) and Cell Imaging and Analysis Network (CIAN).

Work performed in the author's laboratories (P.M.S., C.M.B.) was supported by grants from Natural Sciences and Engineering Research Council of Canada (NSERC) (grants #493616-16, #386084-12), Canadian Institutes of Health Research (CIHR) (grant #CPG-146475) and the Canadian Cancer Society Research Institute CCS i2I grant #705838. A.K. acknowledges support in the form of a Fonds de Recherche du Québec - Santé (FRQS) doctoral studentship. E.V. acknowledges support in the form of CIHR and FRQS master's studentships. P.M.S. is a McGill University William Dawson Scholar.

2.9 REFERENCES

1. Carlton, P.M., et al., *Fast live simultaneous multiwavelength four-dimensional optical microscopy*. Proc Natl Acad Sci U S A, 2010. **107**(37): p. 16016-22.
2. Laissue, P.P., et al., *Assessing phototoxicity in live fluorescence imaging*. Nat Methods, 2017. **14**(7): p. 657-661.
3. Stennett, E.M.S., M.A. Ciuba, and M. Levitus, *Photophysical processes in single molecule organic fluorescent probes*. Chemical Society reviews, 2014. **43**(4): p. 1057-75.
4. Laloi, C. and M. Havaux, *Key players of singlet oxygen-induced cell death in plants*. Front Plant Sci, 2015. **6**: p. 39.
5. Thorpe, G.W., et al., *Cells have distinct mechanisms to maintain protection against different reactive oxygen species: oxidative-stress-response genes*. Proc Natl Acad Sci U S A, 2004. **101**(17): p. 6564-9.
6. Dixit, R. and R. Cyr, *Cell damage and reactive oxygen species production induced by fluorescence microscopy: effect on mitosis and guidelines for non-invasive fluorescence microscopy*. Plant J, 2003. **36**(2): p. 280-90.
7. Icha, J., et al., *Phototoxicity in live fluorescence microscopy, and how to avoid it*. Bioessays, 2017. **39**(8).
8. Magidson, V. and A. Khodjakov, *Circumventing photodamage in live-cell microscopy*. Methods Cell Biol, 2013. **114**: p. 545-60.
9. Douthwright, S. and G. Sluder, *Live Cell Imaging: Assessing the Phototoxicity of 488 and 546 nm Light and Methods to Alleviate it*. J Cell Physiol, 2017. **232**(9): p. 2461-2468.
10. Ettinger, A. and T. Wittmann, *Fluorescence live cell imaging*. Methods Cell Biol, 2014. **123**: p. 77-94.
11. Komarova, Y., et al., *Mammalian end binding proteins control persistent microtubule growth*. J Cell Biol, 2009. **184**(5): p. 691-706.
12. Stepanova, T., et al., *Visualization of microtubule growth in cultured neurons via the use of EB3-GFP (end-binding protein 3-green fluorescent protein)*. J Neurosci, 2003. **23**(7): p. 2655-64.
13. Baird, T.R., D. Kaufman, and C.M. Brown, *Mercury free microscopy: an opportunity for core facility directors*. J Biomol Tech, 2014. **25**(2): p. 48-53.
14. Albeanu, D.F., et al., *LED arrays as cost effective and efficient light sources for widefield microscopy*. PLoS One, 2008. **3**(5): p. e2146.
15. Wagenaar, D.A., *An optically stabilized fast-switching light emitting diode as a light source for functional neuroimaging*. PLoS One, 2012. **7**(1): p. e29822.
16. Frigault, M.M., et al., *Live-cell microscopy - tips and tools*. J Cell Sci, 2009. **122**(Pt 6): p. 753-67.
17. Waldchen, S., et al., *Light-induced cell damage in live-cell super-resolution microscopy*. Sci Rep, 2015. **5**: p. 15348.
18. Knoll, S.G., W.W. Ahmed, and T.A. Saif, *Contractile dynamics change before morphological cues during fluorescence [corrected] illumination*. Sci Rep, 2015. **5**: p. 18513.
19. Mubaid, F. and C.M. Brown, *Less is More: Longer Exposure Times with Low Light Intensity is Less Photo-Toxic*. Microscopy Today, 2017. **25**(6): p. 26-35.
20. Karbowski, M. and R.J. Youle, *Dynamics of mitochondrial morphology in healthy cells and during apoptosis*. Cell Death Differ, 2003. **10**(8): p. 870-80.
21. Ott, M., et al., *Cytochrome c release from mitochondria proceeds by a two-step process*. Proc Natl Acad Sci U S A, 2002. **99**(3): p. 1259-63.
22. Willems, P.H., et al., *Redox Homeostasis and Mitochondrial Dynamics*. Cell Metab, 2015. **22**(2): p. 207-18.
23. Northey, J.J., et al., *Signaling through ShcA is required for TGF- β and New/ErbB-2 induced breast cancer cell motility and invasion*. Mol. Cell. Biol., 2008: p. MCB.01734-07.

24. Northey, J.J., et al., *Distinct phosphotyrosine-dependent functions of the ShcA adaptor protein are required for transforming growth factor beta (TGFbeta)-induced breast cancer cell migration, invasion, and metastasis*. J Biol Chem, 2013. **288**(7): p. 5210-22.
25. Tabaries, S., et al., *Claudin-2 is selectively enriched in and promotes the formation of breast cancer liver metastases through engagement of integrin complexes*. Oncogene, 2011. **30**(11): p. 1318-28.
26. Shcherbakova, D.M., et al., *Bright monomeric near-infrared fluorescent proteins as tags and biosensors for multiscale imaging*. Nat Commun, 2016. **7**: p. 12405.
27. Murray, J.M., *Evaluating the performance of fluorescence microscopes*. Journal of Microscopy, 1998. **191**: p. 128-134.
28. Salmon, W.C. and J.C. Waters, *CCD cameras for fluorescence imaging of living cells*. Cold Spring Harb Protoc, 2011. **2011**(7): p. 790-802.
29. Spring, K.R., *Cameras for digital microscopy*. Methods Cell Biol, 2007. **81**: p. 171-86.
30. Fiszer-Kierzkowska, A., et al., *Liposome-based DNA carriers may induce cellular stress response and change gene expression pattern in transfected cells*. BMC Mol Biol, 2011. **12**: p. 27.
31. Shaner, N.C., P.A. Steinbach, and R.Y. Tsien, *A guide to choosing fluorescent proteins*. Nat Methods, 2005. **2**(12): p. 905-9.
32. Valm, A.M., et al., *Applying systems-level spectral imaging and analysis to reveal the organelle interactome*. Nature, 2017. **546**(7656): p. 162-167.
33. Twig, G., et al., *Fission and selective fusion govern mitochondrial segregation and elimination by autophagy*. EMBO J, 2008. **27**(2): p. 433-46.
34. Choi, C.K., et al., *Actin and alpha-actinin orchestrate the assembly and maturation of nascent adhesions in a myosin II motor-independent manner*. Nat Cell Biol, 2008. **10**(9): p. 1039-50.
35. Zaidel-Bar, R., et al., *Early molecular events in the assembly of matrix adhesions at the leading edge of migrating cells*. J Cell Sci, 2003. **116**(Pt 22): p. 4605-13.
36. Berginski, M.E., et al., *High-resolution quantification of focal adhesion spatiotemporal dynamics in living cells*. PLoS One, 2011. **6**(7): p. e22025.
37. Delorme-Walker, V.D., et al., *Pak1 regulates focal adhesion strength, myosin IIA distribution, and actin dynamics to optimize cell migration*. J Cell Biol, 2011. **193**(7): p. 1289-303.
38. Nayal, A., et al., *Paxillin phosphorylation at Ser273 localizes a GIT1-PIX-PAK complex and regulates adhesion and protrusion dynamics*. J Cell Biol, 2006. **173**(4): p. 587-9.
39. Rose, A.A., et al., *ADAM10 releases a soluble form of the GPNMB/Osteoactivin extracellular domain with angiogenic properties*. PLoS One, 2010. **5**(8): p. e12093.
40. Grashoff, C., et al., *Measuring mechanical tension across vinculin reveals regulation of focal adhesion dynamics*. Nature, 2010. **466**(7303): p. 263-6.
41. Swedlow, J.R., P.D. Andrews, and M. Platani, *In vivo imaging of mammalian cells: image acquisition and analysis*. Cold Spring Harb Protoc, 2009. **2009**(9): p. pdb ip70.
42. Knight, M.M., et al., *Live cell imaging using confocal microscopy induces intracellular calcium transients and cell death*. Am J Physiol Cell Physiol, 2003. **284**(4): p. C1083-9.
43. Alejo, J.L., S.C. Blanchard, and O.S. Andersen, *Small-molecule photostabilizing agents are modifiers of lipid bilayer properties*. Biophys J, 2013. **104**(11): p. 2410-8.
44. Bogdanov, A.M., et al., *Cell culture medium affects GFP photostability: a solution*. Nat Methods, 2009. **6**(12): p. 859-60.
45. Bogdanov, A.M., E.I. Kudryavtseva, and K.A. Lukyanov, *Anti-fading media for live cell GFP imaging*. PLoS One, 2012. **7**(12): p. e53004.
46. Coupe, P., et al., *A CANDLE for a deeper in vivo insight*. Med Image Anal, 2012. **16**(4): p. 849-64.
47. Biggs, D.S., *3D deconvolution microscopy*. Curr Protoc Cytom, 2010. **Chapter 12**: p. Unit 12 19 1-20.
48. Nasser, L. and T. Boudier, *A novel generic dictionary-based denoising method for improving noisy and densely packed nuclei segmentation in 3D time-lapse fluorescence microscopy images*. Sci Rep, 2019. **9**(1): p. 5654.

49. Weigert, M., et al., *Content-aware image restoration: pushing the limits of fluorescence microscopy*. Nat Methods, 2018. **15**(12): p. 1090-1097.
50. Ngan, E., et al., *A complex containing LPP and alpha-actinin mediates TGFbeta-induced migration and invasion of ErbB2-expressing breast cancer cells*. J Cell Sci, 2013. **126**(Pt 9): p. 1981-91.
51. Ngan, E., et al., *LPP is a Src substrate required for invadopodia formation and efficient breast cancer lung metastasis*. Nat Commun, 2017. **8**: p. 15059.
52. Lord, S.J., et al., *SuperPlots: Communicating reproducibility and variability in cell biology*. Journal of Cell Biology, 2020. **219**(6).

2.10 FIGURES AND LEGENDS

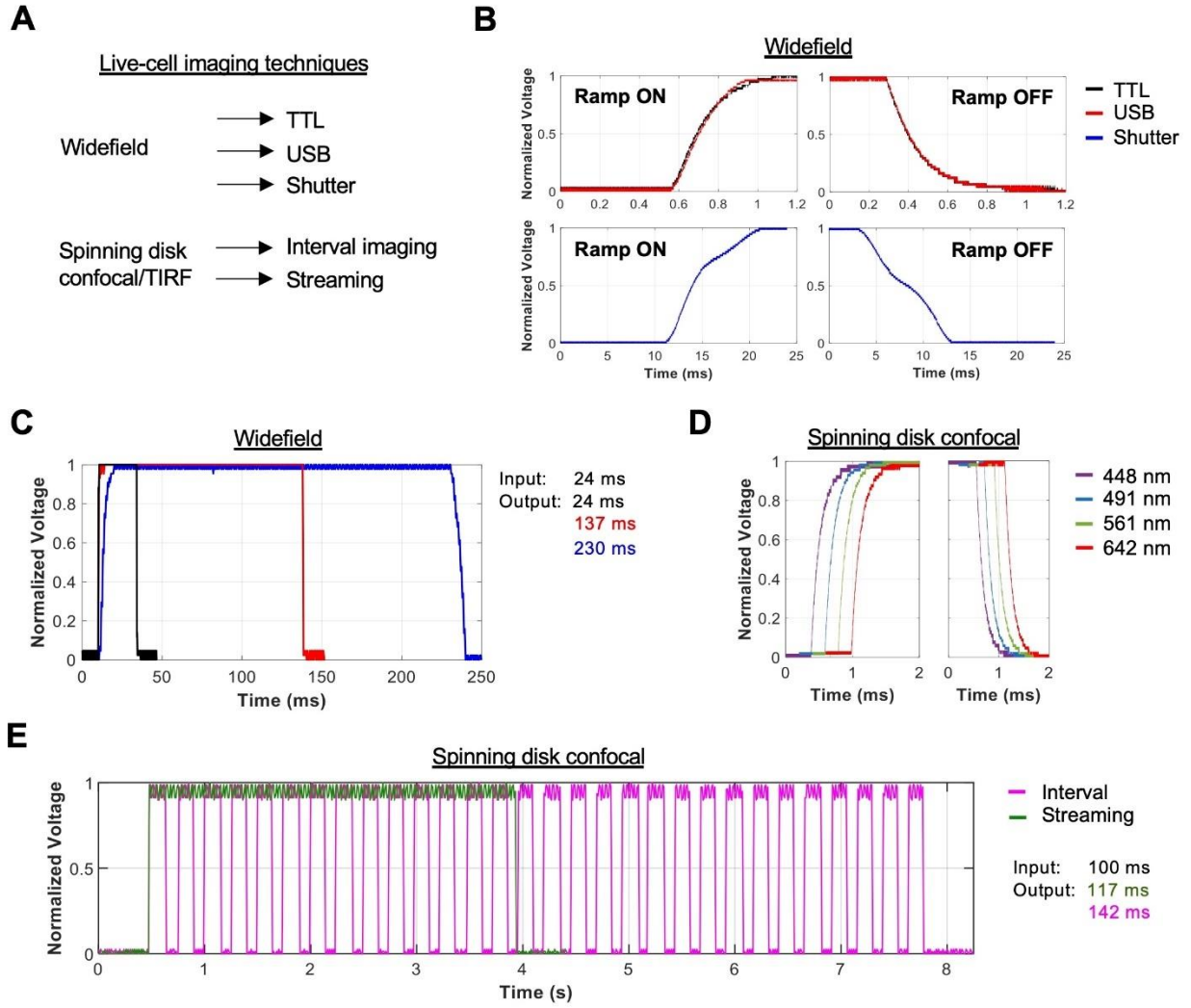


Figure 2.1. Standard imaging protocols deliver additional sample illumination beyond input camera exposure time. (A) Microscopy techniques commonly used for live-cell imaging. Mechanical shutters were traditionally used for sample illumination. Modern LED light sources (widefield microscopy) can be activated through the microscope software using a USB connection or by a transistor-transistor logic (TTL) circuit between the camera and light source. Solid-state lasers (spinning disk confocal microscopy) deliver sample illumination using an acousto-optic tunable filter (AOTF) crystal that is controlled by the microscope software through a USB connection. Interval imaging allows users to set a time delay between subsequent image acquisitions. Stream acquisition allows users to capture images as quickly as possible (up to the camera frame rate) with the sample constantly illuminated. (B) Ramp on/off times were measured on a widefield microscope using a mechanical shutter, USB or TTL light source activation. (C) Total illumination time delivered by the shutter, USB or TTL for an input camera exposure time of 24 ms. (D) Ramp on/off times were measured on the SD confocal microscope using electronic activation (through the AOTF crystal). (E) Total illumination time delivered by interval or stream acquisition on the spinning disk confocal microscope. Camera exposure time was set to 100 ms. A total of 30 frames were captured with the imaging interval set to 0 ms.

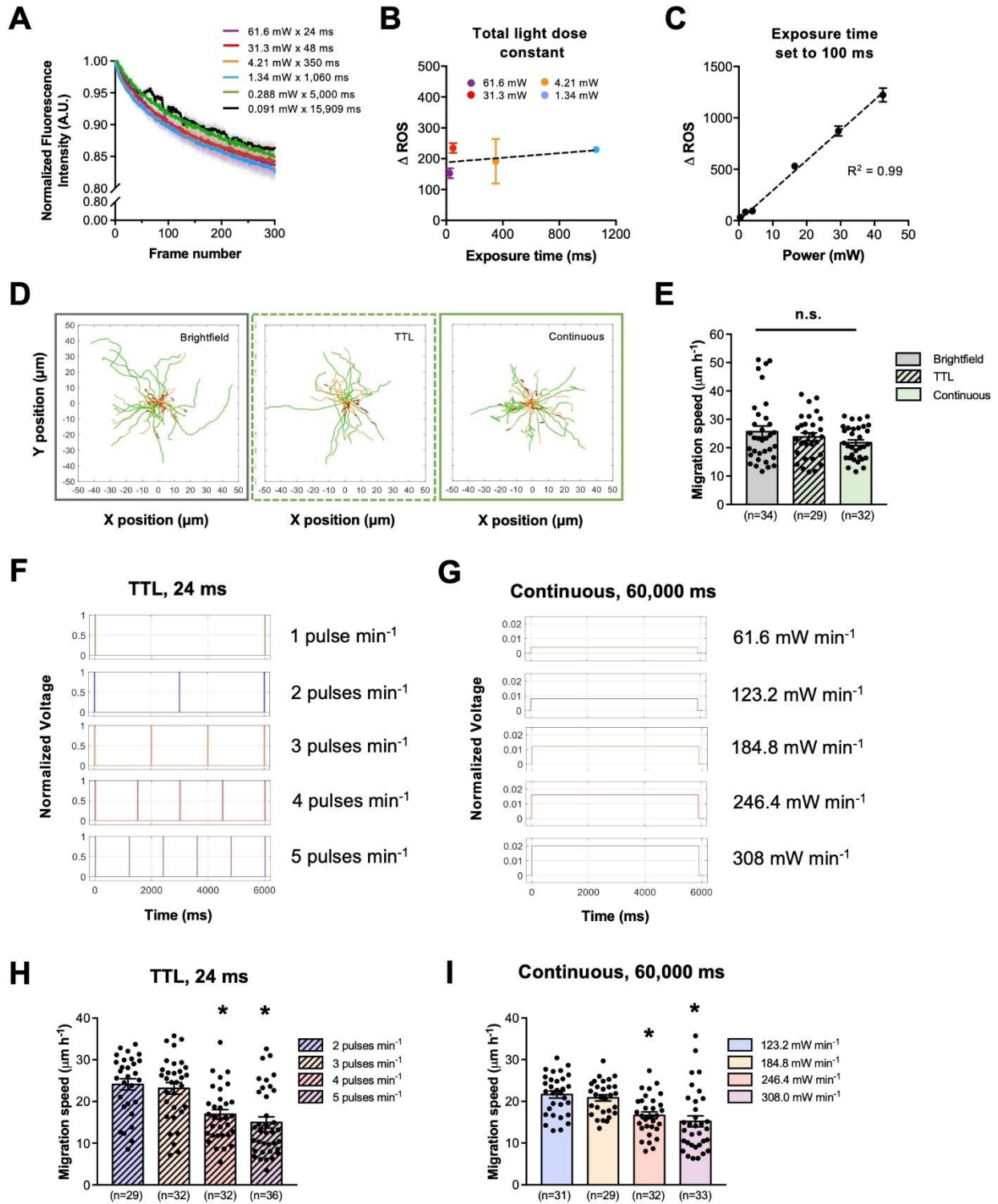


Figure 2.2. Total light dose and ROS are tightly linked processes that cause phototoxicity.

(A) CHO-K1 cells stably expressing paxillin-EGFP were fixed with 4% PFA and repeatedly imaged with a 20×0.8 NA objective lens on a widefield microscope equipped with TTL. Photobleaching decay curves were normalized to the maximum fluorescence intensity of each experiment. Data represents the average of three independent experiments. Shaded areas represent mean±s.e.m. (B) Paxillin-EGFP was photobleached with different light power regiments in the presence of CellROX™. Data represent the mean±s.e.m. of three independent experiments. (C) Paxillin-EGFP was photobleached with increasing light power, and ROS production was imaged through the addition of CellROX™. Camera exposure time was set to 100 ms. Data represent the mean±s.e.m. of three independent experiments. (D) CHO-K1 cell migration tracks in the presence of brightfield (n=34), TTL (61.6 mW×24 ms) (n=29) or continuous (0.0245 mW×60,000 ms) (n=32) illumination. Each line presents the path of a single migrating cell over 1.5 h. Tracks are color-coded based on cell speed calculated for every 10-min interval: <15 $\mu\text{m h}^{-1}$ (red), 15-25 $\mu\text{m h}^{-1}$ (orange), >25 $\mu\text{m h}^{-1}$ (green). (E) Migration speed (mean±s.e.m.) of cells in each condition depicted in D. (F,G) Imaging frequency for TTL, and incident light power for continuous imaging, was increased 2-, 3-, 4- and 5-fold, respectively. (H) Migration speed (mean±s.e.m.) of cells captured with the imaging frequencies described in F. Number of cells analyzed is indicated in parentheses. * $P<0.001$ from 1 pulse min^{-1} (two-tailed Student's t-test). (I) Migration speed (mean±s.e.m.) of cells captured with the different light powers described in G. Number of cells analyzed is indicated in parentheses. * $P<0.001$ from 0.245 mW min^{-1} (two-tailed Student's t-test).

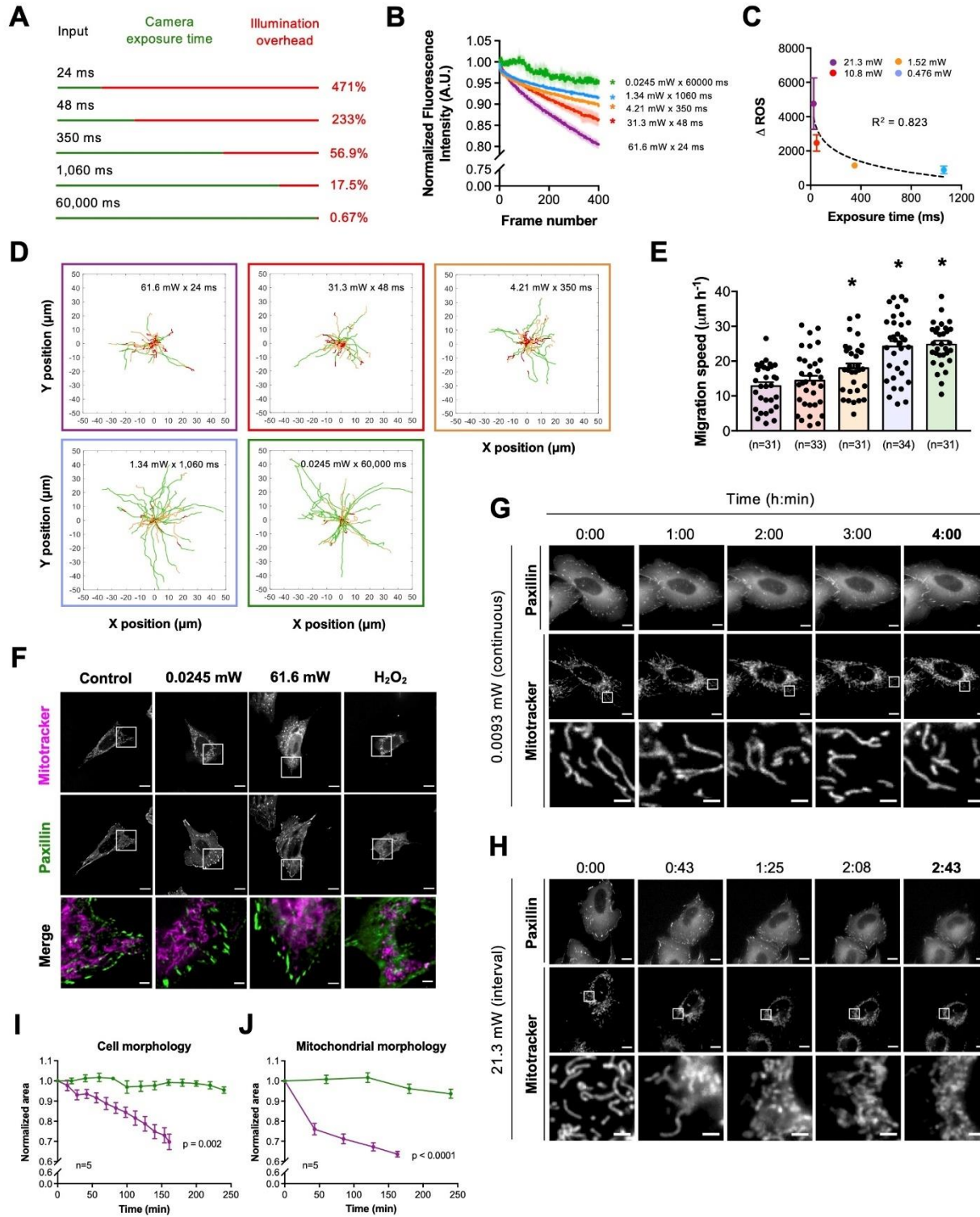


Figure 2.3. Longer exposure times reduce the impact of IO. (A) Percentage contribution of IO for different input camera exposure times when using a USB for light source activation (AOTF crystal). (B) Photobleaching decay curves of CHO-K1 cells expressing paxillin-EGFP in response to different light power regimens. Images were acquired with 20×0.8 NA objective lens on a widefield microscope. Curves were normalized to the maximum fluorescence intensity of each experiment. Data represents the average of three independent experiments. Shaded areas represent mean±s.e.m. ($P < 0.04$ from 61.6 mW×24 ms, two-tailed Student's t-test for area under the curve). (C) Paxillin-EGFP was photobleached with different light power regimens in the presence of CellROX™. Data represent the mean±s.e.m. of three independent experiments. (D) Live-cell migration tracks of CHO-K1 cells expressing paxillin-EGFP in response to different light power regimens (n=31 for 61.6 mW×24 ms; n=33 for 31.3 mW×48 ms; n=31 for 4.21 mW×350 ms; n=34 for 1.34 mW×1060 ms; n=31 for 0.0245 mW×60,000 ms). Each line presents the path of a single migrating cell over 1.5 h. Tracks are color-coded based on cell speed calculated for every 10-min interval: <15 $\mu\text{m h}^{-1}$ (red), 15-25 $\mu\text{m h}^{-1}$ (orange), >25 $\mu\text{m h}^{-1}$ (green). (E) Migration speed (mean±s.e.m.) of each cell depicted in D. Number of cells analyzed is indicated in parentheses. * $P < 0.005$ from 61.6 mW×24 ms (two-tailed Student's t-test). (F) Migrating cells were stained with MitoTracker™Red and fixed with 4% PFA to visualize mitochondrial morphology. Cells were exposed to no light (control), 0.0245 mW of light power continuously for 16 h, 61.6 mW of light power intermittently (24 ms) for 3 h, or 250 μM of H_2O_2 (no light exposure) for 3 h. Scale bars: 10 μm for whole-cell images and 2 μm for magnified images. (G,H) CHO-K1 cells were stained with MitoTracker™ Red and imaged with DLD (0.0093 mW×60,000 ms) or CLD (21.3 mW×24 ms) using a 63×1.4 NA oil objective. Images for paxillin-EGFP and MitoTracker™ Red were acquired every minute and 6 min, respectively. Scale bars: 10 μm for whole-cell images and 2 μm for magnified images. (I,J) Changes in cell area and mitochondrial area over time (n=5 cells from three independent experiments). Measurements were normalized to initial cell area at time zero. Results represent mean±s.e.m. (P -values correspond to Student's t-test for area under the curve).

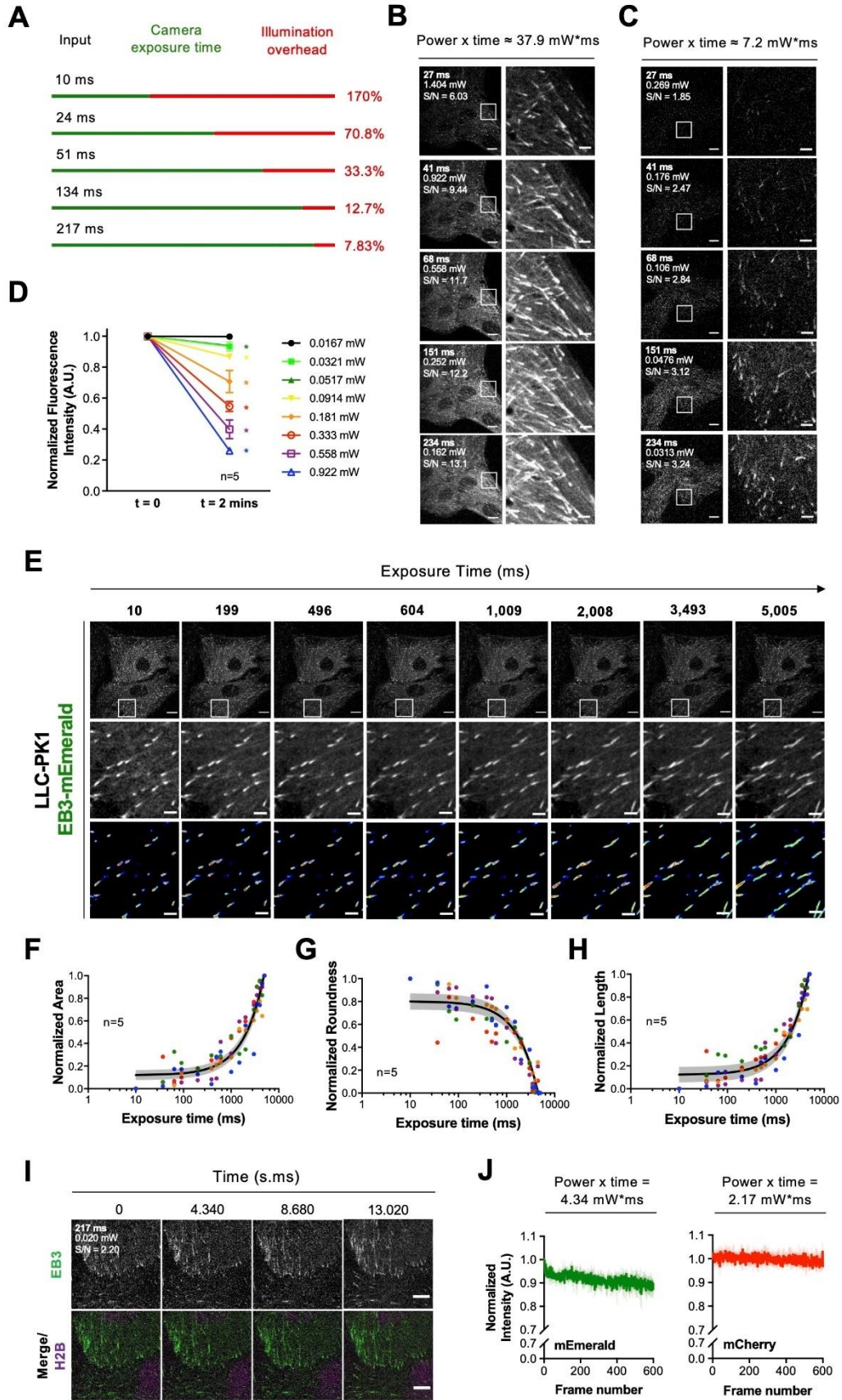


Figure 2.4. Object shape can be used to determine the longest exposure time for a dynamic process. (A) Percentage contribution of IO for several exposure times. IO was found to be 17 ms for stream to RAM image acquisition on the spinning disk confocal microscope. (B,C) Representative images of LLC-PK1 cells stably expressing EB3-mEmerald and H2B-mCherry showing the effect of IO on the S/N. Images were acquired with a 63×1.40 NA oil immersion objective lens. Scale bars: 10 μm for whole-cell images and 2 μm for magnified images. (D) Photobleaching decay curves of EB3-mEmerald in live LLC-PK1 cells (mean \pm s.e.m.; n=5 from three independent experiments). * P <0.05 from 0.0167 mW (two-tailed Student's t-test). (E) LLC-PK1 cells were rapidly imaged on a spinning disk confocal microscope with a 63×1.40 NA oil objective. Maximum intensity projections were generated from 10 ms frames to simulate data captured with different exposure times. Scale bars: 10 μm for whole-cell images and 2 μm for magnified images. (F-H) Area, roundness and length of EB3 signal localized to microtubule tips were determined from images in E. Values were normalized to a scale of 0-1. Individual data points are color-coded by cell (n=5). Shaded areas represent mean \pm s.e.m. (I) Dual-color imaging of EB3-mEmerald and H2B-mCherry. Camera exposure time was set to 200 ms based on EB3 morphology measurements. Scale bar: 5 μm . (J) Photobleaching decay curves of mEmerald and mCherry from fixed LLC-PK1 cells. Curves were normalized to the maximum fluorescence intensity of each experiment. Data represents the average of three independent experiments. Shaded area represents mean \pm s.e.m.

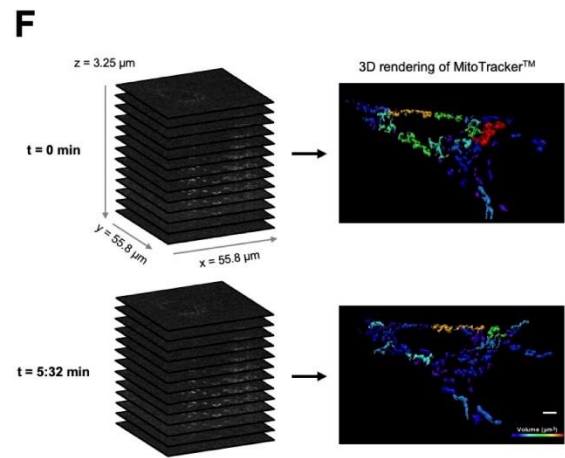
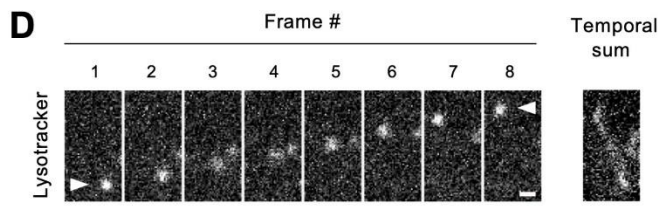
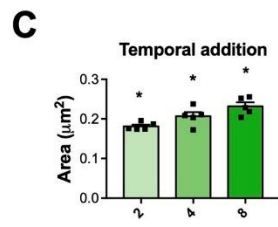
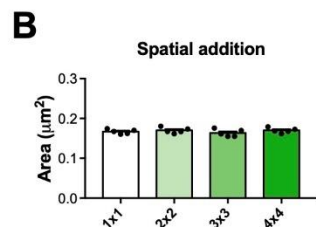
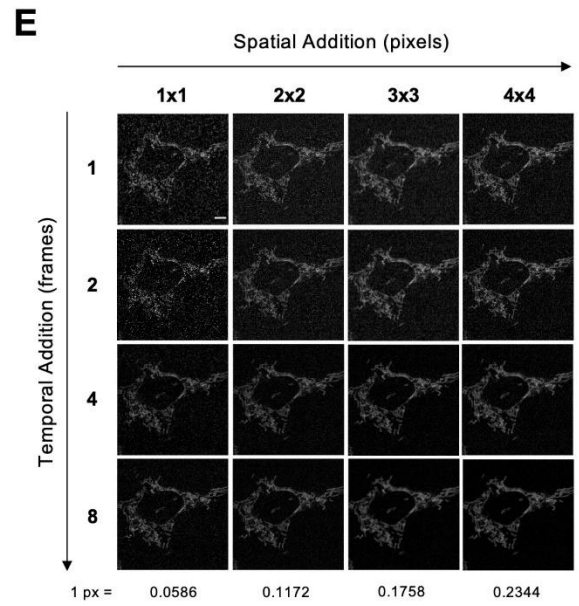
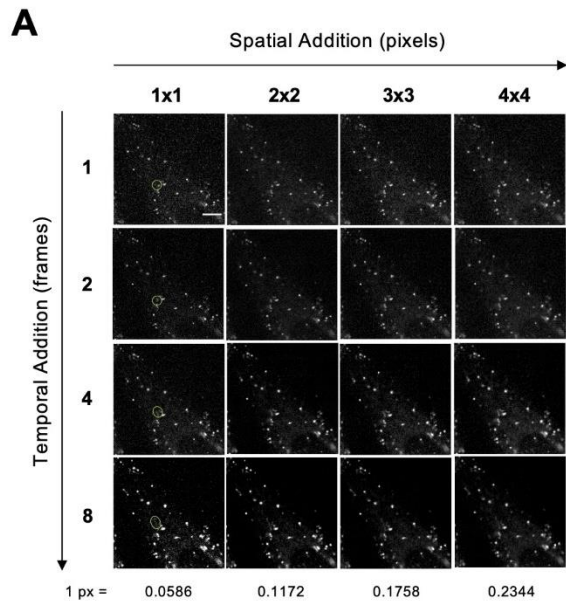


Figure 2.5. Spatial and temporal binning can be used to improve S/N of images. (A) CHO-K1 cells stained with LysotrackerTM Green were imaged on an SD microscope with a 63×1.40 NA oil objective. Camera exposure time was set to 100 ms. Spatial addition was achieved by adding pixels together; temporal addition was achieved by adding images together. Brightness and contrast were adjusted for each image to highlight any changes in morphology. Scale bar: 5 μm . (B,C) Analysis of lysosomal morphology following spatial and temporal addition. Black dots indicate the average for each cell analyzed (n=5). Bars represent mean \pm s.e.m. * P <0.05 from 1×1 binning (Mann-Whitney U-test). (D) High-magnification montage of green oval in A showing the eight image frames that were added together. The white arrowhead points to a rapidly moving lysosome that caused streaking in the temporally binned image. Scale bar: 0.7 μm . (E) CHO-K1 cells stained with MitoTrackerTM Red were imaged with a camera exposure time of 100 ms. Spatial and temporal addition were performed as described for A. Brightness and contrast were adjusted for each image to highlight any changes in morphology. Scale bar: 5 μm . (F) Three-dimensional time-lapse of mitochondrial dynamics. A 13-slice z-stack with a step size of 0.25 μm was continuously acquired for 5.5 min. Surfaces were statistically coded based on volume. Camera exposure time was set to 50 ms with 2×2 binning. Scale bar: 4 μm .

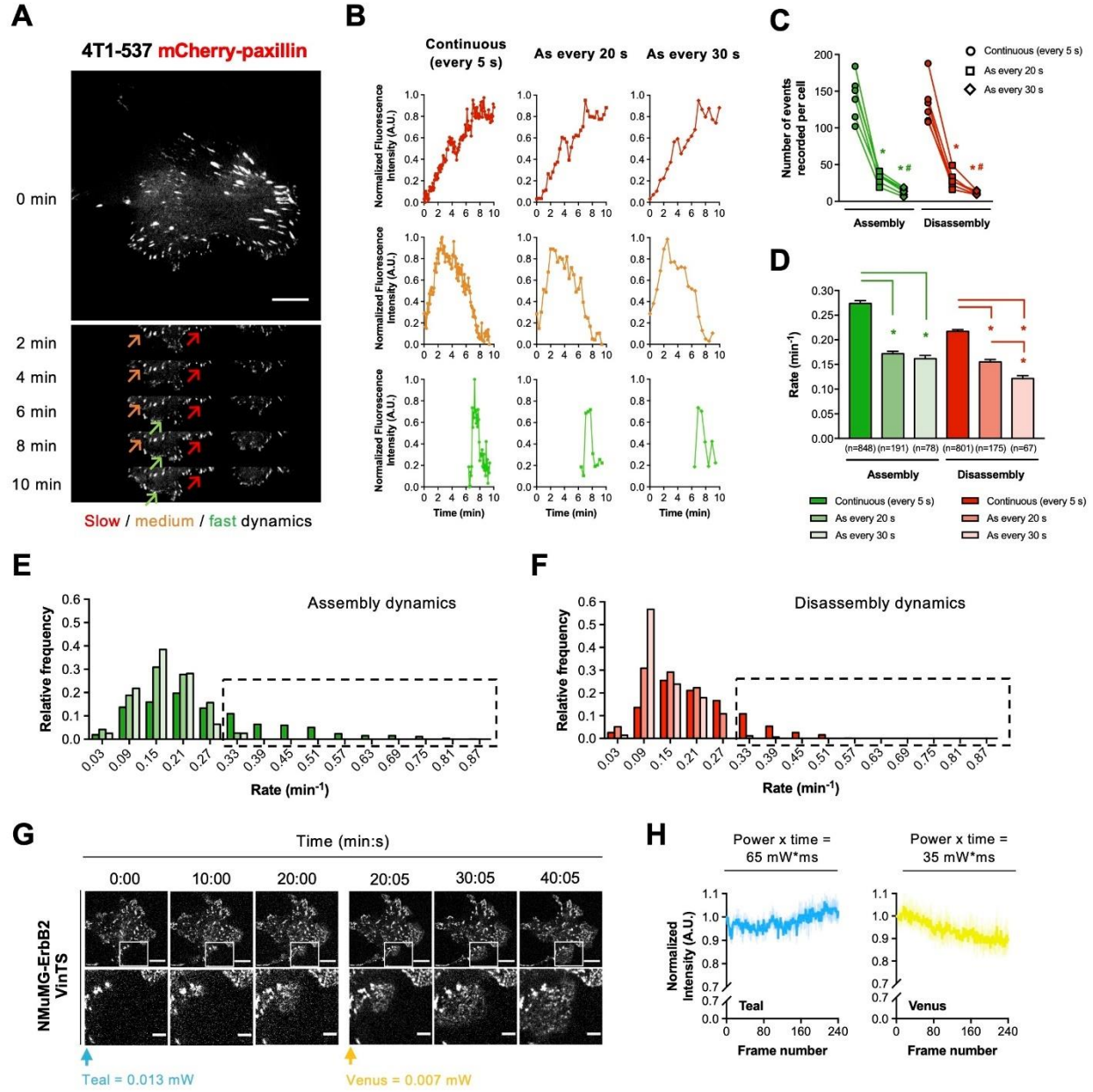


Figure 2.6. Continuous imaging provides enhanced temporal resolution to reveal quantifiable fast adhesion dynamics. (A) Lung-metastatic 4T1 breast cancer cells (4T1-537) were transfected with mCherry-paxillin. Arrows follow adhesions with a slow assembly rate (red), medium assembly and disassembly rates (orange) and fast dynamics (green). Images were captured continuously for 20 min on an SD microscope with a 63×1.40 NA oil immersion objective lens. Camera exposure time was set to 5 s with 2×2 binning. Scale bar: 10 μm . (B) Fluorescence intensity traces of adhesions from A. Circles (\bullet) are continuous imaging, squares (\blacksquare) are every 20 s, and diamonds (\blacklozenge) are every 30 s. (C) The total number of assembly (green) and disassembly (red) events detected for each cell imaged continuously (open circle; \circ) compared to simulated data generated by duplicating every fourth (open square; \square) or sixth (open diamond; \diamond) image frame ($n=6$). A region of interest tool was used to selectively track adhesions in protrusive cell regions. * $P<0.003$ from continuous imaging; # $P<0.005$ from every 20 s (Mann-Whitney U-test). (D) Average assembly and disassembly rates for each data set depicted in C were determined from the rate of change in mean fluorescence intensity. Data represent the mean \pm s.e.m. for dynamic events pooled from six cells imaged for 20 min. Number of events analyzed is indicated in parentheses. * $P<0.0001$ from continuous imaging; # $P<0.001$ from every 20 s (Mann-Whitney U-test). (E,F) Frequency distribution of assembly and disassembly rates from D. Data values were binned into 0.06 min^{-1} segments. Boxed regions in each graph illustrate rapid adhesion dynamics only captured by continuous imaging. (G) NMuMG-ErbB2 cells expressing VinculinTS were continuously imaged for 20 min with a 448 nm laser. Cells were subsequently illuminated for another 20 min with a 491 nm laser. Scale bars: 10 μm for whole-cell images and 3 μm for magnified images. (H) Photobleaching decay curves of fixed NMuMG-ErbB2 cells with VinculinTS. Teal and venus bleaching experiments were conducted independently. Curves were normalized by the maximum fluorescence intensity of each experiment. Data represents the average of three independent experiments. Shaded areas represent mean \pm s.e.m.

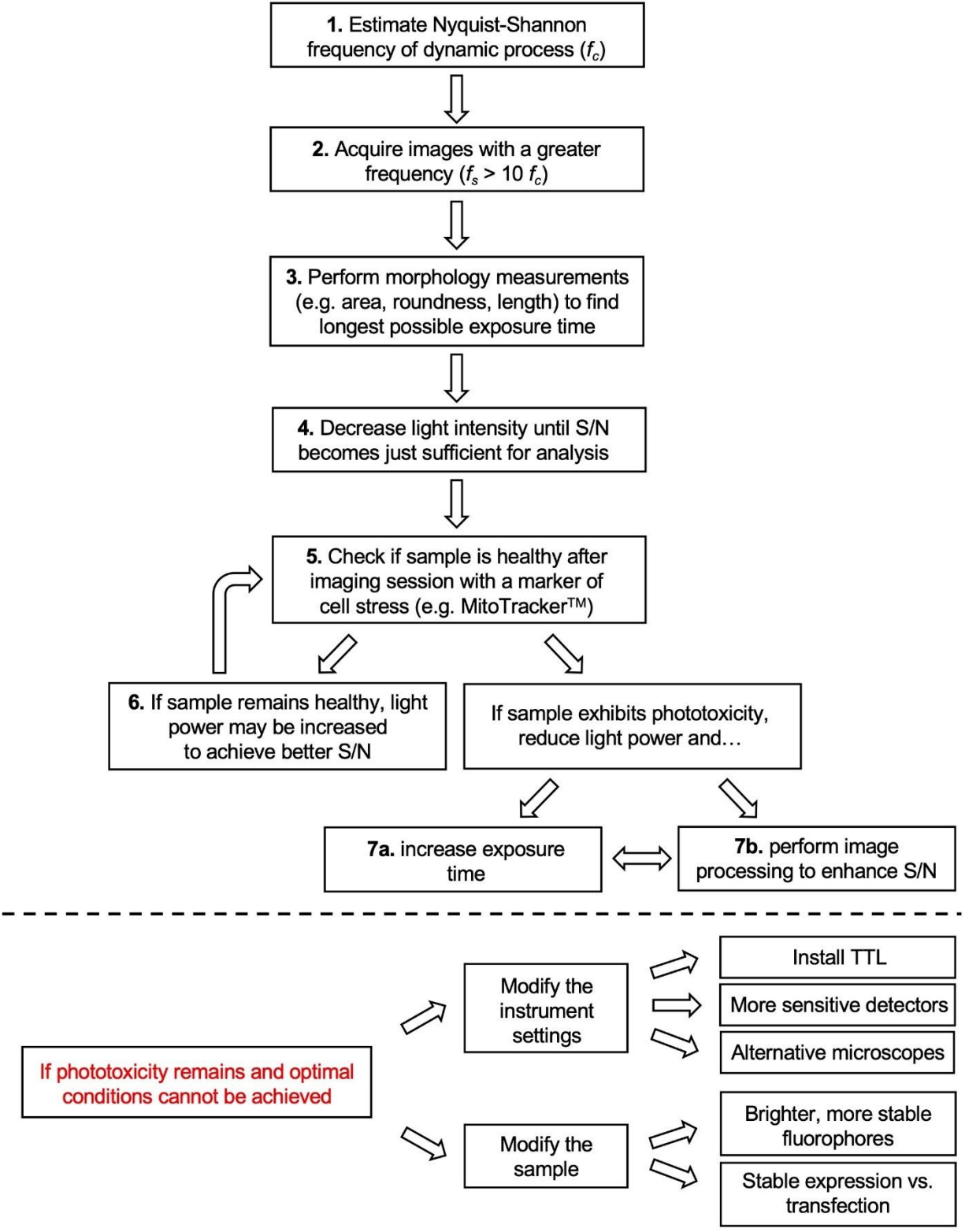


Figure 2.7. Flowchart for optimizing live-cell fluorescence imaging. A workflow for determining exposure time and light power was developed based on the results of the current study. Implementing longer exposure times will help researchers establish optimal live-cell imaging conditions on microscopes without TTL.

2.11 SUPPLEMENTARY INFORMATION

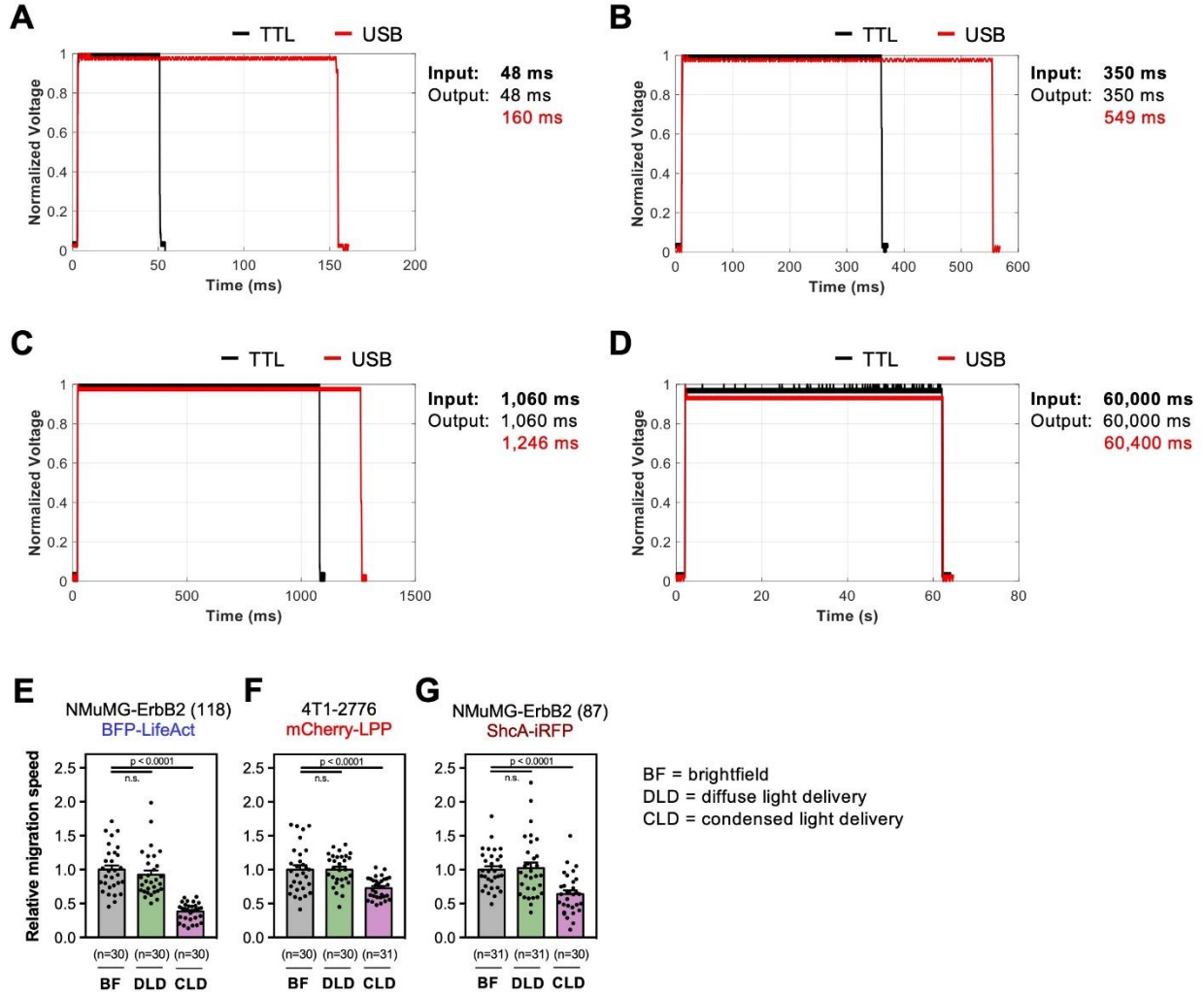
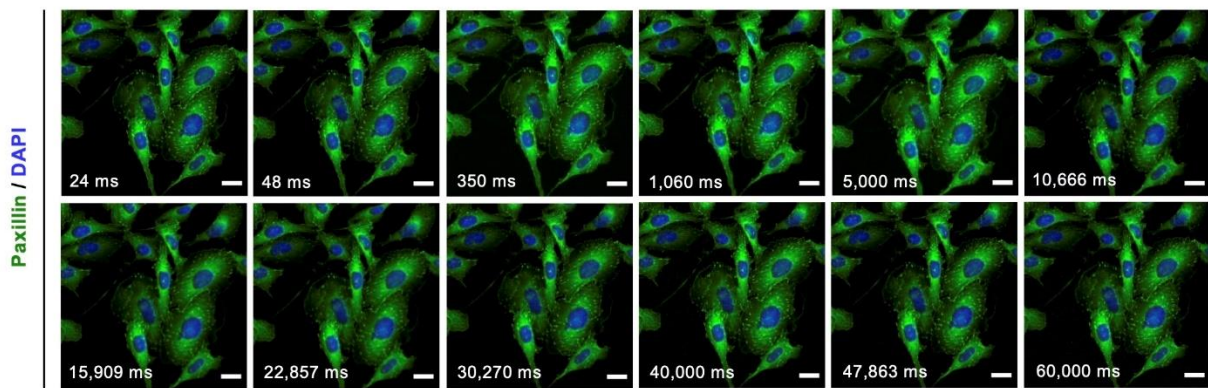
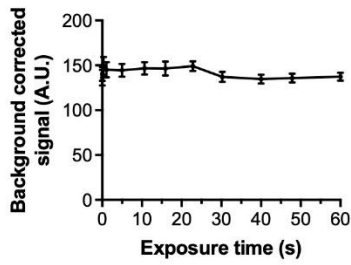
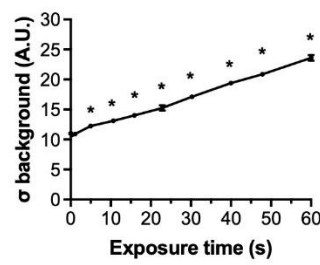
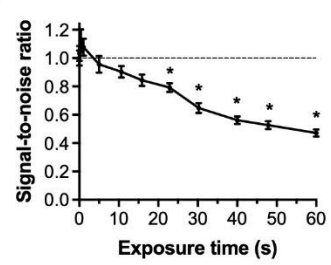
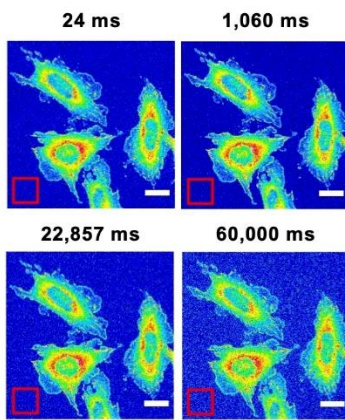
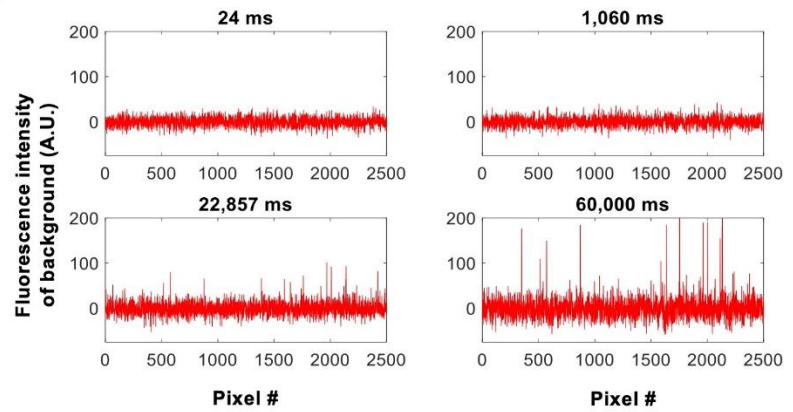


Figure S2.1. Light source activation through USB causes a significant amount of IO which affects many cell types regardless of fluorophore localization or excitation wavelength. (A-D) Total illumination time delivered by TTL or USB activation of the light source in response to different camera input times (48 ms, 350 ms, 1,060 ms and 60,000 ms). The difference between TTL and USB decreases as exposure time increases. **(E-G)** Average migration speeds of NMuMG-ErbB2 (118) cells expressing BFP-LifeAct, 2776-4T1 cells expressing mCherry-LPP and NMuMG-ErbB2 (87) cells expressing ShcA-iRFP under brightfield (BF), diffuse light delivery (DLD) and condensed light delivery (CLD) (Table S5.5). Values were normalized to brightfield. Each data point represents the migration speed of an individual cell. Number of cells analyzed is indicated in parentheses. Error bars represent mean \pm s.e.m. (*P* values from brightfield, Mann-Whitney *U* test).

APower x time $\approx 1456 \text{ mW} \cdot \text{ms}$ **B****C****D****E****F****G**

60,000 ms exposure

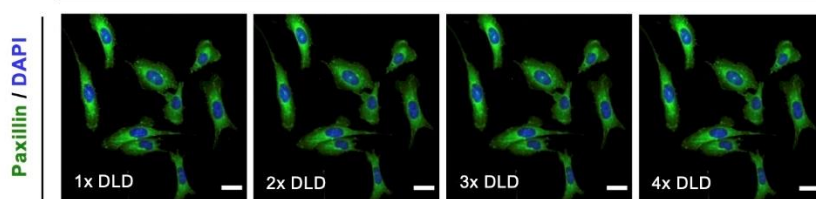
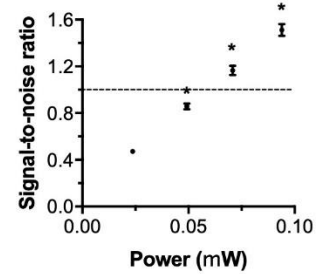
**H**

Figure S2.2. DLD can generate images with comparable signal-to-noise as CLD. CHO-K1 cells expressing paxillin-EGFP were fixed with 4% PFA and stained with DAPI. **(A)** Representative images for the same field of view captured with a 20×0.8NA objective lens and 12 different illumination conditions (Table S5.2). Scale bar is 25 μm . **(B)** Mean intensity of paxillin-EGFP in cells (n=94) from A corrected for background signal. Data represents the average of three independent experiments. **(C)** Standard deviation of the background (σ bkg) for images in A was determined from a 125×125 pixel region of interest. Data represents the average of three independent experiments. Error bars represent mean \pm s.e.m. (* P <0.02 from 24 ms, two-tailed Student's t -test). **(D)** Cells were analyzed in MetaXpress using the Multi Wavelength Cell Scoring application (see methods). S/N of images was calculated by dividing the mean intensity of paxillin-EGFP by σ bkg (Table S5.6). Values were normalized to the S/N of images captured with the 24 ms exposure time condition. Data represents the average of three independent experiments. Error bars represent mean \pm s.e.m. (* P <0.05 from 24 ms, two-tailed Student's t -test). **(E)** A 16-color lookup table was applied to sample images from A to show paxillin-EGFP signal intensity compared to background. Scale bar is 25 μm . **(F)** Fluctuations in fluorescence intensity from boxed regions in E. **(G)** Representative images for the same field of view captured with an exposure time of 60,000 ms and increasing incident light power (Table S5.7). Scale bar is 25 μm . **(H)** S/N of images in G was calculated as described for D. Data represents the average of three independent experiments (n=53 cells). Values were normalized to the S/N of 61.6 mW×24 ms. Error bars represent mean \pm s.e.m. (* P <0.001 from 0.0237 mW, two-tailed Student's t -test).

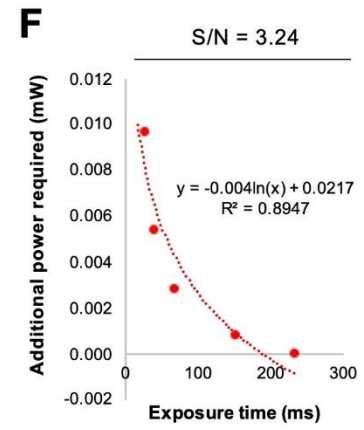
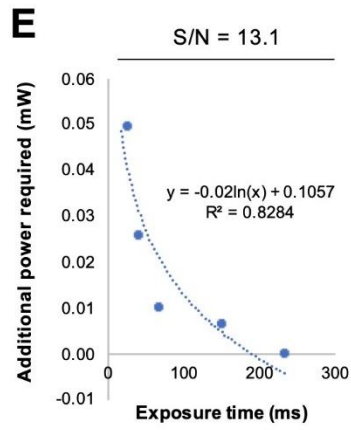
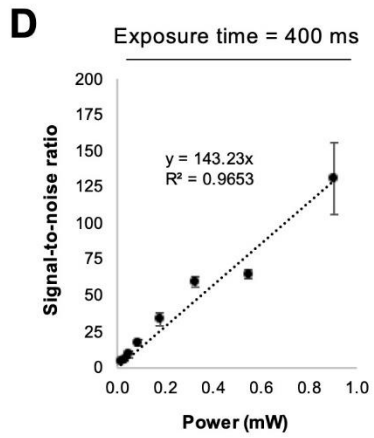
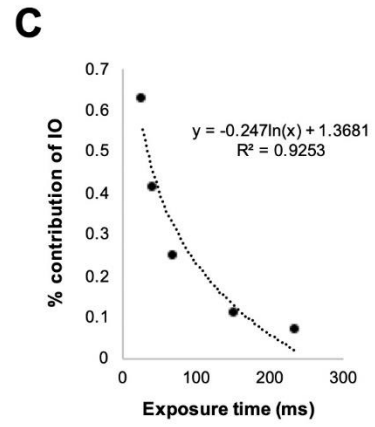
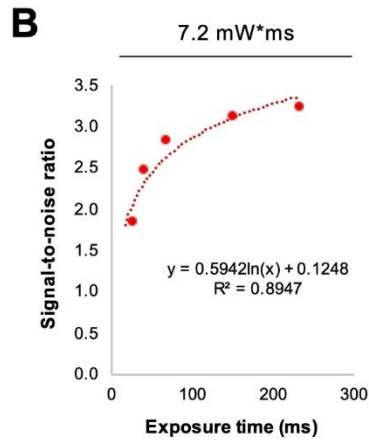
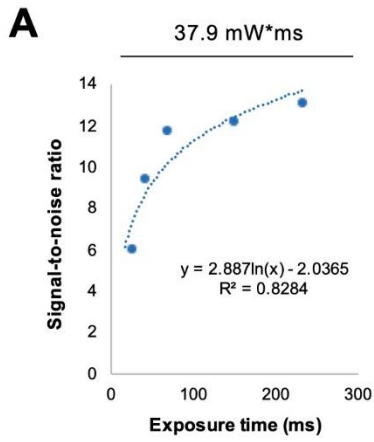


Figure S2.3. Power must be increased exponentially to recover signal-to-noise lost to IO. (A,B) S/N of EB3-mEmerald from images captured with the same total light dose but different powers and exposure times (Table S5.8). Data represents the average S/N of tip proteins ($n > 262$) from images shown in Fig. 4B,C. (C) Percent contribution of IO as a function of exposure time. (D) S/N of EB3-mEmerald from images captured with the same exposure time (400 ms) but increasing light power. Data represents the average of five independent experiments ($n > 58$ tip proteins per cell). Error bars represent $\text{mean} \pm \text{s.e.m.}$ (E,F) Amount of additional power required to obtain the same S/N as images captured with an exposure time of 217 ms. The effect is demonstrated for the two different total light doses shown in Fig. 4B,C.

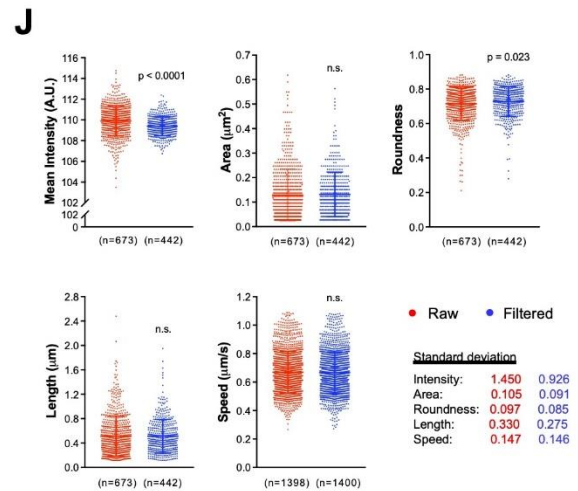
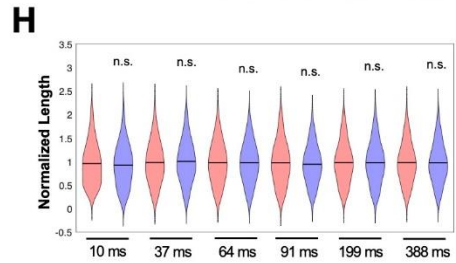
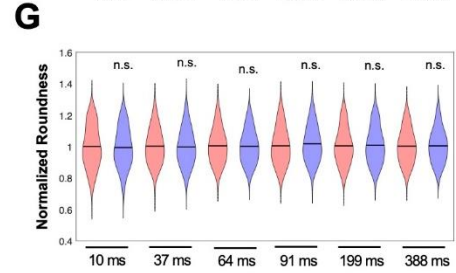
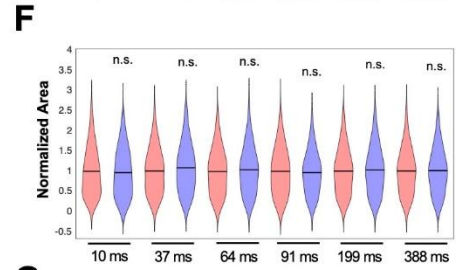
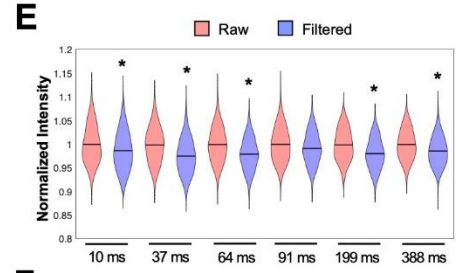
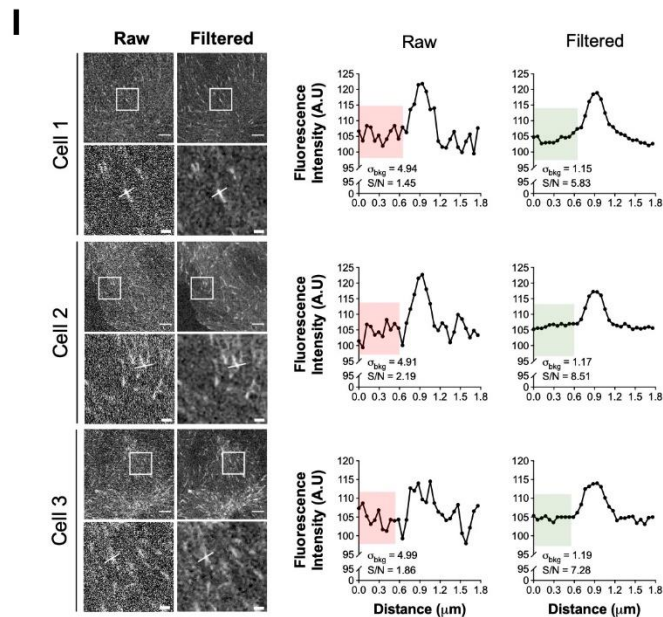
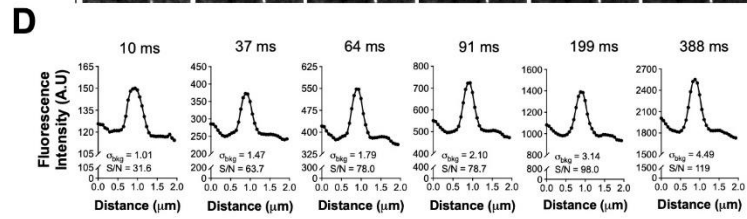
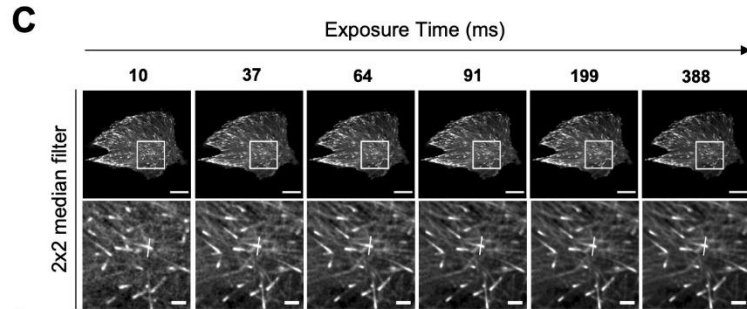
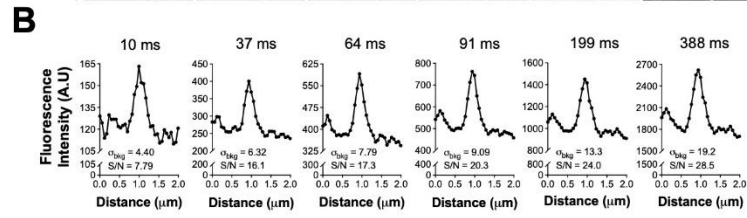
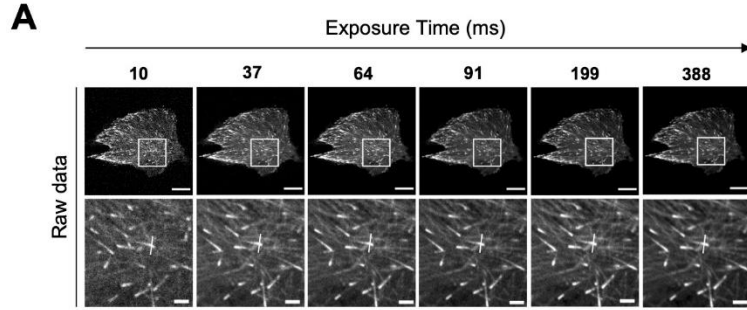


Figure S2.4. Median filtering improves S/N without affecting morphology. (A) LLC-PK1 cells stably expressing EB3-mEmerald and H2B-mCherry were rapidly imaged on a spinning disk confocal microscope with a 63×1.40NA oil immersion objective lens. Frames were summed to simulate data captured with longer exposure times. Brightness and contrast were adjusted for each image for comparability. Scale bar is 10 μm for whole-cell images and 2 μm for regions of interest. (B) Intensity profile across individual EB3-labelled microtubules in images from A are shown by the white lines. The standard deviation of the background (σ_{bkg}) was determined from multiple 250x250 pixel regions of interest. S/N was calculated by dividing the mean intensity of EB3-mEmerald by σ_{bkg} ($n>185$). (C) Images from A were median filtered with a 2x2 grid. Scale bar is 10 μm for whole-cell images and 2 μm for regions of interest. (D) Intensity profile of EB3 in images from C are shown by the white lines. S/N was determined from $n>181$ tip proteins. (E-H) Mean intensity, area, roundness and length of EB3 signal localized to microtubule tips were determined from raw (red) and filtered (blue) images (from A and C images). Measurements were normalized to raw values. Outliers greater or less than 1.5 times the standard deviation of the mean were omitted. Width of the violin plot shows the probability density of the data smoothed with a kernel density estimator. ($P<0.05$ from corresponding raw data, two-tailed Student's t -test). (I) EB3-mEmerald images captured with optimal imaging conditions (0.020 mW×200 ms) (Table S5.9) were median filtered and analyzed for S/N. Filtering improved object detection by removing spurious background noise. S/N was determined from $n>288$ tip proteins. (J) Mean intensity, area, roundness, length and speed of EB3 from raw and filtered timelapse images for Cell 1. Dots indicate individual data points. Number of tip proteins analyzed is indicated in parentheses. Error bars represent mean \pm s.e.m. Standard deviation for each measurement is shown. (P from raw data, two-tailed Student's t -test).

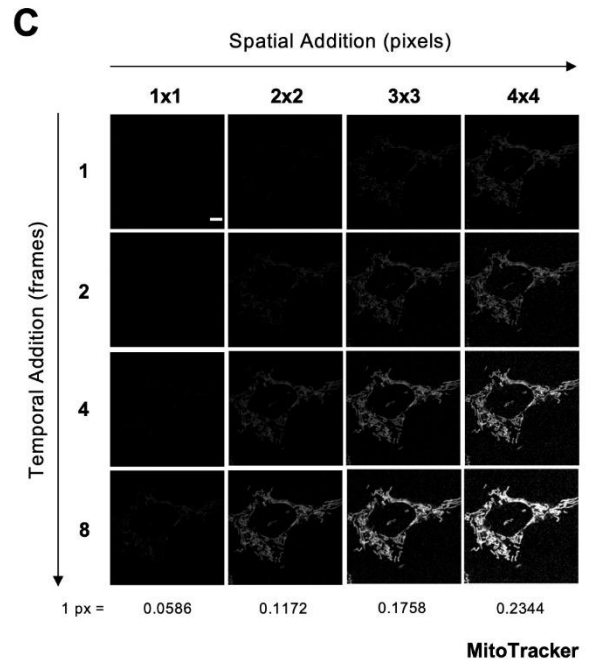
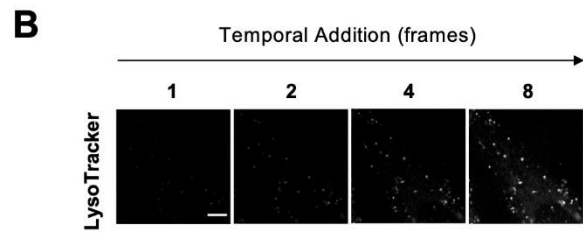
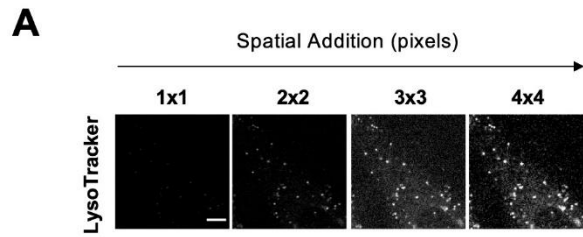


Figure S2.5. Spatial and temporal binning of lysosomes and mitochondria results in greater S/N. CHO-K1 cells stained with LysoTracker™ Green or MitoTracker™ Red were imaged on a spinning disk confocal microscope with a 63×1.40NA oil immersion objective lens. Spatial and temporal addition were performed as described in Fig. 5. Images are shown with equivalent brightness and contrast settings. Scale bar is 5 μm.

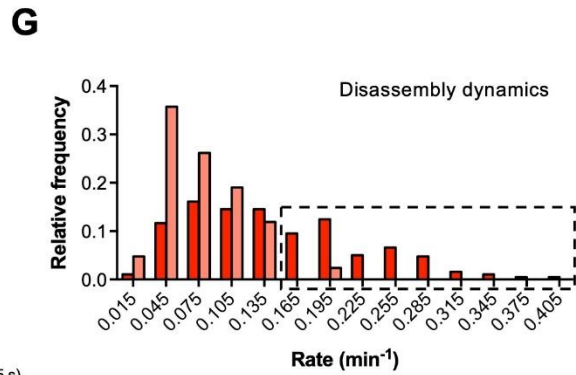
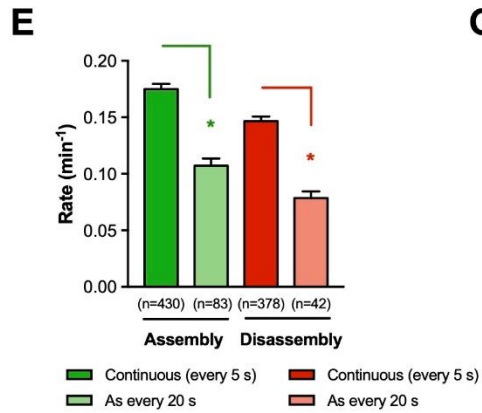
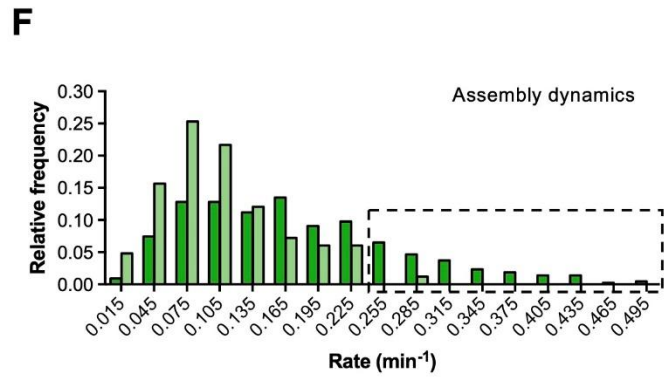
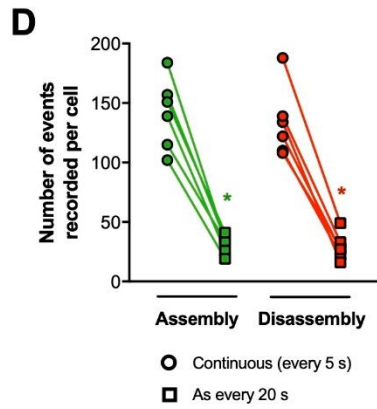
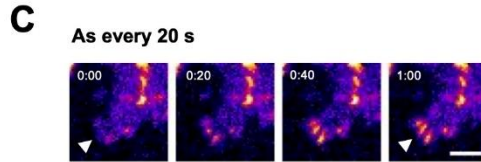
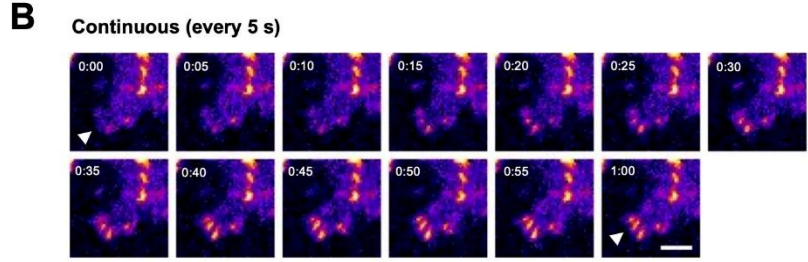
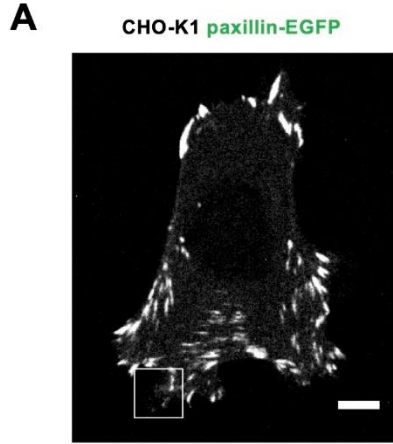


Figure S2.6. Continuous imaging provides enhanced temporal resolution of fast adhesion dynamics in CHO-K1 cells. (A) CHO-K1 cells expressing paxillin-EGFP were continuously imaged on a spinning disk confocal microscope with a 63×1.40NA oil immersion objective lens. Cells were illuminated for 20 min with a 491 nm diode laser set to 0.016 mW. Camera exposure time was set to 5 s (Table S5.9). Scale bar is 5 μm . (B,C) Montage of protrusive cell region in A captured continuously (every 5 s) or every 20 s. White arrow points to the site of adhesion formation. Time is in min:s. Scale bar is 2 μm . (D) The total number of assembly (green) and disassembly (red) events detected for each cell imaged continuously (open circle; \circ) compared to simulated data generated by duplicating every 4th (open square; \square) image frame. A region of interest tool was used to selectively track adhesions in protrusive cell regions. (* $P=0.0022$, Mann-Whitney U test). (E) The average assembly and disassembly rates for each data set depicted in C were determined from the rate of change in mean fluorescence intensity. Data represent dynamic events pooled from six cells. Number of events analyzed is indicated in parentheses. (* $P<0.0001$, Mann-Whitney U test). (F,G) Frequency distribution of assembly and disassembly rates from E. Data values were binned into 0.03 min^{-1} segments. Boxed regions in each graph illustrate highly dynamic adhesions captured only by continuous imaging.

Table S2.1. Illumination overhead continues to be a widespread and relatively unknown phenomenon affecting many microscopes. Surveys of 14 bioimaging facilities throughout Canada and 41 users were conducted to determine the type of equipment being used by researchers and measure the awareness of illumination overhead. The results are likely similar to the situation in many countries.

| Facility Managers | | | | |
|---|--------------------|--------------------|--------------------|-----------------------|
| Q: How many automated fluorescence microscopes are widefield microscopes? | | | | |
| # of microscopes: | <u>1-3</u> 5/14 | <u>4-6</u> 3/14 | <u>7-9</u> 3/14 | <u>>10</u> 3/14 |
| Q: Do any of these widefield microscopes have a mercury/HBO light source? | | | | |
| <u>Yes</u> 9/14 | <u>No</u> 5/14 | | | |
| Q: Do any of these widefield microscopes have a metal halide light source? | | | | |
| <u>Yes</u> 10/14 | <u>No</u> 4/14 | | | |
| Q: Are you aware that depending on how a light source is shuttered there can be additional fluorescence light exposure on the sample beyond the camera exposure time due to delays in shutter open and close times? | | | | |
| <u>Yes</u> 11/14 | <u>No</u> 3/14 | | | |
| Q: Are you aware that these shutter delay times can be on the order of tens to hundreds of milliseconds? | | | | |
| <u>Yes</u> 8/14 | <u>No</u> 6/14 | | | |
| Facility Users | | | | |
| Q: Are you aware that depending on how a light source is shuttered there can be additional fluorescence light exposure on the sample beyond the camera exposure time due to delays in shutter open and close times? | | | | |
| <u>Yes</u> 20/41 | <u>No</u> 21/41 | | | |
| Q: Are you aware that these shutter delay times can be on the order of tens to hundreds of milliseconds? | | | | |
| <u>Yes</u> 14/41 | <u>No</u> 27/41 | | | |

Table S2.2. Illumination conditions used to capture live-cell migration data for CHO-K1 cells expressing paxillin-EGFP. An X-Cite Optical Power Measurement System (XR2100) with an XP750 external sensor was used to measure incident light intensity through a 20×0.8NA objective lens on the Zeiss AxioObserver widefield microscope. Excitation wavelength was set to 488 nm. Exposure times were scaled accordingly to maintain total light exposure of the sample during image acquisition. Power density was determined by measuring the total illumination area of the objective. Measurements were performed on three separate days. Mean±s.e.m. power is shown (*P* values were calculated relative to power × time for 61.6 mW×24 ms, two-tailed Student’s *t*-test).

| 20x/0.8NA objective | | | | | | |
|----------------------|--------------------------|-------------------------------|--------------------------------------|--------------------|----------------------|-----------------|
| Illumination setting | Effective lamp power (%) | Fluorescence light power (mW) | Power density (mW cm ⁻²) | Exposure time (ms) | Power x time (mW*ms) | <i>P</i> values |
| 1 | 21 | 61.6 ± 0.6% | 3814 | 24 | 1477.6 ± 9.6 | N/A |
| 2 | 10 | 31.3 ± 1.0% | 1938 | 48 | 1494.4 ± 12.8 | 0.275 |
| 3 | 1.2 | 4.21 ± 5.0% | 261 | 350 | 1473.5 ± 73.8 | 0.952 |
| 4 | 0.3 | 1.34 ± 6.0% | 83.0 | 1060 | 1423.9 ± 86.5 | 0.528 |
| 5 | 0.12 | 0.288 ± 5.6% | 17.8 | 5000 | 1441.7 ± 77.9 | 0.630 |
| 6 | 0.05 | 0.136 ± 5.9% | 8.42 | 10666 | 1454.1 ± 80.6 | 0.756 |
| 7 | 0.03 | 0.0911 ± 5.5% | 5.64 | 15909 | 1449.8 ± 80.3 | 0.714 |
| 8 | 0.02 | 0.0634 ± 5.4% | 3.93 | 22857 | 1449.9 ± 79.0 | 0.710 |
| 9 | 0.015 | 0.0474 ± 1.7% | 2.93 | 30270 | 1434.8 ± 24.7 | 0.156 |
| 10 | 0.011 | 0.0362 ± 1.9% | 2.24 | 40000 | 1448.0 ± 27.3 | 0.315 |
| 11 | 0.009 | 0.0304 ± 2.0% | 1.88 | 47863 | 1455.0 ± 29.3 | 0.450 |
| 12 | 0.007 | 0.0245 ± 2.0% | 1.52 | 60000 | 1470.0 ± 29.7 | 0.789 |

Table S2.3. Illumination conditions used to measure CHO-K1 cell migration speeds in response to increasing light power. Power and power density were measured as described in Table S5.2. DLD refers to diffuse light dose (0.0245 mW×60,000 ms).

| 20x/0.8NA objective | | | | | |
|----------------------|--------------------------|-------------------------------|--------------------------------------|--------------------|----------------------|
| Illumination setting | Effective lamp power (%) | Fluorescence light power (mW) | Power density (mW cm ⁻²) | Exposure time (ms) | Power x time (mW*ms) |
| 2x DLD | 0.016 | 0.0492 | 3.05 | 60000 | 2952 |
| 3x DLD | 0.024 | 0.0708 | 4.38 | | 4248 |
| 4x DLD | 0.039 | 0.0940 | 5.82 | | 5640 |
| 5x DLD | 0.062 | 0.122 | 7.55 | | 7320 |

Table S2.4. Illumination conditions for paxillin-EGFP used to observe mitochondrial morphology in migrating cells. A PM400 Optical Power and Energy Meter with an S170C Microscope Slide Power Sensor was used to measure incident light intensity through a 63×1.4NA immersion oil objective lens on the Zeiss AxioObserver widefield microscope. Excitation wavelength was set to 488 nm. Power density was determined by measuring the total illumination area of the objective. Measurements were performed on three separate days. Mean±s.e.m. power is shown (*P* values were calculated relative to power × time for 21.3 mW×24 ms, two-tailed Student’s *t*-test).

| 63x/1.4NA objective (immersion oil) | | | | | | |
|-------------------------------------|--------------------------|-------------------------------|--------------------------------------|--------------------|----------------------|-----------------|
| Illumination setting | Effective lamp power (%) | Fluorescence light power (mW) | Power density (mW cm ⁻²) | Exposure time (ms) | Power x time (mW*ms) | <i>P</i> values |
| 1 | 21 | 21.3 ± 7.0% | 10427 | 24 | 510.9 ± 37.0 | N/A |
| 2 | 0.007 | 0.0093 ± 7.2% | 4.55 | 60000 | 560.8 ± 40.2 | 0.326 |

Table S2.5. Illumination conditions for BFP, mCherry and iRFP excitation on the widefield microscope. Power and power density were measured as described in Table S5.2. Excitation wavelengths were set to 385, 587 and 620 nm for BFP, mCherry and iRFP, respectively. CLD refers to condensed light delivery; DLD refers to diffuse light delivery.

| 20x/0.8NA objective | | | | | | |
|---------------------|---------|--------------------------|-------------------------------|--------------------------------------|--------------------|----------------------|
| Fluorophore | Setting | Effective lamp power (%) | Fluorescence light power (mW) | Power density (mW cm ⁻²) | Exposure time (ms) | Power x time (mW*ms) |
| BFP | CLD | 70 | 33.90 | 2099 | 24 | 813.6 |
| | DLD | 0.03 | 0.015 | 0.929 | 60000 | 900.0 |
| mCherry | CLD | 23 | 58.40 | 3616 | 100 | 5840 |
| | DLD | 0.023 | 0.099 | 6.13 | 60000 | 5940 |
| iRFP | CLD | 21 | 63.10 | 3907 | 100 | 6310 |
| | DLD | 0.02 | 0.112 | 6.93 | 60000 | 6720 |

Table S2.6. Signal-to-noise ratio of paxillin-EGFP in response to different exposure times. CHO-K1 cells expressing paxillin-EGFP were fixed with 4% PFA and stained with DAPI. Three independent fields of view were acquired on the Zeiss AxioObserver widefield microscope using the illumination conditions outlined in Table S5.2. Cells were analyzed in MetaXpress using the Multi Wavelength Cell Scoring application (n=94). Mean intensity and standard deviation of the background were determined from a 125×125 pixel region of interest. Mean±s.e.m. are shown. (*P* values were calculated relative to the signal-to-noise ratio for 24 ms, two-tailed Student’s *t*-test).

| 20x/0.8NA objective | | | | | |
|-----------------------------|---------------------------|-------------------------------------|---|------------------------------|------------------------|
| Illumination setting | Exposure time (ms) | Mean intensity of background | Standard deviation of background | Signal-to-noise ratio | <i>P</i> values |
| 1 | 24 | 100.1 ± 3.5 | 11.0 ± 0.3 | 12.4 ± 0.8 | N/A |
| 2 | 48 | 99.3 ± 3.4 | 11.0 ± 0.3 | 12.7 ± 0.8 | 0.689 |
| 3 | 350 | 95.3 ± 2.5 | 10.8 ± 0.1 | 13.9 ± 1.2 | 0.291 |
| 4 | 1060 | 96.5 ± 1.6 | 10.9 ± 0.1 | 13.3 ± 0.9 | 0.399 |
| 5 | 5000 | 127.3 ± 5.3 | 12.2 ± 0.3 | 11.8 ± 0.9 | 0.610 |
| 6 | 10666 | 147.5 ± 3.3 | 13.1 ± 0.1 | 11.2 ± 0.6 | 0.233 |
| 7 | 15909 | 165.8 ± 5.3 | 14.0 ± 0.2 | 10.4 ± 0.6 | 0.088 |
| 8 | 22857 | 187.0 ± 16.7 | 15.2 ± 0.6 | 9.80 ± 0.47 | 0.041 |
| 9 | 30270 | 223.4 ± 7.2 | 17.1 ± 0.3 | 8.02 ± 0.54 | 0.008 |
| 10 | 40000 | 270.4 ± 11.1 | 19.4 ± 0.2 | 6.95 ± 0.40 | 0.006 |
| 11 | 47863 | 295.8 ± 10.9 | 20.9 ± 0.4 | 6.52 ± 0.43 | 0.004 |
| 12 | 60000 | 335.8 ± 23.7 | 23.6 ± 0.6 | 5.83 ± 0.39 | 0.004 |

Table S2.7. Signal-to-noise ratio of paxillin-EGFP in response to increasing light power. CHO-K1 cells expressing paxillin-EGFP were fixed with 4% PFA and stained with DAPI. Three independent fields of view were acquired on the Zeiss AxioObserver widefield microscope using a 20×0.8NA objective lens. Camera exposure time was set to 60,000 ms. Cells were analyzed in MetaXpress using the Multi Wavelength Cell Scoring application (n=53). Mean intensity and standard deviation of the background were determined from a 125×125 pixel region of interest. Mean±s.e.m. are shown. (*P* values were calculated relative to the signal-to-noise ratio for 0.0237 mW (1× diffuse light dose), two-tailed Student’s *t*-test).

| 20x/0.8NA objective | | | | | |
|----------------------|-------------------------------|------------------------------|----------------------------------|-----------------------|-----------------|
| Illumination setting | Fluorescence light power (mW) | Mean intensity of background | Standard deviation of background | Signal-to-noise ratio | <i>P</i> values |
| 1x DLD | 0.0237 | 388.4 ± 23.9 | 23.9 ± 0.7 | 7.62 ± 0.27 | N/A |
| 2x DLD | 0.0492 | 441.0 ± 28.4 | 25.0 ± 0.9 | 13.8 ± 0.5 | 0.0007 |
| 3x DLD | 0.0708 | 478.7 ± 20.8 | 25.7 ± 0.8 | 18.8 ± 0.8 | 0.0014 |
| 4x DLD | 0.0940 | 519.7 ± 13.8 | 26.2 ± 0.4 | 24.4 ± 1.0 | 0.0013 |

Table S2.8. Illumination conditions used to show the effect of IO on the spinning disk confocal microscope. A PM400 Optical Power and Energy Meter with an S170C Microscope Slide Power Sensor was used to measure light intensity through an HCX PL APO 63×1.40NA immersion oil objective lens on the spinning disk confocal microscope. Excitation wavelength was set to 491 nm. Exposure times were scaled accordingly to maintain total light dose. Power density was determined by measuring the total illumination area of the objective.

| 63x/1.40NA objective (immersion oil) | | | | | | |
|--------------------------------------|--------------------------|-------------------------------|--------------------------------------|--------------------------|---------------------------|----------------------|
| Illumination setting | Effective lamp power (%) | Fluorescence light power (mW) | Power density (mW cm ⁻²) | Input exposure time (ms) | Actual exposure time (ms) | Power x time (mW*ms) |
| 1 | 17 | 0.162 | 1588 | 217 | 234 | 37.9 |
| 2 | 21 | 0.252 | 2471 | 134 | 151 | 38.1 |
| 3 | 31 | 0.558 | 5471 | 51 | 68 | 37.9 |
| 4 | 40 | 0.922 | 9039 | 24 | 41 | 37.8 |
| 5 | 50 | 1.404 | 13765 | 10 | 27 | 37.9 |
| 6 | 8 | 0.0313 | 307 | 217 | 234 | 7.3 |
| 7 | 9.9 | 0.0476 | 467 | 134 | 151 | 7.2 |
| 8 | 14.4 | 0.106 | 1039 | 51 | 68 | 7.2 |
| 9 | 18.3 | 0.176 | 1725 | 24 | 41 | 7.2 |
| 10 | 22.4 | 0.269 | 2637 | 10 | 27 | 7.3 |

Table S2.9. Summary of illumination conditions used to capture cellular dynamics on the spinning disk confocal microscope. Images were acquired with an HCX PL APO 63×1.40NA immersion oil objective lens. A PM400 Optical Power and Energy Meter with an S170C Microscope Slide Power Sensor was used to measure light power. Excitation wavelength was set to 448 nm for Teal; 491 nm for mEmerald, LysoTracker™ Green, EGFP and Venus; and 561 nm for MitoTracker™ Red, mCherry and mRuby. Power density was determined by measuring the total illumination area of the objective.

| EB3 dynamics | | | | | |
|--------------|------------|--------------------|-------------------------------|--------------------------------------|--------------|
| Setting | Laser (nm) | Exposure time (ms) | Fluorescence light power (mW) | Power density (mW cm ⁻²) | Probe(s) |
| 1 | 491 | 200 | 0.020 | 196 | EB3-mEmerald |
| 2 | 491 | 200 | 0.020 | 196 | EB3-mEmerald |
| | 561 | | 0.010 | 98.0 | H2B-mCherry |

| Lysosomal and mitochondrial dynamics | | | | | |
|--------------------------------------|------------|--------------------|-------------------------------|--------------------------------------|----------------------|
| Setting | Laser (nm) | Exposure time (ms) | Fluorescence light power (mW) | Power density (mW cm ⁻²) | Probe(s) |
| 1 | 491 | 100 | 0.020 | 196 | LysoTracker Green |
| 2 | 561 | 100 | 0.037 | 363 | MitoTracker Red |
| 3 | 561 | 50 | 0.037 | 363 | MitoTracker Red (3D) |

| Actin and adhesion dynamics | | | | | |
|-----------------------------|------------|--------------------|-------------------------------|--------------------------------------|--------------------|
| Setting | Laser (nm) | Exposure time (ms) | Fluorescence light power (mW) | Power density (mW cm ⁻²) | Probe(s) |
| 1 | 448 | 5000 | 0.013 | 127 | VinculinTS (Teal) |
| | 491 | | 0.007 | 68.6 | VinculinTS (Venus) |
| 2 | 491 | 5000 | 0.016 | 157 | paxillin-EGFP |
| 3 | 491 | 5000 | 0.060 | 588 | LifeAct-EGFP |
| 4 | 561 | 5000 | 0.031 | 304 | mCherry-paxillin |
| 5 | 491 | 5000 | 0.016 | 157 | paxillin-EGFP |
| | 561 | | 0.031 | 304 | LifeAct-mRuby |

CHAPTER 3 – Microscope Hardware and Software Delays Cause Photo-Toxicity

Alex Kiepas^{1,2} and Claire M. Brown^{1,3}

¹Department of Physiology, ²Goodman Cancer Research Centre, and ³Advanced BioImaging Facility (ABIF), McGill University, Montreal, Quebec, Canada

This chapter is an original research article published in:

Microscopy Today, 2020

3.1 PREFACE

Modern fluorescent light microscopes are complex instruments that heavily rely on computer software to coordinate sample illumination, image acquisition and data storage. Automation allows researchers to perform increasingly complex experiments with multiple fluorophores, regions of interest, and a variety of spatial and temporal time scales. Hardware and software components appear to work together seamlessly during most applications; however, live-cell imaging reveals that subtle changes in image acquisition parameters can have a large impact on cell health and image quality. In the previous chapter, we demonstrated that software delays in USB triggering of the light source lead to illumination overhead (IO). IO can severely impact cell health if the additional light dose ($\text{mW} \times \text{ms}$) is sufficiently large. At the same time, we realized that IO may generate inappropriate delays between images if the time interval between subsequent acquisitions is sufficiently small. Therefore, we sought to investigate the impact of hardware and software delays on rapid image acquisition.

3.2 ABSTRACT

Technological advancements in the areas of sample illumination, image acquisition, and image processing have significantly improved the speed and sensitivity of fluorescence microscopy. In particular, light emitting diodes (LEDs) coupled to transistor-transistor logic (TTL) circuits have reduced photo-bleaching and photo-toxicity by limiting sample illumination to the camera exposure time. Unfortunately, many microscopes still rely on bulb-based light sources that cannot be configured with TTL. Moreover, even when TTL is enabled in conventional microscope software, hardware and software delays can still contribute to photo-toxicity and lead to additional delays between subsequent images, introducing errors in time lapse image recordings. The goal of the present article is to highlight the significance of these issues.

3.3 INTRODUCTION

In the November 2017 issue of *Microscopy Today*, our laboratory published an article indicating that longer exposure times with lower light intensities reduced photo-toxicity to live cells [1]. In particular, fluorescence wide-field imaging experiments showed that employing longer exposure times with lower light powers drastically reduced photo-bleaching and increased cell migration and cell protrusion speeds without impacting image quality. Further investigation into this phenomenon pointed us to the issue of illumination overhead (IO). IO is the time fluorescent samples are exposed to incident light, but fluorescence emission is not being collected by the detector [2]. IO leads to excessive light exposure to the sample with no improvement in image quality. The authors were aware of IO when the *Microscopy Today* article was published in 2017, but not the extent of the problem. Since then additional experiments have been conducted to further investigate the impact of IO. Importantly, photo-bleaching and photo-toxicity were not due to increased incident light power.

Modern light sources for fluorescence microscopy, such as light-emitting diodes (LEDs), can be electronically switched on and off within a few milliseconds [3, 4]. This technological advancement has significantly reduced photo-bleaching and photo-toxicity during fluorescence microscopy by changing the way sample illumination is controlled. In the past, mechanical shutters were required to regulate sample exposure time for bulb-based light sources. When using shutters, the microscope software synchronizes shutter opening with camera acquisition time. Image acquisition software introduces a delay so that camera acquisition does not begin until the shutter is fully open [5]. This ensures uniform illumination across the entire field of view; however, samples are exposed to extra illumination (IO) beyond the camera exposure time. The amount of IO samples experience is a function of shutter speed. In contrast, most newer microscopes are equipped with LED-based light sources, and sample illumination is largely controlled by electronic triggering. Electronic activation of light sources is significantly faster than physical shutter speeds, resulting in a dramatic reduction in IO [2]. Triggering can be achieved in two ways: (1) the microscope software directly triggers the light source through a USB connection to the device; or (2) the microscope software initiates camera acquisition, which in turn triggers the light source through a transistor-transistor logic (TTL) circuit.

In this follow-up study, the complexity of IO and interval imaging with USB and TTL triggering was explored. IO generated more reactive oxygen species (ROS) when shorter exposure

times were used, complementing the results of our original work. The percent of IO decreased with longer exposure times; however, the amount of IO samples experienced was not constant across all exposure times. Additionally, results showed that the light source had to be disconnected from the microscope software for TTL light triggering to function properly; otherwise, hardware and software delays continued to contribute significantly to IO. Finally, although TTL successfully eliminated IO, hardware and software delays continued to impact the acquisition interval resulting in inaccurate time resolution of experiments.

3.4 RESULTS

Sample illumination with LED light sources can be controlled through the microscope software by (1) opening and closing a mechanical shutter, (2) electronically triggering the light source via a USB cable connection, or (3) electronically triggering the light source via a TTL cable from the camera to the light source. We previously observed that electronic activation of the light source is ~ 20 -fold faster than opening/closing mechanical shutters [2]. Therefore, we focused on USB and TTL triggering of the light source in the present article. USB and TTL turn the light source on and off at approximately the same rate [2]. A notable advantage of USB triggering is that it allows the microscope software to modify the properties of the light source (for example, light power; for multiple LEDs they can be turned on and off selectively, programmed for different exposure times). In contrast, TTL triggering relies on an electronic circuit between the camera and the light source; when the camera begins acquiring an image, a current is sent to the light source to turn it on. This is an all-or-nothing event, meaning that the light source turns on to a preset user-defined intensity. However, if both USB and TTL cables are connected to the light source, light intensity can be adjusted in the microscope software prior to TTL triggering. Thus, it may be useful to have both connections to the light source, especially if performing multi-color and multi-dimensional acquisition.

Based on this information, we tested three different settings on a Zeiss AxioObserver equipped with an X-Cite 120LED: TTL triggering of the light source with the USB cable (1) disconnected or (2) connected, and (3) USB triggering of the light source with the TTL cable disconnected. TTL effectively synchronized and limited light exposure to the camera image acquisition time within a millisecond or so (Fig. 3.2, *top panel*). Although USB triggering is equally effective in turning the light source on and off [2], light exposure time was almost six times longer with USB triggering when compared to TTL (Fig. 3.2, *bottom panel*). Consequently, USB and TTL triggering of the light source are not equivalent. Interestingly, the USB cable had to be disconnected from the microscope software for TTL triggering to work properly; even if TTL override was enabled, the exposure time was three times longer when the microscope software detected the light source via the USB connection (Fig. 3.2, *middle panel*). This suggests that determination of IO time is complex, as it can arise from both hardware and software delays. IO is an especially important issue for live-cell microscopy, as the extra illumination time with USB triggering results in a significant amount of photo-bleaching and ROS production [2]. The impact

of IO is more drastic when shorter exposure times with higher light powers are used as the relative contribution of IO to photo-bleaching and phototoxicity is greater. For example, when 400 images of paxillin-EGFP were collected with high-power illumination light and a 24 ms exposure time, the sample was illuminated almost six-fold longer (138 ms) for each of the 400 images collected. This resulted in significant ROS production (Fig. 3.1). However, when low-power light was used with 1060 ms exposure times, the contribution of IO was only 10–20%, so there was minimal ROS accumulation even after collecting 400 images (Fig. 3.1).

Further in-depth experiments exploring the issue of IO revealed that the amount of additional sample illumination was not constant but varied with changes in exposure time. Indeed, longer exposure times exhibited longer IO when USB triggering was used, with some variability in the times (Fig. 3.3). Nevertheless, the percentage contribution of IO decreased with longer exposure times, resulting in healthier live-cell imaging conditions [2]. Thus, the conclusion of our *Microscopy Today* article (that is, longer exposure times with lower light power are less photo-toxic) still stands and is especially important if IO is significant. This is especially true for mercury or metal-halide light sources that cannot be electronically switched on and off but rely on mechanical shuttering. If fluorescence light sources, such as LEDs, can be directly triggered by TTL to limit light exposure of the sample to the camera exposure time, then higher light powers and shorter exposure times are compatible with live-cell imaging experiments. It should be noted that increased photo-bleaching was not caused by increased incident light power in our set of experiments [2]. It is possible that the production of ROS over shorter periods of time with high light power could overwhelm cellular systems designed to remove ROS and cause photo-toxicity in live samples; however, further experimentation is required to determine if this is indeed the case.

Another important observation from our studies was that hardware and software delays can also negatively impact the image acquisition interval. When a sufficiently long imaging interval was set in the microscope software, TTL triggering was able to capture images at the desired time resolution (Figure 3.4A, *top panels in black*). Unfortunately, imaging intervals below a certain value could not be realized, even though the time resolution was theoretically possible (Figure 3.4A, *bottom panels in red*). Moreover, the minimum imaging interval appeared to vary with exposure time and did not change in a systematic way (Figure 3.4B). This is especially problematic when imaging dynamic cellular processes that occur on the millisecond to second time scale. As a

result, it is recommended that users verify the time resolution of their experimental system using an oscilloscope or accurate software time stamps indicating exactly when the images were saved. Some hardware and software delays can be mitigated with stream acquisition if it is available in the image acquisition software. In this case, stream acquisition with temporary data storage on random access memory (RAM) allowed rapid imaging with a 5.005 ms delay between images (data not shown). Similar results were obtained on a spinning disk confocal system; stream acquisition reduced IO from ~ 42 to ~ 17 ms [2]. Furthermore, stream acquisition allowed subsequent images to be captured with no time delay beyond ~ 17 ms of IO (Figure 3.5). Longer exposure times with lower light levels and stream acquisition allowed for the simultaneous capture of images of EB3-mEmerald and H2B-mCherry with high time resolution (200 ms camera exposure time plus 17 ms IO) with no apparent photo-bleaching [2]. These parameters could also be used to quantify the speed and persistence of lysosomes using LysoTracker™ Green staining (Figure 3.6).

3.5 DISCUSSION

Overall, our results indicate that IO is a highly complex issue that appears to be caused by hardware and software delays. These hardware and software delays are likely unique to every microscope [6]. Thus, there are many factors that contribute to additional sample illumination (as seen here with USB triggering) and extended image acquisition intervals with TTL triggering. Camera software drivers, computer processing speeds, computer components (video cards, RAM, CPU), software versions, and connections between the computer and microscope components all likely affect IO and image acquisition intervals. The complexity is clear. Indeed, microscopists have previously noted that faster image acquisition can be achieved by imaging a smaller region of interest (ROI) on the camera chip, and the acquisition speed can vary depending on the physical location of the ROI on the chip [7, 8]. Efforts are currently underway to design hardware and software for improved high-speed synchronization of multiple devices [9-11]. In the meantime, microscopists should measure imaging parameters with an oscilloscope to determine the impact of IO and adapt image acquisition parameters for healthy live-cell imaging conditions while maintaining time resolution and accurate time intervals for time lapse imaging.

3.6 MATERIALS AND METHODS

3.6.1 Cell culture

CHO-K1 cells stably expressing paxillin-EGFP were obtained from the lab of Dr. Rick Horwitz (University of Virginia, Charlottesville, VA). Cells were grown in low glucose (1.0 g l^{-1}) Dulbecco's modified Eagle's medium (DMEM; cat. no. 11885-084, Thermo Fisher Scientific), supplemented with 10% fetal bovine serum (FBS; cat. no. 10082147, Thermo Fisher Scientific), 1% non-essential amino acids (NEAA; cat. no. 11140-050, Thermo Fisher Scientific), 25 nM 4-(2-hydroxyethyl)-1-piperazineethanesulfonic acid (HEPES; cat. no. 15630-080, Thermo Fisher Scientific), and 1% penicillin-streptomycin (cat. no. 10378-016, Thermo Fisher Scientific). Cells were maintained in 0.5 mg ml^{-1} Geneticin-418 (G418; cat. no. 11811-031, Thermo Fisher Scientific) antibody selection to maintain paxillin-EGFP expression.

MCF7 cells were obtained from the American Type Culture Collection (ATCC; cat. no. HTB-22). Cells were grown in high glucose (4.5 g l^{-1}) DMEM (cat. no. 319-005-CL, Wisent Bioproducts), supplemented with 10% FBS (cat. no. 12483-020, Gibco) and 1% penicillin-streptomycin (cat. no. 450-201-EL, Wisent Bioproducts).

3.6.2 Measurements of exposure time

A digital oscilloscope (DS1054Z; Rigol, Beijing, China) coupled to a DET36A/M Si Based Detector (Thorlabs, Dachau, Germany) was used to measure the total illumination time delivered through a Plan ApoChromat $\times 20/0.8$ NA objective lens on a Zeiss AxioObserver fully automated inverted microscope (Carl Zeiss, Jena, Germany). An XCite 120LED light source (Excelitas Technologies, Waltham, MA) was used to deliver excitation light via the microscope software (ZEN pro, version 2.6). The light source was electronically triggered via a USB cable connection between the computer and the light source (*scenario 1*) or a TTL cable between an Axiocam 506 camera (Carl Zeiss) and the light source (*scenarios 2 and 3*). In the latter case, the USB cable between the computer and the light source was either connected (*scenario 2*) or disconnected (*scenario 3*). A variety of camera exposure times (24–60,000 ms) and acquisition intervals (25–500 ms) were input into the microscope software, and the light output was recorded.

The oscilloscope was also used to measure the total illumination time delivered through an HC PLAN APO $\times 20/0.7$ NA objective lens on a Leica DMI6000B inverted microscope equipped with a Quorum WaveFx-X1 spinning disk confocal system (Quorum Technologies, Guelph, ON).

A 561 nm diode laser was used to deliver excitation light via an acousto-optic tunable filter (AOTF) crystal controlled by MetaMorph software (version 7.10.2.240; Molecular Devices, Sunnyvale, CA). The AOTF crystal was controlled by USB triggering. Voltage traces were captured with interval imaging or stream to random access memory (RAM) acquisition. Camera exposure time was set to 100 or 200 ms. The acquisition interval was set to 0 ms. Voltage traces obtained from the oscilloscope were analyzed in MATLAB (version 9.8.0, Rel. 2020a; The MathWorks, Natick, MA). IO was determined by subtracting the desired (input) exposure time from the actual (output) exposure time. Dividing IO by input exposure time yielded percent IO.

3.6.3 Measurements of power

A PM400 Optical Power and Energy Meter with an S170C Microscope Slide Power Sensor (Thorlabs) was used to measure incident light intensity through oil immersion objective lenses: Zeiss PlanApo $\times 63/1.4$ NA on the AxioObserver and Leica HCX PL APO $\times 63/1.4$ NA on the spinning disk confocal microscope. Measurements were performed on three separate days and averaged.

3.6.4 ROS production in response to photo-bleaching

CHO-K1 cells expressing paxillin-EGFP were seeded onto μ -slide 8-well plates (cat. no. 80821, IBIDI, Fitchburg, WI) coated with $0.21 \mu\text{g cm}^{-2}$ fibronectin (cat. no. F-0895, Sigma-Aldrich) diluted in 1x phosphate-buffered saline (PBS). Cells were allowed to adhere and grow under exponential conditions for at least 12 h prior to experimentation. Cells were then stained with $0.83 \mu\text{M}$ CellROX™ Deep Red (cat. no. C10422, Thermo Fisher Scientific). Images were acquired on the Zeiss AxioObserver with a PlanApo $\times 63/1.4$ NA oil immersion objective lens and Chamlide TC-L-Z003 stage top environmental control incubator (Live Cell Instrument, Seoul, South Korea). An XCite 120LED was used to deliver excitation light through an EGFP filter cube (filter set 10; 450–490 nm excitation, 515–565 nm emission; Carl Zeiss) at three different intensities: 21.3 mW, 10.8 mW and 0.476 mW. Image acquisition settings were adjusted to maintain a constant number of photons impacting the sample during camera exposure time without taking IO into consideration ($21.3 \text{ mW} \times 24 \text{ ms}$, $10.8 \text{ mW} \times 48 \text{ ms}$, $0.476 \text{ mW} \times 1060 \text{ ms}$). The light source was USB triggered through the microscope software. CellROX™ was imaged before and after paxillin-EGFP photo-bleaching (400 frames) with a total light dose of $1030 \text{ mW} \times \text{ms}$

delivered through a Cy5 filter cube (filter set 49006; 590–650 nm excitation, 662–737 nm emission; Chroma Technologies, Bellows Falls, VT). Exposure time was set to 1000 ms. Paxillin-EGFP and CellROX™ images were pseudo-colored (Rainbow RGB) in ImageJ (National Institutes of Health, Bethesda, MD) to emphasize changes in fluorescence intensity. The intensity scale is the same for all image panels for each fluorophore (Figure 1).

3.6.5 Lysosomal dynamics

MCF7 cells were seeded onto μ -dish 35 mm high glass bottom dishes (cat. no. 81158, IBIDI) coated with $5 \mu\text{g cm}^{-2}$ fibronectin (cat. no. FC010, EMD Millipore) and stained with 200 nM LysoTracker™ Green DND-26 (cat. no. L7526, Thermo Fisher Scientific). Cells were imaged on the spinning disk confocal microscope with a Leica HCX PL APO $\times 63/1.40$ NA oil immersion DIC objective lens, Prime BSI sCMOS camera (Photometrics, Tuscon, AZ), and CU-501 stage-top incubator system (Live Cell Instrument, Seoul, South Korea). Each cell was illuminated with a 491 nm diode laser set to ~ 0.02 mW. Stream to RAM acquisition in MetaMorph was used to acquire images continuously for over 30 s. Camera exposure time was set to 200 ms with 2×2 pixel binning (1 pixel = $0.1172 \mu\text{m} \times 0.1172 \mu\text{m}$). IO was found to contribute an additional 17 ms delay resulting in a time resolution of 217 ms. The pinhole size of the spinning disk was fixed at $50 \mu\text{m}$.

Image stacks were imported into Imaris (version 9.2.0; Bitplane, AG, Zurich, Switzerland) to track the position of lysosomes over time. Lysosomes were masked with the Spots function using an estimated diameter of $0.5 \mu\text{m}$ and local background subtraction. An autoregressive motion algorithm with a maximum distance of $1 \mu\text{m}$ and gap size of 3 frames was used to follow lysosomes. Data were then exported to MATLAB to quantify speed and persistence. Tracks less than 15 frames (3.255 s) were removed by filtering. Average speed was calculated from mean change in x,y position between each time point. Persistence was calculated by dividing the net displacement of each vesicle track after 15 frames by the total distance traveled. Data from three cells were then pooled together and plotted as frequency distributions using Prism 8 (version 8.4.2; GraphPad Software, San Diego, CA).

3.7 AUTHOR CONTRIBUTIONS

A.K. performed experiments. A.K. and C.M.B. conceptualized the project, wrote and edited the manuscript.

3.8 ACKNOWLEDGEMENTS

We thank Dr. Marco Biondini and Leeanna El-Houjeiri (McGill University, Montreal, QC) for preparing MCF7 cells stained with LysoTracker™ Green. Work performed in the author's laboratory (CMB) was supported by grants from the National Sciences and Engineering Research Council (NSERC) (Grant #493616-16, #386084-12) and CIHR (Grant #CPG146475). AK acknowledges support in the form of a Fonds de Recherche Santé (FRQS) doctoral studentship. Imaging experiments were performed at the McGill University Advanced BioImaging Facility (ABIF).

3.9 REFERENCES

1. Mubaid, F. and C.M. Brown, *Less is More: Longer Exposure Times with Low Light Intensity is Less Photo-Toxic*. *Microscopy Today*, 2017. **25**(6): p. 26-35.
2. Kiepas, A., et al., *Optimizing live-cell fluorescence imaging conditions to minimize phototoxicity*. *J Cell Sci*, 2020. **133**(4).
3. Nishigaki, T., et al., *Stroboscopic illumination using light-emitting diodes reduces phototoxicity in fluorescence cell imaging*. *Biotechniques*, 2006. **41**(2): p. 191-7.
4. Bosse, J.B., et al., *Open LED Illuminator: A Simple and Inexpensive LED Illuminator for Fast Multicolor Particle Tracking in Neurons*. *PLoS One*, 2015. **10**(11): p. e0143547.
5. MicroscopyU. *The Automatic Microscope*. Available from: <https://www.microscopyu.com/applications/live-cell-imaging/the-automatic-microscope>.
6. Davis, M.A., *Hardware triggering: maximizing speed and efficiency for live cell imaging*. *Nature Methods*, 2017. **14**(12): p. 1223-1223.
7. Instruments, O. *Cropped sensor mode*. Available from: <https://andor.oxinst.com/learning/view/article/what-is-cropped-sensor-mode>.
8. Almada, P., S. Culley, and R. Henriques, *PALM and STORM: Into large fields and high-throughput microscopy with sCMOS detectors*. *Methods*, 2015. **88**: p. 109-21.
9. uManager. *Hardware-based synchronization in Micro-Manager*. Available from: https://micro-manager.org/wiki/Hardware-based_Synchronization_in_Micro-Manager.
10. Colville, M.J., et al., *High-speed device synchronization in optical microscopy with an open-source hardware control platform*. *Sci Rep*, 2019. **9**(1): p. 12188.
11. Edelstein, A., et al., *Computer control of microscopes using microManager*. *Curr Protoc Mol Biol*, 2010. **Chapter 14**: p. Unit14 20.

3.10 FIGURES AND LEGENDS

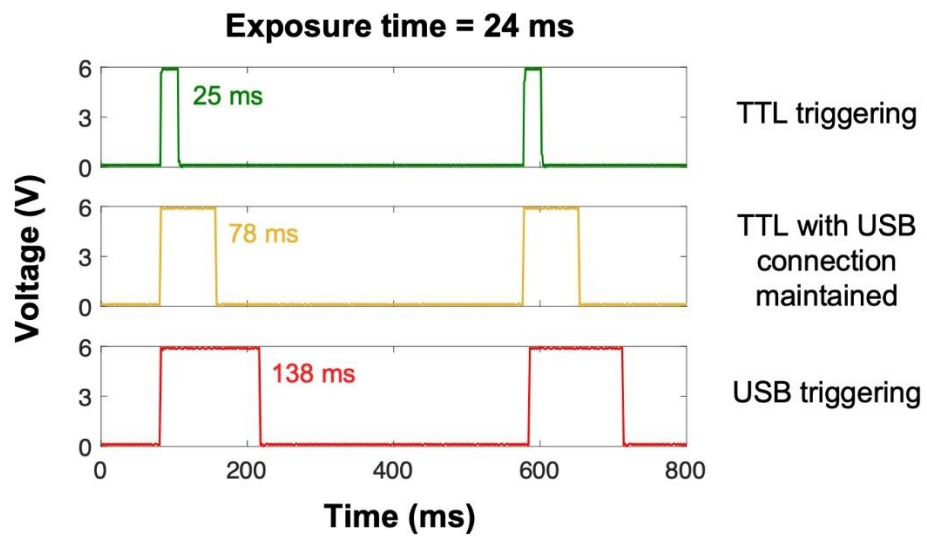


Figure 3.1. USB connection must be disabled for TTL to eliminate IO. CHO-K1 cells expressing paxillin-EGFP were seeded onto fibronectin-coated dishes and stained with CellROX™ Deep Red Reagent. Paxillin-EGFP was repeatedly imaged for 400 frames with USB triggering of the light source. Three different light doses were chosen: 21.3 mW × 24 ms, 10.8 mW × 48 ms, and 0.476 mW × 1060 ms. Light power and exposure time were adjusted such that the total light dose per frame remained constant ($\sim 250 \text{ W} \times \text{ms} \times \text{cm}^{-2}$); in other words, the amount of light on the sample during the camera image acquisition time was constant between conditions. CellROX™ was imaged before and after paxillin-EGFP acquisition to measure ROS production. Images were pseudo-colored to highlight changes in paxillin-EGFP and CellROX™ intensity. Scale bar is 10 μm .

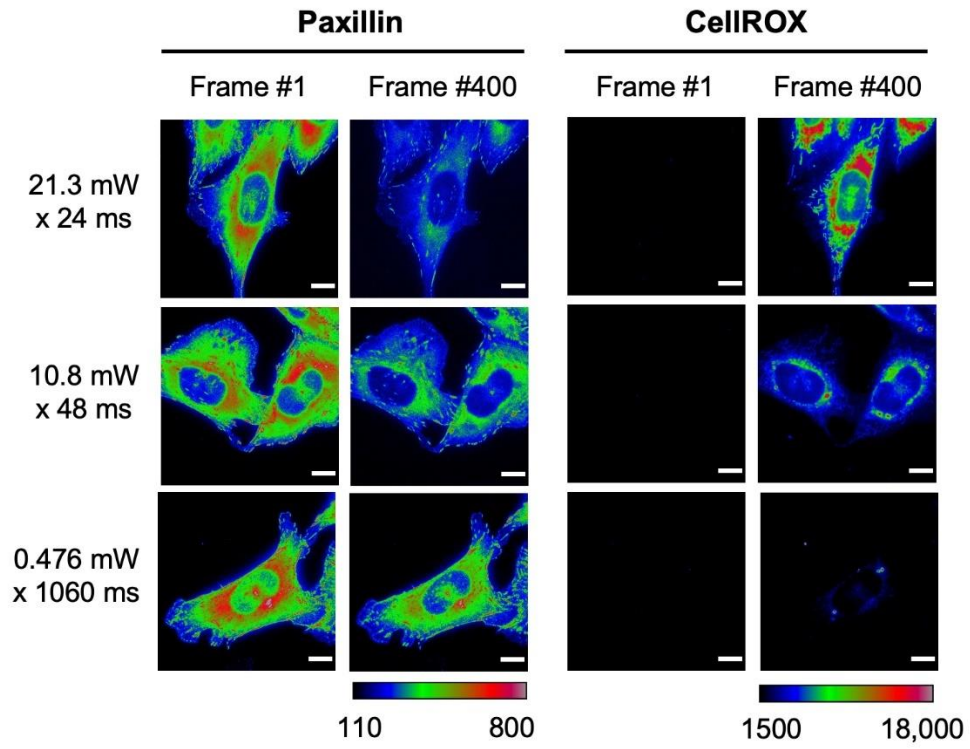


Figure 3.2. IO generates a significant amount of ROS. Oscilloscope measurements showing sample illumination time. Experiments were conducted on a Zeiss AxioObserver microscope running ZEN pro software (version 2.6). An X-Cite 120LED light source was triggered with TTL while the USB connection between the microscope computer/software and light source was disconnected (*green trace*) or connected (*yellow trace*), and USB directly while the TTL cable was disconnected (*red trace*). Exposure time was set to 24 ms in the microscope software; imaging interval was set to 500 ms.

USB triggering

| Input exposure time (ms) | Output exposure time (ms) | Illumination Overhead (ms) | % Illumination Overhead |
|--------------------------|---------------------------|----------------------------|-------------------------|
| 24 | 134 | 110 | 460 |
| 25 | 133 | 108 | 430 |
| 48 | 160 | 112 | 230 |
| 100 | 272 | 172 | 170 |
| 350 | 554 | 204 | 58 |
| 1060 | 1248 | 188 | 18 |
| 60000 | 60350 | 350 | 1.0 |

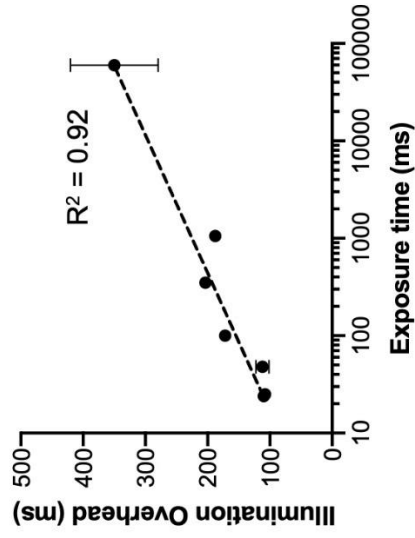


Figure 3.3. IO may vary with exposure time due to software delays. Oscilloscope measurements of sample illumination time compared to input exposure time. An X-Cite 120LED light source was USB triggered through ZEN pro software (version 2.6). The amount of IO changed with exposure time.

TTL triggering

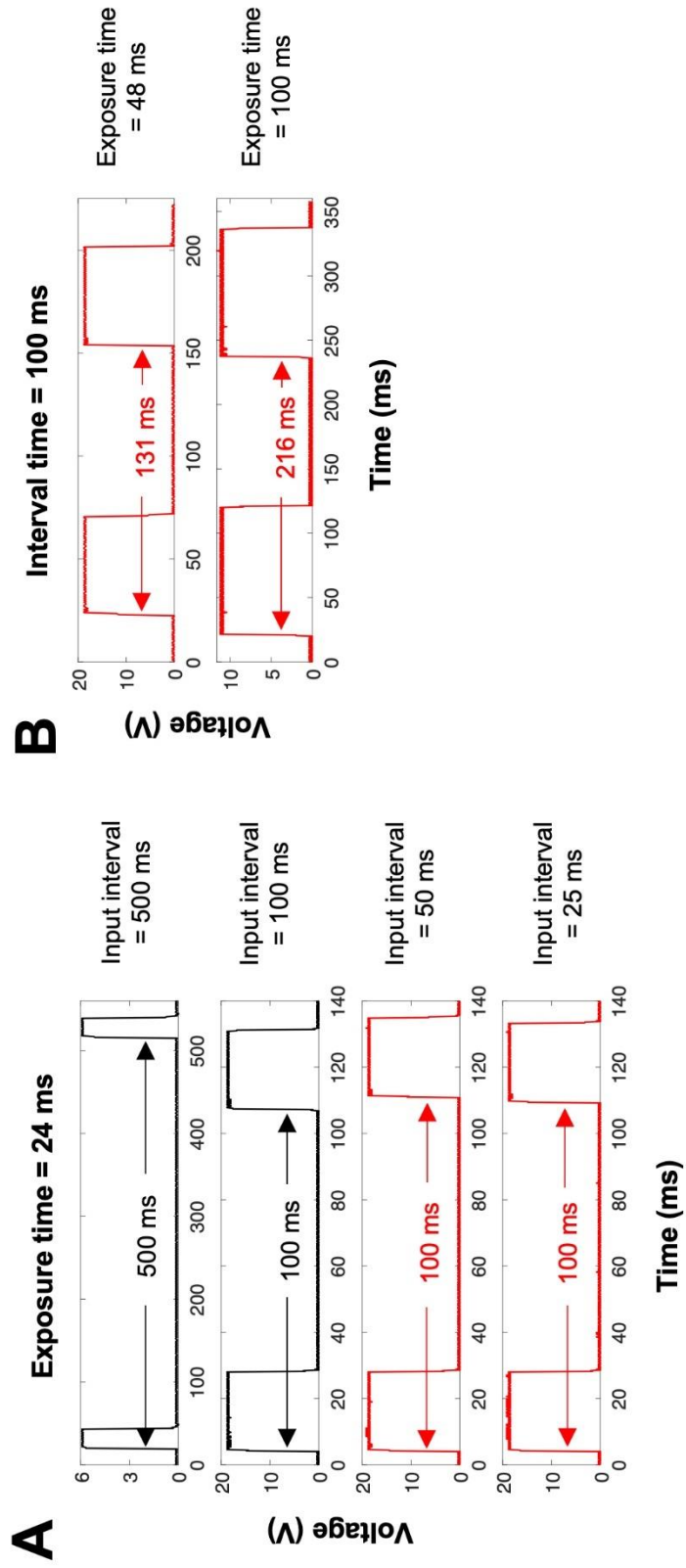
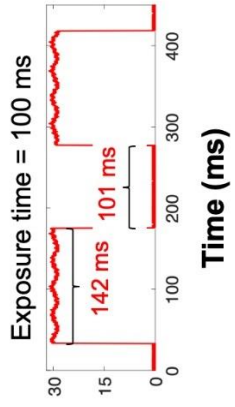
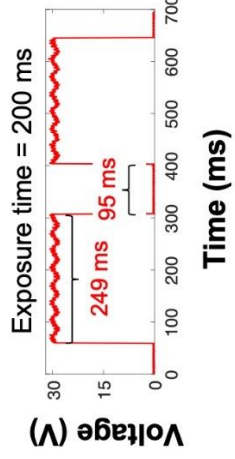


Figure 3.4. Software delays lead to inappropriate delays between images. (A) Time lapse experiments were performed with TTL triggering of the X-Cite 120LED light source. Several camera acquisition intervals were chosen: 500 ms, 100 ms, 50 ms, and 25 ms. Camera exposure time was set to 24 ms. (B) Time lapse experiments in A were repeated with various camera exposure times: 48 ms and 100 ms. The image acquisition interval was set to 100 ms.

Interval imaging



Stream acquisition

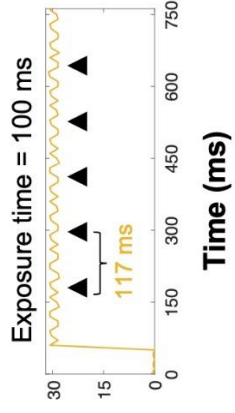


Figure 3.5. Stream acquisition reduces IO and delays between images. Oscilloscope measurements of sample illumination time. Experiments were conducted on a Leica DMI6000B inverted microscope equipped with a Quorum WaveFx-X1 spinning disk confocal system running MetaMorph software (version 7.10.2.240). A 561 nm laser was electronically triggered with an AOTF crystal. Interval imaging resulted in ~42 ms IO and ~100 ms delay between images. Stream acquisition resulted in ~17 ms delay between images (in the form of IO).

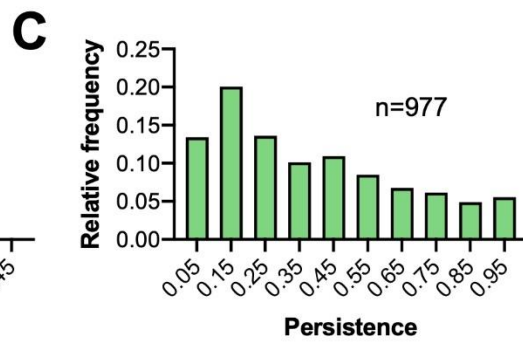
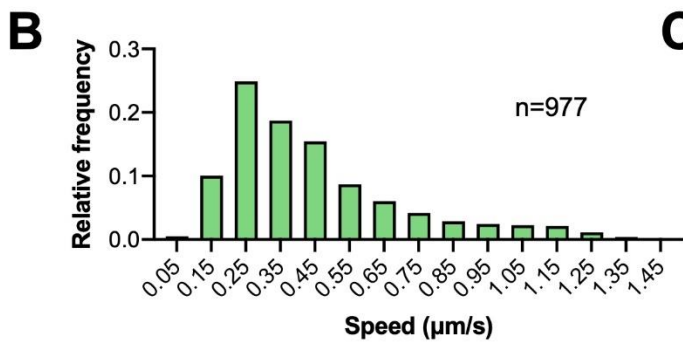
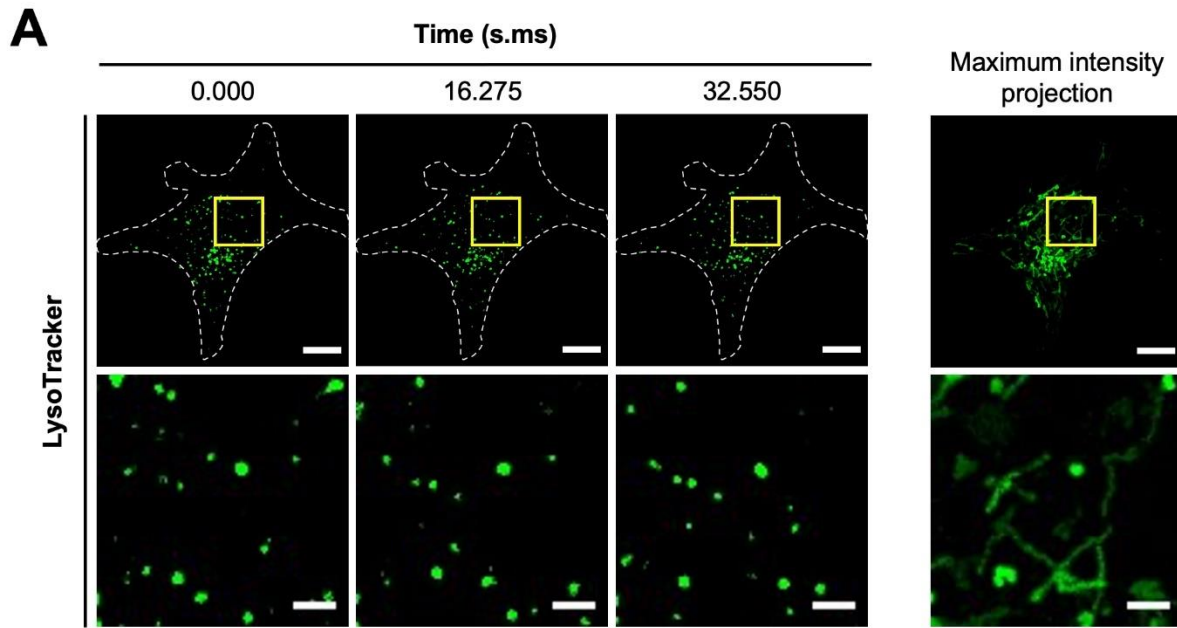


Figure 3.6. Stream acquisition captures rapid lysosomal dynamics accurately. (A) MCF7 cells were seeded onto fibronectin-coated dishes and stained with LysoTracker™ Green DND-26. Images were collected on the spinning disk confocal microscope using stream acquisition and a $\times 63/1.4$ NA oil immersion objective lens. A 491 nm laser (~ 0.02 mW) was used to excite LysoTracker™. Camera exposure time was set to 200 ms. Scale bars are 10 μm for *whole-cell images* and 2 μm for *magnified images*. (B,C) Lysosome positions were tracked and quantified for speed and persistence. Frequency distributions show pooled data for lysosomes from three cells. N indicates the number of lysosomes analyzed.

CHAPTER 4 – The SHCA adapter protein cooperates with lipoma-preferred partner in the regulation of adhesion dynamics and invadopodia formation

Alex Kiepas^{1,2}, Elena Voorand^{2,3}, Julien Senecal^{2,4}, Ryuhjin Ahn^{4,6}, Matthew G. Annis^{2,5}, Kevin Jacquet⁷, George Tali¹, Nicolas Bisson^{7,8}, Josie Ursini-Siegel^{3,6,9}, Peter M. Siegel^{2,3,5} and Claire M. Brown^{1,10}

¹Department of Physiology, ²Goodman Cancer Research Centre, ³Department of Biochemistry, ⁴Division of Experimental Medicine, ⁵Department of Medicine, ⁹Department of Oncology, ¹⁰Advanced BioImaging Facility (ABIF), McGill University, Montreal, Quebec, Canada; ⁶Lady Davis Institute for Medical Research, Montreal, Quebec, Canada; ⁷Centre de recherche du Centre Hospitalier Universitaire (CHU) de Quebec-Universite Laval, Quebec, Quebec, Canada; and ⁸PROTEO network and Cancer Research Centre, Univeriste Laval, Quebec, Quebec, Canada

This chapter is an original research article published in:
Journal of Biological Chemistry. 2020

4.1 PREFACE

Cell migration and invasion are two fundamental cellular processes that facilitate cancer metastasis, which is a major cause of patient mortality. Previous studies by our laboratory have identified two critical mediators of breast cancer cell migration, invasion and metastasis: p46/52ShcA and LPP [1-4]. p46/52ShcA is an adapter protein that propagates ErbB2 signaling by binding phosphotyrosine residues 1226/1227 in the cytoplasmic tail, whereas LPP is a scaffold protein that localizes to adhesions. Interestingly, reduced expression of either protein is sufficient to abrogate TGF β -induced cell migration and invasion across transwell membranes. Fluorescence recovery after photobleaching experiments suggest that p46/52ShcA and LPP may regulate adhesion dynamics [2]. While LPP is a known component of adhesions [2, 5-9], relatively little is known about the role of p46/52ShcA in these structures. Adhesions allow cancer cells in the primary tumor to interact with the surrounding ECM, migrate through tissues, and eventually colonize distant organs [10-12]. Phosphoproteomic analysis of adhesions recently identified p46/52ShcA within isolated adhesion complexes [13]. Tension applied to human endothelial cells via fibronectin-bound paramagnetic beads also stimulates the recruitment of p46/52ShcA to adhesions [14]. Therefore, the aim of the current study was to define the molecular mechanisms through which p46/52ShcA and LPP enhance adhesion dynamics to promote breast cancer metastasis.

4.2 ABSTRACT

SHC adaptor protein (SHCA) and lipoma-preferred partner (LPP) mediate transforming growth factor β (TGF β)-induced breast cancer cell migration and invasion. Reduced expression of either protein diminishes breast cancer lung metastasis, but the reason for this effect is unclear. Here, using total internal reflection fluorescence (TIRF) microscopy, we found that TGF β enhanced the assembly and disassembly rates of paxillin-containing adhesions in an SHCA-dependent manner through the phosphorylation of the specific SHCA tyrosine residues Tyr-239, Tyr-240, and Tyr-313. Using a BioID proximity labeling approach, we show that SHCA exists in a complex with a variety of actin cytoskeletal proteins, including paxillin and LPP. Consistent with a functional interaction between SHCA and LPP, TGF β -induced LPP localization to cellular adhesions depended on SHCA. Once localized to the adhesions, LPP was required for TGF β -induced increases in cell migration and adhesion dynamics. Mutations that impaired LPP localization to adhesions (mLIM1) or impeded interactions with the actin cytoskeleton via α -actinin (Δ ABD) abrogated migratory responses to TGF β . Live-cell TIRF microscopy revealed that SHCA clustering at the cell membrane preceded LPP recruitment. We therefore hypothesize that, in the presence of TGF β , SHCA promotes the formation of small, dynamic adhesions by acting as a nucleator of focal complex formation. Finally, we defined a previously unknown function for SHCA in the formation of invadopodia, a process that also required LPP. Our results reveal that SHCA controls the formation and function of adhesions and invadopodia, two key cellular structures required for breast cancer metastasis.

4.3 INTRODUCTION

Cellular migration and invasion are fundamental processes that are required for metastasis. Some cancer cells employ a mesenchymal mode of cell migration, which is highly dependent on adhesions that link the actin cytoskeleton to the extracellular matrix (ECM). Cellular adhesions consist of a complex network of transmembrane integrin heterodimers and cytoplasmic proteins that form a plaque containing hundreds of components with a multitude of potential protein-protein interactions [15-17]. Together, these protein interactions mediate cellular signaling and allow the cell to generate traction forces that are important for controlling cell migration. Equally important to the metastatic cascade are invadopodia, which are cellular structures that mediate cancer cell invasion through barriers otherwise impenetrable to migratory cells. Invadopodia are F-actin-rich and proteolytically active cell protrusions capable of degrading ECM components and breaching epithelial and endothelial basement membranes [18]. These structures share many protein components with adhesions, such as cortactin (Ctn), but can be distinguished by the presence of Tks5 [18-20]. Together, adhesions and invadopodia are two fundamental structures that enable cancer cells to escape from the primary tumor and establish distant metastases [21-26]. Consequently, up-regulation and/or increased signaling of proteins that enhance adhesion and invadopodia formation are often observed in invasive and metastatic cancer cells [27-31].

Previous work by our group and others showed that ErbB2 and transforming growth factor β (TGF β) signaling pathways cooperate to enhance the metastatic ability of breast cancer cells [32-37]. SHC adapter protein (SHCA) is a critical downstream integrator of these pathways and is essential for breast tumor growth, migration, invasion, and metastasis [1, 3, 38-44]. SHCA is part of a Src-homology/collagen (SHC) family of proteins that also includes SHCB, SHCC, and SHCD. Alternative translational initiation and RNA splicing result in the expression of three different SHCA isoforms: p46, p52, and p66 [45]. All breast cancer cells express p46/52 SHCA isoforms, whereas p66SHCA is more highly expressed in breast cancers with mesenchymal features [46]. Recently, p66SHCA has been shown to be a context-dependent promoter of breast cancer metastasis [47]. Loss of p66SHCA expression results in slower adhesion dynamics, reduced cell migration rates, and diminished lung metastasis [47]. SHCA harbors an N-terminal phosphotyrosine-binding domain (PTB), a central collagen homology domain (CH1) with three key tyrosine residues (Tyr-239/Tyr-240/Tyr-313) and a C-terminal SH2 domain [45]. Our previous studies revealed that the PTB domain, but not the SH2 domain, is required for TGF β -induced

migration and invasion of ErbB2⁺ breast cancer cells [3]. Moreover, phosphorylation of tyrosine residues was required for migratory and invasive phenotypes *in vitro* and breast cancer lung metastasis *in vivo* [3].

More recently, we have characterized lipoma-preferred partner (LPP) as an important regulator of breast cancer cell migration, invasion, and metastasis [2, 4]. LPP is a member of the zyxin family of LIM proteins and is known to promote mesenchymal migration [48]. LPP contains three LIM domains and a proline-rich N-terminal region, which allow it to localize to adhesions and interact with numerous proteins [49]. Whereas loss of SHCA negatively impacts breast tumor initiation and growth [38], LPP is dispensable for primary tumor growth [4]. However, loss of LPP recapitulates the migratory and invasive defects seen in SHCA-depleted cells. Namely, breast cancer cells with diminished LPP expression do not exhibit increased migration and invasion in response to TGF β stimulation [2]. The ability of LPP to localize to adhesions via its LIM domains and interact with α -actinin is required for the pro-migratory and pro-invasive functions of LPP [2]. Src-mediated phosphorylation of LPP, while dispensable for cell migration, is required for invadopodia formation and efficient breast cancer lung metastasis [4].

In the current study, we show for the first time that SHCA acts as a nucleator of focal complex formation by promoting the formation of small, dynamic adhesions in response to TGF β . We suggest that SHCA serves as a molecular scaffold to facilitate the recruitment of actin cytoskeletal and adhesion proteins, including paxillin and LPP. Indeed, TGF β enhances adhesion targeting of paxillin and LPP, which permits faster assembly and disassembly of these structures. TGF β -induced migration and adhesion dynamics require LPP localization to adhesions and interaction with the actin cytoskeleton. Furthermore, we show that tyrosine phosphorylation of SHCA is required for TGF β -induced adhesion dynamics. We also implicate SHCA as an important regulator of invadopodia formation, which requires phosphorylation of tyrosine residues within the CH1 domain. The requirement of SHCA for efficient invadopodia formation is reminiscent of the role of LPP in the formation of these structures [4]. Taken together, we delineate essential roles for SHCA and LPP as critical mediators of adhesion fate and invadopodia formation.

4.4 RESULTS

4.4.1 Cooperation between TGF β and ErbB2 signaling pathways promotes single-cell migration

NMuMG cells expressing activated ErbB2 spontaneously metastasize to the lung from the primary tumor [1]. We have previously observed that cells with constitutively active ErbB2 (ErbB2-NT) exhibit increased movement through porous membranes in response to TGF β [1, 2]. In contrast, NMuMG cells expressing a variant of ErbB2 that lacks five important tyrosine phosphorylation sites (ErbB2-NYPD) fail to exhibit this phenotype [1]. To gain a more in-depth understanding of TGF β -induced migration of ErbB2⁺ breast cancer cells, we employed live-cell time-lapse microscopy. Using this approach, we could readily assess the behavior, mean net displacement, and speed of individual breast cancer cells.

Rose plots of breast cancer cells treated with TGF β demonstrated that ErbB2-NT cells stimulated with TGF β migrated further and faster than untreated cells, a response that was not observed with ErbB2-NYPD breast cancer cells (Fig. 4.1A-C; see Movie S1 in online publication). Population-based analysis of single cells showed that ErbB2-NT cells began to increase in speed after 9 h of TGF β treatment and achieved a maximal speed of $\sim 33 \mu\text{m h}^{-1}$ (Fig. 4.1C). In contrast, ErbB2-NYPD-expressing cells continued to migrate at $\sim 21 \mu\text{m h}^{-1}$ even after 27 h of TGF β stimulation (Fig. 4.1C). These results were confirmed with an independent set of mammary tumor explants generated from mice injected with ErbB2-NT- or ErbB2-NYPD-expressing breast cancer cells (Fig. S4.1).

TGF β is known to induce an epithelial-to-mesenchymal transition (EMT) in ErbB2⁺ breast cancer cells [50]. Cells engaging a mesenchymal mode of migration depend on integrin-mediated adhesion dynamics [51-53]. Therefore, we sought to investigate the assembly and disassembly rates of adhesions using fluorescently labeled paxillin, a *bona fide* marker of adhesions [54, 55]. TGF β significantly increased the assembly and disassembly rates of mCherry-paxillin containing adhesions in protrusive cell regions of ErbB2-NT, but not ErbB2-NYPD, expressing breast cancer cells (Fig. 4.1D). In particular, a larger proportion of rapid events was observed in ErbB2-NT-expressing cells (see Movie S2 in online publication). The observed rapid adhesion dynamics in ErbB2-NT cells following TGF β stimulation correlated well with the TGF β -induced increase in migration speeds exhibited by these cells.

4.4.2 Signaling through the SHCA adapter protein is required for TGF β -induced migration

SHCA is recruited to tyrosine-phosphorylated residues (Tyr-1226/Tyr-1227) in the cytoplasmic tail of the ErbB2 receptor, and this association is required for the development of aggressively growing mammary tumors [56]. Indeed, SHCA has been shown to be important for primary tumor growth and metastasis of ErbB2⁺ breast cancer cells [3, 40, 43]. Therefore, we applied time-lapse microscopy to assess the impact of SHCA loss on cell migration. NMuMG ErbB2-NT cells expressing shRNAs against the 3-UTR of mouse *SHCA* mRNA (SHCA^{low}) or luciferase-targeting shRNAs (SHCA^{endo}) were previously generated in our laboratory [3]. Immunoblot analysis demonstrated that cells from ErbB2-NT/SHCA^{low} explants expressed significantly reduced levels of SHCA (p46, p52, and p66 iso-forms) when compared with parental controls (Fig. 4.2A). Rose plots revealed that ErbB2-NT/SHCA^{endo} cells exhibited an increase in cell migration following TGF β treatment, whereas ErbB2-NT/SHCA^{low} cells did not (Fig. 4.2B). Treatment with TGF β also significantly increased the mean net displacement of cells expressing endogenous levels of SHCA (SHCA^{endo}), which was not observed in cells with low SHCA expression (SHCA^{low}) (Fig. 4.2C). This effect was due to an increase in migration speed, as ErbB2-NT breast cancer cells expressing endogenous levels of SHCA (SHCA^{endo}) exhibited significantly faster speeds after 18 h of TGF β treatment (Fig. 4.2D) rather than a change in directional persistence (data not shown). Results from an independent set of ErbB2-NT/SHCA^{endo} and ErbB2-NT/SHCA^{low} mammary tumor explants supported these findings (Fig. S4.2).

Next, we investigated adhesion dynamics in protrusive cell regions of SHCA^{endo}- and SHCA^{low}-expressing cells. We found that TGF β enhanced the assembly and disassembly rates of mCherry-paxillin-containing adhesions in cells expressing endogenous levels of SHCA, but not in ErbB2-NT/SHCA^{low} cells (Fig. 4.2E). Moreover, TGF β increased the formation of paxillin-bearing adhesions in ErbB2-NT/SHCA^{endo} cells (Fig. 4.3A-C). These newly formed adhesions appeared to be smaller in size (Fig. 4.3D), which is consistent with the idea that smaller adhesions are more dynamic [57]. In contrast, TGF β did not affect the number and size distribution of adhesions in ErbB2-NT/SHCA^{low} cells (Fig. 4.3B-D). Taken together, our results suggest that SHCA is required for the formation of small, dynamic adhesions in response to TGF β stimulation.

4.4.3 Phosphorylation of SHCA is required for TGF β -induced migration

The CH1 domain of SHCA contains three phosphotyrosine residues (Tyr-239/Tyr-240/Tyr-313) that are critical for breast cancer metastasis [3]. Given the importance of SHCA signaling in breast cancer progression, we sought to investigate single-cell migration of ErbB2-NT/SHCA^{low} cells rescued with WT p46/52SHCA or various SHCA mutants that lacked specific tyrosine phosphorylation sites (Shc313F, Y313F; Shc2F, Y239F/Y240F; Shc3F, Y239F/Y240F/Y313F) (Fig. 4.4A). Immunoblot analysis revealed that WT and mutant SHCA alleles were expressed in ErbB2-NT/SHCA^{low} breast cancer cells at comparable levels (Fig. 4.4B). As expected, TGF β stimulated the migration of cells rescued with SHCA-WT in a manner similar to ErbB2-NT/SHCA^{endo} cells (Fig. 4.4C). In particular, the mean net displacement and average speed of cells were increased 18 h after TGF β treatment (Fig. 4.4D,E). Additionally, TGF β promoted an increase in adhesion assembly and disassembly rates in SHCA-WT cells (Fig. 4.4F). In contrast, SHCA-3F cells failed to respond to TGF β . Indeed, the mean net displacement, migration speeds, and adhesion dynamics of SHCA-3F-expressing ErbB2-NT/SHCA^{low} cells was unaffected by TGF β stimulation (Fig. 4.4C-F). Expression of SHCA-313F or SHCA-2F was sufficient to restore responsiveness to TGF β , as measured by mean net displacement and cell speed (Fig. S4.3). We confirmed these results by re-expressing SHCA-WT, SHCA-313F, SHCA-2F, and SHCA-3F in cells from an independent ErbB2-NT/SHCA^{low} explant (Fig. S4.4). Altogether, these results revealed that SHCA controls TGF β -induced migration of ErbB2-overexpressing breast cancer cells by regulating adhesion dynamics, which requires pY239/pY240 or pY313-dependent SHCA signaling.

4.4.4 SHCA regulates LPP recruitment and retention in cellular adhesions

Our data demonstrate a role for SHCA in regulating adhesion dynamics in rapidly migrating cells. To outline the molecular mechanisms by which SHCA impacts cellular adhesions, we sought to delineate its potential protein partners in signaling complexes using BioID proximity labeling. To achieve this, we generated cells expressing WT SHCA fused to a mutant BirA biotin ligase that covalently adds biotin to adjacent proteins (Myc-SHCA-WT-BirA). Biotinylated proteins were pulled down from cell lysates and identified by MS, using Myc-BirA as a control. A biological triplicate was performed, and nonspecific interactions were eliminated using the significance analysis of interactome (SAINT) algorithm [58, 59]. Strikingly, several adhesion and

actin cytoskeletal proteins were identified as proximal to SHCA, including arpin, paxillin (Pxn), talin (Tln), and LPP (Table 4.1; Table S4.1). LPP is a member of the zyxin family of LIM proteins [5]. It is able to localize to adhesions and interact with LIM and SH3 protein (LASP), palladin, protein phosphatase 2A (PP2A), scrib, supervillin, and vasodilator-stimulated phosphoprotein (VASP) [49]. We have previously identified LPP as a promoter of efficient breast cancer lung metastasis [4]. Therefore, we decided to investigate whether SHCA regulates the function of LPP in response to TGF β .

We first validated that the Myc-SHCA-WT-BirA construct biotinylates LPP using an immunoblotting-based method that is orthogonal to BioID (Fig. S4.5). A BirA-only vector was included as a negative control. Next, we introduced mCherry-LPP into ErbB2-NT/SHCA^{endo} and ErbB2-NT/SHCA^{low} cells to assess LPP localization in the absence or presence of TGF β (Fig. 4.5A,B). TGF β enhanced LPP targeting to adhesions in ErbB2-NT/SHCA^{endo} cells, which was not observed in ErbB2-NT/SHCA^{low} breast cancer cells (Fig. 4.5C). In addition to paxillin and LPP, we also investigated the number of vinculin-bearing adhesions found in ErbB2-NT/SHCA^{endo} and ErbB2-NT/SHCA^{low} cells treated with TGF β . Vinculin stabilizes and strengthens adhesions and is therefore an important indicator of more mature adhesions [60, 61]. The number of vinculin-bearing mature adhesions did not change with TGF β treatment (Fig. 4.5D), further supporting the notion that TGF β promotes the formation of more nascent adhesions. Based on these observations, we performed time-lapse imaging to determine the assembly and disassembly rates of cellular adhesions containing LPP. ErbB2-NT/SHCA^{endo} cells treated with TGF β exhibited increased dynamics of LPP-containing adhesions in protrusive cell regions, whereas ErbB2-NT/SHCA^{low} cells did not (Fig. 4.5E). Expression of SHCA-WT in ErbB2-NT/SHCA^{low} cells restored TGF β -induced increases in LPP dynamics; however, expression of the SHCA-3F phosphomutant was not sufficient to rescue this phenotype (Fig. 4.5F). Altogether, our data suggest that SHCA controls paxillin and LPP localization to dynamic adhesions in response to TGF β .

4.4.5 LPP is an important component of adhesions that interacts with α -actinin to mediate TGF β -enhanced migration

Previous studies show that LPP is an important regulator of mesenchymal cell migration [8, 62]. Given that SHCA regulates LPP recruitment to adhesions in response to TGF β , we sought to determine whether LPP also regulates TGF β -enhanced migration and adhesion dynamics.

ErbB2-NT cells with endogenous levels of SHCA were infected with shRNAs against LPP (LPP^{KD}) or LucA (LPP^{endo}) (Fig. 4.6A; Fig. S4.6A). LPP knockdown was also confirmed by immunofluorescence staining and linescan analysis of paxillin-bearing adhesions (Fig. S4.6B-D). Cells with endogenous levels of SHCA and LPP (LPP^{endo}) migrated further and faster in response to TGF β treatment (Fig. 4.6B-D). Cells with LPP knockdown (LPP^{KD}), however, did not exhibit increased migration despite remaining responsive to TGF β -induced signaling (pSmad/Smad) (Fig. 4.6B; Fig. S4.6A). Furthermore, TGF β did not affect assembly and disassembly rates of paxillin-bearing adhesions in LPP^{KD} cells (Fig. 4.6E). Together, these data suggest that both SHCA and LPP are required for enhancing adhesion dynamics in TGF β -stimulated cells.

LPP has three LIM domains, which are necessary for localization to adhesions. LPP also contains an α -actinin-binding domain (ABD), which allows it to interact with the actin cytoskeleton. Previous studies by our group show that LPP must localize to adhesions and interact with the actin cytoskeleton to promote metastasis [4]. Therefore, we rescued LPP^{KD} cells with one of three fluorescently tagged LPP constructs: WT LPP (EGFP-LPP-WT), a mutant that cannot localize to adhesions (EGFP-LPP-mLIM1), or a mutant that cannot interact with α -actinin (EGFP-LPP- Δ ABD) (Fig. S4.7A,B). Immunofluorescence staining and linescan analysis showed co-localization between EGFP-LPP-WT and paxillin in adhesions (Fig. S4.7C-E). LPP- Δ ABD also co-localized with paxillin at adhesions (Fig. S4.7C-E). LPP-mLIM1, however, failed to localize to adhesions despite being expressed at levels comparable with endogenous LPP (Fig. S4.7C-E). Migration and adhesion dynamics of LPP-WT, LPP-mLIM1, and LPP- Δ ABD cells were then analyzed using live-cell microscopy. Re-expression of WT LPP in LPP^{KD} cells successfully rescued the migratory phenotype observed in LPP^{endo} cells (Fig. S4.8). Expression of either LPP-mLIM1 or LPP- Δ ABD, however, was not able to rescue TGF β -enhanced cell migration and adhesion dynamics (Fig. S4.8). Thus, LPP must localize to adhesions and interact with the actin cytoskeleton to facilitate faster cell migration and adhesion dynamics in response to TGF β treatment.

4.4.6 SHCA localizes to adhesions to regulate focal complex formation

Given that SHCA interacts with several adhesion proteins, we explored the possibility that SHCA may also localize to adhesions. Using a far-red fluorescent protein (miRFP670) [63], we generated a WT SHCA construct (SHCA-WT-iRFP) and performed TIRF microscopy to limit

fluorescent illumination to the first 80 nm of the cell. ErbB2-NT/SHCA^{low} cells were infected with SHCA-WT-iRFP or SHCA-3F-iRFP (Fig. 4.7A; Fig. S4.9A) and assessed for their responsiveness to TGF β . The migratory phenotype was successfully rescued with SHCA-WT-iRFP but not the SHCA-3F-iRFP mutant (Fig. S4.9B-D). SHCA-WT-iRFP cells were then infected with mCherry-LPP and fixed to assess the cellular localization of these adapter proteins. TIRF microscopy revealed more SHCA clusters at the plasma membrane after TGF β treatment (Fig. 4.7B). SHCA-positive signals co-localized with mCherry-LPP, suggesting that SHCA is targeted to adhesions upon stimulation (Fig. 4.7C). Image quantification revealed that the number of LPP-bearing adhesions increased upon TGF β treatment, as well as the percentage of LPP-containing adhesions positive for SHCA (Fig. 4.7D,E). Taken together, these results suggest that SHCA facilitates the recruitment of LPP into cellular adhesions in response to TGF β treatment.

Adhesion assembly is a highly regulated process that begins with integrin binding to ECM ligands, such as fibronectin, vitronectin, and laminin. Ligand binding induces a conformational change that unmask the short cytoplasmic tail of integrins, enabling the recruitment of scaffold and signaling proteins [64]. TGF β can regulate the expression of integrin subunits [65-67] and cause clustering of ErbB2 and integrins at the cell membrane [36]. Considering that SHCA regulates the recruitment of LPP, we wondered whether SHCA directs adhesion formation. We performed semi-continuous time-lapse imaging of SHCA-WT-iRFP and EGFP-LPP to obtain high temporal resolution of adhesion dynamics (2-s intervals). SHCA appeared to assemble at the site of an adhesion prior to LPP recruitment (Fig. 4.8A; see Movie S3 in online publication). Once an adhesion formed and began to increase in size, the rate of SHCA recruitment decreased and eventually stabilized (Fig. 4.8B; see Movie S4 in online publication). Occasionally, a second nucleation point or “treadmilling” of SHCA was observed at the growing end of an adhesion (Fig. 4.8C). Interestingly, SHCA fluorescence intensity at some adhesions decreased prior to loss of LPP signal (Fig. 4.8D; see Movie S5 in online publication). Finally, there were instances where SHCA appeared to nucleate an adhesion but LPP was not recruited (Fig. 4.8E; see Movie S6 in online publication). In these cases, the adhesion often disassembled and was characterized by a short lifespan. These adhesions likely coincided with nascent adhesion formation and disassembly. Collectively, these four examples demonstrate that SHCA is an early component of adhesions and is required for the recruitment of LPP.

4.4.7 MAPK and PI3K activation are required for LPP localization to adhesions

In addition to the engagement of Smad proteins, TGF β is known to modulate mitogen-activated protein kinase (MAPK) and phosphatidylinositol 3-kinase (PI3K)/AKT pathways [68-70]. Tyrosine phosphorylation of SHCA by the TGF β receptor complex causes the recruitment of a Grb2/son of sevenless (SOS)/Ras complex, which subsequently triggers activation of the Ras-MAPK pathway [71]. Similarly, TGF β stimulation causes the association of type I TGF β receptor with p85, the regulatory subunit of PI3K, which mediates AKT activation and leads to the phosphorylation of S6 kinase 1 [72, 73]. MAPK and PI3K pathways are also known to regulate cell migration [74-78]. Therefore, LPP recruitment to adhesions was analyzed in the absence or presence of trametinib (a MEK inhibitor) or pictilisib (a PI3K inhibitor) to determine whether these signaling pathways play a role in regulating LPP recruitment to adhesions in response to TGF β stimulation.

NMuMG cells expressing constitutively active ErbB2 (NT118) exhibited increased ERK1/2 phosphorylation (Thr-202/Tyr-204) levels following 24 h of TGF β stimulation; however, S6 phosphorylation (Ser-240/244) levels did not increase significantly (Fig. S4.10A,B). As expected, TGF β promoted the formation of small, dynamic adhesions in control cells (Fig. S4.10C (*top panels*), D-F). Pre-treatment with trametinib effectively eliminated ERK1/2 phosphorylation in both TGF β -stimulated and unstimulated cells (Fig. S4.10A,B). In line with previous observations [79], ERK inhibition resulted in the formation of large adhesions (Fig. S4.10C (*middle panels*), E,F). Cells pretreated with trametinib also exhibited large stress fibers at the trailing edge and a robust lamellipodia (Fig. S4.10C, *middle panels*). However, TGF β stimulation did not affect the number or size of LPP adhesions compared with unstimulated trametinib-treated cells (Fig. S4.10D-F). On the other hand, pretreatment with pictilisib reduced S6 phosphorylation (Fig.S4.10A,B). Cells pretreated with pictilisib also exhibited large adhesions (Fig. S4.10C (*bottom panels*), D-F). TGF β stimulation did not affect the number of LPP adhesions; however, the size of LPP adhesions increased significantly (Fig. S4.10D-F). Together, these results suggest that both MAPK and PI3K signaling are required for LPP recruitment to small, dynamic adhesions in response to TGF β . Additionally, the increased size of LPP-containing adhesions in pictilisib-treated cells stimulated with TGF β suggests that PI3K signaling may be important for the regulation of adhesion disassembly.

4.4.8 SHCA is a mediator of invadopodia formation

Invadopodia structures are unique mechanosensory structures that are central to the metastatic process [80]. We have previously shown that LPP is required for TGF β -induced invadopodia formation [4]. Because SHCA regulates LPP recruitment to adhesions in response to TGF β , we next investigated the effect of SHCA knockdown on invadopodia formation. ErbB2-NT/SHCA^{low} cells were plated onto fluorescently labeled gelatin for 24 h in the absence or presence of TGF β . Cells were then fixed and stained with phalloidin (F-actin) and assessed for gelatin degradation (as indicated by the loss of fluorescence signal). Coverslips without cells were imaged as a control to ensure uniform gelatin coating (Fig. S4.11A). Our data revealed that shRNA-mediated knockdown of SHCA impaired the ability of cells to form invadopodia in response to TGF β (Fig. 4.9A,B). Of note, NMuMG ErbB2-NT cells did not degrade ECM in the absence of TGF β stimulation (Fig. S4.11B). Exogenous expression of WT SHCA restored TGF β -induced gelatin degradation; however, ErbB2-NT/SHCA^{low} cells expressing the SHCA-3F mutant failed to respond to TGF β (Fig. 4.9A,B). These results indicate that phosphorylation of Tyr-239/Tyr-240/Tyr-313 within SHCA is required for efficient invadopodia formation. To ensure that gelatin degradation was coincident with invadopodia formation, cells were stained for Ctnn, a well-characterized marker of invadopodia [20, 25] (Fig. 4.9C). Linescan analysis showed multiple sites of actin and cortactin co-localization at sites of reduced gelatin fluorescence (Fig. 4.9D). ErbB2-NT/SHCA^{low} cells expressing fluorescently tagged SHCA constructs (SHCA-WT-iRFP and SHCA-3F-iRFP) demonstrated a similar phenotype, with cells expressing SHCA-WT-iRFP exhibiting significantly greater TGF β -induced gelatin degradation relative to SHCA-3F-iRFP-expressing cells (Fig. S4.1C-F). Thus, our results indicate that tyrosine phosphorylation of SHCA is required for TGF β -induced invadopodia formation.

4.5 DISCUSSION

In this study, we establish SHCA (p46/52 isoforms) as a critical mediator of cell migration and invasion in ErbB2-overexpressing breast cancer cells. SHCA nucleates focal complex formation in the presence of TGF β by enhancing the recruitment of key adhesion proteins, such as paxillin and LPP (Fig. 4.10). Beyond its function within cell adhesions, we further delineate a novel role for SHCA in TGF β -induced invadopodia formation. In line with our observations that SHCA phosphorylation at Tyr-239/Tyr-240/Tyr-313 mediates adhesion dynamics, SHCA phosphorylation is also required for these invasive structures to form.

Cells that undergo an EMT adopt a mesenchymal mode of migration, which relies on adhesions to generate traction forces for movement [81, 82]. For cells to migrate, nascent adhesions must form, grow into focal contacts, couple to the actin cytoskeleton, and then disassemble as the cell moves forward, a process that generally occurs on the order of minutes [83, 84]. Consequently, changes in adhesion dynamics dramatically affect the migration speed of cells [85]. Our data demonstrate that TGF β stimulates the formation of small, dynamic adhesions, which allow breast cancer cells to move at greater speeds. This is evidenced by a selective increase in the number of nascent paxillin-containing adhesions in response to TGF β , with no change in more stable vinculin-containing mature adhesions. p46/52SHCA is required for this phenotype, as shRNA-mediated knockdown impairs the ability of NMuMG ErbB2-NT cells to enhance assembly and disassembly rates in response to TGF β . Mutating the cytoplasmic tail of ErbB2 such that p46/52SHCA can no longer bind (ErbB2-NYPD) also prevents TGF β -induced migration. Accordingly, lung metastatic burden is significantly reduced when SHCA signaling is disrupted [1, 3]. These data are consistent with findings in triple-negative breast cancer cells, where p66SHCA is required for efficient cell migration and lung metastasis [47]. Loss of p66SHCA expression results in the formation of large, elongated adhesions that exhibit slower assembly and disassembly rates, whereas exogenous expression of p66SHCA induces an EMT in ErbB2⁺ luminal breast cancers [46, 47].

TGF β has been previously shown to induce the association of ErbB2 with the actin cytoskeleton [35, 36]. In addition, TGF β stimulation induces the expression of various α and β integrin subunits, including α_1 , α_2 , α_3 , α_5 , α_v , β_1 , and β_3 [65, 67, 86-88]. Of these integrin subunits, collagens are bound by $\alpha_1\beta_1$ and $\alpha_2\beta_1$; laminin is bound by $\alpha_1\beta_1$, $\alpha_2\beta_1$ and $\alpha_v\beta_3$; and vitronectin is bound by $\alpha_v\beta_1$ and $\alpha_v\beta_3$ [89]. Fibronectin is also a ligand for many of these integrin receptors,

including $\alpha_5\beta_1$, which is widely regarded as the major fibronectin receptor [89]. Immunoprecipitation experiments show that p52SHCA can bind $\alpha_5\beta_1$, $\alpha_1\beta_1$ and $\alpha_v\beta_3$, but not $\alpha_2\beta_1$, $\alpha_3\beta_1$ or $\alpha_6\beta_1$ [90]. Binding to integrin β_3 is facilitated by the PTB domain [91]. SHCA can also interact with the cytoplasmic domain of integrin β_4 through its SH2 or PTB domains upon phosphorylation of Tyr-1440 or Tyr-1526, respectively [92]. Here, we demonstrate that SHCA localizes to integrin-dependent adhesions using a fluorescently tagged construct and time-lapse TIRF microscopy. Our BioID results show that SHCA interacts with a variety of adhesion and actin cytoskeletal proteins, such as arpin, crk, LPP, paxillin, and talin. The SHCA-BirA construct also labeled known interacting partners, including Grb2, Shc SH2 domain-binding protein 1 (Shcbp1), and protein-tyrosine phosphatase nonreceptor type 12 (Ptpn12) [93-95]. Cell migration experiments were performed on fibronectin as it has been implicated in the development of multiple cancers [96-98]. In fact, human breastcancer cells that overexpress $\alpha_5\beta_1$ integrins show a 3-fold increase in cell invasiveness compared with $\alpha_5\beta_1$ -depleted cells due to the generation of greater contractile forces [99]. Given that SHCA regulates cell migration, invasion, and proliferation on collagen [100], laminin [101, 102], vitronectin [100], and fibronectin [1], it would be interesting to investigate adhesion dynamics and SHCA localization in response to different ECM components.

Our imaging results demonstrate that TGF β induces clustering of SHCA in what appear to be nascent adhesions prior to LPP recruitment. In addition to nucleation, SHCA exhibits a treadmilling effect that may allow components to be recruited to the growing end of an adhesion. Three-dimensional super-resolution microscopy reveals that integrins and actin filaments are separated by a core region that spans ~40 nm [16]. This region can be stratified into three spatial and function compartments: an integrin signaling layer, a force transduction layer, and an actin regulatory layer. Paxillin and focal adhesion kinase (FAK) appear to be key players in the membrane-proximal integrin signaling layer; vinculin is observed in the broader central zone responsible for force transduction; and zyxin localizes to the uppermost region that constitutes the actin regulatory layer [16]. The ability of SHCA to engage with integrins and facilitate LPP localization to adhesions in the presence of TGF β is necessary for enhanced cell migration. Moreover, LPP must interact with the actin cytoskeleton through an α -actinin-binding domain (ABD) to mediate adhesion dynamics. Based on the results presented here, it is conceivable that SHCA is localized to the signaling layer, whereas LPP is a constituent of the actin regulatory layer.

Immunofluorescence analysis of motile cells shows that early nascent adhesions are largely composed of integrins, talin, and paxillin [103, 104]. Mass spectrometry of the adhesion machinery shows that paxillin is also one of the first components to dissociate during nocodazole-induced adhesion disassembly, with ~12% abundance remaining after 15 min [105]. This is in contrast to vinculin, which is still an abundant constituent of adhesions (~73%) over this time frame [105]. In comparison, LPP dynamics appear to fall between these two adhesion components (~43%) [105]. It is interesting to note that p46/52SHCA does not appear in proteomics analyses of adhesions [105, 106]. However, human endothelial cells treated with fibronectin-bound paramagnetic microbeads show that all three splice isoforms of SHCA (p46, p52, and p66) are found in adhesions [14]. These results are in line with phosphoproteomic analyses that detect SHCA within isolated adhesion complexes and reveal SHCA phosphorylation on serine 139 [13]. Importantly, our data also show that p46/52SHCA isoforms localize to adhesions following TGF β treatment, which occurs prior to LPP localization. Given the fact that SHCA directly interacts with FAK [14], and FAK is a component of early adhesions [107, 108] that can localize prior to paxillin recruitment [109] and dissociate at roughly the same rate [105], it is conceivable that SHCA localizes to adhesions during the early stages of formation. It would be particularly interesting to generate a superresolution map of SHCA and other adhesion components in ErbB2-overexpressing breast cancer cells and investigate whether SHCA forms multiple nucleation sites along the growing end of an adhesion. Such an approach would provide clarity on the precise relationship between SHCA and LPP within adhesions.

Our data suggest that both MAPK and PI3K signaling pathways are required for LPP recruitment to small, dynamic adhesions in response to TGF β stimulation. However, the observation that trametinib-treated cells are phenotypically different from pictilisib-treated cells suggests that distinct signaling pathways engaged downstream of SHCA differentially impact adhesion dynamics. In particular, trametinib causes LPP localization to stress fibers with no further increases in adhesion size and number following TGF β stimulation. In contrast, pictilisib does not impact the pattern of LPP localization or result in the formation of robust lamellipodia. The size increase of LPP-containing adhesions following PI3K inhibition suggests that it plays a role in regulating adhesion disassembly. This interpretation is consistent with previous observations that knockout of FAK, which is upstream of PI3K [110, 111], specifically affects adhesion disassembly, but not adhesion assembly, rates [112].

LPP is a known regulator of migration in mesenchymal cells that has recently been characterized as a critical mediator of ErbB2⁺ breast cancer metastasis [4]. LPP is also an important component of invadopodia [4]. Invadopodia are mechanosensory structures [80, 113] that allow tumor cells to penetrate the basement membrane and move through dense environments comprised of highly cross-linked ECM fibers [114]. Increasing evidence suggests that invadopodia directly contribute to poor overall survival [27]. Consequently, many studies have attempted to elucidate key regulators of invadopodia formation and target precursor formation. Current models propose three stages of invadopodia formation: precursor core initiation, precursor stabilization, and maturation [115]. Similar to adhesion assembly, SHCA may be involved in invadopodia formation. In the present study, we provide the first evidence that phosphotyrosine-dependent SHCA signaling is required for efficient invadopodia formation in breast cancer cells in response to TGF β treatment. Interestingly, the results of our BioID screen show that SHCA is proximal to Ctnn, a core invadopodia component. Therefore, the finding that SHCA knockdown prevents efficient TGF β -induced invadopodia formation may be due to a loss of LPP recruitment to these structures, a loss of interaction with Ctnn or both.

Several proteins (including LPP and Ctnn [116]) have been identified in both adhesions and invadopodia, suggesting that these structures are intimately linked. Both cellular structures are connected to the actin cytoskeleton, albeit in a different fashion [19]. The actin cytoskeleton couples to adhesions in a tangential orientation to generate traction forces, whereas invadopodia require perpendicular alignment of filaments, with respect to the underlying ECM, to create protrusive forces [117, 118]. Whether invadopodia are discrete structures or derived from adhesions is still debated [119]. Similar to adhesions, invadopodia are frequently surrounded by a multimeric protein complex consisting of integrins and integrin-associated proteins, such as paxillin, talin, and vinculin [120]. These adhesion rings may help anchor invadopodia and promote their maturation. Given that SHCA regulates the recruitment of adhesion components in response to TGF β , it is possible that SHCA may affect the formation of invadopodia anchors. Thus, the mechanisms through which SHCA regulates invadopodia formation awaits further investigation.

4.6 MATERIALS AND METHODS

4.6.1 Cell culture

Normal murine mammary gland (NMuMG) cells were obtained from the American Type Culture Collection (ATCC; catalogue no. CRL-1636) and grown in high-glucose (4.5 g liter⁻¹) Dulbecco's modified Eagle's medium (DMEM; catalogue no. 319-005-CL, Wisent Bioproducts) supplemented with 5% fetal bovine serum (FBS; catalogue no. 10082-147, Thermo Fisher Scientific), 10 µg ml⁻¹ insulin (catalogue no. 511-016-CM, Wisent Bioproducts), 1 mM L-glutamine (catalogue no. 609-065-CM, Wisent Bioproducts), 1% penicillin-streptomycin (catalogue no. 450-201-EL, Wisent Bioproducts), and 0.2% amphotericin B (catalogue no. 450-105-QL, Wisent Bioproducts).

NMuMG cells (NT 118/119 and NYPD 120/121) were previously infected with a pMSCV-puro viral vector to express the rat orthologue of ErbB2 with an activating transmembrane point mutation V664E [1]. Cells were cultured as described above with the addition of 2 µg ml⁻¹ puromycin (catalogue no. ant-pr-1, InvivoGen) antibiotic selection to maintain ErbB2 expression. NMuMG cells (SHCA^{endo} 83/84 and SHCA^{low} 87/92) were also previously infected with a pMSCV-hygro viral vector to express constitutively active ErbB2 (ErbB2-NT) and a pMSCV-puro viral vector containing an shRNA against endogenous SHCA (SHCA^{low}) or an shRNA against luciferase (SHCA^{endo}) [3]. Cells were maintained in 0.8 mg ml⁻¹ hygromycin B (catalogue no. 450-141-XL, Wisent Bioproducts) to maintain ErbB2 expression and 2 µg ml⁻¹ puromycin to maintain SHCA knockdown.

To generate individual explants (NT 118/119, NYPD 120/121, SHCA^{endo} 83/84, and SHCA^{low} 87/92), NMuMG cells were injected into the mammary fat pad of athymic mice and subsequently derived from primary tumors [1, 3]. Explants 87 and 92 (SHCA^{low}) were infected with a pMSCV-blast viral vector harboring a variety of SHCA mutants, including WT SHCA (SHCA-WT), SHCA-313F, SHCA-2F, and SHCA-3F. Finally, explant 87 (SHCA^{low}) was infected with WT SHCA fused to a far-red fluorescent protein (SHCA-WT-iRFP). Cells were maintained in 5 µg ml⁻¹ blasticidin (catalogue no. ant-bl-1, InvivoGen) to maintain SHCA re-expression.

In parallel, NMuMG cells were previously infected with an shRNA against endogenous LPP (LPP^{KD}) or an shRNA against luciferase (LPP^{endo}) [2]. Cells were then infected with constitutively active ErbB2 [2]. Cells were cultured in 2 µg ml⁻¹ puromycin to maintain LPP knockdown and 0.8 mg ml⁻¹ hygromycin B to maintain ErbB2 expression. Finally, NMuMG-

ErbB2 cells with LPP knockdown were infected with a pMSCV-blast vector containing EGFP-LPP-WT, EGFP-LPP-mLIM1, or EGFP-LPP- Δ ABD [4]. Cells were cultured in 5 $\mu\text{g ml}^{-1}$ blasticidin.

MMTV/polyoma virus middle T antigen-expressing mammary tumor cells (MT864) were obtained from the laboratory of Dr. William J. Muller. Cells were cultured in high-glucose DMEM supplemented with 5% FBS, mammary epithelial growth supplement (3 ng ml^{-1} EGF (catalogue no. PHG0311, Invitrogen), 0.5 $\mu\text{g ml}^{-1}$ hydrocortisone (catalogue no. 511-002-UG, Wisent Bioproducts), 5 $\mu\text{g ml}^{-1}$ insulin, 0.4% (v/v) bovine pituitary extract (catalogue no. 002-011-IL, Wisent Bioproducts), 1% penicillin-streptomycin, and 50 $\mu\text{g ml}^{-1}$ gentamycin (catalogue no. 450-135-XL, Wisent Bioproducts). WT SHCA tagged with BirA (Myc-SHCA-WT-BirA) and BirA-only vector were expressed in MMTV middle T antigen mammary epithelial cells. Cells were maintained in 8 $\mu\text{g ml}^{-1}$ blasticidin (catalogue no. 400-190-EM, Wisent Bioproducts) antibiotic selection to maintain SHCA re-expression.

Retroviral production was performed using the Retro-X universal packaging system (catalogue no. 631530, Clontech) according to the manufacturer's protocol. Cells were then incubated with Polybrene (10 $\mu\text{g ml}^{-1}$) and virus-containing medium for 48 h to allow for infection. Mycoplasma screening was routinely performed using the MycoAlert mycoplasma detection kit (catalogue no. LT07-318, Lonza).

4.6.2 DNA constructs

pMSCV-puro-ErbB2, pMSCV-hygro-ErbB2, pMSCV-puro-SHCA (shRNA), pMSCV-puro-LucA (shRNA), pMSCV-blast-SHCA, pMSCV-puro-LPP (shRNA), and pMSCV-EGFP-LPP constructs were previously generated in the laboratory of P. M. S [1, 3, 4].

FLAG-tagged SHCA was subcloned into pcDNA3.1 myc-BioID (catalogue no. 35700, Addgene) using the following primers and NotI and EcoRI restriction enzymes: 5'-CACGAGCGG CCGCAAACAAGCTGAGT-3' and 5'-GCCGGAATTCGAATTTCACTTGTCATCGTC-3'. BirA-SHCA-FLAG was then subcloned into the pQCXIB expression vector (catalogue no. 22266, Addgene) using the following primers and AgeI and EcoRI restriction enzymes: 5'-AGCTGGCAC CGGTAGCCACCATGGAACAAAACTC-3' (a gift from Dr. Marc Fabian) and 5'-GCCGGA ATTCGAATTTCACTTGTCATCGTC-3'.

To create SHCA-iRFP, SHCA was PCR-amplified from the previously generated constructs (pMSCV-SHCA-WT and pMSCV-SHCA-3F) with the following primers: 5'-CCCTTG AACCTCCTCGTTTCGACC-3' and 5'-TAGGTACCGCCTTGTCATCGTCATCCT-3'. XhoI and KpnI restriction enzymes were then used to insert the amplified product into pCMV-miRFP670 [63]. Finally, 5'-CGCAAATGGGCGGTAGGCGTG-3' and 5'-TATAGAATTCTTAGCTCT CAAGCGCGG-3' primers with EcoRI and BglII restriction sites were used to shuttle SHCA-iRFP into pMSCV-blast.

To create cells with stable expression of mCherry-paxillin, pSL301 (Invitrogen) and pmCherryPaxillin (catalogue no.50526, Addgene) were digested with AgeI and XbaI restriction enzymes. The pSL301-mCherryPaxillin intermediate was then digested with HpaI and EcoRI restriction enzymes to shuttle mCherry-paxillin into pMSCV-blast.

To create cells with stable expression of mCherry-LPP, LPP was PCR-amplified from previously generated pMSCV-EGFP-LPP-WT construct with the following primers: 5'-ATTGCG GCCGCGATGTCTCACCCATCTTGG-3' and 5'-GAGACGTGCTACTTCCATTTGTC-3'. NotI and EcoRI restriction enzymes were then used to replace paxillin with the amplified LPP product in pMSCV-blast-mCherryPaxillin.

4.6.3 Cell migration assays

NMuMG ErbB2 cells were seeded onto μ -slide 8-well plates (catalogue no. 80821, ibidi) coated with $5 \mu\text{g cm}^{-2}$ fibronectin (catalogue no. F-0895, Sigma–Aldrich) diluted in $1\times$ PBS. Cells were allowed to adhere and grow under exponential conditions for at least 12 h prior to experimentation. Recombinant human TGF β 1 (2 ng ml^{-1} ; catalogue no. 100-21, PeproTech) was applied to the cells directly before imaging ($t = 0$). Images were acquired on a Zeiss AxioObserver fully automated inverted microscope equipped with a Plan-Neofluar $\times 10/0.3$ NA Ph1 objective lens, AxioCam 506 CCD camera (Carl Zeiss, Jena, Germany) and ChamSlide TC-L-Z003 stage top environmental control incubator (Live Cell Instrument, Seoul, South Korea). Cells were imaged every 10 min in phase-contrast for a total of 30 h.

4.6.3.1 Analysis of cell migration: Cells were manually tracked in MetaXpress analysis software (Molecular Devices, Sunnyvale, CA). x,y position data for each cell track was then exported to MATLAB (version 8.6, release R2015b, The MathWorks, Natick, MA). Rose plots of cell migration were created by superimposing the starting position of each track on the origin (0,

0). Windrose plots were generated by determining the angle and mean net displacement of each track. The mean net displacement for each 45° segment was then plotted. The average speed was calculated by determining the mean distance traveled between each time point over the imaging interval. Speeds were then averaged into 3-h segments. The data shown represent the mean \pm S.E. for all cells analyzed from at least three independent experiments.

4.6.4 Imaging adhesion turnover

NMuMG ErbB2 cells were seeded onto 35-mm coverglass bottom cell culture dishes (catalogue no. FD35-100, World Precision Instruments) coated with fibronectin and transfected with 1 μ g of pmCherry paxillin using Effectene reagent (catalogue no. 301425, Qiagen). Medium was changed 18–24 h after transfection, and cells were allowed to recover for an additional 24 h in the absence or presence of TGF β . NMuMG ErbB2 cells stably expressing mCherry-LPP were also seeded onto 35-mm dishes to analyze the dynamics of LPP. Cells with stable expression of mCherry-LPP were cultured in 5 μ g ml⁻¹ blasticidin to maintain expression. Images were acquired every 30 s for 25 min on a total internal reflection fluorescence (TIRF)-Spinning Disk Spectral Discovery System (Spectral Applied Research, Richmond Hill, Ontario, Canada) coupled to a DMI6000B Leica microscope equipped with a Plan-Apochromat \times 63/1.47 NA oil immersion DIC objective lens (Leica, Wetzlar, Germany), Imagem X2 EM-CCD camera (Hamamatsu Photonics K.K., Hamamatsu City, Japan), and ChamSlide CU-501 top-stage incubator system (Live Cell Instrument, Seoul, South Korea). An EM-CCD camera was chosen at the cost of resolution (1 pixel = 0.155 μ m) because of increased sensitivity. A 561-nm laser with an ET 620/60-nm filter cube was used to visualize mCherry-paxillin or mCherry-LPP (where indicated). The camera exposure time was set to 500 ms with an EM gain of 255 and read speed of 22 MHz. A TIRF prism was used to limit fluorescence excitation to a depth of 100 nm.

4.6.4.1 Calculating adhesion dynamics: Images collected with the TIRF microscope were processed in Imaris (version 8.3.1; Bitplane AG, Zurich, Switzerland) using the Surfaces function. A protruding edge of each cell was manually selected using the region of interest (ROI) tool. Surface detail was smoothed and set to 0.300 μ m with a local background subtraction of 0.300 μ m. Adhesions were then masked by a manual refinement of the autothreshold feature. Finally, adhesions were tracked over time using an autoregressive algorithm with a maximum distance of

2 μm and maximum gap size of three time points. Surfaces smaller than 5 pixels were removed by filtering.

Mean intensity data for each adhesion tracked in Imaris were exported to Excel for further analysis. Curves were visually inspected for assembly and disassembly events. A string of five or more points upward was interpreted as assembly, whereas five or more points downward was interpreted as disassembly. A log-linear fitting method was then used to determine the rate for each event. Fits with an r^2 value greater than 0.7 were considered acceptable. Finally, assembly and disassembly rates were pooled together into a box plot for each condition. The mean for each condition is denoted by a *red line*. The data shown represent the results from at least three independent experiments.

To verify the results of our semi-automatic analysis, a custom algorithm was created in MATLAB [47, 121]. Here, a spline curve was first fitted to each intensity trace to identify segments of assembly and disassembly. The difference in intensity between each time point was calculated, and changes greater than 15% were considered significant. A log-linear fitting method was then used to determine the rate for each event, as described above. Our automatic algorithm generated the same results as the semi-automatic analysis.

4.6.5 Immunoblotting

Cells were cultured to 80% confluence and lysed in ice-cold TNE lysis buffer, as described previously [1]. Where indicated, cells were cultured in the presence of TGF β for 48 h. Total cell lysates (20 μg) were resolved by 6–12% SDS-PAGE. Proteins were transferred onto polyvinylidene difluoride membranes (catalogue no. IPVH00010, Millipore), and membranes were blocked in 5% fat-free milk for 1 h. Membranes were incubated with the following antibodies overnight at 4°C: ErbB2 (1:4000; catalogue no. sc-284, Santa Cruz Biotechnology, Inc.), SHCA (1:4000; catalogue no. 610082, BD Transduction Laboratories), FLAG (1:4000; catalogue no. F1804, Sigma–Aldrich), LPP (1:4000; catalogue no. sc-101434, Santa Cruz Biotechnology), paxillin (1:4000; catalogue no. ab23510, Abcam), Smad2/3 (1:1000; catalogue no. 3102, Cell Signaling), pSmad2 (Ser-465/467) (1:1000; catalogue no. 3101, Cell Signaling), Myc (1:3000; catalogue no. TAG003, BioShop), α -tubulin (1:20,000; catalogue no. T9026, Sigma–Aldrich), and glyceraldehyde-3-phosphate dehydrogenase (1:10,000; catalogue no. MAB374, Millipore). The appropriate horseradish peroxidase–conjugated secondary antibodies (1:10,000; Jackson Immuno

Research Laboratories) were added to the membranes for 1 h. Finally, the membranes were visualized using SuperSignal™ West Pico PLUS Chemiluminescent Substrate (catalogue no. 34578, Thermo Fisher Scientific).

For MAPK and PI3K inhibitor experiments, cells were pre-treated with 500 nM trametinib (catalogue no. T-8123, LC Laboratories) or 500 nM pictilisib (catalogue no. 11600-10, Cayman Chemical) for 12 h. TGFβ was then added to the medium, and cells were cultured for an additional 24 h. Proteins were transferred onto polyvinylidene difluoride membranes (catalogue no. IPFL00010, Millipore), and membranes were blocked with Intercept blocking buffer (catalogue no. 927-60001, LI-COR) for 1 h. Membranes were incubated with the following antibodies overnight at 4°C: ERK1/2 (1:1000; catalogue no. 9107S, Cell Signaling), pErk1/2 (Thr-202/Tyr-204) (1:1000; catalogue no. 9101S, Cell Signaling), S6 (1:500; catalogue no. 2317S, Cell Signaling), and pS6 (Ser-240/244) (1:500; catalogue no. 5364S, Cell Signaling). IR dyes 680RD donkey anti-mouse (1:10,000; catalogue no. 926-68072, LI-COR) and 800CW donkey anti-rabbit (1:10,000; catalogue no. 926-32213, LI-COR) were added to the membranes for 1 h. Finally, the membranes were visualized with the Odyssey Imager (LI-COR, Lincoln, NE). Quantification was performed with ImageJ (National Institutes of Health, Bethesda, MD). Phosphorylated protein levels were normalized by their respective total protein levels. Fold change for each experiment was determined relative to unstimulated cells. The data shown represent the mean ± S.E. for three independent experiments.

4.6.6 Immunofluorescence

Cells were plated onto 35-mm coverglass bottom dishes coated with fibronectin and allowed to settle overnight. Cells were then cultured in the absence or presence of TGFβ for 24 h before being fixed with 4% paraformaldehyde (PFA) for 10 min at 37°C. Cells were permeabilized with 0.3% TritonX-100 for 10 min, rinsed with 100 mM glycine in PBS, and blocked with 10% FBS in PBS for 1 h. Antibodies against LPP (1:500; catalogue no. sc-27312, Santa Cruz Biotechnology) and vinculin (1:1500; catalogue no. V9131, Sigma–Aldrich) were applied overnight at 4°C (where indicated). AlexaFluor 488 (1:1000; catalogue no. A11055, Invitrogen) and Alexa Fluor 546 (1:1000; catalogue no. A10036, Invitrogen) dye-conjugated secondary antibodies were then applied for 1 h at room temperature to visualize LPP and vinculin, respectively. Alexa Fluor 488 phalloidin (1:500; catalogue no. A12379, Invitrogen) was used to

visualize F-actin, and 4',6-diamidino-2-phenylindole (1:20,000; catalogue no. D1306, Thermo Fisher Scientific) was used to visualize nuclei (where indicated). Cells were kept in 1× PBS with 0.05% sodium azide (catalogue no. SAZ001, BioShop).

For MAPK and PI3K inhibitor experiments, cells were seeded onto coverglass bottom dishes and pretreated with 500nM trametinib or 500 nM pictilisib for 12 h. TGFβ was then added to the medium, and cells were cultured for an additional 24 h. Antibodies against LPP (1:1000) and paxillin (1:1000) were applied overnight at 4°C. Alexa Fluor 546 (1:1000) and AlexaFluor 647 (1:1000; catalogue no. A21447, Invitrogen) dye-conjugated secondary antibodies were then applied for 1 h at room temperature to visualize paxillin and LPP, respectively. AlexaFluor 488 phalloidin (1:1000) was used to visualize F-actin. Cells were kept in 1× PBS.

Images were acquired on a Zeiss LSM 710 confocal micro-scope with a Plan-Apochromat ×63/1.4 NA oil immersion DIC objective lens. For Figs. 3 and 5, the following parameters were used: 1 Airy unit, 900 master gain, 1 digital gain, 3.15 μs pixel dwell time, and 4-line averaging. An Ar ion laser tuned to 488-nm (1% power; 488/594-nm beam splitter; 493–556-nm detection) was used to visualize actin, a HeNe Green 543-nm laser (8% power; 488/543/633-nm beam splitter; 548–586 nm detection) was used to visualize vinculin, and a HeNe 594-nm laser (8% power; 458/514/594-nm beam splitter; 599–638-nm detection) was used to visualize mCherry-paxillin or mCherry-LPP. Images were acquired sequentially and saved as 8-bit with 1024 × 1024 pixels. For EGFP-LPP-WT, -mLIM1, and -ΔABD localization (Fig. S7), the following parameters were used: 1 Airy unit, 875 (EGFP-LPP) and 900 (mCherry-paxillin) master gain, 1 digital gain, 0.79 μs pixel dwell time, and 16-line averaging. An Ar ion laser tuned to 488-nm (2–2.4% power; 488-nm beam splitter; 467–560-nm detection) was used to visualize EGFP-LPP constructs, and a 561-nm DPSS laser (3–4% power; 458/561-nm beam splitter; 575–692-nm detection) was used to visualize mCherry-paxillin. Images were saved as 12-bit with 1024 × 1024 pixels. For MAPK and PI3K inhibitor experiments (Fig. S10), the following parameters were used: 1 Airy unit, 850 master gain, 1 digital gain, 6.3 μs pixel dwell time, and 4-line averaging. The 488-nm laser (3.5% power; 488/594-nm beam splitter; 493–556-nm detection) was used to visualize actin, the 543-nm laser (8% power; 458/543-nm beam splitter; 548–643-nm detection) was used to visualize paxillin, and a HeNe Red 633-nm laser (5% power; 488/543/633-nm beam splitter; 638–755-nm detection) was used to visualize LPP. Images were saved as 8-bit with 512 × 512 pixels.

Images were also acquired on a Zeiss LSM 780 confocal microscope with a Plan-Apochromat $\times 63/1.4$ NA oil immersion objective lens. For Fig. S6, the following parameters were used: 1 Airy unit, 800 master gain, 1 digital gain, 6.3 μs pixel dwell time, and 4-line averaging. A 405-nm blue diode laser (1% power; 405-nm beam splitter; 410–514-nm detection) was used to visualize 4',6-diamidino-2-phenylindole, an Ar ion laser tuned to 488-nm (2% power; 488-nm beam splitter; 490–606-nm detection) was used to visualize LPP, and a 561-nm DPSS laser (2% power; 458/561-nm beam splitter; 578–696-nm detection) was used to visualize mCherry-paxillin. Images were saved as 8-bit with 1024×1024 pixels.

4.6.6.1 Determining the number and size of adhesions per cell area: Immunofluorescence images were imported into Imaris for analysis using the Surfaces function. Surface detail was smoothed and set to 0.200 μm with a local background subtraction of 0.200 μm . All cellular adhesions (vinculin, paxillin, and/or LPP signals) were masked by a manual refinement of the autothreshold feature and splitting touching objects with a seed point diameter of 0.500 μm . Surfaces smaller than 10 pixels were removed by filtering. A contour was then manually drawn around the cell to determine the total surface area in contact with the dish. Finally, the number of adhesions for each cell was divided by the total cell area. An intensity threshold was used to classify small adhesions. Adhesions with a mean intensity less than 35 (arbitrary units) were considered to be small. The number of small adhesions in each cell was then divided by the total number of adhesions identified. The data shown represent the mean \pm S.E. for all cells analyzed from three independent experiments.

For MAPK and PI3K inhibitor experiments, surface detail and local background subtraction were uniformly changed to 0.300 μm to accommodate for the larger adhesions present in some conditions. Surfaces smaller than 2 pixels were removed by filtering. Measurements of adhesion size were obtained directly from masked adhesions. The data shown represent the mean \pm S.E. for all cells analyzed from two independent experiments.

4.6.7 BioID assay and streptavidin pulldown

MMTV/MT cells were starved overnight and subsequently treated with 50 μM biotin-supplemented 10% FBS/DMEM growth medium for 24 h. Two 15-cm plates of cells at 70% confluence were used per pulldown sample. The next day, cells were trypsinized, washed with PBS, and centrifuged at 250g for 5 min. Cells collected from each 15-cm plate were lysed with

700 μ l of RIPA lysis buffer (1% Triton X-100, 50 mM Tris-HCl, pH 7.5, 150 mM NaCl, 1 mM EDTA, 1 mM EGTA, 0.1% SDS) supplemented with protease inhibitor mixture, 50 units of benzonase, 0.5% sodium deoxycholate for 1 h on ice. Cells were vortexed every 15 min for 10 s. Lysates were sonicated at 50% amplitude two times for 10 s on ice. Lysates were centrifuged at maximum speed for 30 min at 4°C. Pierce Avidin-agarose beads (30- μ l bead volume per pulldown; catalogue no. 20219, Thermo Fisher Scientific) were used on supernatants from the centrifuged lysates (6% by volume of the supernatant was used as input control). Samples were rotated end-over-end for 3 h at 4°C. Afterward, beads were centrifuged at 3000 rpm for 1 min at 4°C and washed with RIPA buffer three times. *For immunoblots*, both input and pulldown samples were incubated with protein loading dye for 10 min at 95°C. *For elution for MS*, following the wash with RIPA buffer, samples were washed twice with LIGHT buffer (50 mM Tris-HCl, pH 7.5, using HPLC grade water) and eluted with 150 μ l of 50 mM H₃PO₄ (pH 1.5–2) on ice for 10 min. Supernatants were collected. This was repeated two more times, and all three elutions were pooled and kept in 80°C until MS analysis. Three technical replicates per condition were used for MS analysis.

4.6.7.1 Mass spectrometry and analysis of BioID data: Each BioID experiment was performed in triplicate, on different days, and using cells from successive passages. To distinguish background from *bona fide* protein associations, Myc-BirA (no biotin) and Myc-SHCA-WT-BirA (no biotin) were used as controls to perform SAINT analyses [58, 122].

Peptide identification was carried out on an Orbitrap Fusion Tribrid mass spectrometer (Thermo Fisher Scientific) equipped with a nanoelectrospray ion source (Thermo Fisher Scientific) and coupled to an UltiMate 3000 nanoRSLC (Thermo Fisher Scientific). Data-dependent acquisition of mass spectra was performed using Xcalibur (version 3.0.63; Thermo Fisher Scientific). Full scan mass spectra (350–1800 m/z) were acquired in the orbitrap at a resolution of 120,000 using a maximum injection time of 50 ms and automatic gain control target of 4e5. The quadrupole analyzer allowed for the isolation of selected ions in a window of 1.6 m/z and fragmentation by higher-energy collision-induced dissociation with 35% energy. The resulting fragments were detected by the linear ion trap at a rapid scan rate. Dynamic exclusion of previously fragmented peptides was set for a period of 20 s and a tolerance of 10 ppm. All MS/MS peak lists were generated using Thermo Proteome Discoverer (version 1.4.0.288; Thermo Fisher Scientific) with default parameters. MGF sample files were analyzed using Mascot (version 2.5.1; Matrix

Science, London, UK). The software was programmed to search against the Uniprot *Mus musculus* database (November 2014, 84,646 entries), assuming trypsin digestion. Searches were carried out with a fragment ion mass tolerance of 0.60 Da and a parent ion tolerance of 10 ppm. Carbamidomethyl of cysteine was specified as a fixed modification. Variable modifications were deamidation of asparagine and glutamine, oxidation of methionine, and phosphorylation of serine, threonine, and tyrosine. Two miscleavages were allowed.

Validation of the MS/MS-based peptide and protein identifications was carried out using Scaffold software (version 4.7.5; Proteome Software Inc., Portland, OR). Criteria for protein identifications were fixed at greater than 99% probability to achieve an FDR less than 1% and required at least one peptide to be identified. The Protein Prophet algorithm was used to assign peptide and protein probabilities [123, 124]. For proteins that contained similar peptides and could not be differentiated based on MS/MS analysis alone, the principle of parsimony was applied. After being exported from Scaffold, spectral counts were formatted according to SAINT algorithm guidelines [58, 59]. For each prey, the SAINT express statistical analyses were carried out by using the maximal spectral count value from Myc-BirA (no biotin) or Myc-SHCA-WT-BirA (no biotin) as controls. Proteins with a SAINT score ≥ 0.9 were deemed genuine interactors.

4.6.8 Co-localization of ShcA and LPP

NMuMG ErbB2 cells expressing SHCA-WT-iRFP and mCherry-LPP were plated onto 35-mm coverglass bottom dishes coated with fibronectin and allowed to settle overnight. Cells were cultured in the absence or presence of TGF β for 24 h before being fixed with 4% PFA for 10 min at 37°C. Images of SHCA and LPP were acquired sequentially on the TIRF microscope described above. A 561-nm laser with an ET 620/60-nm filter cube was used to visualize mCherry-LPP, whereas a 642-nm laser with an ET 700/75-nm filter cube was used to visualize SHCA-WT-iRFP. The camera exposure time was set to 1 s with an EM gain of 255 and read speed of 22 MHz. The TIRF prism was set to limit fluorescence excitation to a depth of 80 nm.

Images were imported into Imaris for analysis using the Surfaces function. Surface detail was smoothed and set to 0.200 μm with a local background subtraction of 0.200 μm . The LPP signal was used to mask cellular adhesions; manual refinement of the autothreshold feature and splitting touching objects with a seed point diameter of 0.500 μm was used. A contour was then manually drawn around the cell to determine the total surface area in contact with the dish. The

percentage of LPP adhesions positive for SHCA was determined by analyzing the mean intensity of SHCA within each mask. Adhesions with a mean intensity greater than diffuse cytoplasmic signal were considered positive for SHCA. The data shown represent the mean \pm S.E. for all cells analyzed from three independent experiments. Linescan analysis was performed in ImageJ to show overlap of SHCA and LPP signals in fixed cells.

4.6.9 Rapid imaging of adhesion dynamics

NMuMG ErbB2 cells expressing SHCA-WT-iRFP and EGFP-LPP were plated onto 35-mm coverglass bottom dishes coated with fibronectin and allowed to settle overnight. Cells were cultured in the presence of TGF β for 24 h prior to imaging. Images of SHCA and LPP were acquired sequentially on the TIRF microscope described above. A 488-nm laser with an ET525/50 nm filter cube was used to visualize EGFP-LPP, whereas a 642-nm laser with an ET 700/75-nm filter cube was used to visualize SHCA-WT-iRFP. The camera exposure time was set to 350 ms with an EM gain of 255 and read speed of 22 MHz. Images were acquired semi-continuously with the imaging interval set to 2 s. This time delay was chosen to give the filter wheel sufficient time to switch between filters. The exact time of acquisition for each image was recorded. The TIRF prism was set to limit fluorescence excitation to a depth of 80 nm.

Image stacks were analyzed in Imaris, as described in the previous section. Given that SHCA appears at sites of adhesion before LPP, the SHCA signal was used to mask adhesions in these sets of experiments. The mean intensities of SHCA and LPP within an adhesion were then plotted against time. Fluorescence intensity signals were adjusted for local cytoplasmic intensity. Time series data were adjusted for the delay between channels. Image stacks were also analyzed in ImageJ. Linescan analysis (ImageJ) was used to show treadmilling of SHCA, or the formation of a second nucleation point, in mature adhesions. Note that EGFP-LPP was chosen for these sets of experiments because EGFP is brighter than mCherry and there is no spectral overlap with iRFP.

4.6.10 Gelatin degradation assays

Degradation assays were performed on fluorescently conjugated gelatin-coated coverslips. Briefly, 35-mm glass-bottom dishes were coated with a mix of 0.1 mg ml⁻¹ poly-D-lysine (catalogue no. P6407, Sigma–Aldrich) and 5 μ g cm⁻² fibronectin in 1 \times PBS for 20 min, followed by incubation with 0.4% glutaraldehyde for 10 min. Oregon Green 488–conjugated gelatin

(catalogue no. G13186, Invitrogen) was diluted 1:20 with 0.1% unconjugated gelatin (catalogue no. 07903, Stem Cell Technologies) and used to coat dishes for 10 min at 37°C. Coverslips were then incubated with 10 mg ml⁻¹ sodium borohydride for 2 min, followed by 70% ethanol for 20 min. Three washes with 1× PBS were performed between each step. DMEM (37°C) was added to the coverslips 1 h before cell plating.

Cells were pretreated with TGFβ for 24 h in a cell culture dish and counted before plating. Cells seeded onto gelatin dishes (32,000 cells) were allowed to invade for 24 h before fixing with 4% PFA. Cells were then permeabilized with 0.2% Triton X-100, rinsed with 100 mM glycine in PBS, and blocked with 10% FBS in PBS. Antibodies against cortactin (1:1000; catalogue no. 05-180, EMD Millipore) and Atto 647N phalloidin for F-actin (1:2000; catalogue no. 65906, Sigma-Aldrich) were used. AlexaFluor 546 dye-conjugated secondary antibody (1:1000) was used to visualize cortactin. Cells were kept in 1× PBS with 0.05% sodium azide.

Images were acquired on a Zeiss LSM 710 confocal micro-scope with a Plan-Apochromat ×63/1.4 NA oil immersion DIC objective lens with the following parameters: 1 Airy unit, 800–900 master gain, 1 digital gain, 3.15 μs pixel dwell time, 4-line averaging. An Ar ion laser tuned to 488-nm (0.5–2.5% power; 488/594-nm beam splitter; 493–549-nm detection) was used to visualize gelatin, a HeNe Green 543-nm laser (4–5% power; 458/543-nm beam splitter; 566–599-nm detection) was used to visualize cortactin, and a HeNe Red 633-nm laser (1–4% power; 488/543/633-nm beam splitter; 638–759-nm detection) was used to visualize actin. Z-stacks were acquired at 0.26–0.30 μm steps over 2.1–2.4 μm. Images of gelatin alone were captured with a ×20/0.8 NA Plan-Apochromat objective lens. Images were saved as 12-bit with 1024 × 1024 pixels.

Quantification of gelatin degradation was performed in Imaris using the Surfaces function. The lookup table was inverted to make areas of degradation appear bright. Surface detail was smoothed and set to 0.500 μm with a local back-ground subtraction of 0.250 μm. Areas of degradation were then masked by a manual refinement of the autothreshold feature. Finally, orthogonal views were generated with the section viewer. Linescan analysis was performed in ImageJ. The data shown represent the mean ± S.E. for all cells analyzed from three independent experiments.

4.6.11 Statistical analyses

Statistical significance values (p values) were obtained by performing a two-tailed Student's t test or Mann–Whitney U test. Data are presented as mean \pm S.E. (where indicated). Experiments were performed at least three times. For analysis of cell speed, pairwise comparisons between $-TGF\beta$ and $+TGF\beta$ were performed between each 3-hour segment. The number of experiments was chosen as the n value to convey experimental reproducibility. For all other experiments, statistical tests were used to make pairwise comparisons between a base value (untreated cells) and a test condition. An $n > 30$ was chosen to account for normal distribution.

For adhesion dynamics, the *top* and *bottom lines* of box plots indicate the third and first quartile, respectively, whereas the *heavy central lines* indicate the mean. The *whiskers* extend up to 1.5 times the interquartile range. *Black dots* represent outliers. Cell averages were chosen as the n value to prevent p value skewing from many assembly and disassembly events [125].

4.6.12 Data availability

The mass spectrometry proteomics data have been deposited to the ProteomeXchange Consortium via the PRIDE [126] partner repository with the data set identifier PXD018265 and 10.6019/PXD018265.

4.7 AUTHOR CONTRIBUTIONS

A.K. generated several constructs, performed immunoblotting and microscopy experiments, analyzed data, and created MATLAB codes. E.V. performed gelatin degradation assays and helped with immunoblotting experiments. J.S. helped with microscopy, analysis and immunoblotting experiments. R.A. performed streptavidin pulldown assays. M.G.A. generated ShcA-iRFP constructs. K.J. and N.B. performed mass spectrometry analyses. G.T. provided preliminary results for cell migration. J.U.-S. contributed to the design and analysis of the ShcA BioID data. P.M.S. and C.M.B. conceptualized and supervised the project. A.K., E.V., P.M.S. and C.M.B. wrote and edited the manuscript.

4.8 ACKNOWLEDGEMENTS

We thank Dr. William J. Muller (McGill University, Montreal, QC) for providing MMTV Middle T antigen expressing breast cancer cells. We also thank Dr. Marc Fabian (Lady Davis Institute, Montreal, QC) for providing the AgeI-Myc primer used to create Myc-ShcA-WT-BirA. Finally, we thank members of the Ursini-Siegel, Siegel and Brown laboratories for thoughtful discussions about the manuscript. Work performed in the author's laboratories (J.U.-S., P.M.S., C.M.B.) was supported by grants from NSERC (Grant #493616-16, #386084-12), CIHR (Grant #CPG-146475), CCSRI (Grant #702060) and CCS i2I (Grant #705838). A.K. acknowledges support in the form of an FRQS doctoral studentship. E.V. acknowledges support in the form of CIHR and FRQS master's studentships. J.S. acknowledges support in the form of a Rolande and Marcel Gosselin graduate studentship. R.A. acknowledges support in the form of an MICRTP doctoral studentship. K.J. acknowledges support in the form of a studentship from the PROTEO network. N.B. holds a Canada Research Chair (Tier 2) in Cancer Proteomics. J.U-S. holds an FRQS Senior Salary Support award. P.M.S. is a McGill University William Dawson Scholar. Imaging experiments were performed at the McGill Life Sciences Complex Advanced BioImaging Facility (ABIF) and Cell Imaging and Analysis Network (CIAN).

4.9 REFERENCES

1. Northey, J.J., et al., *Signaling through ShcA is required for TGF- β and Neu/ErbB-2 induced breast cancer cell motility and invasion*. Mol. Cell. Biol., 2008: p. MCB.01734-07.
2. Ngan, E., et al., *A complex containing LPP and alpha-actinin mediates TGF β -induced migration and invasion of ErbB2-expressing breast cancer cells*. J Cell Sci, 2013. **126**(Pt 9): p. 1981-91.
3. Northey, J.J., et al., *Distinct phosphotyrosine-dependent functions of the ShcA adaptor protein are required for transforming growth factor beta (TGF β)-induced breast cancer cell migration, invasion, and metastasis*. J Biol Chem, 2013. **288**(7): p. 5210-22.
4. Ngan, E., et al., *LPP is a Src substrate required for invadopodia formation and efficient breast cancer lung metastasis*. Nat Commun, 2017. **8**: p. 15059.
5. Petit, M.M., et al., *LPP, an actin cytoskeleton protein related to zyxin, harbors a nuclear export signal and transcriptional activation capacity*. Mol Biol Cell, 2000. **11**(1): p. 117-29.
6. Petit, M.M., S.M. Meulemans, and W.J. Van de Ven, *The focal adhesion and nuclear targeting capacity of the LIM-containing lipoma-preferred partner (LPP) protein*. J Biol Chem, 2003. **278**(4): p. 2157-68.
7. Janssens, V., et al., *PP2A binds to the LIM domains of lipoma-preferred partner through its PR130/B" subunit to regulate cell adhesion and migration*. J Cell Sci, 2016. **129**(8): p. 1605-18.
8. Jin, L., et al., *Angiotensin II, focal adhesion kinase, and PRX1 enhance smooth muscle expression of lipoma preferred partner and its newly identified binding partner palladin to promote cell migration*. Circ Res, 2007. **100**(6): p. 817-25.
9. Gorenne, I., et al., *LPP, a LIM protein highly expressed in smooth muscle*. Am J Physiol Cell Physiol, 2003. **285**(3): p. C674-685.
10. Pantel, K. and R.H. Brakenhoff, *Dissecting the metastatic cascade*. Nat Rev Cancer, 2004. **4**(6): p. 448-56.
11. van Zijl, F., G. Krupitza, and W. Mikulits, *Initial steps of metastasis: cell invasion and endothelial transmigration*. Mutat Res, 2011. **728**(1-2): p. 23-34.
12. Chambers, A.F., A.C. Groom, and I.C. MacDonald, *Dissemination and growth of cancer cells in metastatic sites*. Nat Rev Cancer, 2002. **2**(8): p. 563-72.
13. Robertson, J., et al., *Defining the phospho-adhesome through the phosphoproteomic analysis of integrin signalling*. Nat Commun, 2015. **6**: p. 6265.
14. Wu, R.F., et al., *p66(Shc) Couples Mechanical Signals to RhoA through Focal Adhesion Kinase-Dependent Recruitment of p115-RhoGEF and GEF-H1*. Mol Cell Biol, 2016. **36**(22): p. 2824-2837.
15. Zaidel-Bar, R., et al., *Functional atlas of the integrin adhesome*. Nat Cell Biol, 2007. **9**(8): p. 858-67.
16. Kanchanawong, P., et al., *Nanoscale architecture of integrin-based cell adhesions*. Nature, 2010. **468**(7323): p. 580-4.
17. Winograd-Katz, S.E., et al., *The integrin adhesome: from genes and proteins to human disease*. Nat Rev Mol Cell Biol, 2014. **15**(4): p. 273-88.
18. Murphy, D.A. and S.A. Courtneidge, *The 'ins' and 'outs' of podosomes and invadopodia: characteristics, formation and function*. Nat Rev Mol Cell Biol, 2011. **12**(7): p. 413-26.
19. Albiges-Rizo, C., et al., *Actin machinery and mechanosensitivity in invadopodia, podosomes and focal adhesions*. J Cell Sci, 2009. **122**(Pt 17): p. 3037-49.
20. Beaty, B.T. and J. Condeelis, *Digging a little deeper: the stages of invadopodium formation and maturation*. Eur J Cell Biol, 2014. **93**(10-12): p. 438-44.
21. Seals, D.F., et al., *The adaptor protein Tks5/Fish is required for podosome formation and function, and for the protease-driven invasion of cancer cells*. Cancer Cell, 2005. **7**(2): p. 155-65.
22. Courtneidge, S.A., et al., *The SRC substrate Tks5, podosomes (invadopodia), and cancer cell invasion*. Cold Spring Harb Symp Quant Biol, 2005. **70**: p. 167-71.
23. Stylli, S.S., et al., *Nck adaptor proteins link Tks5 to invadopodia actin regulation and ECM degradation*. J Cell Sci, 2009. **122**(Pt 15): p. 2727-40.

24. Bowden, E.T., et al., *An invasion-related complex of cortactin, paxillin and PKC μ associates with invadopodia at sites of extracellular matrix degradation.* *Oncogene*, 1999. **18**(31): p. 4440-9.
25. Clark, E.S., et al., *Cortactin is an essential regulator of matrix metalloproteinase secretion and extracellular matrix degradation in invadopodia.* *Cancer Res*, 2007. **67**(9): p. 4227-35.
26. Provenzano, P.P. and P.J. Keely, *The role of focal adhesion kinase in tumor initiation and progression.* *Cell Adh Migr*, 2009. **3**(4): p. 347-50.
27. Blouw, B., et al., *The invadopodia scaffold protein Tks5 is required for the growth of human breast cancer cells in vitro and in vivo.* *PLoS One*, 2015. **10**(3): p. e0121003.
28. Yamaguchi, H. and J. Condeelis, *Regulation of the actin cytoskeleton in cancer cell migration and invasion.* *Biochim Biophys Acta*, 2007. **1773**(5): p. 642-52.
29. Wendt, M.K. and W.P. Schiemann, *Therapeutic targeting of the focal adhesion complex prevents oncogenic TGF- β signaling and metastasis.* *Breast Cancer Res*, 2009. **11**(5): p. R68.
30. Sulzmaier, F.J., C. Jean, and D.D. Schlaepfer, *FAK in cancer: mechanistic findings and clinical applications.* *Nat Rev Cancer*, 2014. **14**(9): p. 598-610.
31. Sakamoto, S., et al., *Talin1 promotes tumor invasion and metastasis via focal adhesion signaling and anoikis resistance.* *Cancer Res*, 2010. **70**(5): p. 1885-95.
32. Ueda, Y., et al., *Overexpression of HER2 (erbB2) in human breast epithelial cells unmasks transforming growth factor β -induced cell motility.* *The Journal of biological chemistry*, 2004. **279**(23): p. 24505-13.
33. Seton-Rogers, S.E., et al., *Cooperation of the ErbB2 receptor and transforming growth factor β in induction of migration and invasion in mammary epithelial cells.* *Proc Natl Acad Sci U S A*, 2004. **101**(5): p. 1257-62.
34. Rexer, B.N. and C.L. Arteaga, *Intrinsic and acquired resistance to HER2-targeted therapies in HER2 gene-amplified breast cancer: mechanisms and clinical implications.* *Crit Rev Oncog*, 2012. **17**(1): p. 1-16.
35. Wang, S.E., et al., *HER2/Neu (ErbB2) signaling to Rac1-Pak1 is temporally and spatially modulated by transforming growth factor β .* *Cancer research*, 2006. **66**(19): p. 9591-600.
36. Wang, S.E., et al., *Transforming growth factor β induces clustering of HER2 and integrins by activating Src-focal adhesion kinase and receptor association to the cytoskeleton.* *Cancer research*, 2009. **69**(2): p. 475-82.
37. Siegel, P.M., et al., *Transforming growth factor β signaling impairs Neu-induced mammary tumorigenesis while promoting pulmonary metastasis.* *Proceedings of the National Academy of Sciences*, 2003. **100**(14): p. 8430-8435.
38. Ursini-Siegel, J., et al., *ShcA signalling is essential for tumour progression in mouse models of human breast cancer.* *EMBO J*, 2008. **27**(6): p. 910-20.
39. Ursini-Siegel, J., et al., *Receptor tyrosine kinase signaling favors a protumorigenic state in breast cancer cells by inhibiting the adaptive immune response.* *Cancer Res*, 2010. **70**(20): p. 7776-87.
40. Ursini-Siegel, J., et al., *The ShcA SH2 domain engages a 14-3-3/PI3'K signaling complex and promotes breast cancer cell survival.* *Oncogene*, 2012. **31**(48): p. 5038-44.
41. Ahn, R., et al., *The ShcA PTB domain functions as a biological sensor of phosphotyrosine signaling during breast cancer progression.* *Cancer Res*, 2013. **73**(14): p. 4521-32.
42. Im, Y.K., et al., *The ShcA adaptor activates AKT signaling to potentiate breast tumor angiogenesis by stimulating VEGF mRNA translation in a 4E-BP-dependent manner.* *Oncogene*, 2015. **34**(13): p. 1729-35.
43. Ha, J.R., et al., *Integration of Distinct ShcA Signaling Complexes Promotes Breast Tumor Growth and Tyrosine Kinase Inhibitor Resistance.* *Mol Cancer Res*, 2018. **16**(5): p. 894-908.
44. Wright, K.D., et al., *The p52 isoform of SHC1 is a key driver of breast cancer initiation.* *Breast Cancer Res*, 2019. **21**(1): p. 74.
45. Ursini-Siegel, J. and W.J. Muller, *The ShcA adaptor protein is a critical regulator of breast cancer progression.* *Cell Cycle*, 2008. **7**(13): p. 1936-43.

46. Hudson, J., et al., *p66ShcA promotes breast cancer plasticity by inducing an epithelial-to-mesenchymal transition*. *Mol Cell Biol*, 2014. **34**(19): p. 3689-701.
47. Lewis, K., et al., *p66ShcA functions as a contextual promoter of breast cancer metastasis*. *Breast Cancer Res*, 2020. **22**(1): p. 7.
48. Grunewald, T.G., S.M. Pasedag, and E. Butt, *Cell Adhesion and Transcriptional Activity - Defining the Role of the Novel Protooncogene LPP*. *Transl Oncol*, 2009. **2**(3): p. 107-16.
49. Ngan, E., et al., *Emerging roles for LPP in metastatic cancer progression*. *J Cell Commun Signal*, 2018. **12**(1): p. 143-156.
50. Muraoka, R.S., et al., *Increased Malignancy of Neu-Induced Mammary Tumors Overexpressing Active Transforming Growth Factor {beta}1*. *Mol. Cell. Biol.*, 2003. **23**(23): p. 8691-8703.
51. Lauffenburger, D.A. and A.F. Horwitz, *Cell migration: a physically integrated molecular process*. *Cell*, 1996. **84**(3): p. 359-69.
52. Friedl, P. and K. Wolf, *Tumour-cell invasion and migration: diversity and escape mechanisms*. *Nat Rev Cancer*, 2003. **3**(5): p. 362-74.
53. Friedl, P., et al., *New dimensions in cell migration*. *Nat Rev Mol Cell Biol*, 2012. **13**(11): p. 743-7.
54. Glenney, J.R., Jr. and L. Zokas, *Novel tyrosine kinase substrates from Rous sarcoma virus-transformed cells are present in the membrane skeleton*. *J Cell Biol*, 1989. **108**(6): p. 2401-8.
55. Turner, C.E., J.R. Glenney, Jr., and K. Burridge, *Paxillin: a new vinculin-binding protein present in focal adhesions*. *J Cell Biol*, 1990. **111**(3): p. 1059-68.
56. Dankort, D., et al., *Grb2 and Shc adapter proteins play distinct roles in Neu (ErbB-2)-induced mammary tumorigenesis: implications for human breast cancer*. *Mol Cell Biol*, 2001. **21**(5): p. 1540-51.
57. Zaidel-Bar, R., et al., *A paxillin tyrosine phosphorylation switch regulates the assembly and form of cell-matrix adhesions*. *J Cell Sci*, 2007. **120**(Pt 1): p. 137-48.
58. Choi, H., et al., *SAINT: probabilistic scoring of affinity purification-mass spectrometry data*. *Nat Methods*, 2011. **8**(1): p. 70-3.
59. Teo, G., et al., *SAINTexpress: improvements and additional features in Significance Analysis of INTeractome software*. *J Proteomics*, 2014. **100**: p. 37-43.
60. Dumbauld, D.W., et al., *Contractility modulates cell adhesion strengthening through focal adhesion kinase and assembly of vinculin-containing focal adhesions*. *J Cell Physiol*, 2010. **223**(3): p. 746-56.
61. Plotnikov, S.V., et al., *Force fluctuations within focal adhesions mediate ECM-rigidity sensing to guide directed cell migration*. *Cell*, 2012. **151**(7): p. 1513-27.
62. Gorenne, I., et al., *LPP expression during in vitro smooth muscle differentiation and stent-induced vascular injury*. *Circ Res*, 2006. **98**(3): p. 378-85.
63. Shcherbakova, D.M., et al., *Bright monomeric near-infrared fluorescent proteins as tags and biosensors for multiscale imaging*. *Nat Commun*, 2016. **7**: p. 12405.
64. Humphries, J.D., A. Byron, and M.J. Humphries, *Integrin ligands at a glance*. *J Cell Sci*, 2006. **119**(Pt 19): p. 3901-3.
65. Pechkovsky, D.V., et al., *Transforming growth factor beta1 induces alphavbeta3 integrin expression in human lung fibroblasts via a beta3 integrin-, c-Src-, and p38 MAPK-dependent pathway*. *J Biol Chem*, 2008. **283**(19): p. 12898-908.
66. Mamuya, F.A. and M.K. Duncan, *α V integrins and TGF-beta-induced EMT: a circle of regulation*. *J Cell Mol Med*, 2012. **16**(3): p. 445-55.
67. Heino, J. and J. Massague, *Transforming growth factor-beta switches the pattern of integrins expressed in MG-63 human osteosarcoma cells and causes a selective loss of cell adhesion to laminin*. *J Biol Chem*, 1989. **264**(36): p. 21806-11.
68. Zhang, L., F. Zhou, and P. ten Dijke, *Signaling interplay between transforming growth factor- β receptor and PI3K/AKT pathways in cancer*. *Trends Biochem Sci*, 2013. **38**(12): p. 612-20.
69. Chapnick, D.A., et al., *Partners in crime: the TGF β and MAPK pathways in cancer progression*. *Cell Biosci*, 2011. **1**: p. 42.

70. Zhang, Y.E., *Non-Smad pathways in TGF-beta signaling*. Cell Res, 2009. **19**(1): p. 128-39.
71. Lee, M.K., et al., *TGF-beta activates Erk MAP kinase signalling through direct phosphorylation of ShcA*. Embo j, 2007. **26**(17): p. 3957-67.
72. Lamouille, S. and R. Derynck, *Cell size and invasion in TGF-beta-induced epithelial to mesenchymal transition is regulated by activation of the mTOR pathway*. J Cell Biol, 2007. **178**(3): p. 437-51.
73. Yi, J.Y., I. Shin, and C.L. Arteaga, *Type I transforming growth factor beta receptor binds to and activates phosphatidylinositol 3-kinase*. J Biol Chem, 2005. **280**(11): p. 10870-6.
74. Huang, C., K. Jacobson, and M.D. Schaller, *MAP kinases and cell migration*. Journal of Cell Science, 2004. **117**(20): p. 4619.
75. Huang, C., et al., *JNK phosphorylates paxillin and regulates cell migration*. Nature, 2003. **424**(6945): p. 219-23.
76. Chin, Y.R. and A. Toker, *Function of Akt/PKB signaling to cell motility, invasion and the tumor stroma in cancer*. Cell Signal, 2009. **21**(4): p. 470-6.
77. Grille, S.J., et al., *The protein kinase Akt induces epithelial mesenchymal transition and promotes enhanced motility and invasiveness of squamous cell carcinoma lines*. Cancer Res, 2003. **63**(9): p. 2172-8.
78. Enomoto, A., et al., *Akt/PKB regulates actin organization and cell motility via Girdin/APE*. Dev Cell, 2005. **9**(3): p. 389-402.
79. Mendoza, M.C., et al., *ERK-MAPK drives lamellipodia protrusion by activating the WAVE2 regulatory complex*. Mol Cell, 2011. **41**(6): p. 661-71.
80. Alexander, N.R., et al., *Extracellular matrix rigidity promotes invadopodia activity*. Curr Biol, 2008. **18**(17): p. 1295-9.
81. Savagner, P., *Leaving the neighborhood: molecular mechanisms involved during epithelial-mesenchymal transition*. Bioessays, 2001. **23**(10): p. 912-23.
82. Condeelis, J. and J.E. Segall, *Intravital imaging of cell movement in tumours*. Nat Rev Cancer, 2003. **3**(12): p. 921-30.
83. Noyal, A., et al., *Paxillin phosphorylation at Ser273 localizes a GIT1-PIX-PAK complex and regulates adhesion and protrusion dynamics*. J Cell Biol, 2006. **173**(4): p. 587-9.
84. Berginski, M.E., et al., *High-resolution quantification of focal adhesion spatiotemporal dynamics in living cells*. PLoS One, 2011. **6**(7): p. e22025.
85. Huttenlocher, A. and A.R. Horwitz, *Integrins in cell migration*. Cold Spring Harb Perspect Biol, 2011. **3**(9): p. a005074.
86. Heino, J., et al., *Regulation of cell adhesion receptors by transforming growth factor-beta. Concomitant regulation of integrins that share a common beta 1 subunit*. J Biol Chem, 1989. **264**(1): p. 380-8.
87. Honda, E., K. Yoshida, and H. Munakata, *Transforming growth factor-beta upregulates the expression of integrin and related proteins in MRC-5 human myofibroblasts*. Tohoku J Exp Med, 2010. **220**(4): p. 319-27.
88. Yeh, Y.C., et al., *Transforming growth factor- β 1 induces Smad3-dependent β 1 integrin gene expression in epithelial-to-mesenchymal transition during chronic tubulointerstitial fibrosis*. Am J Pathol, 2010. **177**(4): p. 1743-54.
89. Plow, E.F., et al., *Ligand binding to integrins*. J Biol Chem, 2000. **275**(29): p. 21785-8.
90. Wary, K.K., et al., *The adaptor protein Shc couples a class of integrins to the control of cell cycle progression*. Cell, 1996. **87**(4): p. 733-43.
91. Deshmukh, L., V. Gorbatyuk, and O. Vinogradova, *Integrin β 3 phosphorylation dictates its complex with the Shc phosphotyrosine-binding (PTB) domain*. J Biol Chem, 2010. **285**(45): p. 34875-84.
92. Dans, M., et al., *Tyrosine phosphorylation of the beta 4 integrin cytoplasmic domain mediates Shc signaling to extracellular signal-regulated kinase and antagonizes formation of hemidesmosomes*. J Biol Chem, 2001. **276**(2): p. 1494-502.

93. Rozakis-Adcock, M., et al., *Association of the Shc and Grb2/Sem5 SH2-containing proteins is implicated in activation of the Ras pathway by tyrosine kinases*. Nature, 1992. **360**(6405): p. 689-692.
94. Habib, T., R. Herrera, and S.J. Decker, *Activators of protein kinase C stimulate association of Shc and the PEST tyrosine phosphatase*. J Biol Chem, 1994. **269**(41): p. 25243-6.
95. Schmandt, R., S.K. Liu, and C.J. McGlade, *Cloning and characterization of mPAL, a novel Shc SH2 domain-binding protein expressed in proliferating cells*. Oncogene, 1999. **18**(10): p. 1867-79.
96. Waalkes, S., et al., *Fibronectin 1 mRNA expression correlates with advanced disease in renal cancer*. BMC Cancer, 2010. **10**: p. 503.
97. Jia, D., et al., *Development of a highly metastatic model that reveals a crucial role of fibronectin in lung cancer cell migration and invasion*. BMC Cancer, 2010. **10**: p. 364.
98. Ioachim, E., et al., *Immunohistochemical expression of extracellular matrix components tenascin, fibronectin, collagen type IV and laminin in breast cancer: their prognostic value and role in tumour invasion and progression*. Eur J Cancer, 2002. **38**(18): p. 2362-70.
99. Mierke, C.T., et al., *Integrin alpha5beta1 facilitates cancer cell invasion through enhanced contractile forces*. J Cell Sci, 2011. **124**(Pt 3): p. 369-83.
100. Collins, L.R., et al., *Bifurcation of cell migratory and proliferative signaling by the adaptor protein Shc*. J Cell Biol, 1999. **147**(7): p. 1561-8.
101. Mainiero, F., et al., *The coupling of alpha6beta4 integrin to Ras-MAP kinase pathways mediated by Shc controls keratinocyte proliferation*. EMBO J, 1997. **16**(9): p. 2365-75.
102. Shaw, L.M., et al., *Activation of phosphoinositide 3-OH kinase by the alpha6beta4 integrin promotes carcinoma invasion*. Cell, 1997. **91**(7): p. 949-60.
103. Zaidel-Bar, R., et al., *Early molecular events in the assembly of matrix adhesions at the leading edge of migrating cells*. J Cell Sci, 2003. **116**(Pt 22): p. 4605-13.
104. Laukaitis, C.M., et al., *Differential dynamics of alpha 5 integrin, paxillin, and alpha-actinin during formation and disassembly of adhesions in migrating cells*. J Cell Biol, 2001. **153**(7): p. 1427-40.
105. Horton, E.R., et al., *Definition of a consensus integrin adhesome and its dynamics during adhesion complex assembly and disassembly*. Nat Cell Biol, 2015. **17**(12): p. 1577-1587.
106. Kuo, J.C., et al., *Analysis of the myosin-II-responsive focal adhesion proteome reveals a role for beta-Pix in negative regulation of focal adhesion maturation*. Nat Cell Biol, 2011. **13**(4): p. 383-93.
107. Lawson, C., et al., *FAK promotes recruitment of talin to nascent adhesions to control cell motility*. J Cell Biol, 2012. **196**(2): p. 223-32.
108. Lawson, C. and D.D. Schlaepfer, *Integrin adhesions: who's on first? What's on second? Connections between FAK and talin*. Cell Adh Migr, 2012. **6**(4): p. 302-6.
109. Hu, Y.-L., et al., *FAK and paxillin dynamics at focal adhesions in the protrusions of migrating cells*. Scientific Reports, 2014. **4**(1): p. 6024.
110. Xia, H., et al., *Focal adhesion kinase is upstream of phosphatidylinositol 3-kinase/Akt in regulating fibroblast survival in response to contraction of type I collagen matrices via a beta 1 integrin viability signaling pathway*. J Biol Chem, 2004. **279**(31): p. 33024-34.
111. Kim, N.G. and B.M. Gumbiner, *Adhesion to fibronectin regulates Hippo signaling via the FAK-Src-PI3K pathway*. J Cell Biol, 2015. **210**(3): p. 503-15.
112. Schober, M., et al., *Focal adhesion kinase modulates tension signaling to control actin and focal adhesion dynamics*. J Cell Biol, 2007. **176**(5): p. 667-80.
113. Parekh, A. and A.M. Weaver, *Regulation of invadopodia by mechanical signaling*. Exp Cell Res, 2016. **343**(1): p. 89-95.
114. Schoumacher, M., et al., *Actin, microtubules, and vimentin intermediate filaments cooperate for elongation of invadopodia*. J Cell Biol, 2010. **189**(3): p. 541-56.
115. Eddy, R.J., et al., *Tumor Cell Invadopodia: Invasive Protrusions that Orchestrate Metastasis*. Trends Cell Biol, 2017. **27**(8): p. 595-607.

116. Tomar, A., et al., *Cortactin as a target for FAK in the regulation of focal adhesion dynamics*. PLoS One, 2012. **7**(8): p. e44041.
117. Artym, V.V., et al., *Dynamic interactions of cortactin and membrane type 1 matrix metalloproteinase at invadopodia: defining the stages of invadopodia formation and function*. Cancer Res, 2006. **66**(6): p. 3034-43.
118. Weaver, A.M., *Invadopodia: specialized cell structures for cancer invasion*. Clin Exp Metastasis, 2006. **23**(2): p. 97-105.
119. Buccione, R., G. Caldieri, and I. Ayala, *Invadopodia: specialized tumor cell structures for the focal degradation of the extracellular matrix*. Cancer Metastasis Rev, 2009. **28**(1-2): p. 137-49.
120. Branch, K.M., D. Hoshino, and A.M. Weaver, *Adhesion rings surround invadopodia and promote maturation*. Biol Open, 2012. **1**(8): p. 711-22.
121. Kiepas, A., et al., *Optimizing live-cell fluorescence imaging conditions to minimize phototoxicity*. J Cell Sci, 2020. **133**(4).
122. Choi, H., et al., *Analyzing protein-protein interactions from affinity purification-mass spectrometry data with SAINT*. Curr Protoc Bioinformatics, 2012. **Chapter 8**: p. Unit8 15.
123. Keller, A., et al., *Empirical statistical model to estimate the accuracy of peptide identifications made by MS/MS and database search*. Anal Chem, 2002. **74**(20): p. 5383-92.
124. Nesvizhskii, A.I., et al., *A statistical model for identifying proteins by tandem mass spectrometry*. Anal Chem, 2003. **75**(17): p. 4646-58.
125. Lord, S.J., et al., *SuperPlots: Communicating reproducibility and variability in cell biology*. Journal of Cell Biology, 2020. **219**(6).
126. Perez-Riverol, Y., et al., *The PRIDE database and related tools and resources in 2019: improving support for quantification data*. Nucleic Acids Res, 2019. **47**(D1): p. D442-d450.

4.10 FIGURES AND LEGENDS

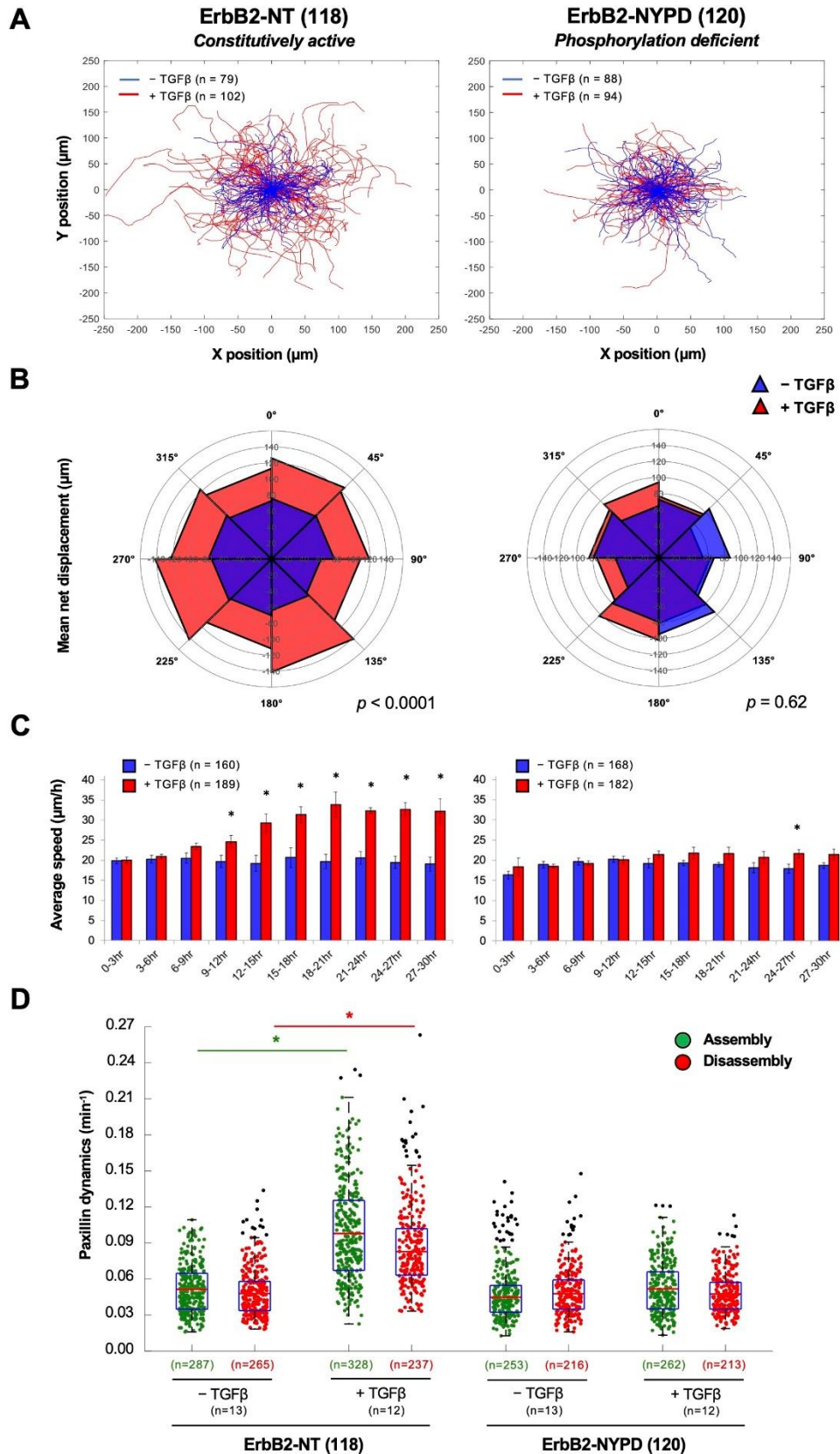


Figure 4.1. TGF β stimulates the migration of ErbB2-NT-expressing breast cancer cells. (A) Live-cell migration tracks for each condition are shown 18 h after treatment with or without TGF β (2 ng ml⁻¹). Each *line* represents the migration path of a single cell over 6 h. The starting point of each cell was superimposed on the origin (0, 0). *Numbers in parentheses* refer to explant cell lines. (B) Cell displacements from A were pooled into 45° segments based on their angle of trajectory and averaged to determine mean net displacement. (C) Average migration speed over time was calculated by determining the mean distance traveled between each imaging time point by all cells in A. The data for each population were then averaged into 3-h segments. Data represent mean \pm S.E. (*error bars*) from five (NT) or six (NYPD) independent experiments. *, $p < 0.05$, two-tailed Student's *t* test. (D) Adhesions in protrusive cell regions were tracked over time using a TIRF Spectral Discovery System coupled to a Leica microscope equipped with a Plan-Apochromat $\times 63/1.47$ NA oil immersion DIC objective lens and EM-CCD camera (1 pixel = 0.155 μ m). Cells were transfected with mCherry-paxillin, a marker of cellular adhesions, 48 h prior to imaging and left untreated or treated with TGF β for 24 h. Average assembly (*green*) or disassembly (*red*) rates were determined from changes in mean fluorescence intensity. Data represent individual assembly and disassembly events from three independent experiments. *Coloured n* values refer to the number of events while *black n* values refer to the number of cells. The *top* and *bottom lines* of the *box* indicate the third and first quartile, respectively, whereas the *heavy central line* indicates the mean. The *whiskers* extend up to 1.5 times the interquartile range. *Black dots* represent outliers. *, $p < 0.0001$ calculated from the cell averages for assembly and disassembly rates; two-tailed Student's *t* test.

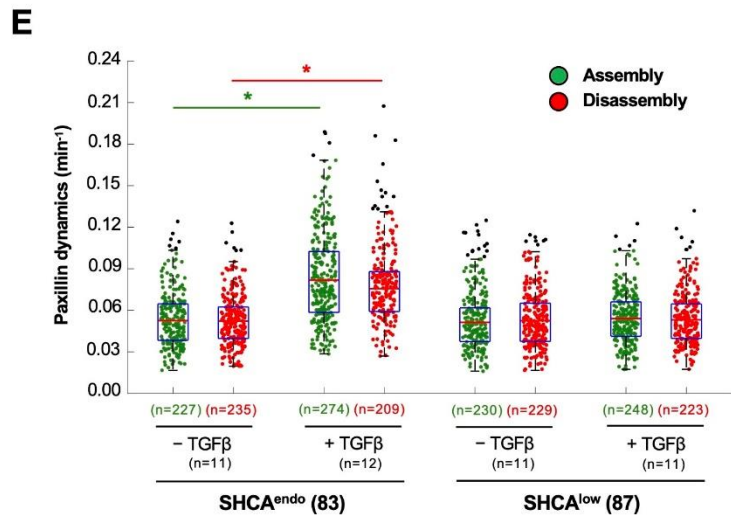
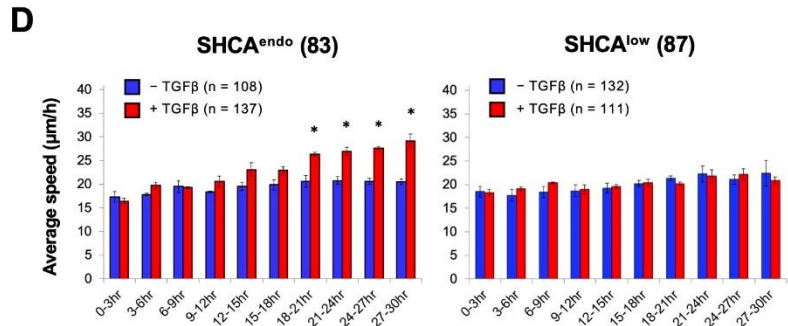
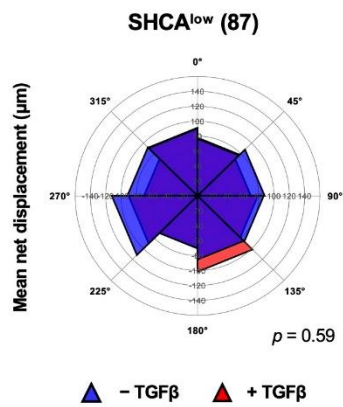
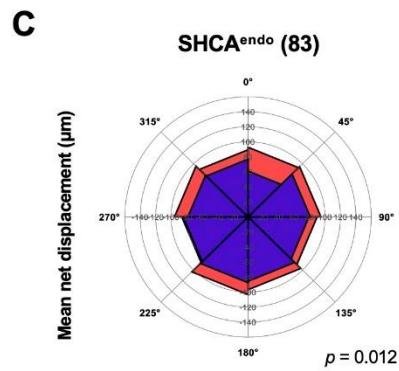
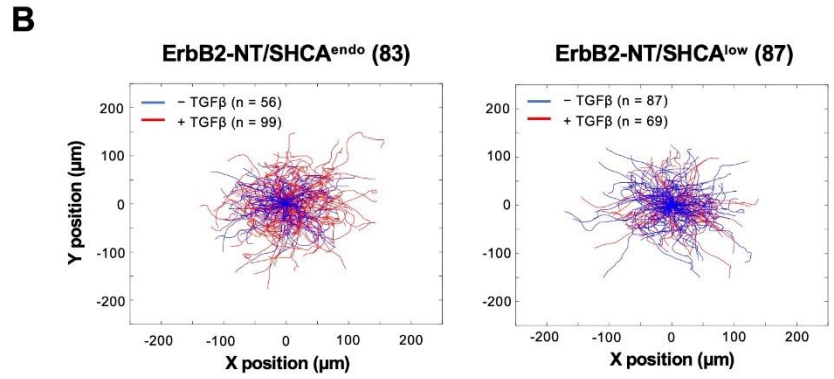
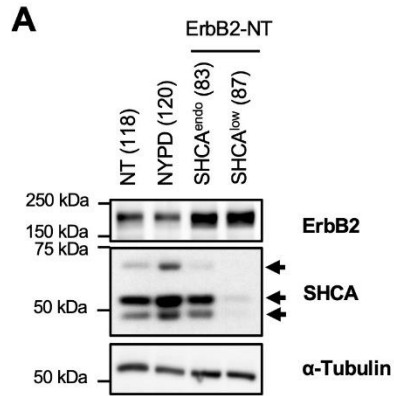
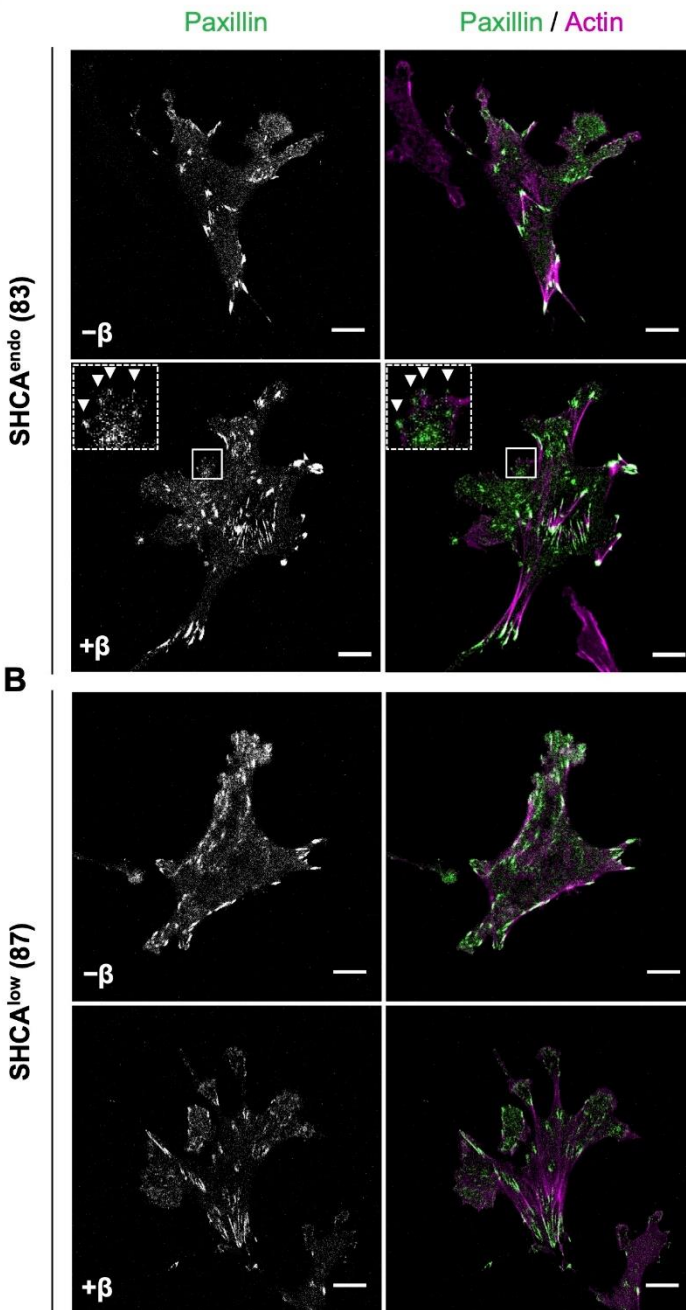
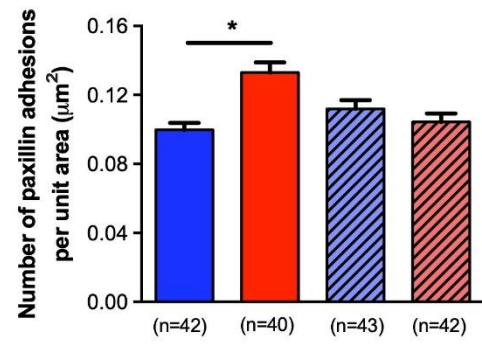
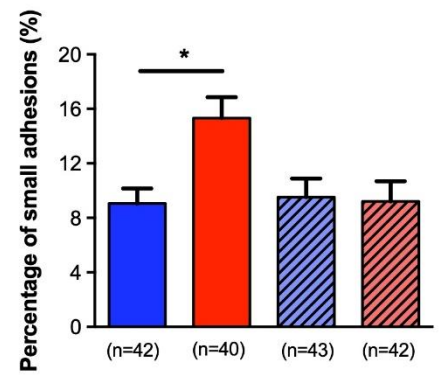


Figure 4.2. The SHCA adapter protein is required for TGF β -induced migration. (A) Total cell lysates showing ErbB2 and SHCA levels in ErbB2-NT (explant 118), ErbB2-NYPD (explant 120), ErbB2-NT/SHCA^{endo} (explant 83), and ErbB2-NT/SHCA^{low} (explant 87) populations. α -Tubulin was used as a loading control. (B) ErbB2-NT/SHCA^{endo} (explant 83) and ErbB2-NT/SHCA^{low} (explant 87) cells were seeded onto fibronectin-coated glass bottom dishes and allowed to migrate in the absence or presence of TGF β (2 ng ml⁻¹). Live-cell migration tracks for each condition are shown 18 h after treatment. Each *line* represents the migration path of a single cell over 6 h. The starting point of each cell was superimposed on the origin (0,0). (C) Cell displacements from *B* were pooled into 45° segments based on their angle of trajectory and averaged to determine mean net displacement. (D) Average migration speed over time was calculated by determining the mean distance traveled between each imaging time point by all cells in *B*. The data for each population was then averaged into 3-h segments. Data represent mean \pm S.E. (*error bars*) from three (ErbB2-NT/SHCA^{endo}) or four (ErbB2-NT/SHCA^{low}) independent experiments. *, $p < 0.05$, two-tailed Student's *t* test. (E) Adhesions in protrusive cell regions were tracked over time using TIRF microscopy. Cells were transfected with mCherry-paxillin 48 h prior to imaging and left untreated or treated with TGF β for 24 h. Average assembly (*green*) or disassembly (*red*) rates were determined from changes in mean fluorescence intensity. Data represent individual assembly and disassembly events from three (ErbB2-NT/SHCA^{endo}) or four (ErbB2-NT/SHCA^{low}) independent experiments. *Coloured n* values refer to the number of events while *black n* values refer to the number of cells. The *top* and *bottom lines* of the *box* indicate the third and first quartile, respectively, whereas the *heavy central line* indicates the mean. The *whiskers* extend up to 1.5 times the interquartile range. *Black dots* represent outliers. *, $p < 0.0001$ calculated from the cell averages for assembly and disassembly rates; two-tailed Student's *t* test.

A**C****D**

■ SHCA^{endo} (83) - β ■ SHCA^{low} (87) - β
■ SHCA^{endo} (83) + β ■ SHCA^{low} (87) + β

Figure 4.3. SHCA is required for the formation of small, dynamic adhesions in breast cancer cells exposed to TGF β . (A and B) ErbB2-NT/SHCA^{endo} (explant 83) and ErbB2-NT/SHCA^{low} (explant 87) cells were infected with mCherry-paxillin, seeded onto fibronectin-coated glass bottom dishes, and cultured in the absence or presence of TGF β (2 ng ml⁻¹) for 24 h. Cells were then fixed with 4% PFA and stained with phalloidin (F-actin). Images were taken on a Zeiss confocal laser-scanning microscope (CLSM) using a Plan-Apochromat $\times 63/1.4$ NA oil immersion DIC objective lens (1 pixel = 0.132 μ m). *Arrowheads* highlight examples of small adhesions formed after treatment with TGF β . *Scale bar*, 10 μ m. (C) Images were imported into Imaris to determine the average number of cellular adhesions for the indicated conditions. Data were normalized by dividing the number of adhesions in each cell by the total cell area. Cell area was determined by drawing a contour around each cell. (D) Cellular adhesions from C were subsequently analyzed for size. An intensity threshold was used to classify small adhesions. Adhesions with a mean intensity less than 35 (arbitrary units) were considered to be small. The number of small adhesions in each cell was then divided by total adhesions identified. Data represent mean \pm S.E. (*error bars*) from three independent experiments. *, $p < 0.003$; Mann–Whitney U test.

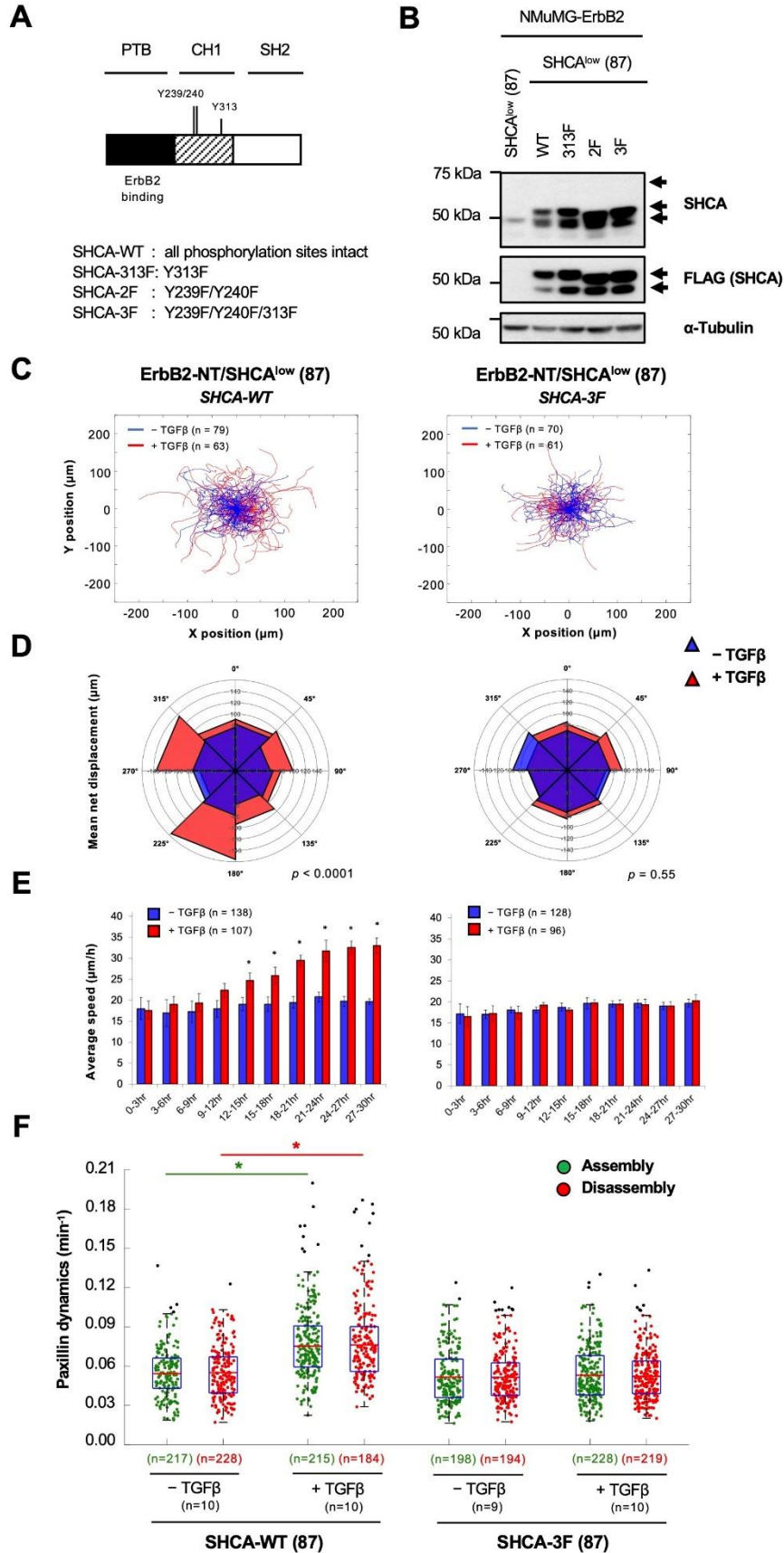


Figure 4.4. Loss of SHCA phosphorylation abrogates TGF β -induced increase in migration speed of ErbB2-expressing breast cancer cells. (A) *Schematic diagram* of SHCA showing the domain structure and location of three tyrosine residues (Y) that were mutated to phenylalanine (F). (B) Immunoblot analysis of whole-cell lysates showing SHCA levels (anti-SHCA or anti-FLAG antibodies) in the indicated cell populations. α -Tubulin was used as a loading control. (C) ErbB2-NT/SHCA-WT (explant 87) and ErbB2-NT/SHCA-3F (explant 87) cells were seeded onto fibronectin-coated glass bottom dishes and allowed to migrate in the absence or presence of TGF β (2 ng ml⁻¹). Live-cell migration tracks for each condition are shown 18 h after treatment. Each *line* represents the migration path of a single cell over 6 h. The starting point of each cell was superimposed on the origin (0,0). (D) Cell displacements from C were pooled into 45° segments based on their angle of trajectory and averaged to determine mean final displacement. (E) Average migration speed over time was calculated by determining the mean distance traveled between each imaging time point by all cells in C. The data for each population were then averaged into 3-h segments. Data represent mean \pm S.E. (*error bars*) from four independent experiments. *, $p < 0.05$, two-tailed Student's *t* test. (F) Adhesions in protrusive cell regions were tracked over time using TIRF microscopy. Cells were transfected with mCherry-paxillin 48 h prior to imaging and left untreated or treated with TGF β for 24 h. Average assembly (*green*) or disassembly (*red*) rates were determined from changes in mean fluorescence intensity. Data represent individual assembly and disassembly events from three independent experiments. *Coloured n* values refer to the number of events while *black n* values refer to the number of cells. The *top* and *bottom lines* of the *box* indicate the third and first quartile, respectively, whereas the *heavy central line* indicates the mean. The *whiskers* extend up to 1.5 times the interquartile range. *Black dots* represent outliers. *, $p < 0.0001$ calculated from the cell averages for assembly and disassembly rates; two-tailed Student's *t* test.

. Table 4.1. BioID analysis to identify novel SHCA-interacting proteins

| Prey | Spectral counts ^a | SAINT score ^b | -Fold change ^c | Function |
|--|------------------------------|--------------------------|---------------------------|---|
| Cellular adhesion proteins (SHCA interactors) | | | | |
| Actr2 | 11.3 ± 2.3 | 0.96 | 4.3 | ATP-binding component of Arp2/3 complex |
| Arhgef10l | 9.3 ± 2.5 | 1 | 93.3 | RhoGEF |
| Arhgef5 | 5.3 ± 3.5 | 0.98 | 53.3 | RhoGEF |
| Arhgef7 | 3.3 ± 1.2 | 0.98 | 33.3 | RhoGEF |
| Arpin | 7.3 ± 2.9 | 1 | 73.3 | Regulates actin polymerization |
| Cd2ap | 24 ± 4 | 1 | 10.3 | Scaffold protein, binds actin |
| Coro1b | 37.3 ± 11.7 | 1 | 12.4 | Actin-binding protein |
| Crk | 5.7 ± 2.9 | 1 | 56.7 | Adaptor protein, cell adhesion, migration |
| Cttn | 25 ± 4.6 | 1 | 18.8 | Focal adhesion protein, cytoskeletal organization |
| Eps8l2 | 25.3 ± 7.5 | 1 | 253.3 | Enhances SOS activity, cytoskeletal organization |
| Lims1 | 4.7 ± 0.6 | 1 | 46.7 | Integrin signaling, focal adhesion protein |
| Lpp | 9.7 ± 5.5 | 0.98 | 9.7 | Focal adhesion protein, adhesion dynamics |
| Pak2 | 8.3 ± 2.3 | 1 | 25 | Ser/Thr kinase, cytoskeletal organization |
| Parva | 3.3 ± 0.6 | 0.96 | 10 | Focal adhesion protein, binds actin |
| Pdlim5 | 20.3 ± 7 | 1 | 15.3 | Cytoskeleton-associated protein, migration |
| Pxn | 2.7 ± 1.2 | 0.96 | 26.7 | Focal adhesion protein, adhesion dynamics |
| Sept10 | 8.3 ± 2.5 | 1 | 12.5 | GTP-binding protein, cytoskeletal organization |
| Sept11 | 27.7 ± 0.6 | 1 | 4.6 | GTP-binding protein, cytoskeletal organization |
| Sept2 | 33 ± 3.6 | 0.97 | 3.1 | GTP-binding protein, cytoskeletal organization |
| Sept6 | 11 ± 2.6 | 1 | 16.5 | GTP-binding protein, cytoskeletal organization |
| Sept7 | 36 ± 3 | 1 | 6.8 | GTP-binding protein, cytoskeletal organization |
| Tln1 | 37 ± 19.5 | 1 | 37 | Focal adhesion protein, binds actin |
| Known SHCA-interacting proteins | | | | |
| Ptpn12 | 10.7 ± 2.9 | 1 | 32 | Protein-tyrosine phosphatase |
| Grb2 | 6.3 ± 3.2 | 1 | 63.3 | Adaptor protein; activates ERK and AKT pathways |
| Shcgp1 | 8.3 ± 1.5 | 1 | 83.3 | SHCA-binding protein |

^a Average of three biological replicates.

^b Cutoff: SAINT score >0.9 (from a total of 113 interacting proteins).

^c -Fold enrichment relative to Myc-BirA alone.

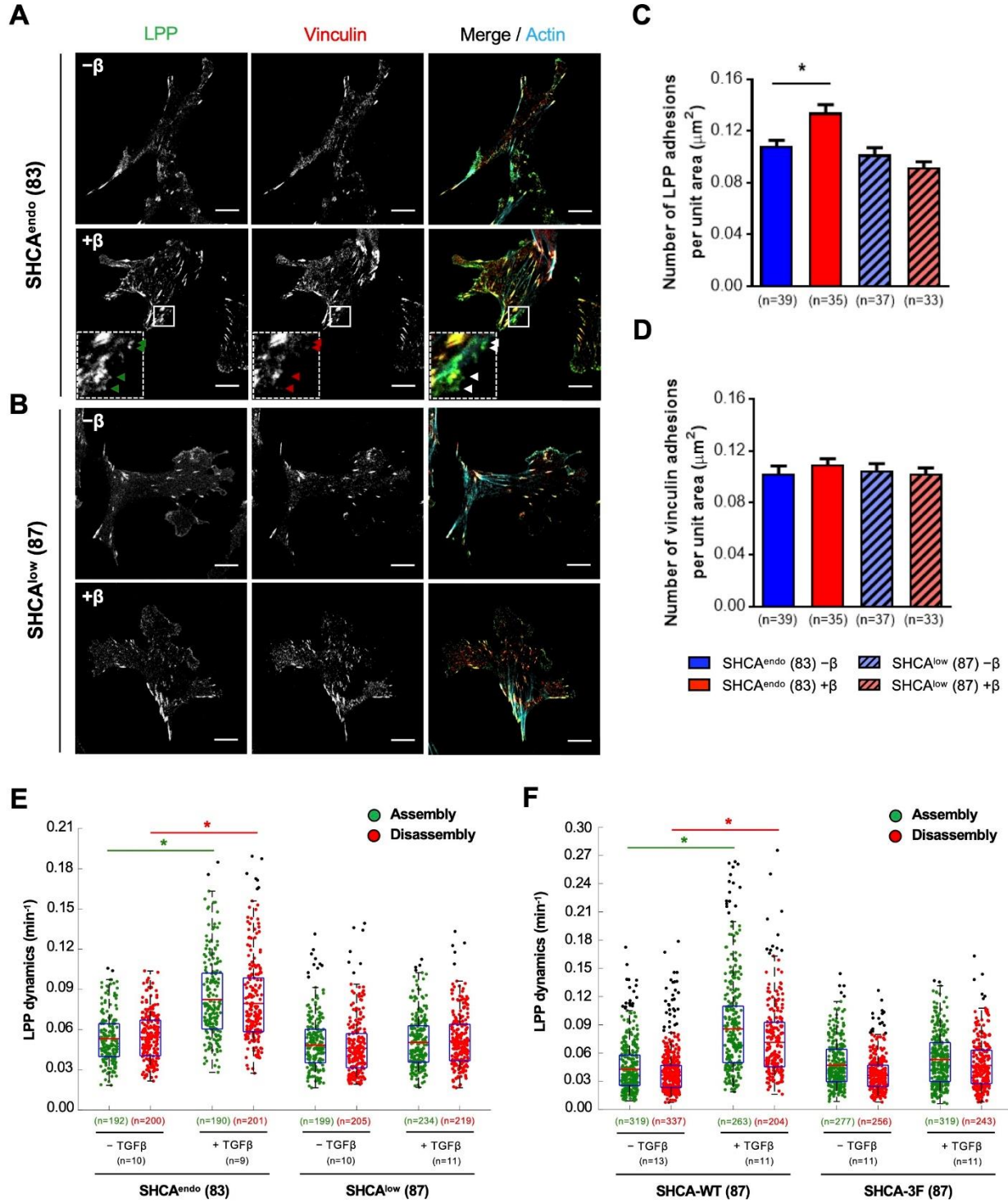


Figure 4.5. LPP targeting to adhesions in response to TGF β requires SHCA. (A and B) ErbB2-NT/SHCA^{endo} (explant 83) and ErbB2-NT/SHCA^{low} (explant 87) cells were infected with mCherry-LPP, seeded onto fibronectin-coated glass bottom dishes, and cultured in the absence or presence of TGF β (2 ng ml⁻¹) for 24 h. Cells were then fixed with 4% PFA and stained with antibodies against vinculin and phalloidin (F-actin). Images were taken on a Zeiss CLSM using a Plan-Apochromat $\times 63/1.4$ NA oil immersion DIC objective lens (1 pixel = 0.132 μ m). The *arrowheads* highlight examples of small adhesions formed after treatment with TGF β . *Scale bar*, 10 μ m. (C and D) Images were imported into Imaris to determine the average number of LPP and vinculin-bearing adhesions over the whole cell for each condition. Data were normalized by dividing the number of adhesions in each cell by the total cell area. Cell area was determined by drawing a contour around each cell. Data represent mean \pm S.E. (*error bars*) from three independent experiments. *, $p < 0.001$, Mann–Whitney U test. (E and F) Adhesions in protrusive cell regions were tracked over time using TIRF microscopy. Average assembly (*green*) or disassembly (*red*) rates were determined from changes in mean fluorescence intensity after 24 h with or without TGF β treatment. Data represent individual assembly and disassembly events from three independent experiments. *Coloured n* values refer to the number of events while *black n* values refer to the number of cells. The *top* and *bottom lines* of the *box* indicate the third and first quartile, respectively, whereas the *heavy central line* indicates the mean. The *whiskers* extend up to 1.5 times the interquartile range. *Black dots* represent outliers. *, $p < 0.001$ calculated from the cell averages for assembly and disassembly rates, two-tailed Student's t test.

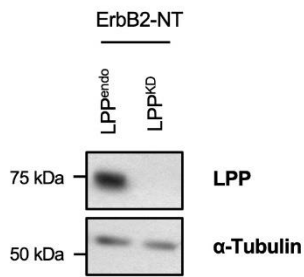
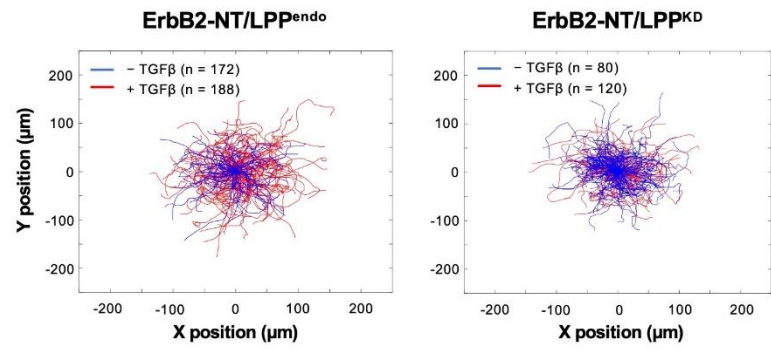
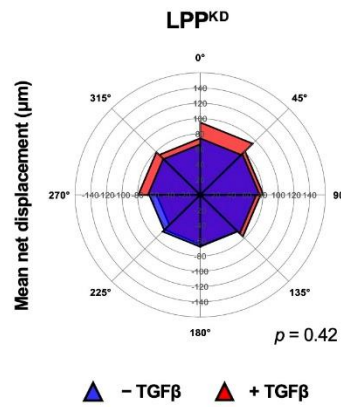
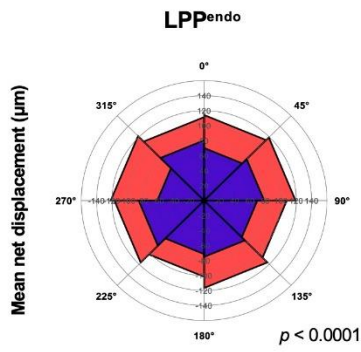
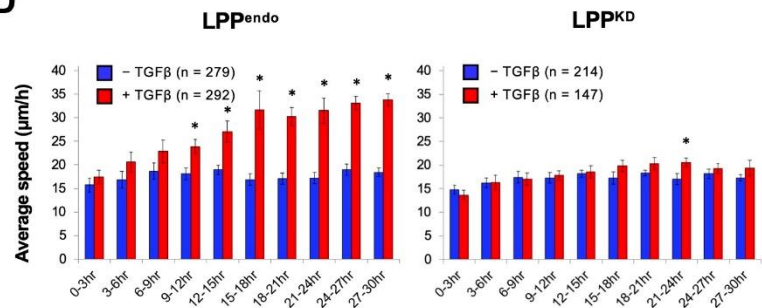
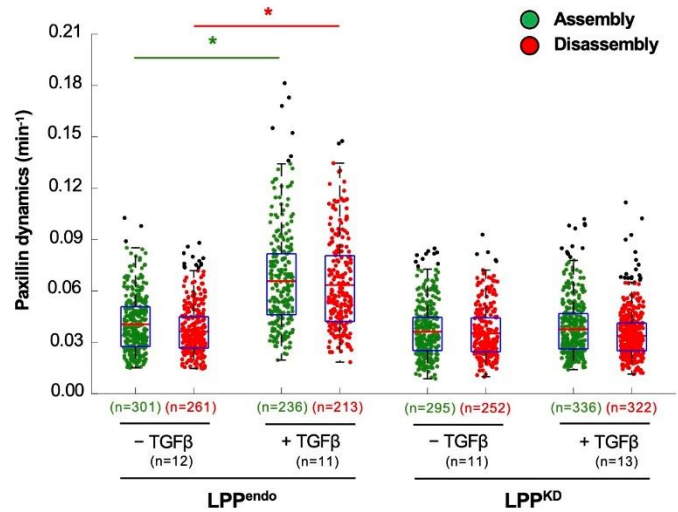
A**B****C****D****E**

Figure 4.6. LPP is required for TGF β -induced migration and adhesion dynamics. (A) Immunoblot analysis of whole cell lysates showing LPP levels in the indicated cell populations. α -Tubulin was used as a loading control. (B) ErbB2-NT/LPP^{endo} and ErbB2-NT/LPP^{KD} cells were seeded onto fibronectin-coated glass bottom dishes and allowed to migrate in the absence or presence of TGF β (2 ng ml⁻¹). Live-cell migration tracks for each condition are shown 18 h after treatment. Each *line* represents the migration path of a single cell over 6 h. The starting point of each cell was superimposed on the origin (0,0). (C) Cell displacements from *B* were pooled into 45° segments based on their angle of trajectory and averaged to determine mean final displacement. (D) Average migration speed over time was calculated by determining the mean distance traveled between each imaging time point by all cells in *B*. The data for each population were then averaged into 3-h segments. Data represent mean \pm S.E. (*error bars*) from four independent experiments. *, $p < 0.05$, two-tailed Student's *t* test. (E) Adhesions in protrusive cell regions were tracked over time using TIRF microscopy. Cells were transfected with mCherry-paxillin 48 h prior to imaging and left untreated or treated with TGF β for 24 h. Average assembly (*green*) or disassembly (*red*) rates were determined from changes in mean fluorescence intensity. Data represent individual assembly and disassembly events from three independent experiments. *Coloured n* values refer to the number of events while *black n* values refer to the number of cells. The *top* and *bottom lines* of the *box* indicate the third and first quartile, respectively, whereas the *heavy central line* indicates the mean. The *whiskers* extend up to 1.5 times the interquartile range. *Black dots* represent outliers. *, $p < 0.0001$ calculated from the cell averages for assembly and disassembly rates; two-tailed Student's *t* test.

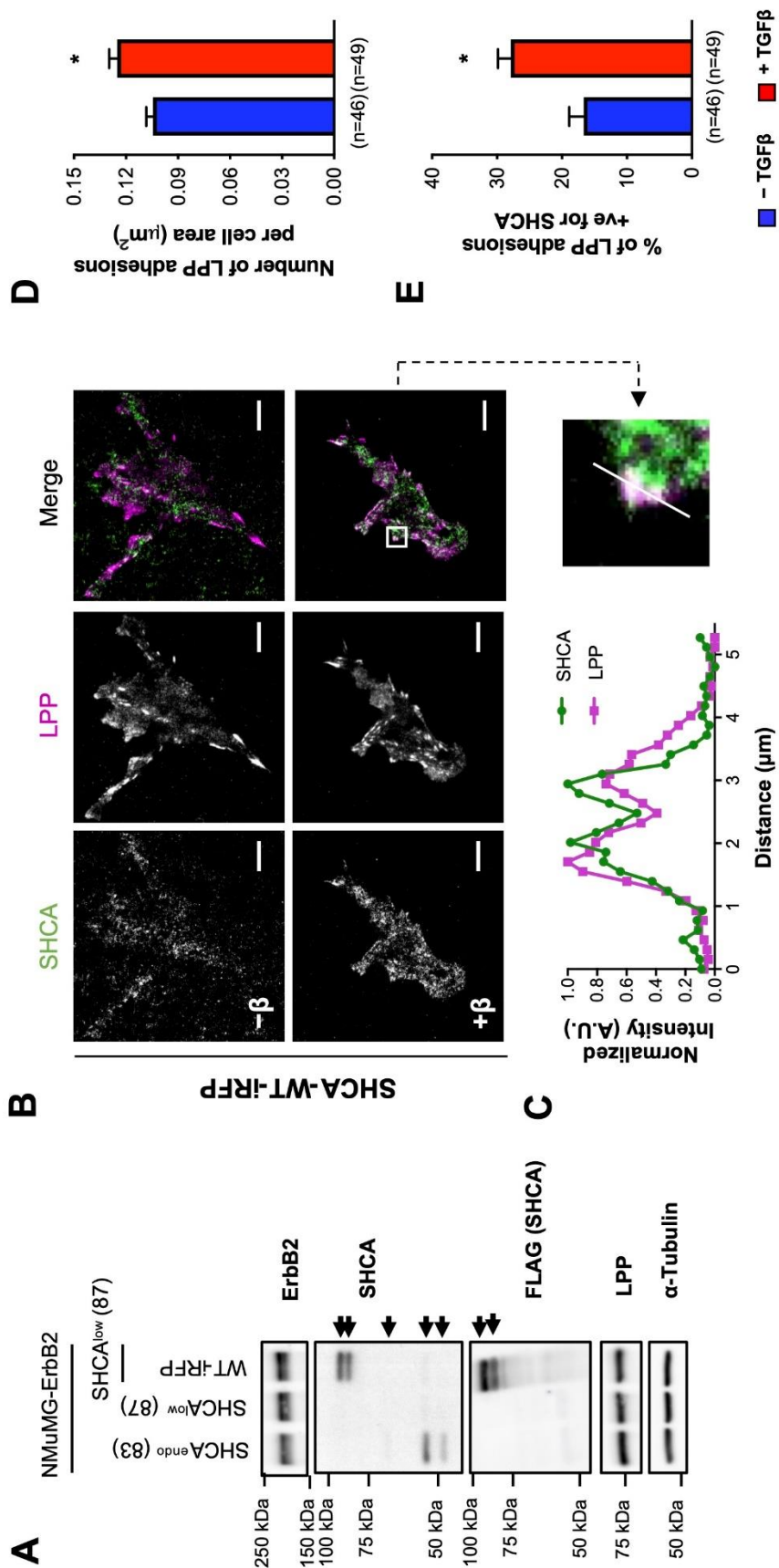


Figure 4.7. SHCA is found in adhesions and co-localizes with LPP upon TGF β treatment.

(A) Immunoblot analyses of whole-cell lysates showing SHCA (anti-SHCA or anti-FLAG antibodies) and LPP levels in ErbB2-NT/SHCA^{endo} (explant 83), ErbB2-NT/SHCA^{low} (explant 87), and ErbB2-NT/SHCA^{low}/SHCA-WT-iRFP (explant 87) cells. α -Tubulin was used as a loading control. (B) NMuMG ErbB2 cells expressing SHCA-WT-iRFP were infected with mCherry-LPP, seeded onto fibronectin-coated glass bottom dishes, and cultured in the absence or presence of TGF β (2 ng ml⁻¹) for 24 h. Cells were then fixed with 4% PFA and imaged using TIRF microscopy. *Scale bar*, 10 μ m. (C) Linescan analysis of SHCA and LPP from the *boxed region* in B. (D and E) Images were imported into Imaris to determine the average number of LPP-bearing adhesions and percentage co-localization with SHCA over the whole cell. Data were normalized by dividing the number of adhesions in each cell by the total cell area. Cell area was determined by drawing a contour around each cell. Adhesions were considered positive for SHCA if the mean intensity of the SHCA channel within the adhesion exceeded the diffuse cytoplasmic signal intensity. Data represent mean \pm S.E. (*error bars*) from three independent experiments. *, $p < 0.0012$; Mann–Whitney U test.

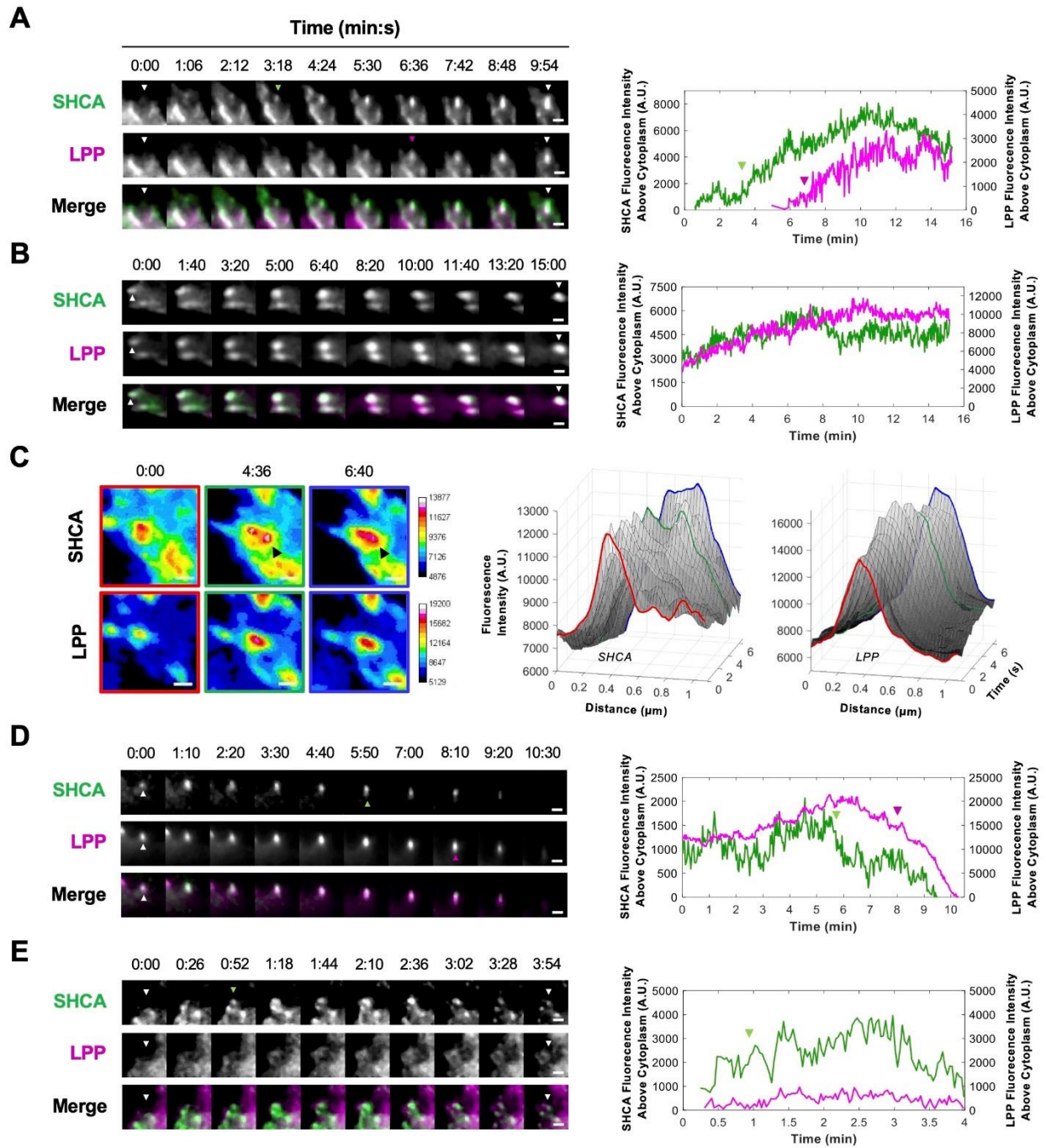


Figure 4.8. SHCA localization to adhesions precedes LPP recruitment. ErbB2-NT/SHCA^{low} (explant 87) cells expressing SHCA-WT-iRFP and EGFP-LPP were seeded onto fibronectin-coated glass bottom dishes and imaged with TIRF microscopy. **(A)** Time-lapse montage of a newly forming adhesion (see Movie S3). *White arrowheads* indicate the site of adhesion nucleation; *green arrowheads* indicate the appearance of SHCA; and *magenta arrowheads* indicate the appearance of LPP. Intensity traces for SHCA and LPP are depicted in the *adjacent graph*. **(B)** Time-lapse montage of a maturing adhesion (see Movie S4). *White arrowheads* indicate the adhesion of interest. Intensity traces for SHCA and LPP are depicted in the *adjacent graph*. **(C)** Pseudo-colored montage (16-color) of SHCA and LPP in a mature adhesion. The *black arrowhead* points to a second nucleation point in the SHCA channel. Linescan analysis was performed every 20 s to show the formation of a second SHCA nucleation point at the growing end of the adhesion. Fluorescence intensity of SHCA and LPP are plotted as a function of distance and time. **(D)** Time-lapse montage of a disassembling adhesion (see Movie S5). *White arrowheads* indicate the adhesion of interest; *green arrowheads* indicate the start of SHCA disassembly; and *magenta arrowheads* indicate the start of LPP disassembly. Intensity traces for SHCA and LPP are depicted in the *adjacent graph*. **(E)** Time-lapse montage of a short-lived adhesion (see Movie S6). *White arrowheads* indicate the site of adhesion nucleation, and *green arrowheads* indicate the appearance of SHCA. Intensity traces for SHCA and LPP are depicted in the *adjacent graph*. *Scale bars*, 2 μm .

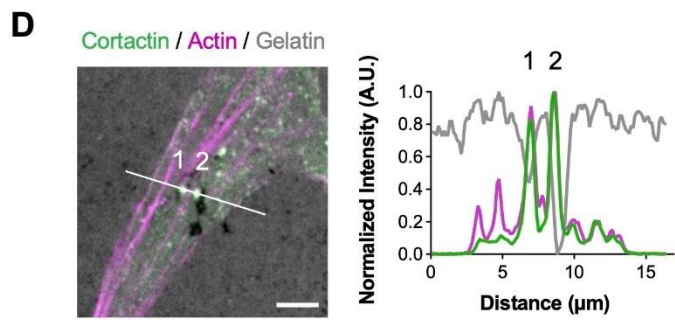
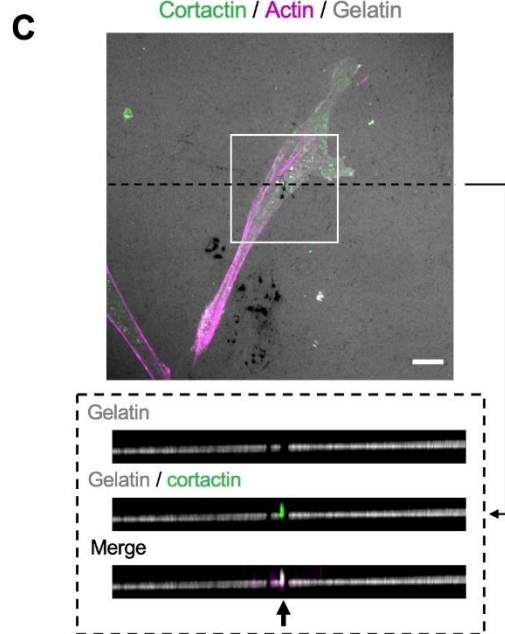
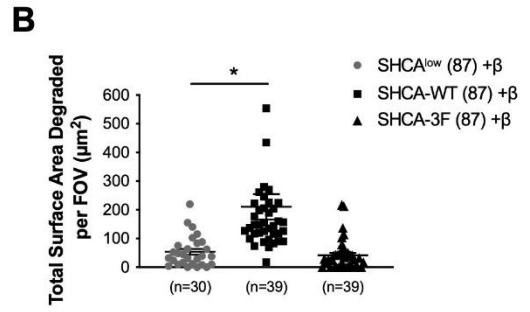
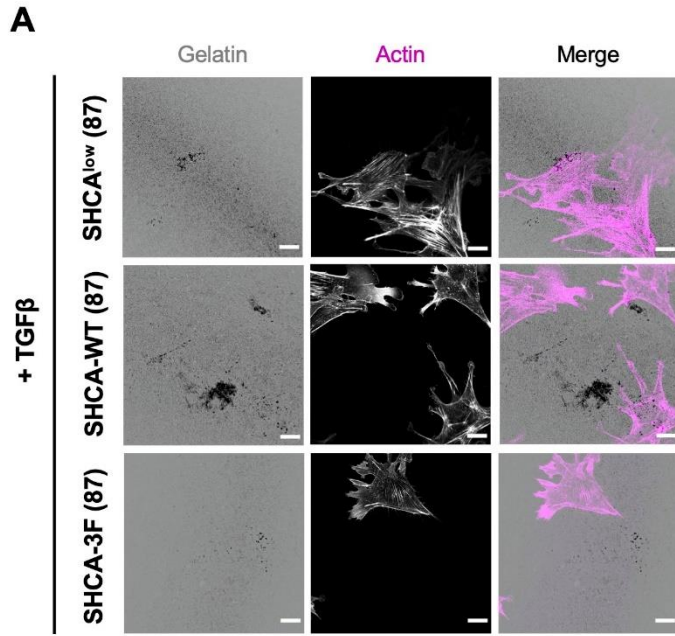


Figure 4.9. SHCA promotes breast cancer cell-mediated gelatin degradation. (A) ErbB2-NT/SHCA^{low}, ErbB2-NT/SHCA^{low}/SHCA-WT and ErbB2-NT/SHCA^{low}/SHCA-3F (explant 87) cells were pre-treated with TGFβ (2 ng ml⁻¹) for 24 h and seeded onto fluorescently-labelled gelatin. Cells were allowed to invade for 24 h before fixing with 4% PFA and staining with antibodies against cortactin and phalloidin (F-actin). Images were taken on a Zeiss CLSM using a Plan-Apochromat ×63/1.4 NA oil immersion DIC objective lens (1 pixel = 0.132 μm). *Scale bar*, 15 μm. (B) Images were imported into Imaris to determine the total surface area degraded per field of view (*FOV*). Data represent mean ± S.E. from three independent experiments. Individual data points are depicted with *symbols*. *, $p < 0.0001$; Mann–Whitney U test. (C) Z-stack acquisition was performed over a depth of 2.1 μm at 0.3 μm intervals. An orthogonal view (x - z plane, *dotted black box*) is presented to highlight an area of gelatin degradation where cortactin and actin are co-localized (*black arrow*). *Scale bar*, 10 μm. (D) Linescan analysis of *zoomed region* from C showing a slice view (x - y plane, *solid white line*) of cortactin and actin co-localization at sites of gelatin degradation. Intensity traces for cortactin, actin, and gelatin are shown in the *adjacent graph*. *Scale bar*, 5 μm.

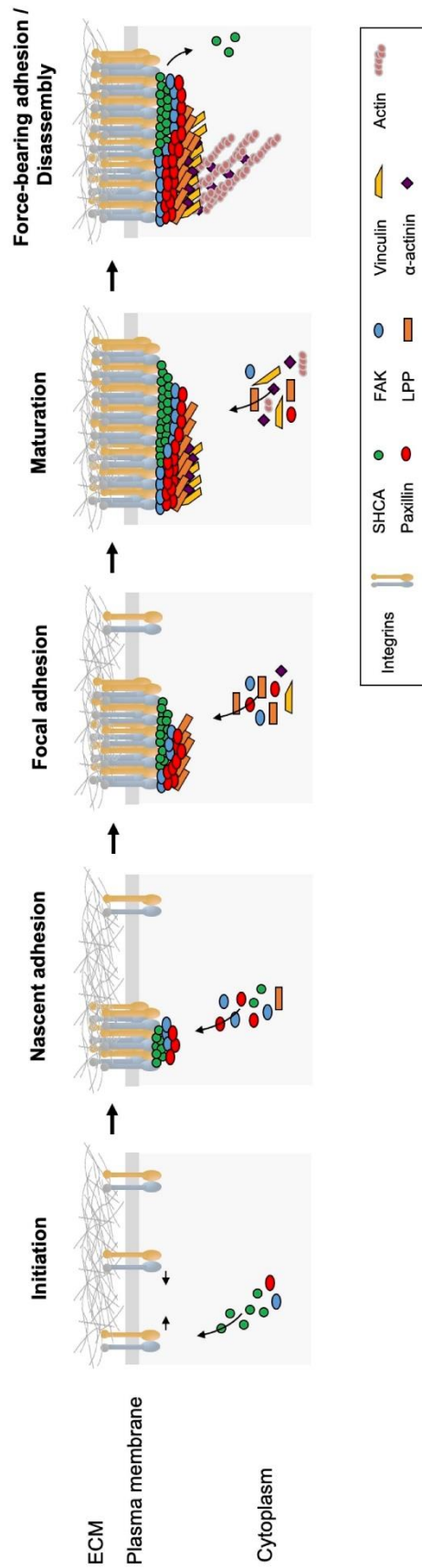


Figure 4.10. SHCA promotes the formation of small, dynamic adhesions in the presence of TGF β by acting as a nucleator of focal complex formation. A *schematic diagram* illustrates the proposed role of SHCA during the different stages of adhesion formation. During initiation, TGF β causes clustering of ErbB2 and integrins at the cell membrane. During nascent adhesion formation, SHCA associates with the cytoplasmic regions of several integrins both directly and indirectly. FAK and paxillin are also recruited. During focal adhesion formation, SHCA interacts with a variety of intracellular adapter/signaling molecules (including LPP) and enhances their recruitment to adhesions. During mature adhesion formation, SHCA exhibits treadmilling as more integrins are engaged. This promotes the recruitment of additional components to the growing end of an adhesion. In force-bearing adhesions, adhesion binding to actin cables establishes a link between the ECM and the cellular cytoskeleton for the generation of traction forces. During disassembly, SHCA begins to leave before other components.

4.11 SUPPLEMENTARY INFORMATION

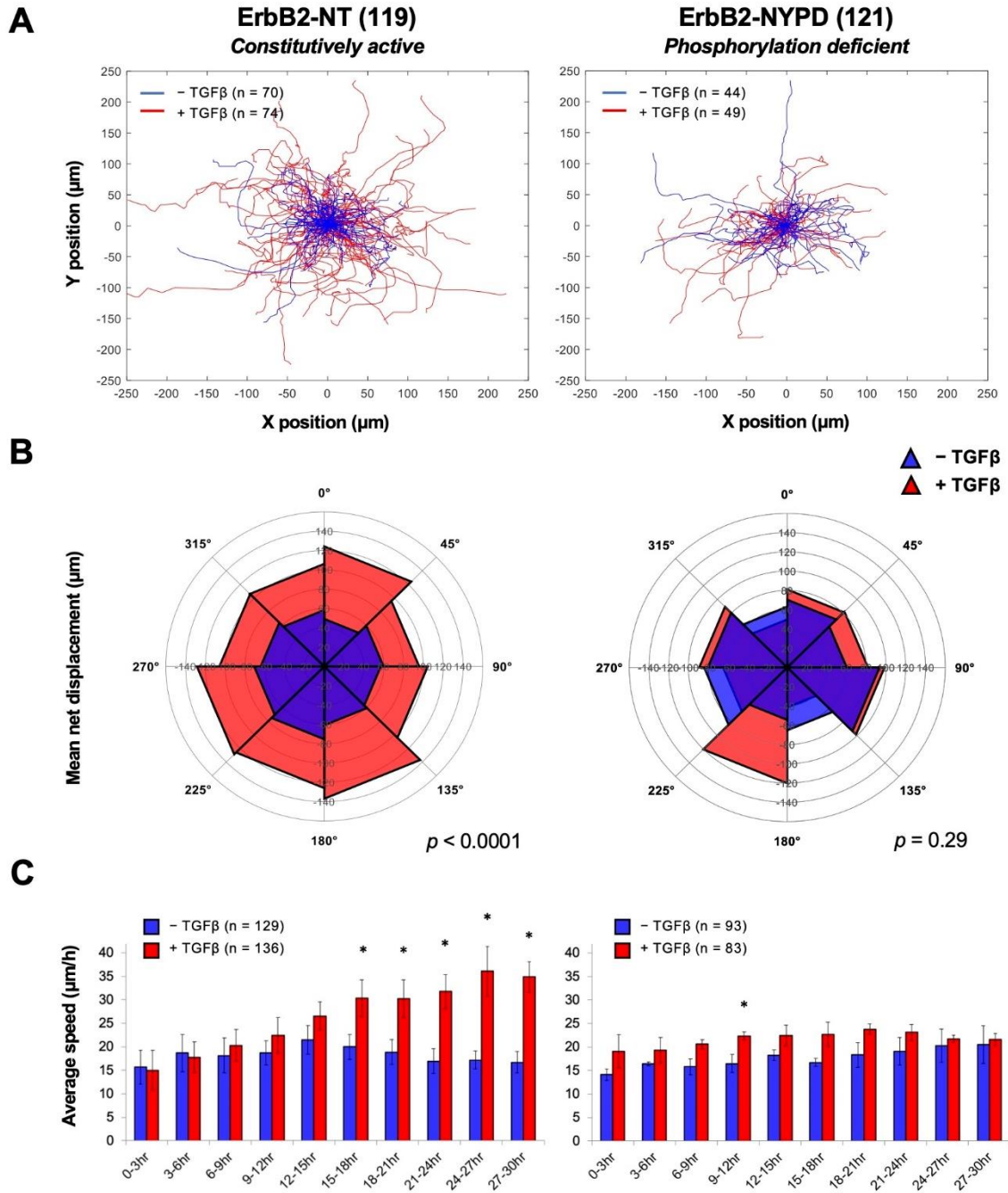


Figure S4.1. TGF β stimulates the migration of ErbB2-NT expressing breast cancer cells in independent mammary tumor explant cell lines. (A) Live-cell migration tracks for ErbB2-NT (explant 119) and ErbB2-NYPD (explant 121) cells are shown 18 h after treatment with or without TGF β (2 ng ml⁻¹). (B) Cell displacements from A were pooled into 45° segments based on their angle of trajectory and averaged to determine mean net displacement. (C) Average migration speed over time was calculated by determining the mean distance travelled between each imaging time point by all cells in A. Data represent mean \pm S.E. (*error bars*) from four (NT) or three (NYPD) independent experiments. *, $p < 0.05$; two-tailed Student's *t* test.

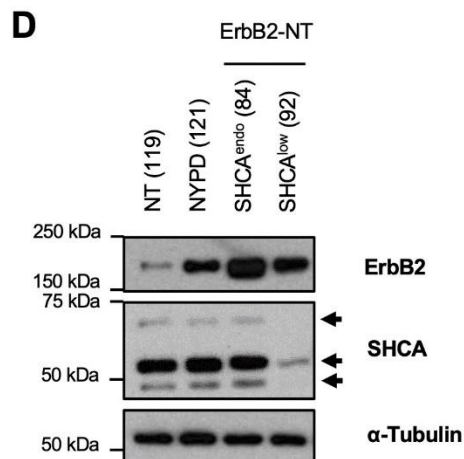
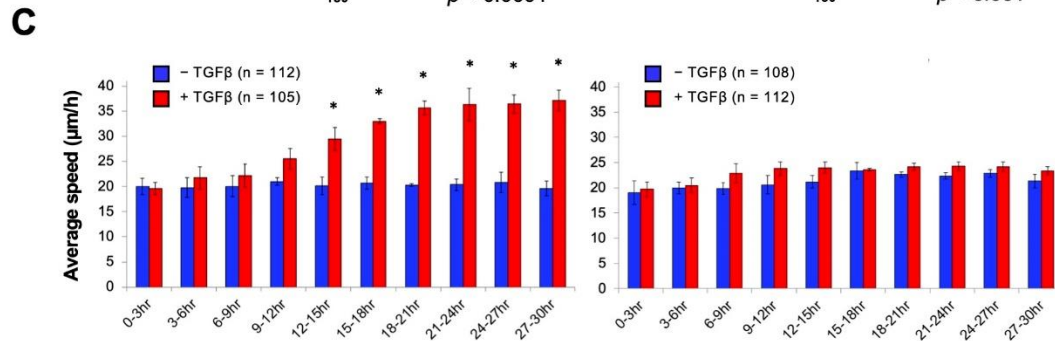
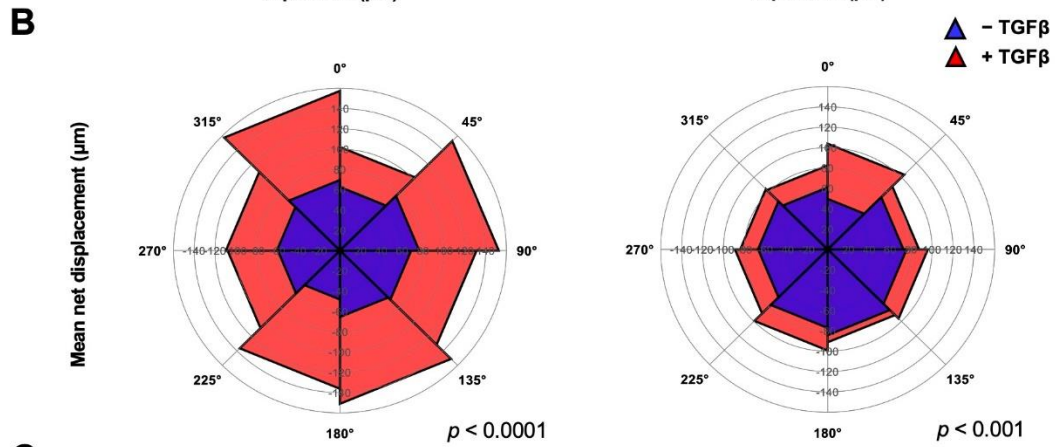
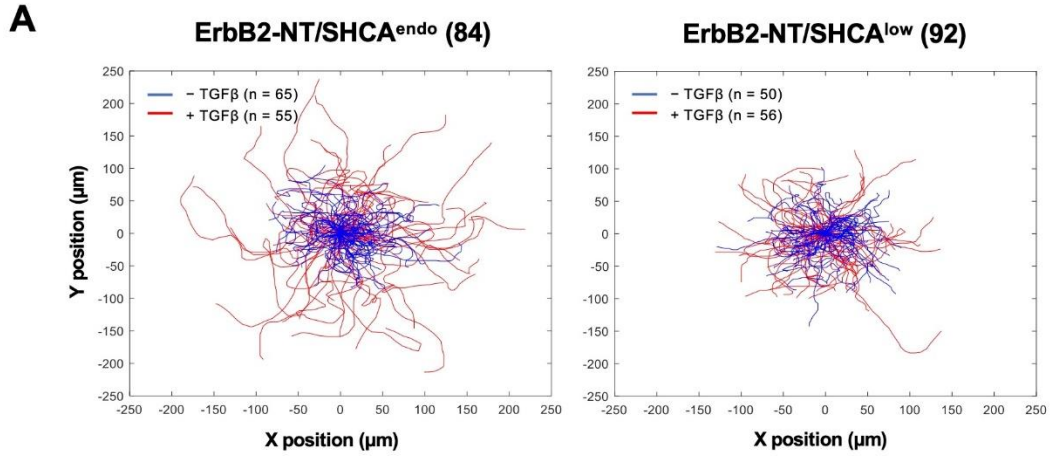


Figure S4.2. The SHCA adapter protein is required for TGF β -induced migration in independent mammary tumor explant cell lines. (A) Live-cell migration tracks for ErbB2-NT/SHCA^{endo} (explant 84) and ErbB2-NT/SHCA^{low} (explant 92) cells are shown 18 h after treatment with or without TGF β (2 ng ml⁻¹). (B) Cell displacements from A were pooled into 45° segments based on their angle of trajectory and averaged to determine mean net displacement. (C) Average migration speed over time was calculated by determining the mean distance travelled between each imaging time point by all cells in A. Data represent mean \pm S.E. (*error bars*) from three independent experiments. *, $p < 0.05$; two-tailed Student's t test. (D) Total cell lysates showing ErbB2 and SHCA levels in ErbB2-NT (explant 119), ErbB2-NYPD (explant 121), ErbB2-NT/SHCA^{endo} (explant 84) and ErbB2-NT/SHCA^{low} (explant 92) populations. α -Tubulin was used as a loading control.

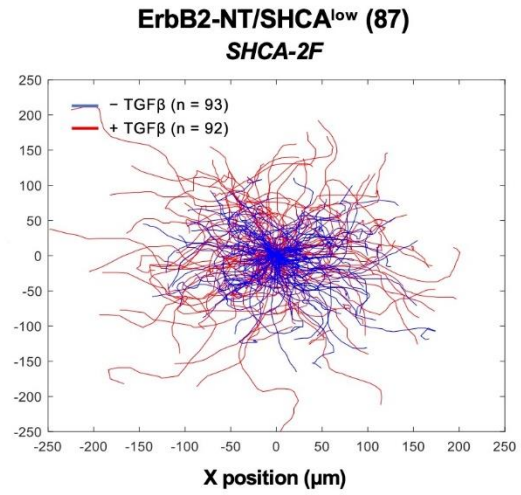
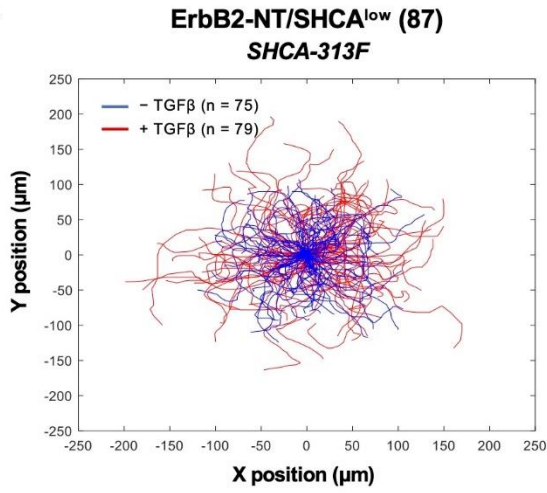
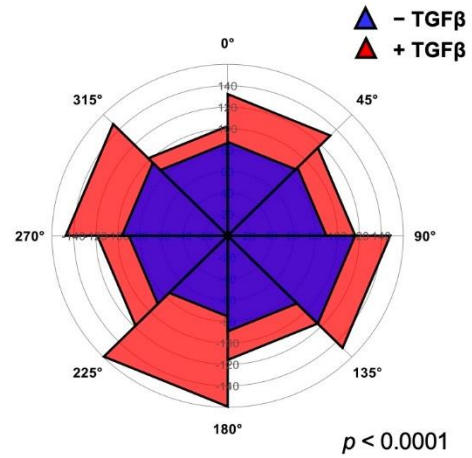
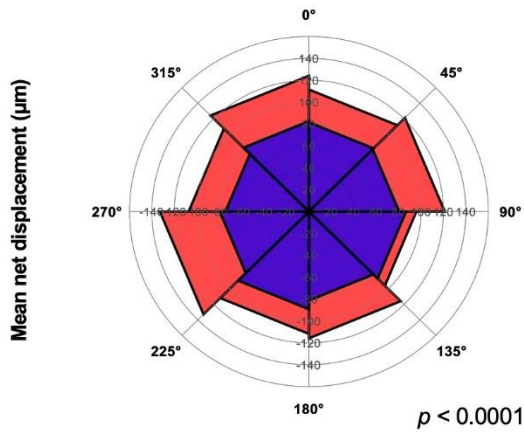
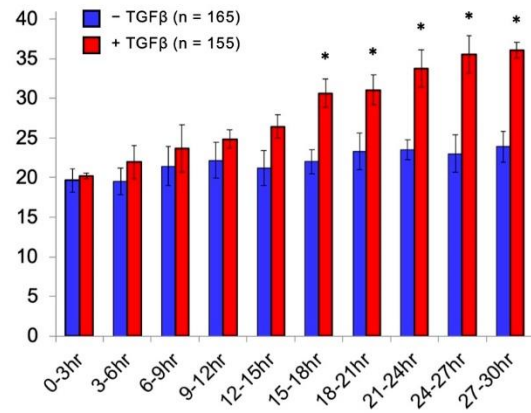
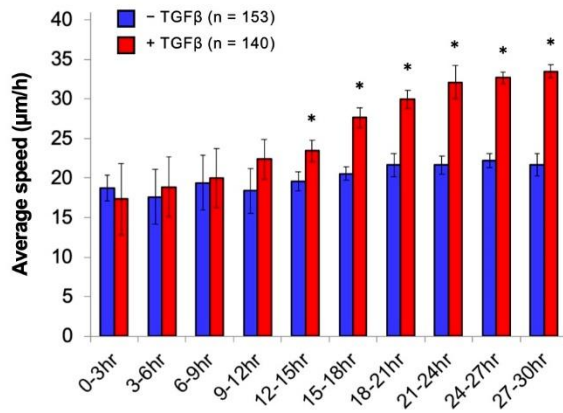
A**B****C**

Figure S4.3. SHCA phosphorylation on Y239/Y240 or Y313 is sufficient for enhanced cell migration in response to TGF β . (A) Live-cell migration tracks of ErbB2NT/SHCA^{low} (explant 87) cells re-expressing SHCA-313F or SHCA-2F after 18 h of treatment with or without TGF β (2 ng ml⁻¹). (B) Cell displacements from A were pooled into 45° segments based on their angle of trajectory and averaged to determine mean net displacement. (C) Average migration speed over time was calculated by determining the mean distance travelled between each imaging time point by all cells in A. Data represent mean \pm S.E. (*error bars*) from four independent experiments. *, $p < 0.05$; two-tailed Student's t test.

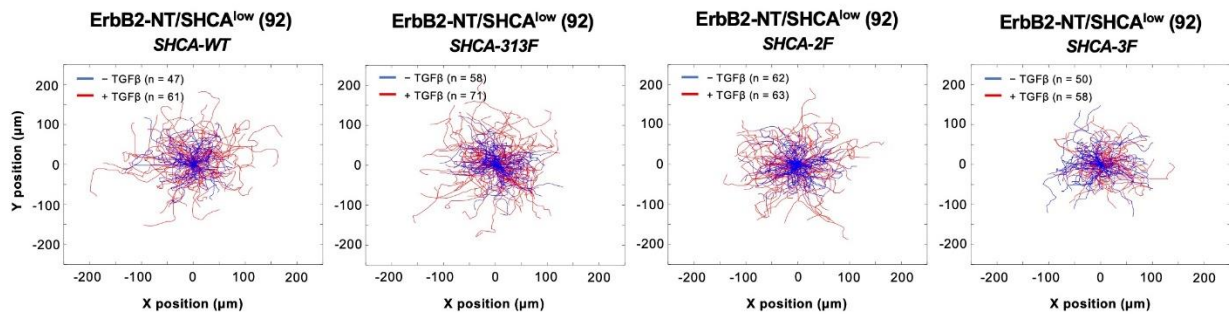
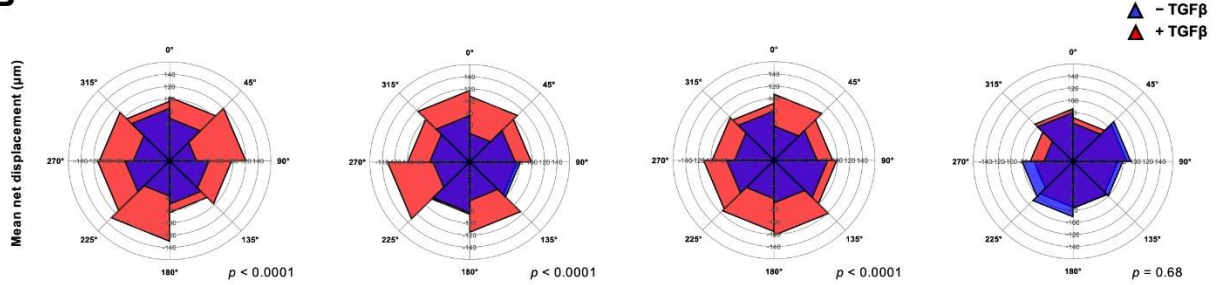
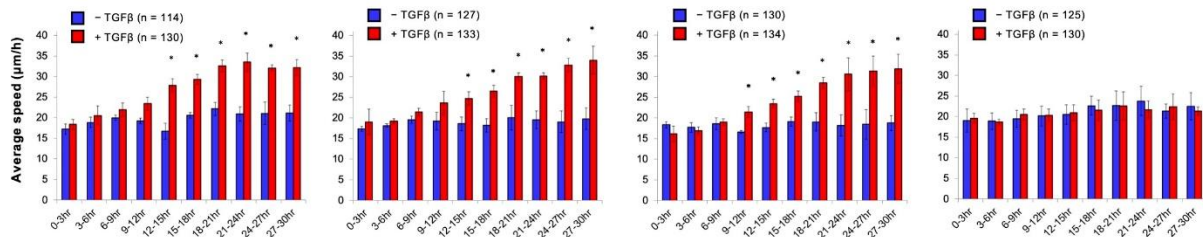
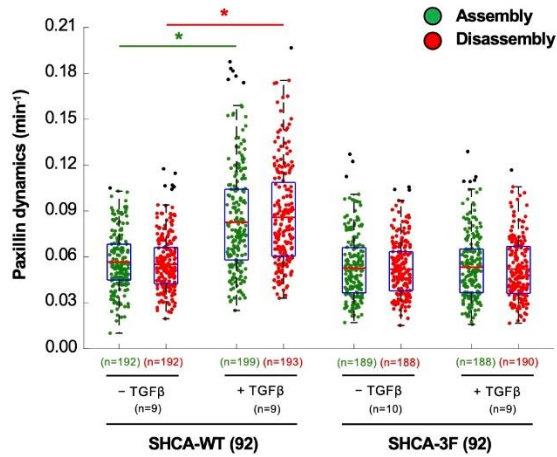
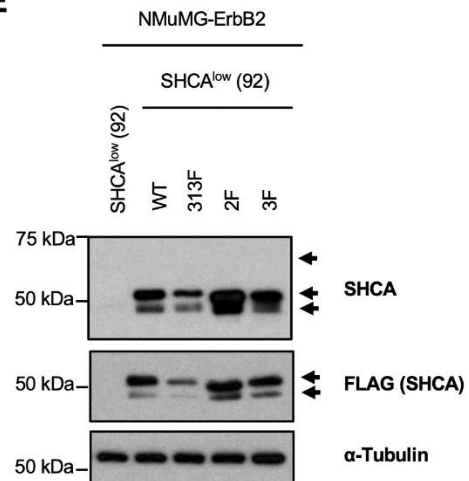
A**B****C****D****E**

Figure S4.4. Loss of SHCA phosphorylation on Y239/Y240/Y313 abrogates TGF β -induced migration of ErbB2-NT expressing breast cancer cells. ErbB2NT/SHCA^{low} (explant 92) cells re-expressing SHCA-WT, SHCA-313F, SHCA-2F or SHCA-3F. **(A)** Live-cell migration tracks for each condition are shown 18 h after treatment with or without TGF β (2 ng ml⁻¹). SHCA-3F cannot rescue TGF β -induced increase in migration. **(B)** Cell displacements from A were pooled into 45° segments based on their angle of trajectory and averaged to determine mean net displacement. **(C)** Average migration speed over time was calculated by determining the mean distance travelled between each imaging time point by all cells in A. Data represent mean \pm S.E. (*error bars*) from three independent experiments. *, $p < 0.05$; two-tailed Student's t test. **(D)** Adhesions in protrusive cell regions were tracked over time using TIRF microscopy for SHCA-WT and SHCA-3F cells. Cells were transfected with mCherry-paxillin 48 h prior to imaging and left untreated or treated with TGF β for 24 h. Data represent individual assembly (*green*) and disassembly (*red*) events from three independent experiments. *Top and bottom lines* of the *box* indicate 3rd and 1st quartile, respectively, while the *heavy central line* indicates mean. The *whiskers* extend up to 1.5 times the interquartile range. *Black dots* represent outliers. *, $p < 0.0001$ calculated from the cell averages for assembly and disassembly rates; two-tailed Student's t test. **(E)** Total cell lysates showing SHCA and FLAG levels. α -Tubulin was used as a loading control.

Table S4.1. Mass spectrometry data for BioID analysis to identify novel SHCA-interacting proteins

| <u>Uniprot Accession #</u> | <u>Gene Name</u> | <u>Spectral Counts (ShcA)</u> | <u>SpecSum</u> | <u>AvgSpec</u> | <u># Replicates</u> | <u>Spectral Counts (Mvc Cont)</u> | <u>SaintScore</u> | <u>logOddsScore</u> | <u>FoldChange</u> | <u>BFDR</u> | <u>Coverage</u> |
|----------------------------|------------------|-------------------------------|----------------|----------------|---------------------|-----------------------------------|-------------------|---------------------|-------------------|-------------|-----------------|
| P61161 | Actr2 | 14 10 10 | 34 | 11.33 | 3 | 2 3 3 | 0.96 | 2.77 | 4.25 | 0.01 | 33.00% |
| AZAWP8-2 | Arhgef10l | 9 12 7 | 28 | 9.33 | 3 | 0 0 0 | 1 | 11.37 | 93.33 | 0 | 17.00% |
| E9Q7D5 | Arhgef5 | 5 9 2 | 16 | 5.33 | 3 | 0 0 0 | 0.98 | 2.86 | 53.33 | 0 | 10.00% |
| Q9E528-2 | Arhgef7 | 4 4 2 | 10 | 3.33 | 3 | 0 0 0 | 0.98 | 2.86 | 33.33 | 0 | 4.90% |
| Q9D0A3 | Arpin | 9 9 4 | 22 | 7.33 | 3 | 0 0 0 | 1 | 6.45 | 73.33 | 0 | 45.00% |
| Q9JLQ0 | Cd2ap | 28 24 20 | 72 | 24 | 3 | 2 2 3 | 1 | 15.33 | 10.29 | 0 | 36.00% |
| A2RS22 | Coro1b | 42 46 24 | 112 | 37.33 | 3 | 3 3 3 | 1 | 17.72 | 12.44 | 0 | 56.00% |
| Q91VM1 | Crk | 4 9 4 | 17 | 5.67 | 3 | 0 0 0 | 1 | 6.45 | 56.67 | 0 | 39.00% |
| Q60598 | Ctnn | 20 26 29 | 75 | 25 | 3 | 1 1 2 | 1 | 19.99 | 18.75 | 0 | 31.00% |
| Q99K30 | Eps8l2 | 25 33 18 | 76 | 25.33 | 3 | 0 0 0 | 1 | 28.11 | 253.33 | 0 | 45.00% |
| A8CVP1 | Lims1 | 5 5 4 | 14 | 4.67 | 3 | 0 0 0 | 1 | 6.45 | 46.67 | 0 | 16.00% |
| Q88FW7 | Lpp | 7 16 6 | 29 | 9.67 | 3 | 2 1 0 | 0.98 | 3 | 9.67 | 0 | 34.00% |
| Q8CIN4 | Pak2 | 7 7 11 | 25 | 8.33 | 3 | 0 1 0 | 1 | 14.04 | 25 | 0 | 25.00% |
| Q9EPC1 | Parva | 4 3 3 | 10 | 3.33 | 3 | 0 1 0 | 0.96 | 2.91 | 10 | 0.01 | 13.00% |
| Q8CI51 | Pdlim5 | 21 27 13 | 61 | 20.33 | 3 | 2 1 1 | 1 | 10.61 | 15.25 | 0 | 41.00% |
| Q8V36-2 | Pxn | 2 4 2 | 8 | 2.67 | 3 | 0 0 0 | 0.96 | 2.86 | 26.67 | 0.01 | 11.00% |
| Q8C650 | Sept10 | 6 8 11 | 25 | 8.33 | 3 | 1 1 0 | 1 | 4.46 | 12.5 | 0 | 19.00% |
| Q8C1B7 | Sept11 | 27 28 28 | 83 | 27.67 | 3 | 5 8 5 | 1 | 12.48 | 4.61 | 0 | 46.00% |
| P42208 | Sept2 | 32 37 30 | 99 | 33 | 3 | 9 13 10 | 0.97 | 2.44 | 3.09 | 0.01 | 62.00% |
| Q9RLT4 | Sept6 | 10 14 9 | 33 | 11 | 3 | 0 2 0 | 1 | 4.67 | 16.5 | 0 | 37.00% |
| E9Q1G8 | Sept7 | 33 39 36 | 108 | 36 | 3 | 4 7 5 | 1 | 20.67 | 6.75 | 0 | 49.00% |
| P26039 | Tln1 | 38 56 17 | 111 | 37 | 3 | 1 2 0 | 1 | 17.76 | 37 | 0 | 21.00% |
| P35831 | Phn12 | 9 14 9 | 32 | 10.67 | 3 | 0 0 1 | 1 | 20.51 | 32 | 0 | 21.00% |
| Q3U1Q4 | Grb2 | 4 10 5 | 19 | 6.33 | 3 | 0 0 0 | 1 | 6.45 | 63.33 | 0 | 53.00% |
| Q9Z179 | Shcbbp1 | 7 9 9 | 25 | 8.33 | 3 | 0 0 0 | 1 | 11.37 | 83.33 | 0 | 17.00% |

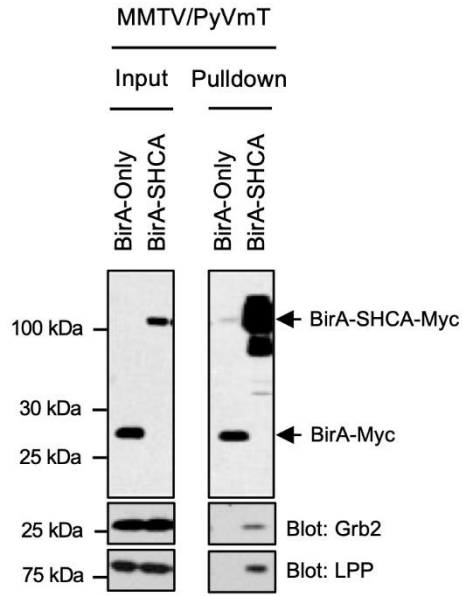


Figure S4.5. SHCA-BirA biotinylates LPP. MMTV/Middle T antigen expressing breast cancer cells harboring wildtype SHCA fused with BirA and Myc (Myc-SHCA-WT-BirA) or Myc-BirA (control) were used for validation of BioID proteomics. Cells were incubated with 50 μ M biotin for 24 h and collected for lysis. Whole cell lysates (input) and streptavidin pulldown (biotinylated proteins) were blotted with Myc and LPP antibodies. Data are representative of three independent experiments.

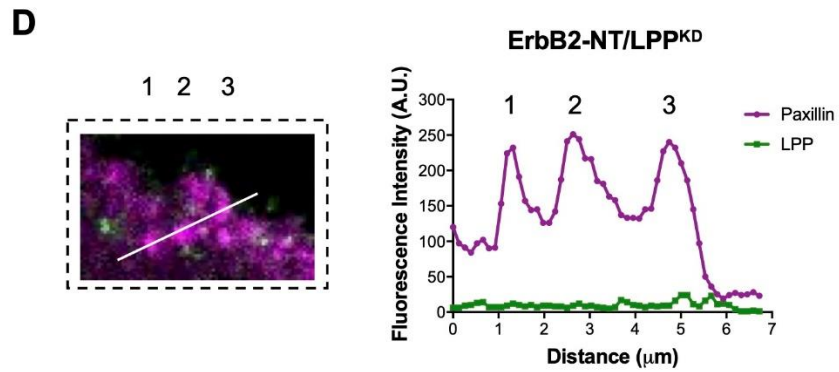
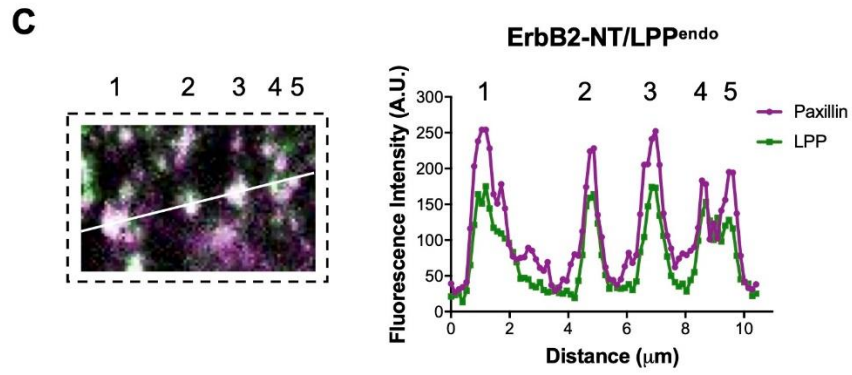
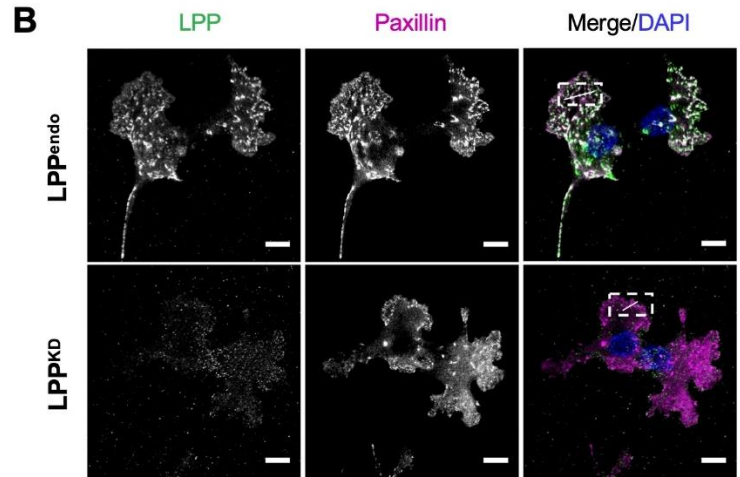
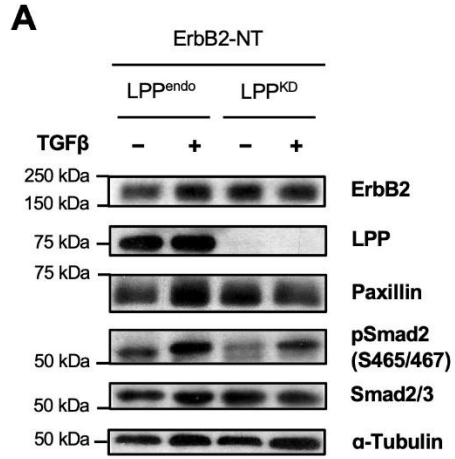


Figure S4.6. LPP is a component of cellular adhesions in breast cancer cells. (A) Immunoblot analysis of ErbB2, LPP, paxillin, Smad and pSmad (S465/467) levels in LPP^{endo} and LPP^{KD} cells 48 h after treatment with or without TGF β (2 ng ml⁻¹). α -Tubulin was used as a loading control. (B) Cells were seeded onto fibronectin-coated glass bottom dishes and transfected with mCherry-paxillin. Cells were then fixed with PFA and stained for LPP and DAPI. Images were taken on a Zeiss CLSM using a PlanApochromat $\times 63/1.4$ NA oil DIC objective lens. *Scale bar*, 10 μ m. (C and D) Linescan analysis of *zoomed regions* from B showing LPP and paxillin signal intensity in LPP^{endo} and LPP^{KD} cellular adhesions.

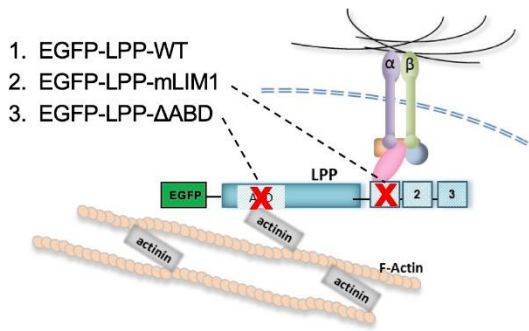
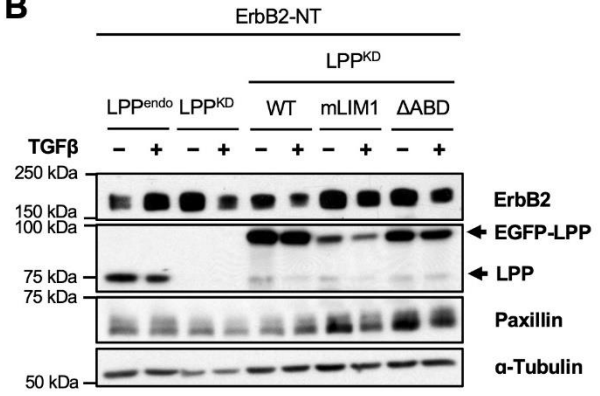
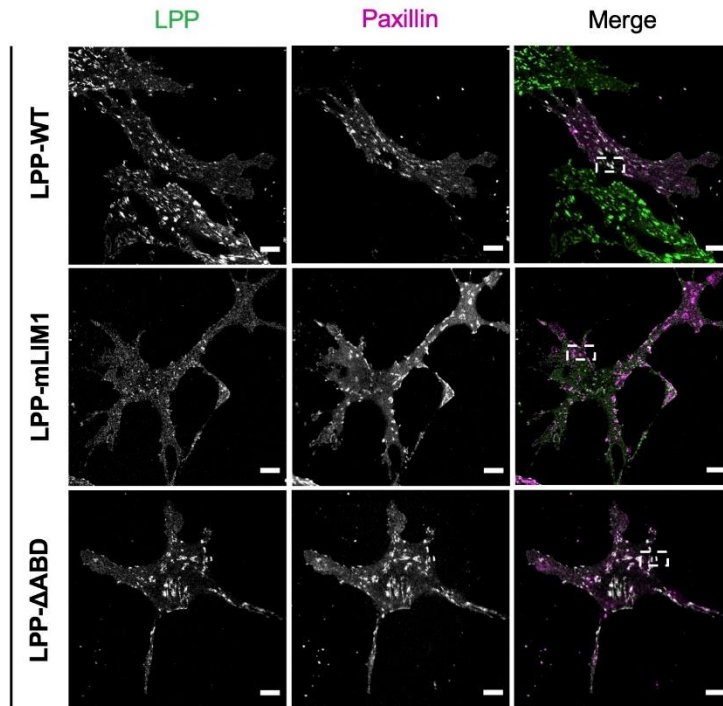
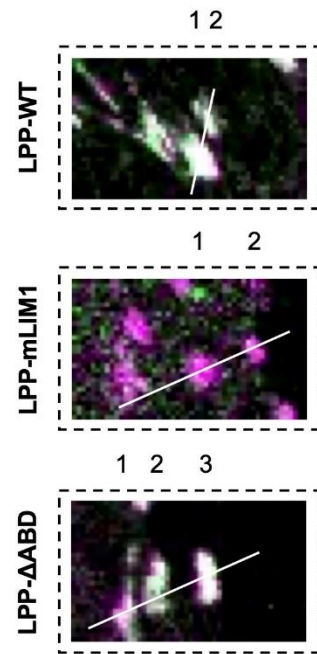
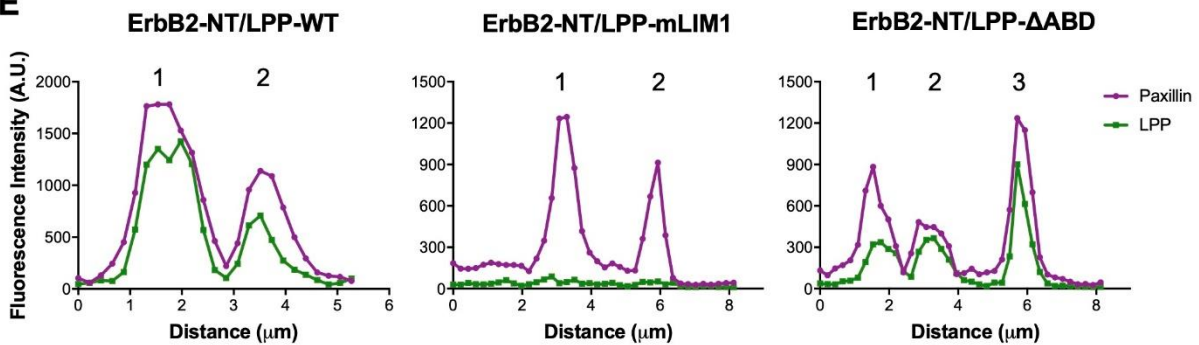
A**B****C****D****E**

Figure S4.7. LPP localization to adhesions requires intact LIM domains. (A) *Schematic diagram* of LPP showing its three LIM domains (1, 2, 3) and α -actinin binding domain (ABD). The LIM domains regulate LPP localization to adhesions, while the ABD domain allows LPP to interact with the actin cytoskeleton. EGFP-LPP-WT, EGFP-LPP-mLIM1 and EGFP-LPP- Δ ABD constructs were previously generated in our lab. (B) Immunoblot analysis showing successful re-expression of WT LPP and the two mutant constructs in LPP^{KD} cells. Cells were cultured in the absence or presence of TGF β (2 ng ml⁻¹) for 48 h and analyzed for ErbB2, LPP and paxillin expression. α -Tubulin was used as a loading control. (C) Cells were seeded onto fibronectin-coated glass bottom dishes and transfected with mCherry-paxillin. Cells were then fixed with PFA and stained for LPP. Images were taken on a Zeiss CLSM using a Plan-Apochromat \times 63/1.4 NA oil DIC objective lens. *Scale bar*, 10 μ m. (D and E) Linescan analysis of zoomed regions from C showing LPP and paxillin signal intensity in LPP-WT, LPP-mLIM1 and LPP Δ ABD cellular adhesions.

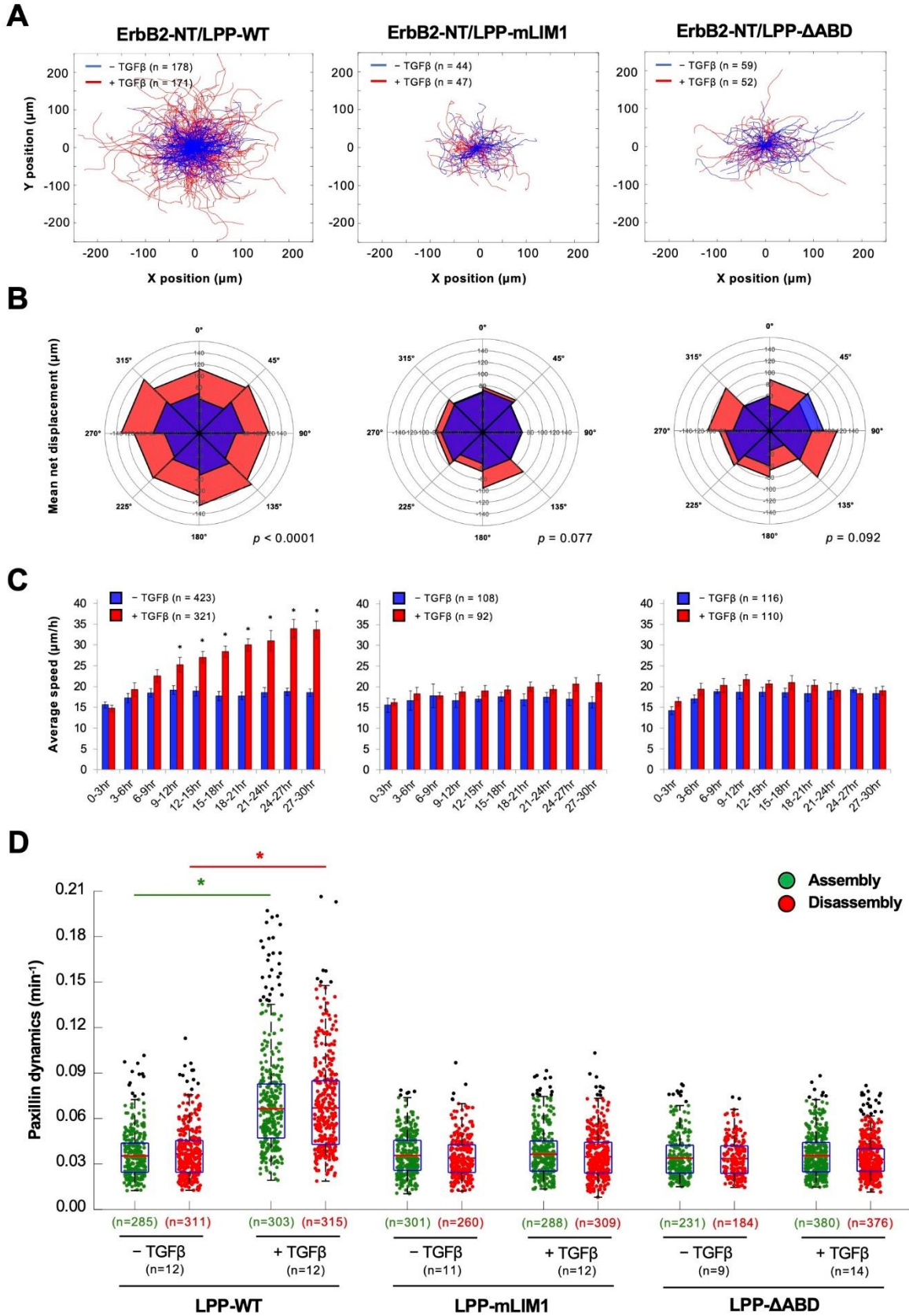


Figure S4.8. LPP must localize to adhesions and interact with the actin cytoskeleton for TGF β -induced migration and adhesion dynamics. ErbB2-NT/LPP^{KD} cells re-expressing LPP-WT, LPP-mLIM1 or LPP- Δ ABD. **(A)** Live-cell migration tracks for each condition are shown 18 h after treatment with or without TGF β (2 ng ml⁻¹). LPP-mLIM1 and LPP- Δ ABD cannot rescue TGF β -induced increase in migration. **(B)** Cell displacements from *A* were pooled into 45° segments based on their angle of trajectory and averaged to determine mean net displacement. **(C)** Average migration speed over time was calculated by determining the mean distance travelled between each imaging time point by all cells in *A*. Data represent mean \pm S.E. (*error bars*) from three independent experiments. *, $p < 0.05$; two-tailed Student's *t* test. **(D)** Adhesions in protrusive cell regions were tracked over time using TIRF microscopy. Cells were transfected with mCherry-paxillin 48 h prior to imaging and left untreated or treated with TGF β for 24 h. LPP-mLIM1 and LPP- Δ ABD cannot rescue TGF β -induced increase in adhesion dynamics. Data represent individual assembly (*green*) and disassembly (*red*) events from three independent experiments. *Top and bottom lines* of the *box* indicate 3rd and 1st quartile, respectively, while the *heavy central line* indicates mean. The *whiskers* extend up to 1.5 times the interquartile range. *Black dots* represent outliers. *, $p < 0.0001$ calculated from the cell averages for assembly and disassembly rates; two-tailed Student's *t* test.

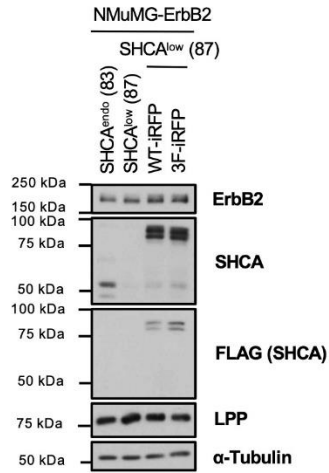
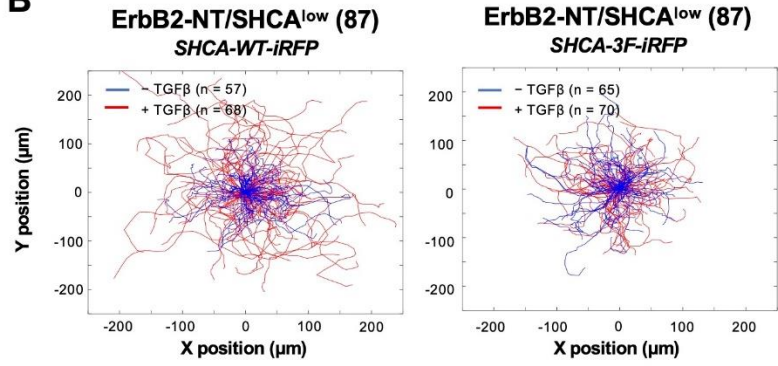
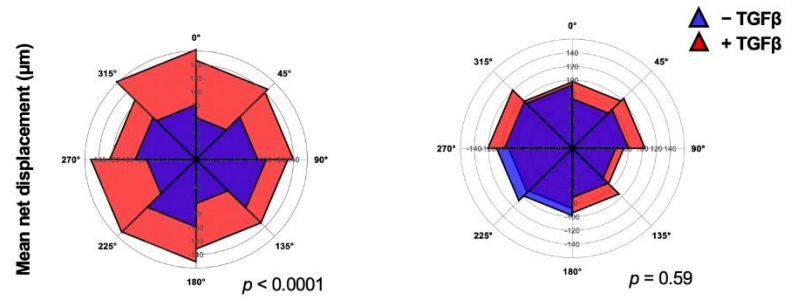
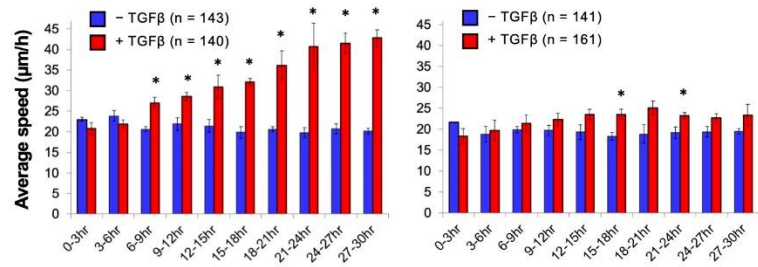
A**B****C****D**

Figure S4.9. Migratory behavior of breast cancer cells with reduced SHCA levels is successfully rescued with SHCA-WT-iRFP but not SHCA-3F-iRFP. (A) Immunoblot analyses of whole cell lysates showing ErbB2, SHCA (anti-SHCA or anti-FLAG antibodies) and LPP levels in SHCA^{endo} (explant 83), SHCA^{low} (explant 87), SHCA^{low}/SHCA-WT-iRFP (explant 87) and SHCA^{low}/SHCA-3F-iRFP (explant 87) cells. α -Tubulin was used as a loading control. (B) Live-cell migration tracks for SHCA-WT-iRFP and SHCA-3F-iRFP are shown after 18 h of treatment with or without TGF β (2 ng ml⁻¹). (C) Cell displacements from *B* were pooled into 45° segments based on their angle of trajectory and averaged to determine mean net displacement. (D) Average migration speed over time was calculated by determining the mean distance travelled between each imaging time point by all cells in *B*. Data represent mean \pm S.E. (*error bars*) from three independent experiments. *, $p < 0.05$; two-tailed Student's *t* test.

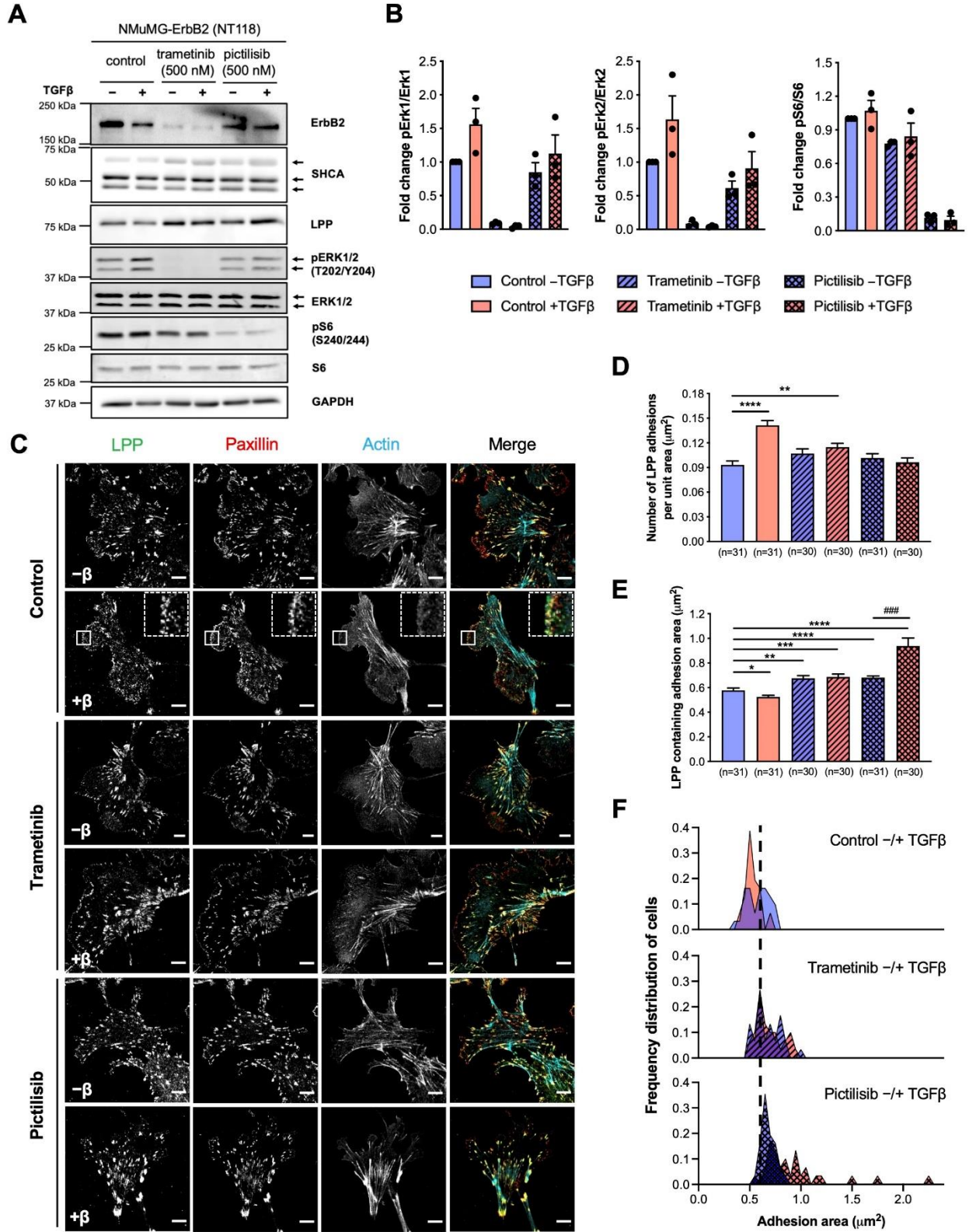


Figure S4.10. MAPK and PI3K signaling are required for the formation of small, dynamic adhesions in response to TGF β stimulation. (A) Immunoblot analyses of whole cell lysates obtained from NMuMG ErbB2-NT (explant 118) cells cultured in the absence or presence of TGF β (2 ng ml⁻¹) for 24 h and trametinib (500 nM) or pictilisib (500 nM) for 36 h. ErbB2, SHCA, LPP, pERK1/2 (T202/Y204), ERK1/2, pS6 (S240/244) and S6 levels are shown. GAPDH was used as a loading control. (B) Quantification of pERK1, pERK2 and pS6 levels in cells from A. Phosphorylation levels were normalized to total ERK1, ERK2 and S6 levels, respectively. Fold change was calculated relative to unstimulated control cells (control -TGF β). Data represent mean \pm S.E. (*error bars*) from three independent experiments. (C) ErbB2-NT (explant 118) cells were seeded onto fibronectin-coated glass bottom dishes and cultured under the same conditions as A. Cells were then fixed with 4% PFA and stained with antibodies against LPP, paxillin and phalloidin (F-actin). Images were taken on a Zeiss CLSM using a Plan-Apochromat \times 63/1.4 NA oil DIC objective lens (1 pixel = 0.264 μ m). *Scale bar*, 10 μ m. (D) Images were imported into Imaris to determine the average number of LPP adhesions over the whole cell for each condition. Data was normalized by dividing the number of adhesions in each cell by its total area. Cell area was determined by drawing a contour around each cell. Data represent mean \pm S.E. (*error bars*) from two independent experiments. **, $p < 0.01$, ****, $p < 0.0001$; two-tailed Student's t test. (E) The average size of LPP adhesions was determined from Imaris analyses performed in D. Data represent mean \pm S.E. (*error bars*) from two independent experiments. *, $p < 0.05$, **, $p < 0.01$, *** and ####, $p < 0.001$, ****, $p < 0.0001$; two-tailed Student's t test. (F) Frequency distribution of average adhesion area per cell determined from E. Data was binned into 0.05 μ m² segments.

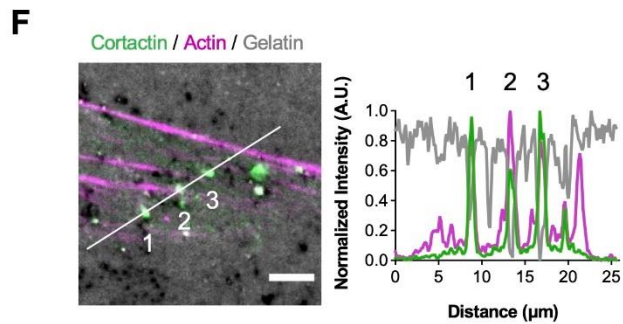
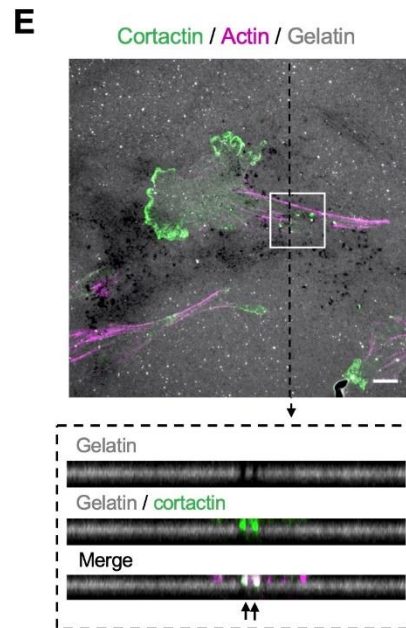
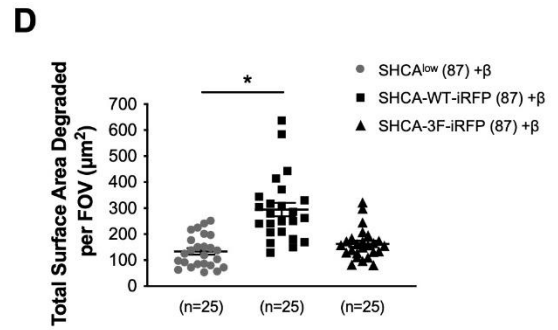
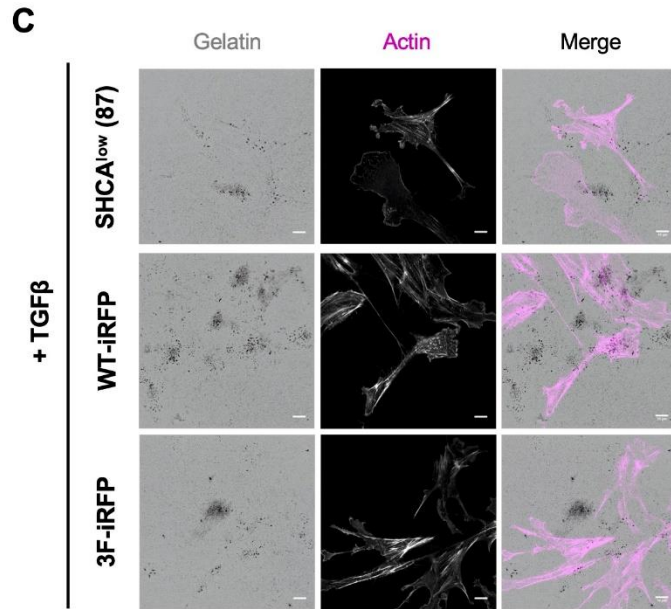
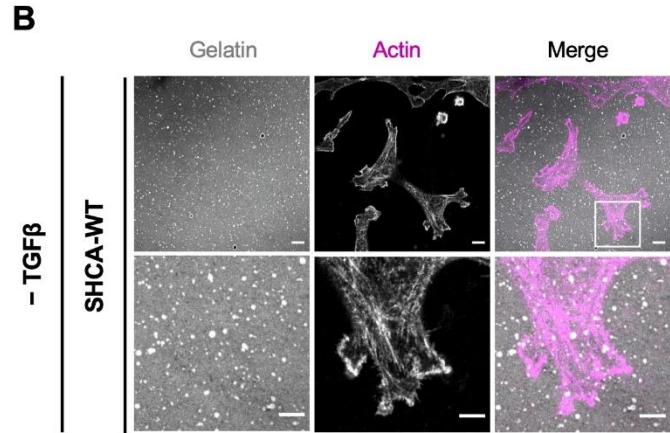
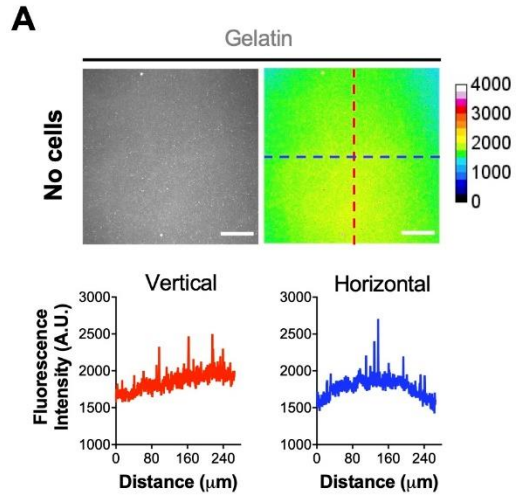


Figure S4.11. Invasive behavior of breast cancer cells is successfully rescued with SHCA-WT-iRFP but not SHCA-3F-iRFP. (A) Representative image of fluorescently labeled gelatin. Linescan analysis was performed to demonstrate the absence of deformities. *Scale bar*, 50 μm . (B) SHCA^{low}/SHCA-WT (explant 87) cells were seeded onto fluorescently labeled gelatin and cultured for 24 h. Cells fail to degrade gelatin in the absence of TGF β . *Scale bar*, 10 μm for *whole image* and 5 μm for *zoomed region*. (C) SHCA^{low} (explant 87), SHCA^{low}/SHCA-WT-iRFP (explant 87) and SHCA^{low}/SHCA-3F-iRFP (explant 87) cells were pre-treated with TGF β for 24 h and then plated onto fluorescently labeled gelatin for an additional 24 h. *Scale bar*, 10 μm . (D) Images were imported into Imaris to determine the total surface area degraded per field of view (*FOV*). Data represent mean \pm S.E. (*error bars*) from three independent experiments. *Individual data points* are depicted with symbols. *, $p < 0.0001$; Mann-Whitney U test. (E) Z-stack acquisition was performed over a depth of 2.38 μm at 0.26 μm intervals. An orthogonal view (x - z plane, *dotted black box*) is presented to highlight an area of gelatin degradation where cortactin and actin are co-localized (*black arrow*). *Scale bar*, 10 μm . (F) Linescan analysis of *zoomed region* from E showing a slice view (x - y plane, *solid white line*) of cortactin and actin colocalization at sites of gelatin degradation. Intensity traces for cortactin, actin and gelatin are shown in the *adjacent graph*. *Scale bar*, 5 μm .

CHAPTER 5 - LPP is a mechanosensitive protein that mediates HER2 and triple-negative breast cancer metastasis

Alex Kiepas^{1,2}, Elena Voorand^{1,3}, Alex Nowakowski^{1,4}, Sebastien Tabaries^{1,5}, Julien Senecal^{1,6}, Haruka Yoshie⁷, Ulrike Boehm⁸, Matthew G. Annis^{1,5}, Teng-Leong Chew⁸, Allen J. Ehrlicher⁷, Claire M. Brown^{2,9} and Peter M. Siegel^{1,3,5}

¹Goodman Cancer Research Centre, ²Department of Physiology, ³Department of Biochemistry, ⁴Department of Anatomy & Cell Biology, ⁵Department of Medicine, ⁷Division of Experimental Medicine, and ⁷Department of Bioengineering, McGill University, Montreal, Quebec, Canada;

⁸Advanced Imaging Center (AIC), Janelia Research Campus, Ashburn, Virginia, USA;

⁹Advanced BioImaging Facility (ABIF), McGill University, Montreal, Quebec, Canada

Manuscript in preparation

5.1 PREFACE

We have previously shown that the adapter/scaffold proteins p46/52ShcA and LPP are required for the migration and invasion of ErbB2⁺ breast cancer cells in response to TGF β [1-5]. Live-cell TIRF microscopy revealed that p46/52ShcA localization to cellular adhesions precedes LPP recruitment to these structures [5]. We found that LPP must localize to adhesions and interact with the actin cytoskeleton to mediate TGF β -enhanced adhesion dynamics. However, three outstanding questions remain. How does LPP modulate the ECM/cytoskeletal linkage to enhance migration in response to changing biophysical cues? What is precise localization of p46/52ShcA and LPP within adhesions? Does LPP promote metastasis to multiple organs in other breast cancer subtypes, such as triple-negative breast cancer (TNBC)? We explore these three questions in this chapter.

5.2 ABSTRACT

Lipoma preferred partner (LPP) is a member of the zyxin family of LIM proteins that has long been characterized as a promoter of mesenchymal migration. We have shown that LPP is an important mediator of ErbB2⁺ breast cancer cell migration and focal adhesion dynamics, particularly in cells that have undergone an epithelial-to-mesenchymal transition (EMT) induced by transforming growth factor beta (TGF β). Here, we employ a fluorescence resonance energy transfer (FRET)-based vinculin tension sensor (VinTS) to measure adhesion forces in ErbB2⁺ breast cancer cells. We find that TGF β enhances adhesion tension in protrusive cell regions. LPP and its α -actinin binding domain (ABD) are required for TGF β -mediated tension as cells expressing an shRNA against LPP (LPP-KD) or an ABD-deficient mutant (LPP- Δ ABD) do not exhibit increased adhesion forces. To understand how LPP modulates the ECM/cytoskeleton linkage, we acquired 3D super-resolution microscopy images of LPP, α -actinin and p46/52ShcA with an interferometric photoactivated localization microscope (iPALM). Preliminary results suggest that LPP- Δ ABD localizes to the same adhesion layer as α -actinin despite a deleted binding domain. We subsequently explored whether LPP is required for substrate stiffness sensing. We find that ErbB2⁺ cells with wildtype LPP prefer to migrate on intermediate stiffnesses (~40 kPa) and invade on soft (<5 kPa) and hard (>100 kPa) substrates. In contrast, cells with LPP-KD migrate at a constant speed (~25 μ m/h) on all stiffnesses. Finally, we investigated whether LPP regulates the migration, invasion and metastasis of other breast cancer subtypes to distinct metastatic sites. Human (MDA-MB-231) and mouse (4T1) triple-negative breast cancer (TNBC) cells require endogenous levels of LPP for TGF β -enhanced migration and invasion. Importantly, liver-metastatic cells (4T1-2776) with LPP-KD produce significantly less liver metastatic burden following splenic injection in mice. Taken together, LPP mediates cellular mechanosensitivity and enhances ErbB2⁺ and TNBC metastasis.

5.3 INTRODUCTION

Cell migration is a fundamental process involved in breast cancer progression to metastatic disease, where it contributes to tumor cell dissemination. Chemokines, cytokines and growth factors in the microenvironment support cell migration (chemotaxis) through the extracellular matrix (ECM) by modulating the actin cytoskeleton and focal adhesion dynamics [6, 7]. Breast cancer cells also sense and respond to ECM stiffness (durotaxis) through adhesion proteins [8, 9].

Adhesions provide a critical link between the ECM and the cytoskeleton. By coupling actin cables to the ECM, adhesions transmit increased mechanical load to the substrate, resulting in greater traction forces [10-13]. Conversely, adhesions can sense and respond to physical changes in the microenvironment [14]. Force application exposes cryptic binding sites within adhesion proteins, resulting in the recruitment of more binding partners [15-17]. As a result, adhesions form or enlarge when force increases and shrink or disassemble when force decreases [18-20]. This mechanosensitive property of adhesions is thought to regulate cell migration in response to substrate stiffness. Previous studies demonstrate that cells rapidly respond to changes in substrate stiffness [21, 22]. Cells grown on stiff substrates also possess larger adhesions than cells grown on soft substrates [23]. The relationship between tissue stiffness and breast cancer progression is also well documented [24-26]. Increased ECM/tissue rigidity promotes breast cancer cell migration/invasion out of the primary tumor and metastasis to essential organs [27-29]. Focal adhesion kinase (FAK), paxillin and vinculin appear to regulate mechanosensing in mouse embryonic fibroblasts (MEFs) [30, 31]; however, several other adhesion proteins have been implicated as well. Consequently, the molecular pathway regulating breast cancer cell migration in response to stiffness remains unknown.

Numerous proteins localize to adhesions and the interplay between them is still under study [32, 33]. We identified lipoma preferred partner (LPP) as an important adhesion protein in ErbB2-overexpressing breast cancer cells [1, 3, 5]. LPP localizes to adhesions and interacts with the actin cytoskeleton through its LIM and α -actinin binding domains, respectively, to enhance cell migration in response to TGF β . Interestingly, these contacts are required for the formation of small, dynamic adhesions [5]. LPP recruitment to adhesions is regulated in part by the adapter protein ShcA (p46/52 isoforms). Cells with reduced levels of p46/52ShcA (ShcA^{low}) do not exhibit TGF β -induced increases in LPP assembly and disassembly rates. Importantly, reduced expression of either adapter protein is sufficient to reduce breast cancer metastasis to the lungs [2, 3]. LPP has a

similar domain structure to zyxin, which has been shown to play a key role in mechanotransduction [34-39]. Thus, LPP may function as a mechanosensory and potentially mechanoregulatory protein in breast cancer cells.

Using a fluorescence resonance energy transfer (FRET)-based tension sensor (VinTS) and interferometric photoactivation localization microscopy (iPALM), we investigated the role of LPP in mediating force generation at adhesions and its 3D localization within these structures. We subsequently generated polydimethylsiloxane (PDMS) substrates of varying stiffness to investigate the response of breast cancer cells to changing substrate stiffness. Finally, we employed multiple triple-negative breast cancer (TNBC) models to demonstrate that LPP regulates the migration, invasion and metastasis of multiple breast cancer subtypes to distinct metastatic sites (lung and liver).

5.4 RESULTS

5.4.1 LPP enhances adhesion tension in response to TGF β

LPP is a scaffold protein that localizes to cellular adhesions and promotes single cell migration in response to TGF β stimulation [1, 5, 40]. We previously observed that NMuMG cells expressing constitutively active ErbB2 (ErbB2-NT) migrate further and faster when treated with TGF β [5]. TGF β stimulates the formation of smaller adhesions with increased dynamics. This phenotype requires LPP expression as knockdown (LPP^{KD}) prevents TGF β -enhanced adhesion dynamics and cell migration. Re-expression of LPP- Δ ABD failed to restore enhanced migration, suggesting that this domain provides a critical link between adhesions and the actin cytoskeleton required to regulate growth factor induced increases in migration (Fig. S5.1A).

Paxillin phosphorylation on tyrosine residues 31 and 118 leads to the formation of dynamic adhesions [41]. These residues are known to interact with vinculin [42, 43] and have been previously implicated in mechanotransduction in MEFs [31]. Interestingly, NMuMG-ErbB2 cells expressing LPP^{KD}, LPP- Δ ABD or LPP-mLIM (a mutant that cannot localize to adhesions) continue to exhibit TGF β -induced phosphorylation of paxillin Y31 and Y118 despite an inability to enhance adhesion dynamics (Fig. 5.1A). Thus, LPP interaction with α -actinin may play an important role in mechanotransduction in breast cancer cells.

To gain a more in-depth understanding of how LPP enhances single cell migration speeds, we employed a vinculin tension sensor to measure mechanical forces transmitted through individual adhesions [44]. VinTS contains teal and venus fluorescent proteins separated by an elastic linker that is calibrated to measure force with piconewton (pN) sensitivity (Fig. 5.1B). We transfected NMuMG-ErbB2 cells with VinTS and performed spectral imaging with linear unmixing on a confocal laser scanning microscope (CLSM) to assess changes in FRET following TGF β treatment (Fig. S5.1B,C). Live-cell imaging revealed that TGF β significantly reduced FRET (or increased adhesion tension) in protrusive cell regions (Fig. 5.1C,D). LPP expression was required for this phenotype, as NMuMG-ErbB2 cells with LPP^{KD} did not exhibit increased adhesion tension after TGF β treatment. Cells expressing LPP-WT successfully regained TGF β -enhanced adhesion tension, whereas cells expressing the LPP- Δ ABD mutant did not (Fig. 5.1E,F). Together, these results demonstrate that LPP interaction with α -actinin is required for increased force transduction at cellular adhesions following TGF β treatment.

Previous work exploring the nanoscale architecture of adhesions reveals three protein-specific strata: an integrin signaling layer containing paxillin, a force transduction layer containing vinculin, and an actin regulatory layer containing α -actinin [45]. Given that the LPP/ α -actinin linkage affects vinculin tension, we endeavoured to characterize the relative substructural localization of LPP-WT and LPP- Δ ABD within cellular adhesions using 3D super resolution microscopy. Photoactivated localization microscopy (PALM) and stochastic optical reconstruction microscopy (STORM) images of LPP and α -actinin were collected with an iPALM microscope (Fig. 5.2A,B). Preliminary results revealed that LPP- Δ ABD localizes to the same region as α -actinin despite an inability to bind this protein (Fig 5.2B). This data supports our finding that the ABD domain provides a critical contact point between LPP and α -actinin; LPP localization to adhesions alone is not sufficient to enhance adhesion tension. We previously identified p46/52ShcA as an important adapter protein that regulates LPP recruitment to adhesions in response to TGF β [5]. Therefore, we subsequently attempted to capture the spatial relationship between p46/52ShcA and LPP within adhesions. NMuMG-ErbB2 cells are difficult to transfect and stable expression of mEos2 abrogates photoconversion (data not shown). As an alternative, we introduced p46/52ShcA into another breast cancer cell line (4T1-2776). iPALM microscopy revealed that p46/52ShcA localized closer to the plasma membrane than LPP (Fig. 5.2C). Together, these results suggest that p46/52ShcA is localized to the signaling layer while LPP interacts with α -actinin in the force transduction layer.

5.4.2 LPP is required for cellular mechanosensitivity

ECM deposition, modification, degradation and organization are modified during breast cancer progression [46]. These modifications impact tissue stiffness and lead to changes in cellular behavior [12, 21, 22, 28, 29, 47-49]. While the normal mammary gland is thought to have a stiffness of \sim 5-7 kPa, malignant lesions may reach \sim 147 \pm 40 kPa [24-26]. Previous data on cell invasion [28, 29] and cell migration [50, 51] suggest that cells prefer to invade on soft and hard substrates and migrate on intermediate stiffnesses (Fig. 5.3A). To test this hypothesis, we generated polydimethylsiloxane (PDMS) substrates coated with fibronectin or fluorescent gelatin (Fig. 5.3B). The PDMS substrates were generated on glass bottom coverslips and tuned to a specific stiffness (1-100 kPa). NMuMG-ErbB2 cells expressing LPP-WT exhibited the fastest migration speeds on 40 kPa (Fig. 5.3C). TGF β stimulation increased cell migration on all stiffnesses without

affecting cell preference for stiffness. Next, we explored the impact of LPP expression on cellular mechanosensing. Given its newly defined role in force mechanotransduction (Fig. 5.1), we hypothesized that LPP localization to adhesions is required for extracellular force transmission. Indeed, NMuMG-ErbB2 cells with LPP^{KD} did not respond to substrate stiffness and continued to migrate at approximately the same speed on all stiffnesses (Fig. 5.3D). Finally, we investigated cell invasion in response to stiffness. NMuMG-ErbB2 cells degrade gelatin very weakly even in the presence of TGF β . Therefore, we employed an ErbB2⁺ ductal carcinoma cell line, HCC1954, which exhibited increased gelatin degradation following TGF β treatment (Fig. S5.2). In accordance with our hypothesis, we found HCC1954 cells degraded gelatin maximally on 90 kPa where NMuMG-ErbB2 / LPP^{KD} / LPP-WT cell migration was only ~25% of its maximum (Fig. 5.3E). In contrast, HCC1954 cells degraded minimally on 20-30 kPa where NMuMG-ErbB2 cells started to approach maximal migration speed (Fig. 5.3E). Further work is required to determine the effect of LPP knockdown on stiffness-mediated cell invasion. HCC1954 cells with LPP^{KD} exhibited significantly reduced invasion (Fig. S5.2), making such analysis difficult to interpret.

5.4.3 LPP expression affects the migration and invasion of triple-negative breast cancer cells

Breast cancer is a heterogenous disease comprised of distinct molecular subtypes. In addition to ErbB2⁺ breast cancers, gene expression profiling has identified luminal A, luminal B and TNBC subtypes [52-54]. TNBCs do not express estrogen receptor, progesterone receptor or ErbB2. Thus, a lack of well-defined clinical targets results in poor overall outcomes for patients with this subtype [55].

TNBC cells often co-express luminal and myoepithelial markers indicative of a partial EMT [56-61]. These cells can often be driven to undergo further EMT resulting in the development of claudin-low breast tumors. Indeed, TGF β reduced E-cadherin levels in murine 4T1 cells resulting in the loss of cell-cell junctions (Fig. 5.4A,B). TGF β also enhanced FAK phosphorylation on Y397, which is required for efficient cell migration [41, 62] (Fig. 5.4A,B). Therefore, we investigated the importance of LPP in TNBC breast cancer cell migration and invasion.

Rose plots of 4T1 cells expressing endogenous LPP, a scrambled siRNA control (siRNA scr), or an siRNA against LPP (siRNA LPP) demonstrated that LPP expression is required for TGF β -enhanced migration of TNBC cells (Fig. 5.4C). 4T1 cells expressing endogenous LPP or control siRNA migrated further and faster following TGF β treatment (Fig. 5.4C,D). In contrast,

cells with LPP knockdown were unable to enhance single cell migration, despite similar levels of E-cadherin and FAK phosphorylation (Fig. 5.4A-D). Similarly, human MDA-MB-231 cells expressing endogenous LPP or an empty vector control (EV) migrated further and faster in response to TGF β , while LPP knockdown (shRNA LPP) abrogated this effect (Fig. 5.4E-G). We subsequently seeded 4T1 and MDA-MB-231 cells on fluorescent gelatin to assess cell invasion. Cells cultured in the presence of TGF β exhibited increased invasion (Fig. 5.4H,I; Fig. S5.3). In contrast, TGF β failed to increase the invasion of MDA-MB-231 cells lacking LPP (Fig. 5.4H,I). Collectively, these results demonstrate that LPP expression affects ErbB2⁺ and TNBC breast cancer cell migration and invasion.

To further characterize the role of LPP in TNBC cells, we quantified the migration and invasion of 4T1 sub-populations that preferentially metastasize to the lungs (4T1-526) or liver (4T1-2776). Lung-metastatic and liver-metastatic cells were previously generated in our lab [63, 64] by serial selection *in vivo* (Fig. 5.5A). 4T1-526 and -2776 cells expressing endogenous LPP or a control shRNA against luciferase (LucA) migrated further and faster following TGF β treatment (Fig. 5.5B-G). TGF β also significantly enhanced gelatin degradation of both cell lines (Fig. 5.5H,I). As expected, LPP knockdown (shRNA LPP) in 4T1-526 and -2776 cells abrogated TGF β -enhanced cell migration (Fig. 5.5B-G). 4T1-526 cells with LPP knockdown also failed to exhibit TGF β -enhanced cell invasion (Fig. 5.5H). While 4T1-2776 cells with LPP knockdown exhibited a small increase in cell invasion following TGF β stimulation, the level of degradation observed was significantly reduced compared to LucA cells (Fig. 5.5I). Thus, LPP expression is required for the migration and invasion of TNBC cells that metastasize to the lungs and liver.

5.4.4 LPP enhances adhesion dynamics in liver-metastatic breast cancer cells

Mesenchymal migration relies on integrin-based adhesions to generate traction forces for movement [65-67]. Our previous results indicate that LPP is required for TGF β -enhanced adhesion dynamics in ErbB2⁺ cells that have undergone an EMT and metastasize to the lungs [3, 5]. Given the parallels between ErbB2⁺ and TNBC cell migration, experiments were conducted to determine whether LPP also regulates the formation of dynamic adhesions in liver-metastatic cells. 4T1-2776 LucA and LPP knockdown cells were infected with fluorescently labelled paxillin and seeded onto fibronectin-coated glass bottom dishes (Fig. 5.6A). Paxillin is an adapter protein found in all adhesion classes (nascent adhesions, focal complexes, focal adhesions and fibrillar adhesions) [41,

68], allowing for the analysis of adhesion size and number. In line with our results from NMuMG-ErbB2 cells [5], a decrease in adhesion size and an increase in adhesion number was observed in 4T1-2776 control knockdown (LucA) cells treated with TGF β (Fig. 5.6A,B). In contrast, LPP knockdown cells treated with TGF β continued to exhibit large adhesions and maintained the same number of adhesions as unstimulated LucA cells (Fig. 5.6A,B). Interestingly, LPP knockdown reduced the number of adhesions in unstimulated shRNA LPP cells below baseline; TGF β treatment subsequently returned adhesion number to the same level as unstimulated LucA cells. To test the biological significance of these findings, we performed live-cell imaging of 4T1-2776 cells using a spinning disk confocal microscope. Analysis of mean fluorescence intensity data from individual paxillin-bearing adhesions revealed that TGF β enhanced average adhesion assembly and disassembly rates in LucA cells (Fig. 5.6C). In contrast, TGF β reduced adhesion assembly and disassembly rates in LPP knockdown cells (Fig. 5.6C). While these results were not significant for cell averages ($p=0.0688$ and 0.1215 , respectively; Mann-Whitney U test), they were highly significant when all assembly and disassembly events were pooled together ($p<0.0001$; Mann-Whitney U test). Hence, the return to baseline adhesion number seen in TGF β -treated LPP knockdown cells was likely due to the formation of larger, more stable adhesions (Fig. 5.6A, *lower right image*).

5.4.5 LPP promotes TNBC metastasis to the liver

Previous work by our group demonstrated that LPP is required for ErbB2⁺ breast cancer metastasis to the lungs [3]. While LPP expression was dispensable for mammary tumor growth, loss of LPP reduced the number of circulating tumor cells and surface lesions observed on the lungs [3]. Based on the novel finding here that LPP affects the migration and invasion of 4T1-2776 cells (Fig. 5.5), we wondered whether LPP expression is required for efficient liver metastasis. 4T1-2776 parental, control knockdown (LucA) and LPP knockdown populations were injected into spleens of BALB/c mice to assess liver metastasis (Fig. 5.7A). After 2.5 weeks post splenic injection, analysis of H&E sections revealed that LPP knockdown significantly reduced the area of the liver occupied by metastatic lesions (Fig. 5.7B,C). Taken together, our results implicate LPP as an important mechanosensitive protein involved in breast cancer metastasis to the lungs and liver.

5.5 DISCUSSION

In this study, we explored the role of LPP as a mechanoregulatory and mechanosensory protein involved in breast cancer cell migration. We show that LPP provides a critical link between the ECM and the actin cytoskeleton, which facilitates increased adhesion tension following TGF β stimulation. LPP interaction with α -actinin in adhesions may allow cells to exert increased traction forces on the underlying substrate [11], resulting in faster cell migration. Conversely, this interaction allows cells to sense changes in substrate stiffness and adjust cellular behavior accordingly. Beyond its function in ErbB2⁺ breast cancer cells, we delineate the role of LPP in triple-negative breast cancer cells. Murine and human TNBC cells require LPP expression for TGF β -enhanced cell migration and invasion. In line with previous observations [5], we show that LPP promotes the formation of small, dynamic adhesions in liver-metastatic cells.

Cells cultured on two-dimensional ECM substrates rely on adhesions to sense stiffness. Adhesions are complex structures composed of >200 different proteins with >690 interactions [32, 33]. A few mechanosensitive proteins have been previously identified, including vinculin [30, 31, 69], talin [15, 70, 71] and zyxin [34-39]; however, adhesion composition and protein interactions vary between cell types and the type of ECM engaged. Consequently, the mechanisms that allow cancer cells to sense the biophysical microenvironment require further investigation. Here, we provide compelling evidence that LPP, a member of the zyxin family of LIM proteins [72], is required for substrate stiffness sensing in ErbB2⁺ breast cancer cells. Previous studies show that cyclic mechanical stretching of cardiac myocytes decreases LPP expression and membrane localization [73, 74]. Similarly, shear stress waveforms and substrate stiffness appear to affect LPP expression and adhesion localization in smooth muscle cells [75]. Our imaging results show that ErbB2⁺ cells with wildtype LPP prefer to migrate on intermediate stiffnesses (~40 kPa); slower migration speeds are observed on soft (<5 kPa) and hard (>100 kPa) substrates where invasion is increased. In contrast, cells with LPP knockdown (LPP^{KD}) migrate at a constant speed (~25 $\mu\text{m h}^{-1}$) regardless of substrate stiffness. These results are consistent with other findings which demonstrate that ECM stiffness affects cell migration and invasion [12, 21-23, 28, 29, 50, 76-80]. Previous studies show that adhesions grow as a function of extracellular stiffness [23]. We expect that small adhesions found on soft substrates exhibit rapid dynamics, whereas large adhesions found on stiff substrates exhibit significantly slower dynamics. On the other hand, we predict that cells with LPP knockdown possess adhesions with similar size and dynamics across a range of

substrate stiffnesses (1-100 kPa). Further work is required to test this hypothesis and determine whether LPP interaction with α -actinin modulates adhesion dynamics in response to substrate stiffness.

We have recently shown that the adapter protein p46/52ShcA is an early component of adhesions that regulates LPP recruitment to these structures in response to TGF β [5]. Here, we show that the substructural localization of p46/52ShcA appears to be distinct from LPP. p46/52ShcA localizations were found closer to reference beads placed on the coverslip similar to previous studies investigating paxillin [45]. Although further PALM/STORM experiments directly comparing the localization of p46/52ShcA to other adhesion proteins such as paxillin, FAK and vinculin are required, our results suggest that p46/52ShcA is part of the signalling layer of adhesions. Thus, p46/52ShcA expression may also be required for stiffness sensing. Several studies demonstrate that FAK and paxillin contribute to mechanosensing and mechanotransduction through a FAK/phosphopaxillin/vinculin pathway [30, 31, 81, 82]. While ECM stiffness may not affect the turnover of signaling proteins [69], the phosphorylation status of these proteins is altered. Prior studies by our group have shown that tyrosine phosphorylation of p46/52ShcA (Y239/240/313) is required for TGF β -enhanced LPP dynamics, cell migration and cell invasion [2, 5]. Therefore, it would be interesting to determine whether shRNA silencing of p46/52ShcA abrogates cellular preference for stiffness like LPP knockdown. In extension, it would be interesting to determine whether p46/52ShcA regulates LPP localization to adhesions in response to substrate stiffness.

Two confounding aspects of the field of mechanobiology are the different methods used to model changes in substrate stiffness and the large variations in stiffness employed. In the present study, we developed PDMS substrates coated with fibronectin or fluorescent gelatin with the intention of directly comparing the migration and invasion activity of the same cell line in response to a pre-defined range of stiffnesses (1-100 kPa). We tested many ErbB2⁺ cell lines (NIC, SKBr3, BT474, BRC36, ZR-75-30, MDA-MB-361 and AU565) and different ECM components (laminin, vitronectin and poly-L-lysine) (data not shown). Unfortunately, we were unable to identify a cell line that exhibited suitable migration and invasion on the cellular assays at hand. NIC and SKBr3 cells display TGF β -enhanced migration across porous membranes; however, NIC cells developed a trailing edge with numerous large adhesions that impede cell movement on 2D substrates (data not shown), and SKBr3 cells do not require LPP expression for enhanced migration [1]. These

results emphasize that regulation of migration and invasion in cancer cells is complex and influenced by many factors. As a result, we compared the relative migration activity of NMuMG-ErbB2 cells (which degrade poorly) to the invasion activity of HCC1954 cells (which migrate poorly). Interestingly, several TNBC cell lines appear to migrate and invade well. Additionally, we found that TGF β treatment enhances the migration of 4T1, MDA-MB-231, MDA-MB-436 and BT-549 cells (data not shown), which is consistent with other studies showing that TGF β can prime TNBC cells for enhanced metastasis [83-85]. These results prompted us to explore the role of LPP in TNBC.

In the present study, we demonstrate that LPP plays an important role in the migration, invasion and metastasis of TNBC cells. TNBC is a highly heterogeneous breast cancer subtype that can be further subdivided into 6 categories, including basal-like, mesenchymal (M) and mesenchymal stem-like (MSL) [86]. The BT-549 cell line belongs to the M subtype while MDA-MB-231 and MDA-MB-436 cells belong to the MSL subtype. The M subtype is enriched in components and pathways involved in cell motility (regulation of actin by Rho), ECM receptor interaction and cell differentiation pathways (including TGF β signaling) [86]. The MSL subtype shares enrichment of genes for similar processes; however, these cells also express components and processes linked to EGFR, PDGF, calcium signaling and ERK1/2 signaling [86]. M and MSL cells are highly migratory under basal conditions. Nevertheless, additional TGF β stimulation can drive TNBC cells further along the EMT spectrum, leading to increased cell migration and invasion [87-90]. Mutant TP53 (found in MDA-MB-231, MDA-MB-436 and BT-549 cells) promotes TGF β pro-migratory responses [91]. In agreement with these studies, we demonstrate that TGF β stimulation enhances the migration and invasion of 4T1 and MDA-MB-231 cells. LPP expression is required for this phenotype, which aligns with its role as an important mediator of mesenchymal cell migration [92-94]. We will continue to investigate the mechanisms through which LPP enhances metastatic phenotypes in TNBC cells. Based on our results from NMuMG-ErbB2 cells, we suspect that TGF β enhances LPP recruitment to adhesions to support increased cell contractility. Indeed, preliminary experiments in 4T1-2776 cells transfected with a talin tension sensor demonstrate that LPP expression is required for TGF β -induced increases in adhesion tension (data not shown). We hypothesize that LPP enhances the structural support of adhesions to facilitate increased actin contractility. TGF β is known to induce actomyosin contractility [95]. This increase in actin contractility is likely the same in the absence of LPP

localization to adhesions; however, we predict that the lack of structural support causes the “molecular clutch” to slip [96]. We will also perform a BioID screen to identify LPP interacting partners. We recently identified ankyrin repeat-containing protein 1 (KANK1) and PDZ and LIM domain 7 (PDLIM7/Enigma) as LPP interacting proteins in NMuMG-ErbB2 cells [97]. KANK1 inversely controls adhesion size and podosome formation by linking talin to microtubules [98], whereas PDLIM7 binds YAP and triggers its activation following mechanical stretching of adhesions [99]. These interactions may explain how LPP regulates cell migration and invasion in response to substrate stiffness. Adhesions and invadopodia primarily vary in the way F-actin is organized (tangential or perpendicular) [100]. An intriguing hypothesis is that invadopodia arise from adhesions [101]. Further work in TNBC cells will allow us to determine if LPP facilitates a switch from migration to invasion in response to stiffness.

Finally, our results demonstrate that LPP is required for TNBC metastasis to the liver. Quiescent hepatic stellate cells express a minute amount of TGF β , which is upregulated shortly after liver injury [102, 103]. This phenotype may explain why 4T1-2776 cells with endogenous LPP expression form larger metastatic lesions. It would be interesting to investigate TNBC breast cancer cell migration/invasion in response to hepatocyte conditioned media. These studies could then be extended to liver organotypic slice culture systems [104]. Additional research into the effect of LPP knockdown on TNBC lung metastasis is also required. Our previous findings show that LPP is required for ErbB2⁺ breast cancer metastasis to the lungs [3]. Here, we show that 4T1 sub-populations that metastasize to the lungs (4T1-526) require LPP expression for TGF β -enhanced migration and invasion. Thus, it is possible that LPP is required for breast cancer to metastasis to the liver, lungs and other organs/tissues. Whether LPP is a universal regulator of breast cancer metastasis to multiple organs/tissues awaits further investigation.

5.6 MATERIALS AND METHODS

5.6.1 Cell culture

Normal murine mammary epithelial gland (NMuMG) cells overexpressing ErbB2 were previously generated in our lab [1, 3]. Cells were grown in high-glucose (4.5 g l⁻¹) Dulbecco's modified Eagle's medium (DMEM; catalogue no. 319-005-CL, Wisent Bioproducts) supplemented with 5% fetal bovine serum (FBS; catalogue no. 10082-147, Thermo Fisher Scientific), 10 µg ml⁻¹ insulin (catalogue no. 511-016-CM, Wisent Bioproducts), 1 mM L-glutamine (catalogue no. 609-065-CM, Wisent Bioproducts), 1% penicillin-streptomycin (catalogue no. 450-201-EL, Wisent Bioproducts), and 0.2% amphotericin B (catalogue no. 450-105-QL, Wisent Bioproducts). Hygromycin B (0.8 mg ml⁻¹; catalogue no. 450-141-XL, Wisent Bioproducts) was used to maintain ErbB2 expression; puromycin (2 µg ml⁻¹; catalogue no. ant-pr-1, InvivoGen) was used to maintain LPP knockdown; and blasticidin (5 µg ml⁻¹; catalogue no. ant-bl-1, InvivoGen) was used to maintain expression of EGFP-LPP-WT, EGFP-LPP-mLIM1 or EGFP-LPP-ΔABD.

HCC1954 cells were obtained from the American Type Culture Collection (ATCC; catalogue no. CRL-2338) and grown in Roswell Park Memorial Institute media (RPMI; catalogue no. 350-000-CL) supplemented with 10% FBS, 1% penicillin-streptomycin and 0.2% amphotericin B. Puromycin (2 µg ml⁻¹) was used to maintain LPP knockdown.

4T1 cells were obtained from the ATCC (catalogue no. CRL-2539) and grown in high-glucose DMEM supplemented with 10% FBS, 1.5 g l⁻¹ sodium bicarbonate (catalogue no. 609-105-EL, Wisent Bioproducts), 10 mM 4-(2-hydroxyethyl)-1-piperazineethanesulfonic acid (HEPES; catalogue no. 330-050-EL, Wisent Bioproducts), 1 mM sodium pyruvate (catalogue no. 600-110-EL, Wisent Bioproducts), 1% penicillin-streptomycin and 0.2% amphotericin B. Lung-metastatic (4T1-526) [64] and liver-metastatic (4T1-2776) [63] sub-populations were previously obtained using *in vivo* selection approaches. Cells were maintained in the same media as the parental 4T1 population. Puromycin (2 µg ml⁻¹) was used to maintain LPP knockdown. Blasticidin (5 µg ml⁻¹) was used to maintain mCherry-paxillin expression.

MDA-MB-231 cells were obtained from the ATCC (catalogue no. HTB-26) and grown in high-glucose DMEM supplemented with 10% FBS, 1x non-essential amino acids (NEAA; catalogue no. 321-011-EL, Wisent Bioproducts), 1% penicillin-streptomycin and 0.2% amphotericin B. Puromycin (2 µg ml⁻¹) was used to maintain LPP knockdown.

All cell populations were stimulated with recombinant human TGF β 1 (2 ng ml⁻¹; catalogue no. 100-21, PeproTech). Retroviral production was performed using the Retro-X universal packaging system (catalogue no. 631530, Clontech) according to the manufacturer's protocol. Cells were then incubated with polybrene (10 μ g ml⁻¹) and virus-containing medium for 48 h to allow for infection. Mycoplasma screening was routinely performed using the MycoAlert mycoplasma detection kit (catalogue no. LT07-318, Lonza).

5.6.2 DNA constructs

Vinculin tension sensor (catalogue no. 26019), vinculin-mTFP1 (catalogue no. 55516), vinculin-venus (catalogue no. 27300) and mEos2- α -actinin (catalogue no. 57346) constructs were obtained from Addgene. MSCV-ShcA-mEos2 was created by subcloning mEos2 into MSCV-ShcA-miRFP670 [5] using the following primers and EcoR1 restriction enzymes: 5'-CAT-GAG-TGC-GAT-TAA-GCC-AGA-CAT-GAA-GAT-CAA-AC-3' and 5'-GAT-TGC-CTG-ACA-ATG-CCA-GAC-GAT-GAG-AAT-TCA-T-3'. Calf intestinal alkaline phosphatase (CIP) was used to remove 5'- and 3'- phosphates. ShcA-mEos2 was subsequently shuttled into pcDNA3.1 using the following primers and NheI and XhoI restriction enzymes: 5'-TAT-GCT-AGC-ACC-ATG-AAC-AAG-CTG-AGT-GGA-G-3' and 5'-TAT-ACT-CGA-GTC-ATC-GTC-TGG-CAT-TGT-CAG-3'. pMSCV-blast-mCherry-paxillin was previously generated in the lab of P.M.S. [5].

LMP-puro-LPP shRNA constructs against human LPP were created with the following fragments: 5'-TGC-TGT-TGA-CAG-TGA-GCG-CCC-CAG-TTT-AAG-ACA-CCA-AAT-ATA-GTG-AAG-CCA-CAG-ATG-TAT-ATT-TGG-TGT-CTT-AAA-CTG-GGT-TGC-CTA-CTG-CCT-CGG-A-3' (shRNA #2) and 5'-TGC-TGT-TGA-CAG-TGA-GCG-CGC-CAA-GTT-AAA-TAG-CAA-ATG-ATA-GTG-AAG-CCA-CAG-ATG-TAT-CAT-TTG-CTA-TTT-AAC-TTG-GCT-TGC-CTA-CTG-CCT-CGG-A-3' (shRNA #3). shRNA #2 and #3 were originally cloned into a vector without EGFP using XhoI and EcoR1 restriction enzymes; however, they were subsequently transferred into an LMP-puro vector containing EGFP (catalogue no. EAV4071, Open Biosystems) using XhoI and AgeI restriction enzymes. HCC1954 cells were infected with shRNA #2 and #3 (no EGFP), whereas MDA-MB-231 cells were infected with shRNA #2 (EGFP).

LMP-puro-LucA and LMP-puro-LPP shRNA constructs against mouse LPP were previously generated in the laboratory of P.M.S [1]. 4T1 cells were transfected with the following

siRNA sequences against LPP: 5'-AGC-GCA-UAG-AGA-AUA-CGA-UU-3' and 5'-AGA-AGA-CCU-AUA-UCA-CAG-AC-3'.

5.6.3 Immunoblotting

Cells were cultured to 80% confluence and lysed in ice-cold TNE lysis buffer, as previously described [5]. Where indicated, cells were cultured in the presence of TGF β for 48 h and low serum (0.5% FBS) for 24 h. Total cell lysates (20 μ g) were resolved by 6-12% SDS-PAGE. Proteins were transferred onto polyvinylidene difluoride membranes (catalogue no. IPVH00010, Millipore) and membranes were blocked in 5% fat-free milk for 1 h. Membranes were incubated overnight at 4°C with the following antibodies: ErbB2 (1:4000; catalogue no. sc-284, Santa Cruz), E-cadherin (1:1000, catalogue no. 3195S, Cell Signalling), FAK (1:4000; catalogue no. 06-543, Millipore), FAK pY397 (1:4000; catalogue no. 3283S, Cell Signalling), LPP (1:4000; catalogue no. sc-101434, Santa Cruz), paxillin (1:10,000; catalogue no. ab23510, Abcam), paxillin pY31 (1:1000; catalogue no. 44-720G, Thermo Fisher Scientific), paxillin pY118 (1:1000; catalogue no. 611724, BD Biosciences) and α -tubulin (1:20,000; catalogue no. T9026, Sigma-Aldrich). The appropriate horseradish peroxidase-conjugated secondary antibodies (1:10,000; Jackson Immuno Research Laboratories) were added to the membranes for 1 h. Finally, the membranes were visualized using SuperSignalTM West Pico PLUS Chemiluminescent Substrate (catalogue no. 34578, Thermo Fisher Scientific).

5.6.4 Fluorescence resonance energy transfer (FRET) to measure adhesion tension

NMuMG-ErbB2 cells were seeded onto μ -dish 35 mm high glass bottom dishes (catalogue no. 81158, ibidi) coated with 5 μ g cm⁻² fibronectin (catalogue no. F-0895, Sigma-Aldrich) diluted in 1x PBS. Cells were immediately transfected with 0.5 μ g of the vinculin tension sensor construct upon seeding using LipofectamineTM LTX with PLUSTM reagent (catalogue no. 15338100, Thermo Fisher Scientific). The medium was changed 18-24 h after transfection, and cells were allowed to recover for an additional 24 h in the absence or presence of TGF β .

Images were acquired on a Zeiss LSM 710 confocal microscope with a Plan-Apochromat \times 63/1.4 NA oil immersion DIC objective lens. A 405 nm blue diode laser was used to excite mTFP1. Spectral acquisition mode with 9.8-nm segments (415-727 nm) and subsequent linear unmixing was used to obtain mTFP1 and venus (FRET) images. For NMuMG-ErbB2 cells with

EGFP-LPP-WT or EGFP-LPP- Δ ABD, the EGFP signal was also unmixed. The following parameters were used: 1 Airy unit (53 μ m), 850-900 master gain, 1 digital gain, 12.6 μ s pixel dwell time and 4-line averaging. Images were saved as 8-bit with 512 \times 512 pixels. Reference spectra for vinculin-mTFP1, EGFP-LPP and vinculin-venus were acquired in separate experiments with the settings described above; however, a 488 nm Ar ion laser was used to excite vinculin-venus with the spectral acquisition window shifted to 493-727 nm. A Chamlide CU-501 top-stage incubator system (Live Cell Instrument, Seoul, South Korea) was used to keep cells in 5% CO₂ at 37°C.

Unmixed images were subsequently imported into Imaris (version 9.2.0; Bitplane AG, Zurich, Switzerland) and analyzed with the Surfaces function. A protruding edge of each cell was manually selected using the region of interest (ROI) tool. Adhesions were then identified using the unmixed mTFP1 channel. Surface detail was smoothed and set to 0.200 μ m with a local background subtraction of 0.200 μ m. Adhesions were then masked by visual inspection and manual refinement of the autothreshold feature. Touching objects were split with a growing estimated diameter of 0.600 μ m and a quality filter. Surfaces smaller than 3 pixels were removed by filtering. Finally, the mean fluorescence intensities of venus (FRET) and mTFP1 within each adhesion was divided to yield FRET ratio images. The inverse of FRET ratio corresponds to adhesion tension.

5.6.5 Interferometric photoactivated localization microscopy (iPALM)

25 mm glass coverslips containing 100 nm Au beads were prepared as previously described [105]. Surface activation was performed by immersing coverslips in 1M HCl for 2 min. Coverslips were then washed with milliQ water, immersed in 70% ethanol for 20-30 min, and washed with 1x PBS for 30-60 min prior to coating with 5 μ g cm⁻² fibronectin. Cells were seeded onto coverslips and transfected with ShcA-mEos2 or mEos2- α -actinin in suspension using LipofectamineTM LTX with PLUSTM reagent. The medium was changed 18-24 h after transfection, and cells were left to recover for an additional 24 h in the absence or presence of TGF β . Cells were fixed with 3% paraformaldehyde (PFA) containing 0.1% Triton X-100 for 10 min at 37°C; rinsed with 0.2% sodium borohydride (NaBH₄) in 1x PBS for 7 min; rinsed with 50 mM glycine in 1x PBS for 3 \times 10 min; and further permeabilized with 0.2% Triton X-100 for 10 min. Cells were then incubated overnight at 4°C with LPP antibody (*for NMuMG-ErbB2 cells*: catalogue no. PA5-82414, Thermo

Fisher Scientific; for *4T1-2776 cells*: catalogue no. sc-101434, Santa Cruz) diluted in blocking solution containing 10% FBS, 1% bovine serum album (BSA) and 0.05% Triton X-100 in 1x PBS. The following day, cells were rinsed with 1% FBS/0.05% Triton X-100 for 5×5 min and incubated with Alexa FluorTM 647 secondary antibody (*rabbit*: catalogue no. A32733, *mouse*: catalogue no. A32728, Thermo Fisher Scientific) diluted in blocking solution for 45 min at room temperature. Finally, cells were rinsed with an abundant amount of 1x PBS for 3×10 min using a coverslip mini rack. After staining, dSTORM buffer consisting of 50 mM Tris (pH 8.0), 10 mM NaCl, 100 mM MEA, 0.5 mg ml⁻¹ glucose oxidase and 0.03 mg ml⁻¹ catalase (Sigma-Aldrich) was applied to the cells. Another 25 mm coverslip was then placed above the cells and sealed using 5 min epoxy and Vaseline.

The sample was imaged on an interferometric photoactivated localization microscope (iPALM) as previously described [105]. A 640 nm laser was used to excite LPP-AF647 (stochastic optical reconstruction microscopy [STORM]) while 405 and 561 nm lasers were used to photoconvert and excite mEos2 (photoactivated localization microscopy [PALM]). Camera positions were calibrated using the Au gold beads as a reference. 30,000-40,000 image frames were then collected by each of the three cameras and combined in Peak Selector software (version 9.5; Howard Hughes Medical Institute, Ashburn, VA). Peaks were filtered by adjusting the following parameters: Sigma X/Y Pos rtNph, Sigma X/Y Pos Full, Group Sigma X/Y Pos, Group Sigma Z, Unwrapped Error Z, Unwrapped Group Z Error and Unwrapped Z. An ROI was selected, and localizations were exported to MATLAB (version 9.8.0, release R2020a; The MathWorks, Natick, MA) for further analysis.

5.6.6 Cellular response to substrate stiffness

Polydimethylsiloxane (PDMS) substrates were prepared as previously described [11, 106]. Part A and B of a high purity dielectric soft silicone gel kit (catalogue no. GEL-8100, Nusil Technology) were mixed in a 1:1 weight ratio. A curing agent from Sylgard 184 silicone encapsulant kit (catalogue no. 184 SIL ELAST KIT, Dow Corning) was then added according to the required substrate modulus (stiffness) [11]. The mixture was slowly rotated end-over-end for 30-45 min. PDMS was applied to Type 0 coverglass 24×60 mm (Cat. No.: 63751-01, Electron Microscopy Sciences) and spin-coated at 300 rpm for 1 min with an acceleration/deceleration of 50 rpm s⁻¹ from 0 to 300 rpm to achieve uniform thickness of 70 μ m. The PDMS was cured on the

coverglass at 100°C for 2 h. Atomic force microscopy was performed by Dr. Allen Ehrlicher's lab (McGill University) to verify the stiffness of each PDMS substrate. Substrates were then activated with Piranha solution and two crosslinkers to uniformly coat surfaces with gelatin or fibronectin. First, the PDMS surface was activated with a Piranha solution (1:3:5 ratio of H₂O:H₂O₂:H₂SO₄). Sulfuric acid (catalogue no. A300-500, Fisher Scientific) was first added to water, followed by hydrogen peroxide (catalogue no. H325-500, Fisher Scientific) (extremely exothermic reaction). Piranha solution was then applied to the PDMS in excess and incubated at room temperature for 15 min. The chemical reaction between H₂SO₄ and H₂O₂ generates reactive oxygen species which attack Si-CH₃ bonds to form silanol groups (Si-OH) on the PDMS surface [107]. De-ionized water was used to rinse the PDMS after activation. A 1% poly(ethyleneimine) (PEI) solution (catalogue no. 408727, Sigma-Aldrich) was then applied for 10 min. The hyperbranched structure of PEI provides amine groups and increases contact possibility with polar analytes. Finally, 0.04% glutaraldehyde (catalogue no. G5882, Sigma-Aldrich) was applied for 10 min. Substrates were rinsed three times with 1x PBS prior to adding fibronectin or fluorescent gelatin.

5.6.6.1 Cell migration assays on PDMS: PDMS was coated with 5 µg cm⁻² fibronectin overnight at 4°C. The following day, PDMS substrates were washed three times with 1× PBS. Cells were then seeded onto the substrates and allowed to grow under exponential conditions for at least 12 h. TGFβ was applied to the cells directly before imaging ($t = 0$). Images were acquired on a Zeiss AxioObserver fully automated inverted microscope equipped with a Plan-Neofluar ×10/0.3 NA Ph1 objective lens, AxioCam 506 CCD camera (Carl Zeiss, Jena, Germany) and Chambridge TC-L-Z003 stage top environmental control incubator (Live Cell Instrument, Seoul, South Korea). Cells were imaged every 10 min in phase contrast for a total of 24 h.

Cells were semi-manually tracked in MetaXpress analysis software (Molecular Devices, Sunnyvale, CA) using the track points application. The x,y position data for each cell track was then exported to MATLAB. Average cell speed was calculated by determining the mean distance travelled between each time point over the imaging period. Speeds reported for cells cultured in TGFβ were calculated from cell tracks measured after 18 h of growth factor treatment.

5.6.6.2 Gelatin degradation assays on PDMS: Oregon GreenTM 488 conjugated gelatin (catalogue no. G13186, Invitrogen) was diluted in 0.1% unlabeled gelatin (catalogue no. 07903, Stem Cell Tech) at a ratio of 1:15 fluorescent/nonfluorescent gelatin, passed through a 0.22 µm filter, and pre-heated to 37 °C for 30 min. The gelatin mixture was applied to the activated PDMS

surfaces and incubated overnight at 4°C to produce a very thin coating (~2 µm). The following day, gelatin-coated surfaces were incubated with 10 mg ml⁻¹ NaBH₄ for 2 min, followed by 70% ethanol for 20 min. Three washes with 1× PBS were performed between each step. DMEM (37°C) was added to the coverslips 1 h before cell plating.

Cells were pre-treated with TGFβ for 24 h in a cell culture dish. Cells (32,000) were then seeded onto gelatin coated PDMS dishes and allowed to invade for 24 h before fixing with 4% PFA. Cells were permeabilized with 0.2% Triton X-100, rinsed with 100 mM glycine in 1× PBS, and blocked with 10% FBS/PBS. Atto 647N phalloidin (1:2000; catalogue no. 65906, Sigma-Aldrich) was used to stain F-actin. Cells were kept in 1x PBS with 0.05% sodium azide.

Images were acquired on a Zeiss LSM 710 confocal microscope with a Plan-Apochromat ×20/0.8 NA objective lens using the following parameters: 1 Airy unit, 850 (gelatin) or 800 (F-actin) master gain, 1 digital gain, 3.15 µs pixel dwell time and 4-line averaging. An Ar ion laser tuned to 488 nm (2% power; 488/594 nm beam splitter; 493-549 nm detection) was used to visualize gelatin and a HeNe Red 633 nm laser (2% power; 488/543/633 nm beam splitter; 638-759 nm detection) was used to visualize F-actin. Images were saved as 12-bit with 1024 × 1024 pixels (1 pixel = 0.415 µm).

Quantification of gelatin degradation was performed in Imaris using the Surfaces function. The lookup table was inverted to make areas of degradation appear bright. Surface detail was smoothed and set to 0.830 µm with a local background subtraction of 0.500 µm. Areas of gelatin degradation were then masked by manual refinement of the autothreshold feature. The total degradation per field of view (FOV) was determined.

5.6.7 Cell migration assays

Cells were seeded onto µ-slide 8-well plates (catalogue no. 80821, ibidi) coated with 5 µg cm⁻² fibronectin. Cells were cultured in the absence or presence of TGFβ for 24 h prior to imaging. Images were acquired on the Zeiss AxioObserver with a Plan-Neofluar ×10/0.3 NA Ph1 objective lens. Images were taken every 5 or 10 min in phase contrast for a total of 10 h. Cells were semi-manually tracked in ImageJ/Fiji (National Institutes of Health, Bethesda, MD) using the manual tracking plugin; *x,y* position data was then exported to MATLAB. Rose plots of cell migration were created by superimposing the starting position of each track on the origin (0, 0). Windrose plots were generated by determining the angle and mean net displacement of each track. The mean

net displacement for each 45° segment was then plotted. Average speed was calculated as described above.

5.6.8 Gelatin degradation assays

Degradation assays were performed on fluorescently conjugated gelatin-coated coverslips as previously described [5]. μ -dish 35 mm high glass bottom dishes were coated with a mix of 0.1 mg ml⁻¹ poly-D-lysine (catalogue no. P6407, Sigma-Aldrich) and 5 μ g cm⁻² fibronectin for 20 min, followed by incubation with 0.4% glutaraldehyde for 10 min. Oregon GreenTM 488 conjugated gelatin was diluted 1:20 with 0.1% unconjugated gelatin and used to coat dishes for 10 min at 37°C. Coverslips were then incubated with 10 mg ml⁻¹ NaBH₄ for 2 min, followed by 70% ethanol for 20 min. Three washes with 1× PBS were performed between each step. DMEM (37°C) was added to the coverslips 1 h before cell plating.

Cells were pre-treated with TGF β for 24 h and allowed to invade for 24 h before fixing and staining. Antibodies against LPP (1:500; catalogue no. 8B3A11, Cell Signaling), cortactin (1:500; catalogue no. ab230992, Abcam) and Atto 647N phalloidin (1:2000) were used. Alexa-Fluor 546 dye-conjugated secondary antibody (1:1000; catalogue no. A11036, Thermo Fisher Scientific) was applied for 1 h at room temperature to visualize LPP.

Images were acquired on the Zeiss LSM 710 confocal microscope with a Plan-Apochromat \times 63/1.4 NA oil immersion DIC objective lens using the following parameters: 1 Airy unit, 1 digital gain, 3.15 μ s pixel dwell time and 4-line averaging. The 488 nm laser (1-2% power; 488/594 nm beam splitter; 493-549 nm detection) and 800-850 master gain was used to image gelatin; a HeNe Green 543 nm laser (7% power; 458/543 nm beam splitter; 566-599 nm detection) and 900 master gain was used to image LPP or cortactin, where indicated; and the 633 nm laser (1-2.5% power; 488/543/633 nm beam splitter; 638-759 nm detection) and 800-900 master gain was used to image F-actin. All images were saved as 12-bit with 1024 \times 1024 pixels (1 pixel = 0.132 μ m).

Quantification of gelatin degradation was performed in Imaris using the Surfaces function. The lookup table was inverted to make areas of degradation appear bright. Surface detail was smoothed and set to 0.264 μ m with a local background subtraction of 0.250 μ m. Areas of gelatin degradation were then masked by manual refinement of the autothreshold feature.

5.6.9 Adhesion dynamics assays

Cells were infected with mCherry-paxillin and seeded onto μ -dish 35 mm high glass bottom dishes coated with $5 \mu\text{g cm}^{-2}$ fibronectin. Cells were left to adhere and grow under exponential conditions for at least 12 h. Cells were then cultured in the absence or presence of TGF β for an additional 24 h before imaging. *For adhesion number*, cells were imaged on a total internal reflection fluorescence (TIRF)-Spinning Disk Spectral Discovery System (Spectral Applied Research, Richmond Hill, ON) coupled to a DMI6000B Leica microscope equipped with a Plan-Apochromat $\times 63/1.47$ NA oil immersion DIC objective lens (Leica, Wetzlar, Germany), ORCA-Flash 4.0 V3 sCMOS camera (Hamamatsu Photonics K.K., Hamamatsu City, Japan), and ChamSlide CU-501 top-stage incubator system. A 561 nm laser with an ET 620/60 nm filter cube was used to visualize mCherry-paxillin. The camera exposure was set to 5 s (1 pixel = 0.062 μm). A TIRF prism was used to limit fluorescent excitation to a depth of 100 nm. *For adhesion dynamics*, cells were imaged on a DMI6000B Leica microscope equipped with a Quorum WaveFx-X1 spinning disk confocal system, HCX PL APO $\times 63/1.40$ NA oil immersion DIC objective lens, and Prime BSI sCMOS camera (Photometrics, Tuscon, AZ). A 561 nm laser with an ET 620/60 nm filter cube was used to visualize mCherry-paxillin. The camera exposure was set to 5 s with 2×2 pixel binning to enhance the signal due to low light levels (1 pixel = 0.1172 μm). The pinhole size of the spinning disk was fixed at 50 μm .

Images were processed in Imaris using the surfaces function. A protruding edge of each cell was manually selected using the ROI tool. Surface detail was smoothed and set to 0.200 μm with a local background subtraction of 0.200 μm . Adhesions were then masked by manual refinement of the autothreshold feature. Touching objects were split with a growing estimated diameter of 0.500 μm and a quality filter. Surfaces smaller than 5 pixels were removed by filtering. Finally, adhesions were tracked over time using an autoregressive algorithm with a maximum distance of 0.800 μm and maximum gap size of 2 time points.

Mean intensity data for each adhesion tracked in Imaris was exported to MATLAB. A custom algorithm was used to calculate assembly and disassembly rates [5, 108, 109]. Intensity changes greater than 20% between subsequent points were considered significant.

5.6.10 Experimental liver metastasis assays

4T1-2776 cell populations (1×10^5 cells) were injected into the spleens of 4-6 week-old female BALB/c mice as previously described [63, 110]. Spleens were removed after cancer cell drainage into the portal vein and mice were monitored for an additional 2.5 weeks before sacrifice and liver resection. The left cardiac lobe of the liver was formalin fixed, paraffin embedded, sectioned and stained with hematoxylin and eosin (H&E). Tumor area/tissue area was quantified from H&E-stained sections using Aperio ImageScope software (Leica). The mice were housed in facilities managed by the McGill University Animal Resources Centre. All animal experiments were conducted under a McGill University-approved Animal Use Protocol (AUP #5129), which was reviewed by the Facility Animal Care Committee for the Faculty of Medicine (Committee A).

5.6.11 Statistical analyses

Statistical significance values (p values) were obtained by performing a two-tailed Student's t test or Mann–Whitney U test. Data are presented as mean \pm s.e.m. Statistical tests were used to make pairwise comparisons between conditions. For VinTS and adhesion dynamics experiments, cell averages were chosen as the n value to prevent p value skewing [111]. For cell migration experiments, cells were pooled together from at least three independent experiments to obtain an $n > 30$. This was done to capture the normal distribution of the data. For *in vivo* studies, we previously determined that a sample size of $n = 8$ is sufficient to provide 95% power and with 0.05 α -error probability and an effect size of 2 [3]. Thus, a sample size of 10 mice per cohort was used for splenic injection experiments to account for the potential loss of animals over the duration of the experiment.

5.7 REFERENCES

1. Ngan, E., et al., *A complex containing LPP and alpha-actinin mediates TGFbeta-induced migration and invasion of ErbB2-expressing breast cancer cells.* J Cell Sci, 2013. **126**(Pt 9): p. 1981-91.
2. Northey, J.J., et al., *Distinct phosphotyrosine-dependent functions of the ShcA adaptor protein are required for transforming growth factor beta (TGFbeta)-induced breast cancer cell migration, invasion, and metastasis.* J Biol Chem, 2013. **288**(7): p. 5210-22.
3. Ngan, E., et al., *LPP is a Src substrate required for invadopodia formation and efficient breast cancer lung metastasis.* Nat Commun, 2017. **8**: p. 15059.
4. Northey, J.J., et al., *Signaling through ShcA is required for TGF- β and New/ErbB-2 induced breast cancer cell motility and invasion.* Mol. Cell. Biol., 2008: p. MCB.01734-07.
5. Kiepas, A., et al., *The SHCA adapter protein cooperates with lipoma-preferred partner in the regulation of adhesion dynamics and invadopodia formation.* J Biol Chem, 2020. **295**(31): p. 10535-10559.
6. Van Haastert, P.J.M. and P.N. Devreotes, *Chemotaxis: signalling the way forward.* Nature Reviews Molecular Cell Biology, 2004. **5**(8): p. 626-634.
7. Roussos, E.T., J.S. Condeelis, and A. Patsialou, *Chemotaxis in cancer.* Nature reviews. Cancer, 2011. **11**(8): p. 573-587.
8. DuChez, B.J., et al., *Durotaxis by Human Cancer Cells.* Biophys J, 2019. **116**(4): p. 670-683.
9. Shellard, A. and R. Mayor, *Durotaxis: The Hard Path from In Vitro to In Vivo.* Dev Cell, 2020.
10. Beningo, K.A., et al., *Nascent focal adhesions are responsible for the generation of strong propulsive forces in migrating fibroblasts.* The Journal of cell biology, 2001. **153**(4): p. 881-888.
11. Yoshie, H., et al., *High Throughput Traction Force Microscopy Using PDMS Reveals Dose-Dependent Effects of Transforming Growth Factor- β ; on the Epithelial-to-Mesenchymal Transition.* JoVE, 2019(148): p. e59364.
12. Marinkovic, A., et al., *Improved throughput traction microscopy reveals pivotal role for matrix stiffness in fibroblast contractility and TGF-beta responsiveness.* Am J Physiol Lung Cell Mol Physiol, 2012. **303**(3): p. L169-80.
13. Vicente-Manzanares, M., C.K. Choi, and A.R. Horwitz, *Integrins in cell migration – the actin connection.* Journal of Cell Science, 2009. **122**(2): p. 199.
14. Geiger, B., J.P. Spatz, and A.D. Bershadsky, *Environmental sensing through focal adhesions.* Nat Rev Mol Cell Biol, 2009. **10**(1): p. 21-33.
15. del Rio, A., et al., *Stretching single talin rod molecules activates vinculin binding.* Science, 2009. **323**(5914): p. 638-41.
16. Ciobanaru, C., B. Faivre, and C. Le Clainche, *Actomyosin-dependent formation of the mechanosensitive talin-vinculin complex reinforces actin anchoring.* Nat Commun, 2014. **5**: p. 3095.
17. Kluger, C., et al., *Different Vinculin Binding Sites Use the Same Mechanism to Regulate Directional Force Transduction.* Biophysical Journal, 2020. **118**(6): p. 1344-1356.
18. Galbraith, C.G., K.M. Yamada, and M.P. Sheetz, *The relationship between force and focal complex development.* J Cell Biol, 2002. **159**(4): p. 695-705.
19. Pankov, R., et al., *Integrin dynamics and matrix assembly: tensin-dependent translocation of alpha(5)beta(1) integrins promotes early fibronectin fibrillogenesis.* J Cell Biol, 2000. **148**(5): p. 1075-90.
20. Choi, C.K., et al., *Actin and alpha-actinin orchestrate the assembly and maturation of nascent adhesions in a myosin II motor-independent manner.* Nat Cell Biol, 2008. **10**(9): p. 1039-50.
21. Pelham, R.J., Jr. and Y. Wang, *Cell locomotion and focal adhesions are regulated by substrate flexibility.* Proc Natl Acad Sci U S A, 1997. **94**(25): p. 13661-5.
22. Lo, C.M., et al., *Cell movement is guided by the rigidity of the substrate.* Biophys J, 2000. **79**(1): p. 144-52.

23. Discher, D.E., P. Janmey, and Y.L. Wang, *Tissue cells feel and respond to the stiffness of their substrate*. Science, 2005. **310**(5751): p. 1139-43.
24. Athanasiou, A., et al., *Breast lesions: quantitative elastography with supersonic shear imaging--preliminary results*. Radiology, 2010. **256**(1): p. 297-303.
25. Evans, A., et al., *Differentiating benign from malignant solid breast masses: value of shear wave elastography according to lesion stiffness combined with greyscale ultrasound according to BI-RADS classification*. Br J Cancer, 2012. **107**(2): p. 224-9.
26. Bae, J.S., et al., *Prediction of invasive breast cancer using shear-wave elastography in patients with biopsy-confirmed ductal carcinoma in situ*. Eur Radiol, 2017. **27**(1): p. 7-15.
27. Provenzano, P.P., et al., *Collagen density promotes mammary tumor initiation and progression*. BMC Med, 2008. **6**: p. 11.
28. Parekh, A., et al., *Sensing and modulation of invadopodia across a wide range of rigidities*. Biophys J, 2011. **100**(3): p. 573-82.
29. Jerrell, R.J. and A. Parekh, *Cellular traction stresses mediate extracellular matrix degradation by invadopodia*. Acta Biomater, 2014. **10**(5): p. 1886-96.
30. Pasapera, A.M., et al., *Myosin II activity regulates vinculin recruitment to focal adhesions through FAK-mediated paxillin phosphorylation*. J Cell Biol, 2010. **188**(6): p. 877-90.
31. Plotnikov, S.V., et al., *Force fluctuations within focal adhesions mediate ECM-rigidity sensing to guide directed cell migration*. Cell, 2012. **151**(7): p. 1513-27.
32. Zaidel-Bar, R., et al., *Functional atlas of the integrin adhesome*. Nat Cell Biol, 2007. **9**(8): p. 858-67.
33. Kuo, J.C., et al., *Analysis of the myosin-II-responsive focal adhesion proteome reveals a role for beta-Pix in negative regulation of focal adhesion maturation*. Nat Cell Biol, 2011. **13**(4): p. 383-93.
34. Yoshigi, M., et al., *Mechanical force mobilizes zyxin from focal adhesions to actin filaments and regulates cytoskeletal reinforcement*. J Cell Biol, 2005. **171**(2): p. 209-15.
35. Hirata, H., H. Tatsumi, and M. Sokabe, *Zyxin emerges as a key player in the mechanotransduction at cell adhesive structures*. Communicative & integrative biology, 2008. **1**(2): p. 192-195.
36. Hirata, H., H. Tatsumi, and M. Sokabe, *Mechanical forces facilitate actin polymerization at focal adhesions in a zyxin-dependent manner*. Journal of cell science, 2008. **121**(Pt 17): p. 2795-804.
37. Uemura, A., et al., *The LIM domain of zyxin is sufficient for force-induced accumulation of zyxin during cell migration*. Biophysical journal, 2011. **101**(5): p. 1069-75.
38. Hoffman, L.M., et al., *Stretch-induced actin remodeling requires targeting of zyxin to stress fibers and recruitment of actin regulators*. Mol Biol Cell, 2012. **23**(10): p. 1846-59.
39. Smith, M.A., et al., *LIM domains target actin regulators paxillin and zyxin to sites of stress fiber strain*. PLoS One, 2013. **8**(8): p. e69378.
40. Ngan, E., et al., *Emerging roles for LPP in metastatic cancer progression*. J Cell Commun Signal, 2018. **12**(1): p. 143-156.
41. Zaidel-Bar, R., et al., *A paxillin tyrosine phosphorylation switch regulates the assembly and form of cell-matrix adhesions*. J Cell Sci, 2007. **120**(Pt 1): p. 137-48.
42. Brown, M.C. and C.E. Turner, *Paxillin: Adapting to Change*. Physiological Reviews, 2004. **84**(4): p. 1315-1339.
43. Webb, D.J., et al., *Paxillin phosphorylation sites mapped by mass spectrometry*. J Cell Sci, 2005. **118**(Pt 21): p. 4925-9.
44. Grashoff, C., et al., *Measuring mechanical tension across vinculin reveals regulation of focal adhesion dynamics*. Nature, 2010. **466**(7303): p. 263-6.
45. Kanchanawong, P., et al., *Nanoscale architecture of integrin-based cell adhesions*. Nature, 2010. **468**(7323): p. 580-4.
46. Winkler, J., et al., *Concepts of extracellular matrix remodelling in tumour progression and metastasis*. Nature Communications, 2020. **11**(1): p. 5120.

47. Levental, K.R., et al., *Matrix crosslinking forces tumor progression by enhancing integrin signaling*. Cell, 2009. **139**(5): p. 891-906.
48. Provenzano, P.P., et al., *Matrix density-induced mechanoregulation of breast cell phenotype, signaling and gene expression through a FAK-ERK linkage*. Oncogene, 2009. **28**(49): p. 4326-43.
49. Wei, S.C., et al., *Matrix stiffness drives epithelial-mesenchymal transition and tumour metastasis through a TWIST1-G3BP2 mechanotransduction pathway*. Nat Cell Biol, 2015. **17**(5): p. 678-88.
50. Dokukina, I.V. and M.E. Gracheva, *A model of fibroblast motility on substrates with different rigidities*. Biophys J, 2010. **98**(12): p. 2794-803.
51. Peyton, S.R. and A.J. Putnam, *Extracellular matrix rigidity governs smooth muscle cell motility in a biphasic fashion*. J Cell Physiol, 2005. **204**(1): p. 198-209.
52. Sorlie, T., et al., *Repeated observation of breast tumor subtypes in independent gene expression data sets*. Proc Natl Acad Sci U S A, 2003. **100**(14): p. 8418-23.
53. Sotiriou, C., et al., *Breast cancer classification and prognosis based on gene expression profiles from a population-based study*. Proc Natl Acad Sci U S A, 2003. **100**(18): p. 10393-8.
54. Sotiriou, C. and M.J. Piccart, *Taking gene-expression profiling to the clinic: when will molecular signatures become relevant to patient care?* Nat Rev Cancer, 2007. **7**(7): p. 545-53.
55. Dai, X., et al., *Breast cancer intrinsic subtype classification, clinical use and future trends*. Am J Cancer Res, 2015. **5**(10): p. 2929-43.
56. Kim, S., et al., *Elevated TGF- β 1 and - β 2 expression accelerates the epithelial to mesenchymal transition in triple-negative breast cancer cells*. Cytokine, 2015. **75**(1): p. 151-8.
57. Hudson, J., et al., *p66ShcA promotes breast cancer plasticity by inducing an epithelial-to-mesenchymal transition*. Mol Cell Biol, 2014. **34**(19): p. 3689-701.
58. Drasin, D.J., T.P. Robin, and H.L. Ford, *Breast cancer epithelial-to-mesenchymal transition: examining the functional consequences of plasticity*. Breast Cancer Res, 2011. **13**(6): p. 226.
59. Côme, C., et al., *Snail and slug play distinct roles during breast carcinoma progression*. Clin Cancer Res, 2006. **12**(18): p. 5395-402.
60. Yang, J., et al., *Twist, a master regulator of morphogenesis, plays an essential role in tumor metastasis*. Cell, 2004. **117**(7): p. 927-39.
61. Taube, J.H., et al., *Core epithelial-to-mesenchymal transition interactome gene-expression signature is associated with claudin-low and metaplastic breast cancer subtypes*. Proc Natl Acad Sci U S A, 2010. **107**(35): p. 15449-54.
62. Sieg, D.J., C.R. Hauck, and D.D. Schlaepfer, *Required role of focal adhesion kinase (FAK) for integrin-stimulated cell migration*. J Cell Sci, 1999. **112** (Pt 16): p. 2677-91.
63. Tabaries, S., et al., *Granulocytic immune infiltrates are essential for the efficient formation of breast cancer liver metastases*. Breast Cancer Res, 2015. **17**: p. 45.
64. Rose, A.A., et al., *ADAM10 releases a soluble form of the GPNMB/Osteoactivin extracellular domain with angiogenic properties*. PLoS One, 2010. **5**(8): p. e12093.
65. Lauffenburger, D.A. and A.F. Horwitz, *Cell migration: a physically integrated molecular process*. Cell, 1996. **84**(3): p. 359-69.
66. Friedl, P. and K. Wolf, *Tumour-cell invasion and migration: diversity and escape mechanisms*. Nat Rev Cancer, 2003. **3**(5): p. 362-74.
67. Friedl, P., et al., *New dimensions in cell migration*. Nat Rev Mol Cell Biol, 2012. **13**(11): p. 743-7.
68. Zaidel-Bar, R., et al., *Early molecular events in the assembly of matrix adhesions at the leading edge of migrating cells*. J Cell Sci, 2003. **116**(Pt 22): p. 4605-13.
69. Stutchbury, B., et al., *Distinct focal adhesion protein modules control different aspects of mechanotransduction*. Journal of cell science, 2017. **130**(9): p. 1612-1624.
70. Austen, K., et al., *Extracellular rigidity sensing by talin isoform-specific mechanical linkages*. Nature cell biology, 2015. **17**(12): p. 1597-1606.
71. Elosegui-Artola, A., et al., *Mechanical regulation of a molecular clutch defines force transmission and transduction in response to matrix rigidity*. Nature Cell Biology, 2016. **18**(5): p. 540-548.

72. Macalma, T., et al., *Molecular characterization of human zyxin*. J Biol Chem, 1996. **271**(49): p. 31470-8.
73. Hooper, C.L., P.R. Dash, and S.Y. Boateng, *Lipoma preferred partner is a mechanosensitive protein regulated by nitric oxide in the heart*. FEBS Open Bio, 2012. **2**: p. 135-44.
74. Hooper, C.L., et al., *Modulation of stretch-induced myocyte remodeling and gene expression by nitric oxide: a novel role for lipoma preferred partner in myofibrillogenesis*. Am J Physiol Heart Circ Physiol, 2013. **304**(10): p. H1302-13.
75. Jin, L., et al., *Mechanical properties of the extracellular matrix alter expression of smooth muscle protein LPP and its partner palladin; relationship to early atherosclerosis and vascular injury*. J Muscle Res Cell Motil, 2009. **30**(1-2): p. 41-55.
76. Gu, Z., et al., *Soft matrix is a natural stimulator for cellular invasiveness*. Mol Biol Cell, 2014. **25**(4): p. 457-69.
77. Aung, A., et al., *3D traction stresses activate protease-dependent invasion of cancer cells*. Biophys J, 2014. **107**(11): p. 2528-37.
78. Alexander, N.R., et al., *Extracellular matrix rigidity promotes invadopodia activity*. Curr Biol, 2008. **18**(17): p. 1295-9.
79. Kai, F., H. Laklai, and V.M. Weaver, *Force Matters: Biomechanical Regulation of Cell Invasion and Migration in Disease*. Trends Cell Biol, 2016. **26**(7): p. 486-497.
80. Chaudhuri, O., et al., *Extracellular matrix stiffness and composition jointly regulate the induction of malignant phenotypes in mammary epithelium*. Nat Mater, 2014. **13**(10): p. 970-8.
81. Klein, E.A., et al., *Cell-cycle control by physiological matrix elasticity and in vivo tissue stiffening*. Curr Biol, 2009. **19**(18): p. 1511-8.
82. Wang, W., et al., *Matrix stiffness regulates vascular integrity through focal adhesion kinase activity*. Faseb j, 2019. **33**(1): p. 1199-1208.
83. Padua, D., et al., *TGFbeta primes breast tumors for lung metastasis seeding through angiopoietin-like 4*. Cell, 2008. **133**(1): p. 66-77.
84. Kang, Y., et al., *Breast cancer bone metastasis mediated by the Smad tumor suppressor pathway*. Proc Natl Acad Sci U S A, 2005. **102**(39): p. 13909-14.
85. González-González, A., et al., *Activating Transcription Factor 4 Modulates TGFβ-Induced Aggressiveness in Triple-Negative Breast Cancer via SMAD2/3/4 and mTORC2 Signaling*. Clin Cancer Res, 2018. **24**(22): p. 5697-5709.
86. Lehmann, B.D., et al., *Identification of human triple-negative breast cancer subtypes and preclinical models for selection of targeted therapies*. J Clin Invest, 2011. **121**(7): p. 2750-67.
87. Kim, S., et al., *Berberine Suppresses Cell Motility Through Downregulation of TGF-β1 in Triple Negative Breast Cancer Cells*. Cellular Physiology and Biochemistry, 2018. **45**(2): p. 795-807.
88. Terashima, M., et al., *Synergistic antitumor effects of S-1 with eribulin in vitro and in vivo for triple-negative breast cancer cell lines*. Springerplus, 2014. **3**: p. 417.
89. Brown, K.A., et al., *Induction by transforming growth factor-β1 of epithelial to mesenchymal transition is a rare event in vitro*. Breast Cancer Research, 2004. **6**(3): p. R215.
90. Luwor, R.B., et al., *Single live cell TGF-β signalling imaging: breast cancer cell motility and migration is driven by sub-populations of cells with dynamic TGF-β-Smad3 activity*. Molecular Cancer, 2015. **14**(1): p. 50.
91. Adorno, M., et al., *A Mutant-p53/Smad complex opposes p63 to empower TGFbeta-induced metastasis*. Cell, 2009. **137**(1): p. 87-98.
92. Jin, L., et al., *Angiotensin II, focal adhesion kinase, and PRX1 enhance smooth muscle expression of lipoma preferred partner and its newly identified binding partner palladin to promote cell migration*. Circ Res, 2007. **100**(6): p. 817-25.
93. Gorenne, I., et al., *LPP expression during in vitro smooth muscle differentiation and stent-induced vascular injury*. Circ Res, 2006. **98**(3): p. 378-85.

94. Vervenne, H.B., et al., *Lpp is involved in Wnt/PCP signaling and acts together with Scrib to mediate convergence and extension movements during zebrafish gastrulation*. Dev Biol, 2008. **320**(1): p. 267-77.
95. Meyer-ter-Vehn, T., et al., *Contractility as a prerequisite for TGF-beta-induced myofibroblast transdifferentiation in human tenon fibroblasts*. Invest Ophthalmol Vis Sci, 2006. **47**(11): p. 4895-904.
96. Case, L.B. and C.M. Waterman, *Integration of actin dynamics and cell adhesion by a three-dimensional, mechanosensitive molecular clutch*. Nature cell biology, 2015. **17**(8): p. 955-963.
97. Voorand, E., *Mechanisms of Adhesion and Invasiveness Regulation During Breast Cancer Metastasis*, in *Biochemistry*. 2020, McGill University.
98. Rafiq, N.B.M., et al., *A mechano-signalling network linking microtubules, myosin IIA filaments and integrin-based adhesions*. Nature Materials, 2019. **18**(6): p. 638-649.
99. Elbediwy, A., et al., *Enigma proteins regulate YAP mechanotransduction*. J Cell Sci, 2018. **131**(22).
100. Albiges-Rizo, C., et al., *Actin machinery and mechanosensitivity in invadopodia, podosomes and focal adhesions*. J Cell Sci, 2009. **122**(Pt 17): p. 3037-49.
101. Oikawa, T., T. Itoh, and T. Takenawa, *Sequential signals toward podosome formation in NIH-src cells*. The Journal of cell biology, 2008. **182**(1): p. 157-169.
102. Gao, C., et al., *Transforming growth factor beta (TGF-beta) expression in isolated and cultured rat hepatocytes*. J Cell Physiol, 1996. **167**(3): p. 394-405.
103. Gressner, O.A., et al., *Activation of TGF-beta within cultured hepatocytes and in liver injury leads to intracrine signaling with expression of connective tissue growth factor*. Journal of cellular and molecular medicine, 2008. **12**(6B): p. 2717-2730.
104. Pearen, M.A., et al., *Murine Precision-Cut Liver Slices as an Ex Vivo Model of Liver Biology*. JoVE, 2020(157): p. e60992.
105. Shtengel, G., et al., *Interferometric fluorescent super-resolution microscopy resolves 3D cellular ultrastructure*. Proc Natl Acad Sci U S A, 2009. **106**(9): p. 3125-30.
106. Yoshie, H., et al., *Traction Force Screening Enabled by Compliant PDMS Elastomers*. Biophys J, 2018. **114**(9): p. 2194-2199.
107. Koh, K.-S., et al., *Quantitative Studies on PDMS-PDMS Interface Bonding with Piranha Solution and its Swelling Effect*. Micromachines, 2012. **3**(2): p. 427-441.
108. Lewis, K., et al., *p66ShcA functions as a contextual promoter of breast cancer metastasis*. Breast Cancer Res, 2020. **22**(1): p. 7.
109. Kiepas, A., et al., *Optimizing live-cell fluorescence imaging conditions to minimize phototoxicity*. J Cell Sci, 2020. **133**(4).
110. Tabaries, S., et al., *Claudin-2 is selectively enriched in and promotes the formation of breast cancer liver metastases through engagement of integrin complexes*. Oncogene, 2011. **30**(11): p. 1318-28.
111. Lord, S.J., et al., *SuperPlots: Communicating reproducibility and variability in cell biology*. Journal of Cell Biology, 2020. **219**(6).

5.8 FIGURES AND LEGENDS

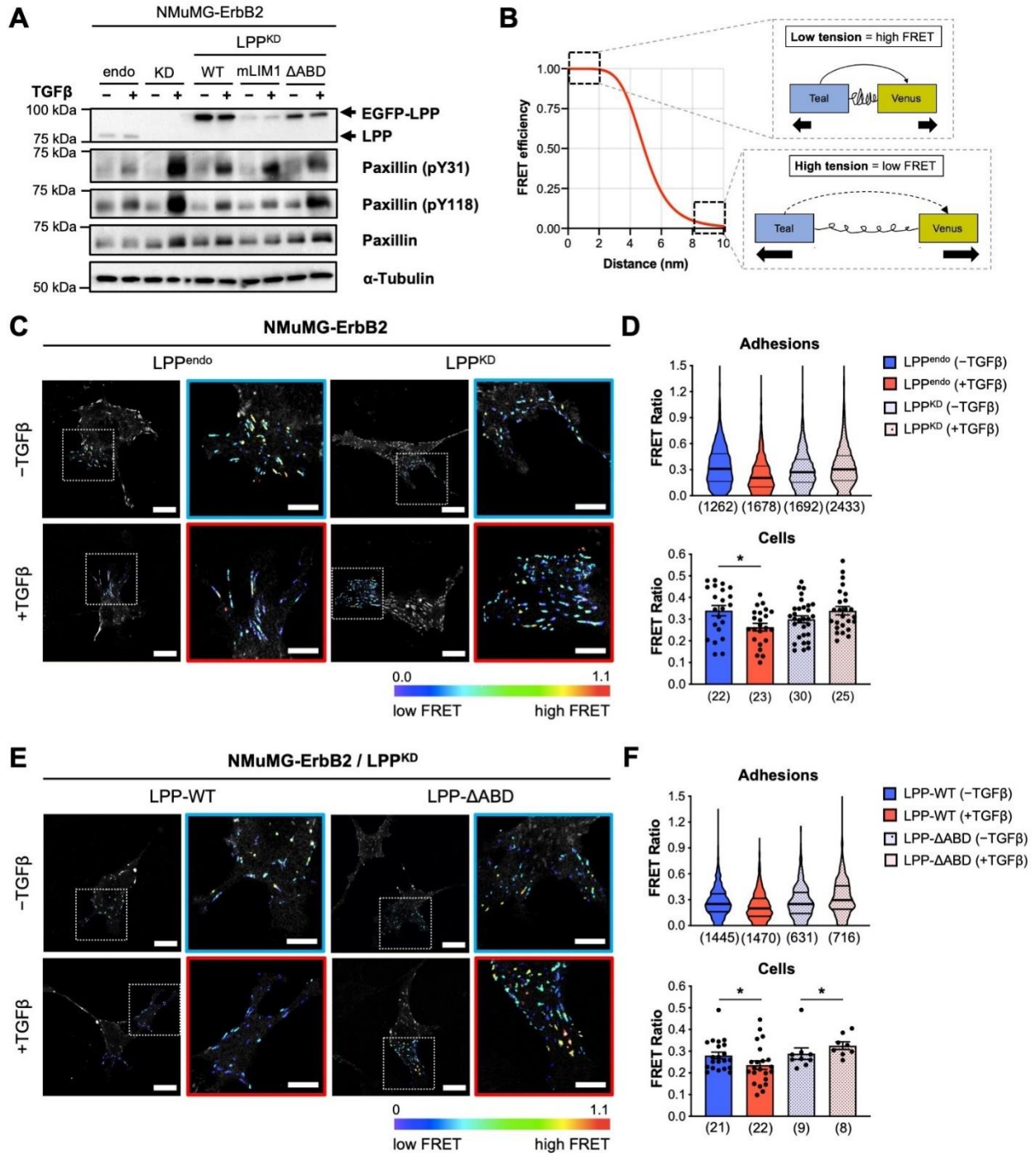


Figure 5.1. LPP mediates TGF β -enhanced adhesion tension through its α -actinin binding domain. (A) Immunoblot analyses of whole-cell lysates showing LPP, paxillin and phospho-paxillin (pY31 and pY118) levels in the indicated cell populations. Cells were cultured in low serum media with or without TGF β (2 ng ml⁻¹) for 24 h. α -Tubulin was used as a loading control. (B) Schematic diagram of the vinculin tension sensor (VinTS) used to measure adhesion tension. Corresponding graph depicts FRET efficiency between teal and venus fluorescent proteins as a function of distance. (C) NMuMG-ErbB2 cells expressing an shRNA against luciferase (LPP^{endo}) or LPP (LPP^{KD}) were transfected with VinTS and cultured in the absence or presence of TGF β (2 ng ml⁻¹) for 24 h. Adhesions were statistically coded based on FRET signal. (D) FRET ratio of individual adhesions pooled together for LPP^{endo} and LPP^{KD} cells with and without TGF β (*top panel*). Width of the violin plot indicates the probability density of the data. The *thin lines* indicate the first and third quartiles whereas the *heavy central line* indicates the mean. *Numbers in parentheses* refer to the number of adhesions analyzed for each condition. FRET ratio of adhesions in individual cells was subsequently averaged and one data point was plotted for each cell under condition (*bottom panel*). *Black dots and numbers in parentheses* indicate individual cells pooled from three independent experiments. Data represent mean \pm s.e.m. (*error bars*). * $p < 0.05$; Mann-Whitney U test. (E and F) NMuMG-ErbB2 cells with LPP knockdown were rescued with wildtype LPP (LPP-WT) or an α -actinin binding domain mutant (LPP- Δ ABD), transfected with VinTS and cultured in the absence or presence of TGF β (2 ng ml⁻¹) for 24 h. Cells were imaged and analyzed as described in C and D, respectively. Data represent mean \pm s.e.m. (*error bars*) from two (LPP-WT) or one (LPP- Δ ABD) independent experiments. * $p < 0.05$; Mann-Whitney U test. Scale bar is 20 μ m for whole-cell images and 2 μ m for magnified images.

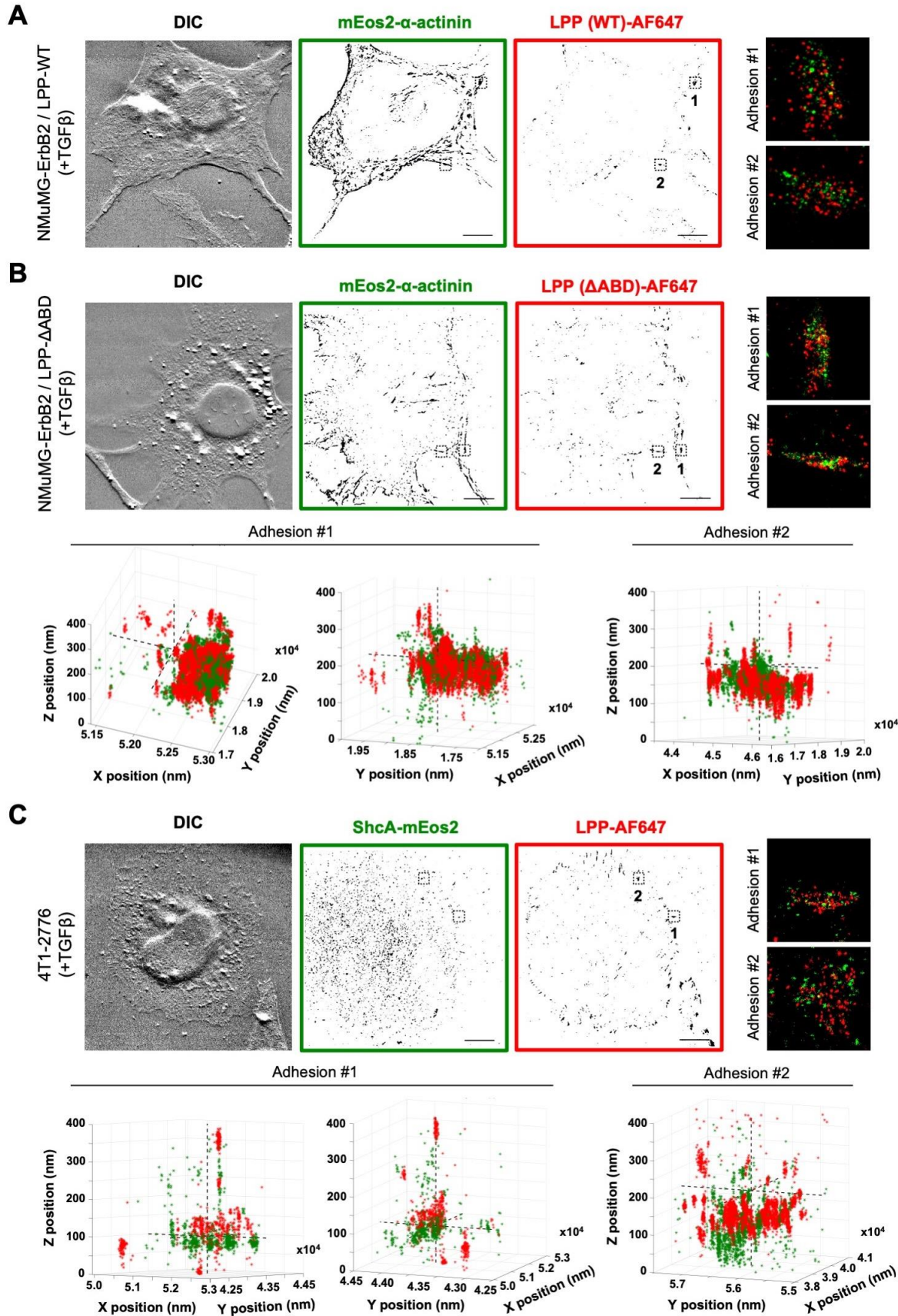


Figure 5.2. LPP localizes to the same adhesion layer as α -actinin. (A and B) NMuMG-ErbB2/LPP^{KD} cells re-expressing LPP-WT or LPP- Δ ABD were transfected with mEos2- α -actinin, treated with TGF β for 24 h, and fixed and stained with a primary antibody against LPP (PA5-82414) and Alexa Fluor 647 secondary antibody. An iPALM microscope with dual Nikon \times 60/1.49 NA objective lenses was used to capture 30,000-40,000 images of mEos2- α -actinin and LPP-AF647 independently [105]. Images captured on three separate cameras (phase separated by 120 $^\circ$) were then mathematically recombined based on the position of Au fiducial markers found in the coverslip. The following filters (max values) were applied for data visualization: Sigma X,Y Pos rtNph = 0.05, Sigma X,Y Pos Full = 0.13, Group Sigma X,Y Pos = 0.13, Group Sigma Z = 30, Unwrapped Z Error = -80 (min)/80 (max), Unwrapped Group Z Error = -80 (min)/80 (max). Frame peaks for indicated adhesions were exported to MATLAB and plotted in 3D. (C) 4T1-2776 cells were transfected with ShcA-mEos2, treated with TGF β for 24 h, and fixed and stained with a primary antibody against LPP (sc-101434) and Alexa Fluor 647 secondary antibody. Images were captured on the iPALM microscope described above. The following filters (max values) were applied for data visualization: Sigma X,Y Pos rtNph = 0.055, Sigma X,Y Pos Full = 0.2, Group Sigma X,Y Pos = 0.2, Group Sigma Z = 30, Unwrapped Z Error = -80 (min)/80 (max), Unwrapped Group Z Error = -80 (min)/80 (max). Whole cell images were median filtered (2 \times 2) and inverted to aid visualization. Adhesion insets were gaussian filtered (2 \times 2). Scale bar is 10 μ m.

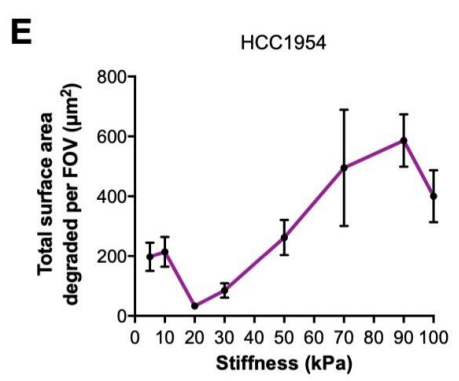
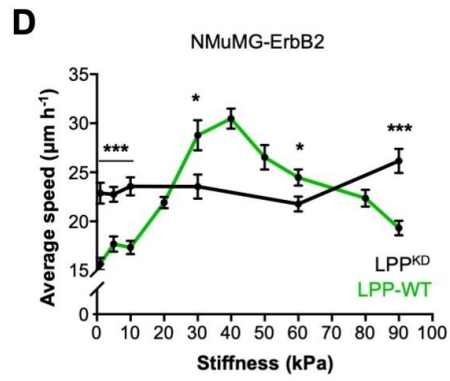
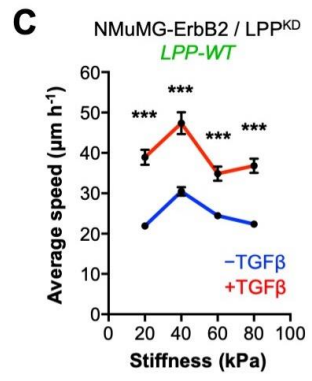
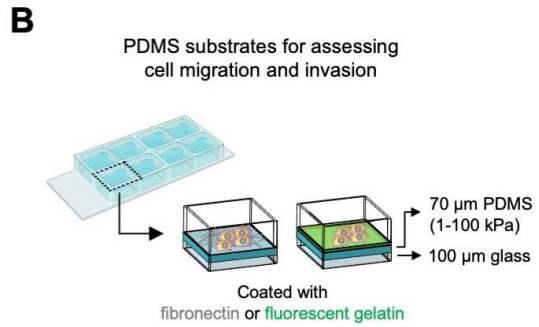
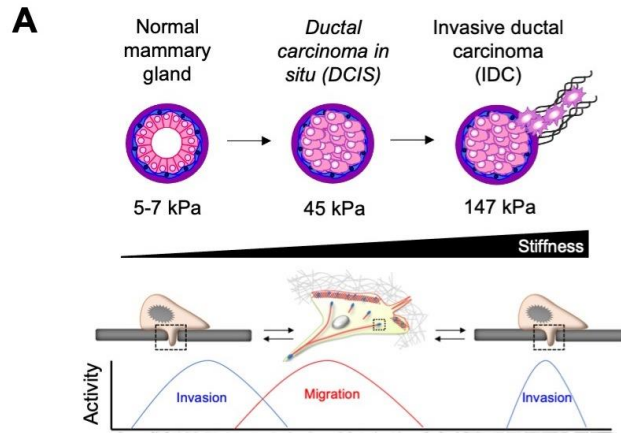


Figure 5.3. LPP is required for sensing substrate stiffness. (A) Schematic diagram showing mammary gland stiffness during breast cancer progression (*top panel*). Young's moduli are based on previously published results [24-26]. A hypothetical schematic depicting breast cancer cell migration and ECM degradation responses on changing substrate stiffness (*bottom panel*). (B) Schematic diagram of polydimethylsiloxane (PDMS) substrates used to assess cell migration and invasion in response to substrate stiffness. A thin PDMS substrate (70 μm) tuned to a specific stiffness (1-100 kPa) was polymerized on a glass coverslip (100 μm). The substrate was then activated and coated with fibronectin or fluorescent gelatin to assess cell migration or invasion, respectively. (C) NMuMG-ErbB2/LPP^{KD} cells expressing LPP-WT were plated onto 20, 40, 60 and 80 kPa substrates coated with fibronectin (5 $\mu\text{g cm}^{-2}$) in the absence or presence of TGF β (2 ng ml⁻¹). The average migration speed of individual cells was measured 18 h after treatment. Data represent mean \pm s.e.m. (*error bars*). Number of cells (*n*) are 44, 46, 34 and 39 for untreated and 20, 17, 17 and 11 for treated cells. *** $p < 0.001$; two-tailed Student's *t* test. (D) NMuMG-ErbB2/LPP^{KD} (*black trace*) and NMuMG-ErbB2/LPP^{KD}/LPP-WT cells (*green trace*) were plated on PDMS substrates coated with fibronectin to assess cell migration. Data represent mean \pm s.e.m. (*error bars*). Number of cells (*n*) are 37, 54, 51, 33, 63 and 35 for LPP^{KD} cells on 1, 5, 10, 30, 60 and 90 kPa, respectively. Number of cells (*n*) are 45, 31, 48, 22, 12 and 41 for LPP-WT cells on 1, 5, 10, 30, 50 and 90 kPa, respectively. The graph also contains migration data from C. * $p < 0.05$, *** $p < 0.001$; two-tailed Student's *t* test. (E) HCC1954 cells pre-treated with TGF β for 24 h were plated on PDMS substrates coated with fluorescently labelled gelatin to assess cell invasion. Cells were allowed to invade for 24 h before fixing with 4% PFA and quantifying invasion. Invasion data is also presented in [97]. Data represent mean \pm s.e.m. (*error bars*). Number of cells (*n*) are 16, 18, 11, 25, 22, 9, 25 and 28 on 5, 10, 20, 30, 50, 70, 90 and 100 kPa, respectively.

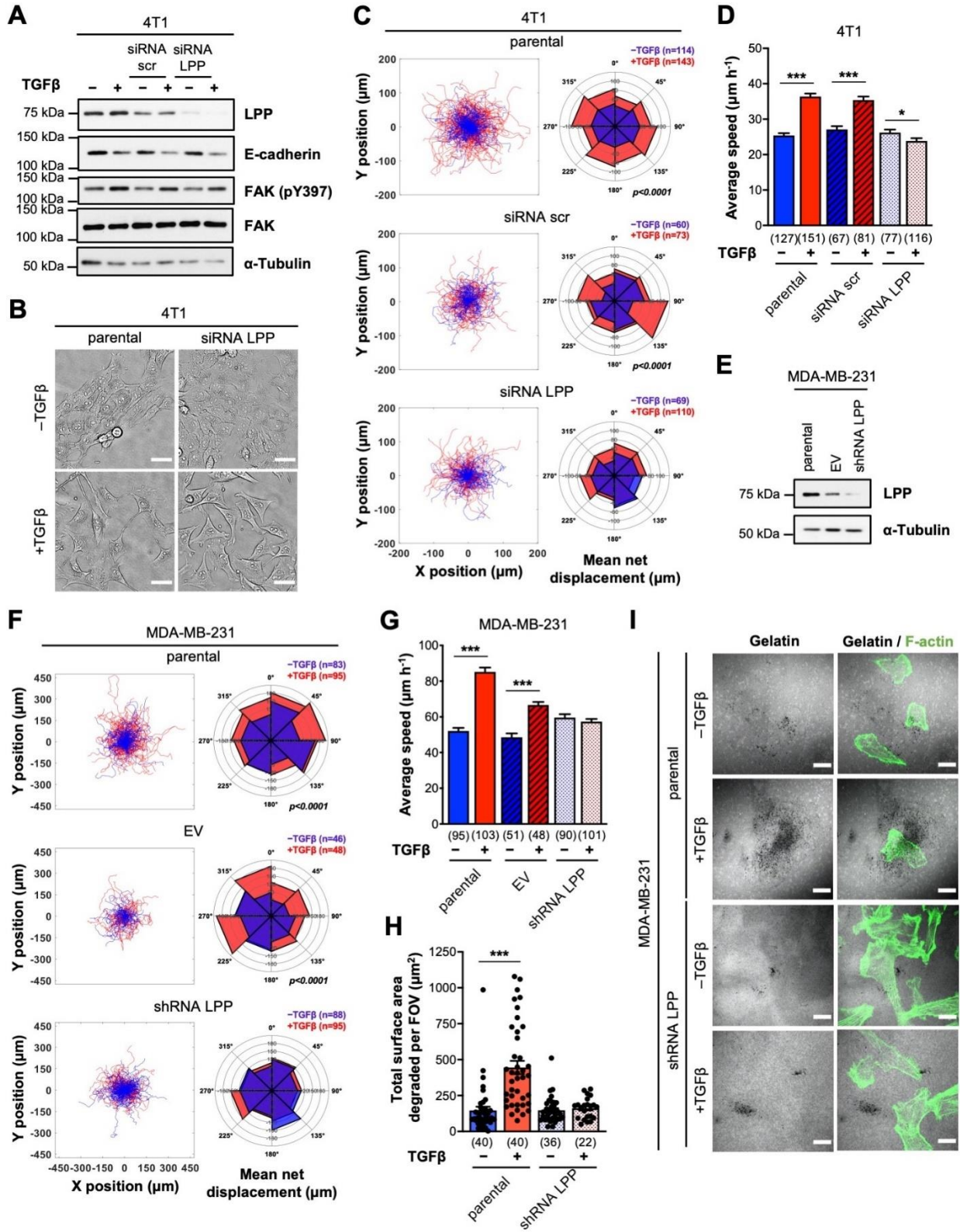


Figure 5.4. LPP is an important regulator of triple-negative breast cancer cell migration and invasion. (A) Immunoblot analyses of whole-cell lysates showing LPP, E-cadherin, FAK and phospho-FAK (pY397) levels in the indicated cell populations. 4T1 triple-negative breast cancer (TNBC) cells were transfected with an siRNA against LPP (siRNA LPP) or a scrambled control (siRNA scr). Cells were then cultured in low serum media with or without TGF β (2 ng ml⁻¹) for 48 h. α -Tubulin was used as a loading control. (B) 4T1 cells cultured in the absence or presence of TGF β for 24 h were seeded onto glass coverslips coated with fibronectin (5 μ g cm⁻²). Images were captured on a Zeiss AxioObserver using a Plan-Apochromat \times 20/0.8 NA objective lens. Scale bar is 40 μ m. (C) 4T1 cells seeded on fibronectin coated coverslips were allowed to migrate in the continued absence or presence of TGF β . Each *line* represents the migration path of a single cell over 5 h (*left panels*). The starting point of each cell was superimposed on the origin (0, 0). Cell displacements were pooled into 45° segments based on their angle of trajectory and averaged to determine mean net displacement (*right panels*). (D) Average migration speed for each condition was calculated by determining the mean distance travelled between each imaging time point. Data represent mean \pm s.e.m. (*error bars*) for five (parental) or three (siRNA scr and siRNA LPP) independent experiments. (E) Immunoblot analyses of whole-cell lysates showing LPP levels in MDA-MB-231 TNBC cells infected with an empty vector (EV) or an shRNA against LPP (shRNA LPP). α -Tubulin was used as a loading control. (F and G) MDA-MB-231 cells cultured in the absence or presence of TGF β (2 ng ml⁻¹) for 24 h were seeded onto glass coverslips coated with fibronectin (5 μ g cm⁻²). Cells were imaged and tracked in the continued absence or presence of TGF β and analyzed for mean net displacement and average migration speed as described in C and D. Data represent mean \pm s.e.m. (*error bars*) for three (parental and shRNA LPP) or two (EV) independent experiments. (H and I) MDA-MB-231 cells cultured in the absence or presence of TGF β for 24 h were seeded onto fluorescently labelled gelatin. Cells were allowed to invade for 24 h before fixing with 4% PFA and staining with phalloidin (F-actin). Images were taken on a Zeiss CLSM using a Plan-Apochromat \times 63/1.4 NA oil immersion DIC objective lens. Scale bar is 20 μ m. Images were subsequently imported into Imaris to determine the total surface area degraded per field of view (FOV). Data represent mean \pm s.e.m. (*error bars*) for three independent experiments. Individual data points are depicted with *black dots*. Numbers in parentheses indicate the number of FOV or individual cells analyzed. * $p < 0.05$, *** $p < 0.001$; Mann-Whitney U test.

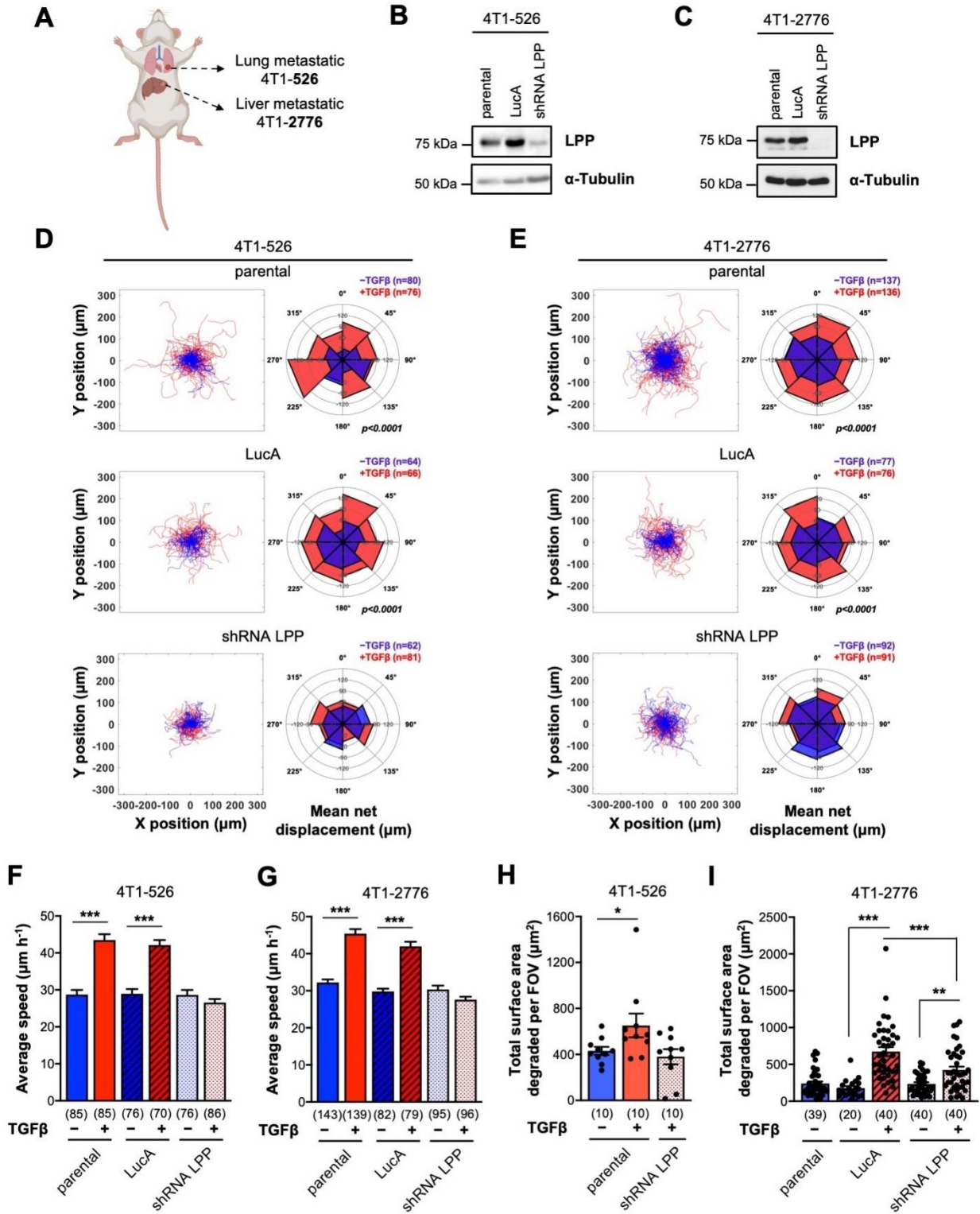


Figure 5.5. LPP is required for TGF β -enhanced migration and invasion of 4T1 derivatives that preferentially metastasize to the lungs and liver. (A) 4T1 sub-populations that metastasize to the lungs (4T1-526) or liver (4T1-2776) were previously isolated by our lab following *in vivo* selection of 4T1 parental cells [63, 64]. (B and C) Immunoblot analyses of LPP levels in 4T1-526 and 4T1-2776 cells expressing an shRNA against LPP (shRNA LPP) or luciferase (LucA). α -Tubulin was used as a loading control. (D and E) 4T1-526 and 4T1-2776 cells cultured in the absence or presence of TGF β (2 ng ml⁻¹) for 24 h were seeded onto glass coverslips coated with fibronectin (5 μ g cm⁻²). Each *line* represents the migration path of a single cell over 5 h (*left panels*). The starting point of each cell was superimposed on the origin (0, 0). Cell displacements were pooled into 45° segments based on their angle of trajectory and averaged to determine mean net displacement (*right panels*). (F and G) Average migration speed for each condition was calculated by determining the mean distance travelled between each imaging time point. Data represent mean \pm s.e.m. (*error bars*) for at least three independent experiments. *Numbers in parentheses* indicate the number of individual cells analyzed. (H and I) 4T1-526 and 4T1-2776 cells cultured in the absence or presence of TGF β for 24 h were seeded onto fluorescently labelled gelatin. Cells were allowed to invade for 24 h before fixing, staining and analysis of total surface area degraded per *FOV*. Data represent mean \pm s.e.m. (*error bars*) for one (4T1-526) or three (4T1-2776) independent experiments. Individual data points are depicted with *black dots*. *Numbers in parentheses* indicate the number of *FOV* analyzed. * $p < 0.05$, ** $p < 0.01$, *** $p < 0.001$; Mann-Whitney *U* test.

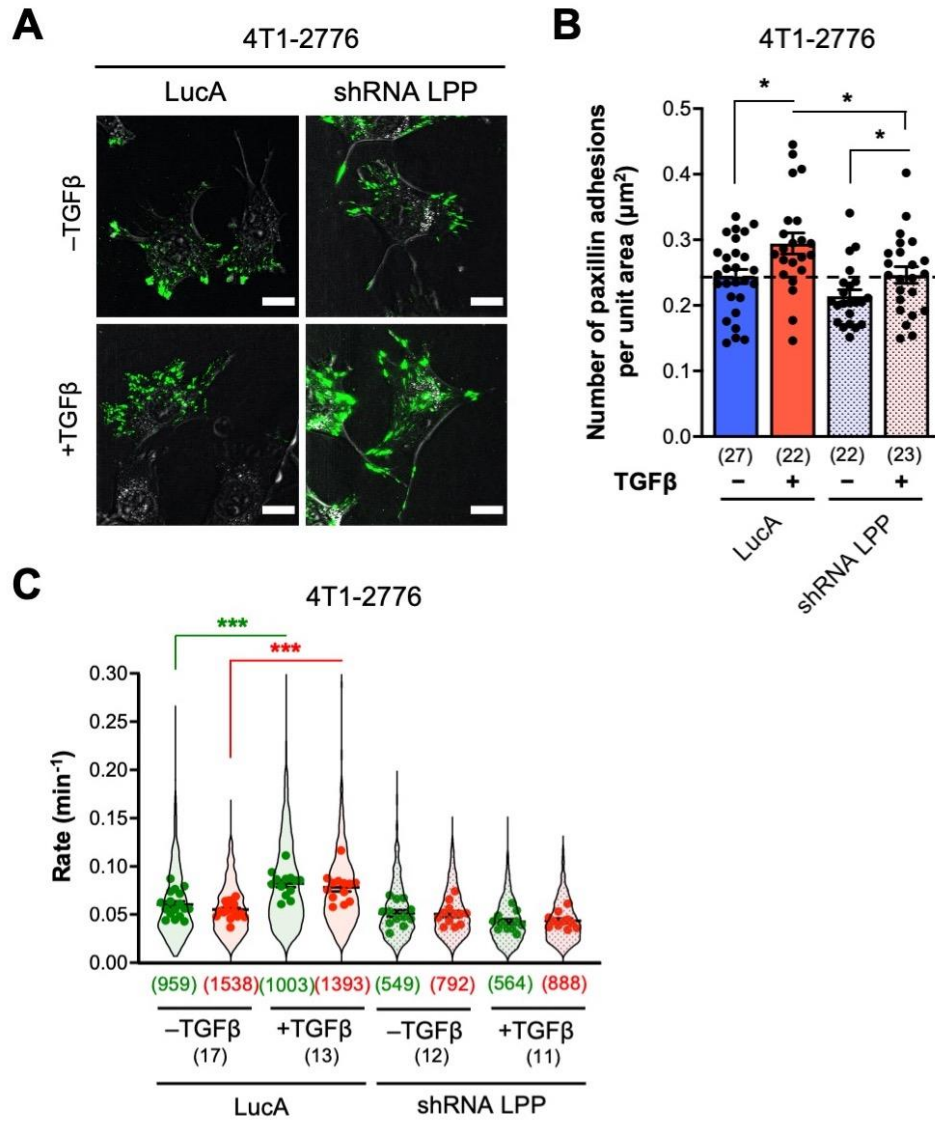


Figure 5.6. TGF β enhances adhesion dynamics in liver metastatic cells in an LPP-dependent manner. (A) 4T1-2776 cells were infected with mCherry-paxillin (a *bona fide* marker of cellular adhesions), seeded onto glass coverslips coated with fibronectin ($5 \mu\text{g cm}^{-2}$), and cultured in the absence or presence of TGF β (2 ng ml^{-1}) for 24 h. Images were acquired on a TIRF Spectral Discovery System coupled to a Leica microscope using a Plan-Apochromat $\times 63/1.47$ NA oil immersion DIC objective lens. mCherry-paxillin fluorescence (*green*) and differential interference contrast (DIC) (*grey*) images were captured for each cell and overlaid. Scale bar is $15 \mu\text{m}$. (B) Images were imported into Imaris to determine the average number of cellular adhesions for the indicated conditions. Data were normalized by dividing the number of adhesions in each cell by the total cell area. Cell area was determined from DIC images by drawing a contour around each cell. Data represent mean \pm s.e.m. (*error bars*) for two independent experiments. *Numbers in parentheses* indicate the number of individual cells analyzed. (C) 4T1-2776 cells expressing mCherry-paxillin were continuously imaged for 15 min. Adhesion assembly (*green*) and disassembly (*red*) rates were calculated from changes in mean intensity; Imaris was used to track adhesions over time whereas a custom algorithm in MATLAB was used to perform rate calculations. Individual assembly and disassembly events for each condition are shown as a violin plot. The width of the plot indicates probability density. The *coloured dots* represent cell averages for assembly and disassembly rates. Data represents mean \pm s.e.m. (*error bars*) for three (LucA) or two (shRNA LPP) independent experiments. *Coloured n* values refer to the number of events while *black n* values refer to the number of cells analyzed. * $p < 0.05$, *** $p < 0.001$; Mann-Whitney *U* test.

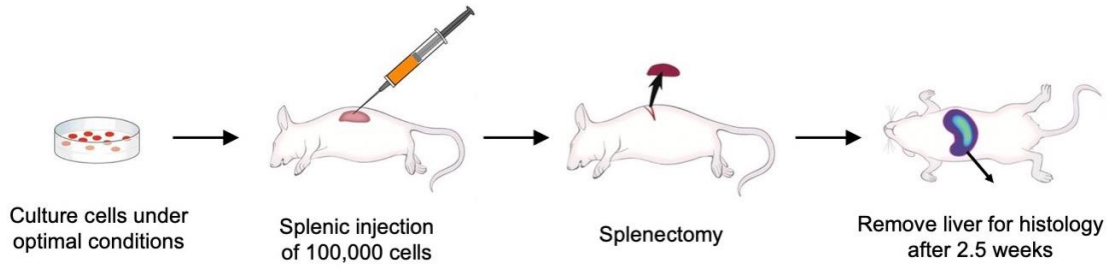
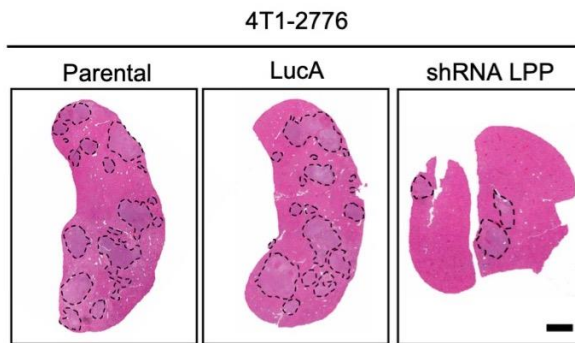
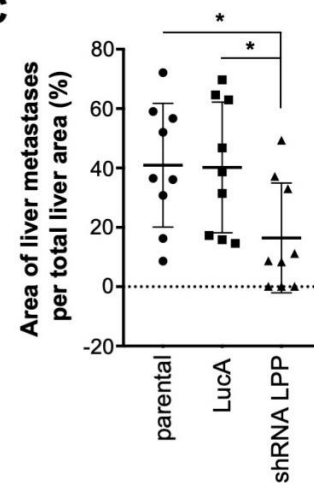
A**B****C**

Figure 5.7. Loss of LPP expression reduces liver-metastatic potential of TNBC cells. (A) Schematic diagram showing the design of the experimental liver metastasis assay. 4T1-2776 cell populations were injected into the spleens of BALB/c mice. Spleens were removed after cancer cell drainage into the portal vein. Mice were monitored for 2.5 weeks post-injection before animals were sacrificed and livers resected. (B) Representative hematoxylin & eosin (H&E) images of metastatic burden in the left cardiac liver lobe following splenic injection. Scale bar is 2 mm. (C) Quantification of tumor burden (tumor area/tissue area). Data represents mean \pm s.e.m. (*error bars*). *Symbols* indicate the total tumor burden for each mouse calculated from four H&E stained step sections (200 μ m/step). $n = 9$ for parental, LucA and shRNA LPP. * $p < 0.05$; Mann-Whitney U test.

5.9 SUPPLEMENTARY INFORMATION

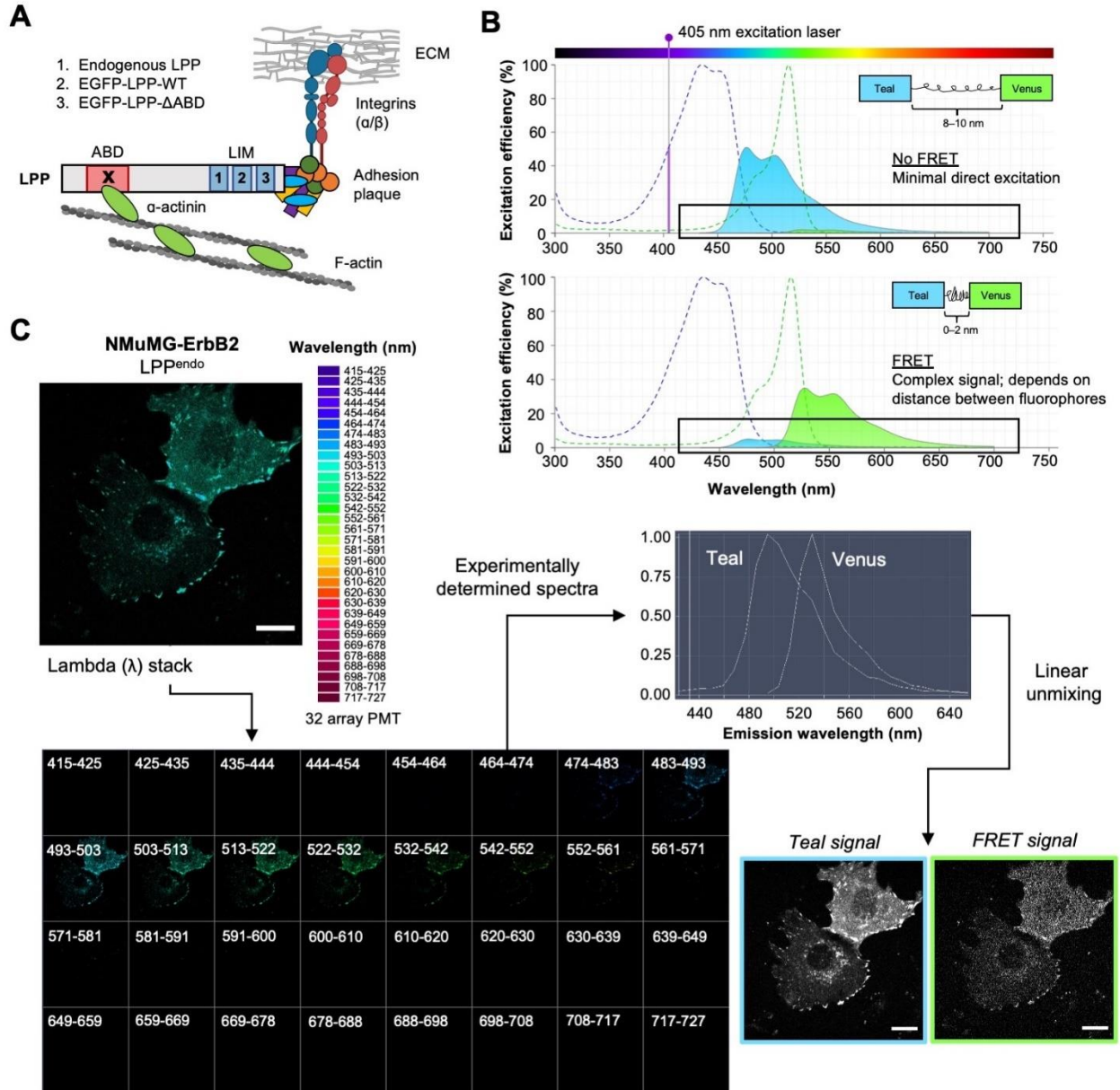


Figure S5.1. Spectral capture and linear unmixing can be used to measure adhesion tension.

(A) Schematic diagram of LPP showing its three LIM domains (1, 2, 3) and α -actinin binding domain (ABD). The LIM domains regulate LPP localization to adhesions, while the ABD domain allows LPP to interact with the actin cytoskeleton. NMuMG-ErbB2 cells with an shRNA against LPP (LPP^{KD}) were rescued with fluorescently labelled wildtype LPP (LPP-WT) or an ABD domain mutant (LPP- Δ ABD). (B) Schematic diagram depicting FRET energy transfer between teal and venus fluorescent proteins in the vinculin tension sensor (VinTS). Under high tension conditions, the elastic linker between teal and venus is stretched, resulting in a large distance between the fluorophores (*top panel*). Sample excitation with 405 nm light causes teal excitation/emission and minimal direct venus excitation. Under low tension conditions, the elastic linker between teal and venus is relaxed, resulting in a small distance between the fluorophores (*bottom panel*). Sample excitation with 405 nm light causes teal excitation; however, a significant amount of energy is transferred to venus. Therefore, the resulting image contains both teal and venus emission. The diagram was made with the help of BD Biosciences Spectrum Viewer. (C) The complex signal obtained from fluorophores undergoing FRET can be mathematically unmixed on a confocal laser scanning microscope (CLSM). First, emission signal is split across a 32 PMT array (9.8 nm segments shown here) and recombined into a lambda (λ) stack. The lambda stack is then compared to experimentally determined spectra for each fluorophore alone (teal-vinculin and venus-vinculin in the case of VinTS). Linear unmixing algorithms generate two unmixed images corresponding to teal and venus (FRET) emission. Finally, teal and FRET fluorescence intensity levels can be compared to determine adhesion tension. Autofluorescence was also measured and found to be insignificant. Scale bar is 20 μ m.

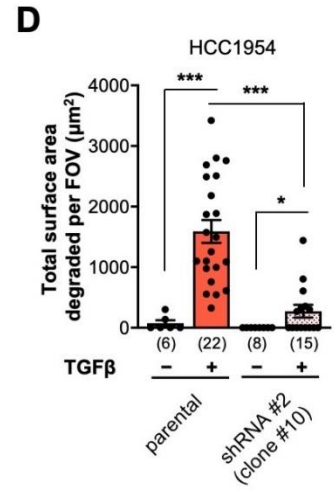
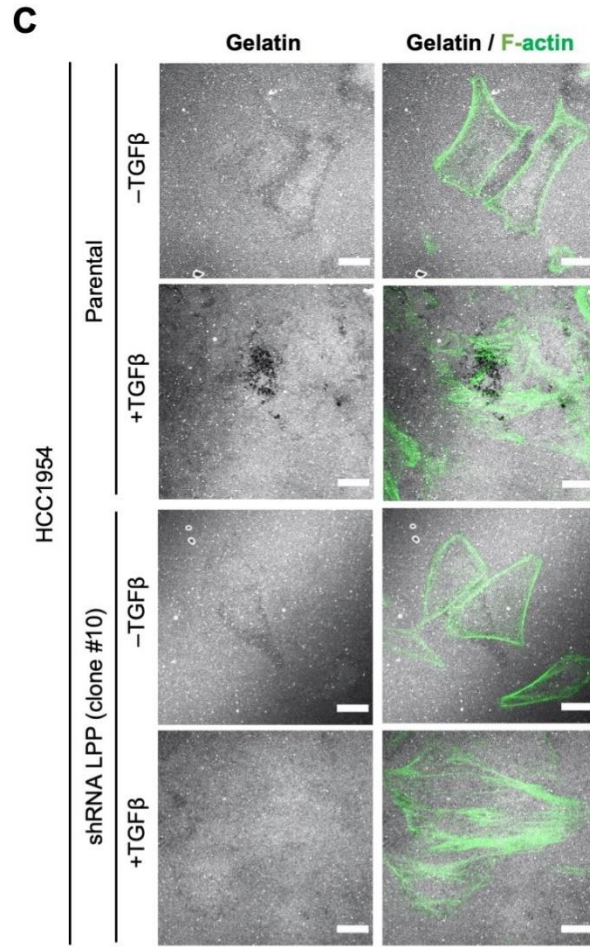
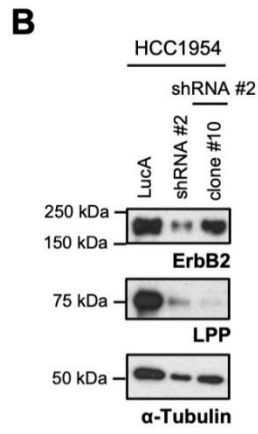
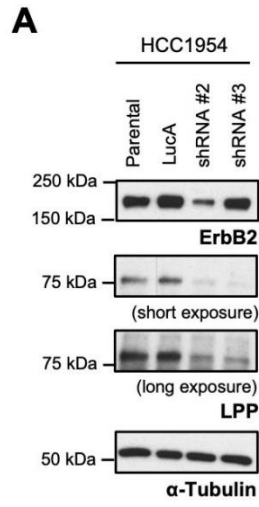
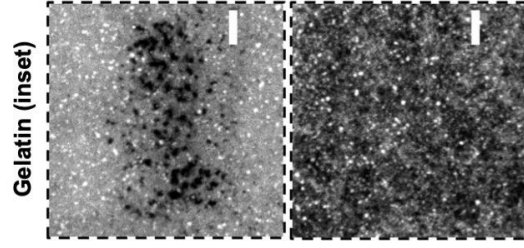
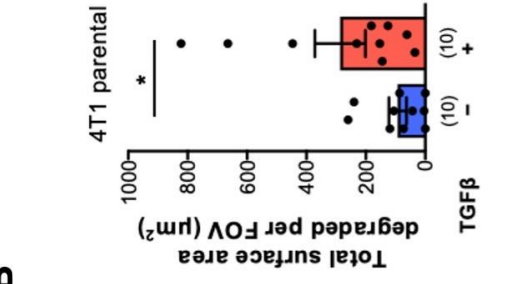


Figure S5.2. LPP is required for TGF β -enhanced invasion of ErbB2⁺ cells. (A and B) Immunoblot analyses of whole-cell lysates showing ErbB2 and LPP levels in parental HCC1954 cells and populations expressing an shRNA against luciferase (LucA) or an shRNA against LPP (shRNA #2 or shRNA #3). Individual clones were selected to identify cells with better LPP silencing. Clone #10 within shRNA #2 was found to exhibit the best LPP knockdown. α -Tubulin was used as a loading control. (C) HCC1954 cells were cultured in the absence or presence of TGF β (2 ng ml⁻¹) for 24 h and seeded onto fluorescently labelled gelatin. Cells were allowed to invade for 24 h before fixing with 4% PFA and staining with phalloidin (F-actin). Images were taken on a Zeiss CLSM using a Plan-Apochromat $\times 63/1.4$ NA oil immersion DIC objective lens. Scale bar is 20 μ m. (D) Images were imported into Imaris to determine the total surface area degraded per field of view (FOV). Data represent mean \pm s.e.m. (*error bars*). Individual data points are depicted with *black dots*. Numbers in parentheses indicate FOV analyzed. * $p < 0.05$, *** $p < 0.001$; Mann-Whitney U test.

B



A

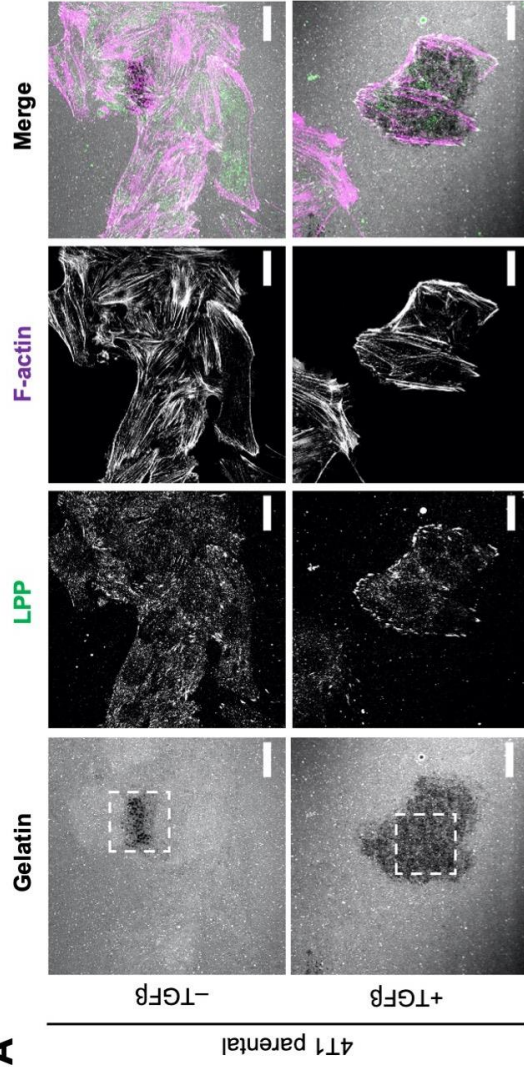


Figure S5.3. 4T1 triple-negative breast cancer cells exhibit enhanced invasion following TGF β stimulation. (A) 4T1 parental cells were cultured in absence or presence of TGF β (2 ng ml⁻¹) for 24 h and seeded onto fluorescently labelled gelatin. Cells were allowed to invade for 24 h before fixing with 4% PFA and staining with antibodies against LPP and phalloidin (F-actin). Images were taken on a Zeiss CLSM using a Plan-Apochromat $\times 63/1.4$ NA oil immersion DIC objective lens. Scale bar is 20 μ m for whole-cell images and 5 μ m for magnified images. (B) Images were imported into Imaris to determine the total surface area degraded per field of view (FOV). Data represent mean \pm s.e.m. (*error bars*). Individual data points are depicted with *black dots*. Numbers in parentheses indicate FOV analyzed. * $p < 0.05$; Mann-Whitney U test.

CHAPTER 6 – General Discussion and Future Directions

6.1 SUMMARY

The work described in this thesis highlights two important aspects of breast cancer cell biology. First, cell migration and invasion are fundamental processes that promote metastasis. Breast cancers that metastasize to essential organs account for most cancer-related deaths [1-3]. Thus, we explored the mechanisms controlling breast cancer cell migration and invasion. Second, fluorescence microscopy provides a convenient and selective way to observe the behavior of cells in response to genetic and pharmacological manipulations. Unfortunately, the process of imaging fluorescent molecules with light can cause phototoxicity. Therefore, we explored ways of optimizing live-cell fluorescence imaging conditions.

In chapter 2, we describe a detailed workflow for fluorescence microscopy to image both slow and fast cellular processes. We show that light beyond the camera exposure time, termed “illumination overhead” (IO), accounts for much of the photobleaching and phototoxicity experienced with live-cell fluorescence imaging. Fast-switching LED lamps with transistor-transistor logic (TTL) circuits can effectively eliminate IO; however, many microscopy platforms cannot take advantage of camera-based TTL triggering. Therefore, the goal of this manuscript [4] is to raise awareness of phototoxicity issues and help researchers develop imaging protocols that more accurately capture cellular events without artifacts due to phototoxicity.

In chapter 3, we show that hardware and software delays can contribute to phototoxicity and lead to inappropriate delays between subsequent images even when TTL is enabled. We found that the LED light source had to be completely disconnected from the microscope acquisition software to prevent IO. Furthermore, we discovered that imaging intervals below a certain value could not be realized, even though the time resolution was theoretically possible. This study [5] underscores the importance of verifying imaging parameters with an oscilloscope and not relying only on the image acquisition software settings. In the future, we will develop a detailed protocol for identifying and measuring IO on any given microscopy platform. Additionally, we will continue to investigate factors that contribute to IO and alter its duration.

We previously found that the adapter/scaffold proteins p46/52ShcA and lipoma preferred partner (LPP) are required for the migration, invasion and metastasis of ErbB2-overexpressing breast cancer cells [6-9]. In chapter 4, we establish that p46/52ShcA and LPP promote further and faster cell migration in response to TGF β . Both adapter proteins are required for the formation of small, dynamic adhesions and invadopodia. p46/52ShcA must be phosphorylated on tyrosine

residues 239/240 or 313, and LPP must localize to adhesions and interact with the actin cytoskeleton through its LIM and α -actinin binding domains, respectively, to mediate these effects. Furthermore, TIRF microscopy reveals that p46/52ShcA is a novel component of adhesions and its localization to these structures precedes LPP [10].

In chapter 5, we show that LPP is an important mechanoregulatory and mechanosensory protein in ErbB2⁺ cells. TGF β enhances adhesion tension in protrusive cell regions in an LPP-dependent manner. The α -actinin binding domain (ABD) is required for TGF β -mediated tension, as cells expressing LPP with a deleted ABD domain (LPP- Δ ABD) do not exhibit increased adhesion forces. Furthermore, we show that LPP is required for substrate stiffness sensing. Cells expressing wildtype LPP migrate maximally on PDMS substrates with intermediate stiffnesses (~40 kPa) and invade maximally on soft (<5 kPa) and hard (>100 kPa) substrates. In contrast, cells lacking LPP are insensitive to substrate stiffness. We also show that LPP is required for the migration, invasion and metastasis of triple-negative breast cancer (TNBC) cells. Human MDA-MB-231 cells, mouse 4T1 cells, and 4T1 derivatives that preferentially metastasize to the lungs (4T1-526) and liver (4T1-2776), fail to exhibit TGF β -induced migration and invasion when LPP expression is silenced. Importantly, 4T1-2776 cells with LPP knockdown show decreased liver metastatic burden following splenic injection.

6.2 MITIGATING PHOTOTOXICITY

6.2.1 Changing the light dose delivery method

In this thesis and previous work [11], we demonstrate that light dose delivery has a profound impact on photobleaching and phototoxicity. We find that longer exposure times with lower light powers are more amenable to live-cell fluorescence imaging. While this is true for conventional microscope setups, longer exposure times do not improve cell health when TTL effectively eliminates IO. Instead, we find that total light dose (exposure time \times light power) affects the amount of ROS produced by fluorescence illumination. Interestingly, several studies show that light pulsing effectively reduces photobleaching and phototoxicity [12-14]. An intriguing hypothesis is that short rest times between subsequent pulses alleviate pressure on cellular mechanisms designed to eliminate ROS. Preliminary studies from our lab demonstrate that short light pulses (width = 25-100 μ s; rest time = 150-300 μ s) significantly reduce photobleaching and support faster cell protrusion rates [15]. Further work is required to determine the effect of light

pulsing on mitochondrial morphology and ROS production; however, based on the results presented in this thesis, we predict that shorter light pulses with longer gap times will reduce ROS accumulation over time.

6.2.2 Reducing ROS

Numerous sites within the electron transport chain produce ROS [16], which negatively impacts cell health by damaging DNA, lipids and proteins [17-19]. Consequently, cells possess several types of antioxidant enzymes to reduce ROS levels, including superoxide dismutase (SOD), catalase, glutathione peroxidase (GPx), peroxiredoxins and thioredoxins. Low or absent expression of these antioxidant enzymes increases cellular sensitivity to oxidative stress. For example, *SOD1* knockout mice ($^{-/-}$) exhibit extensive oxidative damage in the cytoplasm [20, 21], resulting in delayed wound healing [22], an increase in cellular senescence [23], hepatocarcinogenesis [21], and various diseases associated with neurodegeneration [24]. Similarly, mice heterozygous for *SOD2* ($^{+/-}$) show evidence of DNA damage and a 100% increase in tumor incidence compared to wildtype mice [25].

SOD proteins form the first line of defense against oxidative stress by degrading superoxide anion (O_2^-) in the cytoplasm and mitochondria [26-28]. While antioxidant enzymes have been extensively studied in the context of cancer and neurodegeneration, relatively little is known about their roles in alleviating fluorescence-induced ROS. Cancer cells express different levels of SOD depending on context-dependent stimuli [29-33], presenting an opportunity to explore enzyme function in response to phototoxicity. We hypothesize that SOD enzymes offer protection against O_2^- produced by singlet excited fluorescent molecules; cells with higher levels of SOD expression likely clear ROS more effectively, resulting in less ROS accumulation over the same imaging period. A previous study using V79 Chinese hamster cells demonstrates that cells expressing higher levels of SOD1 exhibit faster O_2^- degradation kinetics [34]. It is important to note that SOD enzymes generate H_2O_2 , which must be degraded into H_2O and O_2 by catalase to avoid cellular damage. Stable overexpression of catalase, but not SOD1, increases cellular resistance to H_2O_2 treatment [35]. Similarly, T47D human breast cancer cells expressing higher levels of GPx1 are more resistant to H_2O_2 , cumene hydroperoxide and menadione [36]. Thus, it would be interesting to compare mitochondrial morphology and the migration speed of cells with different levels of both antioxidant enzymes in response to different light doses.

Antioxidant enzymes and other reducing agents are occasionally added to cell culture media in an effort to minimize photobleaching and phototoxicity. Catalase is currently used in an oxygen scavenging system containing glucose oxidase (GOX/CAT); glucose oxidase catalyzes a reaction between glucose and dissolved O₂ to produce gluconic acid and H₂O₂, which is subsequently broken down into O₂ and H₂O by catalase [37]. This cyclic reaction reduces O₂ levels substantially [38] to prevent reactions with excited triplet state fluorophores; however, there are two important caveats to consider: (1) aerobic organisms require oxygen for ATP production and (2) removal of oxygen enhances the lifetime of triplet state fluorophores [39-41]. Indeed, GOX/CAT causes hypoxia within minutes [42] and induces fluorophore blinking [43]. Ascorbic acid (vitamin C) has also been used to diminish photobleaching by reducing excited singlet oxygen (¹O₂) [44-47]. Unfortunately, photobleaching is reduced only for certain fluorophores [38]. Moreover, ascorbic acid can generate other ROS species in living cells depending on the availability of substrates such as Fe and Cu [48-50]. As a result, the diffuse light delivery (DLD) method we employed in our studies is a more attractive option for general use in all imaging situations to reduce phototoxicity. A range of fluorescent probes has recently been developed to measure O₂⁻, H₂O₂ and other reactive oxygen, nitrogen and sulfur species [51]. Measuring the relative amounts of each species generated by fluorescence may reveal new ways, or highlight ideal light delivery techniques, to limit phototoxicity.

6.3 NEW IMAGING APPROACHES ENABLE NOVEL BIOLOGICAL QUESTIONS

The microscopy techniques developed in chapters 2 and 3 will allow us to explore novel biological questions that could not previously be captured due to photobleaching. Diffuse light delivery (DLD) will allow us to perform live-cell imaging of multiple adhesion and invadopodia components over time. Additionally, our workflow may allow us to combine adhesion dynamics, adhesion tension and traction force mapping measurements to determine which proteins play an essential role in transducing intracellular actomyosin forces into extracellular migration forces.

6.3.1 Live-cell imaging of multiple adhesion components

In chapter 4, we explored the dynamics of adhesions in NMuMG-ErbB2 cells. Images were captured every 20 s with a camera exposure time of 500 ms, in line with previous studies exploring the assembly and disassembly of these structures [52-54]. Although we found that TGFβ enhanced

adhesion dynamics, it is important to note that nascent adhesions found at the protruding edge of the cell are typically sub-resolution ($<1 \mu\text{m}$ in diameter) and have a short lifespan ($<1 \text{ min}$) [55, 56]. Therefore, assembly and disassembly events arising from nascent adhesions successfully identified with CLSM were likely missed during time-lapse TIRF imaging.

Interval imaging with short camera exposure times is typically employed to reduce light exposure on the sample and avoid object blurring. In chapter 2, we show that the interval between subsequent images can be dramatically reduced by employing longer exposure times with lower light levels (DLD). Continuous illumination of the sample can capture rapid adhesion dynamics and other cellular processes with no apparent phototoxicity. While this method appears to be counterintuitive, it reduces fluorescence-induced ROS production by decreasing the relative amount of IO delivered to the sample. As a result, it is possible to image the relatively unstable fluorescent proteins found in VinTS (teal and venus fluorescent proteins) continuously for at least 40 min. In chapter 5, we switch to this new method of imaging to quantify adhesion dynamics in 4T1-2776 cells. The assembly and disassembly rates of adhesions within these cells are comparable to the dynamics observed for NMuMG-ErbB2 cells, further solidifying the validity of this method.

In the future, we will continue to use DLD to investigate adhesion dynamics in MDA-MB-231 cells, which exhibit significantly faster cell migration speeds than NMuMG-ErbB2, 4T1-526 and 4T1-2776 cells. Preliminary experiments suggest that MDA-MB-231 cells possess small adhesions with a significant shift to even more rapid adhesions following TGF β treatment. Additionally, DLD will allow us to image several adhesion proteins simultaneously to determine their localization as a function of adhesion maturation. In chapter 4, we show that p46/52ShcA localizes to adhesions before LPP; however, it would be worthwhile to image p46/52ShcA and LPP recruitment in relation to other known adhesion components. Mass spectrometry analysis of adhesions after 15 min of nocodazole-induced disassembly indicates that the signaling proteins paxillin and FAK exhibit $\sim 12\%$ and $\sim 16\%$ abundance, respectively [57]. In contrast, the adapter/scaffold proteins LPP, α -actinin and vinculin exhibit $\sim 43\%$, $\sim 64\%$ and 73% abundance, respectively [57]. This data is roughly in line with previous iPALM imaging of adhesion components in human osteosarcoma cells, which shows that FAK and paxillin are localized closest to the plasma membrane in a signaling layer, vinculin is localized to an intermediate force transduction layer, and zyxin and α -actinin are localized to an uppermost actin-regulatory layer

[58]. Based on live-cell TIRF data (chapter 4) and iPALM imaging (chapter 5), we hypothesize that p46/52ShcA localizes to the signaling layer of adhesions around the same time as FAK and paxillin. On the other hand, we predict that LPP localizes to the force transduction layer occupied by α -actinin. Multi-color live-cell imaging and super-resolution mapping of adhesion components will help us understand how p46/52ShcA regulates LPP recruitment to adhesions to increase adhesion tension following TGF β stimulation.

6.3.2 Live-cell imaging of invadopodia

Invadopodia are specialized degradative structures that mechanically and enzymatically facilitate tumor cell invasion [59-65]. We recently identified LPP as a critical mediator of invadopodia formation in ErbB2⁺ breast cancer cells [9]. In this thesis, we show that p46/52ShcA is also required for ErbB2⁺ cell invasion (chapter 4). Additionally, we demonstrate that LPP is required for TNBC cell invasion (chapter 5). In both chapters, cells were seeded onto glass coverslips coated with a thin layer of fluorescent gelatin. After 24 h, cells were fixed and loss of gelatin fluorescence was quantified as area degraded. Cells were also stained for F-actin and one of two established markers of invadopodia: Tks5 or cortactin [66-70]. Interestingly, NMuMG-ErbB2 cells possessed few actin puncta even after TGF β treatment despite a dramatic increase in gelatin degradation. This result may be explained by the fact that invadopodia are dynamic structures with a typical lifetime of 5 to 15 min [62, 71, 72]. We previously attempted to perform dual-color live-cell microscopy of actin and fluorescent gelatin but found phototoxicity to be a significant impairment, in line with the efforts of other groups [73]. The imaging protocol presented in chapter 2 may now allow us to image invadopodia over time with limited phototoxicity. Current models of invadopodia formation suggest that cofilin, Arp2/3, N-WASP and cortactin are involved in precursor core initiation [62]. Tks5 and SHIP2 are subsequently recruited to stabilize the precursor core to the plasma membrane [62]. Finally, Nck1 and Cdc42 activate the N-WASP-Arp2/3 complex to nucleate actin polymerization; Cdc42 and RhoA also recruit membrane tethered matrix metalloproteinase (MT1-MMP) to the plasma membrane [62]. Multi-color live-cell imaging of LPP and other invadopodia components may reveal how p46/52ShcA and LPP enhance cell invasion in response to TGF β . Our BioID data indicates that p46/52ShcA is proximal to cortactin and actin-related protein 2 (Arp2) (chapter 4). Arp2 is the ATP-binding component of the Arp2/3 complex responsible for actin filament elongation [74, 75].

Furthermore, p46/52ShcA interacts with Septin2, Septin6 and Septin7 (chapter 4), which form a diffusive barrier around nascent podosomes to promote their maturation [76]. Thus, it is possible that p46/52ShcA is an early signaling component involved in invadopodia formation.

6.3.3 Live-cell imaging of adhesion tension and traction force mapping

Finally, DLD will allow us to measure adhesion tension over time using the VinTS construct described in chapter 5. Current methods for FRET imaging require too much light to be applied to the sample for efficient live-cell time-lapse imaging; however, we now demonstrate that teal and venus fluorescent proteins can be imaged continuously on an SD confocal microscope with no apparent phototoxicity (chapter 2). We envision an experimental setup where cells expressing VinTS are seeded on a PDMS substrate containing fluorescent beads for traction force microscopy. First, a laser will be used to excite mTFP1; the returning mTFP1 and venus (FRET) emission will be separated by a beam splitter and the signals will be recorded on two separate sCMOS cameras. The z position of the objective will then be lowered to focus on the fluorescent beads below the cell. After an image of the beads is acquired, the objective focus will return to VinTS within cellular adhesions. Longer exposure times with lower light levels will enable us to measure vinculin adhesion dynamics, adhesion tension and traction force in different adhesion classes and at different stages of adhesion maturation. This experimental setup will also allow us to determine if adhesion tension and traction force are intimately linked processes. Previous studies suggest that traction force and adhesion tension increase as a function of substrate stiffness [77, 78]. These results are congruent with the fact that stiffness induces adhesion maturation [79]. Adhesions are likely more load bearing on stiffer substrates due to the recruitment of additional adapter and scaffold proteins [80-82]; however, the formation of very large adhesions can also impede cell migration [83, 84]. In line with these studies, we find that NMuMG-ErbB2 cells migrate more rapidly on 40 kPa than on 5 kPa or 90 kPa (chapter 5). Therefore, it would be interesting to determine if adhesion tension and traction force increase linearly as very soft substrates increase in stiffness, and whether the relationship between these forces changes at a certain stiffness. Furthermore, we would like to investigate whether LPP linkage to α -actinin is important for adhesion tension and traction force increases as a function of stiffness.

In addition to the experimental setup described above, we may be able to answer these biological questions with newer microscopy platforms that deliver excitation light in a unique way.

Traditional fluorescence microscopes deliver excitation light and capture fluorescence emission with a single objective lens. The objective lens is placed above or below the sample such that the entire volume is illuminated within a field of view. Optical (z) sectioning can be used to record a thin layer of the sample, such as in confocal microscopy; however, these microscopy techniques still excite a large pool of fluorophores whose emission is simply discarded. In contrast, light sheet [85, 86] and lattice light sheet [87] microscopes use an additional objective lens perpendicular to the direction of observation to illuminate a thin slice (hundreds of nanometers to a few micrometers). By exposing a thin sheet of the sample to excitation light, this novel method of light delivery dramatically reduces photobleaching and improves sample health [88, 89]. Moreover, light sheets with sub-micrometer thickness yield incredible resolution in x , y and z : $230 \times 230 \times 370$ nm in dithered mode and $150 \times 150 \times 280$ nm in structured illumination microscopy mode [87].

Lattice light sheet microscopy is quickly becoming the preferred method for observing organellar, cytoskeletal and 3D cell migration dynamics [90-93]. Our lab is in the process of acquiring a lattice light sheet microscope capable of high-speed, high-resolution imaging. We hope to perform high resolution time-lapse imaging of p46/52ShcA, LPP, α -actinin and other proteins within adhesions. It would be particularly interesting to adapt FRET-based adhesion tension sensors to this experimental system to investigate how adhesion architecture and protein dynamics change over time in response to adhesion tension.

6.4 ROLE OF LPP IN CELLULAR MECHANOMEMORY

Recent studies demonstrate that cells acquire mechanomemory of substrate stiffness through a mechanism involving YAP/TAZ [94-96]. Consequently, cells cultured on stiff substrates maintain elevated migration speeds on soft substrates up to 48 h after re-seeding [97]. We show that ErbB2⁺ breast cancer cells with wildtype LPP modulate their migration speed in response to stiffness (chapter 5), which aligns well with previous studies using fibroblasts [83, 98, 99]. We also recently identified PDLIM7/Enigma as an LPP interacting partner in NMuMG-ErbB2 cells through a BioID screen [100]. PDLIM7 is known to bind YAP and trigger its activation following mechanical stretching of adhesions [101]. This interaction requires further investigation as it may provide insight into how LPP influences cell migration and invasion in response to substrate stiffness.

Mechanomemory may have important implications for breast cancer metastasis. The stiffness of the extracellular environment varies widely throughout the body. Notably, brain and bone exhibit Young's moduli of $\sim 1-4$ and $\sim 15,000-20,000$ kPa, respectively [102]. In contrast, the stiffness of tissue culture plastic is ~ 3 GPa. Our group and others have successfully isolated breast cancer cells that preferentially metastasize to the lungs, liver, brain and bone [103-108]. We are interested in exploring whether cells that exhibit site specific metastasis display differences in cell migration and invasion in response to stiffness. In extension, can stiffness be used to prime breast cancer cells for metastasis to certain organs; can existing metastatic preference be re-programmed for metastasis to another tissue/organ; and is LPP a critical mediator of this process? If so, could targeting LPP result in new and novel breast cancer therapeutics?

6.5 OTHER EXTRACELLULAR FORCES THAT INFLUENCE CELL BEHAVIOR

6.5.1 Viscoelasticity

In this thesis, we investigated the role of substrate stiffness on breast cancer cell migration and invasion. Our motivation to pursue this line of research stemmed from the fact that breast tissue stiffens with cancer progression from ~ 5 to 147 kPa [109]. While stiffness is an important prognostic factor that enhances metastatic phenotypes, it is important to note that most biological tissues and ECMs are not perfectly elastic like PDMS [110-114]. Tissues exhibit a time-dependent mechanical response and dissipate a fraction of energy it took to deform them, a property known as viscoelasticity. Soft tissues, such as lung, liver and brain, generally exhibit viscous moduli that are 10-20% of their elastic moduli [115]. Hard tissues, such as bone and cartilage, also exhibit viscosity at about 10% of their elastic moduli [115]. Importantly, malignant lesions are more viscoelastic than benign lesions [116-119].

Malignant tumors have increased collagen density [120, 121]; however, these collagen fibers are structurally different from those of normal ECM stroma [122, 123]. Reduced proteoglycan content and changes in ECM crosslinking decrease viscoelasticity [111, 124-126]. Viscoelasticity enhances the proliferation and differentiation potential of human mesenchymal stem cells [127, 128]. Cells cultured on soft 1.4 kPa substrates exhibit greater cell spreading and stress fiber formation when the substrate is viscoelastic rather than purely elastic [124]. Furthermore, MDA-MB-231 cells can extend invadopodia and mechanically enlarge channels in viscoelastic matrices (~ 1.8 kPa) to enhance migration [129]. In contrast, cells cultured on 9 kPa

substrates exhibit greater cell spreading as viscoelasticity decreases (faster stress relaxation), due to increased nuclear localization of YAP [128]. The molecular mechanisms underlying this dichotomous role are still unknown. Nevertheless, these results highlight the importance of viscoelasticity and substrate stiffness on cellular behavior.

Advancements in materials engineering allow the viscoelastic modulus (or rate of stress relaxation) to be tuned independently of hydrogel stiffness and cell-adhesion ligand density [128]. Given that LPP is required for substrate stiffness sensing, it would be interesting to explore whether its localization to adhesions and interaction with α -actinin is also required for viscoelastic sensing on these substrates. Knockdown of additional adhesion and actin cytoskeleton components may subsequently help elucidate how cells sense and respond to physiologically relevant values of viscoelasticity.

6.5.2 Fractionability

Another physical property that cells may be able to exploit is fractionability. Materials must be ‘strong’ and ‘tough’ to maintain structural integrity; strength refers to a material’s resistance to non-recoverable deformation, whereas toughness measures a material’s resistance to fracture [130]. Unfortunately, these properties tend to be mutually exclusive. Materials with higher strength do not dissipate stresses well and are therefore more prone to fracture. In contrast, materials with lower strength tend to deform more easily; dissipation of local stresses is better and therefore cracking does not occur as easily [130]. Human cortical bone provides an excellent example of a tissue that is strong but highly susceptible to fracture with aging or disease. The intrinsic toughness of bone arises from collagen fibrils. Aging and certain diseases enhance the crosslinking of advanced glycation end products [131, 132]. Repeated load application during daily activities causes the formation of microcracks [133, 134]. The amount of subsequent force required to increase fracture length is decreased, resulting in embrittlement. In the context of cancer, fractionability may explain how cells are able to breach basement membranes, which can exhibit Young’s moduli >1 MPa [135, 136]. Soft tissues may also undergo cracking, albeit to a much lesser extent [137]. Thus, it would be intriguing to assess cell invasion on substrates with similar stiffness but different fractionability.

6.6 LIMITATIONS OF 2D CELL MIGRATION AND INVASION MODELS

To characterize the migration of ErbB2⁺ and TNBC cells, we used glass bottom dishes coated with fibronectin (FN). FN is involved in many cellular processes including cell differentiation, embryonic development, growth and wound healing [138]. FN has also been implicated in the development of multiple cancer types [139-141]. FN plays a critical role in the formation of the pre-metastatic niche [142, 143]. Lysyl oxidase secreted by hypoxic primary tumor cells enhances the expression of FN in the lungs, creating docking sites for disseminating tumor cells [144-146]. Similarly, cancer cells can stimulate hepatic stellate cells to produce more FN in the liver [147]. FN coating the luminal side of liver vascular endothelium allows cancer cells to establish contacts and transmigrate via the adhesion protein talin [148]. MDA-MB-231 cells that overexpress integrins $\alpha_5\beta_1$ show a three-fold increase in cell invasiveness compared to $\alpha_5\beta_1$ -depleted cells due to the generation of greater contractile forces [149]. Mammary epithelial cells that interact with FN are also primed to respond to TGF β ; however, FN is essentially absent from normal adult breast tissue [150]. The major structural protein in the mammary gland is fibrillar (type I) collagen [151, 152]. Moreover, it is well known that breast cancer development is associated with increased collagen deposition [121, 153, 154]. Breast cancer cells recruit surrounding stromal cells to secrete collagen I [155] and re-align collagen fiber at the tumor front to enhance invasion [122, 123]. Previous studies show that different intracellular pathways are activated depending on the integrins engaged [156]. p52ShcA can bind $\alpha_5\beta_1$ (fibronectin), $\alpha_1\beta_1$ (collagen and laminin), $\alpha_v\beta_3$ (vitronectin) [157] and the cytoplasmic domain of integrin β_4 (laminin) [158]. Therefore, it would be interesting to explore whether p46/52ShcA and LPP are required for TGF β -induced cell migration and adhesion dynamics on other ECM components. A previous study shows that p46/52ShcA regulates cell migration on collagen and vitronectin [159]. Given that p46/52ShcA affects LPP recruitment to adhesions on FN, we predict that LPP is required for TGF β -induced migration on other ECM components as well.

To characterize cellular invasion, we seeded cells onto fluorescently labelled gelatin and determined the total area degraded per field of view. 2D matrix degradation assays are commonly used to assess invadopodia or podosome formation [160]. While these assays provide valuable insight into the ability of cells to breach barriers, there are a few limitations to consider. First, basement membranes are thin, dense sheets composed of two independent polymeric networks: laminin and type IV collagen [161]. The gelatin used in our experiments was denatured collagen

(derived from pig skin) bonded to glass coverslips with glutaraldehyde. Unfortunately, these substrates lack laminin, which forms an important barrier in the breast and inhibits the dissemination of normal epithelial cells [162]. Matrigel is a laminin-rich hydrogel that is commonly used to assess invasion through transwell assays. Although Matrigel is derived from tumor cell extracts, it also fails to approximate the crosslinked, mechanically rigid properties of basement membranes found *in vivo* [163, 164]. Consequently, there is a concerted effort to develop new substrates that better mimic the mechanical properties of tissues [165, 166]. Second, cells can degrade gelatin physically, by extending invadopodia into the substrate, or enzymatically by activating ECM proteases [167, 168]. There are three main classes of proteases present in invadopodia: MMPs, cathepsin cysteine proteases, and serine proteases [169]. MMPs are frequently upregulated in breast cancer and correlate with poor survival [170-172]. Therefore, it may be difficult to distinguish between invadopodia formation and MMP activity using gelatin degradation assays alone. A *bona fide* marker of invadopodia, such as Tks5 [66, 67, 69], is often needed to make conclusive statements about invadopodia formation. In a previous study, we showed that LPP knockdown does not affect MMP expression or activity in NMuMG-ErbB2 cells [9]; however, further studies are required to verify this phenotype in TNBC cells. Finally, 2D matrix degradation assays force cells to migrate using adhesions or invade using invadopodia. In contrast, cells in 3D environments exhibit a large range of behaviors that are not strictly confined to a single category [173-175]. For example, lobopodial migration uses asymmetric intracellular pressure to generate bleb-like protrusions at the leading edge; cells adhere and exert pulling forces on the ECM, while the nucleus moves forward in a piston-like manner [176]. This type of cell migration appears to be a hybrid between mesenchymal and ameboid migration.

An important distinction between 2D and 3D models is that cell migration and invasion are intimately linked processes in 3D. Mesenchymal migration is associated with high proteolytic activity, while ameboid migration allows cells to adapt to the environment and navigate through tissues by selecting the path of least resistance [174, 177-179]. A high degree of plasticity exists such that cells can switch between strategies and become proteolytic in environments where ameboid propulsion is not sustainable [180-183]. Consequently, we are also interested in determining how LPP expression affects the migration/invasion of ErbB2⁺ and TNBC breast cancer cells in 3D environments.

6.7 3D CELL MIGRATION

Cell migration on 2D substrates requires the formation of actin-rich lamellipodia and integrin-based adhesions that interact with the ECM. Adhesions are present on the ventral surface of cells and allow cells to transduce actomyosin-based contractility into traction forces [184]. In contrast, cells embedded in 3D hydrogels are exposed to a complex network of proteoglycans and fibrous proteins (collagens, elastins, fibronectins and laminins) [163]. Fiber architecture and cross-linking density regulate ECM porosity, stiffness and viscoelasticity [115, 173, 174, 185]. Extracellular fluid (ECF), which hydrates the ECM, also possesses physical attributes, such as osmotic pressure and hydrostatic pressure [186-193]. Consequently, cells employ a range of protrusive structures to traverse through the ECM, including filopodia, blebs, lobopodia and pseudopods [175, 194].

Intravital imaging and 3D cell migration experiments demonstrate that tumor cells can migrate along collagen fibers using adhesions [195-197]. Similar to 2D cell migration, a balance between cytoskeletal tension and ECM/adhesion coupling is required for efficient 3D cell migration [196]. Decreasing bulk matrix stiffness does not necessarily inhibit the formation of elongated adhesions as cells can form adhesions where collagen fibers are present [197]. While antibodies against integrin β_1 reduce the migration speed of mesenchymal cells [177, 183, 198], adhesions are not required for efficient migration in all 3D microenvironments [199]. For example, confining microenvironments induce a switch from integrin-dependent, actomyosin-based motile mechanisms to one that operates independently of either component and instead relies on microtubule dynamics [177, 199]. Interestingly, cells can also generate locomotive forces through actin flow given appropriate topographical features [200].

Advances in multiphoton microscopy reveal that the tissue microenvironment contains confining pores varying from 1 to 20 μm in diameter and channel-like tracks ranging from 3 to 30 μm in width and up to 600 μm in length [201]. Although cells can proteolytically cleave the physical scaffold to migrate through tissues, mesenchymal cell migration is severely impeded in confining microenvironments [183, 198]. The nucleus must often be compressed for cells to migrate through ECM pores [202]. Cells with reduced lamin A expression possess more malleable nuclei and traverse pores more quickly; however, the chance of apoptosis is increased due to nuclear rupture [203-206]. Thus, there is a delicate balance between nuclear compression and cell migration.

LPP may play an important role in 3D cell migration. First, cell-matrix adhesions are important for 3D cell migration along collagen fibers [195-197]. Our group and others have established that LPP is an important component of adhesions in a variety of cells [7, 10, 207-211]. Second, using a BioID proximity labelling approach we recently uncovered that LPP may interact with microtubules through KANK1 [100]. Finally, zyxin, a closely related family member, is required for the formation of a perinuclear actin cap that wraps around the nucleus [212]. This actin cap is connected to the apical surface of the nucleus through the linker of nucleoskeleton and cytoskeleton (LINC) complex. The LINC complex is composed a network of SUN and nesprin proteins connect lamin to the actin cytoskeleton [213]. Inhibition of SUN or nesprin proteins prevents nuclear movement [205, 214]. Similarly, lamin A inhibition causes transmembrane actin-associated nuclear lines to slip over the nucleus, resulting in slower cell migration [215, 216]. Cells with zyxin knockdown cannot form a perinuclear actin cap in response to low shear stress [212]. Thus, it would be interesting to explore the roles of LPP in 3D cell migration.

6.8 MOVING BEYOND 3D CELL MIGRATION MODELS

More widespread use of 3D models has facilitated the development of new concepts of plasticity and adaptability in cell migration [217, 218]. Many different types of hydrogels have been created to mimic various aspects of the tissue microenvironment. Collagen [196, 219, 220], fibrin [219, 221, 222] and basement membrane (Matrigel) ECM matrices [162, 183, 223] are frequently used; however, the composition of these gels (matrix fiber thickness, spacing, crosslinking, elastic modulus) is often ill-defined following synthesis [224]. Consequently, it may be unclear which biophysical signals contribute to the phenotype observed. More recently, polyethylene glycol (PEG) [219, 225], hyaluronic acid [226-228] and alginate [128, 229, 230] hydrogels have gained popularity due to high reproducibility and facile tuning of mechanical properties. These hydrogels are often coupled to integrin binding ligands at fixed densities to mimic *in vivo* scaffolds.

Despite our best efforts, an incomplete understanding of 3D tissue geometry and molecular topology precludes us from generating models that fully recapitulate physiological environments. There are often compromises regarding the precise biochemical composition, stiffness, gradients of soluble factors, fluid flow and other microenvironmental factors. The effects of this compromise are evident from studies that culture cells in different 3D ECM environments. The amount of cell

spreading, distribution of actin fibers, shape of adhesions, and cell migration speed differ between hydrogels [231]. Furthermore, primary human breast carcinomas invade aggressively in collagen I matrices but largely fail to invade into Matrigel; re-embedding cells from Matrigel in collagen I rescues invasion [162]. In order to truly mimic ECM, it is necessary to develop materials whose mechanical and chemical properties can be tuned on the time and length scales of cell development [165]. For example, basement membranes are subject to turnover at variable rates in normal tissue. An equilibrium exists wherein macromolecular constituents are constantly removed and deposited in a dynamic process to preserve overall basement membrane architecture [161, 232-234]. Normal cellular processes are inhibited unless the hydrogels are designed to degrade over time [219, 235, 236]. *In vivo* imaging of cancer metastasis is the ultimate goal; however, intravital microscopy is still largely limited to the brain due to convenience of access [195, 237-239]. As a result, *ex vivo* embryo, organ and tissue slice culture systems are increasingly employed as model systems [240-244].

6.9 CONCLUDING REMARKS

Cell migration is a complex process involving numerous intracellular pathways and proteins. In this thesis, we focused on two adapter proteins that localize to cell-matrix adhesions: p46/52ShcA and LPP. We found that p46/52ShcA and LPP are required for the migration and invasion of ErbB2⁺ breast cancer cells in response to TGF β . Furthermore, we found that LPP facilitates the migration, invasion and metastasis of TNBC cells. We will continue to investigate the molecular mechanisms through which LPP enhances TNBC metastasis. Based on our results from NMuMG-ErbB2 cells, we suspect that TGF β enhances LPP recruitment to adhesions to support increased cell contractility. Indeed, preliminary experiments in 4T1-2776 cells transfected with a talin tension sensor demonstrate that LPP expression is required for TGF β -induced increases in adhesion tension. Additionally, we will investigate whether LPP is required for the migration and invasion of breast cancer cells that preferentially metastasize to the brain and bone [104-106]. Preliminary results indicate that bone-metastatic 4T1-590 cells require LPP expression to migrate further and faster in response to TGF β . Cranial injection experiments using MDA-MB-231 cells suggest that LPP expression is also required to form brain metastases in mice. Although further experimentation is required to verify these phenotypes, our results suggest that LPP is a universal mediator of breast cancer metastasis to multiple different organs/tissues.

Finally, we would like to extend our studies to 3D models of cell migration. Cells must sense, integrate and interpret diverse chemical and physical cues within the tissue microenvironment to define the direction of migration and engage underlying motility mechanisms. Numerous physical and biochemical properties can be tuned in hydrogels, resulting in a variety of migration modes [174, 175]. ECM/adhesion coupling is required for efficient 3D cell migration along collagen fibers [196, 197]; however, confining environments rapidly induce a mesenchymal-to-ameboid transition [180, 183, 198]. This type of cell migration relies heavily on microtubule polymerization [199]. As cells migrate through confining pores, compressive forces are also transmitted to the nucleus through the LINC complex [205, 206]. Our BioID results indicate that LPP may interact with microtubules through KANK1 [100]. Furthermore, LPP is closely related to zyxin, which has been shown to interact with the LINC complex [212]. Thus, the role of LPP in 3D cell migration awaits further investigation. I believe that studying cellular behaviors and biophysical forces in 3D environments that more closely resemble human tissues will help us better understand cancer metastasis and identify inhibitors of tumor invasion.

6.10 REFERENCES

1. Institute, N.C. *Cancer stat facts: female breast cancer*. Available from: <https://seer.cancer.gov/statfacts/html/breast.html>.
2. Society, C.C. *Survival statistics for breast cancer*. Available from: <https://www.cancer.ca/en/cancer-information/cancer-type/breast/prognosis-and-survival/survival-statistics/?region=on>.
3. Society, C.C. *Breast cancer statistics*. Available from: <https://www.cancer.ca/en/cancer-information/cancer-type/breast/statistics/?region=on>.
4. Kiepas, A., et al., *Optimizing live-cell fluorescence imaging conditions to minimize phototoxicity*. J Cell Sci, 2020. **133**(4).
5. Kiepas, A. and C.M. Brown, *Microscope Hardware and Software Delays Cause Photo-Toxicity*. Microscopy Today, 2020. **28**(4): p. 30-36.
6. Northey, J.J., et al., *Signaling through ShcA is required for TGF- β and Neu/ErbB-2 induced breast cancer cell motility and invasion*. Mol. Cell. Biol., 2008: p. MCB.01734-07.
7. Ngan, E., et al., *A complex containing LPP and alpha-actinin mediates TGF β -induced migration and invasion of ErbB2-expressing breast cancer cells*. J Cell Sci, 2013. **126**(Pt 9): p. 1981-91.
8. Northey, J.J., et al., *Distinct phosphotyrosine-dependent functions of the ShcA adaptor protein are required for transforming growth factor beta (TGF β)-induced breast cancer cell migration, invasion, and metastasis*. J Biol Chem, 2013. **288**(7): p. 5210-22.
9. Ngan, E., et al., *LPP is a Src substrate required for invadopodia formation and efficient breast cancer lung metastasis*. Nat Commun, 2017. **8**: p. 15059.
10. Kiepas, A., et al., *The SHCA adapter protein cooperates with lipoma-preferred partner in the regulation of adhesion dynamics and invadopodia formation*. J Biol Chem, 2020. **295**(31): p. 10535-10559.
11. Mubaid, F. and C.M. Brown, *Less is More: Longer Exposure Times with Low Light Intensity is Less Photo-Toxic*. Microscopy Today, 2017. **25**(6): p. 26-35.
12. Donnert, G., C. Eggeling, and S.W. Hell, *Triplet-relaxation microscopy with bunched pulsed excitation*. Photochemical & Photobiological Sciences, 2009. **8**(4): p. 481-485.
13. Donnert, G., et al., *Macromolecular-scale resolution in biological fluorescence microscopy*. Proceedings of the National Academy of Sciences, 2006. **103**(31): p. 11440.
14. Oracz, J., et al., *Photobleaching in STED nanoscopy and its dependence on the photon flux applied for reversible silencing of the fluorophore*. Scientific Reports, 2017. **7**(1): p. 11354.
15. Mubaid, F., *Incident Light Modulation by Means of Power Variations and Light Pulsing Reduces Photo Induced Toxicity and Bleaching*, in *Physiology*. 2019, McGill University.
16. Holmstrom, K.M. and T. Finkel, *Cellular mechanisms and physiological consequences of redox-dependent signalling*. Nat Rev Mol Cell Biol, 2014. **15**(6): p. 411-21.
17. Cadet, J. and J.R. Wagner, *DNA base damage by reactive oxygen species, oxidizing agents, and UV radiation*. Cold Spring Harb Perspect Biol, 2013. **5**(2).
18. Cui, H., Y. Kong, and H. Zhang, *Oxidative stress, mitochondrial dysfunction, and aging*. J Signal Transduct, 2012. **2012**: p. 646354.
19. Dizdaroglu, M., et al., *Free radical-induced damage to DNA: mechanisms and measurement*. Free Radic Biol Med, 2002. **32**(11): p. 1102-15.
20. Fischer, L.R., et al., *Absence of SOD1 leads to oxidative stress in peripheral nerve and causes a progressive distal motor axonopathy*. Exp Neurol, 2012. **233**(1): p. 163-71.
21. Elchuri, S., et al., *CuZnSOD deficiency leads to persistent and widespread oxidative damage and hepatocarcinogenesis later in life*. Oncogene, 2005. **24**(3): p. 367-80.
22. Iuchi, Y., et al., *Spontaneous skin damage and delayed wound healing in SOD1-deficient mice*. Mol Cell Biochem, 2010. **341**(1-2): p. 181-94.
23. Zhang, Y., et al., *A new role for oxidative stress in aging: The accelerated aging phenotype in Sod1(-)/(-) mice is correlated to increased cellular senescence*. Redox Biol, 2017. **11**: p. 30-37.

24. Wang, Y., et al., *Superoxide dismutases: Dual roles in controlling ROS damage and regulating ROS signaling*. J Cell Biol, 2018. **217**(6): p. 1915-1928.
25. Van Remmen, H., et al., *Life-long reduction in MnSOD activity results in increased DNA damage and higher incidence of cancer but does not accelerate aging*. Physiol Genomics, 2003. **16**(1): p. 29-37.
26. Okado-Matsumoto, A. and I. Fridovich, *Subcellular distribution of superoxide dismutases (SOD) in rat liver: Cu,Zn-SOD in mitochondria*. J Biol Chem, 2001. **276**(42): p. 38388-93.
27. Culotta, V.C., M. Yang, and T.V. O'Halloran, *Activation of superoxide dismutases: putting the metal to the pedal*. Biochim Biophys Acta, 2006. **1763**(7): p. 747-58.
28. Fridovich, I., *Superoxide anion radical (O₂⁻), superoxide dismutases, and related matters*. J Biol Chem, 1997. **272**(30): p. 18515-7.
29. Oberley, L.W. and G.R. Buettner, *Role of superoxide dismutase in cancer: a review*. Cancer Res, 1979. **39**(4): p. 1141-9.
30. Hempel, N., P.M. Carrico, and J.A. Melendez, *Manganese superoxide dismutase (Sod2) and redox-control of signaling events that drive metastasis*. Anticancer Agents Med Chem, 2011. **11**(2): p. 191-201.
31. Kim, Y.S., et al., *Insights into the Dichotomous Regulation of SOD2 in Cancer*. Antioxidants (Basel), 2017. **6**(4).
32. Chung-man Ho, J., et al., *Differential expression of manganese superoxide dismutase and catalase in lung cancer*. Cancer Res, 2001. **61**(23): p. 8578-85.
33. Davison, C.A., et al., *Antioxidant enzymes mediate survival of breast cancer cells deprived of extracellular matrix*. Cancer Res, 2013. **73**(12): p. 3704-15.
34. Teixeira, H.D., R.I. Schumacher, and R. Meneghini, *Lower intracellular hydrogen peroxide levels in cells overexpressing CuZn-superoxide dismutase*. Proceedings of the National Academy of Sciences, 1998. **95**(14): p. 7872.
35. Mann, H., et al., *Overexpression of superoxide dismutase and catalase in immortalized neural cells: toxic effects of hydrogen peroxide*. Brain Res, 1997. **770**(1-2): p. 163-8.
36. Mirault, M.E., et al., *Overexpression of seleno-glutathione peroxidase by gene transfer enhances the resistance of T47D human breast cells to clastogenic oxidants*. J Biol Chem, 1991. **266**(31): p. 20752-60.
37. Benesch, R.E. and R. Benesch, *Enzymatic removal of oxygen for polarography and related methods*. Science, 1953. **118**(3068): p. 447-8.
38. Aitken, C.E., R.A. Marshall, and J.D. Puglisi, *An oxygen scavenging system for improvement of dye stability in single-molecule fluorescence experiments*. Biophys J, 2008. **94**(5): p. 1826-35.
39. Song, L., et al., *Influence of the triplet excited state on the photobleaching kinetics of fluorescein in microscopy*. Biophys J, 1996. **70**(6): p. 2959-68.
40. Widengren, J. and R. Rigler, *Mechanisms of photobleaching investigated by fluorescence correlation spectroscopy*. Bioimaging, 1996. **4**(3): p. 149-157.
41. Zheng, Q., et al., *On the Mechanisms of Cyanine Fluorophore Photostabilization*. J Phys Chem Lett, 2012. **3**(16): p. 2200-2203.
42. Mueller, S., G. Millonig, and G.N. Waite, *The GOX/CAT system: a novel enzymatic method to independently control hydrogen peroxide and hypoxia in cell culture*. Adv Med Sci, 2009. **54**(2): p. 121-35.
43. Ha, T. and P. Tinnefeld, *Photophysics of fluorescent probes for single-molecule biophysics and super-resolution imaging*. Annu Rev Phys Chem, 2012. **63**: p. 595-617.
44. Dijk, M.A., et al., *Combining optical trapping and single-molecule fluorescence spectroscopy: enhanced photobleaching of fluorophores*. J Phys Chem B, 2004. **108**(20): p. 6479-84.
45. Widengren, J., et al., *Strategies to improve photostabilities in ultrasensitive fluorescence spectroscopy*. J Phys Chem A, 2007. **111**(3): p. 429-40.
46. Petrou, A.L., et al., *A Possible Role for Singlet Oxygen in the Degradation of Various Antioxidants. A Meta-Analysis and Review of Literature Data*. Antioxidants (Basel), 2018. **7**(3).

47. Krumova, K. and G. Cosa, *Chapter 1 Overview of Reactive Oxygen Species*, in *Singlet Oxygen: Applications in Biosciences and Nanosciences, Volume 1*. 2016, The Royal Society of Chemistry. p. 1-21.
48. Kaźmierczak-Barańska, J., et al., *Two Faces of Vitamin C-Antioxidative and Pro-Oxidative Agent*. *Nutrients*, 2020. **12**(5): p. 1501.
49. Podmore, I.D., et al., *Vitamin C exhibits pro-oxidant properties*. *Nature*, 1998. **392**(6676): p. 559-559.
50. Carr, A. and B. Frei, *Does vitamin C act as a pro-oxidant under physiological conditions?* *The FASEB Journal*, 1999. **13**(9): p. 1007-1024.
51. Wu, L., et al., *Reaction-Based Fluorescent Probes for the Detection and Imaging of Reactive Oxygen, Nitrogen, and Sulfur Species*. *Accounts of Chemical Research*, 2019. **52**(9): p. 2582-2597.
52. Nayal, A., et al., *Paxillin phosphorylation at Ser273 localizes a GIT1-PIX-PAK complex and regulates adhesion and protrusion dynamics*. *J Cell Biol*, 2006. **173**(4): p. 587-9.
53. Delorme-Walker, V.D., et al., *Pak1 regulates focal adhesion strength, myosin IIA distribution, and actin dynamics to optimize cell migration*. *J Cell Biol*, 2011. **193**(7): p. 1289-303.
54. Berginski, M.E., et al., *High-resolution quantification of focal adhesion spatiotemporal dynamics in living cells*. *PLoS One*, 2011. **6**(7): p. e22025.
55. Choi, C.K., et al., *Actin and alpha-actinin orchestrate the assembly and maturation of nascent adhesions in a myosin II motor-independent manner*. *Nat Cell Biol*, 2008. **10**(9): p. 1039-50.
56. Zaidel-Bar, R., et al., *Early molecular events in the assembly of matrix adhesions at the leading edge of migrating cells*. *J Cell Sci*, 2003. **116**(Pt 22): p. 4605-13.
57. Horton, E.R., et al., *Definition of a consensus integrin adhesome and its dynamics during adhesion complex assembly and disassembly*. *Nat Cell Biol*, 2015. **17**(12): p. 1577-1587.
58. Kanchanawong, P., et al., *Nanoscale architecture of integrin-based cell adhesions*. *Nature*, 2010. **468**(7323): p. 580-4.
59. Parekh, A., et al., *Sensing and modulation of invadopodia across a wide range of rigidities*. *Biophys J*, 2011. **100**(3): p. 573-82.
60. Parekh, A. and A.M. Weaver, *Regulation of invadopodia by mechanical signaling*. *Exp Cell Res*, 2016. **343**(1): p. 89-95.
61. Alexander, N.R., et al., *Extracellular matrix rigidity promotes invadopodia activity*. *Curr Biol*, 2008. **18**(17): p. 1295-9.
62. Eddy, R.J., et al., *Tumor Cell Invadopodia: Invasive Protrusions that Orchestrate Metastasis*. *Trends Cell Biol*, 2017. **27**(8): p. 595-607.
63. Schoumacher, M., et al., *Actin, microtubules, and vimentin intermediate filaments cooperate for elongation of invadopodia*. *J Cell Biol*, 2010. **189**(3): p. 541-56.
64. Blouw, B., et al., *The invadopodia scaffold protein Tks5 is required for the growth of human breast cancer cells in vitro and in vivo*. *PLoS One*, 2015. **10**(3): p. e0121003.
65. Murphy, D.A. and S.A. Courtneidge, *The 'ins' and 'outs' of podosomes and invadopodia: characteristics, formation and function*. *Nat Rev Mol Cell Biol*, 2011. **12**(7): p. 413-26.
66. Stylli, S.S., et al., *Nck adaptor proteins link Tks5 to invadopodia actin regulation and ECM degradation*. *J Cell Sci*, 2009. **122**(Pt 15): p. 2727-40.
67. Courtneidge, S.A., et al., *The SRC substrate Tks5, podosomes (invadopodia), and cancer cell invasion*. *Cold Spring Harb Symp Quant Biol*, 2005. **70**: p. 167-71.
68. Clark, E.S., et al., *Cortactin is an essential regulator of matrix metalloproteinase secretion and extracellular matrix degradation in invadopodia*. *Cancer Res*, 2007. **67**(9): p. 4227-35.
69. Seals, D.F., et al., *The adaptor protein Tks5/Fish is required for podosome formation and function, and for the protease-driven invasion of cancer cells*. *Cancer Cell*, 2005. **7**(2): p. 155-65.
70. Beaty, B.T. and J. Condeelis, *Digging a little deeper: the stages of invadopodium formation and maturation*. *Eur J Cell Biol*, 2014. **93**(10-12): p. 438-44.

71. Sharma, V.P., D. Entenberg, and J. Condeelis, *High-resolution live-cell imaging and time-lapse microscopy of invadopodium dynamics and tracking analysis*. Methods in molecular biology (Clifton, N.J.), 2013. **1046**: p. 343-357.
72. Dalaka, E., et al., *Direct measurement of vertical forces shows correlation between mechanical activity and proteolytic ability of invadopodia*. Science Advances, 2020. **6**(11): p. eaax6912.
73. Rajadurai, C.V., et al., *5'-Inositol phosphatase SHIP2 recruits Mena to stabilize invadopodia for cancer cell invasion*. J Cell Biol, 2016. **214**(6): p. 719-34.
74. Nolen, B.J., R.S. Littlefield, and T.D. Pollard, *Crystal structures of actin-related protein 2/3 complex with bound ATP or ADP*. Proceedings of the National Academy of Sciences of the United States of America, 2004. **101**(44): p. 15627.
75. Pollard, T.D., L. Blanchoin, and R.D. Mullins, *Molecular mechanisms controlling actin filament dynamics in nonmuscle cells*. Annu Rev Biophys Biomol Struct, 2000. **29**: p. 545-76.
76. Collins, K.B., et al., *Septin2 mediates podosome maturation and endothelial cell invasion associated with angiogenesis*. Journal of Cell Biology, 2019. **219**(2).
77. Kumar, A., et al., *Talin tension sensor reveals novel features of focal adhesion force transmission and mechanosensitivity*. J Cell Biol, 2016. **213**(3): p. 371-83.
78. Marinkovic, A., et al., *Improved throughput traction microscopy reveals pivotal role for matrix stiffness in fibroblast contractility and TGF-beta responsiveness*. Am J Physiol Lung Cell Mol Physiol, 2012. **303**(3): p. L169-80.
79. Discher, D.E., P. Janmey, and Y.L. Wang, *Tissue cells feel and respond to the stiffness of their substrate*. Science, 2005. **310**(5751): p. 1139-43.
80. del Rio, A., et al., *Stretching single talin rod molecules activates vinculin binding*. Science, 2009. **323**(5914): p. 638-41.
81. Kluger, C., et al., *Different Vinculin Binding Sites Use the Same Mechanism to Regulate Directional Force Transduction*. Biophysical Journal, 2020. **118**(6): p. 1344-1356.
82. Ciobanasu, C., B. Faivre, and C. Le Clainche, *Actomyosin-dependent formation of the mechanosensitive talin-vinculin complex reinforces actin anchoring*. Nat Commun, 2014. **5**: p. 3095.
83. Lo, C.M., et al., *Cell movement is guided by the rigidity of the substrate*. Biophys J, 2000. **79**(1): p. 144-52.
84. Galbraith, C.G., K.M. Yamada, and M.P. Sheetz, *The relationship between force and focal complex development*. J Cell Biol, 2002. **159**(4): p. 695-705.
85. Huisken, J. and D.Y.R. Stainier, *Selective plane illumination microscopy techniques in developmental biology*. Development, 2009. **136**(12): p. 1963.
86. Power, R.M. and J. Huisken, *A guide to light-sheet fluorescence microscopy for multiscale imaging*. Nat Methods, 2017. **14**(4): p. 360-373.
87. Chen, B.C., et al., *Lattice light-sheet microscopy: imaging molecules to embryos at high spatiotemporal resolution*. Science, 2014. **346**(6208): p. 1257998.
88. Icha, J., et al., *Phototoxicity in live fluorescence microscopy, and how to avoid it*. Bioessays, 2017. **39**(8).
89. Wu, Y., et al., *Inverted selective plane illumination microscopy (i>SPIM) enables coupled cell identity lineaging and neurodevelopmental imaging in Caenorhabditis elegans*. Proceedings of the National Academy of Sciences, 2011. **108**(43): p. 17708.
90. Chen, C.-Y., et al., *The Applications of Lattice Light-sheet Microscopy for Functional Volumetric Imaging of Hippocampal Neurons in a Three-Dimensional Culture System*. Micromachines, 2019. **10**(9): p. 599.
91. Fritz-Laylin, L.K., et al., *Actin-based protrusions of migrating neutrophils are intrinsically lamellar and facilitate direction changes*. eLife, 2017. **6**: p. e26990.
92. Liu, T.L., et al., *Observing the cell in its native state: Imaging subcellular dynamics in multicellular organisms*. Science, 2018. **360**(6386).

93. Tharp, K.M., et al., *Adhesion-mediated mechanosignaling forces mitohormesis*. bioRxiv, 2020: p. 2020.03.06.979583.
94. Yang, C., et al., *Mechanical memory and dosing influence stem cell fate*. Nature materials, 2014. **13**(6): p. 645-652.
95. Liu, F., et al., *Mechanosignaling through YAP and TAZ drives fibroblast activation and fibrosis*. American Journal of Physiology-Lung Cellular and Molecular Physiology, 2014. **308**(4): p. L344-L357.
96. Peng, T., et al., *A mathematical model of mechanotransduction reveals how mechanical memory regulates mesenchymal stem cell fate decisions*. BMC Systems Biology, 2017. **11**(1): p. 55.
97. Nasrollahi, S., et al., *Past matrix stiffness primes epithelial cells and regulates their future collective migration through a mechanical memory*. Biomaterials, 2017. **146**: p. 146-155.
98. Pelham, R.J., Jr. and Y. Wang, *Cell locomotion and focal adhesions are regulated by substrate flexibility*. Proc Natl Acad Sci U S A, 1997. **94**(25): p. 13661-5.
99. Dokukina, I.V. and M.E. Gracheva, *A model of fibroblast motility on substrates with different rigidities*. Biophys J, 2010. **98**(12): p. 2794-803.
100. Voorand, E., *Mechanisms of Adhesion and Invadopodia Regulation During Breast Cancer Metastasis*, in *Biochemistry*. 2020, McGill University.
101. Elbediwy, A., et al., *Enigma proteins regulate YAP mechanotransduction*. J Cell Sci, 2018. **131**(22).
102. Handorf, A.M., et al., *Tissue stiffness dictates development, homeostasis, and disease progression*. Organogenesis, 2015. **11**(1): p. 1-15.
103. Tabaries, S., et al., *Granulocytic immune infiltrates are essential for the efficient formation of breast cancer liver metastases*. Breast Cancer Res, 2015. **17**: p. 45.
104. Rose, A.A., et al., *ADAM10 releases a soluble form of the GPNMB/Osteoactivin extracellular domain with angiogenic properties*. PLoS One, 2010. **5**(8): p. e12093.
105. Kang, Y., et al., *A multigenic program mediating breast cancer metastasis to bone*. Cancer Cell, 2003. **3**(6): p. 537-49.
106. Bos, P.D., et al., *Genes that mediate breast cancer metastasis to the brain*. Nature, 2009. **459**(7249): p. 1005-9.
107. Minn, A.J., et al., *Lung metastasis genes couple breast tumor size and metastatic spread*. Proceedings of the National Academy of Sciences of the United States of America, 2007. **104**(16): p. 6740-6745.
108. Minn, A.J., et al., *Genes that mediate breast cancer metastasis to lung*. Nature, 2005. **436**(7050): p. 518-24.
109. Athanasiou, A., et al., *Breast lesions: quantitative elastography with supersonic shear imaging--preliminary results*. Radiology, 2010. **256**(1): p. 297-303.
110. Li, W., D.E.T. Shepherd, and D.M. Espino, *Frequency dependent viscoelastic properties of porcine brain tissue*. J Mech Behav Biomed Mater, 2020. **102**: p. 103460.
111. Perepelyuk, M., et al., *Normal and Fibrotic Rat Livers Demonstrate Shear Strain Softening and Compression Stiffening: A Model for Soft Tissue Mechanics*. PLOS ONE, 2016. **11**(1): p. e0146588.
112. Palchesko, R.N., et al., *Development of Polydimethylsiloxane Substrates with Tunable Elastic Modulus to Study Cell Mechanobiology in Muscle and Nerve*. PLOS ONE, 2012. **7**(12): p. e51499.
113. Yoshie, H., et al., *Traction Force Screening Enabled by Compliant PDMS Elastomers*. Biophys J, 2018. **114**(9): p. 2194-2199.
114. McDonald, S.J., et al., *Early fracture callus displays smooth muscle-like viscoelastic properties ex vivo: implications for fracture healing*. J Orthop Res, 2009. **27**(11): p. 1508-13.
115. Chaudhuri, O., et al., *Effects of extracellular matrix viscoelasticity on cellular behaviour*. Nature, 2020. **584**(7822): p. 535-546.

116. Sinkus, R., et al., *MR elastography of breast lesions: Understanding the solid/liquid duality can improve the specificity of contrast-enhanced MR mammography*. *Magnetic Resonance in Medicine*, 2007. **58**(6): p. 1135-1144.
117. Qiu, Y., et al., *Ultrasonic viscoelasticity imaging of nonpalpable breast tumors: preliminary results*. *Academic radiology*, 2008. **15**(12): p. 1526-1533.
118. Bayat, M., et al., *Automated In Vivo Sub-Hertz Analysis of Viscoelasticity (SAVE) for Evaluation of Breast Lesions*. *IEEE Trans Biomed Eng*, 2018. **65**(10): p. 2237-2247.
119. Kumar, V., et al., *Viscoelastic parameters as discriminators of breast masses: Initial human study results*. *PLOS ONE*, 2018. **13**(10): p. e0205717.
120. Boyd, N.F., et al., *Evidence that breast tissue stiffness is associated with risk of breast cancer*. *PLoS One*, 2014. **9**(7): p. e100937.
121. Li, T., et al., *The association of measured breast tissue characteristics with mammographic density and other risk factors for breast cancer*. *Cancer Epidemiol Biomarkers Prev*, 2005. **14**(2): p. 343-9.
122. Acerbi, I., et al., *Human breast cancer invasion and aggression correlates with ECM stiffening and immune cell infiltration*. *Integr Biol (Camb)*, 2015. **7**(10): p. 1120-34.
123. Cheung, K.J., et al., *Collective invasion in breast cancer requires a conserved basal epithelial program*. *Cell*, 2013. **155**(7): p. 1639-51.
124. Chaudhuri, O., et al., *Substrate stress relaxation regulates cell spreading*. *Nature communications*, 2015. **6**: p. 6364-6364.
125. Xu, B., H. Li, and Y. Zhang, *Understanding the viscoelastic behavior of collagen matrices through relaxation time distribution spectrum*. *Biomatter*, 2013. **3**(3).
126. Shen, Z.L., et al., *Viscoelastic properties of isolated collagen fibrils*. *Biophysical journal*, 2011. **100**(12): p. 3008-3015.
127. Cameron, A.R., J.E. Frith, and J.J. Cooper-White, *The influence of substrate creep on mesenchymal stem cell behaviour and phenotype*. *Biomaterials*, 2011. **32**(26): p. 5979-93.
128. Chaudhuri, O., et al., *Hydrogels with tunable stress relaxation regulate stem cell fate and activity*. *Nature materials*, 2016. **15**(3): p. 326-334.
129. Wisdom, K.M., et al., *Matrix mechanical plasticity regulates cancer cell migration through confining microenvironments*. *Nature Communications*, 2018. **9**(1): p. 4144.
130. Ritchie, R.O., *The conflicts between strength and toughness*. *Nature Materials*, 2011. **10**(11): p. 817-822.
131. Verzijl, N., et al., *Crosslinking by advanced glycation end products increases the stiffness of the collagen network in human articular cartilage: A possible mechanism through which age is a risk factor for osteoarthritis*. *Arthritis & Rheumatism*, 2002. **46**(1): p. 114-123.
132. Saito, M. and K. Marumo, *Collagen cross-links as a determinant of bone quality: a possible explanation for bone fragility in aging, osteoporosis, and diabetes mellitus*. *Osteoporosis International*, 2010. **21**(2): p. 195-214.
133. O'Brien, F.J., et al., *Visualisation of three-dimensional microcracks in compact bone*. *Journal of anatomy*, 2000. **197 Pt 3**(Pt 3): p. 413-420.
134. Nalla, R.K., et al., *Effect of aging on the toughness of human cortical bone: evaluation by R-curves*. *Bone*, 2004. **35**(6): p. 1240-1246.
135. Candiello, J., et al., *Biomechanical properties of native basement membranes*. *Febs j*, 2007. **274**(11): p. 2897-908.
136. Chlasta, J., et al., *Variations in basement membrane mechanics are linked to epithelial morphogenesis*. *Development*, 2017. **144**(23): p. 4350-4362.
137. Taylor, D., et al., *The fracture toughness of soft tissues*. *Journal of the Mechanical Behavior of Biomedical Materials*, 2012. **6**: p. 139-147.
138. Fernandez-Garcia, B., et al., *Expression and prognostic significance of fibronectin and matrix metalloproteases in breast cancer metastasis*. *Histopathology*, 2014. **64**(4): p. 512-22.

139. Waalkes, S., et al., *Fibronectin 1 mRNA expression correlates with advanced disease in renal cancer*. BMC Cancer, 2010. **10**: p. 503.
140. Jia, D., et al., *Development of a highly metastatic model that reveals a crucial role of fibronectin in lung cancer cell migration and invasion*. BMC Cancer, 2010. **10**: p. 364.
141. Ioachim, E., et al., *Immunohistochemical expression of extracellular matrix components tenascin, fibronectin, collagen type IV and laminin in breast cancer: their prognostic value and role in tumour invasion and progression*. Eur J Cancer, 2002. **38**(18): p. 2362-70.
142. Psaila, B. and D. Lyden, *The metastatic niche: adapting the foreign soil*. Nature Reviews Cancer, 2009. **9**(4): p. 285-293.
143. Doglioni, G., S. Parik, and S.-M. Fendt, *Interactions in the (Pre)metastatic Niche Support Metastasis Formation*. Frontiers in oncology, 2019. **9**: p. 219-219.
144. Erler, J.T., et al., *Hypoxia-induced lysyl oxidase is a critical mediator of bone marrow cell recruitment to form the premetastatic niche*. Cancer Cell, 2009. **15**(1): p. 35-44.
145. Kaplan, R.N., et al., *VEGFR1-positive haematopoietic bone marrow progenitors initiate the pre-metastatic niche*. Nature, 2005. **438**(7069): p. 820-7.
146. Canesin, G., et al., *Lysyl oxidase-like 2 (LOXL2) and E47 EMT factor: novel partners in E-cadherin repression and early metastasis colonization*. Oncogene, 2015. **34**(8): p. 951-64.
147. Costa-Silva, B., et al., *Pancreatic cancer exosomes initiate pre-metastatic niche formation in the liver*. Nat Cell Biol, 2015. **17**(6): p. 816-26.
148. Barbazán, J., et al., *Liver Metastasis Is Facilitated by the Adherence of Circulating Tumor Cells to Vascular Fibronectin Deposits*. Cancer Res, 2017. **77**(13): p. 3431-3441.
149. Mierke, C.T., et al., *Integrin alpha5beta1 facilitates cancer cell invasion through enhanced contractile forces*. J Cell Sci, 2011. **124**(Pt 3): p. 369-83.
150. Park, J. and J.E. Schwarzbauer, *Mammary epithelial cell interactions with fibronectin stimulate epithelial-mesenchymal transition*. Oncogene, 2014. **33**(13): p. 1649-57.
151. Schedin, P. and P.J. Keely, *Mammary gland ECM remodeling, stiffness, and mechanosignaling in normal development and tumor progression*. Cold Spring Harbor perspectives in biology, 2011. **3**(1): p. a003228-a003228.
152. Monaghan, P., et al., *Topographical arrangement of basement membrane proteins in lactating rat mammary gland: comparison of the distribution of type IV collagen, laminin, fibronectin, and Thy-1 at the ultrastructural level*. Proc Natl Acad Sci U S A, 1983. **80**(11): p. 3344-8.
153. Provenzano, P.P., et al., *Collagen density promotes mammary tumor initiation and progression*. BMC Med, 2008. **6**: p. 11.
154. Levental, K.R., et al., *Matrix crosslinking forces tumor progression by enhancing integrin signaling*. Cell, 2009. **139**(5): p. 891-906.
155. Wang, K., et al., *Breast cancer cells alter the dynamics of stromal fibronectin-collagen interactions*. Matrix Biol, 2017. **60-61**: p. 86-95.
156. Kutys, M.L. and K.M. Yamada, *An extracellular-matrix-specific GEF-GAP interaction regulates Rho GTPase crosstalk for 3D collagen migration*. Nat Cell Biol, 2014. **16**(9): p. 909-17.
157. Wary, K.K., et al., *The adaptor protein Shc couples a class of integrins to the control of cell cycle progression*. Cell, 1996. **87**(4): p. 733-43.
158. Deshmukh, L., V. Gorbatyuk, and O. Vinogradova, *Integrin {beta}3 phosphorylation dictates its complex with the Shc phosphotyrosine-binding (PTB) domain*. J Biol Chem, 2010. **285**(45): p. 34875-84.
159. Collins, L.R., et al., *Bifurcation of cell migratory and proliferative signaling by the adaptor protein Shc*. J Cell Biol, 1999. **147**(7): p. 1561-8.
160. Artym, V.V., K.M. Yamada, and S.C. Mueller, *ECM degradation assays for analyzing local cell invasion*. Methods Mol Biol, 2009. **522**: p. 211-9.
161. Jayadev, R. and D.R. Sherwood, *Basement membranes*. Curr Biol, 2017. **27**(6): p. R207-R211.

162. Nguyen-Ngoc, K.V., et al., *ECM microenvironment regulates collective migration and local dissemination in normal and malignant mammary epithelium*. Proc Natl Acad Sci U S A, 2012. **109**(39): p. E2595-604.
163. Frantz, C., K.M. Stewart, and V.M. Weaver, *The extracellular matrix at a glance*. Journal of Cell Science, 2010. **123**(24): p. 4195.
164. Rowe, R.G. and S.J. Weiss, *Navigating ECM barriers at the invasive front: the cancer cell-stroma interface*. Annu Rev Cell Dev Biol, 2009. **25**: p. 567-95.
165. Tibbitt, M.W. and K.S. Anseth, *Hydrogels as extracellular matrix mimics for 3D cell culture*. Biotechnology and bioengineering, 2009. **103**(4): p. 655-663.
166. Giobbe, G.G., et al., *Extracellular matrix hydrogel derived from decellularized tissues enables endodermal organoid culture*. Nature Communications, 2019. **10**(1): p. 5658.
167. Radisky, E.S. and D.C. Radisky, *Matrix metalloproteinases as breast cancer drivers and therapeutic targets*. Frontiers in bioscience (Landmark edition), 2015. **20**: p. 1144-1163.
168. Paolillo, M. and S. Schinelli, *Extracellular Matrix Alterations in Metastatic Processes*. International journal of molecular sciences, 2019. **20**(19): p. 4947.
169. Murphy, D.A. and S.A. Courtneidge, *The 'ins' and 'outs' of podosomes and invadopodia: characteristics, formation and function*. Nature Reviews Molecular Cell Biology, 2011. **12**(7): p. 413-426.
170. McGowan, P.M. and M.J. Duffy, *Matrix metalloproteinase expression and outcome in patients with breast cancer: analysis of a published database*. Ann Oncol, 2008. **19**(9): p. 1566-72.
171. Roy, D.M. and L.A. Walsh, *Candidate prognostic markers in breast cancer: focus on extracellular proteases and their inhibitors*. Breast cancer (Dove Medical Press), 2014. **6**: p. 81-91.
172. Têtu, B., et al., *The influence of MMP-14, TIMP-2 and MMP-2 expression on breast cancer prognosis*. Breast Cancer Res, 2006. **8**(3): p. R28.
173. Doyle, A.D., et al., *Dimensions in cell migration*. Current opinion in cell biology, 2013. **25**(5): p. 642-649.
174. Yamada, K.M. and M. Sixt, *Mechanisms of 3D cell migration*. Nature Reviews Molecular Cell Biology, 2019. **20**(12): p. 738-752.
175. Petrie, R.J. and K.M. Yamada, *Multiple mechanisms of 3D migration: the origins of plasticity*. Current opinion in cell biology, 2016. **42**: p. 7-12.
176. Petrie, R.J., et al., *Nonpolarized signaling reveals two distinct modes of 3D cell migration*. J Cell Biol, 2012. **197**(3): p. 439-55.
177. Wolf, K., et al., *Compensation mechanism in tumor cell migration: mesenchymal-amoeboid transition after blocking of pericellular proteolysis*. J Cell Biol, 2003. **160**(2): p. 267-77.
178. Wolf, K. and P. Friedl, *Extracellular matrix determinants of proteolytic and non-proteolytic cell migration*. Trends Cell Biol, 2011. **21**(12): p. 736-44.
179. Renkawitz, J., et al., *Nuclear positioning facilitates amoeboid migration along the path of least resistance*. Nature, 2019. **568**(7753): p. 546-550.
180. Pankova, K., et al., *The molecular mechanisms of transition between mesenchymal and amoeboid invasiveness in tumor cells*. Cell Mol Life Sci, 2010. **67**(1): p. 63-71.
181. van den Berg, M.C.W., et al., *Proteolytic and Opportunistic Breaching of the Basement Membrane Zone by Immune Cells during Tumor Initiation*. Cell Rep, 2019. **27**(10): p. 2837-2846.e4.
182. Infante, E., et al., *LINC complex-Lis1 interplay controls MT1-MMP matrix digest-on-demand response for confined tumor cell migration*. Nat Commun, 2018. **9**(1): p. 2443.
183. Zaman, M.H., et al., *Migration of tumor cells in 3D matrices is governed by matrix stiffness along with cell-matrix adhesion and proteolysis*. Proceedings of the National Academy of Sciences, 2006. **103**(29): p. 10889.
184. Gardel, M.L., et al., *Mechanical integration of actin and adhesion dynamics in cell migration*. Annu Rev Cell Dev Biol, 2010. **26**: p. 315-33.
185. van Helvert, S., C. Storm, and P. Friedl, *Mechanoreciprocity in cell migration*. Nature cell biology, 2018. **20**(1): p. 8-20.

186. Gonzalez-Molina, J., et al., *The extracellular fluid macromolecular composition differentially affects cell-substrate adhesion and cell morphology*. Scientific Reports, 2019. **9**(1): p. 8505.
187. Li, Y. and S.X. Sun, *Transition from Actin-Driven to Water-Driven Cell Migration Depends on External Hydraulic Resistance*. Biophysical journal, 2018. **114**(12): p. 2965-2973.
188. Li, Y., et al., *On the energy efficiency of cell migration in diverse physical environments*. Proceedings of the National Academy of Sciences, 2019. **116**(48): p. 23894.
189. Zhao, R., et al., *Cell sensing and decision-making in confinement: The role of TRPM7 in a tug of war between hydraulic pressure and cross-sectional area*. Science Advances, 2019. **5**(7): p. eaaw7243.
190. Prentice-Mott, H.V., et al., *Biased migration of confined neutrophil-like cells in asymmetric hydraulic environments*. Proceedings of the National Academy of Sciences, 2013. **110**(52): p. 21006.
191. Piotrowski-Daspit, A.S., J. Tien, and C.M. Nelson, *Interstitial fluid pressure regulates collective invasion in engineered human breast tumors via Snail, vimentin, and E-cadherin*. Integrative biology : quantitative biosciences from nano to macro, 2016. **8**(3): p. 319-331.
192. Lee, H.J., et al., *Fluid shear stress activates YAP1 to promote cancer cell motility*. Nature Communications, 2017. **8**(1): p. 14122.
193. Gonzalez-Molina, J., et al., *Extracellular fluid viscosity enhances liver cancer cell mechanosensing and migration*. Biomaterials, 2018. **177**: p. 113-124.
194. Petrie, R.J. and K.M. Yamada, *At the leading edge of three-dimensional cell migration*. Journal of Cell Science, 2012. **125**(24): p. 5917.
195. Condeelis, J. and J.E. Segall, *Intravital imaging of cell movement in tumours*. Nat Rev Cancer, 2003. **3**(12): p. 921-30.
196. Doyle, A.D., et al., *Local 3D matrix microenvironment regulates cell migration through spatiotemporal dynamics of contractility-dependent adhesions*. Nature Communications, 2015. **6**(1): p. 8720.
197. Kubow, K.E., S.K. Conrad, and A.R. Horwitz, *Matrix microarchitecture and myosin II determine adhesion in 3D matrices*. Curr Biol, 2013. **23**(17): p. 1607-19.
198. Wolf, K., et al., *Physical limits of cell migration: control by ECM space and nuclear deformation and tuning by proteolysis and traction force*. J Cell Biol, 2013. **201**(7): p. 1069-84.
199. Balzer, E.M., et al., *Physical confinement alters tumor cell adhesion and migration phenotypes*. FASEB J, 2012. **26**(10): p. 4045-56.
200. Reversat, A., et al., *Cellular locomotion using environmental topography*. Nature, 2020. **582**(7813): p. 582-585.
201. Weigelin, B., G.J. Bakker, and P. Friedl, *Intravital third harmonic generation microscopy of collective melanoma cell invasion: Principles of interface guidance and microvesicle dynamics*. Intravital, 2012. **1**(1): p. 32-43.
202. Friedl, P., K. Wolf, and J. Lammerding, *Nuclear mechanics during cell migration*. Current opinion in cell biology, 2011. **23**(1): p. 55-64.
203. Harada, T., et al., *Nuclear lamin stiffness is a barrier to 3D migration, but softness can limit survival*. The Journal of cell biology, 2014. **204**(5): p. 669-682.
204. Denais, C.M., et al., *Nuclear envelope rupture and repair during cancer cell migration*. Science (New York, N.Y.), 2016. **352**(6283): p. 353-358.
205. Mistriotis, P., et al., *Confinement hinders motility by inducing RhoA-mediated nuclear influx, volume expansion, and blebbing*. J Cell Biol, 2019. **218**(12): p. 4093-4111.
206. Wisniewski, E.O., et al., *Dorsoventral polarity directs cell responses to migration track geometries*. Sci Adv, 2020. **6**(31): p. eaba6505.
207. Petit, M.M., et al., *LPP, an actin cytoskeleton protein related to zyxin, harbors a nuclear export signal and transcriptional activation capacity*. Mol Biol Cell, 2000. **11**(1): p. 117-29.

208. Petit, M.M., S.M. Meulemans, and W.J. Van de Ven, *The focal adhesion and nuclear targeting capacity of the LIM-containing lipoma-preferred partner (LPP) protein*. J Biol Chem, 2003. **278**(4): p. 2157-68.
209. Janssens, V., et al., *PP2A binds to the LIM domains of lipoma-preferred partner through its PR130/B" subunit to regulate cell adhesion and migration*. J Cell Sci, 2016. **129**(8): p. 1605-18.
210. Jin, L., et al., *Angiotensin II, focal adhesion kinase, and PRX1 enhance smooth muscle expression of lipoma preferred partner and its newly identified binding partner palladin to promote cell migration*. Circ Res, 2007. **100**(6): p. 817-25.
211. Gorenne, I., et al., *LPP, a LIM protein highly expressed in smooth muscle*. Am J Physiol Cell Physiol, 2003. **285**(3): p. C674-685.
212. Chambliss, A.B., et al., *The LINC-anchored actin cap connects the extracellular milieu to the nucleus for ultrafast mechanotransduction*. Sci Rep, 2013. **3**: p. 1087.
213. Crisp, M., et al., *Coupling of the nucleus and cytoplasm: role of the LINC complex*. J Cell Biol, 2006. **172**(1): p. 41-53.
214. Luxton, G.W.G., et al., *Linear arrays of nuclear envelope proteins harness retrograde actin flow for nuclear movement*. Science (New York, N.Y.), 2010. **329**(5994): p. 956-959.
215. Folker, E.S., et al., *Lamin A variants that cause striated muscle disease are defective in anchoring transmembrane actin-associated nuclear lines for nuclear movement*. Proc Natl Acad Sci U S A, 2011. **108**(1): p. 131-6.
216. Lee, J.S., et al., *Nuclear lamin A/C deficiency induces defects in cell mechanics, polarization, and migration*. Biophys J, 2007. **93**(7): p. 2542-52.
217. Friedl, P. and K. Wolf, *Plasticity of cell migration: a multiscale tuning model*. J Cell Biol, 2010. **188**(1): p. 11-9.
218. Friedl, P., et al., *New dimensions in cell migration*. Nat Rev Mol Cell Biol, 2012. **13**(11): p. 743-7.
219. Raeber, G.P., M.P. Lutolf, and J.A. Hubbell, *Molecularly Engineered PEG Hydrogels: A Novel Model System for Proteolytically Mediated Cell Migration*. Biophysical Journal, 2005. **89**(2): p. 1374-1388.
220. Wolf, K., et al., *Collagen-based cell migration models in vitro and in vivo*. Seminars in cell & developmental biology, 2009. **20**(8): p. 931-941.
221. Brown, L.F., et al., *Fibroblast migration in fibrin gel matrices*. The American journal of pathology, 1993. **142**(1): p. 273-283.
222. Salam, N., et al., *Assessment of Migration of Human MSCs through Fibrin Hydrogels as a Tool for Formulation Optimisation*. Materials (Basel, Switzerland), 2018. **11**(9): p. 1781.
223. Kleinman, H.K. and G.R. Martin, *Matrigel: basement membrane matrix with biological activity*. Semin Cancer Biol, 2005. **15**(5): p. 378-86.
224. Caliari, S.R. and J.A. Burdick, *A practical guide to hydrogels for cell culture*. Nature methods, 2016. **13**(5): p. 405-414.
225. Ehrbar, M., et al., *Elucidating the role of matrix stiffness in 3D cell migration and remodeling*. Biophys J, 2011. **100**(2): p. 284-93.
226. Burdick, J.A., et al., *Controlled Degradation and Mechanical Behavior of Photopolymerized Hyaluronic Acid Networks*. Biomacromolecules, 2005. **6**(1): p. 386-391.
227. Burdick, J.A. and G.D. Prestwich, *Hyaluronic acid hydrogels for biomedical applications*. Advanced materials (Deerfield Beach, Fla.), 2011. **23**(12): p. H41-H56.
228. Lei, Y., et al., *The spreading, migration and proliferation of mouse mesenchymal stem cells cultured inside hyaluronic acid hydrogels*. Biomaterials, 2011. **32**(1): p. 39-47.
229. Rowley, J.A., G. Madlambayan, and D.J. Mooney, *Alginate hydrogels as synthetic extracellular matrix materials*. Biomaterials, 1999. **20**(1): p. 45-53.
230. Augst, A.D., H.J. Kong, and D.J. Mooney, *Alginate hydrogels as biomaterials*. Macromol Biosci, 2006. **6**(8): p. 623-33.

231. Hakkinen, K.M., et al., *Direct comparisons of the morphology, migration, cell adhesions, and actin cytoskeleton of fibroblasts in four different three-dimensional extracellular matrices*. Tissue Eng Part A, 2011. **17**(5-6): p. 713-24.
232. Matsubayashi, Y., et al., *Rapid Homeostatic Turnover of Embryonic ECM during Tissue Morphogenesis*. Developmental Cell, 2020. **54**(1): p. 33-42.e9.
233. Daley, W.P., S.B. Peters, and M. Larsen, *Extracellular matrix dynamics in development and regenerative medicine*. Journal of Cell Science, 2008. **121**(3): p. 255.
234. Bonnans, C., J. Chou, and Z. Werb, *Remodelling the extracellular matrix in development and disease*. Nature reviews. Molecular cell biology, 2014. **15**(12): p. 786-801.
235. Alsberg, E., et al., *Regulating Bone Formation via Controlled Scaffold Degradation*. Journal of Dental Research, 2003. **82**(11): p. 903-908.
236. Lutolf, M.P., et al., *Synthetic matrix metalloproteinase-sensitive hydrogels for the conduction of tissue regeneration: Engineering cell-invasion characteristics*. Proceedings of the National Academy of Sciences, 2003. **100**(9): p. 5413.
237. Kienast, Y., et al., *Real-time imaging reveals the single steps of brain metastasis formation*. Nature Medicine, 2010. **16**(1): p. 116-122.
238. Ghaffari, A., et al., *Intravital imaging reveals systemic ezrin inhibition impedes cancer cell migration and lymph node metastasis in breast cancer*. Breast cancer research : BCR, 2019. **21**(1): p. 12-12.
239. Alieva, M., et al., *Intravital imaging of glioma border morphology reveals distinctive cellular dynamics and contribution to tumor cell invasion*. Scientific Reports, 2019. **9**(1): p. 2054.
240. Ribatti, D., *The chick embryo chorioallantoic membrane (CAM) assay*. Reprod Toxicol, 2017. **70**: p. 97-101.
241. Eisemann, T., et al., *An advanced glioma cell invasion assay based on organotypic brain slice cultures*. BMC Cancer, 2018. **18**(1): p. 103.
242. Koch, A., et al., *Murine precision-cut liver slices (PCLS): a new tool for studying tumor microenvironments and cell signaling ex vivo*. Cell communication and signaling : CCS, 2014. **12**: p. 73-73.
243. Misra, S., et al., *Ex vivo organotypic culture system of precision-cut slices of human pancreatic ductal adenocarcinoma*. Scientific Reports, 2019. **9**(1): p. 2133.
244. Pearen, M.A., et al., *Murine Precision-Cut Liver Slices as an Ex Vivo Model of Liver Biology*. JoVE, 2020(157): p. e60992.